

Emerging Methodologies and Applications in Modelling, Identification and Control

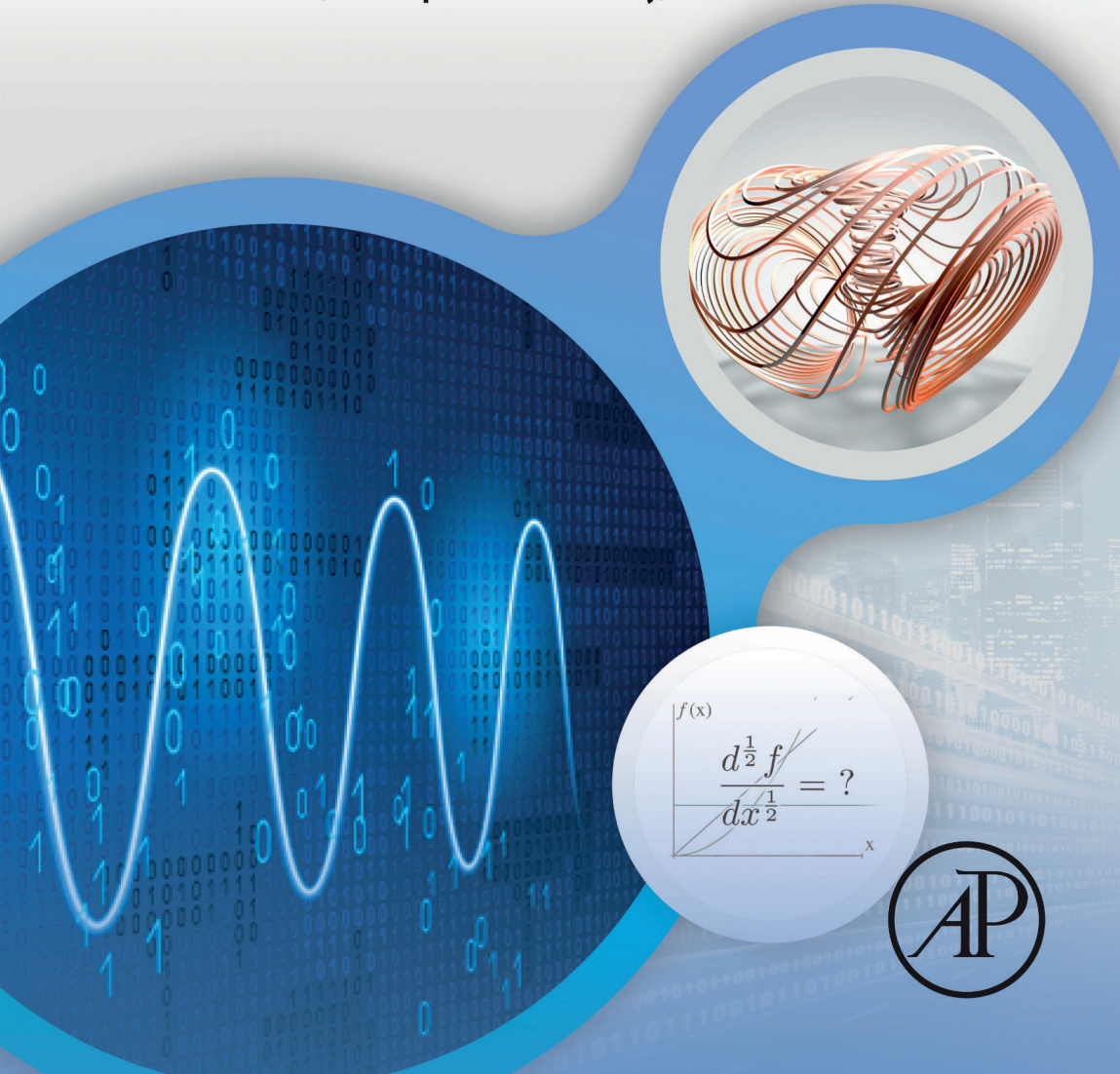
Series Editor: Quan Min Zhu

Volume 2

Fractional-Order Modeling of Dynamic Systems with Applications in Optimization, Signal Processing, and Control

Edited by

Ahmed G. Radwan, Farooq Ahmad Khanday, and Lobna A. Said



**FRACTIONAL-ORDER
MODELING OF
DYNAMIC SYSTEMS
WITH APPLICATIONS IN
OPTIMIZATION, SIGNAL
PROCESSING, AND
CONTROL**

This page intentionally left blank

FRACTIONAL-ORDER MODELING OF DYNAMIC SYSTEMS WITH APPLICATIONS IN OPTIMIZATION, SIGNAL PROCESSING, AND CONTROL

Edited by

AHMED G. RADWAN

*Engineering Mathematics and Physics Department
Cairo University, Giza, Egypt*

*School of Engineering and Applied Sciences
Nile University, Giza, Egypt*

FAROOQ AHMAD KHANDAY

*Department of Electronics and Instrumentation Technology
University of Kashmir, Srinagar, India*

LOBNA A. SAID

*Nanoelectronics Integrated Systems Center (NISC)
Nile University, Giza, Egypt*

Series editor

QUAN MIN ZHU



ACADEMIC PRESS

An imprint of Elsevier

Academic Press is an imprint of Elsevier
125 London Wall, London EC2Y 5AS, United Kingdom
525 B Street, Suite 1650, San Diego, CA 92101, United States
50 Hampshire Street, 5th Floor, Cambridge, MA 02139, United States
The Boulevard, Langford Lane, Kidlington, Oxford OX5 1GB, United Kingdom

Copyright © 2022 Elsevier Inc. All rights reserved.

MATLAB[®] is a trademark of The MathWorks, Inc. and is used with permission. The MathWorks does not warrant the accuracy of the text or exercises in this book. This book's use or discussion of MATLAB[®] software or related products does not constitute endorsement or sponsorship by The MathWorks of a particular pedagogical approach or particular use of the MATLAB[®] software.

No part of this publication may be reproduced or transmitted in any form or by any means, electronic or mechanical, including photocopying, recording, or any information storage and retrieval system, without permission in writing from the publisher. Details on how to seek permission, further information about the Publisher's permissions policies and our arrangements with organizations such as the Copyright Clearance Center and the Copyright Licensing Agency, can be found at our website: www.elsevier.com/permissions.

This book and the individual contributions contained in it are protected under copyright by the Publisher (other than as may be noted herein).

Notices

Knowledge and best practice in this field are constantly changing. As new research and experience broaden our understanding, changes in research methods, professional practices, or medical treatment may become necessary.

Practitioners and researchers must always rely on their own experience and knowledge in evaluating and using any information, methods, compounds, or experiments described herein. In using such information or methods they should be mindful of their own safety and the safety of others, including parties for whom they have a professional responsibility.

To the fullest extent of the law, neither the Publisher nor the authors, contributors, or editors, assume any liability for any injury and/or damage to persons or property as a matter of products liability, negligence or otherwise, or from any use or operation of any methods, products, instructions, or ideas contained in the material herein.

Library of Congress Cataloging-in-Publication Data

A catalog record for this book is available from the Library of Congress

British Library Cataloguing-in-Publication Data

A catalogue record for this book is available from the British Library

ISBN: 978-0-323-90089-8

For information on all Academic Press publications
visit our website at <https://www.elsevier.com/books-and-journals>

Publisher: Mara Conner
Acquisitions Editor: Sonnini R. Yura
Editorial Project Manager: Charlotte Rowley
Production Project Manager: Kamesh Ramajogi
Designer: Matthew Limbert

Typeset by VTeX



Contents

List of contributors

xi

1. Continuous and discrete symmetry methods for fractional differential equations	1
Youness Chatibi, El Hassan El Kinani, and Abdelaziz Ouhadan	
1.1. Introduction	1
1.2. Continuous and discrete symmetry for classical differential equations	3
1.3. Continuous symmetry for fractional differential equation	14
1.4. Discrete symmetry for fractional Harry Dym equation	30
1.5. Conclusion	33
References	33
2. Some theoretical and computation results about COVID-19 by using a fractional-order mathematical model	37
Muhammad Arfan, Kamal Shah, and Aman Ullah	
2.1. Introduction	37
2.2. Background materials	42
2.3. Main work	46
2.4. Series solution of the considered system (2.2) under normal Caputo derivative	52
2.5. General series solution of the considered system (2.3)	58
Declaration of competing interest	65
References	65
3. Spatial-fractional derivatives for fluid flow and transport phenomena	69
Mohamed F. El-Amin	
3.1. Introduction	69
3.2. Preliminary concepts	70
3.3. Spatial-fractional mass conservation equation	72
3.4. Fractional Navier–Stokes equation	75
3.5. Special cases	76
3.6. Fractional models of flow in porous media	81
3.7. Fractional natural gas equation	83
3.8. Fractional multiphase flows in porous media	85
3.9. Special cases of two-phase flow	88
3.10. Fractional convection-diffusion equation	91

3.11. Conclusion	93
References	94
4. On the hybrid fractional chaotic systems: a numerical approach	97
N.H. Sweilam and S.M. AL-Mekhlafi	
4.1. Introduction	97
4.2. Preliminaries and notations	98
4.3. Hybrid fractional chaotic models	99
4.4. Numerical methods for solving hybrid fractional models	106
4.5. Numerical simulations	109
4.6. Conclusions	114
Declaration of competing interest	116
References	116
5. Iterative processes with fractional derivatives	119
Giro Candelario, Alicia Cordero, Juan R. Torregrosa, and María P. Vassileva	
5.1. Introduction	119
5.2. Preliminary concepts	121
5.3. Design and analysis of iterative methods using fractional derivatives	123
5.4. Numerical analysis of the proposed methods	132
5.5. Concluding remarks	144
Acknowledgments	149
References	149
6. Design of fractional-order finite-time sliding mode controllers for quadrotor UAVs subjected to disturbances and uncertainties	151
Moussa Labbadi, Yassine El houm, Yassine Boukal, Karima Boudaraia, and Mohamed Cherkaoui	
6.1. Introduction	151
6.2. Preliminary results	156
6.3. Quadrotor system dynamics	157
6.4. Fractional-order SMC controllers for quadrotors	159
6.5. Simulation results and discussion	169
6.6. Conclusion	174
References	176
7. Performance evaluation of fractional character vector control applied for doubly fed induction generator operating in a network-connected wind power system	179
Abdellatif Kasbi and Abderrafii Rahali	
7.1. Introduction	179

7.2.	Variable-speed wind power system modeling	182
7.3.	Vector control scheme of DFIG using fractional-order PI controllers	187
7.4.	Design of FOPI controllers applied in the power and current regulation loops	191
7.5.	Numerical results and analysis	201
7.6.	Conclusion	208
	References	210
8.	Finite time synchronization of discontinuous fractional order Cohen–Grossberg memristive neural networks with discrete delays under sliding mode control strategies	213
	Pratap Anbalagan, Raja Ramachandran, and Evren Hincal	
8.1.	Introduction	213
8.2.	Preliminaries	217
8.3.	Main results	226
8.4.	A numerical example	239
8.5.	Conclusions	244
	Acknowledgments	244
	References	244
9.	Variable-order control systems: a steady-state error analysis	249
	Hamidreza Ghazisaeedi and Mohammad Saleh Tavazoei	
9.1.	Introduction	249
9.2.	Variable-order operators	250
9.3.	Main results	251
9.4.	A method for numerical simulation	259
9.5.	Numerical examples	260
9.6.	Conclusion	266
	References	268
10.	Theoretical study in conformal thermal antennas optimized by a fractional energy	271
	Rabha W. Ibrahim	
10.1.	Introduction	271
10.2.	Conformal mapping	273
10.3.	Thermal optimization approach	276
10.4.	CTA optimization	281
10.5.	Conformal fractional energy	284
10.6.	Conclusion	289
	References	289

11. Optimal design of fractional-order Butterworth filter with improved accuracy and stability margin	293
Shibendu Mahata, Rajib Kar, and Durbadal Mandal	
11.1. Introduction	293
11.2. Proposed technique	300
11.3. Simulation results and discussion	304
11.4. Conclusions	315
References	317
12. Pseudospectral methods for the Riesz space-fractional Schrödinger equation	323
Mahmoud A. Zaky, Mohamed A. Abdelkawy, Samer S. Ezz-Eldien, and Eid H. Doha	
12.1. Introduction	323
12.2. Space-fractional couplers	326
12.3. Gegenbauer polynomials and their properties	327
12.4. Numerical schemes	330
12.5. Numerical experiments	337
12.6. Conclusion and discussion	346
References	349
13. Transmission line modeling by fractional and topological generalization of the telegrapher's equation	355
Dušan Zorica and Stevan M. Cvetičanin	
13.1. Classical and fractional telegrapher's equations	355
13.2. Reduction of fractional telegrapher's equations to special cases	364
13.3. Transmission line model	366
13.4. Transmission line in transient regime	373
13.5. Transmission line in steady-state regime and its frequency characteristics	382
Appendix 13.A	394
References	399
14. System approach for the frequency analysis of a fractional-order acoustic tube: application for the resonator of the flute instrument	403
Xavier Moreau, Gaby Abou Haidar, and Roy Abi Zeid Daou	
14.1. Introduction	403
14.2. Modeling	405
14.3. Frequency response analysis	411
14.4. System approach	412

14.5.	Frequency analysis of the system approach	415
14.6.	Conclusions and future work	425
	References	425
15.	Fractional-order dynamics to study neuronal function	429
	Antonio Coronel-Escamilla, Rohisha Tuladhar, Ivanka Stamova, and Fidel Santamaria	
15.1.	Introduction	429
15.2.	Fractional calculus definitions	431
15.3.	Fractional-order dynamics in neuroscience	435
15.4.	Discussions and conclusions	449
	References	451
16.	Modeling woody plant tissue using different fractional-order circuits	457
	Menna Mohsen, Mohamed S. Ghoneim, Lobna A. Said, Ahmed S. Elwakil, Ahmed H. Madian, and Ahmed G. Radwan	
16.1.	Introduction	457
16.2.	Woody cell structure	462
16.3.	Bio-impedance models overview	463
16.4.	Experimental setup	465
16.5.	Conclusion	468
	Acknowledgment	469
	References	469
17.	Analog and digital implementation of fractional-order FitzHugh–Nagumo (FO-FHN) neuron model	475
	Mohammad Rafiq Dar, Nasir Ali Kant, Farooq Ahmad Khanday, Shakeel Ahmad Malik, and Mubashir Ahmad Kharadi	
17.1.	Introduction	475
17.2.	Fractional-order FitzHugh–Nagumo (FO-FHN) neuron model	477
17.3.	Analog implementations of the FO-FHN neuron model	481
17.4.	FPAA implementation of FO-FHN neuron network	493
17.5.	FPGA implementation of FO-FHN neuron model	495
17.6.	Conclusion	499
	References	501
	<i>Index</i>	<i>505</i>

This page intentionally left blank

List of contributors

Mohamed A. Abdelkawy

Department of Mathematics, Faculty of Science, Beni-Suef University, Beni-Suef, Egypt
Department of Mathematics and Statistics, College of Science, Imam Mohammad Ibn Saud Islamic University (IMSIU), Riyadh, Saudi Arabia

Roy Abi Zeid Daou

Lebanese German University, Biomedical Technologies Department, Jounieh, Lebanon
MART, Learning, Education and Training Center, Chaniir, Lebanon

Gaby Abou Haidar

Bordeaux University, CNRS, IMS Lab., Bordeaux, France
American University of Science and Technology, Faculty of Engineering, Zahle, Lebanon

S.M. AL-Mekhlafi

Mathematics Department, Faculty of Education, Sana'a University, Sana'a, Yemen

Pratap Anbalagan

Department of Mathematics, Alagappa University, Alagappapuram, Tamilnadu, India
Department of Mathematics, Near East University TRNC, Mersin, Turkey

Muhammad Arfan

Department of Mathematics, University of Malakand, Chakdara,
Dir(L), Khyber Pakhtunkhwa, Pakistan

Karima Boudaraia

Engineering for Smart and Sustainable Systems Research Center, Mohammadia School of Engineers, Mohammed V University in Rabat, Rabat, Morocco

Yassine Boukal

Aeronautics, Space & Defense division, ALTRAN, Blagnac, France

Giro Candelario

Instituto Tecnológico de Santo Domingo (INTEC), Área de Ciencia Básica,
Santo Domingo, Dominican Republic

Youness Chatibi

Laboratory of Mathematics, Statistics and Applications, CeReMAR Center,
Department of Mathematics, Faculty of Sciences, Mohammed V University in Rabat,
Rabat, Morocco

Mohamed Cherkaoui

Engineering for Smart and Sustainable Systems Research Center, Mohammadia School of Engineers, Mohammed V University in Rabat, Rabat, Morocco

Alicia Cordero

Universitat Politècnica de Valencia, Instituto de Matemática Multidisciplinar, Valencia,
Spain

Antonio Coronel-Escamilla

Department of Biology, University of Texas at San Antonio, San Antonio, TX,
United States

Stevan M. Cvetičanin

University of Novi Sad, Faculty of Technical Sciences, Department of Power, Electronic
and Telecommunication Engineering, Novi Sad, Serbia

Mohammad Rafiq Dar

Department of Electronics and Instrumentation Technology, University of Kashmir,
Srinagar, India

Eid H. Doha

Department of Mathematics, Faculty of Science, Cairo University, Giza, Egypt

Mohamed F. El-Amin

Effat University, College of Engineering, Energy Research lab., Jeddah, Saudi Arabia
Aswan University, Faculty of Science, Mathematics Department, Aswan, Egypt

Yassine El houm

Engineering for Smart and Sustainable Systems Research Center, Mohammadia School of
Engineers, Mohammed V University in Rabat, Rabat, Morocco

El Hassan El Kinani

Laboratory of Modeling, Analysis and Control of Systems, Department of Mathematics,
Faculty of Sciences, Moulay Ismail University, Meknes, Morocco

Ahmed S. Elwakil

Nanoelectronics Integrated Systems Center (NISC), Nile University, Giza, Egypt
Department of Electrical and Computer Engineering, University of Sharjah, Sharjah,
United Arab Emirates
Department of Electrical and Computer Engineering, University of Calgary, Calgary, AB,
Canada

Samer S. Ezz-Eldien

Department of Mathematics, Faculty of Science, New Valley University, El-Kharga, Egypt

Hamidreza Ghazisaeeidi

Electrical Engineering Department, Sharif University of Technology, Tehran, Iran

Mohamed S. Ghoneim

Nanoelectronics Integrated Systems Center (NISC), Nile University, Giza, Egypt

Evren Hincal

Department of Mathematics, Near East University TRNC, Mersin, Turkey

Rabha W. Ibrahim

IEEE: 94086547, Kuala Lumpur, Malaysia

Nasir Ali Kant

Department of Electronics and Instrumentation Technology, University of Kashmir,
Srinagar, India

Rajib Kar

National Institute of Technology Durgapur, Department of Electronics and Communication Engineering, Durgapur, West Bengal, India

Abdellatif Kasbi

Laboratory of Optics, Information Processing, Mechanics, Energy and Electronics, Faculty of Sciences, Moulay Ismail University, Meknes, Morocco

Farooq Ahmad Khanday

Department of Electronics and Instrumentation Technology, University of Kashmir, Srinagar, India

Mubashir Ahmad Kharadi

Department of Electronics and Instrumentation Technology, University of Kashmir, Srinagar, India

Moussa Labbadi

Engineering for Smart and Sustainable Systems Research Center, Mohammadia School of Engineers, Mohammed V University in Rabat, Rabat, Morocco

Ahmed H. Madian

Nanoelectronics Integrated Systems Center (NISC), Nile University, Giza, Egypt
Radiation Engineering Dept., NCRRT, Egyptian Atomic Energy, Cairo, Egypt

Shibendu Mahata

National Institute of Technology Durgapur, Department of Electronics and Communication Engineering, Durgapur, West Bengal, India

Shakeel Ahmad Malik

Department of Electronics and Communication Engineering, Islamic University of Science and Technology, Awantipora, India

Durbadal Mandal

National Institute of Technology Durgapur, Department of Electronics and Communication Engineering, Durgapur, West Bengal, India

Menna Mohsen

Nanoelectronics Integrated Systems Center (NISC), Nile University, Giza, Egypt

Xavier Moreau

Bordeaux University, CNRS, IMS Lab., Bordeaux, France

Abdelaziz Ouhadan

Regional Center for Education and Training Professions, Fez-Meknes, Morocco

Ahmed G. Radwan

Engineering Mathematics and Physics Department, Cairo University, Giza, Egypt
School of Engineering and Applied Sciences, Nile University, Giza, Egypt

Abderrafii Rahali

Laboratory of Optics, Information Processing, Mechanics, Energy and Electronics, Faculty of Sciences, Moulay Ismail University, Meknes, Morocco

Raja Ramachandran

Ramanujan Centre for Higher Mathematics, Alagappa University, Alagappapuram, Tamilnadu, India

Lobna A. Said

Nanoelectronics Integrated Systems Center (NISC), Nile University, Giza, Egypt

Fidel Santamaria

Department of Biology, University of Texas at San Antonio, San Antonio, TX, United States

Kamal Shah

Department of Mathematics, University of Malakand, Chakdara, Dir(L), Khyber Pakhtunkhwa, Pakistan

Ivanka Stamova

Department of Mathematics, University of Texas at San Antonio, San Antonio, TX, United States

N.H. Sweilam

Mathematics Department, Faculty of Science, Cairo University, Giza, Egypt

Mohammad Saleh Tavazoei

Electrical Engineering Department, Sharif University of Technology, Tehran, Iran

Juan R. Torregrosa

Universitat Politècnica de Valencia, Instituto de Matemática Multidisciplinar, Valencia, Spain

Rohisha Tuladhar

Department of Biology, University of Texas at San Antonio, San Antonio, TX, United States

Aman Ullah

Department of Mathematics, University of Malakand, Chakdara, Dir(L), Khyber Pakhtunkhwa, Pakistan

María P. Vassileva

Instituto Tecnológico de Santo Domingo (INTEC), Área de Ciencia Básica, Santo Domingo, Dominican Republic

Mahmoud A. Zaky

National Research Centre, Department of Applied Mathematics, Cairo, Egypt
Department of Mathematics, Nazarbayev University, Nur-Sultan, Kazakhstan

Dušan Zorica

Serbian Academy of Arts and Sciences, Mathematical Institute, Beograd, Serbia
University of Novi Sad, Faculty of Sciences, Department of Physics, Novi Sad, Serbia

Continuous and discrete symmetry methods for fractional differential equations

Youness Chatibi^a, El Hassan El Kinani^b, and Abdelaziz Ouhadan^c

^aLaboratory of Mathematics, Statistics and Applications, CeReMAR Center, Department of Mathematics, Faculty of Sciences, Mohammed V University in Rabat, Rabat, Morocco

^bLaboratory of Modeling, Analysis and Control of Systems, Department of Mathematics, Faculty of Sciences, Moulay Ismail University, Meknes, Morocco

^cRegional Center for Education and Training Professions, Fez-Meknes, Morocco

1.1. Introduction

Differential equations are the main instrument used by scientists to describe natural phenomena. These phenomena are generally modeled by ordinary differential equations (ODEs) or partial differential equations (PDEs). The search for explicit solutions of these latter has many applications in modeling because they provide information and predict the behavior of the phenomena studied. Several analytical and numerical methods have been studied and developed for the resolution of differential equations. Among these methods we find the Lie symmetry method.

Historically, the Lie symmetry method for the resolution of differential equations was introduced towards the end of the 19th century by the Norwegian mathematician S. Lie [21]. The basic idea of this theory is based on the invariance of a differential equation under a transformation of independent and dependent variables. Lie's most striking contribution was the discovery that the majority of integration methods were intrinsically linked. This crucial consideration by S. Lie in the field of differential equations has been brought up-to-date thanks to various fundamental contributions over the past decades, notably the works of L.V. Ovsiannikov [29], N.H. Ibragimov [17], G. Bluman [5], P.J. Olver [23], H. Stephani [34], P. Hydon [16], W.H. Steeb [33], A. Ouhadan, and E.H. El Kinani [24,25].

The determination of continuous or discrete symmetries of a differential equation leads to several applications. Among these, it is used to build new nontrivial solutions from trivial ones. For ODEs, the invariance under a one-parameter group of transformations reduces the order of one. And for

PDEs, the dependent and independent variables can be combined in order to reduce the number of independent variables.

Recently, the application of the fractional derivative in the physical sciences and engineering, particularly in mechanics and rheology, is the subject of contributions by several authors [10,14,22]. Indeed, it has been used as a modeling tool in particular to describe the viscoelastic behavior of materials which preserve the memory of past deformations and whose behavior is said to be viscoelastic. These fields of application of fractional calculus have been the subject of a wide range of studies; we cite for example the works of A.A. Kilbas et al. [18] and S. Das [10].

Historically, the first definition of fractional integral and fractional derivative was introduced by Riemann and Liouville as a consequence of the solution of Abel's integral equations. This approach is based on the iteration of the classical integral operator n times [31]. Other versions of the fractional derivative have been introduced to take account of certain physical considerations, in particular the Caputo approach, which was introduced to take account of the initial conditions of a system when these are required. Other approaches have emerged since then (see, e.g., [30]).

In [12,13], the authors developed the Lie symmetry method for FDEs in the sense of Riemann–Liouville and Caputo. Since then, several authors have taken an interest in this subject. We mention the works of R.A. Leo et al., who showed the existence of Lie symmetries of an FDE [20], Q. Huang and R. Zhdanov, who studied the fractional Harry Dym equation [15], and A. Ouhadan and E.H. El Kinani, who studied the fractional Kolmogorov equation [27] and others [2,3,7,8,26,28].

The main purpose of this chapter is to discuss the basics of continuous and discrete symmetry methods to construct some exact solutions of FDEs. These methods are presented with several illustrative examples.

This chapter is organized as follows. Section 1.2 contains basic definitions and facts about continuous and discrete symmetry methods and the prolongation of the generator of symmetry for ODEs and PDEs. Some applications of this technique are considered. A possibility to find exact solutions of ODEs and PDEs is illustrated. Section 1.3 contains the definitions of fractional derivatives in the senses of Riemann–Liouville and Caputo and some results of symmetry analysis for some classes of FDEs with examples of constructing solutions. Section 1.4 is devoted to construct discrete symmetries of the fractional Harry Dym equation.



1.2. Continuous and discrete symmetry for classical differential equations

1.2.1 Continuous symmetry method

Let us consider the general case of a differential equation of order n in p -independent and q -dependent variables given by

$$\Delta(x, u_{(n)}) = 0, \tag{1.1}$$

where $x = (x^1, \dots, x^p)$, $u = (u^1, \dots, u^q)$, and $u_{(n)}$ represents all the derivatives of u of all orders from 0 to n .

We consider the invertible transformations

$$T_\epsilon : \bar{x}^i = \phi^i(x, u, \epsilon), \quad \bar{u}^j = \psi^j(x, u, \epsilon), \quad 1 \leq i \leq p, \quad 1 \leq j \leq q, \tag{1.2}$$

where $\bar{x}^i|_{\epsilon=0} = x^i$, $\bar{u}^j|_{\epsilon=0} = u^j$, ϕ^i and ψ^j are two functions, and $\epsilon \in \Omega \subset \mathbb{R}$ belongs to some neighborhood Ω of point $\epsilon = 0$. These transformations form a one-parameter group G if for all $\epsilon_1, \epsilon_2, \epsilon_1 + \epsilon_2 \in \Omega$ the following conditions hold:

$$T_0 = I \in G, \quad T_{\epsilon_1} T_{\epsilon_2} = T_{\epsilon_1 + \epsilon_2} \in G, \quad T_{\epsilon_1}^{-1} = T_{-\epsilon_1} \in G, \tag{1.3}$$

where I is the identity transformation.

A first-order linear differential operator

$$X = \sum_{i=1}^p \xi^i(x, u) \partial_{x^i} + \sum_{j=1}^q \eta^j(x, u) \partial_{u^j}, \tag{1.4}$$

where $\partial_{x^i} = \partial/\partial x^i$, $\partial_{u^j} = \partial/\partial u^j$,

$$\xi^i(x, u) = \left. \frac{\partial \phi^i(x, u, \epsilon)}{\partial \epsilon} \right|_{\epsilon=0}, \quad \text{and} \quad \eta^j(x, u) = \left. \frac{\partial \psi^j(x, u, \epsilon)}{\partial \epsilon} \right|_{\epsilon=0}, \tag{1.5}$$

is called the infinitesimal generator of the one-parameter group (1.2).

A symmetry group of a differential equation is a group of transformations acting on the independent and dependent variables of this equation such that it maps its solutions to other solutions. To be more precise, let S_Δ denote the space of all solutions of Eq. (1.1), a symmetry G is a mapping of S_Δ into itself, i.e., $G : S_\Delta \rightarrow S_\Delta$. Thus if $u \in S_\Delta$, then we must have $G \cdot u \in S_\Delta$.

We consider a one-parameter group of infinitesimal transformations acting on x and u ,

$$\bar{x}^i = x^i + \epsilon \xi^i(x, u) + o(\epsilon), \quad (1.6)$$

$$\bar{u}^j = u^j + \epsilon \eta^j(x, u) + o(\epsilon). \quad (1.7)$$

The infinitesimal generator X associated with the above group of transformations can also be written as

$$X = \sum_{i=1}^p \xi^i(x, u) \partial_{x^i} + \sum_{j=1}^q \eta^j(x, u) \partial_{u^j}. \quad (1.8)$$

The group transformations corresponding to the infinitesimal generators are found by solving the Lie equations

$$\frac{d\bar{x}^i}{d\epsilon} = \xi^i(x, u), \quad \frac{d\bar{u}^j}{d\epsilon} = \eta^j(x, u), \quad (1.9)$$

with the initial conditions

$$\bar{x}^i|_{\epsilon=0} = x^i, \quad \bar{u}^j|_{\epsilon=0} = u^j. \quad (1.10)$$

The invariance of Eq. (1.1) under the infinitesimal transformations leads to the invariance condition [23]

$$X^{(n)}[\Delta(x, u_{(n)})] = 0 \quad \text{whenever} \quad \Delta(x, u_{(n)}) = 0, \quad (1.11)$$

where $X^{(n)}$ is the n th-order prolongation of the infinitesimal generator X given by [23]

$$X^{(n)} = X + \sum_{\sigma=1}^q \sum_J \eta_J^\sigma(x, u_{(n)}) \partial_{u_J^\sigma}, \quad (1.12)$$

with $J = (j^1, \dots, j^k)$, $1 \leq j^k \leq p$, $1 \leq k \leq n$, $\sum_J = \sum_{j^1=1}^p \sum_{j^2=1}^p \dots \sum_{j^k=1}^p$, and

$$\eta_J^\sigma(x, u_{(n)}) = D_J \left(\eta^\sigma - \sum_{i=1}^p \xi^i u_i^\sigma \right) + \sum_{i=1}^p \xi^i u_{J,i}^\sigma, \quad (1.13)$$

where $D_J = D_{j^1} D_{j^2} \dots D_{j^k}$, $u_i^\sigma = \frac{\partial u^\sigma}{\partial x^i}$, $u_J^\sigma = \frac{\partial^k u^\sigma}{\partial x^{j^1} \dots \partial x^{j^k}}$, and $u_{J,i}^\sigma = \frac{\partial u_J^\sigma}{\partial x^i}$.

Conditions on infinitesimals ξ^i and η^j are determined by equating coefficients of like derivatives of monomials in u_{x^i} and higher derivatives by zero. This leads to a system of PDEs from which we can determine ξ^i and η^j .

For an ODE, the n th-order prolongation of the infinitesimal generator $X = \xi(x, y)\partial_x + \eta(x, y)\partial_y$ is written [23]

$$X^{(n)} = X + \sum_{k=1}^n \eta^{[k]} \frac{\partial}{\partial y^{(k)}}, \tag{1.14}$$

where

$$\eta^{[k]} = D_x(\eta^{[k-1]}) - y^{(k)} D_x(\xi), \tag{1.15}$$

and D_x denotes the total derivation operator defined by

$$D_x = \partial_x + y^{(1)}\partial_y + y^{(2)}\partial_{y^{(1)}} + y^{(3)}\partial_{y^{(2)}} + \dots \tag{1.16}$$

The generators of a continuous symmetry group of a differential equation form a Lie algebra, so any linear combination of generators of symmetry of this group is also a generator of symmetry.

Now, we give two examples of construction of continuous symmetry groups for an ODE and for a PDE.

Example 1.1 (Ordinary differential equation). We consider the following equation:

$$y^{(2)}(x) = 0. \tag{1.17}$$

Let $X = \xi(x, y)\partial_x + \eta(x, y)\partial_y$ be a generator of a group of symmetries of this equation. Its second-order prolongation is given by

$$X^{(2)} = X + \eta^{(1)}\partial_{y^{(1)}} + \eta^{(2)}\partial_{y^{(2)}}. \tag{1.18}$$

The invariance criterion is written

$$X^{(2)}[\Delta]|_{\Delta=0} = \eta^{(2)}|_{\Delta=0} = 0, \quad \text{where } \Delta(x, y) = y^{(2)}(x). \tag{1.19}$$

The system of determining equations is written in the form

$$\begin{aligned} (y^{(1)})^3 : & \quad \xi_{yy} = 0, \\ (y^{(1)})^2 : & \quad \eta_{yy} - 2\xi_{xy} = 0, \\ y^{(1)} : & \quad 2\eta_{xy} - \xi_{xx} = 0, \\ 1 : & \quad \eta_{xx} = 0. \end{aligned}$$

The resolution of this system gives

$$\begin{aligned}\xi(x, y) &= (a_1x + a_2)y + p_1x^2 + b_1x + b_2 \quad \text{and} \\ \eta(x, y) &= a_1y^2 + (p_1x + p_2)y + q_1x + q_2,\end{aligned}\tag{1.20}$$

where $a_1, a_2, b_1, b_2, p_1, p_2, q_1,$ and q_2 are arbitrary constants.

It follows that the Lie algebra of symmetries of Eq. (1.17) is generated by the following eight generators:

$$\begin{aligned}X_1 &= x\gamma\partial_x + \gamma^2\partial_y, & X_2 &= \gamma\partial_x, & X_3 &= x^2\partial_x + x\gamma\partial_y, & X_4 &= x\partial_x, \\ X_5 &= \partial_x, & X_6 &= \gamma\partial_y, & X_7 &= x\partial_y, & X_8 &= \partial_y.\end{aligned}$$

Example 1.2 (Partial differential equation). We consider the following equation:

$$u_t = u_{xx}, \quad u = u(t, x).\tag{1.21}$$

The Lie algebra of symmetries of this equation is generated by the following six generators:

$$\begin{aligned}X_1 &= \partial_x, & X_2 &= \partial_t, & X_3 &= u\partial_u, \\ X_4 &= x\partial_x + 2t\partial_t, & X_5 &= 2t\partial_x - xu\partial_u, & X_6 &= 4tx\partial_x + 4t^2\partial_t - (2t + x^2)u\partial_u,\end{aligned}$$

and by the infinite family of generators $X_\beta = \beta(t, x)\partial_u$, where $\beta(t, x)$ is an arbitrary solution of (1.21).

From these generators, we can construct the symmetry groups of the heat equation (1.21) which are presented in Table 1.1.

Table 1.1 Symmetry groups of the heat equation (1.21).

Groups	\bar{x}	\bar{t}	\bar{u}	Symmetry transformations
G_1	$x + \epsilon$	t	u	Space translation
G_2	x	$t + \epsilon$	u	Time translation
G_3	x	t	$e^\epsilon u$	Scale transformation
G_4	$e^\epsilon x$	$e^{2\epsilon} t$	u	Scale transformation
G_5	$x + 2\epsilon t$	t	$ue^{-(\epsilon x + \epsilon^2 t)}$	Galilean boost
G_6	$\frac{x}{1-4\epsilon t}$	$\frac{t}{1-4\epsilon t}$	$u\sqrt{1-4\epsilon t} \exp\left(\frac{-\epsilon x^2}{1-4\epsilon t}\right)$	Projection
G_β	x	t	$u + \epsilon\beta(t, x)$	Superposition principle

By applying the group G_6 to a trivial solution $u(t, x) = 1$, we obtain a nontrivial solution of the heat equation

$$G_6 \cdot u = \frac{1}{\sqrt{1 + 4\epsilon t}} \exp\left(\frac{-\epsilon x^2}{1 + 4\epsilon t}\right). \tag{1.22}$$

Among the applications of the continuous symmetry groups of a differential equation is the construction of its solutions. Often, for some equations it is not easy to get exact solutions. However, a class of solutions, namely invariant solutions, can be determined in certain situations. We say that a solution $u = u(t, x)$ of Eq. (1.1) is an invariant solution if it is a solution of the characteristic equation

$$\frac{dx^i}{\xi^i(x, u)} = \frac{du^j}{\eta^j(x, u)}, \quad 1 \leq i \leq p, \quad 1 \leq j \leq q. \tag{1.23}$$

In order to obtain an invariant solution one must solve Eq. (1.23) and examine whether the solutions found are indeed solutions of the initial differential equation. Some examples of this technique have been discussed in the literature (see for example [23]).

We can also reduce the order of an n th-order ODE by using the invariant solutions drawn from the equation

$$\frac{dx^i}{\xi^i(x, u)} = \frac{du^j}{\eta^j(x, u)} = \frac{du^{(k)}}{\eta^{[k]}} , \quad 1 \leq i \leq p, \quad 1 \leq j \leq q, \quad 1 \leq k \leq n. \tag{1.24}$$

For more details, see [23].

Other applications of continuous symmetry analysis exist; we cite for example integrating factor, canonical coordinates, linearization of nonlinear PDEs, and determination of conservation laws.

1.2.2 Discrete symmetry method

We consider Eq. (1.1) and we assume that the Lie algebra \mathfrak{g} of continuous symmetry generators of this equation is r -dimensional and that the generators

$$X_i = \sum_{\gamma=1}^q \xi_i^\gamma(z) \partial_{z^\gamma}, \quad \text{when } z^\gamma \in \{x^1, \dots, x^p, u^1, \dots, u^q\}, \quad i = 1, \dots, r, \tag{1.25}$$

form a basis for \mathfrak{g} , with $[X_i, X_j] = c_{ij}^k X_k$. Let $\Gamma : X_i \mapsto \tilde{X}_i$ be a discrete symmetry. Then each X_i can be written as a linear combination of \tilde{X}_i 's as follows [16]:

$$X_i = \sum_{l=1}^r b_i^l \tilde{X}_l, \quad (1.26)$$

where b_i^l satisfy the relations

$$\sum_{l=1}^r \sum_{m=1}^r c_{lm}^n b_i^l b_j^m = \sum_{k=1}^r c_{ij}^k b_k^n, \quad \text{when } 1 \leq i < j \leq n, \quad 1 \leq n \leq r. \quad (1.27)$$

The coefficients b_i^l are constants which are determined by symmetry Γ and the basis $\{X_1, \dots, X_r\}$ is useful to regard these coefficients as elements of an $r \times r$ matrix $B = (b_i^l)$.

In [16], it is shown that if $X_i \in \mathfrak{g}$, then

$$\tilde{X}_i = \Gamma X_i \Gamma^{-1} = \sum_p \xi_i^p(\tilde{z}^p) \partial_{\tilde{z}^p} \quad (1.28)$$

generates a group of symmetries of the differential equation (1.1).

Moreover, at least some of the continuous symmetries can be factored out using their adjoint action upon the generators in \mathfrak{g} ,

$$Ad(\exp(\epsilon_j X_j)) X_i = X_i - \epsilon_j [X_j, X_i] + \frac{\epsilon_j^2}{2!} [X_j, [X_j, X_i]] - \dots = a_i^p(\epsilon_j, j) X_p. \quad (1.29)$$

Let $A(\epsilon_j, j) = \exp(\epsilon_j C(j))$ denote the matrix whose components are $a_i^p(\epsilon_j, j)$. System (1.26) is equivalent under the group generated by X_j to

$$X_i = \sum_{l=1}^r \tilde{b}_i^l \tilde{X}_l, \quad (1.30)$$

where \tilde{b}_i^l are the coefficients of $\tilde{B} = A(\epsilon_j, j)B$. First, we replace B by either $BA(\epsilon_j, j)$ or $A(\epsilon_j, j)B$, and then choose a value that simplifies, at least, one entry in the new matrix. The aim is to create zeros in matrix B , in order to simplify the determining equations and nonlinear constraints. Each matrix $A(\epsilon_j, j)$ should be used at most once.

Example 1.3. We consider the nonlinear diffusion equation that describes the behavior of the collective displacement of particles in a medium caused

by the random movement [6]

$$u_t = (uu_x)_x, \quad \text{where } u = u(t, x). \tag{1.31}$$

In [12], Gazizov et al. found that this equation has four continuous symmetry groups generated by the generators

$$X_1 = \partial_t, \quad X_2 = \partial_x, \quad X_3 = 2t\partial_t + x\partial_x, \quad X_4 = x\partial_x + 2u\partial_u. \tag{1.32}$$

The commutation relations of these generators are written

$$[X_1, X_2] = [X_3, X_4] = 0, \quad [X_1, X_3] = 2X_1, \quad [X_2, X_3] = [X_3, X_4] = X_2. \tag{1.33}$$

The nonzero structure constants are $c_{13}^1 = 2, c_{23}^2 = c_{24}^2 = 1$. Matrices $C(j)$ are

$$C(1) = \begin{pmatrix} 0 & 0 & 0 & 0 \\ 0 & 0 & 0 & 0 \\ -2 & 0 & 0 & 0 \\ 0 & 0 & 0 & 0 \end{pmatrix}, \quad C(2) = \begin{pmatrix} 0 & 0 & 0 & 0 \\ 0 & 0 & 0 & 0 \\ 0 & -1 & 0 & 0 \\ 0 & -1 & 0 & 0 \end{pmatrix},$$

$$C(3) = \begin{pmatrix} 2 & 0 & 0 & 0 \\ 0 & 1 & 0 & 0 \\ 0 & 0 & 0 & 0 \\ 0 & 0 & 0 & 0 \end{pmatrix}, \quad C(4) = \begin{pmatrix} 0 & 0 & 0 & 0 \\ 0 & 1 & 0 & 0 \\ 0 & 0 & 0 & 0 \\ 0 & 0 & 0 & 0 \end{pmatrix}.$$

Using matrices $\epsilon C(j)$ and adjoint action, we get

$$A(1) = \begin{pmatrix} 1 & 0 & 0 & 0 \\ 0 & 1 & 0 & 0 \\ -2\epsilon & 0 & 1 & 0 \\ 0 & 0 & 0 & 1 \end{pmatrix}, \quad A(2) = \begin{pmatrix} 1 & 0 & 0 & 0 \\ 0 & 1 & 0 & 0 \\ 0 & -\epsilon & 1 & 0 \\ 0 & -\epsilon & 0 & 1 \end{pmatrix},$$

$$A(3) = \begin{pmatrix} e^{2\epsilon} & 0 & 0 & 0 \\ 0 & e^\epsilon & 0 & 0 \\ 0 & 0 & 1 & 0 \\ 0 & 0 & 0 & 1 \end{pmatrix}, \quad A(4) = \begin{pmatrix} 1 & 0 & 0 & 0 \\ 0 & e^\epsilon & 0 & 0 \\ 0 & 0 & 1 & 0 \\ 0 & 0 & 0 & 1 \end{pmatrix}. \tag{1.34}$$

Using the relations (1.27), we obtain the nonlinear constraints for (1.31) which are presented in Table 1.2.

After solving the above constraints, using the adjoint matrices to factor out the Lie symmetries, so far, we have been able to simplify B to the

Table 1.2 Nonlinear constraints for nonlinear diffusion equation (1.31).

(i, j)	$n = 1$	$n = 2$	$n = 3$	$n = 4$
(1,2)	-	-	-	-
(1,3)	$b_1^1 b_3^3 = b_1^1$	$b_1^2 (b_3^3 + b_3^4) = 2b_1^2$	$b_1^3 = 0$	$b_1^4 = 0$
(1,4)	$b_1^1 b_4^4 = 0$	$b_1^2 (b_4^3 + b_4^4) = 0$	-	-
(2,3)	$2b_3^1 b_3^3 = b_2^1$	$b_2^2 (b_3^3 + b_3^4) = b_2^2$	$b_2^3 = 0$	$b_2^4 = 0$
(2,4)	$2b_4^1 b_4^3 = b_2^1$	$b_2^2 (b_4^3 + b_4^4) = b_2^2$	$b_2^3 = 0$	$b_2^4 = 0$
(3,4)	$2(b_3^1 b_4^3 - b_3^3 b_4^1) = 0$	$b_3^2 (b_4^3 + b_4^4) = b_4^2 (b_3^3 + b_3^4)$	-	-

following:

$$B_1 = \begin{pmatrix} b_1^1 & 0 & 0 & 0 \\ 0 & b_2^2 & 0 & 0 \\ b_3^1 & b_3^2 & 1 & 0 \\ 0 & b_3^2 & 0 & 1 \end{pmatrix}, \quad B_2 = \begin{pmatrix} 0 & b_1^2 & 0 & 0 \\ b_1^2 & 0 & 0 & 0 \\ b_3^1 & b_3^2 & 1/2 & 3/2 \\ b_3^1 & 0 & 1/2 & -1/2 \end{pmatrix}. \quad (1.35)$$

From the expression

$$\tilde{B}_1 = A(1, b_3^1/2b_1^1)A(2, b_3^2/b_2^2)A(3, -\ln|b_1^1|/2)A(4, -\ln|b_1^1|)B_1, \quad (1.36)$$

we find

$$B_1 = \begin{pmatrix} \lambda & 0 & 0 & 0 \\ 0 & \mu & 0 & 0 \\ 0 & 0 & 1 & 0 \\ 0 & 0 & 0 & 1 \end{pmatrix}, \quad \lambda, \mu = \pm 1. \quad (1.37)$$

The determining equations for the discrete symmetries are given by the system

$$\begin{pmatrix} X\tilde{t} & X\tilde{x} & X\tilde{u} \\ Y\tilde{t} & Y\tilde{x} & Y\tilde{u} \\ Z\tilde{t} & Z\tilde{x} & Z\tilde{u} \\ T\tilde{t} & T\tilde{x} & T\tilde{u} \end{pmatrix} = B_1 \begin{pmatrix} 1 & 0 & 0 \\ 0 & 1 & 0 \\ 2\tilde{t} & \tilde{x} & 0 \\ 0 & \tilde{x} & 2\tilde{u} \end{pmatrix}. \quad (1.38)$$

The solution of the above system is given by $\tilde{t} = \lambda t$, $\tilde{x} = \mu x$, $\tilde{u} = cu$, with c being an arbitrary nonzero constant. Substituting this solution into the symmetry condition, we find that $c = 1/\lambda\mu = \pm 1$. Hence, the discrete symmetry groups are

$$\begin{aligned} \Gamma_1 : (t, x, u) &\mapsto (t, x, u), & \Gamma_2 : (t, x, u) &\mapsto (-t, -x, u), \\ \Gamma_3 : (t, x, u) &\mapsto (t, -x, -u), & \Gamma_4 : (t, x, u) &\mapsto (-t, x, -u). \end{aligned} \quad (1.39)$$

In [35], Wazwaz obtained a solution of (1.31) given by $u_1(t, x) = \frac{x^2}{C - 6t}$, $x > 0$, where C is an arbitrary positive constant.

Applying groups Γ_2 , Γ_3 , and Γ_4 to this solution, we obtain other new solutions,

$$u_2(t, x) = \frac{x^2}{C + 6t}, \quad u_3(t, x) = \frac{(ix)^2}{C - 6t}, \quad u_4(t, x) = \frac{(ix)^2}{C + 6t}, \quad (1.40)$$

where i is the complex number $\sqrt{-1}$.

Example 1.4. In mathematical finance, the Black–Scholes equation governs the price evolution of a European call or European put under the Black–Scholes model [4]

$$V_t + \frac{1}{2}\sigma^2 S^2 V_{SS} + rSV_S - rV = 0, \quad (S, t) \in \mathbb{R}^+ \times (0, T), \quad (1.41)$$

where $V(t, S)$ is the price of the option as a function of stock price S and time t , r is the risk-free interest rate, and σ is the volatility of the stock.

Its generators of continuous symmetry were computed by Gazizov and Ibragimov in [11] and are

$$\begin{aligned} Y_1 &= \partial_t, & Y_2 &= S\partial_S, \\ Y_3 &= 2t\partial_t + (\ln(S) + Dt)S\partial_S + 2rtV\partial_V, \\ Y_4 &= \sigma^2 t S \partial_S + (\ln(S) - Dt)V\partial_V, \\ Y_5 &= 2\sigma^2 t^2 \partial_t + 2\sigma^2 t S \ln(S)\partial_S + [(\ln(S) - Dt)^2 + 2\sigma^2 r t^2 - \sigma^2 t]V\partial_V, \\ Y_6 &= V\partial_V, & Y_\infty &= f(t, S)\partial_V, \end{aligned} \quad (1.42)$$

where $D = r - \frac{\sigma^2}{2} \neq 0$ and f is an arbitrary solution of (1.41).

By solving the Lie equations (1.9), we find the continuous symmetry groups as follows:

$$\begin{aligned} G_1 &: (t, S, V) \mapsto (t + \epsilon, S, V), \\ G_2 &: (t, S, V) \mapsto (t, \epsilon S, V), \quad \epsilon \neq 0, \\ G_3 &: (t, S, V) \mapsto (\epsilon^2 t, S^\epsilon \exp(D(\epsilon^2 - \epsilon)t), V \exp(r(\epsilon^2 - 1)t)), \\ G_4 &: (t, S, V) \mapsto \left(t, S \exp(\epsilon \sigma^2 t), V S^\epsilon \exp \left\{ \left(\frac{\sigma^2}{2} \epsilon^2 - D\epsilon \right) t \right\} \right), \end{aligned}$$

$$G_5 : (t, S, V) \mapsto \left(\frac{t}{1 - 2\sigma^2\epsilon t}, S^{\frac{t}{1 - 2\sigma^2\epsilon t}}, V\sqrt{1 - 2\sigma^2\epsilon t} \exp \left\{ \frac{[(\ln(S) - Dt)^2 + 2\sigma^2 r t^2]\epsilon}{1 - 2\sigma^2\epsilon t} \right\} \right),$$

$$G_6 : (t, S, V) \mapsto (t, S, \epsilon V), \quad \epsilon \neq 0,$$

$$G_\infty : (t, S, V) \mapsto (t, S, V + f(t, S)).$$

Consequently, if $V = V(t, S)$ is a solution of Eq. (1.41), so are the functions

$$V_1 = G_1 \cdot V(t, S) = V(t - \epsilon, S),$$

$$V_2 = G_2 \cdot V(t, S) = V(t, S/\epsilon),$$

$$V_3 = G_3 \cdot V(t, S) = \exp \left\{ r \left(1 - \frac{1}{\epsilon^2} \right) t \right\} V \left(\frac{t}{\epsilon^2}, S^{1/\epsilon^2} \exp \left\{ D \left(\frac{1}{\epsilon^2} - \frac{1}{\epsilon} \right) t \right\} \right),$$

$$V_4 = G_4 \cdot V(t, S) = S^\epsilon \exp \left\{ - \left(\frac{\sigma^2 \epsilon^2}{2} + D\epsilon \right) t \right\} V(t, S \exp \{-\epsilon \sigma^2 t\}),$$

$$V_5 = G_5 \cdot V(t, S) = \frac{1}{\sqrt{1 + 2\sigma^2\epsilon t}} \exp \left\{ \frac{[(\ln(S) - Dt)^2 + 2r\sigma^2 t^2]\epsilon}{1 + 2\sigma^2\epsilon t} \right\} \\ \times V \left(\frac{t}{1 + 2\sigma^2\epsilon t}, S^{\frac{t}{1 + 2\sigma^2\epsilon t}} \right),$$

$$V_6 = G_6 \cdot V(t, S) = \epsilon V(t, S),$$

$$V_\infty = G_\infty \cdot V(t, S) = V(t, S) + f(t, S).$$

If we choose $V(t, S) = e^t$, using group G_4 with $\epsilon = 1$, we obtain the solution

$$V_4(t, S) = S, \quad (1.43)$$

and if we apply group G_5 , we get the following solution:

$$V_{5,4}(t, S) = \frac{S^{\frac{t}{1 + 2\sigma^2 t}}}{\sqrt{1 + 2\sigma^2 t}} \exp \left\{ \frac{(\ln(S) - Dt)^2 + 2r\sigma^2 t^2}{1 + 2\sigma^2 t} \right\}. \quad (1.44)$$

Thus, beginning with the simplest solution (1.43) we arrive at the rather complicated solution (1.44). The iteration of this procedure yields more complex solutions.

In order to simplify the computations, we change the set of generators (1.42) of the Lie algebra as follows:

$$\begin{aligned} X_1 &= \frac{1}{\sigma^2}(Y_1 + DY_2 + rY_6), & X_2 &= Y_2, & X_3 &= Y_3 - \frac{1}{2}Y_6, \\ X_4 &= Y_4, & X_5 &= \frac{1}{2}Y_5, & X_6 &= Y_6. \end{aligned}$$

The discrete symmetries of Eq. (1.41) are [32]

$$\begin{aligned} \Gamma_1 &: (t, S, V) \mapsto (t, S, V), \\ \Gamma_2 &: (t, S, V) \mapsto (t, \exp\{2Dt - \ln(S)\}, V), \\ \Gamma_3 &: (t, S, V) \mapsto \left(-\sigma^{-4}t^{-1}, \exp\{\sigma^{-2}D - \sigma^{-4}Dt^{-1} - \sigma^{-2}t^{-1}\ln(S)\}, \right. \\ &\quad \left. \sigma\sqrt{t}\exp\left\{-\frac{\sigma^{-2}}{2}[(\ln(S) - Dt)^2 + 2\sigma^2rt^2 + 2\sigma^{-2}r]\right\}V \right), \\ \Gamma_4 &: (t, S, V) \mapsto \left(-\sigma^{-4}t^{-1}, \exp\{\sigma^{-2}D - \sigma^{-4}Dt^{-1} + \sigma^{-2}t^{-1}\ln(S)\}, \right. \\ &\quad \left. \sigma\sqrt{t}\exp\left\{-\frac{\sigma^{-2}}{2}[(\ln(S) - Dt)^2 + 2\sigma^2rt^2 - 2\sigma^{-2}r]\right\}V \right). \end{aligned}$$

Like for continuous symmetries, other solutions of the Black–Scholes equation (1.41) can be constructed by using the above discrete symmetry groups.

Example 1.5. We consider the Harry Dym equation that represents an evolution system in which dispersion and nonlinearity are coupled together [19]:

$$u_t = u^3 u_{xxx}. \tag{1.45}$$

This equation has a 5D Lie algebra of continuous symmetry spanned by [23]

$$X_1 = \partial_x, \quad X_2 = x\partial_x + u\partial_u, \quad X_3 = x^2\partial_x + 2xu\partial_u, \quad X_4 = \partial_t, \quad X_5 = \partial_t - \frac{u}{3}\partial_u. \tag{1.46}$$

Eq. (1.45) admits eight groups of discrete symmetry, namely [16]

$$\begin{aligned}
 \Gamma_1 : (t, x, u) &\mapsto (t, x, u), & \Gamma_2 : (t, x, u) &\mapsto (-t, -x, u), \\
 \Gamma_3 : (t, x, u) &\mapsto (t, -x, -u), & \Gamma_4 : (t, x, u) &\mapsto (-t, x, -u), \\
 \Gamma_5 : (t, x, u) &\mapsto (t, -\frac{1}{x}, \frac{u}{x^2}), & \Gamma_6 : (t, x, u) &\mapsto (-t, \frac{1}{x}, \frac{u}{x^2}), \\
 \Gamma_7 : (t, x, u) &\mapsto (t, \frac{1}{x}, -\frac{u}{x^2}), & \Gamma_8 : (t, x, u) &\mapsto (-t, -\frac{1}{x}, -\frac{u}{x^2}).
 \end{aligned} \tag{1.47}$$

If we choose $u(t, x) = [-3a(x + 4a^2t)]^{\frac{2}{3}}$, which is a solution of the Harry Dym equation (1.45), where a is an arbitrary constant, we can generate other solutions of this equation. For example,

$$\begin{aligned}
 \Gamma_2 \cdot u &= [3a(x + 4a^2t)]^{\frac{2}{3}}, \\
 \Gamma_3 \cdot u &= -[3a(x - 4a^2t)]^{\frac{2}{3}}, \\
 \Gamma_4 \cdot u &= -[-3a(x - 4a^2t)]^{\frac{2}{3}}.
 \end{aligned}$$



1.3. Continuous symmetry for fractional differential equation

1.3.1 Some basic results on fractional calculus

Recall that, in the literature, there are two popular approaches to define fractional derivatives. The first one is the Riemann–Liouville approach. The second one is the Caputo approach, which is usually used in cases of initial value problems of FDEs. For more results, we refer to [30,31].

The Riemann–Liouville fractional integral is defined by

$$J_t^\alpha u(t, x) := \frac{1}{\Gamma(\alpha)} \int_0^t (t - \tau)^{\alpha-1} u(\tau, x) d\tau, \tag{1.48}$$

where $\alpha \in \mathbb{R}^+$ and Γ is the Euler Gamma function

$$\Gamma(\alpha) = \int_0^{+\infty} s^{\alpha-1} e^{-s} ds. \tag{1.49}$$

By definition, we have $J_t^0 u(t, x) = u(t, x)$ and it satisfies the semigroup property: $J_t^\alpha J_t^\beta u(t, x) = J_t^{\alpha+\beta} u(t, x)$.

The Riemann–Liouville fractional derivative of $u = u(t, x)$ for order α is defined as follows [30]: for $m \in \mathbb{N}$,

$$D_t^\alpha u(t, x) := \begin{cases} \frac{1}{\Gamma(m - \alpha)} \frac{\partial^m}{\partial t^m} \int_0^t (t - \tau)^{m-\alpha-1} u(\tau, x) d\tau, & m - 1 \leq \alpha < m, \\ \frac{\partial^m u}{\partial t^m}, & \alpha = m. \end{cases} \tag{1.50}$$

The Riemann–Liouville integral and the Riemann–Liouville derivative satisfy the following properties [30]:

$$D_t^\alpha J_t^\alpha u(t, x) = u(t, x), \tag{1.51}$$

$$J_t^\alpha D_t^\alpha u(t, x) = u(t, x) - \sum_{k=0}^{m-1} \frac{D_t^{\alpha-k-1} u(0, x)}{\Gamma(\alpha - k)} t^{\alpha-k-1}. \tag{1.52}$$

Let $u \in AC^m([0, t])$, where $AC^m([0, t])$ is the class of functions which are continuously differentiable in $[0, t]$ up to order $(m - 1)$ with $u^{(m-1)} \in AC([0, t])$. The Caputo fractional derivative is given by: for $m \in \mathbb{N}$,

$${}^C D_t^\alpha u(t, x) := \begin{cases} \frac{1}{\Gamma(m - \alpha)} \int_0^t (t - \tau)^{m-\alpha-1} \frac{\partial^m u(\tau, x)}{\partial \tau^m} d\tau, & m - 1 \leq \alpha < m, \\ \frac{\partial^m u}{\partial t^m}, & \alpha = m. \end{cases} \tag{1.53}$$

The Caputo derivative (1.53) and the Riemann–Liouville integral (1.48) satisfy the following properties:

$${}^C D_t^\alpha J_t^\alpha u(t, x) = u(t, x), \tag{1.54}$$

$$J_t^\alpha {}^C D_t^\alpha u(t, x) = u(t, x) - \sum_{k=0}^{m-1} \frac{u_t^{(k)}(0, x)}{k!} t^k. \tag{1.55}$$

The relation between the Caputo fractional derivative and the Riemann–Liouville fractional derivative is

$$D_t^\alpha u(t, x) = {}^C D_t^\alpha u(t, x) + \sum_{k=0}^{m-1} \frac{u_t^{(k)}(0, x)}{\Gamma(k - \alpha + 1)} t^{k-\alpha}. \tag{1.56}$$

1.3.2 Continuous symmetry for fractional ordinary differential equations

We consider the fractional ODE (FODE) [12]

$$D_x^\alpha \gamma(x) = F(x, \gamma, \gamma^{(1)}, \dots, \gamma^{(n)}), \quad \text{where} \quad \gamma^{(k)} = \frac{d^k \gamma}{dx^k} \quad \text{for} \quad k = 1, \dots, n, \quad (1.57)$$

and a one-parameter group of transformations in the infinitesimal form

$$\bar{x} = x + \epsilon \xi(x, \gamma) + o(\epsilon), \quad \bar{\gamma} = \gamma + \epsilon \eta(x, \gamma) + o(\epsilon), \quad (1.58)$$

where $\gamma = \gamma(x)$ and

$$\xi(x, \gamma) = \left. \frac{\partial \bar{x}}{\partial \epsilon} \right|_{\epsilon=0}, \quad \eta(x, \gamma) = \left. \frac{\partial \bar{\gamma}}{\partial \epsilon} \right|_{\epsilon=0}. \quad (1.59)$$

Along with (1.58), we consider the infinitesimal operator

$$X = \xi(x, \gamma) \frac{\partial}{\partial x} + \eta(x, \gamma) \frac{\partial}{\partial \gamma}. \quad (1.60)$$

With the condition of invariance of Eq. (1.57) in $x = 0$, we get

$$\xi(x, \gamma)|_{x=0} = 0. \quad (1.61)$$

For simplicity, we denote

$$\xi[x] = \xi(x, \gamma) \quad \text{and} \quad \eta[x] = \eta(x, \gamma). \quad (1.62)$$

We find the infinitesimal transformation of the fractional derivative $D_x^\alpha \gamma$

$$\begin{aligned} D_x^\alpha \bar{\gamma}(\bar{x}) &= \frac{1}{\Gamma(1-\alpha)} \frac{d}{d\bar{x}} \int_0^{\bar{x}} \frac{\bar{\gamma}(\bar{t})}{(\bar{x} - \bar{t})^\alpha} d\bar{t} \\ &= \frac{1}{\Gamma(1-\alpha)} \frac{1}{1 + \epsilon D(\xi[x])} \frac{d}{dx} \int_0^{x + \epsilon \xi[x]} \frac{\gamma(\bar{t} - \epsilon \xi[\bar{t}]) + \epsilon \eta(\bar{t} - \epsilon \xi[\bar{t}])}{(x + \epsilon \xi[x] - \bar{t})^\alpha} d\bar{t}. \end{aligned}$$

As $\bar{t} = t + \epsilon \xi[t]$ we have $d\bar{t} = (1 + \epsilon D(\xi[t])) dt$, where D is first derivative. Then

$$\begin{aligned} D_x^\alpha \bar{\gamma}(\bar{x}) &= \frac{1}{\Gamma(1-\alpha)} \frac{1}{1 + \epsilon D(\xi[x])} \frac{d}{dx} \int_0^x \frac{(y(t) + \epsilon \eta[t])(1 + \epsilon D(\xi[t]))}{(x + \epsilon \xi[x] - t - \epsilon \xi[t])^\alpha} dt \\ &= \frac{1 - \epsilon D(\xi[x])}{\Gamma(1-\alpha)} \frac{d}{dx} \int_0^x \frac{\gamma(t) + \epsilon \eta[t] + \epsilon \gamma(t) D(\xi[t])}{(x - t)^\alpha} \left(1 + \epsilon \frac{\xi[x] - \xi[t]}{x - t} \right) dt. \end{aligned}$$

Consider the second factor in the denominator of the integrand. Owing to the smallness of the parameter ϵ it can be written

$$\left(1 + \epsilon \frac{\xi[x] - \xi[t]}{x - t}\right)^\alpha = 1 + \alpha \epsilon \frac{\xi[x] - \xi[t]}{x - t} + o(\epsilon). \tag{1.63}$$

This relation is valid if the function $\xi[x]$ is continuously differentiable as a function of x for $x \geq 0$. Then

$$\begin{aligned} D_x^\alpha \bar{y}(\bar{x}) &= \frac{1 - \epsilon D(\xi[x])}{\Gamma(1 - \alpha)} \frac{d}{dx} \int_0^x \frac{\gamma(t) + \epsilon \eta[t] + \epsilon \gamma(t) D(\xi[t])}{(x - t)^\alpha \left(1 + \alpha \epsilon \frac{\xi[x] - \xi[t]}{x - t}\right)} dt \\ &= \frac{1 - \epsilon D(\xi[x])}{\Gamma(1 - \alpha)} \frac{d}{dx} \int_0^x \frac{\gamma(t) + \epsilon \eta[t] + \epsilon \gamma(t) D(\xi[t])}{(x - t)^\alpha} \\ &\quad \times \left(1 - \alpha \epsilon \frac{\xi[x] - \xi[t]}{x - t}\right) dt \\ &= \frac{1 - \epsilon D(\xi[x])}{\Gamma(1 - \alpha)} \frac{d}{dx} \int_0^x \frac{\gamma(t)}{(x - t)^\alpha} dt + \frac{\epsilon}{\Gamma(1 - \alpha)} \frac{d}{dx} \int_0^x \frac{\eta[t]}{(x - t)^\alpha} dt \\ &\quad + \frac{\epsilon}{\Gamma(1 - \alpha)} \frac{d}{dx} \int_0^x \frac{\gamma(t) D(\xi[t])}{(x - t)^\alpha} dt \\ &\quad - \frac{\epsilon \alpha}{\Gamma(1 - \alpha)} \frac{d}{dx} \int_0^x \frac{\gamma(t) (\xi[x] - \xi[t])}{(x - t)^{1+\alpha}} dt. \end{aligned}$$

Then,

$$D_x^\alpha \bar{y}(\bar{x}) = D_x^\alpha \gamma - \epsilon D_x(\xi) D_x^\alpha \gamma + \epsilon D_x^\alpha \eta + \epsilon D_x^\alpha (\gamma D_x(\xi)) - \epsilon \frac{d}{dx} I_\alpha(x, \gamma), \tag{1.64}$$

where D_x is the total derivative and

$$I_\alpha(x, \gamma) = \frac{\alpha}{\Gamma(1 - \alpha)} \int_0^x \frac{\gamma(t) (\xi[x] - \xi[t])}{(x - t)^{1+\alpha}} dt. \tag{1.65}$$

Let us simplify $I_\alpha(x, \gamma)$. From [31] we know that a differentiable function $f(x)$ has the representation

$$D_x^\alpha f(x) = \frac{f(x)}{\Gamma(1 - \alpha)x^\alpha} + \frac{\alpha}{\Gamma(1 - \alpha)} \int_0^x \frac{f(x) - f(t)}{(x - t)^{1+\alpha}} dt. \tag{1.66}$$

Then

$$\begin{aligned}
 I_\alpha(x, \gamma) &= \frac{\alpha}{\Gamma(1-\alpha)} \int_0^x \frac{\gamma(t)(\xi[x] - \xi[t])}{(x-t)^{1+\alpha}} dt \\
 &= \frac{\alpha}{\Gamma(1-\alpha)} \int_0^x \frac{\gamma(t)(\xi[x] - \xi[t]) + \gamma(x)\xi[x] - \gamma(x)\xi[x]}{(x-t)^{1+\alpha}} dt \\
 &= \frac{\alpha}{\Gamma(1-\alpha)} \left(\xi[x] \int_0^x \frac{\gamma(t) - \gamma(x)}{(x-t)^{1+\alpha}} dt + \int_0^x \frac{\gamma(x)\xi[x] - \gamma(t)\xi[t]}{(x-t)^{1+\alpha}} dt \right) \\
 &= \frac{\alpha}{\Gamma(1-\alpha)} \left(\frac{\Gamma(1-\alpha)}{\alpha} (D_x^\alpha(\xi\gamma) - \xi D_x^\alpha(\gamma)) \right) \\
 &= D_x^\alpha(\xi\gamma) - \xi D_x^\alpha(\gamma).
 \end{aligned}$$

Differentiating $I_\alpha(x, \gamma)$ we obtain

$$\frac{d}{dx} I_\alpha(x, \gamma) = D_x^{\alpha+1}(\xi\gamma) - D_x(\xi)D_x^\alpha\gamma - \xi D_x^{\alpha+1}\gamma. \quad (1.67)$$

Substituting (1.67) in (1.64), we find the desired infinitesimal transformation fractional derivative

$$D_x^\alpha \bar{\gamma} = D_x^\alpha \gamma + \epsilon \zeta_\alpha + o(\epsilon), \quad (1.68)$$

where

$$\zeta_\alpha = D_x^\alpha \eta + D_x^\alpha (D_x(\xi)\gamma) + \xi D_x^{\alpha+1}\gamma - D_x^{\alpha+1}(\xi\gamma). \quad (1.69)$$

Applying the generalized Leibniz rule [31]

$$D_x^\alpha (f(x)g(x)) = \sum_{n=0}^{\infty} \binom{\alpha}{n} D_x^{\alpha-n} f(x) D_x^n g(x), \quad (1.70)$$

where

$$\binom{\alpha}{n} = \frac{(-1)^{n-1} \alpha \Gamma(n-\alpha)}{\Gamma(1-\alpha) \Gamma(n+1)},$$

for the second and last terms of (1.69), we find

$$\begin{aligned}
 \zeta_\alpha &= D_x^\alpha \eta - \alpha D_x(\xi) D_x^\alpha(\gamma) + \sum_{n=1}^{\infty} \left[\binom{\alpha}{n} - \binom{\alpha+1}{n+1} \right] D_x^{\alpha-n}(\gamma) D_x^{n+1}(\xi) \\
 &= D_x^\alpha \eta - \alpha D_x(\xi) D_x^\alpha(\gamma) - \sum_{n=1}^{\infty} \binom{\alpha}{n+1} D_x^{\alpha-n}(\gamma) D_x^{n+1}(\xi).
 \end{aligned}$$

We can explain the derivation $D_x^\alpha(\eta) = D_x^\alpha(\eta(x, y))$ using Leibniz's formula (1.70) as

$$D_t^\alpha(\eta) = D_t^\alpha(1 \cdot \eta) = \sum_{n=0}^{\infty} \binom{\alpha}{n} D_t^{\alpha-n}(1) D_t^n(\eta), \tag{1.71}$$

and given the generalization of the chain rule for composite functions, we find

$$D_t^n[\eta] = \sum_{m=0}^n \binom{n}{m} \sum_{k=0}^m \sum_{r=0}^k \binom{k}{r} \frac{1}{k!} [-u(t, x)]^r D_t^m[u^{k-r}(t, x)] \times \frac{\partial^{n-m+k} \eta(t, x, u(t, x))}{\partial t^{n-m} \partial u^k}.$$

Then,

$$D_t^n[\eta] = \sum_{n=0}^{\infty} \sum_{m=0}^n \sum_{k=0}^m \sum_{r=0}^k \binom{\alpha}{n} \binom{m}{n} \binom{k}{r} \frac{1}{k!} \frac{t^{n-\alpha}}{\Gamma(n+1-\alpha)} \times [-u(t, x)]^r D_t^m[u^{k-r}(t, x)] \frac{\partial^{n-m+k} \eta(t, x, u)}{\partial t^{n-m} \partial u^k}.$$

Therefore

$$D_t^\alpha(\eta) = \frac{\partial^\alpha \eta}{\partial t^\alpha} + \eta_u \frac{\partial^\alpha u}{\partial t^\alpha} - u \frac{\partial^\alpha \eta_u}{\partial t^\alpha} - \sum_{n=1}^{\infty} \binom{\alpha}{n} \frac{\partial^n(\eta_u)}{\partial t^n} D_t^{\alpha-n}(u) + \mu,$$

where

$$\mu = \sum_{n=0}^{\infty} \sum_{m=0}^n \sum_{k=0}^m \sum_{r=0}^k \binom{\alpha}{n} \binom{m}{n} \binom{k}{r} \frac{1}{k!} \frac{t^{n-\alpha}}{\Gamma(n+1-\alpha)} \times [-u(t, x)]^r D_t^m[u^{k-r}(t, x)] \frac{\partial^{n-m+k} \eta(t, x, u)}{\partial t^{n-m} \partial u^k}.$$

In summary,

$$\zeta_\alpha = \frac{\partial^\alpha \eta}{\partial t^\alpha} + \left(\eta_u - \alpha D_t(\tau) \right) \frac{\partial^\alpha u}{\partial t^\alpha} - u \frac{\partial^\alpha \eta_u}{\partial t^\alpha} + \mu + \sum_{n=1}^{\infty} \left[\binom{\alpha}{n} \frac{\partial^n \eta_u}{\partial t^n} - \binom{\alpha}{n+1} D_t^{n+1}(\tau) \right] D_t^{\alpha-n}(u)$$

$$- \sum_{n=1}^{\infty} \binom{\alpha}{n} D_t^n(\xi) D_t^{\alpha-n}(u_x).$$

If η is linear, then μ vanishes.

Similarly, with a continuation of order α it is possible to construct an extension of order $\alpha + 1$. Then $\zeta_{\alpha+1}$ has the form

$$\begin{aligned} \zeta_{\alpha+1} &= D_x(\zeta_\alpha) - D_x(\xi) D_x^{\alpha+1}(y) \\ &= D_x^{\alpha+1} \eta + D_x^{\alpha+1}(D_x(\xi)y) + \xi D_x^{\alpha+2} y - D_x^{\alpha+2}(\xi y) \\ &= D_x^{\alpha+1} \eta - (\alpha + 1) D_x(\xi) D_x^{\alpha+1}(y) - \frac{\alpha(\alpha + 1)}{2} D_x^2(\xi) D_x^\alpha(y) \\ &\quad - \sum_{n=0}^{\infty} \binom{\alpha + 1}{n + 2} D_x^{\alpha-n}(y) D_x^{n+2}(\xi). \end{aligned}$$

In general, we can generalize to an arbitrary extension order $\alpha + n$, $\alpha \in (0, 1)$, and $n \in \mathbb{Z}$,

$$\zeta_{\alpha+n} = D_x^{\alpha+n} \eta + D_x^{\alpha+n}(D_x(\xi)y) + \xi D_x^{\alpha+1+n} y - D_x^{\alpha+1+n}(\xi y). \quad (1.72)$$

The prolongation formula order α for the Caputo fractional derivative has the form

$${}^C \zeta_\alpha = {}^C D_x^\alpha(\eta) - \alpha D_x(\xi) {}^C D_x^\alpha(y) - \sum_{n=1}^{\infty} \binom{\alpha}{n+1} I_x^n ({}^C D_x^\alpha(y)) D_x^{n+1}(\xi). \quad (1.73)$$

Also, this formula is easily generalized to an arbitrary order $(\alpha + n)$.

Example 1.6. We consider the following FODE:

$$D_x^\alpha y(x) = 0. \quad (1.74)$$

For this equation, the determining equation

$$\zeta_\alpha |_{D_x^\alpha y(x)=0} = 0 \quad (1.75)$$

can be rewritten in the following form:

$$\frac{\partial^\alpha \eta}{\partial x^\alpha} - y \frac{\partial^\alpha \eta_y}{\partial x^\alpha} + \mu + \sum_{n=1}^{\infty} \left[\binom{\alpha}{n} \frac{\partial^n \eta_y}{\partial x^n} - \binom{\alpha}{n+1} D_t^{n+1}(\xi) \right] D_x^{\alpha-n}(y) = 0. \quad (1.76)$$

Variables $x, y, y' = \frac{dy}{dx}, y'' = \frac{d^2y}{dx^2}, \dots$ (contained in $\mu, D_x^{n+1}(\xi)$ and $D_x^{\alpha-n}(y)$) are considered independent here. Splitting with respect to $D_x^{\alpha-n}(y)$ leads to an infinite overdetermined system of linear FDEs:

$$\begin{aligned} \frac{\partial^\alpha \eta}{\partial x^\alpha} - y \frac{\partial^\alpha \eta_y}{\partial x^\alpha} + \mu &= 0, \\ \binom{\alpha}{n} \frac{\partial^n \eta_y}{\partial x^n} - \binom{\alpha}{n+1} D_t^{n+1}(\xi) &= 0, \quad n \in \mathbb{N}. \end{aligned}$$

Further splitting allows to solve this system and to find admitted operators

$$X_1 = x\partial_x, \quad X_2 = y\partial_y, \quad X_3 = x^2\partial_x + (\alpha - 1)x y\partial_y, \quad X_4 = x^{\alpha-1}\partial_y. \tag{1.77}$$

Below are the one-parameter groups of transformations associated to the above infinitesimal generators:

$$X_1 : \quad \bar{x} = e^\epsilon x, \quad \bar{y} = y, \tag{1.78}$$

$$X_2 : \quad \bar{x} = x, \quad \bar{y} = e^\epsilon y, \tag{1.79}$$

$$X_3 : \quad \bar{x} = \frac{x}{1 - \epsilon x}, \quad \bar{y} = \frac{y}{(1 - \epsilon x)^{\alpha-1}}, \tag{1.80}$$

$$X_4 : \quad \bar{x} = x, \quad \bar{y} = y + \epsilon x^{\alpha-1}. \tag{1.81}$$

By using the last two groups above, and from a solution $y = \gamma(x)$ of (1.74), we can construct two other solutions of Eq. (1.74), which are

$$\gamma_3(x) = (1 + \epsilon x)^{\alpha-1} \gamma\left(\frac{x}{1 + \epsilon x}\right), \quad \gamma_4(x) = \gamma(x) + \epsilon x^{\alpha-1}. \tag{1.82}$$

Example 1.7. Let us consider a fractional Riccati equation,

$$D_x^\alpha \gamma + a\gamma^2 = \frac{b}{x^{2\alpha}}, \quad 0 < \alpha < 1, \tag{1.83}$$

where a and b are arbitrary constants.

This equation admits a generator of continuous symmetry which is defined by

$$X = x\partial_x - \alpha y\partial_y. \tag{1.84}$$

The invariant solution of (1.83) corresponding to X is $\gamma(x) = \frac{c}{x^\alpha}$, where the constant c satisfies

$$ac^2 + \frac{\Gamma(1 - \alpha)}{\Gamma(1 - 2\alpha)} c - b = 0. \tag{1.85}$$

1.3.3 Continuous symmetry for fractional partial differential equations

Here, we consider a time fractional PDE (FPDE) with two independent variables given in the following form:

$$D_t^\alpha u(t, x) = F(t, x, u, u_x, u_{xx}, \dots), \quad 0 < \alpha < 1, \quad (1.86)$$

where u_t, u_x, u_{xx}, \dots represent the partial derivatives of the dependent variable u .

Similarly to the case of FODEs, we can construct the prolongation formula for the generator of continuous symmetry. We consider the continuous group of transformations

$$\begin{aligned} \bar{t} &= t + \epsilon \tau(t, x, u) + o(\epsilon), \\ \bar{x} &= x + \epsilon \xi(t, x, u) + o(\epsilon), \\ \bar{u} &= u + \epsilon \eta(t, x, u) + o(\epsilon), \end{aligned} \quad (1.87)$$

where τ, ξ , and η are the infinitesimals of the transformations.

When transformations (1.87) are applied to usual partial derivatives u_x, u_{xx}, \dots , we have

$$\begin{aligned} \bar{u}_{\bar{x}}(\bar{t}, \bar{x}) &= u_x(t, x) + \epsilon \eta^x + o(\epsilon), \\ \bar{u}_{\bar{x}\bar{x}}(\bar{t}, \bar{x}) &= u_{xx}(t, x) + \epsilon \eta^{xx} + o(\epsilon), \\ &\vdots \\ \bar{u}_{\bar{k}\bar{x}}(\bar{t}, \bar{x}) &= u_{kx}(t, x) + \epsilon \eta^{kx} + o(\epsilon), \quad k \in \mathbb{N}^*, \\ D_t^\alpha \bar{u}(\bar{t}, \bar{x}) &= D_t^\alpha u(t, x) + \epsilon \zeta_\alpha + o(\epsilon), \end{aligned}$$

where $\eta^x, \eta^{xx}, \dots, \eta^{kx}$, and ζ_α are extended infinitesimals of order 1, 2, ..., k and α , respectively, defined by prolongation formulas

$$\begin{aligned} \eta^x &= D_x(\eta) - u_t D_t(\tau) - u_x D_x(\xi), \\ \eta^{xx} &= D_x(\eta^x) - u_{xt} D_t(\tau) - u_{xx} D_x(\xi), \\ &\vdots \\ \eta^{kx} &= D_x(\eta^{(k-1)x}) - u_{(k-1)x,t} D_t(\tau) - u_{kx} D_x(\xi), \\ \zeta_\alpha &= D_t^\alpha(\eta) + \xi D_t^\alpha(u_x) - D_t^\alpha(\xi u_x) + D_t^\alpha(D_t(\tau)u) \\ &\quad - D_t^{\alpha+1}(\tau u) + \tau D_t^{\alpha+1}(u), \end{aligned}$$

where $u_{kx} = \frac{\partial^k u}{\partial x^k}$.

With the Caputo derivative we have

$${}^C \zeta_\alpha = {}^C D_t^\alpha(\eta) + \xi {}^C D_t^\alpha(u_x) - {}^C D_t^\alpha(\xi u_x) + \tau {}^C D_t^\alpha(u_t) - {}^C D_t^\alpha(\tau u_t). \quad (1.88)$$

The infinitesimal generator X can be written in the following form:

$$X = \tau(t, x, u)\partial_t + \xi(t, x, u)\partial_x + \eta(t, x, u)\partial_u. \quad (1.89)$$

A solution $u = \theta(t, x)$ is said to be an invariant solution of (1.86) if and only if:

1. $u = \theta(t, x)$ is an invariant surface, i.e., $X\theta = \tau\theta_t + \xi\theta_x + \eta\theta_u = 0$;
2. $u = \theta(t, x)$ satisfies Eq. (1.86).

The infinitesimal generator X must satisfy the invariance conditions for Eq. (1.86), which are given as follows:

$$X^{(\alpha)}[\Delta u]|_{\Delta u=0} = 0, \quad (1.90)$$

where $\Delta u = D_t^\alpha u - F$ and $X^{(\alpha)}$ denotes the α -extended prolongation of generator X given by

$$X^{(\alpha)} = X + \zeta_\alpha \frac{\partial}{\partial (D_t^\alpha u)} + \sum_{i=1}^k \eta^{kx} \frac{\partial}{\partial u_{kx}}, \quad (1.91)$$

with

$$\begin{aligned} \zeta_\alpha &= \frac{\partial^\alpha \eta}{\partial t^\alpha} + \left(\eta_u - \alpha D_t(\tau) \right) \frac{\partial^\alpha u}{\partial t^\alpha} - u \frac{\partial^\alpha \eta_u}{\partial t^\alpha} + \mu \\ &+ \sum_{n=1}^{\infty} \left[\binom{\alpha}{n} \frac{\partial^n \eta_u}{\partial t^n} - \binom{\alpha}{n+1} D_t^{n+1}(\tau) \right] D_t^{\alpha-n}(u) \\ &- \sum_{n=1}^{\infty} \binom{\alpha}{n} D_t^n(\xi) D_t^{\alpha-n}(u_x). \end{aligned}$$

As the lower limit $t = 0$ of the integral in the definition of Riemann–Liouville fractional partial derivative is fixed, it should be invariant with respect to the transformations (1.87). Such invariance condition arrives at

$$\tau(t, x, u)|_{t=0} = 0. \quad (1.92)$$

1.3.4 Some illustrative examples

Example 1.8. We consider the time-fractional heat equation

$$D_t^\alpha u = u_{xx}, \quad t > 0, \quad 0 < \alpha < 1. \quad (1.93)$$

The invariance condition for this equation is written

$$(\zeta_\alpha - \eta^{xx})|_{D_t^\alpha u = u_{xx}} = 0. \quad (1.94)$$

Substituting ζ_α and η^{xx} into the invariance condition and eliminating u_{xx} by setting $u_{xx} = D_t^\alpha u$, we get a system of equations for unknown functions ξ_1 , ξ_2 , and η . This system contains the variables t , x , u , u_x , u_t , and u_{tx} and fractional derivatives of orders α and $\alpha + 1$ with respect to t as follows:

$$\begin{aligned} u_x^3 : & \quad \xi_{uu} = 0, \\ u_x^2 : & \quad \eta_{uu} - 2\xi_{xu} = 0, \\ u_x : & \quad 2\eta_{xu} - \xi_{xx} = 0, \\ u_x u_t : & \quad \tau_{xu} = 0, \\ u_x^2 u_t : & \quad \tau_{uu} = 0, \\ u_{tx} : & \quad \tau_x = 0, \\ u_x u_{tx} : & \quad \tau_u = 0, \\ u_x D_t^\alpha u : & \quad \xi_u = 0, \\ D_t^{\alpha-k} u_x : & \quad D_t^k(\xi) = 0, \quad k = 1, 2, \dots \end{aligned}$$

Solving the above system, we find

$$\tau = \tau(t), \quad \xi = \xi(x), \quad \eta = \beta(t, x) + \left(\frac{1}{2}\xi_x + a(t)\right)u, \quad (1.95)$$

where $a(t)$ is an arbitrary function and $\beta(t, x)$ is an arbitrary solution of Eq. (1.93).

Substituting (1.95) into the remaining part of the determining equation and applying the generalized Leibnitz rule, we get the equation

$$\begin{aligned} D_t^\alpha \beta - \beta_{xx} + \left(2\xi_x - \alpha\tau_t - \frac{1}{2}\tau_{xxx}u\right)D_t^\alpha(u) \\ + \sum_{k=1}^{\infty} \binom{\alpha}{k} D_t^{\alpha-k}(u) \left(a^{(k)} - \frac{k-\alpha}{k+1}(\tau)^{(k+1)}\right) = 0. \end{aligned} \quad (1.96)$$

Splitting this equation with respect to u , $D_t^\alpha u$, and $D_t^{\alpha-k} u$, $k = 1, 2, \dots$, we obtain the overdetermined system

$$D_t^\alpha \beta = \beta_{xx}, \quad 2\xi_x = C, \quad \alpha \tau_t = C, \quad a^{(k)} = \frac{k-\alpha}{k+1} (\tau)^{(k+1)}, \quad k = 1, 2, \dots, \tag{1.97}$$

where C is an arbitrary constant. The solution of this system satisfying the condition $\tau(0) = 0$ has the form

$$\tau = 2C_2 t, \quad \xi = \alpha C_2 x + C_1, \quad a(t) = C_3, \quad \beta = \beta(t, x), \tag{1.98}$$

where $C_1, C_2 = C/2\alpha$, and C_3 are arbitrary constants.

Then we obtain the following generators of continuous symmetry for (1.93):

$$X_1 = \partial_x, \quad X_2 = 2t\partial_t + \alpha x\partial_x, \quad X_3 = u\partial_u, \quad X_\infty = \beta(t, x)\partial_u. \tag{1.99}$$

Invariant solution under the generator $X = X_1 + \rho X_3$, where $\rho = cte$, has the form

$$u_R(t, x) = \phi(t)e^{\rho x}, \tag{1.100}$$

where $\phi(t)$ satisfies the equation $D_t^\alpha \phi(t) = \rho^2 \phi(t)$, which gives

$$u_R(t, x) = t^{\alpha-1} E_{\alpha,\alpha}(\rho^2 t^\alpha) e^{\rho x}, \tag{1.101}$$

where $E_{\alpha,\alpha}$ is the generalized Mittag-Leffler function defined as $E_{\alpha,\alpha}[z] = \sum_{k=0}^{\infty} \frac{z^k}{\Gamma(\alpha k + \alpha)}$.

Similarly, if we replace the Riemann–Liouville derivative in Eq. (1.93) by the Caputo derivative, we obtain the following solution:

$$u_C(t, x) = E_\alpha(\rho^2 t^\alpha) e^{\rho x}, \tag{1.102}$$

where E_α is the classical Mittag-Leffler function: $E_\alpha[z] = \sum_{k=0}^{\infty} \frac{z^k}{\Gamma(\alpha k + 1)}$.

If $\alpha \rightarrow 1$, we get the solution $u(t, x) = e^{\rho(x+\rho t)}$, which is obviously a solution of the classical heat equation.

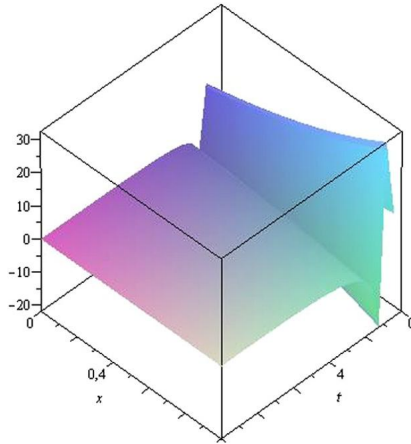


Figure 1.1 The solution $u_R(t, x)$ of (1.93).

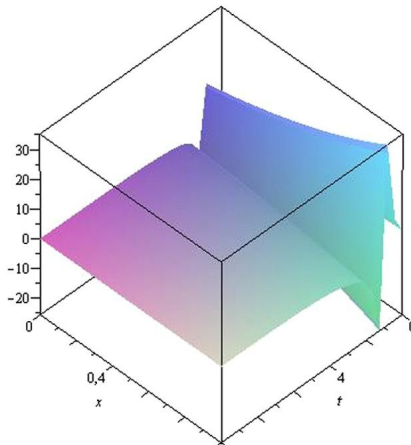


Figure 1.2 The solution $u_C(t, x)$ of (1.93).

The graphical representations of the above solutions $u_R(t, x)$, $u_C(t, x)$, and $u(t, x)$ are respectively displayed in Fig. 1.1, Fig. 1.2, and Fig. 1.3 for $\rho = 1$ and $\alpha = 0.5$.

Example 1.9. We consider the time-fractional Black–Scholes equation given by [36]

$$\frac{\partial^\alpha V}{\partial t^\alpha} + \frac{1}{2}\sigma^2 S^2 V_{SS} + rSV_S - rV = 0, \quad 0 < \alpha < 1. \quad (1.103)$$

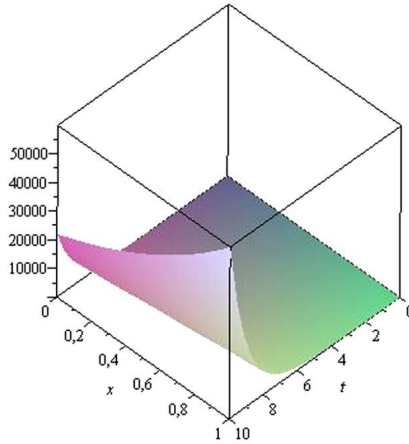


Figure 1.3 The solution $u(t, x)$ of (1.93).

Using the Lie symmetry analysis described in the last section, we retrieve the invariance criterion of the form

$$\zeta_\alpha + \sigma^2 S \xi V_{SS} + r \xi V_S + \frac{1}{2} \sigma^2 S^2 \eta^{SS} + r S \eta^S - r \eta = 0. \tag{1.104}$$

Then, we can obtain the determining equations for the symmetry group of Eq. (1.103):

$$\begin{aligned} \tau_S = \tau_V = \xi_t = \xi_V = 0, \\ \frac{1}{2} \sigma^2 S^2 (\eta_V - 2 \xi_S) - \frac{1}{2} \sigma^2 S^2 (\eta_V - \alpha D_t(\tau)) + \sigma^2 S \xi = 0, \\ \frac{1}{2} \sigma^2 S^2 (2 \eta_{SV} - \xi_{SS}) - r S (\eta_V - \alpha D_t(\tau)) + r S (\eta_V - \xi_S) + r \xi = 0, \\ \frac{\partial^\alpha \eta}{\partial t^\alpha} - V \frac{\partial^\alpha \eta_V}{\partial t^\alpha} + \frac{1}{2} \sigma^2 S^2 \eta_{SS} + r S \eta_S + r (\eta_V - \alpha D_t(\tau)) V - r \eta = 0, \\ \binom{\alpha}{n} \frac{\partial^n \eta_V}{\partial t^n} - \binom{\alpha}{n+1} D_t^{n+1}(\tau) = 0. \end{aligned} \tag{1.105}$$

The solution of the system is given by

$$\begin{aligned} \tau = at + b, \quad \xi = \frac{a\alpha}{2} S \ln(S) + cS, \\ \eta = \left[\left(\frac{a(\alpha - 1)}{2} + d \right) - \frac{a\alpha}{2\sigma^2} D \ln(S) \right] V + v(t, S), \end{aligned}$$

where a , b , c , and d are arbitrary constants, $D = r - \sigma^2/2 \neq 0$, and $v(t, S)$ is an arbitrary solution of the time-fractional Black–Scholes equation.

Consequently, the Lie algebra of continuous symmetry \mathfrak{g} is spanned by the following generators:

$$\begin{aligned} X_1 &= t\partial_t + \frac{\alpha}{2}S\ln(S)\partial_S + \left[\frac{\alpha-1}{2} - \frac{\alpha}{2\sigma^2}D\ln(S) \right] V\partial_V, \\ X_2 &= S\partial_S, \quad X_3 = V\partial_V, \quad X_\infty = v(t, S)\partial_V. \end{aligned}$$

Using these continuous symmetry, we obtain some invariant solutions of the studied equation.

– If $X = X_2$, the invariance solution with respect to X_2 will be of the form $V(t, S) = V(t)$, and it yields the reduced equation $\partial_t^\alpha V = rV$. Then, the solution is given by

$$V_1(t, S) = K_1 t^{\alpha-1} E_{\alpha, \alpha}[rt^\alpha],$$

where K_1 is an arbitrary constant.

– If $X = X_3$ or $X = X_\infty$, we get a trivial solution.

– If $X = X_2 + \mu X_3$ where $\mu = -D/\sigma^2$, the similarity variable and similarity transformation corresponding to this infinitesimal generator can be obtained by solving the associated characteristic equations

$$\frac{dt}{0} = \frac{dS}{S} = \frac{dV}{\mu V}.$$

Hence, an exact solution of Eq. (1.103) is obtained of the form

$$V_2(t, S) = K_2 t^{\alpha-1} E_{\alpha, \alpha} \left[(1-\mu) \left(r + \frac{\mu\sigma^2}{2} \right) t^\alpha \right] S^\mu,$$

where K_2 is an arbitrary constant.

If $\alpha \rightarrow 1$, we get the solutions

$$V_1(t, S) = K_1 e^{rt} \quad \text{and} \quad V_2(t, S) = K_2 e^{(1-\mu)\left(r + \frac{\mu\sigma^2}{2}\right)t} S^\mu, \quad (1.106)$$

which are obviously solutions of the classical Black–Scholes equation.

Example 1.10. We consider the time-fractional Kolmogorov equation

$$D_t^\alpha u = xu_{xx} + f(x)u_x, \quad \alpha \in]0, 1]. \quad (1.107)$$

The above equation has been extensively studied in the case of $\alpha = 1$ in [9] with different expressions of the drift function f which satisfies a family of Riccati type differential equations.

In [28], A. Ouhadan and E.H. El Kinani found its continuous symmetries when $f(x) = \lambda \in \mathbb{R}$ or $f(x) = \frac{1+3\sqrt{x}}{2(1+\sqrt{x})}$.

Case 1: We have $f(x) = \lambda$.

- **Subcase 1:** If $\lambda = \frac{1}{2}$, a basis for the Lie algebra of symmetries admitted by (1.107) is

$$\begin{aligned} X_1 &= t\partial_t + \alpha x\partial_x, & X_2 &= \sqrt{x}\partial_x, & X_3 &= \partial_t, & X_4 &= \partial_u, \\ X_\infty &= h(t, x)\partial_u, \end{aligned} \tag{1.108}$$

with h being an arbitrary solution of (1.107).

The corresponding invariant solution for generator $X = X_2 + X_4$ has the form

$$u(t, x) = \frac{1}{2} e^{2\sqrt{x}} \sum_{k=0}^{q-1} \left\{ E_t \left(-k\frac{\alpha}{2}, 1 \right) - (-1)^{q-k-1} E_t \left(-k\frac{\alpha}{2}, (-1)^q \right) \right\}, \tag{1.109}$$

where function E_t is defined by

$$E_t(a, b) = t^a \sum_{k=0}^{\infty} \frac{(bt)^k}{\Gamma(a + k + 1)}. \tag{1.110}$$

- **Subcase 2:** If $\lambda = \frac{3}{2}$, the Lie algebra is spanned by X_1, X_3, X_4, X_∞ , and the infinitesimal generator X_5 given by

$$X_5 = \sqrt{x}\partial_x - \frac{1}{2\sqrt{x}}u\partial_u. \tag{1.111}$$

The corresponding invariant solution for generator X_5 is given by

$$u(t, x) = \frac{ct^{\alpha-1}}{\sqrt{x}}, \tag{1.112}$$

with c being an arbitrary constant.

- **Subcase 3:** Therefore, if the drift does not belong to $\{\frac{1}{2}, \frac{2}{3}\}$, the only possible symmetries are X_1, X_3, X_4 , and X_∞ .

Case 2: If $f(x) = \frac{1 + 3\sqrt{x}}{2(1 + \sqrt{x})}$, the symmetry algebra admitted by (1.107) is spanned by X_3, X_4, X_∞ , and the infinitesimal generators

$$X_6 = t\partial_t + \alpha x\partial_x + \frac{\alpha}{2(\sqrt{x} + 1)}u\partial_u, \quad X_7 = \sqrt{x}\partial_x - \frac{1}{2(\sqrt{x} + 1)}u\partial_u. \quad (1.113)$$

The corresponding invariant solution for the generator X_7 is

$$u(t, x) = \frac{c}{\sqrt{x} + 1}t^{\alpha-1}, \quad (1.114)$$

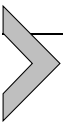
with c being an arbitrary constant.

By using the continuous symmetry group generated by X_6 ,

$$G_6 : (t, x, u) \mapsto \left(e^{\alpha\epsilon}x, e^\epsilon t, \frac{\sqrt{x} + 1}{\sqrt{x} + e^{-\frac{\alpha}{2}\epsilon}}u \right), \quad (1.115)$$

and if $u = u(t, x)$ is a solution of Eq. (1.107), we can derive a new exact solution of (1.107) which is defined by

$$G_6 \cdot u(t, x) = \frac{\sqrt{x} + e^{\frac{\alpha}{2}\epsilon}}{\sqrt{x} + 1}u(e^{-\epsilon}t, e^{-\alpha\epsilon}x). \quad (1.116)$$



1.4. Discrete symmetry for fractional Harry Dym equation

We consider the fractional Harry Dym equation [15]

$$D_t^\alpha u(x, t) = u^3 u_{xxx}, \quad 0 < \alpha < 1. \quad (1.117)$$

This equation has a 4D Lie algebra \mathfrak{g} of continuous symmetry [15]. The basis of \mathfrak{g} is spanned by the generators

$$X_1 = \partial_x, \quad X_2 = x\partial_x + u\partial_u, \quad X_3 = t\partial_t - \frac{\alpha u}{3}\partial_u, \quad X_4 = x^2\partial_x + 2xu\partial_u. \quad (1.118)$$

The following nonzero structure constants c_{ij}^k are

$$c_{12}^1 = -c_{21}^1 = 1, \quad c_{14}^2 = -c_{41}^2 = 2, \quad c_{24}^4 = -c_{42}^4 = 1. \tag{1.119}$$

By using the matrices $C(j)$, we obtain

$$A(1; \epsilon_1) = \begin{pmatrix} 1 & 0 & 0 & 0 \\ -\epsilon & 1 & 0 & 0 \\ 0 & 0 & 1 & 0 \\ \epsilon^2 & -2\epsilon & 0 & 1 \end{pmatrix}, \quad A(2; \epsilon_2) = \begin{pmatrix} e^\epsilon & 0 & 0 & 0 \\ 0 & 1 & 0 & 0 \\ 0 & 0 & 1 & 0 \\ 0 & 0 & 0 & e^{-\epsilon} \end{pmatrix},$$

$$A(3; \epsilon_3) = \begin{pmatrix} 1 & 2\epsilon & 0 & \epsilon^2 \\ 0 & 1 & 0 & \epsilon \\ 0 & 0 & 1 & 0 \\ 0 & 0 & 0 & 1 \end{pmatrix}.$$

The nonlinear constraints of (1.117) are presented in Table 1.3.

Table 1.3 Nonlinear constraints (1.27) for fractional Harry Dym equation (1.117).

(i, j)	$n = 1$	$n = 2$	$n = 3$	$n = 4$
(1,2)	$b_1^1 b_2^2 - b_1^2 b_2^1 = b_1^1$	$2(b_1^1 b_2^4 - b_1^4 b_2^1) = b_1^2$	$b_1^3 = 0$	$b_1^2 b_4^4 - b_1^4 b_2^2 = b_1^4$
(1,3)	$b_1^1 b_3^3 - b_1^3 b_3^1 = 0$	$b_1^1 b_3^4 - b_1^4 b_3^1 = 0$	-	$b_1^2 b_3^4 - b_1^4 b_3^2 = 0$
(1,4)	$b_1^1 b_4^4 - b_1^4 b_4^1 = 2b_1^2$	$b_1^1 b_4^4 - b_1^4 b_4^1 = b_2^2$	$b_2^3 = 0$	$b_1^2 b_4^4 - b_1^4 b_2^2 = 2b_2^4$
(2,3)	$b_2^1 b_3^3 - b_2^3 b_3^1 = 0$	$b_2^1 b_3^4 - b_2^4 b_3^1 = 0$	-	$b_2^2 b_3^4 - b_2^4 b_3^2 = 0$
(2,4)	$b_2^1 b_4^4 - b_2^4 b_4^1 = b_4^1$	$2(b_2^1 b_4^4 - b_2^4 b_4^1) = b_4^2$	$b_4^3 = 0$	$b_2^2 b_4^4 - b_2^4 b_2^2 = b_4^4$
(3,4)	$b_3^1 b_4^4 - b_3^4 b_4^1 = 0$	$b_3^1 b_4^4 - b_3^4 b_4^1 = 0$	-	$b_3^2 b_4^4 - b_3^4 b_4^2 = 0$

After solving these constraints and using the adjoint matrices to factor out the Lie symmetries, so far, we have been able to simplify B to the following:

$$B_1 = \begin{pmatrix} b_1^1 & b_2^1 & 0 & \frac{(b_1^2)^2}{4b_1^1} \\ 0 & 1 & 0 & \frac{1}{2b_1^1} \\ 0 & 0 & b_3^3 & 0 \\ 0 & 0 & 0 & \frac{1}{b_1^1} \end{pmatrix}, \quad B_2 = \begin{pmatrix} 0 & 0 & 0 & b_1^4 \\ 0 & -1 & 0 & \frac{-b_1^4 b_4^2}{2} \\ 0 & 0 & b_3^3 & 0 \\ \frac{1}{b_1^4} & b_4^2 & 0 & \frac{b_1^4 (b_4^2)^2}{4} \end{pmatrix}. \tag{1.120}$$

The remaining three equivalence transformations can be used to make two more simplifications where $A(1; \epsilon_1)B_1$ with $\epsilon_1 = 2/(b_1^2)^2$ gives

$$B_{1,1} = \begin{pmatrix} b_1^1 & b_1^2 & 0 & \frac{(b_1^2)^2}{4b_1^1} \\ 0 & 1 & 0 & 0 \\ 0 & 0 & b_3^3 & 0 \\ 0 & 0 & 0 & \frac{1}{b_1^1} \end{pmatrix}, \quad (1.121)$$

$A(2; \epsilon_2)B_1$ with $\epsilon_2 = -\ln|b_1^1|$ gives

$$B_{1,2} = \begin{pmatrix} \lambda & b_1^2 & 0 & \frac{(b_1^2)^2}{4\lambda} \\ 0 & 1 & 0 & 0 \\ 0 & 0 & b_3^3 & 0 \\ 0 & 0 & 0 & \lambda \end{pmatrix}, \quad \text{where } \lambda \in \{-1, +1\}, \quad (1.122)$$

and finally, $A(3; \epsilon_3)B_{1,2}$ with $\epsilon_3 = -b_1^2/2$ gives

$$B_{1,3} = \begin{pmatrix} \lambda & 0 & 0 & 0 \\ 0 & 1 & 0 & 0 \\ 0 & 0 & b_3^3 & 0 \\ 0 & 0 & 0 & \lambda \end{pmatrix}, \quad \text{with } \lambda \in \{-1, +1\}. \quad (1.123)$$

We also need to consider the case B_2 and in the same manner we obtain another simplified matrix B_2 but it is singular since its determinant is equal to zero. Therefore, the simplified matrix to be used with the Lie symmetry algebra (1.118) is given by B_1 .

In order to keep the fractional derivative unchanged, we must consider that $b_3^3 = 1$. The determining equations for the discrete symmetries are given by the system

$$\begin{pmatrix} X_1\tilde{x} & X_1\tilde{t} & X_1\tilde{u} \\ X_2\tilde{x} & X_2\tilde{t} & X_2\tilde{u} \\ X_3\tilde{x} & X_3\tilde{t} & X_3\tilde{u} \\ X_4\tilde{x} & X_4\tilde{t} & X_4\tilde{u} \end{pmatrix} = B_1 \begin{pmatrix} 1 & 0 & 0 \\ \tilde{x} & 0 & \tilde{u} \\ 0 & \tilde{t} & \frac{-\alpha}{3}\tilde{u} \\ \tilde{x}^2 & 0 & 2\tilde{x}\tilde{u} \end{pmatrix} = \begin{pmatrix} \lambda & 0 & 0 \\ \tilde{x} & 0 & \tilde{u} \\ 0 & \tilde{t} & \frac{-\alpha}{3}\tilde{u} \\ \lambda\tilde{x}^2 & 0 & 2\lambda\tilde{x}\tilde{u} \end{pmatrix}. \quad (1.124)$$

The solution of the previous system is given by

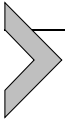
$$\tilde{x} = \lambda x, \quad \tilde{t} = t, \quad \tilde{u} = cu, \quad (1.125)$$

with c being an arbitrary nonzero constant. Substituting (1.125) into the fractional Harry Dym equation (1.117), we find that $c = \lambda$ is required for

the symmetry condition to be satisfied. Consequently, the discrete symmetry groups are

$$\Gamma_1 : (x, t, u) \mapsto (x, t, u), \quad \Gamma_2 : (x, t, u) \mapsto (-x, t, -u). \quad (1.126)$$

Similarly, we can use its discrete symmetry groups to build solutions of the fractional Harry Dym equation from the solutions found in [1].



1.5. Conclusion

During the last two decades, fractional calculus has increasingly been used in practice for modeling systems with memory and spatial nonlocality. Finding exact solutions of FODEs and FPDEs is a challenging problem, especially for nonlinear problems. On the other hand, the Lie symmetry method has been developed considerably and it is the most important approach for constructing analytical solutions of ODEs, PDEs, and recently FODEs and FPDEs.

The purpose of this chapter is to present continuous and discrete symmetries for ODEs, PDEs, FODEs, and FPDEs. We restrict our attention to FDEs with the Riemann–Liouville and Caputo fractional derivatives since these derivatives are the most commonly used in practice. Using symmetry analysis techniques, some exact solutions are constructed for different equations.

Finally, we hope that this chapter will be useful to researchers concerned with fractional calculus and Lie symmetry analysis.

References

- [1] C. Baishya, R. Rangarajan, A new application of G'/G -expansion method for travelling wave solutions of fractional PDEs, *Int. J. Eng. Res. Appl.* 13 (11) (2018) 9936–9942.
- [2] T. Bakkyaraj, R. Sahadevan, Group formalism of Lie transformations to time-fractional partial differential equations, *Pramana J. Phys.* 85 (2015) 849–860.
- [3] T. Bakkyaraj, R. Sahadevan, Invariant analysis of nonlinear fractional ordinary differential equations with Riemann–Liouville fractional derivative, *Nonlinear Dyn.* 80 (2015) 447–455.
- [4] F. Black, M. Scholes, The pricing of options and corporate liabilities, *J. Polit. Econ.* 81 (3) (1973) 637–654.
- [5] G.W. Bluman, S. Anco, *Symmetry and Integration Methods for Differential Equations*, Springer-Verlag, New York, 2002.
- [6] C.J. Budd, G.J. Collins, An invariant moving mesh scheme for the nonlinear diffusion equation, *Appl. Numer. Math.* 26 (1–2) (1998) 23–39.
- [7] Y. Chatibi, E.H. El Kinani, A. Ouhadan, On the discrete symmetry analysis of some classical and fractional differential equations, *Math. Methods Appl. Sci.* (2019) 1–11.

- [8] Y. Chatibi, E.H. El Kinani, A. Ouhadan, Lie symmetry analysis and conservation laws for the time fractional Black–Scholes equation, *Int. J. Geom. Methods Mod. Phys.* 17 (1) (2020) 2050010.
- [9] M. Craddock, E. Platen, Symmetry group methods for fundamental solutions, *J. Differ. Equ.* 207 (2004) 285–302.
- [10] S. Das, *Functional Fractional Calculus for System Identification and Controls*, Springer-Verlag, Berlin Heidelberg, 2008.
- [11] R.K. Gazizov, N.H. Ibragimov, Lie symmetry analysis of differential equations in finance, *Nonlinear Dyn.* 17 (1998) 387–407.
- [12] R.K. Gazizov, A.A. Kasatkin, S.Y. Lukashchuk, Continuous transformation groups of fractional differential equations, *Vestnik USATU* 9 (2007) 125–135.
- [13] R.K. Gazizov, A.A. Kasatkin, S.Y. Lukashchuk, Symmetry properties of fractional diffusion equations, *Phys. Scr.* 136 (2009) 014016.
- [14] I. Hilfer, *Applications of Fractional Calculus in Physics*, World Scientific Publishing Company, Singapore, 2000.
- [15] Q. Huang, R. Zhdanov, Symmetries and exact solutions of the time fractional Harry–Dym equation with Riemann–Liouville derivative, *Physica A: Stat. Mech. Appl.* 409 (2014) 110–118.
- [16] P.E. Hydon, *Symmetry Methods for Differential Equations*, Cambridge University Press, Cambridge, 2000.
- [17] N.H. Ibragimov, *CRC Handbook of Lie Group Analysis of Differential Equations: Symmetries, Exact Solutions and Conservation Laws*, CRC Press, Boca Raton, 1994.
- [18] A.A. Kilbas, H.M. Srivastava, J.J. Trujillo, *Theory and Applications of Fractional Differential Equations*, North Holland Mathematics Studies, vol. 204, Elsevier, Amsterdam, 2006.
- [19] M. Kruskal, Nonlinear wave equations, in: Jürgen Moser (Ed.), *Dynamical Systems, Theory and Applications*, in: *Lecture Notes in Physics*, vol. 38, Springer-Verlag, New York, 1975.
- [20] R.A. Leo, G. Sicuro, P. Tempesta, A theorem on the existence of symmetries of fractional PDEs, *C. R. Acad. Sci. Paris Ser. I* 352 (3) (2014) 219–222.
- [21] S. Lie, Theorie der Transformationsgruppen I, *Math. Ann.* 16 (1880) 441–528.
- [22] K. Oldham, J. Spanier, *The Fractional Calculus Theory and Applications of Differentiation and Integration to Arbitrary Order*, Academic Press, New York, 1974.
- [23] P.J. Olver, *Application of Lie Groups to Differential Equations*, Cambridge University Press, New York, 1986.
- [24] A. Ouhadan, E.H. El Kinani, Lie symmetries of the equation $u_t(x, t) + g(u)u_x(x, t) = 0$, *Adv. Appl. Clifford Algebras* 17 (1) (2007) 95–106.
- [25] A. Ouhadan, E.H. El Kinani, Lie symmetries analysis of the Shallow Water equations, *Appl. Math. E-Notes* 9 (2009) 281–288.
- [26] A. Ouhadan, E.H. El Kinani, Invariant subspace method and some exact solutions of time fractional modified Kuramoto–Sivashinsky equation, *Br. J. Math. Comput. Sci.* 15 (4) (2013) 1–10.
- [27] A. Ouhadan, E.H. El Kinani, Exact solution of time fractional Kolmogorov equation by using Lie symmetry analysis, *J. Fract. Calc. Appl.* 5 (2014) 97–104.
- [28] A. Ouhadan, E.H. El Kinani, Lie symmetry analysis of some time fractional partial differential equations, *Int. J. Mod. Phys. Conf. Ser.* 38 (2015) 1560075.
- [29] L.V. Ovsiannikov, *Group Analysis of Differential Equations*, Academic Press, New York, 1982.
- [30] I. Podlubny, *Fractional Differential Equations*, Academic Press, San Diego, 1999.
- [31] S.G. Samko, A.A. Kilbas, O.I. Marichev, *Fractional Integrals and Derivatives: Theory and Applications*, Gordon and Breach Science Publishers, Yverdon, 1993.
- [32] G. Silberberg, Discrete symmetries of the Black–Scholes equation, in: *Proceedings of 10th International Conference in Modern Group Analysis*, 2005, pp. 190–197.

- [33] W.H. Steeb, *Continuous Symmetries, Lie Algebras, Differential Equations and Computer Algebra*, World Scientific Publishing Company, Singapore, 2007.
- [34] H. Stephani, *Differential Equations and Their Solutions Using Symmetries*, Cambridge University Press, Cambridge, 1989.
- [35] A.M. Wazwaz, Exact solutions to nonlinear diffusion equations obtained by the decomposition method, *Appl. Math. Comput.* 123 (2001) 109–122.
- [36] W. Wyss, The fractional Black-Scholes equation, *Fract. Calc. Appl. Anal.* 3 (1) (2000) 51–61.

This page intentionally left blank

Some theoretical and computation results about COVID-19 by using a fractional-order mathematical model

Muhammad Arfan, Kamal Shah, and Aman Ullah

Department of Mathematics, University of Malakand, Chakdara, Dir(L), Khyber Pakhtunkhwa, Pakistan

2.1. Introduction

Presently the whole globe is facing a pandemic of COVID-19, which originates from Wuhan, a large city in China. Between December 2019 and 18 July 2020, 0.59 million people died due to the mentioned disease, and 13.81 million have had the infection all over the world. Also 7.72 million infected people have recovered from the disease, according to the WHO [1]. The death-to-recovery ratio is different in different countries and depends on the health situation of the people of the respective areas. Different researchers and policy makers are struggling to control the disease from further spreading. One big factor influencing the spread of this disease is migration of infected people, which affect more people and hence spread this disease. Therefore, on an international level, many countries have banned air traffic for some time, and they have also announced lockdown in cities to reduce loss of human lives. Also, each country tries to reduce unnecessary traveling of people and to reduce the number of new cases of infection [2,3]. It is remarkable that such outbreaks in the past have caused the death of millions of people around the globe. Researchers are trying to develop a cure or a vaccine so that the pandemic may be controlled in the future.

During March and April of 2020, Italy, Iran, and Spain reported the highest numbers of COVID-19 cases. Recently, the USA, the UK, Russia, Brazil, and India became the top countries with most COVID-19 cases. Currently, the disease is spreading at a very high rate all over the world.

During March, April, May, and June 2020, various countries implemented lockdowns. Some countries, like Saudi Arabia, UAE, and Qatar, announced curfew, but the infection is still spreading at high rates in these countries. Researchers and medical specialists are working day and night to prepare a vaccine. The economical situation of many countries in the world is very bad. A large numbers of companies and organizations have been stopped production. As a result, millions of people have lost their jobs. Therefore, poverty and unemployment have greatly increased in various countries. Moreover, the healthcare systems of some of the most powerful countries, like the USA, European countries, Middle Eastern countries, and some South Asian countries like India and Pakistan, have collapsed due to COVID-19. In short, the world is facing a severe situation. Throughout human history, such outbreaks have occurred, and millions of people lost their lives. During the Spanish flu outbreak in 1920, nearly 10 million people died worldwide. Such outbreak again appeared during the 1970s, killing 50 million people in Europe and North and South America. In 2003 and 2008, SARS and MARS, two serious infectious diseases, broke out. But these diseases did not result in global pandemics. Moreover, cures were introduced, and these controlled the spread of the diseases.

COVID-19 is an infectious disease caused by severe acute respiratory syndrome coronavirus 2 (SARS-CoV-2). Fever, cough, fatigue, shortness of breath, and loss of smell and taste are common symptoms of the disease. However, in some people the symptoms do not appear clearly. Such people are silent spreaders of the disease. Since the infection is transmitted from person to person, silent spreaders transmit it easily. Therefore, many countries have advised their public to keep social distance and avoid gathering and other social activities where many people are crowding. The duration from exposure to onset of symptoms is typically around 5 days, but may range from 2 to 14 days. Basically, the virus spreads between people during close contact and via small droplets released by coughing, sneezing, and talking. Various methods are adopted to cure infected people. Also some precautionary measures are taken, including frequent hand washing, maintaining social distance (especially from people with symptoms), quarantine (especially people with symptoms), covering coughs, and avoiding to touch one's face without washing hands (for details see [3,4]).

From a medical engineering point of view, infectious diseases can be well understood by using mathematical models. This concept was started during in 1927. Since then, various mathematical models have been estab-

lished for different diseases. For some famous studies, we refer to [5–8] and the papers cited therein.

Researchers have investigated COVID-19 from several points of view (for details see [9–12]). Mathematical models can help us understand and construct disease control strategies and establish precautionary measures. In this regard, some SARS-CoV-2 models have been studied (for details see [13]). Since the infection is rapidly transmitted from person to person, people are advised to keep social distance. Some authors have considered the effects of migration on the transmission dynamics of this disease by considering a modified version of the susceptible–infected (SI) model [14] given by

$$\begin{aligned}\dot{\mathcal{H}} &= a\mathcal{H}(t) - b\mathcal{H}(t)\mathcal{I}(t) + e\mathcal{H}(t), \\ \dot{\mathcal{I}} &= b\mathcal{H}(t)\mathcal{I}(t) + (c - d - e)\mathcal{I}(t), \\ \mathcal{H}(0) &= \mathcal{H}_0, \quad \mathcal{I}(0) = \mathcal{I}_0.\end{aligned}\tag{2.1}$$

The mathematical models that we use in this chapter are inspired by the SI model [15,16] for analyzing computational dynamics. The classic model has been suitably modified to build the healthy–infected individual population dynamics model. The healthy individual population is given by $\mathcal{H}(t)$ at time t . The infected individual population is given by $\mathcal{I}(t)$ at time t . The infection rate is given by $b = (1 - \textit{protectionrate})$. The migration rate of healthy individuals is given by a . The migration rate of infected individuals is given by c . The collective death rate (natural+ due to corona) is given by d and the cure rate is given by e . This model is just an indication to see what happens in a community if migration of individuals is not controlled.

Keeping in mind the aforementioned points, we are going to study the model given in (2.1) for fractional order derivative with $0 < \sigma \leq 1$ as given by

$$\begin{aligned}\mathcal{D}^\sigma \mathcal{H}(t) &= a\mathcal{H}(t) - b\mathcal{H}(t)\mathcal{I}(t) + e\mathcal{H}(t), \\ \mathcal{D}^\sigma \mathcal{I}(t) &= b\mathcal{H}(t)\mathcal{I}(t) + (c - d - e)\mathcal{I}(t), \\ \mathcal{H}(0) &= \mathcal{H}_0 > 0, \quad \mathcal{I}(0) = \mathcal{I}_0,\end{aligned}\tag{2.2}$$

where $\mathcal{H}_0 > 0$ and $\mathcal{I}_0 \geq 0$ are the initial values for healthy and infected class population density in percent. In the last few years, the concepts of modern calculus of fractional differentials and integrals have attracted much interest of researchers, because of the realistic applications of modern calculus, producing precise and accurate output in many applied and medical fields,

regarding various phenomena. Arbitrary-order differential and antidifferential operators are generally global operators which involve global problems. Due to this, the mentioned calculus has received more interest, and many articles from different areas touch the aforesaid fields [17–20]. Such fields have been analyzed for various aspects like existence and uniqueness of approximate solutions. In this regard a lot of papers, and monographs are available in the current literature.

It should be kept in mind that classical calculus and differential equations (DEs) have been extended to many fields of pure and applied mathematics; for example, classical calculus has been extended to modern calculus and fuzzy calculus. Similarly, DEs have been extended to fractional-order DEs (FODEs) and FODEs have been extended to fuzzy fractional differential equations. Different problems in our daily life have been formulated by DEs and systems of DEs, and models of individual small organisms and large animals have been described using computative models, SIR, SEIR, etc. Most of the models in the beginning were of natural or integer order, so scientists have extended the integer-order models to any real order models. Such models are well comparable with integer-order models but more reliable with respect to output [21–24]. FODEs have been studied by many authors for existence theory of solutions [25–27]. For this, various researchers applied basic theories like “topological degree theory,” “Banach contraction,” and Leray–Schauder fixed point theory” [28].

Keeping in mind the above discussed points, we are now going to study the system taken in (2.2) for fuzzy arbitrary-order derivative where uncertainty lies in initial data with fractional order $0 < \sigma \leq 1$ as given by

$$\begin{cases} {}^c\mathcal{D}_t^\sigma(\tilde{u}(t)) = a\tilde{u}(t) - b\tilde{u}(t)\tilde{v}(t) + e\tilde{u}(t), \\ {}^c\mathcal{D}_t^\sigma(\tilde{v}(t)) = b\tilde{u}(t)\tilde{v}(t) + (c - d - e)\tilde{v}(t), \\ \tilde{u}(0) = \tilde{u}_0 = (\underline{u}_0, \bar{u}_0), \quad \tilde{v}(0) = \tilde{v}_0 = (\underline{v}_0, \bar{v}_0), \end{cases} \quad (2.3)$$

where \tilde{u}_0 and \tilde{v}_0 are the initial values for healthy and infected population density in fuzzy form.

One of the extensions we make here is to extend FODEs to the area in which fuzziness lies in some output results such as natural and physical sciences. For this, Zadeh [29] defined fuzzy concepts about set theory in 1965. It is obvious that the ideas of fuzziness have been used in a variety of areas, including fixed point theory of fuzziness, topological fuzziness, fuzziness in control systems, etc. Chang and Zadeh [30] extended the notion of fuzzy set to provide a definition about fuzzy mapping and control. Upon

fuzzy function and control, many scholars generalized such aspects to define new calculus for basic fuzziness [31–33]. Since the beginning of the 21st century, fuzzy arbitrary-order differential and antidifferential equations have got significant attention in the area of physical fields. Dobius and Prada defined the basic concept of fuzzy antidifferential equations [34]. Therefore, where data imprecision or vagueness occurs, the fuzzy concept is better to describe the parameters instead of the crisp number. Hence fuzzy calculus of differentiation and integration plays a central role in modeling such processes. This area has received much attention recently.

Fuzzy integral equations have much more applications due to many practical problems in industrial engineering, computer science, physics, and artificial intelligence. Also operations research may be converted to uncertain process problems of fractional order. They have great significance in the fuzzy analysis theory and its applications in fuzzy control models, artificial intelligence, quantum optics, measure theory, and atmosphere studies [35–38]. In a few cases, results about real-life problems, which are always pervaded with uncertainty, are included. This uncertainty results from several factors, such as measurement errors, deficient data, or the determination of constraint conditions. The Volterra integro-differential equations under uncertainty concerned with fractional derivatives are simply generalizations of classical forms, which have various uses in physics and engineering.

Partial differential equations (PDEs) have significant applications in modeling of many real-world problems like heat transfer problems, propagation of sound in wave form, water waves, tidal energy, etc. (see [39–41]). The concerned area has been further extended to fractional calculus and many fruitful results have been established in the literature. For some applications of kinds of PDEs under the concept of fractional calculus, we refer to [42,43]. Further, fuzzy fractional-order PDEs have many applications in dynamical systems, nonlinear propagation of traveling waves, damped nonlinear strings, electronics, telecommunications, etc. For more details about the applications, we refer to [44–46].

Therefore, we investigated the effects of different migration values on the transmission dynamics of the current pandemic. We obtained the output results for parameter values of migration rates present in model (2.2) and (2.3) applying a fractional order, predicting future transmission.

Significant work has been performed to investigate and mathematically model COVID-19. Very detailed contributions have been provided by different researchers in this regard. In the present study, we considered a simple

model under the concept of fractional calculus by involving migration type parameters. This model indicates the effects of increasing the values of some parameters or reducing its margin on the transmission dynamics of the disease and its control. Furthermore, we have also investigated the model under uncertainty, i.e., a fuzzy concept, and we evaluated the model using fuzzy Laplace transform. The results are presented graphically for various orders using both the classical model and the fuzzy concept.



2.2. Background materials

Here, we recall some definition from [18,47].

Definition 2.2.1. For a function $\mathcal{H}(t)$ we define the fractional integral corresponding to t as

$$\mathcal{I}_t^\sigma \mathcal{H}(t) = \frac{1}{\Gamma(\sigma)} \int_0^t (t - \eta)^{\sigma-1} d\eta, \quad \sigma > 0,$$

such that the integral on the right-hand side exists.

Definition 2.2.2. [44,47] Let us take a continuous fuzzy mapping \tilde{u} on some interval $[0, c] \subset \mathbb{R}$. We formulate the arbitrary-order antiderivative in fuzzy form with respect to t in the ‘‘Riemann–Liouville’’ sense given as

$$\mathbf{I}^\sigma \tilde{u}(t) = \frac{1}{\Gamma(\sigma)} \int_0^t (t - \eta)^{\sigma-1} \tilde{u}(\eta) d\eta, \quad \sigma, \eta \in (0, \infty).$$

Next, if $\tilde{u} \in \text{interval}C^F[0, c] \cap L^F[0, c]$, where $C^F[0, b]$ is the space of continuous mappings in fuzzy form and $L^F[0, c]$ is the space of ‘‘Lebesgue integrable functions’’ in fuzzy form, then the arbitrary antiderivative in fuzzy form is given as

$$[\mathbf{I}^\sigma \tilde{u}(t)]_p = [\mathbf{I}^\sigma \underline{u}_p(t), \mathbf{I}^\sigma \bar{u}_p(t)], \quad 0 \leq p \leq 1,$$

such that

$$\begin{aligned} \mathbf{I}^\sigma \underline{u}_p(t) &= \int_0^t \frac{(t - \eta)^{\sigma-1} \underline{u}_p(\eta)}{\Gamma(\sigma)} d\eta, \quad \sigma, \eta \in (0, \infty), \\ \mathbf{I}^\sigma \bar{u}_p(t) &= \int_0^t \frac{(t - \eta)^{\sigma-1} \bar{u}_p(\eta)}{\Gamma(\sigma)} d\eta, \quad \sigma, \eta \in (0, \infty). \end{aligned}$$

Definition 2.2.3. For a function $\mathcal{H}(t)$, we define the Caputo fractional derivative corresponding to t as

$$\mathcal{D}^\sigma \mathcal{H}(t) = \frac{1}{\Gamma(n-\sigma)} \int_0^t (t-\eta)^{n-\sigma-1} [\mathcal{H}^{(n)}(\eta)] d\eta, \quad \sigma > 0,$$

with the right-hand side being pointwise defined on \mathbf{R}^+ and $n = [\sigma] + 1$. If $\sigma \in (0, 1]$, then one has

$$\mathcal{D}^\sigma \mathcal{H}(t) = \frac{1}{\Gamma(1-\sigma)} \int_0^t (t-\eta)^{-\sigma} [\mathcal{H}^{(1)}(\eta)] d\eta.$$

Definition 2.2.4. [44,47] In the same sense for a mapping $\tilde{u} \in C^F[0, c] \cap L^F[0, c]$, such that $\tilde{u} = [\underline{u}_p(t), \bar{u}_p(t)]$, $0 \leq p \leq 1$ and $t_0 \in (0, c)$, then the ‘‘Caputo fractional derivative’’ is given as

$$[\mathcal{D}^\sigma \tilde{u}(t_0)]_p = [\mathcal{D}^\sigma \underline{u}_p(t_0), \mathcal{D}^\sigma \bar{u}_p(t_0)], \quad 0 < \sigma \leq 1,$$

where

$$\begin{aligned} \mathcal{D}^\sigma \underline{u}_p(t_0) &= \frac{1}{\Gamma(n-\sigma)} \left[\int_0^t (t-\eta)^{n-\sigma-1} \frac{d^n}{d\eta^n} \underline{u}_p(\eta) d\eta \right]_{t=t_0}, \\ \mathcal{D}^\sigma \bar{u}_p(t_0) &= \frac{1}{\Gamma(n-\sigma)} \left[\int_0^t (t-\eta)^{n-\sigma-1} \frac{d^n}{d\eta^n} \bar{u}_p(\eta) d\eta \right]_{t=t_0}. \end{aligned}$$

The antiderivative on the right-hand sides exists and $n = [\sigma]$. As $\sigma \in (0, 1]$, $n = 1$.

Lemma 2.2.5. [18] *The solution of*

$$\mathcal{D}^\sigma \mathcal{H}(t) = h(t), \quad 0 < \sigma \leq 1,$$

is given by

$$\mathcal{H}(t) = c_0 + \frac{1}{\Gamma(1-\sigma)} \int_0^t h(\eta)(t-\eta)^{\sigma-1} d\eta.$$

Lemma 2.2.6. [18] *The Laplace transform of $\mathcal{D}^\sigma \mathcal{H}(t)$ for $0 < \sigma \leq 1$ is provided by*

$$\mathcal{L} \left[\mathcal{D}^\sigma \mathcal{H}(t) \right] = s^\sigma \mathcal{L}[\mathcal{H}(t)] - s^{\sigma-1} \mathcal{H}(0).$$

Lemma 2.2.7. [44,48,49] The “Laplace transform” to a fuzzy mapping of $\frac{{}^c d^\gamma \tilde{u}(t)}{dt^\gamma}$ for $0 < \gamma \leq 1$ is given as

$$\mathcal{L} \left[\frac{{}^c d^\gamma \tilde{u}(t)}{dt^\gamma} \right] = s^\gamma \mathcal{L}[\tilde{u}(t)] - s^{\gamma-1}[\tilde{u}(0)].$$

Definition 2.2.8. [44,48,49] A “fuzzy number” is a mapping $P : \mathfrak{R} \rightarrow [0, 1]$ if it obeys the following conditions:

- (i) P will be “upper semicontinuous”;
- (ii) $P\{\mu(u_1) + \mu(u_2)\} \geq \min\{P(u_1), P(u_2)\}$;
- (iii) $\exists u_0 \in \mathfrak{R}$ such that $P(u_0) = 1$, i.e., P is “normal”;
- (iv) $cl\{u \in \mathfrak{R}, P(u) > 0\}$ is “compact.”

Here we denote the set of all fuzzy numbers by E .

Definition 2.2.9. [44,48,49] The “parametric form” of a fuzzy number can be written in the form of order pair as

$$[\underline{P}(\theta), \overline{P}(\theta)], \quad \text{such that } 0 \leq \theta \leq 1$$

and satisfying following conditions:

- (i) $\underline{P}(\theta)$ is a left continuous, bounded, and increasing function over $(0, 1]$ and right continuous at 0;
- (ii) $\overline{P}(\theta)$ is a right continuous, bounded decreasing function over $[0, 1]$ and right continuous at 0;
- (iii) $\underline{P}(\theta) \leq \overline{P}(\theta)$.

Here, θ is called the “crisp number” if $\underline{P}(\theta) = \overline{P}(\theta) = \theta$.

Let E denote the set of “upper semicontinuous,” “convex,” and “normal fuzzy numbers” with bounded θ -level interval. If $v \in E$, then the θ -level set

$$[v]^\theta = \{t : v(t) \geq \theta\}, \quad 0 \leq \theta \leq 1,$$

whose bounded and closed interval is represented by

$$[v]^\theta = [\underline{v}(\theta), \overline{v}(\theta)].$$

For arbitrary fuzzy number

$$v = (\underline{v}(\theta), \overline{v}(\theta)), \quad \omega = (\underline{\omega}(\theta), \overline{\omega}(\theta)),$$

and for $\kappa_1 \geq 0$, various operations are defined as follows:

- (i) Addition: $(\underline{v}(\theta) + \underline{\omega}(\theta), \overline{v}(\theta) + \overline{\omega}(\theta)) = (\underline{v}(\theta) + \underline{\omega}(\theta), \overline{v}(\theta) + \overline{\omega}(\theta))$.
- (ii) Subtraction: $(\underline{v}(\theta) - \underline{\omega}(\theta), \overline{v}(\theta) - \overline{\omega}(\theta)) = (\underline{v}(\theta) - \underline{\omega}(\theta), \overline{v}(\theta) - \overline{\omega}(\theta))$.
- (iii) Scalar multiplication: $\kappa_1 \cdot v(\theta) = \begin{cases} (\kappa_1 \underline{v}(\theta), \kappa_1 \overline{v}(\theta)), & \kappa_1 \geq 0, \\ (\kappa_1 \overline{v}(\theta), \kappa_1 \underline{v}(\theta)), & \kappa_1 < 0. \end{cases}$

Definition 2.2.10. [44] Let $D_1 : E \times E \rightarrow R_+ \cup \{0\}$ be a mapping, and let $v = (\underline{v}(\theta), \overline{v}(\theta))$ and $\omega = (\underline{\omega}(\theta), \overline{\omega}(\theta))$ be any two fuzzy numbers in parametric form. Then the ‘‘Hausdorff distance’’ between (v, ω) is measured as

$$D_1(v, \omega) = \sup_{\theta \in [0,1]} \max\{|\underline{v}(\theta) - \underline{\omega}(\theta)|, |\overline{v}(\theta) - \overline{\omega}(\theta)|\}.$$

In E , a metric D_1 as defined above has the following properties (see [44]):

- (i) $D_1(v + v, \omega + v) = D_1(v, \omega)$ for all $v, v, \omega \in E$,
- (ii) $D_1(\kappa_1 \cdot v, \kappa_1 \cdot \omega) = |\kappa_1| D_1(v, \omega)$ for all $\kappa_1 \in R, v, \omega \in E$,
- (iii) $D_1(v + \mu, \omega + v) \leq D_1(v, \omega) + D_1(\mu, v)$ for all $v, \omega, \mu, v \in E$,
- (iv) (E, D_1) is a complete metric space.

Definition 2.2.11. [44] Suppose that $\gamma_1, \gamma_2 \in E$. If there exist $\gamma_3 \in E$ such that

$$\gamma_1 = \gamma_2 + \gamma_3,$$

then γ_3 is said to be the H-difference of γ_1 and γ_2 denoted as $\gamma_1 \ominus \gamma_2$.

Definition 2.2.12. [44,48,49] Consider the fuzzy mapping $h : R \rightarrow E$. Then h is called continuous for any fixed $\gamma_0 \in [\beta_1, \beta_2]$, if for every $\epsilon > 0$, there exist $\delta > 0$ such that $|y - \gamma_0| < \delta$, which implies that

$$D_1(h(y), h(\gamma_0)) < \epsilon.$$

Definition 2.2.13. [48] A levelwise continuous mapping $h : [\beta_1, \beta_2] \subset R \rightarrow E$ is defined at $a \in [\beta_1, \beta_2]$ if the set-valued mapping $h_\theta(y) = [h(y)]^\theta$ is continuous at $y = a$ with respect to the H-metric D_1 for all $\theta \in [0, 1]$.

Theorem 2.2.14. [48] Consider the following:

- (i) $h(y)$ is a levelwise continuous function on $[a, a + \gamma_0]$, $\gamma_0 > 0$;
- (ii) $k(y, s)$ is a levelwise continuous function on $\Delta : a \leq s \leq y \leq a + \gamma_0$ and $D_1(v(y), h(\gamma_0)) < \gamma_1$, where $\gamma_1 > 0$;

(iii) for any $(\gamma, s, \nu(s)), (\gamma, s, \omega(s)) \in \Delta$, we have

$$D_1([k(\gamma, s, \nu(s))]^\theta, [k(\gamma, s, \omega(s))]^\theta) \leq MD_1([\nu(s)]^\theta, [\omega(s)]^\theta),$$

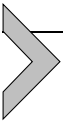
where the constant $M > 0$ is given and for any $\theta \in [0, 1]$.

Then, the levelwise continuous solution $\nu(\gamma)$ exists and is unique for Eq. (2.3) and defined for $\gamma \in (a, a + \theta)$, where $\theta = \min\{\gamma_0, \frac{\gamma_1}{N}\}$, and $N = D_1(k(\gamma, s, \nu(s)), (\gamma, s, \omega(s))) \in \Delta$, where we keep in mind that $\gamma = (u, \nu)$.

Theorem 2.2.15 (Fuzzy convolution theorem). [49] Let ϕ_1 and ϕ_2 be fuzzy γ -valued functions of exponential order $c > 0$, which are piecewise continuous on $[0, \infty)$. Then

$$\mathcal{L}[(\phi_1 * \phi_2)(s)] = \mathcal{L}[\phi_1(s)] \cdot \mathcal{L}[\phi_2(s)], \quad (2.4)$$

where \mathcal{L} represents the integral transform due to Laplace.



2.3. Main work

2.3.1 Qualitative analysis of (2.2)

In this section we discuss “existence and uniqueness” of the arbitrary-order system (2.2). The “existence” of a physical model is discussed by the “fixed point theory” approach. So we will apply the Schauder and Banach fixed point theorems to prove the main results. We consider the arbitrary-order system (2.2) using $\mathcal{U} = \mathcal{H}(t) + \mathcal{I}(t)$. We have

$$\begin{aligned} \mathcal{D}^\sigma \mathcal{U}(t) &= \mathcal{F}(t, \mathcal{U}), \quad 0 < \sigma \leq 1, \\ \mathcal{H}(0) &= \mathcal{H}_0. \end{aligned} \quad (2.5)$$

On using Lemma 2.2.5, Eq. (2.5) is equivalent to the integral equation given by

$$\mathcal{U}(t) = \mathcal{H}_0 + \frac{1}{\Gamma(\sigma)} \int_0^t (t - \eta)^{\sigma-1} \mathcal{F}(\eta, \mathcal{U}(\eta)) d\eta. \quad (2.6)$$

Furthermore, letting $0 \leq t \leq T < \infty$, we define the Banach space by $\mathcal{E}_1 = C[0, T]$ under the norm

$$\|\mathcal{U}\| = \max_{t \in [0, T]} |\mathcal{U}(t)|.$$

To derive the “existence and uniqueness,” we imposed some growth conditions on the nonlinear function as follows:

(A1) There exists a constant $L_{\mathcal{F}} > 0$ such that for each $\mathcal{U}, \bar{\mathcal{U}} \in \mathcal{E}$

$$|\mathcal{F}(t, \mathcal{U}) - \mathcal{F}(t, \bar{\mathcal{U}})| \leq L_{\mathcal{F}}|\mathcal{U} - \bar{\mathcal{U}}|.$$

(A2) There exist constants $C_{\mathcal{F}} > 0$ and $M_{\mathcal{F}} > 0$ such that

$$|\mathcal{F}(t, \mathcal{U}(t))| \leq C_{\mathcal{F}}|\mathcal{U}| + M_{\mathcal{F}}.$$

Theorem 2.3.1. *Under the continuity of \mathcal{F} and with Assumption (A2), problem (2.5) has one or more than one solution.*

Proof. By the Schauder fixed point theorem, we will prove the result. Let us define a closed subset \mathbf{B} of \mathcal{E} as

$$\mathbf{B} = \{\mathcal{U} \in \mathcal{E} : \|\mathcal{U}\| \leq \mathcal{R}, \mathcal{R} > 0\}.$$

We define an operator $\mathbf{T} : \mathbf{B} \rightarrow \mathbf{B}$ by using (2.6) as

$$\mathbf{T}(\mathcal{U}) = \mathcal{U}_0(t) + \frac{1}{\Gamma(\sigma)} \int_0^t (t - \eta)^{\sigma-1} \mathcal{F}(\eta, \mathcal{U}(\eta)) d\eta. \quad (2.7)$$

For any $\mathcal{U} \in \mathbf{B}$, we have

$$\begin{aligned} |\mathbf{T}(\mathcal{U})(t)| &\leq |\mathcal{U}_0| + \frac{1}{\Gamma(\sigma)} \int_0^t (t - \eta)^{\sigma-1} |\mathcal{F}(\eta, \mathcal{U}(\eta))| d\eta \\ &\leq |\mathcal{U}_0| + \frac{1}{\Gamma(\sigma)} \int_0^t (t - \eta)^{\sigma-1} [C_{\mathcal{F}}|\mathcal{U}| + M_{\mathcal{F}}] ds \\ &\leq |\mathcal{U}_0| + \frac{T^\sigma}{\Gamma(\sigma + 1)} [C_{\mathcal{F}}\|\mathcal{U}\| + M_{\mathcal{F}}], \end{aligned}$$

which implies that

$$\begin{aligned} \|\mathbf{T}(\mathcal{U})\| &\leq |\mathcal{U}_0| + \frac{T^\sigma}{\Gamma(\sigma + 1)} [C_{\mathcal{F}}\|\mathcal{U}\| + M_{\mathcal{F}}] \\ &\leq \mathcal{R}. \end{aligned} \quad (2.8)$$

From (2.8), one implies that $\mathcal{U} \in \mathbf{B}$. Thus $\mathbf{T}(\mathbf{B}) \subset \mathbf{B}$. Also this proves that operator \mathbf{T} is “bounded.” For “complete continuity” we proceed as follows.

Let $t_1 < t_2 \in [0, T]$. Then consider

$$\begin{aligned}
 & |\mathbf{T}(\mathcal{U})(t_2) - \mathbf{T}(\mathcal{U})(t_1)| \\
 &= \left| \frac{1}{\Gamma(\sigma)} \int_0^{t_2} (t_2 - \eta)^{\sigma-1} \mathcal{F}(s, \mathcal{U}(\eta)) d\eta - \frac{1}{\Gamma(\sigma)} \int_0^{t_1} (t_1 - \eta)^{\sigma-1} \mathcal{F}(\eta, \mathcal{U}(\eta)) d\eta \right| \\
 &\leq \frac{1}{\Gamma(\sigma)} \left[\int_0^{t_2} (t_2 - \eta)^{\sigma-1} - \int_0^{t_1} (t_1 - \eta)^{\sigma-1} \right] (C_{\mathcal{F}}\mathcal{R} + M_{\mathcal{F}}) d\eta \\
 &\leq \frac{(C_{\mathcal{F}}\mathcal{R} + M_{\mathcal{F}})}{\Gamma(\sigma + 1)} [t_2^\sigma - t_1^\sigma]. \tag{2.9}
 \end{aligned}$$

Now from (2.9), we see that as $t_1 \rightarrow t_2$, the right-hand side also goes to zero. So we see that

$$|\mathbf{T}(\mathcal{U})(t_2) - \mathbf{T}(\mathcal{U})(t_1)| \rightarrow 0, \text{ as } t_1 \rightarrow t_2.$$

Consequently we have

$$\|\mathbf{T}(\mathcal{U})(t_2) - \mathbf{T}(\mathcal{U})(t_1)\| \rightarrow 0, \text{ as } t_1 \rightarrow t_2.$$

Hence \mathbf{T} is an ‘‘equicontinuous’’ operator. By using the Arzela–Ascoli theorem, the operator \mathbf{T} is a ‘‘completely continuous operator’’ and also uniformly bounded, as proved already. By Schauder’s fixed point theorem the given system (2.2) has at least one solution. \square

Next we provide results about the uniqueness of solution.

Theorem 2.3.2. *Under Assumption (A1), the considered system has a unique solution if $\frac{T^\sigma}{\Gamma(\sigma+1)}L_{\mathcal{F}} < 1$.*

Proof. As $\mathbf{T} : \mathcal{E} \rightarrow \mathcal{E}$, defined already, we take \mathcal{U} and $\bar{\mathcal{U}} \in \mathcal{E}$ and consider

$$\begin{aligned}
 \|\mathbf{T}(\mathcal{U}) - \mathbf{T}(\bar{\mathcal{U}})\| &= \max_{t \in [0, T]} \left| \frac{1}{\Gamma(\sigma)} \int_0^t (t - \eta)^{\sigma-1} \mathcal{F}(\eta, \mathcal{U}(\eta)) d\eta \right. \\
 &\quad \left. - \frac{1}{\Gamma(\sigma)} \int_0^t (t - \eta)^{\sigma-1} \mathcal{F}(\eta, \bar{\mathcal{U}}(\eta)) d\eta \right| \\
 &\leq \frac{T^\sigma}{\Gamma(\sigma + 1)} L_{\mathcal{F}} \|\mathcal{U} - \bar{\mathcal{U}}\|. \tag{2.10}
 \end{aligned}$$

From (2.10), we have

$$\|\mathbf{T}(\mathcal{U}) - \mathbf{T}(\bar{\mathcal{U}})\| \leq \frac{2T^\sigma}{\Gamma(\sigma + 1)} L_{\mathcal{F}} \|\mathcal{U} - \bar{\mathcal{U}}\|. \tag{2.11}$$

Hence F is a contraction. By the Banach contraction theorem, the considered system has a unique solution. \square

2.3.2 Qualitative analysis for (2.3)

In this section we discuss qualitative analysis of an arbitrary-order system (2.3). The existence of a physical model is discussed by the fixed point theory approach. So we will apply the Schauder and Banach fixed point theorems to prove the main results. We have considered the arbitrary-order system (2.3) as

$$\begin{aligned} {}^c\mathcal{D}_t^\sigma \tilde{u}(t) &= f_1(t, \tilde{u}(t), \tilde{v}(t)), \\ {}^c\mathcal{D}_t^\sigma \tilde{v}(t) &= f_2(t, \tilde{u}(t), \tilde{v}(t)), \\ \tilde{u}(0) &= \tilde{u}_0, \quad \tilde{v}(0) = \tilde{v}_0, \quad 0 < \sigma \leq 1. \end{aligned} \quad (2.12)$$

Applying a fuzzy arbitrary-order integral of order σ as I^σ to (2.12), using initial conditions, we get

$$\begin{aligned} \tilde{u}(t) &= \tilde{u}_0 + \frac{1}{\Gamma(\sigma)} \int_0^t (t-\zeta)^{\sigma-1} f_1(\zeta, \tilde{u}(\zeta), \tilde{v}(\zeta)) d\zeta, \\ \tilde{v}(t) &= \tilde{v}_0 + \frac{1}{\Gamma(\sigma)} \int_0^t (t-\zeta)^{\sigma-1} f_2(\zeta, \tilde{u}(\zeta), \tilde{v}(\zeta)) d\zeta. \end{aligned} \quad (2.13)$$

We express system (2.13) as

$$\tilde{\mathbf{Y}}(t) = \tilde{\mathbf{Y}}_0(t) + \frac{1}{\Gamma(\sigma)} \int_0^t (t-\eta)^{\sigma-1} \Psi(\eta, \tilde{\mathbf{Y}}(\eta)) d\eta, \quad (2.14)$$

where

$$\tilde{\mathbf{Y}}(t) = \begin{cases} \tilde{u}(t), \\ \tilde{v}(t), \end{cases} \quad \tilde{\mathbf{Y}}_0(t) = \begin{cases} \tilde{u}_0(t), \\ \tilde{v}_0(t), \end{cases} \quad \Psi(t, \tilde{\mathbf{Y}}(t)) = \begin{cases} f_1(t, \tilde{u}(t), \tilde{v}(t)), \\ f_2(t, \tilde{u}(t), \tilde{v}(t)). \end{cases} \quad (2.15)$$

For a discussion of existence and uniqueness, let us define the Banach space by $\mathcal{B} = B_1 \times B_2$ under the fuzzy norm $\|(\tilde{u}, \tilde{v})\| = \max_{t \in [0, T]} |\tilde{u}(t)| + \max_{t \in [0, T]} |\tilde{v}(t)|$. Furthermore, we make some assumptions as growth conditions on the nonlinear vector mapping as

$$\psi : [0, T] \times \mathbb{R} \times \mathbb{R} \rightarrow \mathbb{R}$$

as:

(B1) There exists a constant $L_\psi > 0$ such that for each $\tilde{\mathbf{Y}}(t), \tilde{\mathbf{Y}}^-(t) \in \mathbb{R} \times \mathbb{R}$ such that

$$|\psi(t, \tilde{\mathbf{Y}}(t)) - \psi(t, \tilde{\mathbf{Y}}^-(t))| \leq L_\psi |\tilde{\mathbf{Y}}(t) - \tilde{\mathbf{Y}}^-(t)|.$$

(B2) There exist constants $C_\psi > 0$ and $M_\psi > 0$ such that

$$|\psi(t, \tilde{\mathbf{Y}}(t))| \leq C_\psi |\tilde{\mathbf{Y}}| + M_\psi.$$

Theorem 2.3.3. *Let ψ be continuous, fulfilling Assumption (B2). It is guaranteed that at least one solution to system (2.14) will exist.*

Proof. By the Schauder fixed point theorem, we will prove the theorem. Define a closed subset \mathcal{G} of \mathcal{B} given as

$$\mathcal{G} = \{\tilde{\mathbf{Y}} \in \mathcal{B} : \mathcal{R} \geq \|\tilde{\mathbf{Y}}\|\}.$$

Define a mapping $\tau : \mathcal{G} \rightarrow \mathcal{G}$ by using (2.13) as

$$\tau(\tilde{\mathbf{Y}}) = \tilde{\mathbf{Y}}_0(t) + \frac{1}{\Gamma(\sigma)} \int_0^t (t-\eta)^{\sigma-1} \Psi(\eta, \tilde{\mathbf{Y}}(\eta)) d\eta, \quad (2.16)$$

For any $\tilde{\mathbf{Y}} \in \mathcal{G}$, we have

$$\begin{aligned} |\tau(\tilde{\mathbf{Y}})| &\leq |\tilde{\mathbf{Y}}_0| + \frac{1}{\Gamma(\sigma)} \int_0^t (t-\eta)^{\sigma-1} |\Psi(\eta, \tilde{\mathbf{Y}}(\eta))| d\eta \\ &\leq |\tilde{\mathbf{Y}}_0| + \frac{1}{\Gamma(\sigma)} \int_0^t (t-\eta)^{\sigma-1} [C_\psi |\tilde{\mathbf{Y}}| + M_\psi] d\eta \\ &\leq |\tilde{\mathbf{Y}}_0| + \frac{T^\sigma}{\Gamma(\sigma+1)} [C_\psi \|\tilde{\mathbf{Y}}\| + M_\psi], \end{aligned}$$

which implies that

$$\begin{aligned} \|\tau(\tilde{\mathbf{Y}})\| &\leq |\tilde{\mathbf{Y}}_0| + \frac{T^\gamma}{\Gamma(\gamma+1)} [C_\psi \|\tilde{\mathbf{Y}}\| + M_\psi] \\ &\leq \mathcal{R}. \end{aligned} \quad (2.17)$$

From (2.17), one implies that $\tilde{\mathbf{Y}} \in \mathcal{G}$. Thus $\tau(\mathcal{G}) \subset \mathcal{G}$. This also proves that operator τ is bounded. For “complete continuity” we go ahead as follows.

Let “ $t_1 < t_2 \in [0, T]$.” Then

$$\begin{aligned}
 & |\boldsymbol{\tau}(\tilde{\mathbf{Y}})(t_2) - \boldsymbol{\tau}(\tilde{\mathbf{Y}})(t_1)| \\
 &= \left| \frac{1}{\Gamma(\sigma)} \int_0^{t_2} (t_2 - \eta)^{\sigma-1} \Psi(s, \tilde{\mathbf{Y}}(\eta)) d\eta \right. \\
 &\quad \left. - \frac{1}{\Gamma(\sigma)} \int_0^{t_1} (t_1 - \eta)^{\sigma-1} \Psi(\eta, \tilde{\mathbf{Y}}(\eta)) d\eta \right| \\
 &\leq \frac{1}{\Gamma(\sigma)} \left[\int_0^{t_2} (t_2 - \eta)^{\sigma-1} - \int_0^{t_1} (t_1 - \eta)^{\sigma-1} \right] (C_\Psi \mathcal{R} + M_\Psi) d\eta \\
 &\leq \frac{(C_\Psi \mathcal{R} + M_\Psi)}{\Gamma(\sigma + 1)} [t_2^\sigma - t_1^\sigma]. \tag{2.18}
 \end{aligned}$$

Now from (2.18), we see that as “ $t_1 \rightarrow t_2$,” the right-hand side will clearly go to zero. So we conclude as

$$|\boldsymbol{\tau}(\tilde{\mathbf{Y}})(t_2) - \boldsymbol{\tau}(\tilde{\mathbf{Y}})(t_1)| \rightarrow 0, \text{ as } t_1 \rightarrow t_2.$$

By this we can write

$$\|\boldsymbol{\tau}(\tilde{\mathbf{Y}})(t_2) - \boldsymbol{\tau}(\tilde{\mathbf{Y}})(t_1)\| \rightarrow 0, \text{ as } t_1 \rightarrow t_2.$$

By this we have proved that $\boldsymbol{\tau}$ is an equicontinuous operator. By using the Arzelá–Ascoli theorem, operator $\boldsymbol{\tau}$ is a completely continuous operator and also uniformly bounded, as proved already. By Schauder’s fixed point theorem, the given model (2.3) has one or more than one solution. \square

Furthermore, we provide results about uniqueness of solution as follows.

Theorem 2.3.4. *Under Assumption (B1), system (2.14) will have a unique solution if $\frac{T^\sigma}{\Gamma(\sigma+1)} L_\Psi < 1$.*

Proof. As $\boldsymbol{\tau} : \mathcal{B} \rightarrow \mathcal{B}$, defined already, we take $\tilde{\mathbf{Y}}$ and $\tilde{\tilde{\mathbf{Y}}} \in \mathcal{B}$ and consider

$$\begin{aligned}
 \|\boldsymbol{\tau}(\tilde{\mathbf{Y}}) - \boldsymbol{\tau}(\tilde{\tilde{\mathbf{Y}}})\| &= \max_{t \in [0, T]} \left| \frac{1}{\Gamma(\sigma)} \int_0^t (t - \eta)^{\sigma-1} \Psi(\eta, \tilde{\mathbf{Y}}(\eta)) d\eta \right. \\
 &\quad \left. - \frac{1}{\Gamma(\sigma)} \int_0^t (t - \eta)^{\sigma-1} \Psi(\eta, \tilde{\tilde{\mathbf{Y}}}(\eta)) d\eta \right| \\
 &\leq \frac{T^\sigma}{\Gamma(\sigma + 1)} L_\Psi \|\tilde{\mathbf{Y}} - \tilde{\tilde{\mathbf{Y}}}\|. \tag{2.19}
 \end{aligned}$$

From (2.19), we have

$$\|\tau(\tilde{\mathbf{Y}}) - \tau(\tilde{\tilde{\mathbf{Y}}})\| \leq \frac{2T^\sigma}{\Gamma(\sigma + 1)} L_\Psi \|\tilde{\mathbf{Y}} - \tilde{\tilde{\mathbf{Y}}}\|. \quad (2.20)$$

Hence τ is a contraction. By the Banach contraction theorem, the considered system has a unique solution. \square



2.4. Series solution of the considered system (2.2) under normal Caputo derivative

To produce a semianalytical solution to the considered model, consider a general problem as

$$D^\sigma \mathcal{U}(t) = \mathcal{N}(\mathcal{U}) + L(\mathcal{U}), \quad 0 < \sigma \leq 1, \quad (2.21)$$

$$\mathcal{U}(0) = \mathcal{U}_0, \quad \mathcal{U}_0 \in \mathbb{R}^+, \quad (2.22)$$

where $\mathcal{N}(\mathcal{U})$ is a nonlinear term and $L(\mathcal{U})$ represents the linear term. Taking the Laplace transform of (2.21) and using initial conditions, we have

$$\mathcal{L}[\mathcal{U}(t)] = \frac{1}{s} \mathcal{U}_0 + \frac{1}{s^\sigma} \mathcal{L}[\mathcal{N}(\mathcal{U}) + L(\mathcal{U})]. \quad (2.23)$$

Let us consider the needed solution as $\mathcal{U}(t) = \sum_{n=0}^{\infty} \mathcal{U}_n(t)$. The nonlinear term $\mathcal{N}(\mathcal{U})$ may be expressed as $\mathcal{N}(\mathcal{U}) = \sum_{n=0}^{\infty} \mathcal{P}_n(t)$, where \mathcal{P}_n is defined by

$$\mathcal{P}_n = \frac{1}{\Gamma(n+1)} \frac{d}{d\xi} \left[\mathcal{N} \left(\sum_{k=0}^n \mathcal{U}_k \right) \right] \Big|_{\xi=0}.$$

Therefore (2.23) becomes

$$\mathcal{L} \left[\sum_{n=0}^{\infty} \mathcal{U}_n(t) \right] = \frac{1}{s} \mathcal{U}_0 + \frac{1}{s^\sigma} \mathcal{L} \left[\sum_{n=0}^{\infty} \mathcal{P}_n(\mathcal{H}, \mathcal{I}) + L \left(\sum_{n=0}^{\infty} \mathcal{U}_n \right) \right].$$

Comparing terms on both sides, we have

$$\begin{aligned} \mathcal{L}[\mathcal{U}_0(t)] &= \frac{1}{s} \mathcal{U}_0, \\ \mathcal{L}[\mathcal{U}_1(t)] &= \frac{1}{s^\sigma} \mathcal{L} \left[\mathcal{P}_0(\mathcal{H}, \mathcal{I}) + L(\mathcal{U}_0) \right], \end{aligned}$$

$$\begin{aligned}\mathcal{L}\left[\mathcal{U}_2(t)\right] &= \frac{1}{s^\sigma} \mathcal{L}\left[\mathcal{P}_1(\mathcal{H}, \mathcal{I}) + L(\mathcal{U}_1)\right], \\ \mathcal{L}\left[\mathcal{U}_3(t)\right] &= \frac{1}{s^\sigma} \mathcal{L}\left[\mathcal{P}_2(\mathcal{H}, \mathcal{I}) + L(\mathcal{U}_2)\right], \\ &\vdots \\ \mathcal{L}\left[\mathcal{U}_{n+1}(t)\right] &= \frac{1}{s^\sigma} \mathcal{L}\left[\mathcal{P}_n(\mathcal{H}, \mathcal{I}) + L(\mathcal{U}_n)\right], \quad n \geq 0.\end{aligned}$$

Evaluating the inverse Laplace transform, we have

$$\begin{aligned}\mathcal{U}_0(t) &= \mathcal{U}_0, \\ \mathcal{U}_1(t) &= \mathcal{L}^{-1}\left[\frac{1}{s^\sigma} \mathcal{L}\left[\mathcal{P}_0(\mathcal{H}, \mathcal{I}) + L(\mathcal{U}_0)\right]\right], \\ \mathcal{U}_2(t) &= \mathcal{L}^{-1}\left[\frac{1}{s^\sigma} \mathcal{L}\left[\mathcal{P}_1(\mathcal{H}, \mathcal{I}) + L(\mathcal{U}_1)\right]\right], \\ &\vdots \\ \mathcal{U}_{n+1} &= \mathcal{L}^{-1}\left[\frac{1}{s^\sigma} \mathcal{L}\left[\mathcal{P}_n(\mathcal{H}, \mathcal{I}) + L(\mathcal{U}_n)\right]\right].\end{aligned}\tag{2.24}$$

Hence the required series solution of (2.2) will be obtained as

$$\mathcal{U}(t) = \mathcal{U}_0(t) + \mathcal{U}_1(t) + \mathcal{U}_2(t) + \dots.\tag{2.25}$$

Remark 2.4.1. Convergence of the series (2.25) is easy to establish.

2.4.1 Approximate solution and discussion for (2.2)

To compute the approximate results of the considered model by using the procedure given in (2.24), we now take some values for parameters of (2.1) under fractional order. Let us assume the healthy population is 0.5 and the infected population is 0.5. Taking various values for transmission rates we discuss certain cases as follows:

$$\begin{cases} \mathcal{D}^\sigma \mathcal{H}(t) = a\mathcal{H}(t) - b\mathcal{H}(t)\mathcal{I}(t) + c\mathcal{H}(t), \\ \mathcal{D}^\sigma \mathcal{I}(t) = b\mathcal{H}(t)\mathcal{I}(t) + (c - d - e)\mathcal{I}(t), \\ \mathcal{H}(0) = 0.5, \quad \mathcal{I}(0) = 0.5. \end{cases}\tag{2.26}$$

Using the proposed algorithm to (2.26) as constructed in (2.24), analogously one has

$$\left\{ \begin{array}{l}
 \mathcal{H}_0(t) = 0.5, \quad \mathcal{I}_0(t) = 0.5, \\
 \mathcal{H}_1(t) = [0.5a - 0.25b + 0.5e] \frac{t^\sigma}{\Gamma(\sigma + 1)}, \\
 \mathcal{I}_1(t) = [0.25b - 0.5c - 0.5d - 0.5e] \frac{t^\sigma}{\Gamma(\sigma + 1)}, \\
 \mathcal{H}_2(t) = [a\mathcal{H}_{11} + e\mathcal{I}_{11}] \frac{t^{2\sigma}}{\Gamma(2\sigma + 1)} - [b\mathcal{H}_{11}\mathcal{I}_{11}] \left(\frac{\Gamma(2\sigma + 1)}{\Gamma^2(\sigma + 1)} \right) \frac{t^{3\sigma}}{\Gamma(3\sigma + 1)}, \\
 \mathcal{I}_2(t) = [b\mathcal{H}_{11}\mathcal{I}_{11}] \left(\frac{\Gamma(2\sigma + 1)}{\Gamma^2(\sigma + 1)} \right) \frac{t^{3\sigma}}{\Gamma(3\sigma + 1)} + [(c - d - e)\mathcal{I}_{11}] \frac{t^{2\sigma}}{\Gamma(2\sigma + 1)}, \\
 \mathcal{H}_3(t) = a\mathcal{H}_{111} \frac{t^{3\sigma}}{\Gamma(3\sigma + 1)} - a\mathcal{I}_{111} \frac{\Gamma(2\sigma + 1)}{\Gamma^2(\sigma + 1)} \frac{t^{4\sigma}}{\Gamma(4\sigma + 1)} \\
 \quad - b\mathcal{H}_{111}\mathcal{I}_{111} \frac{\Gamma(5\sigma + 1)}{\Gamma^2(\sigma + 1)\Gamma(3\sigma + 1)\Gamma(6\sigma + 1)} t^{6\sigma} \\
 \quad - b\mathcal{H}_{111}\mathcal{I}_{22} \frac{\Gamma(4\sigma + 1)}{\Gamma^2(2\sigma + 1)\Gamma(5\sigma + 1)} t^{5\sigma} \\
 \quad + b(\mathcal{I}_{111})^2 \frac{\Gamma^2(2\sigma + 1)}{\Gamma^4(\sigma + 1)\Gamma^2(3\sigma + 1)} t^{6\sigma} \\
 \quad + b\mathcal{I}_{111}\mathcal{I}_{22} \frac{1}{\Gamma^2(\sigma + 1)\Gamma(3\sigma + 1)} t^{5\sigma} \\
 \quad + e\mathcal{I}_{111} \frac{\Gamma(2\sigma + 1)}{(\Gamma(\sigma + 1))^2\Gamma(4\sigma + 1)} t^{4\sigma} + e\mathcal{I}_{22} \frac{t^{3\sigma}}{\Gamma(3\sigma + 1)}, \\
 \mathcal{I}_3(t) = b\mathcal{H}_{111}\mathcal{I}_{111} \frac{\Gamma(5\sigma + 1)}{\Gamma^2(\sigma + 1)\Gamma(3\sigma + 1)\Gamma(6\sigma + 1)} t^{6\sigma} \\
 \quad + b\mathcal{H}_{111}\mathcal{I}_{22} \frac{\Gamma(4\sigma + 1)}{\Gamma^2(2\sigma + 1)\Gamma(5\sigma + 1)} t^{5\sigma} \\
 \quad - b(\mathcal{I}_{111})^2 \frac{\Gamma^2(2\sigma + 1)}{\Gamma^4(\sigma + 1)\Gamma^2(3\sigma + 1)} t^{6\sigma} \\
 \quad - b\mathcal{I}_{111}\mathcal{I}_{22} \frac{1}{\Gamma^2(\sigma + 1)\Gamma(3\sigma + 1)} t^{5\sigma} \\
 \quad + (c - d - e)\mathcal{I}_{111} \frac{\Gamma(2\sigma + 1)}{\Gamma^2(\sigma + 1)\Gamma(4\sigma + 1)} t^{4\sigma} \\
 \quad + (c - d - e)\mathcal{I}_{22} \frac{t^{3\sigma}}{\Gamma(3\sigma + 1)},
 \end{array} \right. \tag{2.27}$$

and so on. Further terms can be calculated in the same way. The unknown values in (2.27) are given as

$$\begin{aligned}
 \mathcal{H}_{11} &= 0.5a - 0.25b + 0.5e, \quad \mathcal{I}_{11} = 0.25b - 0.5c - 0.5d - 0.5e, \\
 \mathcal{H}_{111} &= a\mathcal{H}_{11} + e\mathcal{I}_{11}, \quad \mathcal{I}_{111} = b\mathcal{H}_{11}\mathcal{I}_{11}, \quad \mathcal{I}_{22} = (c - d - e)\mathcal{I}_{11}.
 \end{aligned}$$

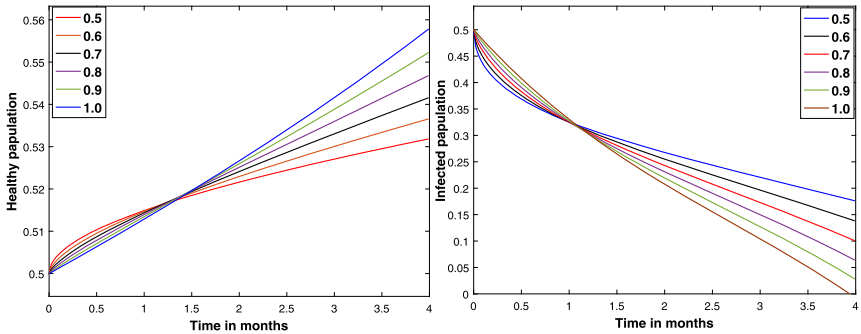


Figure 2.1 Dynamical behaviors of population dynamics in the absence of migration corresponding to different fractional orders.

Case I

We simulate the results above taking $a = 0.000001$, $b = 0.03$, $c = 0.05$, $d = 0.03$, $e = 0.05$. Here the migration of both infected and healthy individuals is taken as zero, as shown in Fig. 2.1.

From Fig. 2.1, we see that in the absence of migration, there is no transfer of healthy or infected people from one place to another, producing a great impact on the control of the infection. In other words, isolation and social distance greatly help in controlling the current outbreak from further spread. The growth and decay of the different compartments have been shown for different fractional orders. The order of derivatives also produces a certain impact on the process; at smaller order the initial process of growth is faster, up to 45 days. After that, the process starts to exhibit reverse behavior. The same behavior is observed for the infected class after one month.

Case II

We simulate the results taking $a = 0.0$, $b = 0.03$, $c = 0.05$, $d = 0.03$, $e = 0.05$. Here the migration of infected individuals is included, and migration of the healthy population is taken as zero (Fig. 2.2). We see that migration of the infected class greatly disturbs the balance of the healthy population. This disturbance is different at different fractional orders, while the infection class shows the same decay as in Fig. 2.1, because it leaves the community.

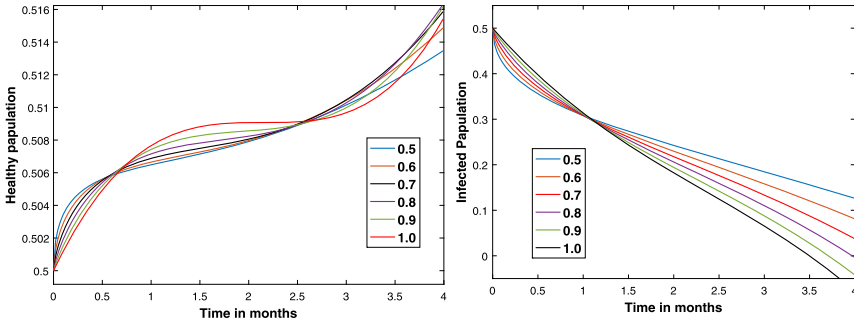


Figure 2.2 Dynamical behaviors of population dynamics in the absence of migration corresponding to different fractional orders.

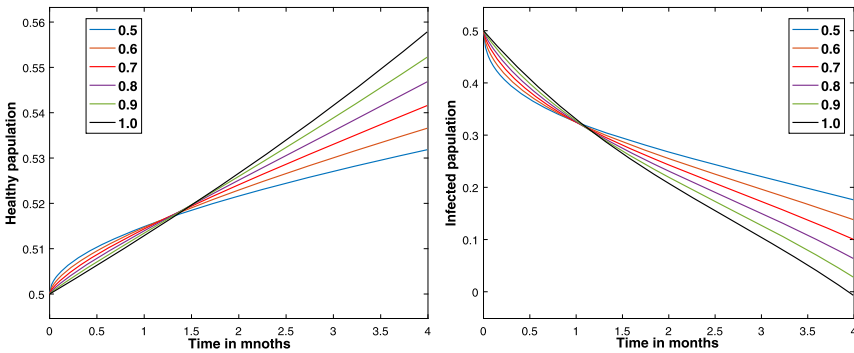


Figure 2.3 Dynamical behaviors of population dynamics in the absence of migration of infected individuals corresponding to different fractional orders.

Case III

We simulate the results taking $a = 0.05$, $b = 0.03$, $c = 0.05$, $d = 0.03$, $e = 0.0$. Here the migration of infected individuals is included and migration of the healthy population is taken as zero (Fig. 2.3) If proper protection is allowed, then migration of the healthy class in the absence of migration of infected individuals and its dynamical behaviors are shown. The effect of the fractional order derivative can be observed which globalize the dynamics.

Case IV

We simulate the results taking $a = 0.0005$, $b = 0.05$, $c = 0.003$, $d = 0.004$, $e = 0.0009$. Here the migration of infected as well as healthy individuals

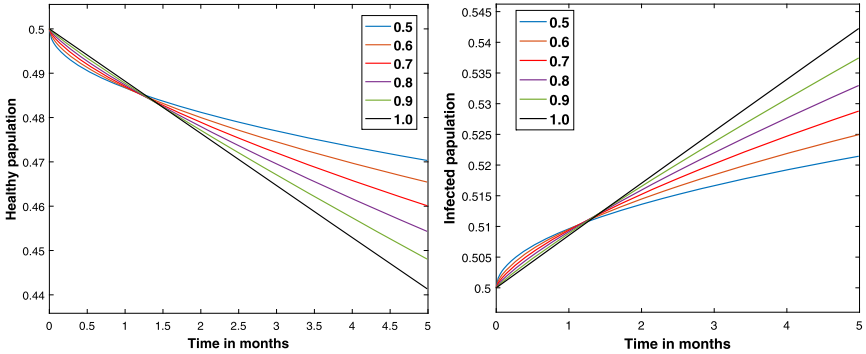


Figure 2.4 Dynamical behaviors of population dynamics in the presence of migration of both populations corresponding to different fractional orders.

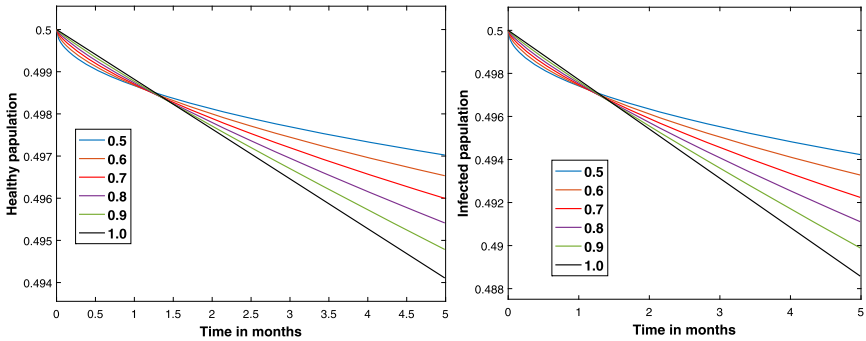


Figure 2.5 Dynamical behaviors of population dynamics in the presence of very low migration of both populations corresponding to different fractional orders.

is included (Fig. 2.4). We see that if migration of both classes is present, then the healthy population density decreases while the infected population density increases with different rates due to the fractional order.

Case V

Here we present the results for very low values of migration of both classes from a community with $a = 0.00005$, $b = 0.005$, $c = 0.003$, $d = 0.004$, $e = 0.00009$ (Fig. 2.5). The corresponding migration values are low. The dynamical behaviors for both classes are presented corresponding to the different fractional orders in Fig. 2.5. Both class densities decrease.

Remark 2.4.2. Clearly from (2.26), corresponding to the given values of parameters, the conditions of Theorem 2.3.3 and Theorem 2.3.4 are

satisfied with $L_{\mathcal{F}} = 0.05$, $T = 4$. We see that $\frac{L_{\mathcal{F}} T^{\sigma}}{\Gamma(\sigma+1)} = \frac{0.20}{\Gamma(\sigma+1)} < 1$, for all $\sigma \in (0, 1]$. The same can be verified for other cases.



2.5. General series solution of the considered system (2.3)

To produce a semianalytical solution to the considered model, we first generated a general algorithm by using system (2.3). We apply the fuzzy Laplace transform to (2.3) on both sides as

$$\begin{aligned}\mathcal{L}[\mathcal{D}_t^{\gamma} \tilde{u}(t)] &= \mathcal{L}\left[f_1(t, \tilde{u}(t), \tilde{v}(t))\right], \\ \mathcal{L}[\mathcal{D}_t^{\gamma} \tilde{v}(t)] &= \mathcal{L}\left[f_2(t, \tilde{u}(t), \tilde{v}(t))\right],\end{aligned}\quad (2.28)$$

and using initial conditions, we have

$$\begin{aligned}s^{\gamma} \mathcal{L}\left[\tilde{u}(t)\right] &= s^{\gamma-1} \tilde{u}_0 + \mathcal{L}\left[f_1(t, \tilde{u}(t), \tilde{v}(t))\right], \\ s^{\gamma} \mathcal{L}\left[\tilde{v}(t)\right] &= s^{\gamma-1} \tilde{v}_0 + \mathcal{L}\left[f_2(t, \tilde{u}(t), \tilde{v}(t))\right],\end{aligned}\quad (2.29)$$

or

$$\begin{aligned}\mathcal{L}\left[\tilde{u}(t)\right] &= \frac{1}{s} \tilde{u}_0 + \frac{1}{s} \mathcal{L}\left[f_1(t, \tilde{u}(t), \tilde{v}(t))\right], \\ \mathcal{L}\left[\tilde{v}(t)\right] &= \frac{1}{s} \tilde{v}_0 + \frac{1}{s} \mathcal{L}\left[f_2(t, \tilde{u}(t), \tilde{v}(t))\right].\end{aligned}\quad (2.30)$$

Considering the unknown as

$$\tilde{u}(t) = \sum_{n=0}^{\infty} \tilde{u}_n(t), \quad \tilde{v}(t) = \sum_{n=0}^{\infty} \tilde{v}_n(t)$$

and considering the product of two terms $\tilde{u}(t)\tilde{v}(t)$ may be written as

$$\tilde{u}(t)\tilde{v}(t) = \sum_{n=0}^{\infty} \tilde{u}_n(t) \sum_{n=0}^{\infty} \tilde{v}_n(t),$$

(2.30) becomes

$$\begin{aligned}\mathcal{L}\left[\sum_{n=0}^{\infty}\tilde{u}_n(t)\right] &= \frac{1}{s}\tilde{u}_0 + \frac{1}{s^\gamma}\mathcal{L}\left[f_1\left(t, \sum_{n=0}^{\infty}\tilde{u}_n(t), \sum_{n=0}^{\infty}\tilde{v}_n(t)\right)\right], \\ \mathcal{L}\left[\sum_{n=0}^{\infty}\tilde{v}_n(t)\right] &= \frac{1}{s}\tilde{v}_0 + \frac{1}{s^\alpha}\mathcal{L}\left[f_2\left(t, \sum_{n=0}^{\infty}\tilde{u}_n(t), \sum_{n=0}^{\infty}\tilde{v}_n(t)\right)\right].\end{aligned}\quad (2.31)$$

We take $\tilde{u}(t) = (\underline{u}(t), \bar{u}(t))$, $\tilde{v}(t) = (\underline{v}(t), \bar{v}(t))$. Comparing terms on both sides,

$$\begin{aligned}\mathcal{L}\left[\underline{u}_0(t)\right] &= \frac{1}{s}\underline{u}_0, & \mathcal{L}\left[\bar{u}_0(t)\right] &= \frac{1}{s}\bar{u}_0, \\ \mathcal{L}\left[\underline{v}_0(t)\right] &= \frac{1}{s}\underline{v}_0, & \mathcal{L}\left[\bar{v}_0(t)\right] &= \frac{1}{s}\bar{v}_0, \\ \mathcal{L}\left[\underline{u}_1(t)\right] &= \frac{1}{s^\gamma}\mathcal{L}\left[f_1\left(t, \underline{u}_0(t), \underline{v}_0(t)\right)\right], \\ \mathcal{L}\left[\bar{u}_1(t)\right] &= \frac{1}{s^\gamma}\mathcal{L}\left[f_2\left(t, \bar{u}_0(t), \bar{v}_0(t)\right)\right], \\ \mathcal{L}\left[\underline{v}_1(t)\right] &= \frac{1}{s^\gamma}\mathcal{L}\left[f_1\left(t, \underline{u}_0(t), \underline{v}_0(t)\right)\right], \\ \mathcal{L}\left[\bar{v}_1(t)\right] &= \frac{1}{s^\gamma}\mathcal{L}\left[f_2\left(t, \bar{u}_0(t), \bar{v}_0(t)\right)\right], \\ \mathcal{L}\left[\underline{u}_2(t)\right] &= \frac{1}{s^\gamma}\mathcal{L}\left[f_1\left(t, \underline{u}_1(t), \underline{v}_1(t)\right)\right], \\ \mathcal{L}\left[\bar{u}_2(t)\right] &= \frac{1}{s^\gamma}\mathcal{L}\left[f_2\left(t, \bar{u}_1(t), \bar{v}_1(t)\right)\right], \\ \mathcal{L}\left[\underline{v}_2(t)\right] &= \frac{1}{s^\gamma}\mathcal{L}\left[f_1\left(t, \underline{u}_1(t), \underline{v}_1(t)\right)\right], \\ \mathcal{L}\left[\bar{v}_2(t)\right] &= \frac{1}{s^\gamma}\mathcal{L}\left[f_2\left(t, \bar{u}_1(t), \bar{v}_1(t)\right)\right], \\ &\vdots \\ \mathcal{L}\left[\underline{u}_{n+1}(t)\right] &= \frac{1}{s^\gamma}\mathcal{L}\left[f_1\left(t, \underline{u}_n(t), \underline{v}_n(t)\right)\right], \\ \mathcal{L}\left[\bar{u}_{n+1}(t)\right] &= \frac{1}{s^\gamma}\mathcal{L}\left[f_2\left(t, \bar{u}_n(t), \bar{v}_n(t)\right)\right],\end{aligned}$$

$$\begin{aligned}\mathcal{L}\left[\underline{v}_{n+1}(t)\right] &= \frac{1}{s^\gamma} \mathcal{L}\left[f_1(t, \underline{u}_n(t), \underline{v}_n(t))\right], \\ \mathcal{L}\left[\bar{v}_{n+1}(t)\right] &= \frac{1}{s^\gamma} \mathcal{L}\left[f_2(t, \bar{u}_n(t), \bar{v}_n(t))\right].\end{aligned}$$

Taking the inverse Laplace transform, one has

$$\begin{aligned}\left[\underline{u}_0(t)\right] &= \underline{u}_0, & \left[\bar{u}_0(t)\right] &= \bar{u}_0, \\ \left[\underline{v}_0(t)\right] &= \underline{v}_0, & \left[\bar{v}_0(t)\right] &= \bar{v}_0, \\ \left[\underline{u}_1(t)\right] &= \mathcal{L}^{-1}\left[\frac{1}{s^\gamma} \mathcal{L}\left[f_1(t, \underline{u}_0(t), \underline{v}_0(t))\right]\right], \\ \left[\bar{u}_1(t)\right] &= \mathcal{L}^{-1}\left[\frac{1}{s^\gamma} \mathcal{L}\left[f_2(t, \bar{u}_0(t), \bar{v}_0(t))\right]\right], \\ \left[\underline{v}_1(t)\right] &= \mathcal{L}^{-1}\left[\frac{1}{s^\gamma} \mathcal{L}\left[f_1(t, \underline{u}_0(t), \underline{v}_0(t))\right]\right], \\ \left[\bar{v}_1(t)\right] &= \mathcal{L}^{-1}\left[\frac{1}{s^\gamma} \mathcal{L}\left[f_2(t, \bar{u}_0(t), \bar{v}_0(t))\right]\right], \\ \left[\underline{u}_2(t)\right] &= \mathcal{L}^{-1}\left[\frac{1}{s^\gamma} \mathcal{L}\left[f_1(t, \underline{u}_1(t), \underline{v}_1(t))\right]\right], \\ \left[\bar{u}_2(t)\right] &= \mathcal{L}^{-1}\left[\frac{1}{s^\gamma} \mathcal{L}\left[f_2(t, \bar{u}_1(t), \bar{v}_1(t))\right]\right], \\ \left[\underline{v}_2(t)\right] &= \mathcal{L}^{-1}\left[\frac{1}{s^\gamma} \mathcal{L}\left[f_1(t, \underline{u}_1(t), \underline{v}_1(t))\right]\right], \\ \left[\bar{v}_2(t)\right] &= \mathcal{L}^{-1}\left[\frac{1}{s^\gamma} \mathcal{L}\left[f_2(t, \bar{u}_1(t), \bar{v}_1(t))\right]\right]. \\ &\vdots\end{aligned}$$

Conversely, one may write general terms for $n \geq 0$ as

$$\begin{aligned}\left[\underline{u}_{n+1}(t)\right] &= \mathcal{L}^{-1}\left[\frac{1}{s^\gamma} \mathcal{L}\left[f_1(t, \underline{u}_n(t), \underline{v}_n(t))\right]\right], \\ \left[\bar{u}_{n+1}(t)\right] &= \mathcal{L}^{-1}\left[\frac{1}{s^\gamma} \mathcal{L}\left[f_2(t, \bar{u}_n(t), \bar{v}_n(t))\right]\right], \\ \left[\underline{v}_{n+1}(t)\right] &= \mathcal{L}^{-1}\left[\frac{1}{s^\gamma} \mathcal{L}\left[f_1(t, \underline{u}_n(t), \underline{v}_n(t))\right]\right], \\ \left[\bar{v}_{n+1}(t)\right] &= \mathcal{L}^{-1}\left[\frac{1}{s^\gamma} \mathcal{L}\left[f_2(t, \bar{u}_n(t), \bar{v}_n(t))\right]\right].\end{aligned}\tag{2.32}$$

Hence the required series solution of the system (2.3) will be

$$\begin{cases} \underline{u}(t) = \underline{u}_0(t) + \underline{u}_1(t) + \underline{u}_2(t) + \dots, \\ \bar{u}(t) = \bar{u}_0(t) + \bar{u}_1(t) + \bar{u}_2(t) + \dots, \\ \underline{v}(t) = \underline{v}_0(t) + \underline{v}_1(t) + \underline{v}_2(t) + \dots, \\ \bar{v}(t) = \bar{v}_0(t) + \bar{v}_1(t) + \bar{v}_2(t) + \dots. \end{cases} \quad (2.33)$$

2.5.1 Numerical results and discussion for (2.3)

For the justification of the numerical results, we now take the example of (2.1) in fuzzy fractional form. Let the healthy population be $\tilde{u}_0 = (\underline{u}_0, \bar{u}_0) = (\theta - 1, 1 - \theta)$ and let the infected population be $\tilde{v}_0 = (\underline{v}_0, \bar{v}_0) = (\theta - 1, 1 - \theta)$. Taking various values for rates we discuss certain cases below, where

$$\begin{cases} {}^c\mathcal{D}_t^\gamma (\tilde{u}(t)) = a\tilde{u}(t) - b\tilde{u}(t)\tilde{v}(t) + c\tilde{u}(t), \\ {}^c\mathcal{D}_t^\gamma (\tilde{v}(t)) = b\tilde{u}(t)\tilde{v}(t) + (c - d - e)\tilde{v}(t), \\ \tilde{u}(0) = \tilde{u}_0 = (\theta - 1, 1 - \theta), \quad \tilde{v}(0) = \tilde{v}_0 = (\theta - 1, 1 - \theta). \end{cases} \quad (2.34)$$

Applying the proposed method to (2.34) as in (2.32), we get

$$\begin{aligned} \underline{u}_0(t) &= \theta - 1, & \bar{u}_0(t) &= 1 - \theta, \\ \underline{v}_0(t) &= \theta - 1, & \bar{v}_0(t) &= 1 - \theta, \\ \underline{u}_1(t) &= \left[(\theta - 1)a - (\theta - 1)^2b + (\theta - 1)e \right] \frac{t^\gamma}{\Gamma(\gamma + 1)}, \\ \bar{u}_1(t) &= \left[(1 - \theta)a - (1 - \theta)^2b + (1 - \theta)e \right] \frac{t^\gamma}{\Gamma(\gamma + 1)}, \\ \underline{v}_1(t) &= \left[(\theta - 1)^2b - (\theta - 1)c - (\theta - 1)d - (\theta - 1)e \right] \frac{t^\gamma}{\Gamma(\gamma + 1)}, \\ \bar{v}_1(t) &= \left[(1 - \theta)^2b - (1 - \theta)c - (1 - \theta)d - (1 - \theta)e \right] \frac{t^\gamma}{\Gamma(\gamma + 1)}, \\ \underline{u}_2(t) &= \left[a\underline{u}_{11} + e\underline{v}_{11} \right] \frac{t^{2\gamma}}{\Gamma(2\gamma + 1)} - \left[b\underline{u}_{11}\underline{v}_{11} \right] \left(\frac{\Gamma(2\gamma + 1)}{\Gamma^2(\gamma + 1)} \right) \frac{t^{3\gamma}}{\Gamma(3\gamma + 1)}, \\ \bar{u}_2(t) &= \left[a\bar{u}_{11} + e\bar{v}_{11} \right] \frac{t^{2\gamma}}{\Gamma(2\gamma + 1)} - \left[b\bar{u}_{11}\bar{v}_{11} \right] \left(\frac{\Gamma(2\gamma + 1)}{\Gamma^2(\gamma + 1)} \right) \frac{t^{3\gamma}}{\Gamma(3\gamma + 1)}, \\ \underline{v}_2(t) &= \left[b\underline{u}_{11}\underline{v}_{11} \right] \left(\frac{\Gamma(2\gamma + 1)}{\Gamma^2(\gamma + 1)} \right) \frac{t^{3\gamma}}{\Gamma(3\gamma + 1)} + \left[(c - d - e)\underline{v}_{11} \right] \frac{t^{2\gamma}}{\Gamma(2\gamma + 1)}, \end{aligned}$$

$$\begin{aligned}
\bar{v}_2(t) &= \left[b\bar{u}_{111}\bar{v}_{111} \right] \left(\frac{\Gamma(2\gamma+1)}{\Gamma^2(\gamma+1)} \right) \frac{t^{3\gamma}}{\Gamma(3\gamma+1)} + \left[(c-d-e)\bar{v}_{111} \right] \frac{t^{2\gamma}}{\Gamma(2\gamma+1)}, \\
\underline{u}_3(t) &= a\underline{u}_{111} \frac{t^{3\gamma}}{\Gamma(3\gamma+1)} - a\underline{v}_{111} \frac{\Gamma(2\gamma+1)}{\Gamma^2(\gamma+1)} \frac{t^{4\gamma}}{\Gamma(4\gamma+1)} \\
&\quad - b\underline{u}_{111}\underline{v}_{111} \frac{\Gamma(5\gamma+1)}{\Gamma^2(\gamma+1)\Gamma(3\gamma+1)\Gamma(6\gamma+1)} t^{6\gamma} \\
&\quad - b\underline{u}_{111}\underline{v}_{22} \frac{\Gamma(4\gamma+1)}{\Gamma^2(2\gamma+1)\Gamma(5\gamma+1)} t^{5\gamma} \\
&\quad + b(\underline{v}_{111})^2 \frac{\Gamma^2(2\gamma+1)}{\Gamma^4(\gamma+1)\Gamma^2(3\gamma+1)} t^{6\gamma} + b\underline{v}_{111}\underline{v}_{22} \frac{1}{\Gamma^2(\gamma+1)\Gamma(3\gamma+1)} t^{5\gamma} \\
&\quad + e\underline{v}_{111} \frac{\Gamma(2\gamma+1)}{(\Gamma(\gamma+1))^2(\Gamma(4\gamma+1))} t^{4\gamma} + e\underline{v}_{22} \frac{t^{3\gamma}}{\Gamma(3\gamma+1)}, \\
\bar{u}_3(t) &= a\bar{u}_{111} \frac{t^{3\gamma}}{\Gamma(3\gamma+1)} - a\bar{v}_{111} \frac{\Gamma(2\gamma+1)}{\Gamma^2(\gamma+1)} \frac{t^{4\gamma}}{\Gamma(4\gamma+1)} \\
&\quad - b\bar{u}_{111}\bar{v}_{111} \frac{\Gamma(5\gamma+1)}{\Gamma^2(\gamma+1)\Gamma(3\gamma+1)\Gamma(6\gamma+1)} t^{6\gamma} \\
&\quad - b\bar{u}_{111}\bar{v}_{22} \frac{\Gamma(4\gamma+1)}{\Gamma^2(2\gamma+1)\Gamma(5\gamma+1)} t^{5\gamma} \\
&\quad + b(\bar{v}_{111})^2 \frac{\Gamma^2(2\gamma+1)}{\Gamma^4(\gamma+1)\Gamma^2(3\gamma+1)} t^{6\gamma} + b\bar{v}_{111}\bar{v}_{22} \frac{1}{\Gamma^2(\gamma+1)\Gamma(3\gamma+1)} t^{5\gamma} \\
&\quad + e\bar{v}_{111} \frac{\Gamma(2\gamma+1)}{(\Gamma(\gamma+1))^2(\Gamma(4\gamma+1))} t^{4\gamma} + e\bar{v}_{22} \frac{t^{3\gamma}}{\Gamma(3\gamma+1)}, \\
\underline{v}_3(t) &= b\underline{u}_{111}\underline{v}_{111} \frac{\Gamma(5\gamma+1)}{\Gamma^2(\gamma+1)\Gamma(3\gamma+1)\Gamma(6\gamma+1)} t^{6\gamma} \\
&\quad + b\underline{u}_{111}\underline{v}_{22} \frac{\Gamma(4\gamma+1)}{\Gamma^2(2\gamma+1)\Gamma(5\gamma+1)} t^{5\gamma} \\
&\quad - b(\underline{v}_{111})^2 \frac{\Gamma^2(2\gamma+1)}{\Gamma^4(\gamma+1)\Gamma^2(3\gamma+1)} t^{6\gamma} - b\underline{v}_{111}\underline{v}_{22} \frac{1}{\Gamma^2(\gamma+1)\Gamma(3\gamma+1)} t^{5\gamma} \\
&\quad + (c-d-e)\underline{v}_{111} \frac{\Gamma(2\gamma+1)}{\Gamma^2(\gamma+1)(\Gamma(4\gamma+1))} t^{4\gamma} \\
&\quad + (c-d-e)\underline{v}_{22} \frac{t^{3\gamma}}{\Gamma(3\gamma+1)}, \\
\bar{v}_3(t) &= b\bar{u}_{111}\bar{v}_{111} \frac{\Gamma(5\gamma+1)}{\Gamma^2(\gamma+1)\Gamma(3\gamma+1)\Gamma(6\gamma+1)} t^{6\gamma} \\
&\quad + b\bar{u}_{111}\bar{v}_{22} \frac{\Gamma(4\gamma+1)}{\Gamma^2(2\gamma+1)\Gamma(5\gamma+1)} t^{5\gamma} \\
&\quad - b(\bar{v}_{111})^2 \frac{\Gamma^2(2\gamma+1)}{\Gamma^4(\gamma+1)\Gamma^2(3\gamma+1)} t^{6\gamma} - b\bar{v}_{111}\bar{v}_{22} \frac{1}{\Gamma^2(\gamma+1)\Gamma(3\gamma+1)} t^{5\gamma}
\end{aligned}$$

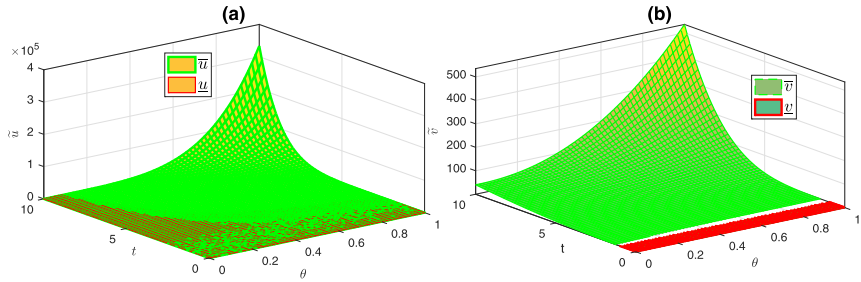


Figure 2.6 Graphical presentation of fuzzy approximate solutions for fractional order 0.75 in the space of uncertainty and time.

$$\begin{aligned}
 &+ (c - d - e)\bar{v}_{111} \frac{\Gamma(2\gamma + 1)}{\Gamma^2(\gamma + 1)(\Gamma(4\gamma + 1))} t^{4\gamma} \\
 &+ (c - d - e)\bar{v}_{22} \frac{t^{3\gamma}}{\Gamma(3\gamma + 1)}.
 \end{aligned}$$

Further terms can be computed in a similar fashion. The unknown values in the above expressions are given in (2.35) as

$$\begin{aligned}
 \underline{u}_{11} &= (\theta - 1)a - (\theta - 1)^2b + (\theta - 1)e, \\
 \bar{u}_{11} &= (1 - \theta)a - (1 - \theta)^2b + (1 - \theta)e, \\
 \underline{v}_{11} &= (\theta - 1)^2b - (\theta - 1)c - (\theta - 1)d - (\theta - 1)e, \\
 \bar{v}_{11} &= (1 - \theta)^2b - (1 - \theta)c - (1 - \theta)d - (1 - \theta)e, \\
 \underline{u}_{111} &= a\underline{u}_{11} + e\underline{v}_{11}, \quad \bar{u}_{111} = a\bar{u}_{11} + e\bar{v}_{11}, \\
 \underline{v}_{111} &= b\underline{v}_{11}\underline{v}_{11}, \quad \bar{v}_{111} = b\bar{v}_{11}\bar{v}_{11}, \\
 \underline{v}_{22} &= (c - d - e)\underline{v}_{11}, \quad \bar{v}_{22} = (c - d - e)\bar{v}_{11}.
 \end{aligned} \tag{2.35}$$

We can now simulate the results above for taking the values $a = 0.5, b = 0.5, c = 0.5, d = 0.5, e = 0.5$ to discuss the dynamics of the healthy and infected populations under fuzzy concept. Let the populations be $u(0) = 0.5, v(0) = 0.5$. We take given values of parameters included in the model and graphically present the fuzzy solutions in Figs. 2.6–2.9 in the space of uncertainty and time.

In Figs. 2.6–2.9, we have presented approximate fuzzy solutions for initial few terms corresponding to different fractional order in $t\theta$ -space. From the figures one can observe that the fuzzy concept can be combined with fractional derivatives for more useful results.

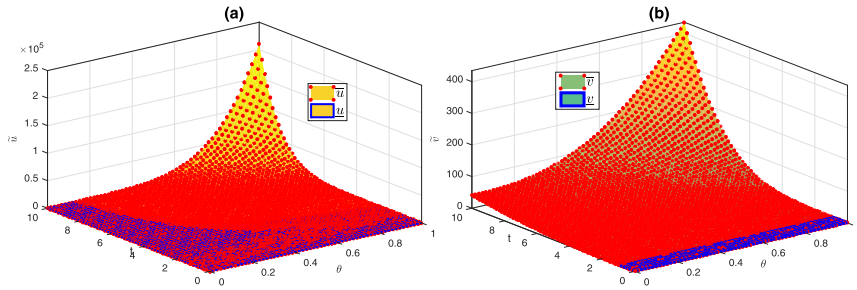


Figure 2.7 Graphical presentation of fuzzy approximate solutions for fractional order 0.85 in the space of uncertainty and time.

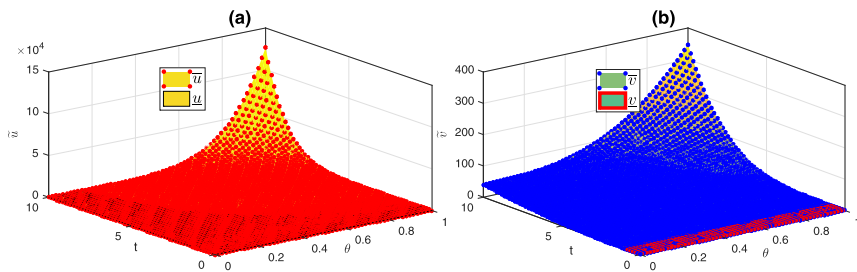


Figure 2.8 Graphical presentation of fuzzy approximate solutions for fractional order 0.95 in the space of uncertainty and time.

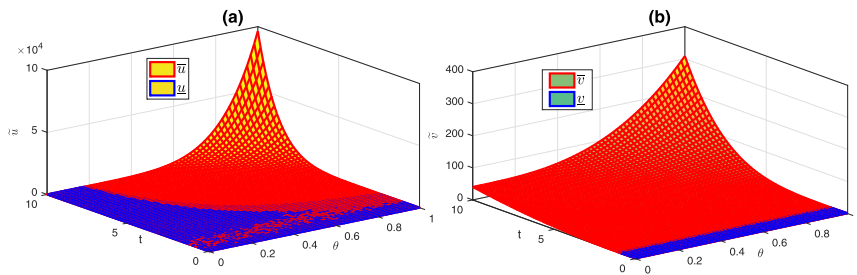


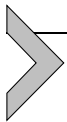
Figure 2.9 Graphical presentation of fuzzy approximate solutions for order 1 in the space of uncertainty and time.

2.5.2 Conclusion

In this chapter a population dynamical model addressing the current COVID-19 pandemic has been investigated from two different scenarios. In the first scenario we have studied the considered model under usual Caputo derivatives. We have proved its existence and the required results about at

least one approximate solution. Furthermore, by assigning different values taken from [14] to a , b , c , d , and e , we have presented its series type solution by graphs. For the required series solution, we have utilized Laplace transform and the decomposition method. It can be observed that by increasing the rates of protection and cure and decreasing the rate of migration, we can eventually decrease the number of infected individuals to minimum or towards stability. By studying such dynamical systems one can know easily how to protect the healthy population from being infected and discourage migration of infected individuals. This model can be applied to populations where social gatherings occur locally or globally. Furthermore, such model exists in the real world, as proved by using fixed point theory. The rates of decay and growth have been shown thorough fractional differentiation in global ways. Hence fractional calculus can be used to comprehensively explain the model. If the recovered class is also included, then we can further extend this model to see the effects of migration on the recovered population also.

When uncertainty exists in data, fuzzy concepts are usually used. Under fuzziness the existence of the considered model and its approximate solutions have been investigated by using the aforementioned tools under fuzzy concepts. Nearly the same behavior has been observed. Hence fractional calculus combined with the fuzzy concept can be used to comprehensively explain many epidemiological models. If the recovered class is also included, then we can further extend this model to see the effects of migration on the recovered population also under a fuzzy concept. Keep in mind that the model we consider here just provides indications about COVID-19 and how migration and protection influence the transmission dynamics of COVID-19.



Declaration of competing interest

There does not exist any kind of competing interest regarding this work.

References

- [1] World Health Organization, Coronavirus disease 2019 (COVID-19) Situation Report-62, [https://www.who.int/docs/default-source/coronaviruse/situation-reports/20200322-sitrep-62-covid-19.pdf?sfvrsn=f7764c462](https://www.who.int/docs/default-source/coronaviruse/situation-reports/20200322-sitrep-62-covid-19.pdf?sfvrsn=f7764c462_2020), 2020.
- [2] C. Nanshan, et al., Epidemiological and clinical characteristics of 99 cases of 2019 novel coronavirus pneumonia in Wuhan, China: a descriptive study, *The Lancet* 395 (10223) (2020) 507–513.

- [3] P. Forida, et al., The symptoms, contagious process, prevention and post treatment of Covid-19, *European Journal of Physiotherapy and Rehabilitation Studies* 1 (1) (2020), 11 pages.
- [4] World Health Organization, Advice on the use of masks in the context of COVID-19: interim guidance, 18 July 2020. No. WHO/2019-nCov/IPC_Masks/2020.4, World Health Organization, 2020.
- [5] M. Goyal, H.M. Baskonus, A. Prakash, An efficient technique for a time fractional model of lassa hemorrhagic fever spreading in pregnant women, *The European Physical Journal Plus* 134 (481) (2019) 1–10.
- [6] W. Gao, P. Veerasha, D.G. Prakasha, H.M. Baskonus, G. Yel, New approach for the model describing the deathly disease in pregnant women using Mittag-Leffler function, *Chaos, Solitons and Fractals* 134 (2020) 109696.
- [7] D. Kumar, J. Singh, M. Al-Qurashi, D. Baleanu, A new fractional SIRS-SI malaria disease model with application of vaccines, anti-malarial drugs, and spraying, *Advances in Difference Equations* 278 (2019) 1–10.
- [8] K. Shah, M.A. Alqudah, F. Jarad, T. Abdeljawad, Semi-analytical study of Pine Wilt Disease model with convex rate under Caputo-Febrizio fractional order derivative, *Chaos, Solitons and Fractals* 135 (2020) 109754.
- [9] X. Tian, et al., Potent binding of 2019 novel coronavirus spike protein by a SARS coronavirus-specific human monoclonal antibody, *Emerging Microbes & Infections* 9 (1) (2020) 382–385.
- [10] X.Y. Ge, et al., Isolation and characterization of a bat SARS-like coronavirus that uses the ACE2 receptor, *Nature* 503 (2013) 535–538.
- [11] H. Lu, et al., Outbreak of pneumonia of unknown etiology in Wuhan, China: the mystery and the miracle, *Journal of Medical Virology* 92 (2020) 401–402, <https://doi.org/10.1002/jmv.25678>.
- [12] J. Riou, C.L. Althaus, Pattern of early human-to-human transmission of Wuhan 2019 novel coronavirus (2019-nCoV), December 2019 to 15 January 2020, *Eurosurveillance* 25 (4) (2020).
- [13] Q. Lin, et al., A conceptual model for the coronavirus disease 2019 (COVID-19) outbreak in Wuhan, China with individual reaction and governmental action, *International Journal of Infectious Diseases* 93 (2020) 211–216.
- [14] S. Nag, A mathematical model in the time of Covid-19, preprint, 13 March 2020.
- [15] V. Lakshmikantham, S. Leela, Naguma-type uniqueness result for fractional differential Equations, *Nonlinear Analysis* 71 (2009) 2886–2889.
- [16] J.A. Lotka, Contribution to the theory of periodic reactions, *The Journal of Physical Chemistry* (2002) 271–274.
- [17] I. Podlubny, *Fractional Differential Equations*, Mathematics in Science and Engineering, Academic Press, New York, 1999.
- [18] V. Lakshmikantham, S. Leela, J. Vasundhara, *Theory of Fractional Dynamic Systems*, Cambridge Academic Publishers, Cambridge, UK, 2009.
- [19] R. Hilfer, *Applications of Fractional Calculus in Physics*, World Scientific, Singapore, 2000.
- [20] Y.A. Rossikhin, M.V. Shitikova, Applications of fractional calculus to dynamic problems of linear and nonlinear hereditary mechanics of solids, *Applied Mechanics Reviews* 50 (1997) 15–67.
- [21] K.S. Miller, B. Ross, *An Introduction to the Fractional Calculus and Fractional Differential Equations*, Wiley, New York, 1993.
- [22] H. Eltayeb, A. Kiliçman, A note on solutions of wave, Laplace's and heat equations with convolution terms by using a double Laplace transform, *Applied Mathematics Letters* 21 (12) (2008) 1324–1329.

- [23] K. Shah, H. Khalil, R.A. Khan, Analytical solutions of fractional order diffusion equations by natural transform method, *Iranian Journal of Science and Technology, Transactions A: Science* 42 (3) (2018) 1479–1490.
- [24] B. Ahmad, S. Sivasundaram, On four-point nonlocal boundary value problems of nonlinear integro-differential equations of fractional order, *Applied Mathematics and Computation* 217 (2010) 480–487.
- [25] Z. Bai, On positive solutions of a nonlocal fractional boundary value problem, *Nonlinear Analysis* 72 (2010) 916–924.
- [26] R.A. Khan, K. Shah, Existence and uniqueness of solutions to fractional order multi-point boundary value problems, *Communications in Applied Analysis* 19 (2015) 515–526.
- [27] K. Shah, N. Ali, R.A. Khan, Existence of positive solution to a class of fractional differential equations with three point boundary conditions, *Mathematical Sciences Letters* 5 (3) (2016) 291–296.
- [28] J. Wang, Y. Zhou, W. Wei, Study in fractional differential equations by means of topological Degree methods, *Numerical Functional Analysis and Optimization* 33 (2012) 216–238.
- [29] L.A. Zadeh, Fuzzy sets, *Information and Control* 8 (3) (1965) 338–353.
- [30] S.S. Chang, L.A. Zadeh, On fuzzy mapping and control, in: *Fuzzy Sets, Fuzzy Logic, and Fuzzy Systems: Selected Papers by Lotfi A Zadeh*, World Scientific, 1996.
- [31] H. Prade, D. Dubois, Towards fuzzy differential calculus, *Fuzzy Sets and Systems* 8 (1982) 225–233.
- [32] J.R. Goetschel, W. Voxman, Elementary fuzzy calculus, *Fuzzy Sets and Systems* 18 (1) (1986) 31–43.
- [33] O. Kaleva, Fuzzy differential equations, *Fuzzy Sets and Systems* 24 (3) (1987) 301–317.
- [34] L. Wang, L. Wang, *A Course in Fuzzy Systems and Control*, Prentice Hall PTR, Upper Saddle River, NJ, 1997.
- [35] H. Zhang, X. Liao, J. Yu, Fuzzy modeling and synchronization of hyperchaotic systems, *Chaos, Solitons and Fractals* 26 (2005) 835–843.
- [36] M.S. El Naschie, From experimental quantum optics to quantum gravity via a fuzzy Kähler manifold, *Chaos, Solitons and Fractals* 25 (2005) 969–977.
- [37] P. Diamond, Time-dependent differential inclusions, cocycle attractors and fuzzy differential equations, *IEEE Transactions on Fuzzy Systems* 7 (1999) 734–740.
- [38] G. Feng, G. Chen, Adaptive control of discrete time chaotic systems a fuzzy control approach, *Chaos, Solitons and Fractals* 23 (2005) 459–467.
- [39] H. Richard, *Elementary Applied Partial Differential Equations*, Prentice Hall, Englewood Cliffs, NJ, 1983.
- [40] E.J. Rizzo, D.J. Shippy, A method of solution for certain problems of transient heat conduction, *AIAA Journal* 8 (1970) 2004–2009.
- [41] M. Al-Smadi, O.A. Arqub, Computational algorithm for solving fredholm time-fractional partial integrodifferential equations of Dirichlet functions type with error estimates, *Applied Mathematics and Computation* 342 (2019) 280–294.
- [42] O.A. Arqub, Z. Odiat, M. Al-Smadi, Numerical solutions of time-fractional partial integrodifferential equations of Robin functions types in Hilbert space with error bounds and error estimates, *Nonlinear Dynamics* 94 (2018) 1819–1834.
- [43] O.A. Arqub, M. Al-Smadi, Numerical algorithm for solving time-fractional partial integrodifferential equations subject to initial and Dirichlet boundary conditions, *Numerical Methods for Partial Differential Equations* 34 (2018) 1577–1597.
- [44] N.A.A. Rahman, M.Z. Ahmad, Solving fuzzy fractional differential equations using fuzzy Sumudu transform, *Journal of Nonlinear Sciences and Applications* 10 (2017) 2620–2632.

- [45] T. Allahviranloo, N. Taheri, An analytic approximation to the solution of fuzzy heat equation by Adomian decomposition method, *International Journal of Contemporary Mathematical Sciences* 4 (2009) 105–114.
- [46] R. Liu, J.R. Wang, D.O. Regan, On the solutions of first order linear impulsive fuzzy differential equations, *Fuzzy Sets and Systems* 400 (2020) 34–89.
- [47] Y. Zhang, Initial boundary value problem for fractal heat equation in the semi-infinite region by Yang-Laplace transform, *Thermal Science* 2014 (2014) 677–681.
- [48] T. Allahviranloo, M. Barkhordari Ahmadi, Fuzzy Laplace transform, *Soft Computing* 14 (3) (2010) 235–243.
- [49] J.Y. Park, Y.C. Kwan, J.V. Jeong, Existence and uniqueness theorem for a solution of fuzzy Volterra integral equations, *Fuzzy Sets and Systems* 105 (1999) 481–488.

Spatial-fractional derivatives for fluid flow and transport phenomena

Mohamed F. El-Amin^{a,b}

^aEffat University, College of Engineering, Energy Research lab., Jeddah, Saudi Arabia

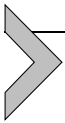
^bAswan University, Faculty of Science, Mathematics Department, Aswan, Egypt

3.1. Introduction

In recent years the fractional derivative models have been utilized successfully in many engineering and science applications. The fractional calculus idea originated around 300 years ago, similar to traditional calculus. The idea of fractional derivatives was discussed by Leibniz and l'Hopital in 1695 [1]. Fractional calculus was then developed by notable names in mathematics such as Wey, Liouville, Fourier, Riemann, Abel, Letnikov, and Grunwald. Recently, fractional modeling has been considered in many science and engineering problems, particularly in fluid dynamics and transport phenomena [2,3]. The two basic types of fractional derivatives, namely, time- and space-fractional derivatives, have been used; however, the time-fractional one was intensively studied. The spatial-fractional development was a bit slower than the temporal one and still requires comprehensive investigation. In this chapter, the emphasis will be on the spatial-fractional modeling or the mixed time-space one. The advection-dispersion phenomenon is a clear example of potential application of spatial fractional modeling [4–6]. On the other hand, Yang [7,8] and Yang et al. [9] have developed a time-space fractional version for Navier–Stokes (NS) equations for incompressible flow on fractal medium. Mohammadein et al. [10] introduced fractional transformation and advanced similarity solutions for the spatial-fractional boundary layer flow model. Yang and Baleanu [11] have proposed a spatial-fractional version of the heat conduction equation in fractal media. The flow in porous media is another example that one may consider spatial-fractional modeling because of its complexity. Thus, solute transport in an underground reservoir does not obey Fick's law [12]. Caputo [13] proposed a fractional Darcy's law with time memory, while the

authors of [14] developed it with space memory. Based on the fractional Taylor series, Wheatcraft and Meerschaerton [15] developed a fractional mass conservation equation of flow in porous media. An analytical solution of the fractional gas flow equation in porous media using fractional power series has been introduced by El-Amin et al. [16], which go back to its traditional original case [17]. Also, Chang et al. [18] presented a spatial fractional Darcy law. Moreover, Chang and Sun [19] developed the time-space fractional carbon dioxide model in porous media. In general, several motivations for using spatial-fractional models to explain fluid flows can be found in the literature. The most appropriate spatial-fractional models are highlighted in this chapter.

The rest of the chapter is organized as follows. In Section 3.2, some concepts of fractional calculus are presented. Section 3.3 introduces a motivation for utilizing spatial-fractional derivatives in fluid flow modeling and derivation of the fractional mass conservation law. The spatial-fractional NS equations are discussed in Section 3.4. Section 3.5 presents two special cases of space-fractional fluid flows, including Poiseuille flow and boundary layer flow. Section 3.6 presents the fractional models of flow in porous media, while Section 3.7 discusses the analytical solution of the space-fractional gas equation. The diffusion/conduction advection/convection equation has been presented in Section 3.8 with two special cases of the fractional heat conduction equation and the solute transport equation.



3.2. Preliminary concepts

In fractional calculus, there exist some basic definitions for fractional derivatives. The current section presents the most important basic definitions applicable and related to the theme of this chapter [2,3]. One of the important basic definitions is the Riemann–Liouville fractional integral. The fractional integral of order $\alpha > 0$ for the integrable function $f(\cdot)$ such that $t \in [a, b]$ may be given as

$${}_a I_t^\alpha f(t) = \begin{cases} \frac{1}{\Gamma(\alpha)} \int_a^t (t - \tau)^{\alpha-1} f(\tau) d\tau, & \alpha \geq 0, \quad t > a, \quad \alpha > 0, \\ f(t), & \alpha = 0, \end{cases} \quad (3.1)$$

such that the Gamma function is given by

$$\Gamma(z) = \int_0^\infty e^{-t} t^{z-1} dt \quad (\text{Re}(z) > 0). \quad (3.2)$$

Moreover, since $f(\cdot)$ is a continuous function with $n - 1 < \alpha \leq n$, $n \in \mathbb{N}$, the Riemann–Liouville fractional derivative can be defined as

$$D_t^\alpha f(t) = \begin{cases} \frac{1}{\Gamma(\alpha-n)} \frac{d^n}{dt^n} \int_a^t \frac{f(\tau)}{(t-\tau)^{\alpha+1-n}} d\tau, & n-1 < \alpha < n, \quad n \in \mathbb{N}, \\ \frac{d^n f(t)}{dt^n}, & \alpha = n \in \mathbb{N}. \end{cases} \quad (3.3)$$

The Caputo fractional derivative is defined by

$${}_a^C D_t^\alpha f(t) = \begin{cases} \frac{1}{\Gamma(\alpha-n)} \int_a^t \frac{f^{(n)}(\tau)}{(t-\tau)^{\alpha+1-n}} d\tau, & n-1 < \alpha < n, \quad n \in \mathbb{N}, \\ \frac{d^n f(t)}{dt^n}, & \alpha = n \in \mathbb{N}. \end{cases} \quad (3.4)$$

For $n = 1$ and lower terminal $a = 0$, the fractional derivative becomes

$${}_0^C D_t^\alpha f(t) = \frac{1}{\Gamma(\alpha-1)} \int_0^t \frac{f'(\tau)}{(t-\tau)^\alpha} d\tau, \quad 0 < \alpha < 1. \quad (3.5)$$

On the other hand, one of the most common identities is the fractional derivative of order α of the power function which is defined by

$$D_\eta^\alpha \eta^\beta = \frac{\Gamma(1+\beta)}{\Gamma(1+\beta-\alpha)} \eta^{\beta-\alpha}. \quad (3.6)$$

Furthermore, we assume $f(\cdot)$ is a differentiable function in the interval $[a, b]$ and $\alpha > 0$. Therefore, one may prove the following:

$$\begin{aligned} {}_a^C D_{ta}^\alpha I_t^\alpha f(t) &= f(t), \\ {}_a^C I_{ta}^\alpha D_t^\alpha f(t) &= f(t) - \sum_{k=0}^{n-1} f^{(k)}(a) \frac{(t-a)^k}{k!}. \end{aligned} \quad (3.7)$$

The integer-order derivative may be generalized to generate a fractional derivative under circumstances that should be collapsed to the integer-order derivative. For example, the Grunwald–Letnikov definition is a generalization of the n th integer derivative to a fractional one. We consider the n th derivative of the continuous function $f \in \mathbb{R}$ as

$$f^{(n)}(t) = \frac{d^n f}{dt^n} = \lim_{h \rightarrow 0} \frac{1}{h^n} \sum_{i=0}^n (-1)^i \binom{n}{i} f(t-ih). \quad (3.8)$$

If one replaces the integer n with a real number $\alpha \in \mathbb{R}$, the definition of the Grunwald–Letnikov fractional derivative will be obtained in the following

form:

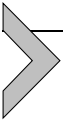
$$\begin{aligned} {}_a D_t^\alpha f(t) &= \lim_{h \rightarrow 0} h^{-\alpha} \sum_{i=0}^{\left[\frac{t-a}{h} \right]} (-1)^i \binom{\alpha}{i} f(t-ih), \quad a < t, \\ {}_t D_b^\alpha f(t) &= \lim_{h \rightarrow 0} h^{-\alpha} \sum_{i=0}^{\left[\frac{b-t}{h} \right]} (-1)^i \binom{\alpha}{i} f(t+ih), \quad b > t, \end{aligned} \quad (3.9)$$

where

$$\binom{\alpha}{i} = \frac{\Gamma(\alpha+1)}{\Gamma(\alpha-i+1)\Gamma(i+1)} \quad (3.10)$$

and $[x]$ denotes the integer part of x . In fact, this formula is unstable; therefore, the shifted Grunwald–Letnikov definition can alternatively be used [32]:

$$D_x^\alpha f(x, t) = h^{-\alpha} \sum_{k=0}^{\left[\frac{x}{h} \right]} \frac{\Gamma(k-\alpha)}{\Gamma(-\alpha)\Gamma(k+1)} f(x-(k-1)h, t). \quad (3.11)$$



3.3. Spatial-fractional mass conservation equation

One of the strongest motivations for using the fractional derivative in modeling fluid flow and transport phenomena is the derivation of the mass conservation equation. So, this section presents the derivation of both integer and fractional derivatives of the mass conservation equation. Consider a control volume of a rectangular cube with volume $\Delta V = \Delta x \Delta y \Delta z$ (Fig. 3.1). Every two opposite faces of the control volume represent the inflow and outflow of the mass flux across them. The quantity of mass across the inflow surface should equal the mass outflow across the opposite surface. From Fig. 3.1, the mass inflow across the first face of the x -axis is given by

$$F(x) = \Delta y \Delta z (\rho u_x), \quad (3.12)$$

and the mass outflow across at $x + \Delta x$ (the opposite side of x) is

$$F(x + \Delta x) = \Delta y \Delta z (\rho u_x) + \Delta y \Delta z \frac{\partial (\rho u_x)}{\partial x} \Delta x. \quad (3.13)$$

Traditionally, the equation of mass conservation of the fluid flow in porous media is derived using the first-order Taylor series to represent the

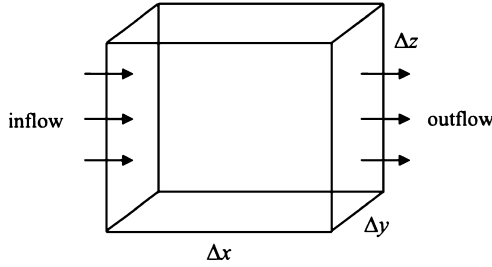


Figure 3.1 Sketch of rectangular control volume.

linear mass flux through a control volume. Alternatively, the fractional Taylor series of order α has been employed to represent the mass flux [15]. The fractional mass flux component in the x -direction can be described using the two-term fractional Taylor series expanding around x ; thus,

$$F(x + \Delta x) = \Delta y \Delta z (\rho u_x) + \Delta y \Delta z \frac{\partial^\alpha (\rho u_x)}{\partial x^\alpha} \frac{(\Delta x)^\alpha}{\Gamma(\alpha + 1)}, \quad (3.14)$$

where the fractional derivative can be defined by the Caputo fractional derivative of order $0 < \alpha < 1$ as

$$\frac{\partial^\alpha f(x)}{\partial x^\alpha} = \frac{1}{\Gamma(1 - \alpha)} \int_{x_i}^x (x - \xi)^{-\alpha} \frac{\partial f(x, \xi)}{\partial \xi} d\xi, \quad (3.15)$$

where $\Gamma(x)$ is the Gamma function. Here, the medium is assumed to be heterogeneous and isotropic. Also, α has been assumed to have the same value in all directions. The net mass flux in the x -direction can be obtained by

$$F(x) - F(x + \Delta x) = -\Delta y \Delta z \frac{\partial^\alpha (\rho u_x)}{\partial x^\alpha} \frac{(\Delta x)^\alpha}{\Gamma(\alpha + 1)}. \quad (3.16)$$

Similarly, the net mass fluxes in the y - and z -directions are given by

$$F(y) - F(y + \Delta y) = -\Delta x \Delta z \frac{\partial^\alpha (\rho u_y)}{\partial y^\alpha} \frac{(\Delta y)^\alpha}{\Gamma(\alpha + 1)} \quad (3.17)$$

and

$$F(z) - F(z + \Delta z) = -\Delta x \Delta y \frac{\partial^\alpha (\rho u_z)}{\partial z^\alpha} \frac{(\Delta z)^\alpha}{\Gamma(\alpha + 1)}. \quad (3.18)$$

Therefore, the net mass flux through the control volume is obtained by summing (3.16)–(3.18):

$$\Delta F = -\frac{\Delta V}{\Gamma(\alpha + 1)} \left[(\Delta x)^{\alpha-1} \frac{\partial^\alpha (\rho u_x)}{\partial x^\alpha} + (\Delta y)^{\alpha-1} \frac{\partial^\alpha (\rho u_y)}{\partial y^\alpha} + (\Delta z)^{\alpha-1} \frac{\partial^\alpha (\rho u_z)}{\partial z^\alpha} \right]. \quad (3.19)$$

Based on the mass conservation concept, the net mass flux, Eq. (3.19), should equal the accumulation term, $\frac{\partial}{\partial t}(\Delta V \rho)$. Then, the mass conservation of the fluid flow can be written as

$$\frac{\partial}{\partial t}(\Delta V \rho) = -\frac{\Delta V}{\Gamma(\alpha + 1)} \left[(\Delta x)^{\alpha-1} \frac{\partial^\alpha (\rho u_x)}{\partial x^\alpha} + (\Delta y)^{\alpha-1} \frac{\partial^\alpha (\rho u_y)}{\partial y^\alpha} + (\Delta z)^{\alpha-1} \frac{\partial^\alpha (\rho u_z)}{\partial z^\alpha} \right] + q, \quad (3.20)$$

where φ is porosity and q is the source/sink term. In other notations, assuming $(x, y, z) \equiv (x_1, x_2, x_3)$ and $(u_x, u_y, u_z) \equiv (u_1, u_2, u_3)$, one can write this equation as

$$\frac{\partial}{\partial t}(\Delta V \rho) + \frac{\Delta V}{\Gamma(\alpha + 1)} \sum_{i=1}^3 (\Delta x_i)^{\alpha-1} \frac{\partial^\alpha (\rho u_i)}{\partial x_i^\alpha} = q. \quad (3.21)$$

In the above equation, $(\Delta x_i)^{\alpha-1}$ is a scaling variable which has to be provided. On the other hand, if $\alpha = 1$ this variable will disappear from the equation, i.e.,

$$\frac{\partial}{\partial t}(\Delta V \rho) + \Delta V \sum_{i=1}^3 \frac{\partial (\rho u_i)}{\partial x_i} = q, \quad (3.22)$$

which is the traditional mass conservation equation.

Considering an anisotropic fractional derivative, i.e., the fractional orders are different in the x -, y -, and z -directions, and for simplicity assuming that $(\Delta x_i)^{\alpha-1} / \Gamma(\alpha + 1) = 1$, the space-fractional mass conservation equation can be written as

$$\frac{\partial \rho}{\partial t} + \frac{\partial^{\alpha_1} (\rho u_x)}{\partial x^{\alpha_1}} + \frac{\partial^{\alpha_2} (\rho u_y)}{\partial y^{\alpha_2}} + \frac{\partial^{\alpha_3} (\rho u_z)}{\partial z^{\alpha_3}} = q, \quad (3.23)$$

where α_1 , α_2 , and α_3 are, respectively, the space-fractional orders in x -, y -, and z -directions.



3.4. Fractional Navier–Stokes equation

The NS equations are widely used and play a crucial role in fluid mechanics to model fluid flow phenomena. Recently, the fractional calculus generalizations of NS equations have gained comprehensive attention. The utilization of fractional modeling to describe various transport phenomena has been of great interest [23]. For example, Xu and Tan [24] found out that it is more convincing to use fractional differential equations to represent the turbulent wind flow rather than the traditional ones. In early times, the space-fractional NS equations were developed by replacing the Laplace operator in the NS equations with a fractional one (see Chen and Holm [26]). Also, Chen [27] introduced a statistical-mechanical model of the chaos-induced turbulence diffusion based on a fractional formulation. In addition, Pozrikids [25] proposed a space-fractional implicit constitutive equation to study fractional Stokes flow. On the other hand, Li and Zhai [22] studied the solution properties of space-fractional NS equations. In [20,21], different sorts of numerical techniques for solving fractional differential equations have been presented.

Using a similar fashion of deriving the fractional mass conservation equation (Section 3.3), the fractional time/space momentum (NS) equations can be provided in their general form as

$$\left\{ \begin{array}{l} \rho \left(\frac{\partial^\alpha u_x}{\partial t^\alpha} + u_x \frac{\partial^{\alpha_1} u_x}{\partial x^{\alpha_1}} + u_y \frac{\partial^{\alpha_2} u_x}{\partial y^{\alpha_2}} + u_z \frac{\partial^{\alpha_3} u_x}{\partial z^{\alpha_3}} \right) \\ \quad = -\frac{\partial^\beta p}{\partial x^\beta} + \mu \left(\frac{\partial^{\gamma_1} u_x}{\partial x^{\gamma_1}} + \frac{\partial^{\gamma_2} u_x}{\partial y^{\gamma_2}} + \frac{\partial^{\gamma_3} u_x}{\partial z^{\gamma_3}} \right) + \rho b_x, \\ \rho \left(\frac{\partial^\alpha u_y}{\partial t^\alpha} + u_x \frac{\partial^{\alpha_1} u_y}{\partial x^{\alpha_1}} + u_y \frac{\partial^{\alpha_2} u_y}{\partial y^{\alpha_2}} + u_z \frac{\partial^{\alpha_3} u_y}{\partial z^{\alpha_3}} \right) \\ \quad = -\frac{\partial^\beta p}{\partial y^\beta} + \mu \left(\frac{\partial^{\gamma_1} u_y}{\partial x^{\gamma_1}} + \frac{\partial^{\gamma_2} u_y}{\partial y^{\gamma_2}} + \frac{\partial^{\gamma_3} u_y}{\partial z^{\gamma_3}} \right) + \rho b_y, \\ \rho \left(\frac{\partial^\alpha u_z}{\partial t^\alpha} + u_x \frac{\partial^{\alpha_1} u_z}{\partial x^{\alpha_1}} + u_y \frac{\partial^{\alpha_2} u_z}{\partial y^{\alpha_2}} + u_z \frac{\partial^{\alpha_3} u_z}{\partial z^{\alpha_3}} \right) \\ \quad = -\frac{\partial^\beta p}{\partial z^\beta} + \mu \left(\frac{\partial^{\gamma_1} u_z}{\partial x^{\gamma_1}} + \frac{\partial^{\gamma_2} u_z}{\partial y^{\gamma_2}} + \frac{\partial^{\gamma_3} u_z}{\partial z^{\gamma_3}} \right) + \rho b_z, \end{array} \right. \quad (3.24)$$

where $\mathbf{u} = (u_x, u_y, u_z)$ is the velocity vector, $\mathbf{b} = (b_x, b_y, b_z)$ represents the acceleration given by the external force, $0 > \alpha > 1$ is the time-fractional order, $0 > \alpha_1 > 1$, $0 > \alpha_2 > 1$, and $0 > \alpha_3 > 1$ are, respectively, the space-fractional orders of the advection terms in the x -, y -, and z -directions, $0 > \beta > 1$ is the space-fractional order, and $1 > \gamma_1 > 2$, $1 > \gamma_2 > 2$, and $1 > \gamma_3 > 2$ are, respectively, the space-fractional orders of the diffusion terms in the x -, y -, and z -directions.

The above general formula of NS equations may be difficult to implement. For example, if one assumes integer time derivatives ($\alpha = 1$) and

isotropic space-fractional derivatives in both advection and viscous terms, namely, $0 > \alpha_1 = \alpha_2 = \alpha_3 = \alpha > 1$ and $1 > \gamma_1 = \gamma_2 = \gamma_3 = \gamma > 2$, the space-fractional NS equations can be written as

$$\begin{cases} \frac{\partial u_x}{\partial t} + u_x \frac{\partial^\alpha u_x}{\partial x^\alpha} + u_y \frac{\partial^\alpha u_x}{\partial y^\alpha} + u_z \frac{\partial^\alpha u_x}{\partial z^\alpha} = -\frac{1}{\rho} \frac{\partial^\beta p}{\partial x^\beta} + \nu \left(\frac{\partial^\gamma u_x}{\partial x^\gamma} + \frac{\partial^\gamma u_x}{\partial y^\gamma} + \frac{\partial^\gamma u_x}{\partial z^\gamma} \right) + b_x, \\ \frac{\partial u_y}{\partial t} + u_x \frac{\partial^\alpha u_y}{\partial x^\alpha} + u_y \frac{\partial^\alpha u_y}{\partial y^\alpha} + u_z \frac{\partial^\alpha u_y}{\partial z^\alpha} = -\frac{1}{\rho} \frac{\partial^\beta p}{\partial y^\beta} + \nu \left(\frac{\partial^\gamma u_y}{\partial x^\gamma} + \frac{\partial^\gamma u_y}{\partial y^\gamma} + \frac{\partial^\gamma u_y}{\partial z^\gamma} \right) + b_y, \\ \frac{\partial u_z}{\partial t} + u_x \frac{\partial^\alpha u_z}{\partial x^\alpha} + u_y \frac{\partial^\alpha u_z}{\partial y^\alpha} + u_z \frac{\partial^\alpha u_z}{\partial z^\alpha} = -\frac{1}{\rho} \frac{\partial^\beta p}{\partial z^\beta} + \nu \left(\frac{\partial^\gamma u_z}{\partial x^\gamma} + \frac{\partial^\gamma u_z}{\partial y^\gamma} + \frac{\partial^\gamma u_z}{\partial z^\gamma} \right) + b_z, \end{cases} \quad (3.25)$$

where $\mu = \nu/\rho$. We may model many special cases by considering different fractional derivatives. In the following section, we present selected special cases. Also, the above formulas are collapsed to the traditional formula of NS equations for incompressible flow as $\alpha = 1$, $\beta = 1$, $\gamma = 2$:

$$\begin{cases} \frac{\partial u_x}{\partial t} + u_x \frac{\partial u_x}{\partial x} + u_y \frac{\partial u_x}{\partial y} + u_z \frac{\partial u_x}{\partial z} = -\frac{1}{\rho} \frac{\partial p}{\partial x} + \nu \left(\frac{\partial^2 u_x}{\partial x^2} + \frac{\partial^2 u_x}{\partial y^2} + \frac{\partial^2 u_x}{\partial z^2} \right) + b_x, \\ \frac{\partial u_y}{\partial t} + u_x \frac{\partial u_y}{\partial x} + u_y \frac{\partial u_y}{\partial y} + u_z \frac{\partial u_y}{\partial z} = -\frac{1}{\rho} \frac{\partial p}{\partial y} + \nu \left(\frac{\partial^2 u_y}{\partial x^2} + \frac{\partial^2 u_y}{\partial y^2} + \frac{\partial^2 u_y}{\partial z^2} \right) + b_y, \\ \frac{\partial u_z}{\partial t} + u_x \frac{\partial u_z}{\partial x} + u_y \frac{\partial u_z}{\partial y} + u_z \frac{\partial u_z}{\partial z} = -\frac{1}{\rho} \frac{\partial p}{\partial z} + \nu \left(\frac{\partial^2 u_z}{\partial x^2} + \frac{\partial^2 u_z}{\partial y^2} + \frac{\partial^2 u_z}{\partial z^2} \right) + b_z. \end{cases} \quad (3.26)$$



3.5. Special cases

3.5.1 Poiseuille flow

Poiseuille flow is fluid flow between two stationary parallel plates at the points $y = 0$ and $y = h$. (See Fig. 3.2.) Initially, the fluid is at rest, and it starts its motion suddenly under a pressure gradient. This problem can be modeled using a 1D simplified NS equation, and here three fractional models will be considered [37]:

$$\frac{\partial u}{\partial t} = -\frac{1}{\rho} \frac{\partial p}{\partial x} + \nu \frac{\partial^\alpha u}{\partial y^\alpha}. \quad (3.27)$$

Along with the initial and boundary conditions,

$$\begin{aligned} u(y, 0) &= 0, \quad 0 < y < h, \\ u(0, t) &= u(h, t) = 0, \quad t \geq 0. \end{aligned} \quad (3.28)$$

If one assumes a uniform effective pressure gradient in the x -direction, i.e., $-\partial p/\partial x = kH(t)$, k is a constant, and $H(\cdot)$ is the Heaviside step function,

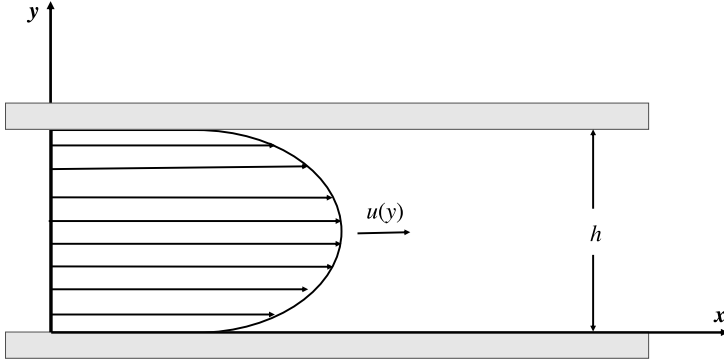


Figure 3.2 Sketch of Poiseuille flow.

the above system can be nondimensionalized to the form

$$\begin{aligned} \frac{\partial}{\partial t} u(y, t) &= 1 + \frac{1}{Re} \frac{\partial^\alpha}{\partial y^\alpha} u(y, t), \\ u(y, 0) &= 0, \quad 0 < y < 1, \\ u(0, t) &= u(1, t) = 0, \quad t \geq 0, \end{aligned} \quad (3.29)$$

where $Re = \sqrt{k/h\rho} \cdot h^\alpha / \nu$ is the generalized Reynolds number.

The fractional derivative $\partial^\alpha / \partial y^\alpha$ is called Riesz operator with $1 < \alpha \leq 2$, which can be defined on the finite intervals $y \in [0, h]$, $t \in [0, T]$ as [1,38]

$$\frac{\partial^\alpha}{\partial y^\alpha} = -c_\alpha \left({}_0D_y^\alpha + {}_yD_h^\alpha \right), \quad (3.30)$$

where $c_\alpha = \frac{1}{2\cos(\pi\alpha/2)}$. The left-hand side and right-hand side Riemann–Liouville fractional derivatives can be, respectively, written as

$$\begin{aligned} {}_0D_y^\alpha u(y, t) &= \frac{1}{\Gamma(2-\alpha)} \frac{\partial^2}{\partial y^2} \int_0^y \frac{u(\xi, t) d\xi}{(y-\xi)^{\alpha-1}}, \\ {}_yD_h^\alpha u(y, t) &= \frac{1}{\Gamma(2-\alpha)} \frac{\partial^2}{\partial y^2} \int_y^h \frac{u(\xi, t) d\xi}{(\xi-y)^{\alpha-1}}. \end{aligned} \quad (3.31)$$

The discrete approximation version can be written as [1,38]

$${}_0D_y^\alpha u(y_j, t_k) \approx \frac{1}{h^\alpha} \sum_{l=0}^{j+1} g_l u_{j-l+1}^k \quad \text{and} \quad {}_yD_1^\alpha u(y_j, t_k) \approx \frac{1}{h^\alpha} \sum_{l=0}^{M-j+1} g_l u_{j+l-1}^k, \quad (3.32)$$

where $g_0 = 1$, $g_l = (-1)^l \alpha(\alpha - 1) \cdots (\alpha - l + 1)/l!$, $l \geq 1$, with the uniform discretizations (y_j, t_k) : $y_j = jh$, $t_k = k\tau$, $j = 0, 1, \dots, M$, $k = 0, 1, \dots, N$, such that $M, N \in \mathbb{N}^+$, $h = 1/M$, and $\tau = T/N$.

Therefore, the implicit difference scheme can be written as

$$\frac{u_j^k - u_j^{k-1}}{\tau} = 1 - \frac{1}{Re} \cdot \frac{1}{2h^\alpha \cos \frac{\pi\alpha}{2}} \cdot \left(\sum_{l=0}^{j+1} g_l u_{j-l+1}^k + \sum_{l=0}^{M-j+1} g_l u_{j+l-1}^k \right). \quad (3.33)$$

Along with the numerical initial and boundary conditions,

$$u_j^0 = 0, \quad u_0^k = u_M^k = 0, \quad j = 0, 1, 2, \dots, M, \quad k = 0, 1, 2, \dots, N, \quad (3.34)$$

which must be comparable with the exact solution of the traditional case, $\alpha = 2$,

$$u(y, t) = \frac{y(1-y)}{2} Re - 2Re \sum_{n=1}^{\infty} \frac{1 - (-1)^n}{(n\pi)^3} \exp\left(-\frac{n^2\pi^2}{Re} t\right) \sin n\pi y. \quad (3.35)$$

3.5.2 Boundary layer flow

In this section, we consider the fractional-derivative model and solution of the boundary layer flow on an infinite vertical plate embedded in a viscous fluid [10]. The boundary layer theory has been developed and used in many applications in different industrial areas and fundamental fluid dynamics analyses (see Schlichting [28] and El-Amin and Kanayama [29,30]). Considering the x -axis to be parallel to the plate and the y -axis to be perpendicular to it, applying a fractional operator of order $0 < \alpha < 1$, the governing equations may be given as

$$\begin{aligned} \frac{\partial u}{\partial x} + \frac{\partial v}{\partial y} &= 0, \\ u \frac{\partial u}{\partial x} + v \frac{\partial u}{\partial y} &= \nu \frac{\partial^{\alpha+1} u}{\partial y^{\alpha+1}}, \end{aligned} \quad (3.36)$$

subject to the boundary conditions

$$u(x, 0) = 0, \quad v(x, 0) = 0, \quad \text{and} \quad u(x, \infty) = u_\infty, \quad (3.37)$$

where u and v are the velocity components in the x - and y -directions, respectively, ν is the kinematic viscosity, and u_∞ is a constant representing the outer free-stream velocity. (See Fig. 3.3.)

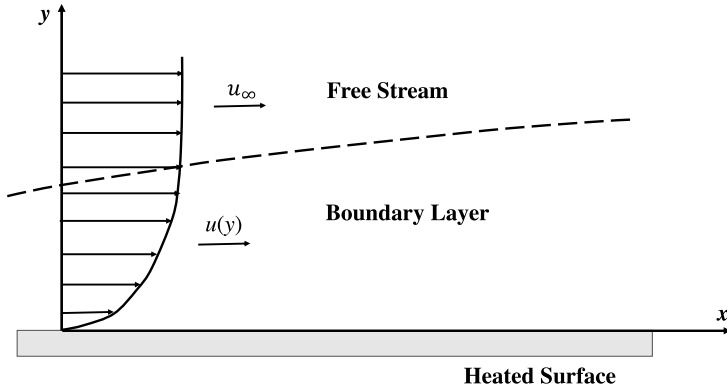


Figure 3.3 Sketch of the boundary layer flow.

Mohammadein et al. [10] have introduced the following generalized similarity variable:

$$\begin{aligned} \eta(x, y) &= \frac{b(x)y^\alpha}{\Gamma(\alpha + 1)}, & \psi(x, y) &= \nu c(x)f(\eta), \\ u &= \frac{\partial \psi}{\partial y}, & v &= -\frac{\partial \psi}{\partial x}. \end{aligned} \quad (3.38)$$

Using Eqs. (3.38), we can write Eq. (3.36) as

$$\alpha \eta f^{(\alpha+2)} + (\alpha - 1)f^{(\alpha+1)} = (3\alpha - 1)\eta f'^2 - 3\alpha \eta f f'' - 3(\alpha - 1)ff', \quad (3.39)$$

with boundary conditions

$$f(0) = f'(0) = 0, \quad f'(\infty) = 1. \quad (3.40)$$

Both fractional dimensionless transformations and fractional differential equations are collapsed into their traditional forms as $\alpha = 1$ [31]. Eq. (3.39) along with the boundary conditions (3.40) can be solved using the power-series technique. Let the function $f(\eta)$ be continuous and assume it can be represented by the fractional power series [10]

$$f(\eta) = \sum_{n=0}^{\infty} a_n \eta^{\alpha n}. \quad (3.41)$$

Then apply the Caputo fractional derivative definition to find

$$\begin{cases} f^{(\alpha)} = \sum_{n=1}^{\infty} a_n \frac{\Gamma(1+\alpha n)}{\Gamma(1+\alpha n-\alpha)} \eta^{\alpha n-\alpha}, \\ f^{(\alpha+1)} = \sum_{n=2}^{\infty} (\alpha n - \alpha) a_n \frac{\Gamma(1+\alpha n)}{\Gamma(1+\alpha n-\alpha)} \eta^{\alpha n-\alpha-1}, \\ f^{(\alpha+2)} = \sum_{n=2}^{\infty} (\alpha n - \alpha)(\alpha n - \alpha - 1) a_n \frac{\Gamma(1+\alpha n)}{\Gamma(1+\alpha n-\alpha)} \eta^{\alpha n-\alpha-2}. \end{cases} \quad (3.42)$$

Similarly, the integer first- and second-order derivatives of the function $f(\eta)$ can be calculated as

$$f' = \sum_{n=1}^{\infty} \alpha n a_n \eta^{\alpha n-1}, \quad f'' = \sum_{n=2}^{\infty} \alpha n (\alpha n - 1) a_n \eta^{\alpha n-2}, \quad (3.43)$$

holding the rule of series product, one obtains,

$$\sum_{n=0}^{\infty} a_n \eta^n \cdot \sum_{n=0}^{\infty} b_n \eta^n = \sum_{n=0}^{\infty} c_n \eta^n, \quad c_n = \sum_{k=0}^n a_k b_{n-k}. \quad (3.44)$$

Therefore, one can estimate the following nonlinear terms of Eq. (3.39):

$$\begin{cases} f'^2 = \sum_{n=2}^{\infty} \sum_{k=0}^n \alpha k a_k \cdot \alpha (n-k) a_{n-k} \eta^{\alpha n-2}, \\ f f' = \sum_{n=1}^{\infty} \sum_{k=0}^n a_k \cdot \alpha (n-k) a_{n-k} \eta^{\alpha n-1}, \\ f f'' = \sum_{n=1}^{\infty} \sum_{k=0}^n a_k \cdot \alpha (n-k) (\alpha (n-k) - 1) a_{n-k} \eta^{\alpha n-2}. \end{cases} \quad (3.45)$$

Substituting all the above terms into Eq. (3.39) and then comparing the coefficients on both sides of the resulting equation for $\eta^{\alpha n-1}$, we get the following recurrence relation:

$$\begin{aligned} & \alpha n (\alpha^2 n - 1) \frac{\Gamma(\alpha(n+1)+1)}{\Gamma(\alpha n+1)} a_{n+1} \\ & = \sum_{k=0}^n \alpha (n-k) (3 - k\alpha + 3(2k-n)\alpha^2) a_k a_{n-k}, \quad \forall n \geq 2. \end{aligned} \quad (3.46)$$

In order to determine the series coefficients, the boundary conditions will be utilized. From $f(0) = 0$, we find that $a_0 = 0$, and from $f'(0) = 0$, we get $a_1 = 0$. From $f'(\infty) = 1$ and for large values of L (approaching infinity),

$f'(L) = \sum_{n=0}^{\infty} \alpha n a_n L^{\alpha n-1} = 1$. On the other hand, the coefficients a_{3k} and a_{3k+1} , $k \geq 0$, vanish, while the coefficients a_{3k+2} , $k \geq 1$, may have the form

$$\gamma_{3n+2} a_{3n+2} = \sum_{i=0}^{n-1} g_{3i+2, (3n+1)-(3i+2)} a_{3i+2} a_{(3n+1)-(3i+2)}, \quad \forall n \geq 1, \quad (3.47)$$

where $\gamma_{r+1} = \frac{r(r\alpha^2-1)\Gamma((r+1)\alpha+1)}{\Gamma(r\alpha+1)}$ and $g_{k,n-k} = (n-k)(3-k\alpha+3(2k-n)\alpha^2)$.

The solution convergence has been proved, and for results and discussions, refer to [10].

3.6. Fractional models of flow in porous media

A solid material containing pores (voids) is called a porous medium or a porous material. The solid skeletal portion is called the “matrix” or “frame” of the material (see Fig. 3.4). A porous medium is distinguished most of all by its porosity and permeability. In multiphase flows, some other properties are dependent on the respective properties of their solid matrix and fluid, such as relative permeability and phase mobility.

One of the crucial areas where fractional models are applied is fluid flow in porous media [19,36]. Fluid flow in porous media such as carbonate rocks is mainly driven by the pressure gradient and governed traditionally

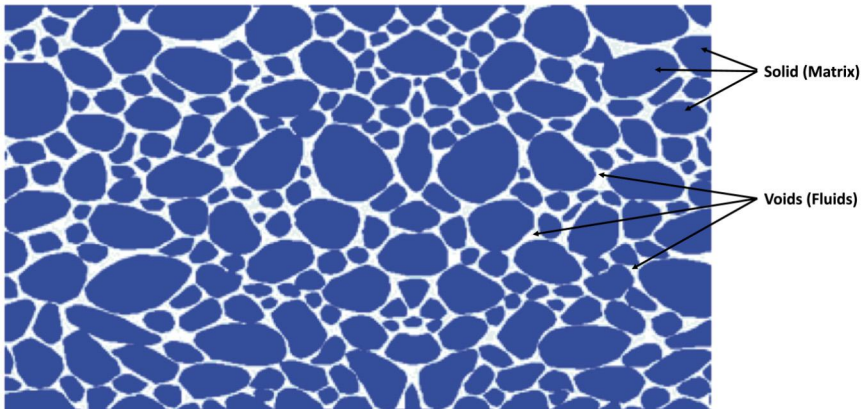


Figure 3.4 Sketch of the flow in porous media.

by Darcy's law as

$$q_m = -\rho \frac{K}{\mu} \nabla p, \quad (3.48)$$

where q_m is the fluid mass flow rate per unit area, which is proportional to the gradient of the pore pressure p . The proportional coefficient is $\eta = K/\mu$, such that K is the permeability of the medium and μ is the fluid viscosity. Alternatively, Eq. (3.48) can be written as

$$\mathbf{u} = -\eta \nabla p, \quad (3.49)$$

where $\mathbf{u} = (u_x, u_y, u_z)$ is the fluid velocity vector.

3.6.1 Fractional Darcy's law with time memory

Assuming that the permeability decreases with time, the fluid pressure effect is then delayed and the flow happens as though the medium had a memory. Caputo [13] has proposed a generalized Darcy law with time memory to accommodate the effect of decreasing permeability. The proportional coefficient η is assumed to be a function of time and the pressure gradient is under a time-fractional operator, i.e.,

$$\mathbf{u} = -\eta(t) \left(\frac{\partial^\alpha}{\partial t^\alpha} \nabla p \right), \quad (3.50)$$

where $0 \leq \alpha \leq 1$. We have

$$\frac{\partial^\alpha}{\partial t^\alpha} \{f(x, t)\} = \frac{1}{\Gamma(1-\alpha)} \int_0^t (t-\tau)^{-\alpha} \frac{\partial f(x, \tau)}{\partial \tau} d\tau.$$

Moreover, Obembe et al. [33] suggested a variable order $\alpha(t)$ time-fractional model as

$$\mathbf{u} = -\xi_0 \eta \left(\frac{\partial^{\alpha(t)}}{\partial t^{\alpha(t)}} \nabla p \right), \quad (3.51)$$

where ξ_0 is the transmissibility conversion factor.

3.6.2 Fractional Darcy law with space memory

He [14] proposed a space memory based on the fractional derivative as

$$\mathbf{u} = -\eta \nabla^\alpha p, \quad 0 \leq \alpha \leq 1, \quad (3.52)$$

where

$$\nabla^\alpha = \left(\frac{\partial^\alpha}{\partial x^\alpha}, \frac{\partial^\alpha}{\partial y^\alpha}, \frac{\partial^\alpha}{\partial z^\alpha} \right).$$

The Caputo fractional derivative is given by

$$\frac{\partial^\alpha}{\partial x^\alpha} \{f(x)\} = \frac{1}{\Gamma(1-\alpha)} \int_0^x (x-\xi)^{-\alpha} \frac{\partial f(x, \xi)}{\partial \xi} d\xi.$$

Chang et al. [18] have shown comparisons between experimental results and the best-fit curve produced by the spatial fractional Darcy law for two different permeabilities. The fractional order $\alpha = 0.45$ results fit well with the permeability value of $2.36 \times 10^{-15} \text{ m}^{1.45}$, while the fractional order $\alpha = 0.76$ results fit well with the permeability value of $1.58 \times 10^{-16} \text{ m}^{1.76}$.



3.7. Fractional natural gas equation

This section introduces a fractional derivative gas transport equation for model gas transport around a production well. Consider natural gas transport in a porous medium withholding the ideal gas law with a deviation factor. The flow has been assumed to be isothermal, and no gas sorption and desorption take place. Therefore, the radial governing equation can be expressed as [16]

$$\gamma \varphi \frac{\partial p}{\partial t} = \frac{1}{r} \frac{\partial}{\partial r} \left(\frac{rk\rho_0}{\mu} \frac{\partial^\alpha p}{\partial r^\alpha} \right), \quad (3.53)$$

where r is the radial coordinate variable. The Dirichlet–Dirichlet boundary conditions are

$$p = p_w \quad \text{for} \quad \eta = 0, \quad p = p_0 \quad \text{for} \quad \eta = \infty, \quad (3.54)$$

and the Dirichlet–Neumann boundary conditions are

$$p = p_w \quad \text{for} \quad \eta = 0, \quad \frac{\partial p}{\partial \eta} = \frac{Q\mu}{2\pi kH} \quad \text{for} \quad \eta = \infty. \quad (3.55)$$

Eq. (3.53) can be rewritten as

$$\frac{1}{\chi} \frac{\partial p}{\partial t} = \frac{\partial^{\alpha+1} p}{\partial r^{\alpha+1}} + \frac{1}{r} \frac{\partial^\alpha p}{\partial r^\alpha}, \quad (3.56)$$

where $\frac{1}{\chi} = \frac{kp_0}{\varphi\mu}$. The generalized fractional Boltzmann change of variable was presented by El-Amin et al. [16]:

$$\eta = \frac{r^{\alpha+1}}{2\Gamma(\alpha+2)t\chi}, \quad t > 0. \quad (3.57)$$

Applying this transformation with some mathematical manipulation, we obtain

$$\eta \frac{\partial p}{\partial \eta} + \frac{\partial^\alpha p}{\partial \eta^\alpha} + \frac{\alpha+1}{2} \eta \frac{\partial^{\alpha+1} p}{\partial \eta^{\alpha+1}} = 0. \quad (3.58)$$

We have the following fractional power series:

$$p(\eta) = \sum_{n=0}^{\infty} a_n \eta^{\alpha n}. \quad (3.59)$$

Then applying the Caputo fractional-order space derivative, the governing equation can be given as

$$\sum_{m=1}^{\infty} \alpha m a_m \eta^{\alpha m} + \sum_{n=1}^{\infty} \left(\frac{a_n \Gamma(\alpha n + 1)}{\Gamma(\alpha(n-1))} \left(\frac{1}{\alpha(n-1)} - \frac{\alpha+1}{2} \right) \right) \eta^{\alpha(n-1)} = 0. \quad (3.60)$$

The powers of the first term of the above equation are $\{\alpha, 2\alpha, 3\alpha, \dots\}$, while the powers of the second term are $\{0, \alpha, 2\alpha, 3\alpha, \dots\}$. So, there is one step between n and m , i.e., $a_1 = 0$, and

$$\alpha m a_m + \left(\frac{\Gamma(\alpha(m+1)+1)}{\Gamma(\alpha m)} \left(\frac{1}{\alpha m} - \frac{\alpha+1}{2} \right) \right) a_{m+1} = 0. \quad (3.61)$$

Consequently, we obtain the recurrence relation

$$a_{m+1} = - \frac{\alpha m}{\left(\frac{\Gamma(\alpha(m+1)+1)}{\Gamma(\alpha m)} \left(\frac{1}{\alpha m} - \frac{\alpha+1}{2} \right) \right)} a_m, \quad m > 1, \quad (3.62)$$

while a_0 and a_2 have to be found. Using the boundary conditions, we can find

$$p_w = a_0, \quad p_0 = p_w + a_2 L^{2\alpha} + a_3 L^{3\alpha} + a_4 L^{4\alpha} + a_5 L^{5\alpha} + \dots \quad (3.63)$$

Then,

$$p_0 - p_w = a_2 L^{2\alpha} \left(1 + \sum_{j=1}^{\infty} \beta_j L^{j\alpha} \right). \quad (3.64)$$

Thus,

$$a_2 = \frac{p_0 - p_w}{L^{2\alpha} \left(1 + \sum_{j=1}^{\infty} \beta_j j^{\alpha} \right)},$$

$$\beta_j = -\frac{(j+1)\alpha}{\left(\frac{\Gamma(j+2)\alpha+1}{\Gamma(j+1)\alpha} \left(\frac{1}{\theta+1} - \frac{\alpha+1}{2} \right) \right)} \beta_{j-1}, \quad \beta_0 = 1. \quad (3.65)$$

On the other hand, the Neumann boundary condition results in

$$\frac{dp}{d\eta} = \alpha \sum_{n=2}^{\infty} n a_n \eta^{\alpha n - 1}. \quad (3.66)$$

We have $a_1 = 0$ and

$$a_2 = \frac{\frac{Q\mu}{2\pi kH}}{\alpha L^{2\alpha-1} \left(2 + \sum_{j=1}^{\infty} (j+2)\beta_j L^{\alpha} \right)}. \quad (3.67)$$

Moreover, the solution convergence has been provided in [16] and it was found that solutions are unconditionally converged.



3.8. Fractional multiphase flows in porous media

Multiphase flows in porous media have many applications, such as oil/gas reservoir simulation, enhanced oil recovery, carbon dioxide sequestration, and water soil infiltration. In this section, the fractional mass and momentum conservation laws of multiphase flow in porous media are derived using the fractional Taylor series approximation. Multiphase flows in porous media are described by very complicated nonlinear models. The traditional models were developed based on the continuum approach utilizing the concept of linear flux to derive the conservation equations [39–44].

In the following, we introduce the fractional mass equation of the multiphase flow. Eq. (3.21) represents the mass equation of the single-phase flow which can be extended to a multiphase immiscible flow. Referring to each fluid phase by β , one can write [45]

$$\frac{\partial}{\partial t} (S_{\beta} \Delta V \varphi \rho_{\beta}) + \frac{\Delta V}{\Gamma(\alpha+1)} \sum_{i=1}^3 (\Delta x_i)^{\alpha-1} \frac{\partial^{\alpha} (\rho_{\beta} u_{\beta i})}{\partial x_i^{\alpha}} = q_{\beta}, \quad (3.68)$$

such that S_{β} is the saturation of phase β , which is defined as the ratio between volume of pore spaces occupied by fluid phase and the total pore

volume. Therefore, if one considers multiphase flow, the summation of saturation of all phases should equal one, i.e.,

$$\sum_{\beta} S_{\beta} = 1. \quad (3.69)$$

Assuming that the control volume, phase density, and porosity vary with pressure and time, the phase saturation varies with time as [45]

$$\begin{aligned} & \frac{\partial}{\partial t} (S_{\beta} \Delta V \varphi \rho_{\beta}) \\ &= \Delta V \varphi \rho_{\beta} \frac{\partial S_{\beta}}{\partial t} + \left(S_{\beta} \varphi \rho_{\beta} \frac{\partial \Delta V}{\partial p} + \Delta V S_{\beta} \rho_{\beta} \frac{\partial \varphi}{\partial p} + \Delta V S_{\beta} \varphi \frac{\partial \rho_{\beta}}{\partial p} \right) \frac{\partial p}{\partial t}. \end{aligned} \quad (3.70)$$

The bulk volume equals the pore volume plus the rock volume; thus,

$$\Delta V = \Delta V_p + \Delta V_s. \quad (3.71)$$

In terms of porosity, the pore volume plus the rock volume are defined, respectively, as

$$\Delta V_s = (1 - \varphi) \Delta V \quad (3.72)$$

and

$$\Delta V_p = \varphi \Delta V. \quad (3.73)$$

Now, let us provide the following terms.

The bulk compressibility coefficient, c_b , is given by

$$c_b = -\frac{1}{\Delta V} \frac{\partial \Delta V}{\partial p}, \quad (3.74)$$

the solid matrix compressibility, c_s , is written as

$$c_s = -\frac{1}{\Delta V_s} \frac{\partial \Delta V_s}{\partial p}, \quad (3.75)$$

which can be expressed in terms of porosity as

$$c_s = -\frac{1}{(\Delta V_s / \Delta V)} \frac{\partial (\Delta V_s / \Delta V)}{\partial p} = \frac{1}{1 - \varphi} \frac{\partial \varphi}{\partial p}, \quad (3.76)$$

and the pore compressibility, c_p , is

$$c_p = -\frac{1}{\Delta V_p} \frac{\partial \Delta V_p}{\partial p}. \quad (3.77)$$

Therefore, the bulk compressibility can be given with respect to a unit change in the pressure p as

$$c_b = (1 - \varphi)c_s + \varphi c_p. \quad (3.78)$$

The fluid phase compressibility $c_{f\beta}$ is defined in terms of the fluid density as

$$c_{f\beta} = \frac{1}{\rho_\beta} \frac{\partial \rho_\beta}{\partial p}. \quad (3.79)$$

Using the above equations, the fractional derivative mass conservation equation of multiphase flow is given by

$$\begin{aligned} \varphi \rho_\beta \frac{\partial S_\beta}{\partial t} + S_\beta \rho_\beta [(1 - \varphi)^2 c_s - \varphi^2 c_p + \varphi c_{f\beta}] \frac{\partial p}{\partial t} \\ + \frac{1}{\Gamma(\alpha + 1)} \sum_{i=1}^3 (\Delta x_i)^{\alpha-1} \frac{\partial^\alpha (\rho_\beta u_{\beta i})}{\partial x_i^\alpha} = q_\beta. \end{aligned} \quad (3.80)$$

As a special case, the fractional single-phase mass conservation equation becomes

$$\rho [(1 - \varphi)^2 c_s - \varphi^2 c_p + \varphi c_{f\beta}] \frac{\partial p}{\partial t} + \frac{1}{\Gamma(\alpha + 1)} \sum_{i=1}^3 (\Delta x_i)^{\alpha-1} \frac{\partial^\alpha (\rho u_i)}{\partial x_i^\alpha} = q. \quad (3.81)$$

The integer-derivative version of Eq. (3.81) is

$$\rho [(1 - \varphi)^2 c_s - \varphi^2 c_p + \varphi c_{f\beta}] \frac{\partial p}{\partial t} + \sum_{i=1}^3 \frac{\partial (\rho u_i)}{\partial x_i} = q. \quad (3.82)$$

Considering another special case for incompressible fluid flow, for which $c_{f\beta} = 0$, neglecting the rock compressibility, i.e., $c_s = c_p = 0$, Eq. (3.81) collapses to

$$\varphi \rho_\beta \frac{\partial S_\beta}{\partial t} + \frac{1}{\Gamma(\alpha + 1)} \sum_{i=1}^3 (\Delta x_i)^{\alpha-1} \frac{\partial^\alpha (\rho_\beta u_{\beta i})}{\partial x_i^\alpha} = q_\beta. \quad (3.83)$$

If we select $\alpha = 1$, the traditional mass conservation equation for immiscible multiphase flow is

$$\phi \frac{\partial S_\beta}{\partial t} + \sum_{i=1}^3 \frac{\partial u_{\beta i}}{\partial x_i} = Q_\beta, \quad (3.84)$$

where $Q_\beta = q_\beta / \rho_\beta$. So, we can have several special cases based on the physical and modeling aspects.



3.9. Special cases of two-phase flow

3.9.1 Imbibition flow

Hydrocarbon reservoirs are naturally fractured and consist of two essential parts, fractures and matrix blocks (Fig. 3.5). The fracture's permeability is much greater than that of the matrix. However, the amount of hydrocarbons in the matrix blocks is much more significant than that of the fractures. In oil recovery, water is injected, and oil is extracted into fractures from the matrix blocks and then into production wells. Imbibition is regarded as a typical oil extraction process, whereas water moves oil from the matrix into the adjacent fracture.

The schematic diagram of the two-phase countercurrent imbibition in porous media provided is shown in Fig. 3.6. The immiscible two-phase flow in porous media is governed by Darcy's law and the equations of mass conservation [46,47],

$$u_w = -\zeta_w \frac{\partial P_w}{\partial x}, \quad (3.85)$$

$$u_{nw} = -\zeta_{nw} \frac{\partial P_{nw}}{\partial x}, \quad (3.86)$$

where $\zeta_w = Kk_{rw} / \mu_w$ and $\zeta_{nw} = Kk_{rnw} / \mu_{nw}$,

$$\phi \frac{\partial S_w}{\partial t} + \frac{\partial u_w}{\partial x} = 0, \quad (3.87)$$

$$\phi \frac{\partial S_{nw}}{\partial t} + \frac{\partial u_{nw}}{\partial x} = 0. \quad (3.88)$$

The saturations of the phases are constrained by

$$S_w + S_{nw} = 1, \quad (3.89)$$

where the subscripts w and nw designate the wetting phase and nonwetting phase, respectively, P is the pressure, S is the saturation, k_r is the relative

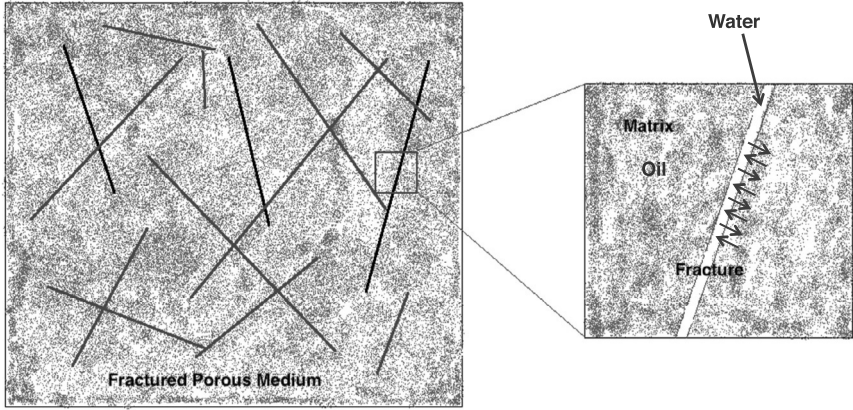


Figure 3.5 Sketch of the fractured porous media.

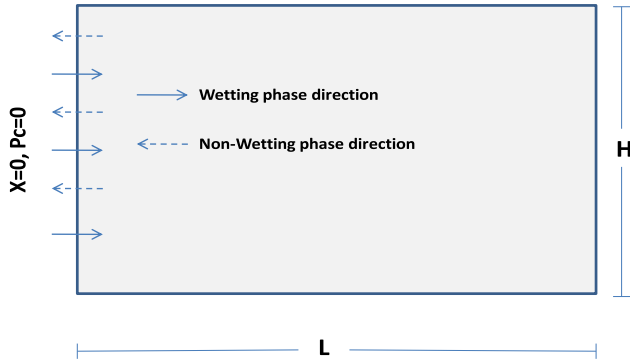


Figure 3.6 Schematic diagram of the two-phase countercurrent imbibition in porous media.

permeability, which is generally a function of saturation defined below, and μ is the viscosity.

3.9.2 Fractional momentum with time memory

Considering the memory formalism explained above, one can write

$$u_w = -\zeta_w(t) \frac{\partial^\alpha}{\partial t^\alpha} \left(\frac{\partial P_w}{\partial x} \right), \tag{3.90}$$

$$u_{nw} = -\zeta_{nw}(t) \frac{\partial^\alpha}{\partial t^\alpha} \left(\frac{\partial P_{nw}}{\partial x} \right). \tag{3.91}$$

It is clear that memory implies the use of more than one parameter, namely α .

For the countercurrent imbibition, the sum of the velocities of the wetting and nonwetting phases vanishes. Thus,

$$\zeta_w(t) \frac{\partial^a}{\partial t^a} \frac{\partial P_w}{\partial x} + \zeta_{nw}(t) \frac{\partial^a}{\partial t^a} \frac{\partial P_{nw}}{\partial x} = 0. \quad (3.92)$$

The capillary pressure P_c is defined as a difference between the nonwetting and wetting phase pressures:

$$P_c = P_{nw} - P_w. \quad (3.93)$$

Therefore,

$$\frac{\partial^a}{\partial t^a} \frac{\partial P_w}{\partial x} = - \frac{\zeta_{nw}(t)}{\zeta_w(t) + \zeta_{nw}(t)} \frac{\partial^a}{\partial t^a} \frac{\partial P_c}{\partial x}. \quad (3.94)$$

One may write

$$u_w = \frac{\zeta_w(t)\zeta_{nw}(t)}{\zeta_w(t) + \zeta_{nw}(t)} \frac{\partial^a}{\partial t^a} \frac{\partial P_c}{\partial x}. \quad (3.95)$$

Then,

$$\varphi \frac{\partial S_w}{\partial t} + \frac{\partial}{\partial x} \left[\frac{\zeta_w(t)\zeta_{nw}(t)}{\zeta_w(t) + \zeta_{nw}(t)} \frac{\partial^a}{\partial t^a} \frac{\partial P_c}{\partial x} \right] = 0. \quad (3.96)$$

3.9.3 Fractional mass equation with time memory

The fractional mass equation with traditional momentum equation (Darcy's law) for the above imbibition model can be written as [45]

$$\frac{\partial S}{\partial t} + \frac{\gamma}{\varphi^{1/2} K^{1/2} (1 - S_\alpha - S_{wi})} \frac{(\Delta x)^{\alpha+1}}{\Gamma(\alpha+1)} \frac{\partial^{\alpha+1}}{\partial x^{\alpha+1}} \left[\frac{\xi_w \xi_{nw}}{\xi_w + \xi_{nw}} \frac{1}{S} \frac{\partial S}{\partial x} \right] = 0 \quad (3.97)$$

and

$$\frac{\partial^{\alpha+1}}{\partial x^{\alpha+1}} \left\{ \frac{\xi_w \xi_{nw}}{\xi_w + \xi_{nw}} \frac{1}{S} \frac{\partial S}{\partial x} \right\} = \frac{1}{\Gamma(-\alpha)} \int_{x_b}^x (x - \varsigma)^{-\alpha-1} \frac{\partial}{\partial \varsigma} \left(\frac{\xi_w \xi_{nw}}{\xi_w + \xi_{nw}} \frac{1}{S} \frac{\partial S}{\partial x} \right) d\varsigma. \quad (3.98)$$

3.9.4 Fractional mass and momentum with time memory

The fractional mass conservation equation and fractional momentum conservation equation (Darcy's law) with time memory can be written as [45]

$$\varphi \frac{\partial S_w}{\partial t} - \frac{1}{\Gamma(\alpha_1 + 1)} \left[(\Delta x)^{\alpha_1 - 1} \frac{\partial^{\alpha_1}}{\partial x^{\alpha_1}} \right] \cdot \zeta_w(t) \frac{\partial^{\alpha_1}}{\partial t^{\alpha_2}} \left(\frac{\partial P_w}{\partial x} \right) = 0 \quad (3.99)$$

and

$$\varphi \frac{\partial S_{mw}}{\partial t} - \frac{1}{\Gamma(\alpha_1 + 1)} \left[(\Delta x)^{\alpha_1 - 1} \frac{\partial^{\alpha_1}}{\partial x^{\alpha_1}} \right] \cdot \zeta_{mw}(t) \frac{\partial^{\alpha_2}}{\partial t^{\alpha_2}} \left(\frac{\partial P_{mw}}{\partial x} \right) = 0. \quad (3.100)$$

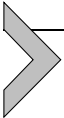
3.9.5 Fractional mass and momentum with space memory

The following equations represent the fractional mass conservation equation and the fractional momentum conservation equation (Darcy's law) with space memory [45]:

$$\varphi \frac{\partial S_w}{\partial t} - \frac{1}{\Gamma(\alpha_1 + 1)} \left[(\Delta x)^{\alpha_1 - 1} \frac{\partial^{\alpha_1}}{\partial x^{\alpha_1}} \right] \cdot \zeta_w \frac{\partial^{\alpha_2}}{\partial x^{\alpha_2}} P_w = 0 \quad (3.101)$$

and

$$\varphi \frac{\partial S_{\kappa w}}{\partial t} - \frac{1}{\Gamma(\alpha_1 + 1)} \left[(\Delta x)^{\alpha_1 - 1} \frac{\partial^{\alpha_1}}{\partial x^{\alpha_1}} \right] \cdot \zeta_{mw} \frac{\partial^{\alpha_2}}{\partial x^{\alpha_2}} P_{mw} = 0. \quad (3.102)$$



3.10. Fractional convection-diffusion equation

3.10.1 Fractional heat conduction model

The heat flux in the 1D domain given by Fourier's law can be written as

$$q = -k \frac{dT}{dx}, \quad (3.103)$$

such that k is the heat transfer coefficient. The definition of Fourier's law leads to the heat governing equation in the form

$$\rho c_p \frac{\partial T}{\partial t} = k \left(\frac{\partial^2 T}{\partial x^2} + \frac{\partial^2 T}{\partial y^2} + \frac{\partial^2 T}{\partial z^2} \right). \quad (3.104)$$

In some nonhomogeneous domains, it would be more convenient to use a fractional model rather than the traditional one. The generalized frac-

tional Fourier law can be written as

$$q(x) = -k_x \frac{d^{\beta_1} T(x)}{dx^{\beta_1}}, \quad (3.105)$$

where k_x denotes the thermal conductivity in the fractional mode and $0 < \beta_1 < 1$ is the order of the fractional derivative. Therefore, the time/space generalized fractional heat conduction equation can be expressed as

$$\rho c_p \frac{\partial^\alpha T}{\partial t^\alpha} = k_x \frac{\partial^{\beta_1} T}{\partial x^{\beta_1}} + k_y \frac{\partial^{\beta_1} T}{\partial y^{\beta_1}} + k_z \frac{\partial^{\beta_1} T}{\partial z^{\beta_1}}, \quad (3.106)$$

where k_x , k_y , and k_z are, respectively, thermal conductivity coefficients in the x -, y -, and z -directions, $0 < \alpha < 1$ is the order of the time-fractional derivative, and $1 < \beta_1, \beta_2, \beta_3 < 2$ are, respectively, the orders of space-fractional derivatives in the x -, y -, and z -directions. In order to solve the fractional-order model numerically, the Grunwald–Letnikov definition may be used:

$$\frac{\partial^\alpha T(x, t)}{\partial t^\alpha} = \frac{\sum_{j=0}^{N_j} c_j T(x, t - j\Delta t)}{\Delta t^\alpha}, \quad (3.107)$$

such that

$$N_f = \min \left\{ \left[\frac{t}{\Delta t} \right], \left[\frac{L}{\Delta t} \right] \right\}, \quad c_0 = 1, \quad c_j = \left(1 - \frac{1 + \alpha}{j} \right) c_{j-1}, \quad j \geq 1, \quad (3.108)$$

where L is the length memory.

3.10.2 Fractional transport equation

The bulk mass flux is defined as a summation of convective and diffusive fluxes, i.e.,

$$J = \mathbf{u}C(x, t) - D\nabla C(x, t). \quad (3.109)$$

The convection–diffusion gas transport equation can be written as

$$\frac{\partial C(x, t)}{\partial t} = -\nabla(\mathbf{u}C(x, t) - D\nabla C(x, t)). \quad (3.110)$$

In heterogeneous media, the general mass flux [32] may be developed to take the general form

$$J = \frac{\partial^{1-\alpha}}{\partial t^{1-\alpha}} (\mathbf{u}C(x, t) - D\nabla C(x, t)). \quad (3.111)$$

Consequently, the fractional generalized convection-diffusion gas transport equation becomes

$$\frac{\partial C(x, t)}{\partial t} = \nabla \cdot \left[\frac{\partial^{1-\alpha}}{\partial t^{1-\alpha}} (D \nabla C(x, t) - \mathbf{u} C(x, t)) \right]. \quad (3.112)$$

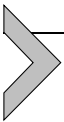
On the other hand, the rapid movement of gas molecules can be described by a nonlocal space-fractional derivative term such as

$$\frac{\partial^\alpha C(x, t)}{\partial t^\alpha} = -u \frac{\partial C(x, t)}{\partial x} + K \frac{\partial^\beta C(x, t)}{\partial x^\beta}, \quad 0 < \alpha \leq 1, \quad 1 < \beta \leq 2, \quad (3.113)$$

where α is the order of the time-fractional derivative while β is the order of the space-fractional derivative.

3.10.3 Applications in cooling and heating systems

Newton's law of cooling predicts that the instantaneous rate of temperature change of any warm body for time is proportional to the body's temperature difference with the ambient, measured in integer units of time. Modol et al. [34] conducted experiments of cooling different liquids and found that the results did not fit the theoretical predictions of Newton's law of cooling. They tried the fractional model of both Caputo and Riemann-Liouville types. They found that liquid cooling has an identical value of the fractional derivative of time, increasing with the liquid's viscosity. The fractional derivative generalized Newton law of cooling has been used in mathematical modeling of the heating and cooling processes of a common type of luminaires, consisting of a single light-emitting diode source in thermal contact with an aluminum passive heat sink [35].



3.11. Conclusion

This chapter presented the spatial-fractional modeling of some essential fluid flow problems. Both fundamentals and computational aspects are discussed, and some applications are highlighted. The chapter contains a number of new formulations of different models researchers still may need to work on to find solutions and study their features. This chapter also could be the starting point of a book that can be written under a similar title.

References

- [1] K.S. Miller, B. Ross, *An Introduction to the Fractional Calculus and Fractional Differential Equations*, John Wiley and Sons Inc., New York, 1993.
- [2] I. Podlubny, *Fractional Differential Equations*, Mathematics in Science and Engineering, vol. 198, Academic Press, New York, NY, USA, 1999.
- [3] K.B. Oldham, J. Spanier, *The Fractional Calculus Theory and Applications of Differentiation and Integration to Arbitrary Order*, Academic Press, New York, NY, USA, 1974.
- [4] B. Baeumer, D.A. Benson, M.M. Meerschaert, Advection and dispersion in time and space, *Physica A* 350 (2005) 245–262.
- [5] D.A. Benson, *The fractional advection–dispersion equation: development and application*, Ph.D. dissertation, Univ. of Nev., Reno, 1998.
- [6] D.A. Benson, S.W. Wheatcraft, M.M. Meerschaert, Application of a fractional advection–dispersion equation, *Water Resour. Res.* 36 (6) (2000) 1403–1412.
- [7] X.J. Yang, *Local Fractional Functional Analysis and Its Applications*, Asian Academic Publisher Limited, Hong Kong, 2011.
- [8] X.J. Yang, *Advanced Local Fractional Calculus and Its Applications*, World Science Publisher, New York, NY, 2012.
- [9] X.J. Yang, H.M. Srivastava, J.H. He, D. Baleanu, Cantor–type cylindrical-coordinate method for differential equations with local fractional derivatives, *Phys. Lett. A* 377 (28–30) (2013) 1696–1700.
- [10] A.S. Mohanmadein, M.F. El-Amin, H.M. Ali, An approximate similarity solution for spatial fractional boundary-layer flow over an infinite vertical plate, *Comput. Appl. Math.* 39 (2020) 114.
- [11] X.J. Yang, D. Baleanu, Fractal heat conduction problem solved by local fractional variation iteration method, *Therm. Sci.* 17 (2) (2013) 625–628.
- [12] M.F. El-Amin, *Advanced Topics in Mass Transfer*, INTECH, 2011.
- [13] M. Caputo, Models of flux in porous media with memory, *Water Resour. Res.* 36 (2000) 693–705.
- [14] J. He, Approximate analytical solution for seepage flow with fractional derivatives in porous media, *Comput. Methods Appl. Mech. Eng.* 167 (1998) 57–68.
- [15] S.W. Wheatcraft, M.M. Meerschaert, Fractional conservation of mass, *Adv. Water Resour.* 31 (2008) 1377–1381.
- [16] M.F. El-Amin, A.G. Radwan, S. Sun, Analytical solution for fractional derivative gas-flow equation in porous media, *Results Phys.* 7 (2017) 2432–2438.
- [17] M.F. El-Amin, Analytical solution of the apparent–permeability gas-transport equation in porous media, *Eur. Phys. J. Plus* 132 (2017) 129.
- [18] A. Chang, H. Sun, Y. Zhang, C. Zheng, F. Min, Spatial fractional Darcy’s law to quantify fluid flow in natural reservoirs, *Physica A* 519 (2019) 119–126.
- [19] A. Chang, H.G. Sun, Time-space fractional derivative models for CO₂ transport in heterogeneous media, *Fract. Calc. Appl. Anal.* 21 (1) (2018) 151–173.
- [20] D. Baleanu, K. Diethelm, E. Scalas, J.J. Trujillo, *Fractional Calculus: Models and Numerical Methods*, second ed., World Scientific, New Jersey, 2016.
- [21] C.P. Li, F.H. Zeng, *Numerical Methods for Fractional Calculus*, CRC Press, Boca Raton, 2015.
- [22] P.T. Li, Z.C. Zhai, Well-posedness and regularity of generalized Navier–Stokes equations in some critical Q-spaces, *J. Funct. Anal.* 259 (2010) 2457–2519.
- [23] M. El-Shahed, A. Salem, On the generalized Navier–Stokes equations, *Appl. Math. Comput.* 156 (2004) 287–293.
- [24] M.Y. Xu, W.C. Tan, Intermediate process and critical phenomena: theory, method and progress of fractional operators and their applications to modern mechanics, *Sci. China G* 49 (2006) 257–272.

- [25] C. Pozrikids, *The Fractional Laplacian*, CRC Press, Boca Raton, 2016.
- [26] W. Chen, S. Holm, Fractional Laplacian time-space models for linear and nonlinear lossy media exhibiting arbitrary frequency power-law dependency, *J. Acoust. Soc. Am.* 115 (2004) 1424–1430.
- [27] W. Chen, A speculative study of 2/3-order fractional Laplacian modeling of turbulence: some thoughts and conjectures, *Chaos* 16 (2006) 023126.
- [28] H. Schlichting, *Boundary Layer Theory*, 7th ed., McGraw-Hill, New York, 1978.
- [29] M.F. El-Amin, H. Kanayama, Boundary layer theory approach to the concentration layer adjacent to the ceiling wall of a hydrogen leakage: axisymmetric impinging and far regions, *Int. J. Hydrog. Energy* 34 (3) (2009) 1620–1626.
- [30] M.F. El-Amin, H. Kanayama, Boundary layer theory approach to the concentration layer adjacent to a ceiling wall at impinging region of a hydrogen leakage, *Int. J. Hydrog. Energy* 33 (21) (2008) 6393–6400.
- [31] B. Gebhart, Y. Jaluria, R.L. Mahajan, B. Sammakia, *Buoyancy-Induced Flows and Transport*, Hemisphere Publishing Corporation, USA, 1988.
- [32] M. Meerschaert, C. Tadjeran, Finite difference approximations for fractional advection-dispersion flow equations, *J. Comput. Appl. Math.* 172 (1) (2004) 65–77.
- [33] A.D. Obembe, M.E. Hossain, S.A. Abu-Khamsin, Variable-order derivative time fractional diffusion model for heterogeneous porous media, *J. Pet. Sci. Eng.* 152 (2017) 391–405.
- [34] A. Mondol, R. Gupta, S. Das, T. Dutta, An insight into Newton's cooling law using fractional calculus, *J. Appl. Phys.* 123 (2018) 064901.
- [35] E. Balvís, A. Paredes, I. Area, R. Bendaña, A.V. Carpentier, H. Michinel, S. Zaragoza, A fractional derivative modeling of heating and cooling of LED luminaires, *Mathematics* 8 (2020) 362.
- [36] M.F. El-Amin, A.G. Radwan, J. Kou, A. Salama, S. Sun, Fractional derivative modeling of double-diffusive free convection with von Neumann stability analysis, *Int. J. Model. Simul.* (2020), <https://doi.org/10.1080/02286203.2020.1843934>, published online.
- [37] H. Xu, H. Jianga, B. Yu, Numerical analysis of the space fractional Navier-Stokes equations, *Appl. Math. Lett.* 69 (2018) 94–100.
- [38] J.H. Kang, F.B. Zhou, T.Q. Xia, G.B. Ye, Numerical modeling and experimental validation of anomalous time and space subdiffusion for gas transport in porous coal matrix, *Int. J. Heat Mass Transf.* 100 (2016) 747–757.
- [39] Z. Chen, G. Huan, Y. Ma, *Computational Methods for Multiphase Flows in Porous Media*, SIAM Computational Science and Engineering, Philadelphia, PA, USA, 2006.
- [40] M.F. El-Amin, *Mass Transfer in Multiphase Systems and Its Applications*, Intech, 2011.
- [41] M.F. El-Amin, S. Abbdel-Naeem, Multiscale numerical modeling of solute transport with two-phase flow in a porous cavity, *J. Appl. Comput. Mech.* 6 (SI) (2020) 1499–1506.
- [42] M.F. El-Amin, Iterative numerical scheme for non-isothermal two-phase flow in heterogeneous porous media, *Algorithms* 12 (6) (2019) 117.
- [43] M.F. El-Amin, S. Abbdel-Naeem, Numerical algorithm for unsteady nonisothermal two-phase flow in a porous cavity, in: 2020 International Conference on Intelligent Engineering and Management (ICIEEM), London, United Kingdom, 2020, pp. 460–464, <https://doi.org/10.1109/ICIEEM48762.2020.9160335>.
- [44] M.F. El-Amin, J. Kou, S. Sun, Numerical investigation of solute transport in fractured porous media using the discrete fracture model, in: V. Krzhizhanovskaya, et al. (Eds.), *Computational Science, ICCS 2020*, in: *Lecture Notes in Computer Science*, vol. 12143, Springer, Cham, 2020.
- [45] M.F. El-Amin, Derivation of fractional-derivative models of multiphase fluid flows in porous media, *J. King Saud Univ., Sci.* 33 (2) (2021) 101364.

-
- [46] M.F. El-Amin, A. Salama, S. Sun, Numerical and dimensional investigation of two-phase countercurrent imbibition in porous media, *J. Comput. Appl. Math.* 242 (2013) 285–296.
- [47] M.F. El-Amin, A. Salama, S. Sun, Effects of gravity and inlet location on a two-phase countercurrent imbibition in porous media, *Int. J. Chem. Eng.* 2012 (2012) 210128, <https://doi.org/10.1155/2012/210128>.

On the hybrid fractional chaotic systems: a numerical approach

N.H. Sweilam^a and S.M. AL-Mekhlafi^b

^aMathematics Department, Faculty of Science, Cairo University, Giza, Egypt

^bMathematics Department, Faculty of Education, Sana'a University, Sana'a, Yemen

4.1. Introduction

The study of chaotic systems began with systems represented by a set of first-order differential equations. However, real-life systems are best described by other mathematical expressions than first-order differential equations. The methods of chaos analysis were soon extended to the study of discrete chaotic equations, where the present state is dependent on previous states of the systems. The chaotic behavior exists in many natural systems, such as climate, weather, and fluid flow. These behaviors have a serious effect on everyday life (for example, [15], [21], [30]). The classical Bloch equation is used for modeling of nuclear magnetization as a function of time [6], [16], [17].

Fractional differential equations (FDEs) can describe the dynamics of several complex and nonlocal systems with memory. It is a hot topic of research in many scientific fields, especially in mathematics and engineering. Fractional derivatives can be described with long-range memory (for more details, see [3], [7], [11], [14]). To understand the physical meaning of the fractional models, we refer to some articles explaining fractional calculus geometrically; see for examples [9], [10] and the references cited therein.

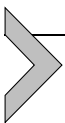
There are several definitions for derivatives of fractional order. The most common one is Caputo's derivative, which has several applications [5], [3], [19], [28]. The advantage of using the Caputo fractional derivative in modeling physical processes is that the fractional derivative of constant functions is zero. This shows that time-independent solutions are also solutions of the time-dependent problem, but this is not the case for the Riemann–Liouville fractional time derivative [29].

The solution of such fractional-order differential equations is difficult to find analytically. Hence, it is very important to develop numerical techniques to approximate the solutions of these models. The nonstandard

finite difference method (NSFDM) is becoming increasingly common. This method was developed by Mickens in 1980. It is universally known to maintain positivity, boundedness, fixed points, and stability of nonlinear systems. Some applications for this method in different fields can be found in [1], [18], [23–27].

In this chapter, we consider a new operator which combines the ideas of the Caputo derivative and the proportional derivative in a new way to create a hybrid fractional operator calculus [2]. This operator is defined based on the Caputo derivative and the Riemann–Liouville integral. An efficient NSFDM with the constant proportional Caputo operator derivative (CPC-NSFDM) is applied to study the behavior of two hybrid fractional-order chaotic systems: a hyperchaotic finance system and a Bloch system with time delay. Also, another numerical method using Caputo’s definition with NSFDM (C-NSFDM) is given. Comparative studies between these methods are given. Stability analysis of the CPC-NSFDM was also conducted.

This chapter is organized as follows. The basic mathematical formulas are introduced in Section 4.2. In Section 4.3 a class of new models of hybrid fractional-order derivatives and some properties of the proposed models such as the existence, uniqueness, equilibrium point, and stability are presented. Two nonstandard numerical methods and their stability analysis are presented in Section 4.4. Numerical simulations are discussed in Section 4.5. Finally, the conclusions are presented in Section 4.6.



4.2. Preliminaries and notations

In the following, we give some important definitions of fractional calculus.

Definition 4.2.1. The Caputo fractional-order derivative can be defined as follows [19]:

$${}^C D_t^\alpha \gamma(t) = \frac{1}{\Gamma(1-\alpha)} \int_0^t \gamma'(s)(t-s)^{-\alpha} ds, \quad 0 < \alpha < 1, \quad (4.1)$$

where Γ is the Euler Gamma function.

Definition 4.2.2. The Riemann–Liouville integral can be defined as follows [19]:

$${}^{RL}I_t^\alpha \gamma(t) = \left[\int_0^t \gamma(s)(t-s)^{\alpha-1} ds \right] \frac{1}{\Gamma(\alpha)}, \quad (4.2)$$

where $0 < \alpha < 1$ and $\gamma(t)$ is an integrable function.

Definition 4.2.3. The proportional Caputo hybrid operator is defined either in a general way [2],

$$\begin{aligned} {}^{PC}D_t^\alpha \gamma(t) &= \left(\int_0^t (K_1(\alpha, s)\gamma(s) + K_0(\alpha, s)\gamma'(s))(t-s)^{-\alpha} ds \right) \frac{1}{\Gamma(1-\alpha)} \\ &= \left(\frac{t^\alpha}{\Gamma(1-\alpha)} \right) (\gamma(t)K_1(\alpha, t) + \gamma'(t)K_0(\alpha, t)), \end{aligned} \quad (4.3)$$

where $K_0(\alpha, t) = \alpha t^{(1-\alpha)}$, $K_1(\alpha, t) = (1-\alpha)t^\alpha$, or as [2]

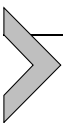
$$\begin{aligned} {}^{CPC}D_t^\alpha \gamma(t) &= \left(\int_0^t (t-s)^{-\alpha} (K_1(\alpha)\gamma(s) + K_0(\alpha)\gamma'(s)) ds \right) \frac{1}{\Gamma(1-\alpha)} \\ &= K_1(\alpha) {}^{RL}I_t^{1-\alpha} \gamma(t) + K_0(\alpha) {}^C D_t^\alpha \gamma(t), \end{aligned} \quad (4.4)$$

where $K_1(\alpha)$ and $K_0(\alpha)$ are constants. Here we consider $K_0(\alpha) = \alpha Q^{(1-\alpha)}$, $K_1(\alpha) = (1-\alpha)Q^\alpha$, where Q is a constant.

In (4.3) the operator PC stands for proportional Caputo and in (4.4) the operator CPC stands for constant proportional Caputo. In both of these formulas, the function space domain is given by requiring that γ is differentiable and both γ and γ' are locally $L1$ functions on the positive reals.

Definition 4.2.4. The inverse operators to the fractional CPC derivatives are given by [2]

$${}^{CPC}I_t^\alpha \gamma(t) = \left(\int_0^t \exp \left[\frac{K_1(\alpha)}{K_0(\alpha)} (t-s) \right] {}^{RL}D_t^{1-\alpha} \gamma(s) ds \right) \frac{1}{K_0(\alpha)}. \quad (4.5)$$



4.3. Hybrid fractional chaotic models

In this section, two new models of hybrid fractional–order derivatives are presented.

4.3.1 A hybrid fractional hyperchaotic finance system

Finance models are developed to reveal the characteristics of the economy (for more details, see [15], [21], [30]). The fractional-order derivatives for the finance system are studied in [13]. Here we present the hybrid fractional hyperchaotic finance system. This system is more general than the system given in [13]. It is given as follows:

$$\begin{aligned} {}_0^{CPC}D_t^{\alpha_1} X &= Z + (Y - a)X + W, \\ {}_0^{CPC}D_t^{\alpha_2} Y &= 1 - bY - X^2, \\ {}_0^{CPC}D_t^{\alpha_3} Z &= -X - cZ, \\ {}_0^{CPC}D_t^{\alpha_4} W &= -0.05XZ - dW, \end{aligned} \quad (4.6)$$

where a is the saving parameter, b is the per investment cost parameter, c is the elasticity of demands of commercial parameter, and all these parameters are positive constants; $W = W_0$, $Z = Z_0$, $Y = Y_0$, and $X = X_0$ are given data. The definitions of all variables of system (4.6) are given in Table 4.1.

Table 4.1 System (4.6) variables [13].

Variable	Definition
X	Interest rate
Y	Finance demand
Z	The index of price
W	The mean of profit margin

4.3.2 Existence and uniqueness of the solution

In the following, we will use the fixed point theory [31]. For this we rewrite (4.6) as follows [32]:

$${}_0^{CPC}D_t^\alpha \gamma(t) = q(\gamma(t), t), \quad \gamma(0) = \gamma_0 \geq 0. \quad (4.7)$$

The vector $\gamma(t) = (X, Y, Z, W)^T$ represents the state variables and q is a continuous vector function such that

$$\begin{pmatrix} q_1 \\ q_2 \\ q_3 \\ q_4 \end{pmatrix} = \begin{pmatrix} Z + (Y - a)X + W \\ 1 - bY - X^2 \\ -X - cZ \\ -0.05XZ - dW \end{pmatrix},$$

with initial condition γ_0 . Moreover, the Lipschitz condition is satisfied by q , where q is a quadratic vector function, i.e., there exists $M^0 \in \mathbb{R}$ such that [32]

$$\|q(\gamma_1(t), t) - q(\gamma_2(t), t)\| = M^0 \|\gamma_1(t) - \gamma_2(t)\|. \tag{4.8}$$

Theorem 4.3.1. *The fractional proposed model (4.6) has a unique solution if the following condition holds:*

$$\frac{M^0 \gamma_{max}^\alpha X_{max}^\alpha}{\Gamma(\alpha - 1)K_0(\alpha)} \leq 1. \tag{4.9}$$

Proof. Using (4.4) and (4.7), we get

$$\gamma(t) = \gamma(t_0) + \frac{1}{K_0(\alpha)} \int_0^t \exp\left(-\frac{K_1(\alpha)}{K_0(\alpha)}(t-s)\right) {}_0^{RL}D_t^{1-\alpha} q(\gamma(s), s) ds. \tag{4.10}$$

Let $K = (0, T)$ and let the operator $B: \mathbb{C}(K, \mathbb{R}^4) \rightarrow \mathbb{C}(K, \mathbb{R}^4)$ such that

$$B[\gamma(t)] = \gamma(t_0) + \frac{1}{K_0(\alpha)} \int_0^t \exp\left(-\frac{K_1(\alpha)}{K_0(\alpha)}(t-s)\right) {}_0^{RL}D_t^{1-\alpha} q(\gamma(s), s) ds. \tag{4.11}$$

It gives

$$B[\gamma(t)] = \gamma(t).$$

Let $\|\cdot\|_K$ denote the supremum norm on K . Thus

$$\|\gamma(t)\|_K = \sup_{t \in K} \|\gamma(t)\|, \quad \gamma(t) \in \mathbb{C}(K, \mathbb{R}^4).$$

So, $\mathbb{C}(K, \mathbb{R}^4)$ with $\|\cdot\|_K$ is a Banach space. Moreover, the following relation holds:

$$\left\| \int_0^t \varphi(s, t) \gamma(s) ds \right\| \leq \Lambda \|\varphi(s, t)\|_K \|\gamma(s)\|_K,$$

with $\gamma(t) \in \mathbb{C}(K, \mathbb{R}^4)$, $\varphi(s, t) \in \mathbb{C}(K^2, \mathbb{R}^4)$ such that

$$\|\varphi(s, t)\|_K = \sup_{t, s \in K} |\varphi(s, t)|.$$

Thus (4.11) can be written as

$$\|B[\gamma_1(t)] - B[\gamma_2(t)]\|_K \leq \left\| \frac{1}{K_0(\alpha)} \int_0^t \exp\left(-\frac{K_1(\alpha)}{K_0(\alpha)}(t-s)\right) {}_0^{RL}D_t^{1-\alpha} q(\gamma_1(s), s) - {}_0^{RL}D_t^{1-\alpha} q(\gamma_2(s), s) ds \right\|_K. \tag{4.12}$$

Since

$$\begin{aligned} & {}_0^{RL}D_t^{1-\alpha}(q(\gamma_1(t), t) - q(\gamma_2(t), t)) \\ &= \frac{1}{\Gamma(\alpha - 1)} \int_0^t (t-s)^{\alpha-2} (q(\gamma_1(s), s) - q(\gamma_2(s), s)) ds, \end{aligned}$$

we have

$$\begin{aligned} & \|B[\gamma_1(t)] - B[\gamma_2(t)]\|_K \\ & \leq \frac{\Upsilon_{max}^\alpha}{\Gamma(\alpha - 1)K_0(\alpha)} \left\| \int_0^t (t-s)^{\alpha-2} (q(\gamma_1(s), s) - q(\gamma_2(s), s)) ds \right\|_K \\ & \leq \frac{\Upsilon_{max}^\alpha X_{max}^\alpha}{\Gamma(\alpha - 1)K_0(\alpha)} \|q(\gamma_1(t), t) - q(\gamma_2(t), t)\|_K \\ & \leq \frac{M^0 \Upsilon_{max}^\alpha X_{max}^\alpha}{\Gamma(\alpha - 1)K_0(\alpha)} \|\gamma_1(t) - \gamma_2(t)\|_K. \end{aligned} \tag{4.13}$$

Finally, we obtain

$$\|B[\gamma_1(t)] - B[\gamma_2(t)]\|_K \leq L \|\gamma_1(t) - \gamma_2(t)\|_K, \tag{4.14}$$

where

$$L = \frac{M^0 \Upsilon_{max}^\alpha X_{max}^\alpha}{\Gamma(\alpha - 1)K_0(\alpha)}.$$

If $L \leq 1$, then the operator B is called a contraction. Hence, the fractional system (4.6) has a unique solution. \square

4.3.3 Equilibrium points and stability

The equilibrium points of system (4.6) can be evaluated by setting [33]

$${}_0^{CPC}D_t^{\alpha_1} X = {}_0^{CPC}D_t^{\alpha_2} Y = {}_0^{CPC}D_t^{\alpha_3} Z = {}_0^{CPC}D_t^{\alpha_4} W = 0.$$

Then we can claim that system (4.6) has the following three equilibrium points: $E_{1,2} = (\lambda, \frac{1-\lambda^2}{b}, -\frac{\lambda}{c}, -\frac{\lambda^2}{20cd})$, $(0, \frac{1}{b}, 0, 0)$, where $\lambda = \frac{-b \mp \sqrt{\Delta}}{40cd}$ and $\Delta = b^2 - 4 \times 20cd \times 20d \times (abc + b - c)$. The Jacobian matrix at the equilibrium point $E_\kappa (X_\kappa^*, Y_\kappa^*, Z_\kappa^*, W_\kappa^*)$, $\kappa = 1, 2, 3$, is

$$J(E_\kappa) \begin{pmatrix} Y_\kappa^* - a & X_\kappa^* & 1 & 1 \\ -2X_\kappa^* & -b & 0 & 0 \\ -1 & 0 & -c & 0 \\ -0.05Z_\kappa^* & 0 & -0.05X_\kappa^* & -d \end{pmatrix},$$

where $d = 0.6$, $c = 1$, $b = 0.1$, and $a = 0.9$. The characteristic polynomial of system (4.6) at E_3 can be written as follows:

$$\Delta\eta = \eta^4 - 7.4\eta^3 - 13.71\eta^2 - 6.5\eta - 0.486 = 0.$$

Then the eigenvalues of the Jacobian matrix are

$$\eta_1 = -0.9, \quad \eta_2 = -0.6, \quad \eta_3 = -0.1, \quad \eta_4 = 9.$$

The stability condition is not satisfied for $\eta_4 = 9$. Hence, the necessary condition to exhibit a chaotic attractor for the fractional-order system (4.6) is satisfied at $\alpha \in (0, 1]$. For the equilibrium point at E_1 , the eigenvalues are given as follows:

$$\eta_{1,2} = 0.409 \mp 1.471i, \quad \eta_3 = -1.0181, \quad \eta_4 = -0.425.$$

This implies that the point E_1 is stable if $\alpha < 0.8274$, because $\min_\kappa |\arg(\eta_i)| = 1.3$, $i = 1, 2, 3, 4$. Similarly, for the equilibrium point at E_2 , the fractional order chaotic system is locally asymptotically stable in the Lyapunov sense if the following condition is satisfied [8]:

$$\frac{\pi}{\sigma} - \min_\eta |\arg \eta_i| < 0,$$

where σ is the least common multiple of the denominators ϖ , $\Delta(\eta) = \det(J - \text{diag}(\eta^{\sigma\alpha_1}, \eta^{\sigma\alpha_2}, \dots, \eta^{\sigma\alpha_k}))$, $\alpha_j = \frac{p}{\varpi}$, $(P, \varpi) = 1$, $P, \varpi \in \mathbb{Z}^+$, $j = 1, 2, \dots, k$.

4.3.4 A hybrid fractional Bloch model with time delay

The Bloch system is one of the known chaotic system. This system describes the dynamics of nuclear magnetization in the presence of static and time-varying magnetic fields (for more details, see [16], [17]). In the following we present a new delay model of the hybrid fractional. This model

is more general than the fractional-order delay model given in [4]. We have

$$\begin{aligned} {}_0^{CPC}D_t^{\alpha_1} X &= \delta Y + aZ(t - \tau_c)(X \sin(\theta) - Y \cos(\theta)) - bX, \\ {}_0^{CPC}D_t^{\alpha_2} Y &= -\delta X - Z + aZ(t - \tau_c)(Y \sin(\theta) + X \cos(\theta)) - bY, \\ {}_0^{CPC}D_t^{\alpha_3} Z &= Y - a \sin(\theta)(X^2 + Y^2) - c(Z - 1), \end{aligned} \tag{4.15}$$

where θ is the phase of the feedback magnetic field and δ is the longitudinal time (for more details, see [20]). The variables X , Y , and Z represent the system magnetization in the x , y , and z -directions, $\tau_c > 0$ is the time delay, and $X(0) = X_0$, $Y(0) = Y_0$, $Z(0) = Z_0$.

4.3.5 Existence and uniqueness of the time-delayed fractional solution

Let us consider the following time-delayed fractional system:

$$\begin{aligned} {}_0^{CPC}D_t^\alpha \gamma(t) &= g(\gamma(t), \gamma(t - \tau_c), t), \quad \gamma(0) = \gamma_0 \geq 0, \quad 0 < \alpha < 1, \quad 0 \leq t \leq T, \\ \gamma(t) &= f(t), \quad \tau_c \leq t \leq 0, \end{aligned} \tag{4.16}$$

where $T \in \mathbb{R}^3$, $f(t)$ and the coefficients of $\gamma(t)$ and $\gamma(t - \tau_c)$ represent smooth functions, and $\tau_c \in \mathbb{R}^3$ denotes the delay. If g is continuous, the solution of Eq. (4.16) can be rewritten as follows:

$$\gamma(t) = \gamma(t_0) + \left(\int_0^t \exp \left[\frac{K_1(\alpha)}{K_0(\alpha)} (t - s) \right] {}_0^{RL}D_t^{1-\alpha} \gamma(s - \tau_c) ds \right) \frac{1}{K_0(\alpha)}. \tag{4.17}$$

Consider the following space:

$$V_{(T_{max}, \gamma_{max})} = \Lambda_{T_{max}} \times M_{\gamma_{max}}. \tag{4.18}$$

We define

$$\begin{aligned} \Lambda_{T_{max}} &= [t_0 - t_{max}, t_0 + t_{max}], \\ M_{\gamma_{max}} &= [\gamma_0 - \gamma_{max}, \gamma_0 + \gamma_{max}], \end{aligned}$$

and $V_{(T_{max}, \gamma_{max})}$ is a compact cylinder of function g defined in Eqs. (4.16) and (4.17). Let $K = \sup \|g\|_\infty$. The Banach fixed point theorem will be applied

using the metric on $V_{(T_{max}, \gamma_{max})}$ which induces the uniform norm:

$$\|\Psi\|_{\infty} = \sup_{t \in \Lambda_{max}} |\Psi|.$$

Consider the Picard operator

$$\Psi : V_{(T_{max}, \gamma_{max})} \longrightarrow V_{(T_{max}, \gamma_{max})},$$

defined by

$$\Psi\beta(t) = \gamma(t_0) + \left(\int_0^t \exp \left[\frac{K_1(\alpha)}{K_0(\alpha)}(t-s) \right] {}_0^R D_t^{1-\alpha} g(\beta(s), \beta(s-\tau_c), s) ds \right) \frac{1}{K_0(\alpha)}. \quad (4.19)$$

We construct the condition for well-posedness as follows.

Let us consider two different functions β_1 and β_2 in $\mathbb{C}[\Lambda_{T_{max}}(t_0), M_{\gamma_{max}}(\gamma_0)]$. Then let us evaluate the following:

$$\begin{aligned} \|\Psi\beta_1(t) - \Psi\beta_2(t)\|_{\infty} &\leq \frac{\gamma_{max}^{\alpha}}{\Gamma(\alpha-1)K_0(\alpha)} \left\| \int_0^t (t-s)^{\alpha-2} (g(\beta_1(s), \beta_1(s-\tau_c), s) \right. \\ &\quad \left. - (g(\beta_2(s), \beta_2(s-\tau_c), s))) ds \right\|_{\infty} \\ &\leq \frac{\gamma_{max}^{\alpha} X_{max}^{\alpha}}{\Gamma(\alpha-1)K_0(\alpha)} \left\| (g(\beta_1(t), \beta_1(t-\tau_c), t) \right. \\ &\quad \left. - (g(\beta_2(t), \beta_2(t-\tau_c), t))) \right\|_{\infty} \\ &\leq \frac{M^0 \gamma_{max}^{\alpha} X_{max}^{\alpha}}{\Gamma(\alpha-1)K_0(\alpha)} \|\beta_1(t) - \beta_2(t)\|_{\infty}. \end{aligned} \quad (4.20)$$

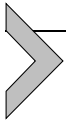
Finally, we obtain

$$\|\Psi\beta_1(t) - \Psi\beta_2(t)\|_{\infty} \leq L \|\beta_1(t) - \beta_2(t)\|_{\infty}, \quad (4.21)$$

where

$$L = \frac{M^0 \gamma_{max}^{\alpha} X_{max}^{\alpha}}{\Gamma(\alpha-1)K_0(\alpha)}.$$

Under the above condition the constructed Picard operation is a contraction on a Banach space with the metric induced by uniform norm; thus, β has the property that there exists a unique function β such that $\Psi\beta = \beta$, which is the unique solution of Eq. (4.16). This completes the proof of existence and uniqueness.



4.4. Numerical methods for solving hybrid fractional models

4.4.1 CPC-NSFDM

In this section, we construct a nonstandard method with a new hybrid fractional operator. The new method is called CPC-NSFDM. This method has advantages compared with the standard method [1], [8], [12], [23] such as better accuracy and higher stability. In addition, this method can be easily formulated as follows. Consider the general form of the fractional differential equation with CPC operator:

$${}_0^{CPC}D_t^{\alpha_v} \gamma(t) = \xi(t, \gamma(t)), \quad 0 < \alpha_v \leq 1, \quad \gamma(0) = \gamma_0, \quad v = 1, 2, \dots, n. \quad (4.22)$$

Now, we can discretize (4.22) using the Grunwald–Letnikov (GL) definition and (4.3). Then we have

$$\frac{1}{\phi(\tau)^{\alpha_v-1} \Gamma(2-\alpha_v)} \sum_{i=0}^n \left((1-\alpha_v) t_i^\alpha \gamma_{n-i+1} + \alpha_v t_i^{(1-\alpha_v)} \frac{\gamma_{n-i+1} - \gamma_{n-i}}{\phi(\tau)} \right) \left[(i+1)^{(1-\alpha_v)} - (i)^{(1-\alpha_v)} \right] = \xi(t_i, \gamma(t_i)), \quad (4.23)$$

where

$$\phi(\tau) = \tau + O(\tau^2), \quad 0 < \phi(\tau) < 1, \quad \tau \longrightarrow 0.$$

Or, using the definition (4.4) and GL approximation to approximate the Caputo fractional derivatives,

$$\frac{Q^{\alpha_v} (1-\alpha_v)}{\phi(\tau)^{\alpha_v-1} \Gamma(2-\alpha_v)} \sum_{i=0}^{n+1} \gamma_{n-i+1} \left[(i+1)^{(1-\alpha_v)} - (i)^{(1-\alpha_v)} \right] + \frac{\alpha Q^{(1-\alpha_v)}}{\phi(\tau)^{\alpha_v}} \left(\gamma_{n+1} - \sum_{i=1}^{n+1} \mu_i \gamma_{n+1-i} - q_{n+1} \gamma_0 \right) = \xi(t_i, \gamma(t_i)), \quad (4.24)$$

where $K_0(\alpha_v) = \alpha_v Q^{(1-\alpha_v)}$, $K_1(\alpha_v) = (1-\alpha_v) Q^{\alpha_v}$, $v = 1, \dots, 4$. $t^n = n\tau$, $\tau = \frac{T_f}{N_n}$, $N_n \in \mathbb{N}$, $\mu_i = (-1)^{i-1} \binom{\alpha_v}{i}$, $\mu_1 = \alpha_v$, $q_i = \frac{i^{\alpha_v}}{\Gamma(1-\alpha_v)}$, and $i = 1, 2, \dots, n+1$.

Additionally, consider the following [22], [23]:

$$\begin{aligned} 0 < \mu_{i+1} < \mu_i < \dots < \mu_1 = \alpha_\nu < 1, \\ 0 < q_{i+1} < q_i < \dots < q_1 = \frac{1}{\Gamma(1 - \alpha_\nu)}. \end{aligned}$$

We can claim the following Caputo discrete form if we put in (4.24) $K_0(\alpha_\nu) = 1$, $K_1(\alpha_\nu) = 0$:

$$\frac{1}{\phi(\tau)^{\alpha_\nu}} \left(\gamma_{n+1} - \sum_{i=1}^{n+1} \mu_i \gamma_{n+1-i} - q_{n+1} \gamma_0 \right) = \xi(t_i, \gamma(t_i)). \quad (4.25)$$

Let

$$r_1 = \frac{Q^{\alpha_\nu} (1 - \alpha_\nu)}{\phi(\tau)^{(1-\alpha_\nu)}}, \quad r_2 = \frac{\alpha_\nu Q^{(1-\alpha_\nu)}}{\phi(\tau)^{\alpha_\nu}}.$$

The discretization of system (4.6) using CPC-NSFDM can be formulated as follows:

$$\begin{aligned} X^{n+1} &= \frac{1}{r_1 + r_2 + a} \left(r_2 \sum_{i=1}^{n+1} \mu_i X^{n+1-i} + r_2 q_{n+1} X^0 \right. \\ &\quad \left. - r_1 \sum_{i=1}^{n+1} X^{n+1-i} \left[(i+1)^{1-\alpha_1} - i^{\alpha_1} \right] \right. \\ &\quad \left. + (Z^n + Y^n X^n + W^n) \right), \\ Y^{n+1} &= \frac{1}{r_1 + r_2 + b} \left(r_2 \sum_{i=1}^{n+1} \mu_i Y^{n+1-i} + r_2 q_{n+1} Y^0 \right. \\ &\quad \left. - r_1 \sum_{i=1}^{n+1} Y^{n+1-i} \left[(i+1)^{1-\alpha_2} - i^{\alpha_2} \right] + (1 - (X^2)^{n+1}) \right), \\ Z^{n+1} &= \frac{1}{r_1 + r_2 + c} \left(r_2 \sum_{i=1}^{n+1} \mu_i Z^{n+1-i} + r_2 q_{n+1} Z^0 \right. \\ &\quad \left. - r_1 \sum_{i=1}^{n+1} Z^{n+1-i} \left[(i+1)^{1-\alpha_3} - i^{\alpha_3} \right] - (X^{n+1}) \right), \end{aligned}$$

$$\begin{aligned}
W^{n+1} = & \frac{1}{r_1 + r_2 + d} \left(r_2 \sum_{i=1}^{n+1} \mu_i W^{n+1-i} + r_2 q_{n+1} W^0 \right. \\
& - r_1 \sum_{i=1}^{n+1} W^{n+1-i} \left[(i+1)^{1-\alpha_4} - i^{\alpha_4} \right] \\
& \left. + \left(-0.05 X^{n+1} Z^{n+1} - d W^{n+1} \right) \right). \quad (4.26)
\end{aligned}$$

Also, the discretization of system (4.15) using CPC-NSFDM is given as follows:

$$\begin{aligned}
X^{n+1} = & \frac{1}{r_1 + r_2 + a} \left(r_2 \sum_{i=1}^{n+1} \mu_i X^{n+1-i} + r_2 q_{n+1} X^0 \right. \\
& - r_1 \sum_{i=1}^{n+1} X^{n+1-i} \left[(i+1)^{1-\alpha_1} - j^{\alpha_1} \right] \\
& \left. + \left(\delta Y^n + a Z^k \left(X^n \sin(\theta) - Y^n \cos(\theta) \right) \right) \right), \\
Y^{1+n} = & \frac{1}{r_1 + r_2 + b} \left(r_2 \sum_{i=1}^{1+n} \mu_i Y^{1+n-i} + r_2 q_{n+1} Y^0 \right. \\
& - r_1 \sum_{i=1}^{1+n} Y^{1+n-i} \left[(i+1)^{1-\alpha_2} - i^{\alpha_2} \right] \\
& \left. + \left(\delta X^{n+1} + Z^n - a Z^k \left(Y^n \sin(\theta) + X^n \cos(\theta) \right) \right) \right), \\
Z^{n+1} = & \frac{1}{r_1 + r_2 + c} \left(r_2 \sum_{i=1}^{n+1} \mu_i Z^{n+1-i} + r_2 q_{n+1} Z^0 \right. \\
& - r_1 \sum_{i=1}^{n+1} Z^{n+1-i} \left[(i+1)^{1-\alpha_3} - i^{\alpha_3} \right] \\
& \left. + \left(Y^{n+1} - a \sin(\theta) \left((X^2)^{n+1} + (Y^2)^{n+1} \right) + c \right) \right). \quad (4.27)
\end{aligned}$$

4.4.2 Stability of CPC-NSFDM

Let us consider the following hybrid fractional-order chaotic system in general form [8]:

$$\begin{aligned}
 {}_0^{CPC}D_t^\alpha \gamma_l(t) &= \xi_l(\gamma_1, \gamma_2, \dots, \gamma_k) - \gamma_l f_l(\gamma_1, \gamma_2, \dots, \gamma_k), \\
 \gamma_l(t_0) &= \gamma_{l,0}, \quad l = 1, \dots, k,
 \end{aligned}
 \tag{4.28}$$

where ξ_l and g_l are continuous functions on \mathbb{R}^k .

Theorem 4.4.1. *The CPC-NSFDM is a stable method.*

Proof. By (4.24) and (4.28), we have

$$\begin{aligned}
 g_1 \gamma_{l,n+1} + g_1 \sum_{i=1}^{n+1} \gamma_{l,n+1-i} B^{1-\alpha} + g_2 \gamma_{l,n+1} - g_2 \sum_{i=1}^{n+1} \mu_i \gamma_{l,n+1-i} - g_2 q_{l,n+1} \gamma_{l,0} \\
 = \xi_l(\gamma_{1,n}, \gamma_{2,n}, \dots, \gamma_{k,n}) - \gamma_{l,n+1} f_l(\gamma_{1,n+1}, \gamma_{2,n+1}, \dots, \gamma_{k,n+1}),
 \end{aligned}
 \tag{4.29}$$

where

$$g_1 = \frac{Q^\alpha(1-\alpha)}{(\phi(\tau))^{\alpha-1}}, \quad g_2 = \frac{Q^{1-\alpha}\alpha}{(\phi(\tau))^\alpha}, \quad B^{1-\alpha} = \left[(i+1)^{1-\alpha} - i^{1-\alpha} \right].$$

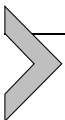
Then from the boundedness theorem [1] we have

$$\left| \gamma_{l,n+1} \right| = \left| \frac{-g_1 \sum_{i=1}^{n+1} \gamma_{l,n+1-i} B^{1-\alpha} + g_2 \sum_{i=1}^{n+1} \mu_i \gamma_{l,n+1-i} + g_2 q_{l,n+1} \gamma_{l,0} + \xi_l(\gamma_{1,n}, \gamma_{2,n}, \dots, \gamma_{k,n})}{g_1 + g_2 + f_l(\gamma_{1,n+1}, \gamma_{2,n+1}, \dots, \gamma_{k,n+1})} \right|,
 \tag{4.30}$$

and since

$$g_1 + g_2 + f_l(\gamma_{1,n+1}, \gamma_{2,n+1}, \dots, \gamma_{k,n+1}) > 1,$$

we have $|\gamma_{l,1}| \leq |\gamma_{l,0}|$ and $|\gamma_{l,n+1}| \leq |\gamma_{l,n}| < |\gamma_{l,n-1}| \dots \leq |\gamma_{l,1}| \leq |\gamma_{l,0}|$. So the proposed scheme is stable. □



4.5. Numerical simulations

In the following, we consider the numerical simulations for system (4.6). The parameter values are given as follows: $d = 0.6$, $c = 1$, $b = 0.1$, and $a = 0.9$. The initial conditions are given as follows [8]: $W(0) = 0.7$, $Z(0) = 0.2$, $Y(0) = 0.5$, and $X(0) = 0.1$. Also, for the numerical simulations of system (4.15), we consider the values of the parameters as follows [8]: $a = 10$, $b = 2$, $c = 4$, and $\delta = 1.26$. The initial conditions are given as follows: $X(0) = 0$, $Y(0) = 0.01$, $Z(0) = 0$. The numerical simulation of the

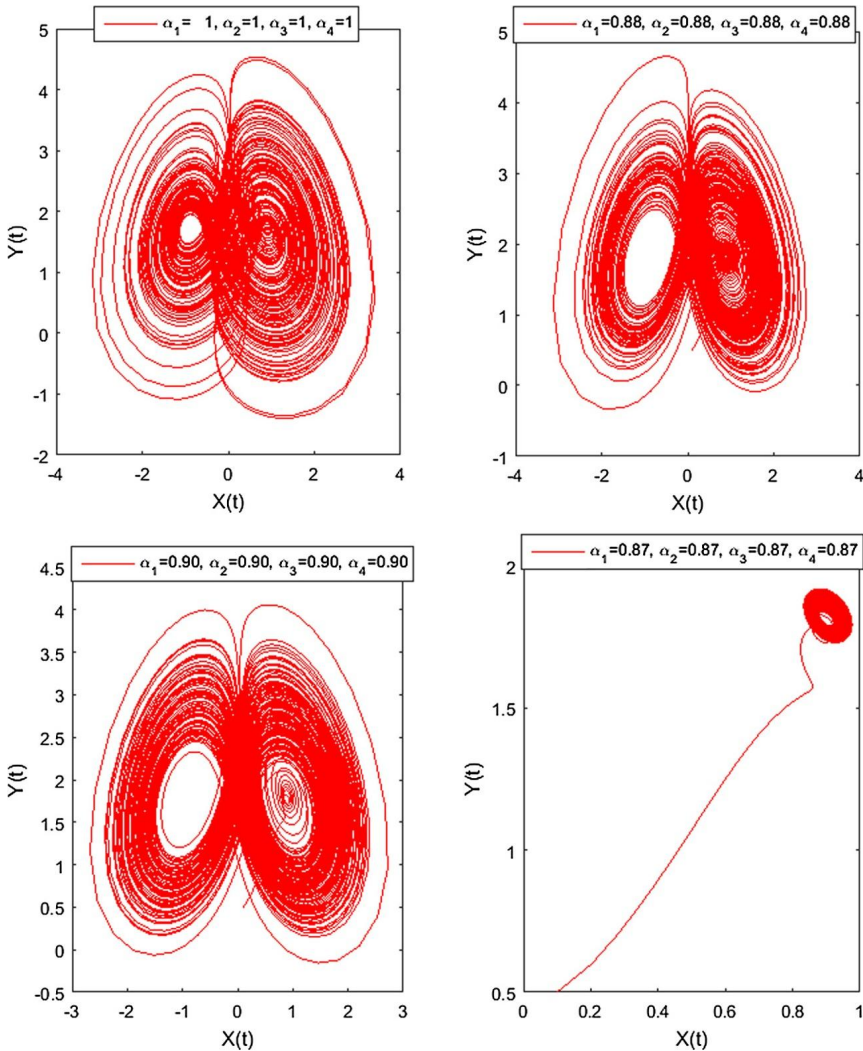


Figure 4.1 Phase portraits of the model (4.6) using CPC-NSFDM at $\alpha_1 = \alpha_2 = \alpha_3 = \alpha_4$, $Q = 0.25$.

chaotic models using two efficient numerical methods are presented. These methods are CPC-NSFDM and C-NSFDM.

The approximate solutions of the proposed hybrid fractional-order systems (4.6) and (4.15) are given in Figs. 4.1–4.7 for different values of $0 < \alpha_\nu \leq 1$. The discretization of CPC-NSFDM for the hybrid fractional order systems (4.6) and (4.15) are given in (4.26) and (4.27), respectively.

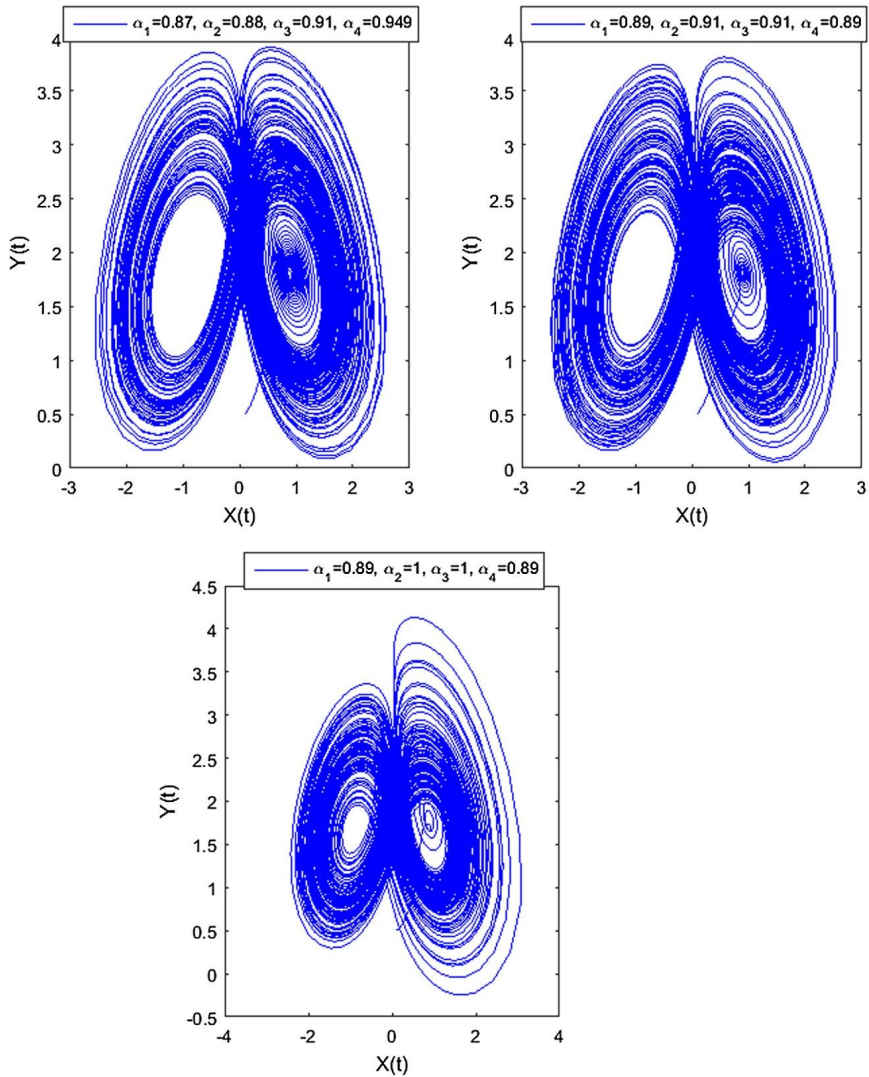


Figure 4.2 Phase portraits of the model (4.6) using CPC-NSFDM at different $\alpha_1, \alpha_2, \alpha_3$.

We can obtain the discretization of the Caputo operator with NSFDM as a special case of this discretization when we put $K_1(\alpha_\nu) = 0$. This means the new operator CPC is more general than the Caputo operator. Fig. 4.1 shows the relationship between the variables X and Y in model (4.6) using CPC-NSFDM at $\alpha_1 = \alpha_2 = \alpha_3 = \alpha_4$, $Q = 0.25$. Also, the approximate solutions at different values of $\alpha_1, \alpha_2, \alpha_3, \alpha_4$ are given in Fig. 4.2. The

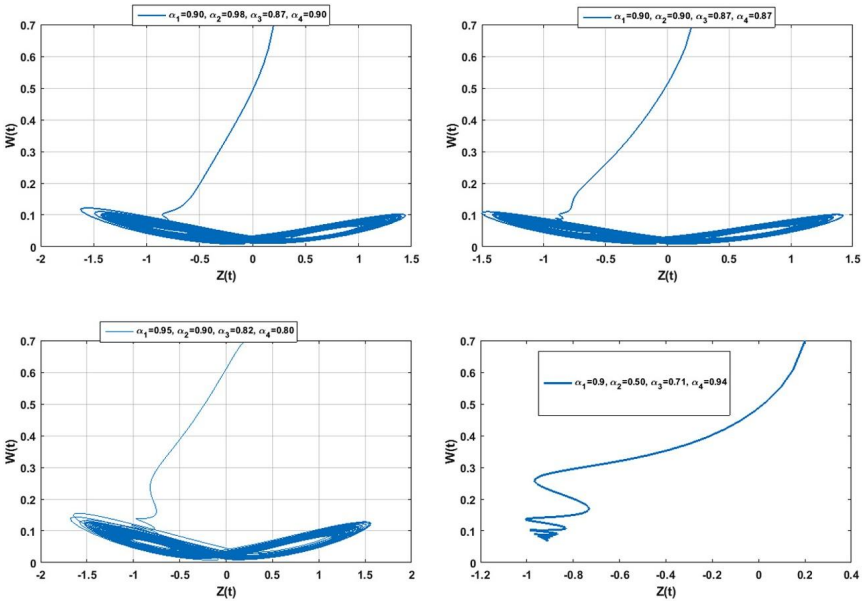


Figure 4.3 Phase portraits of the model (4.6) using CPC-NSFDM at different $\alpha_1, \alpha_2, \alpha_3, Q = 0.25$.

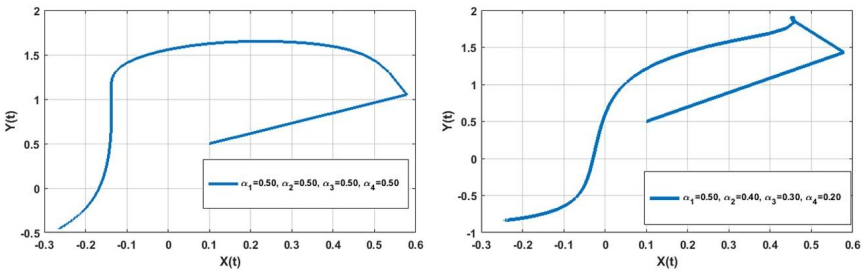


Figure 4.4 Phase portraits of the model (4.6) using CPC-NSFDM at different $\alpha_1, \alpha_2, \alpha_3, Q = 0.00025$.

relationship between the variables W and Z in model (4.6) using CPC-NSFDM at different values of $\alpha_1, \alpha_2, \alpha_3, \alpha_4$ is given in Fig. 4.3. We observe that the behavior of the chaotic system changes when α takes different values. Fig. 4.4 shows the behavior of solution at $0 < \alpha_1, \alpha_2, \alpha_3 \leq 0.5, Q = 0.25$.

The simulation results of (4.15) are given in Figs. 4.5–4.8. These figures explain how the behavior of chaotic systems is different when we use different values of α . Table 4.2 shows the CPU time for the proposed model (4.6)

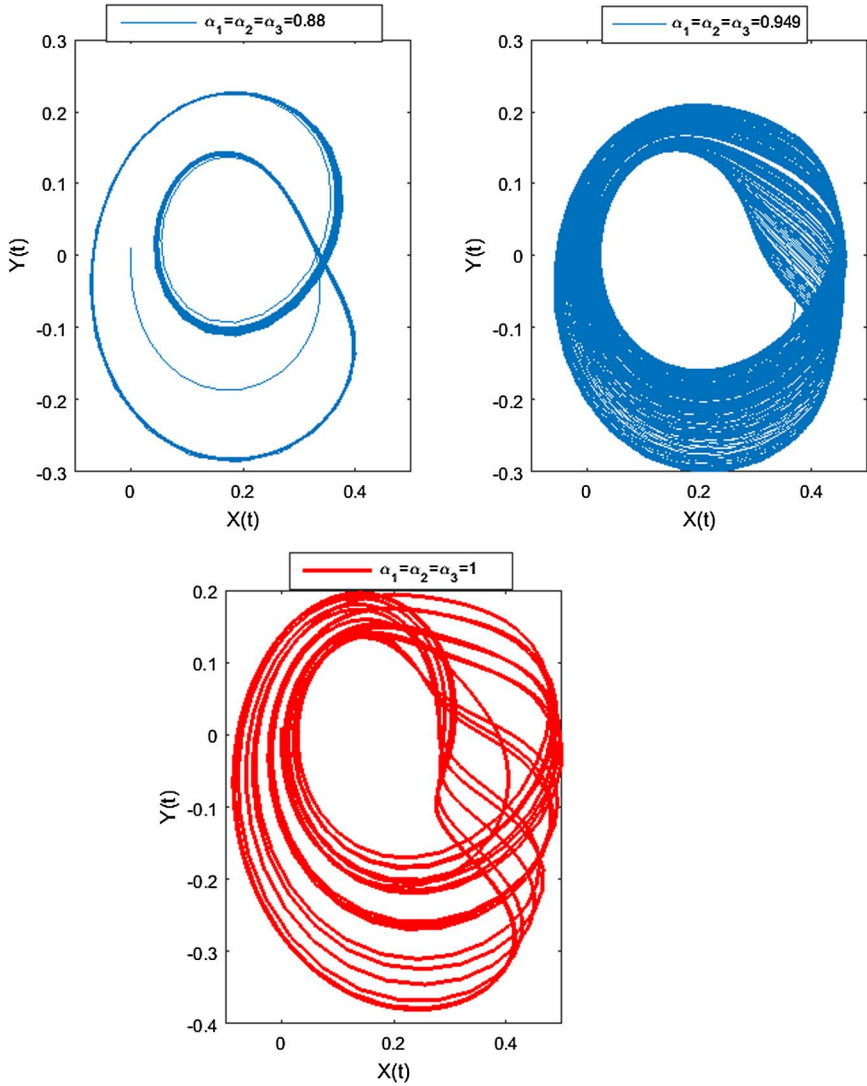


Figure 4.5 Phase portraits of the model (4.15) using CPC-NSFDM at $\alpha_1 = \alpha_2 = \alpha_3$ and time delay $\tau_c = 0.001$, $Q = 0.25$.

using CPC-NSFDM and C-NSFDM with different values of α . We conclude that CPC-NSFDM is more efficient than C-NSFDM. The results obtained with this new operators and CPC-NSFDM are interesting, and our analysis will open new doors for investigations by researchers in the future.

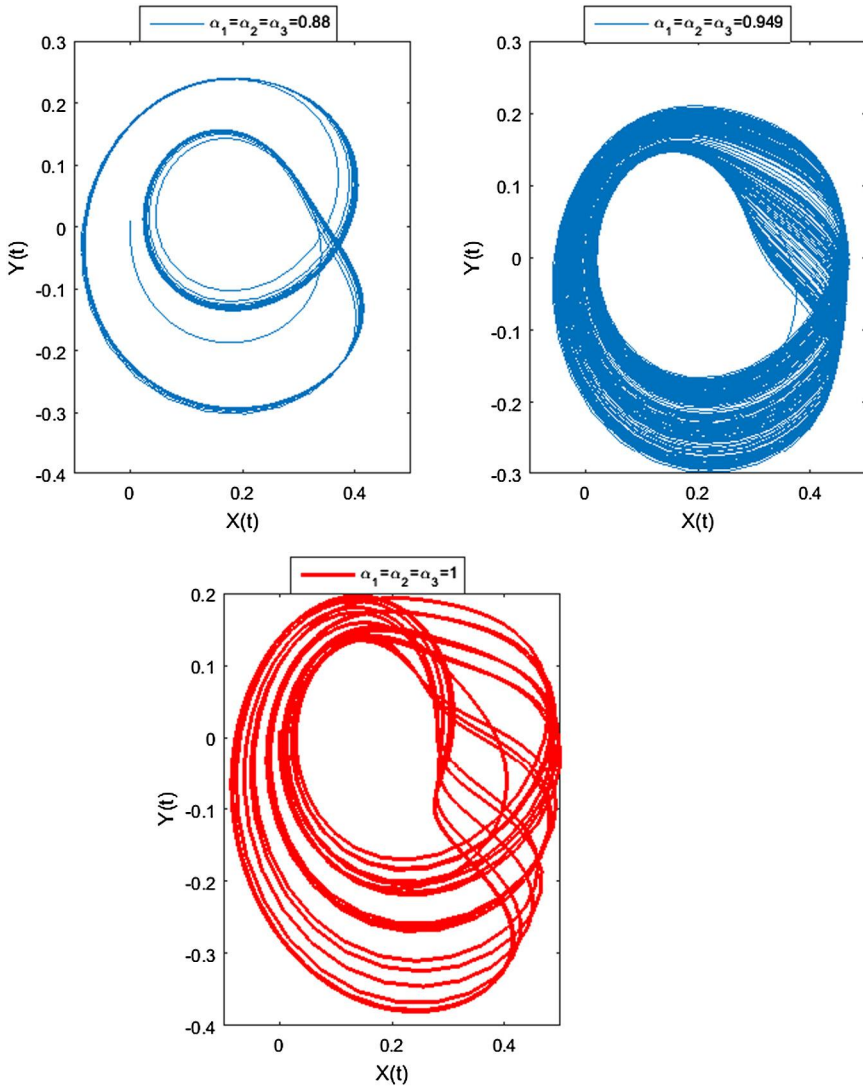
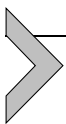


Figure 4.6 Phase portraits of the model (4.15) using C-NSFDM at $\alpha_1 = \alpha_2 = \alpha_3$ and time delay $\tau_c = 0.001$.



4.6. Conclusions

In this chapter, we considered two novel hybrid fractional-order chaotic systems. The new operator which is given in [2] is successfully used to construct these chaotic systems. The NSFDM is constructed with

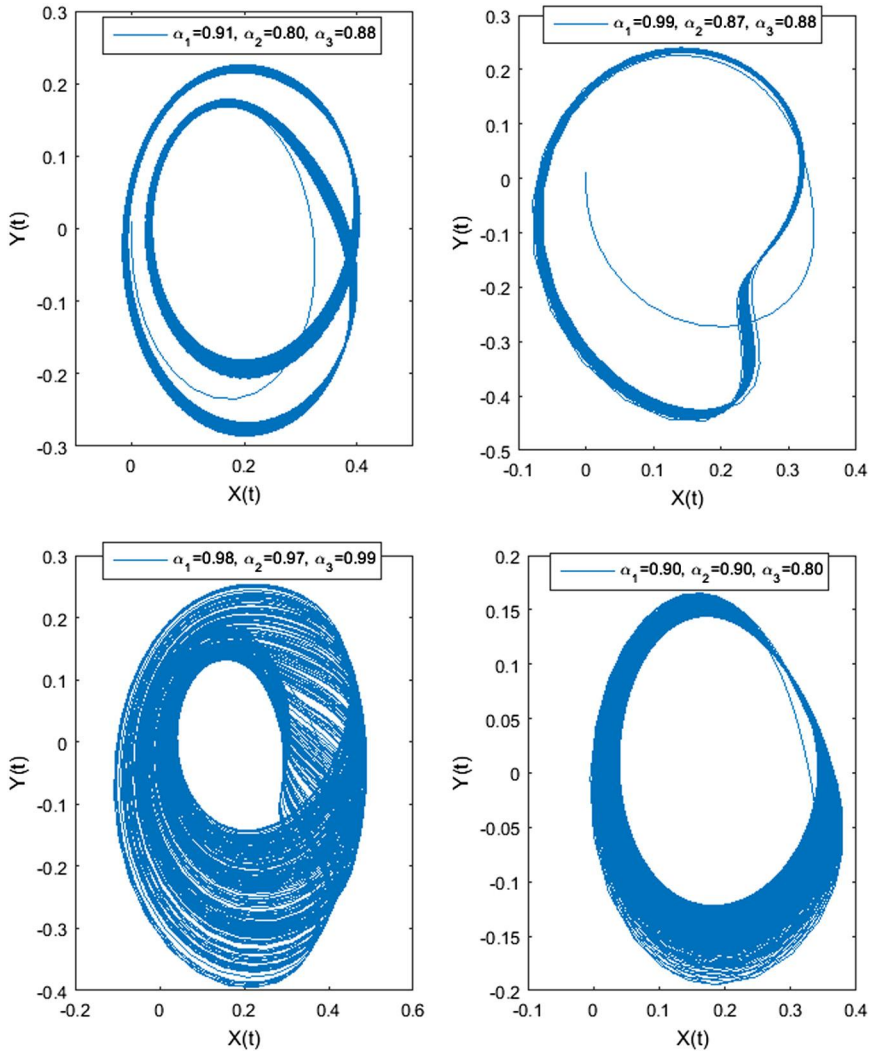


Figure 4.7 Phase portraits of the model (4.15) using CPC-NSFDM at different $\alpha_1, \alpha_2, \alpha_3$ and time delay $\tau_c = 0.001, Q = 0.25$.

the new operator to simulate the proposed models. The stability analysis for the proposed method is conducted. Numerical simulations in this chapter are implemented for different values of α . We conclude that the behavior of the chaotic system changes when α takes different values. Also, the CPC-NSFDM is efficient and more general than the C-NSFDM. The combination of chaotic systems and the hybrid fractional-order derivative

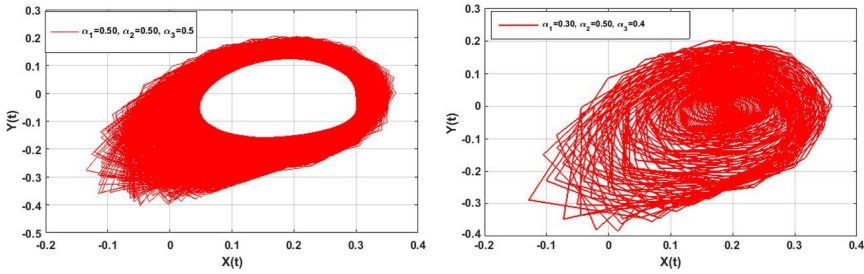
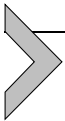


Figure 4.8 Phase portraits of the model (4.15) using CPC-NSFDM at different $\alpha_1, \alpha_2, \alpha_3$ and time delay $\tau_c = 0.001, Q = 0.00025$.

Table 4.2 CPU time in seconds for the solution of hybrid fractional-order system (4.6) using CPC-NSFDM and C-NSFDM at different values of α at $T_f = 2000$.

α_i	CPU time of CPC-NSFDM	CPU time of C-NSFDM
$\alpha_1 = \alpha_2 = \alpha_3 = \alpha_4 = 1$	19.085150	30.277742
$\alpha_1 = \alpha_2 = \alpha_3 = \alpha_4 = 0.90$	172.668507	178.452882
$\alpha_1 = 0.87, \alpha_2 = 0.88, \alpha_3 = 0.91, \alpha_4 = 0.94$	150.146368	153.114388

in the model improves the models and increases complexity. The fractional derivative in the sense of CPC is a novel topic and has very useful applications in different fields.



Declaration of competing interest

The authors have declared no conflict of interest.

References

- [1] A.J. Arenas, G. González-Parra, B.M. Chen-Charpentier, Construction of nonstandard finite difference schemes for the SI and SIR epidemic models of fractional order, *Mathematics and Computers in Simulation* 121 (2016) 48–63.
- [2] D. Baleanu, A. Fernandez, A. Akgül, On a fractional operator combining proportional and classical differintegrals, *Mathematics* 8 (2020), <https://doi.org/10.3390/math8030360>.
- [3] D. Baleanu, K. Diethelm, E. Scalas, J.J. Trujillo, *Fractional Calculus Models and Numerical Methods*, Series on Complexity, Nonlinearity and Chaos, World Scientific Publishing Co. Pte. Ltd., Hackensack, NJ, USA, 2012.
- [4] D. Baleanu, R. Magin, S. Bhalekar, V. Daftardar-Gejji, Chaos in the fractional order nonlinear Bloch equation with delay, *Communications in Nonlinear Science and Numerical Simulation* 25 (1–3) (2015) 41–49.
- [5] D. Baleanu, A.M. Lopes, *Handbook of Fractional Calculus with Applications: Volume 8, Applications in Engineering, Life and Social Sciences, Part B*, De Gruyter, Berlin, Germany, 2019, ISBN 9783110571929, 3110571927.

- [6] S. Bhalekar, V. Daftardar-Gejji, D. Baleanu, R.L. Magin, Transient chaos in fractional Bloch equations, *Computers & Mathematics with Applications* 64 (2012) 3367–3376.
- [7] J.F. Gómez-Aguilar, Chaos and multiple attractors in a fractal-fractional Shinriki's oscillator model, *Physica A: Statistical Mechanics and its Applications* 539 (2020) 122918.
- [8] M. Hajipour, A. Jajarmi, D. Baleanu, An efficient nonstandard finite difference scheme for a class of fractional chaotic systems, *Journal of Computational and Nonlinear Dynamics* 13 (2018) 1–9, <https://doi.org/10.1115/1.4038444>.
- [9] J.H. He, A tutorial review on fractal space time and fractional calculus, *International Journal of Theoretical Physics* 53 (11) (2014).
- [10] J.H. He, S.K. Elagan, Z.B. Li, Geometrical explanation of the fractional complex transform and derivative chain rule for fractional calculus, *Physics Letters A* 376 (4) (2012) 257–259.
- [11] A.S. Hendy, M.A. Zaky, Global consistency analysis of $L1$ -Galerkin spectral schemes for coupled nonlinear space-time fractional Schrödinger equations, *Applied Numerical Mathematics* 156 (2020) 276–302.
- [12] Z. Iqbal, N. Ahmed, D. Baleanu, W. Adel, M. Rafiq, M.A. Rehman, A.S. Alshomrani, Positivity and boundedness preserving numerical algorithm for the solution of fractional nonlinear epidemic model of HIV/AIDS transmission, *Chaos, Solitons and Fractals* 134 (2020) 109706.
- [13] A. Jajarmi, M. Hajipour, D. Baleanu, New aspects of the adaptive synchronization and hyperchaos suppression of a financial model, *Chaos, Solitons and Fractals* 99 (2017) 285–296.
- [14] A.A. Kilbas, H.M. Srivastava, J.J. Trujillo, *Theory and Applications of Fractional Differential Equations*, Elsevier, San Diego, 2006.
- [15] Y. Lin, Y. Chen, Q. Cao, Nonlinear and chaotic analysis of a financial complex system, *Applied Mathematics and Mechanics* 31 (2010) 1305–1316.
- [16] R.L. Magin, O. Abdullah, D. Baleanu, X.H.J. Zhou, Anomalous diffusion expressed through fractional order differential operators in the Bloch-Torrey equation, *Journal of Magnetic Resonance* 190 (2) (2008) 255–270.
- [17] R.L. Magin, X. Feng, D. Baleanu, Solving the fractional order Bloch equation, *Concepts in Magnetic Resonance. Part A* 34A (1) (2009) 16–23.
- [18] R. Mickens, *Nonstandard Finite Difference Models of Differential Equations*, World Scientific, Singapore, 1994.
- [19] I. Podlubny, *Fractional Differential Equations*, Academic Press, New York, 1999.
- [20] B. Rakshit, P. Saha, A.R. Chowdhury, Chaos and control in nonlinear Bloch system, [arXiv:nlin/0501004](https://arxiv.org/abs/nlin/0501004), 2005.
- [21] A. Serletis, Is there chaos in economic time series, *Canadian Journal of Economics* 29 (1996) 210–212.
- [22] R. Scherer, S. Kalla, Y. Tang, J. Huang, The Grünwald-Letnikov method for fractional differential equations, *Computers & Mathematics with Applications* 62 (2011) 902–917.
- [23] N.H. Sweilam, M.M. Abou Hasan, D. Baleanu, New studies for general fractional financial models of awareness and trial advertising decisions, *Chaos, Solitons and Fractals* 104 (2017) 772–784.
- [24] N.H. Sweilam, S.M. AL-Mekhlafi, D. Baleanu, Optimal control for a fractional tuberculosis infection model including the impact of diabetes and resistant strains, *Journal of Advanced Research* 17 (2019) 125–137.
- [25] N.H. Sweilam, S.M. AL-Mekhlafi, D. Baleanu, Nonstandard finite difference method for solving complex-order fractional Burgers equations, *Journal of Advanced Research* 25 (2020) 19–29.
- [26] N.H. Sweilam, S.M. AL-Mekhlafi, A novel numerical method for solving 2-D time fractional Cable equation, *The European Physical Journal Plus* 134 (2019) 1–11.

- [27] N.H. Sweilam, S.M. AL-Mekhlafi, Optimal control for a nonlinear mathematical model of tumor under immune suppression: a numerical approach, *Optimal Control Applications & Methods* 39 (2018) 1581–1596.
- [28] M.A. Zaky, Recovery of high order accuracy in Jacobi spectral collocation methods for fractional terminal value problems with non-smooth solutions, *Journal of Computational and Applied Mathematics* 357 (2019) 103–122.
- [29] M.A. Zaky, A.S. Hendy, Convergence analysis of an $L1$ -continuous Galerkin method for nonlinear time-space fractional Schrödinger equations, <https://doi.org/10.1080/00207160.2020.1822994>, 2020.
- [30] L.L. Zhang, G.L. Cai, X.L. Fang, Stability for a novel time-delay financial hyperchaotic system by adaptive periodically intermittent linear control, *Journal of Applied Analysis and Computation* 7 (2017) 79–91.
- [31] H. Afshari, D. Baleanu, Applications of some fixed point theorems for fractional differential equations with Mittag-Leffler kernel, *Advances in Difference Equations* (2020) 140, <https://doi.org/10.1186/s13662-020-02592-2>.
- [32] E. Bonyah, A.K. Sagoe, D. Kumar, S. Deniz, Fractional optimal control dynamics of coronavirus model with Mittag-Leffler law, *Ecological Complexity* 45 (2020) 100880, <https://doi.org/10.1016/j.ecocom.2020.100880>.
- [33] M. Awais, F.S. Alshammari, S. Ullah, M.A. Khand, S. Islam, Modeling and simulation of the novel coronavirus in Caputo derivative, *Results in Physics* 19 (2020) 103588, <https://doi.org/10.1016/j.rinp.2020.103588>.



Iterative processes with fractional derivatives

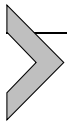
Giro Candelario^a, Alicia Cordero^b, Juan R. Torregrosa^b, and
María P. Vassileva^a

^aInstituto Tecnológico de Santo Domingo (INTEC), Área de Ciencia Básica, Santo Domingo, Dominican Republic

^bUniversitat Politècnica de Valencia, Instituto de Matemática Multidisciplinar, Valencia, Spain

Chapter points

- It is possible to define iterative methods for solving nonlinear equations by using fractional derivatives, whose order of convergence depends of the index of the fractional derivative.
- There are several advantages in the numerical performance of the designed fractional procedures: the same initial guess is useful for detecting all the roots of an equation, changing the index of the derivatives involved. Moreover, complex roots can be found even with real initial estimations.
- This is a recent area of research, which can yield substantial advances in the next years.



5.1. Introduction

Around 1695, Leibniz and l'Hopital devised the concept of the semiderivative, which marked the beginning of the development of fractional calculus simultaneously with classical calculus. Other researchers from this time, such as Riemann, Liouville, and Euler, were also interested in this idea. From then to the present, fractional calculus has evolved both in theoretical aspects and in its applications in medicine, economics, and mechanical engineering, among others, where problems arise that are modeled by differential equations with derivatives of fractional order (see [3,4,11–13,15,18,20,21,25,27] and references therein for examples).

The reason why fractional calculus has many applications in science and engineering is the higher degree of freedom of fractional calculus tools compared to classical ones. The use of fractional derivatives is often necessary in the modeling of problems whose hereditary properties must be preserved (see, for instance, [19]). Frequently the differential equation

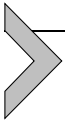
that represents the problem is nonlinear; this can yield, via discretization, a system of nonlinear equations to be solved. Hence, the idea of adopting iterative techniques for their resolution using fractional derivatives is novel and interesting. This area of research is very recent, and it starts with the introduction of iterative methods that use fractional derivatives in their iterative expressions, in the scalar case.

Let us consider the problem of computing a zero of a nonlinear function $f : I \subseteq \mathbb{R} \rightarrow \mathbb{R}$. This can be made by means of an iterative method (see, for example, [24,28]). The aim of this research is the design of new iterative methods with high order of convergence, by introducing fractional derivatives of Riemann–Liouville and Caputo type, and also employing parameters depending on the index of the derivative. Therefore, it is needed to study the convergence and stability of these schemes.

In the recent literature, some fractional one-point Newton type methods have been proposed in order to find roots of nonlinear equations using fractional derivatives. For example, the adaptation of Newton’s method for fractional derivatives was the objective of the recent work by Brambila et al. [5], in which the order of convergence was left without proof. However, in [2] the authors proved the need of adding a damping parameter related with the fractional order of the fractional derivative used, in order to reach the 2α th order of convergence. This result was improved in [6], where a new iterative expression was derived from the fractional Taylor development and order $1 + \alpha$ was obtained.

On the other hand, it is known that increasing the order of convergence of point-to-point iterative methods is achieved by using integer derivatives of second or higher order or developing multipoint methods. This was the following step in the development of this area of research: in [9], several Chebyshev type point-to-point schemes were derived by using fractional derivatives in their iterative expressions. Moreover, in [6] this idea was extended to multipoint Traub type procedures.

The structure of this work is as follows. In Section 5.2, the fundamental concepts related to fractional derivatives are exposed and in Section 5.3 we develop the fractional iterative methods, stating their respective order of convergence. In Section 5.4, numerical tests are performed and the dependence on initial estimations of these methods is studied with the use of planes of convergence. Finally, we derive some conclusions and raise open questions.



5.2. Preliminary concepts

In this section, we introduce some general concepts that we will use in the development of this work such as some special functions used, the Caputo and Riemann–Liouville fractional derivatives [23], [26], the fractional Taylor series [10], [22], and the fractional binomial coefficient [1].

Firstly, we define the Gamma function as

$$\Gamma(x) = \int_0^{+\infty} u^{x-1} e^{-u} du,$$

whenever $x > 0$. This function is a generalization of the factorial function to the complex plane, taking into account that $\Gamma(1) = 1$ and $\Gamma(n + 1) = n!$, when $n \in \mathbb{N}$.

Let us now remember the notion of fractional Caputo and Riemann–Liouville derivatives.

Definition 5.1 (Caputo fractional derivative of order α). Let $f : I \subseteq \mathbb{R} \rightarrow \mathbb{R}$ be an element of $C^{+\infty}([a, x])$ ($-\infty < a < x < +\infty$), with $\alpha \geq 0$ and $n = [\alpha] + 1$, with $[\alpha]$ being the integer part of α . Then, the Caputo fractional derivative of order α of $f(x)$ is defined as follows:

$$({}_a D_a^\alpha) f(x) = \begin{cases} \frac{1}{\Gamma(n - \alpha)} \int_a^x \frac{d^n f(t)}{dt^n} \frac{dt}{(x - t)^{\alpha - n + 1}}, & \alpha \notin \mathbb{N}, \\ \frac{d^{n-1} f(x)}{dx^{n-1}}, & \alpha = n - 1 \in \mathbb{N} \cup \{0\}. \end{cases} \tag{5.1}$$

Definition 5.2 (Riemann–Liouville fractional derivative of order α). Let $f : I \subseteq \mathbb{R} \rightarrow \mathbb{R}$ be an element of $L^1([a, x])$ ($-\infty < a < x < +\infty$), with $\alpha \geq 0$ and $n = [\alpha] + 1$, with $[\alpha]$ being the integer part of α . Then, the Riemann–Liouville fractional derivative of order α of $f(x)$ is defined as

$$(D_{a^+}^\alpha) f(x) = \begin{cases} \frac{1}{\Gamma(n - \alpha)} \frac{d^n}{dx^n} \int_a^x \frac{f(t)}{(x - t)^{\alpha - n + 1}} dt, & \alpha \notin \mathbb{N}, \\ \frac{d^{n-1} f(x)}{dx^{n-1}}, & \alpha = n - 1 \in \mathbb{N} \cup \{0\}. \end{cases} \tag{5.2}$$

Moreover, to prove the order of convergence of the iterative fractional methods we need a generalization of the classical Taylor series expansion of $f(x)$ around the zero of the nonlinear function, \bar{x} , using both the Caputo and the Riemann–Liouville fractional derivatives [10,22,29]. These generalizations are given in the following two results.

Theorem 5.1 (Taylor series expansion using Caputo fractional derivatives [22]). *Let us suppose that $cD_a^{j\alpha}f(x) \in C([a, b])$, for $j = 1, 2, \dots, n + 1$, where $\alpha \in (0, 1]$. Then we have*

$$f(x) = \sum_{i=0}^n cD_a^{i\alpha}f(a) \frac{(x-a)^{i\alpha}}{\Gamma(i\alpha+1)} + cD^{(n+1)\alpha}f(\xi) \frac{(x-a)^{(n+1)\alpha}}{\Gamma((n+1)\alpha+1)}, \quad (5.3)$$

with $a \leq \xi \leq x$, for all $x \in (a, b]$, where $cD_a^{n\alpha} = cD_a^\alpha \cdot cD_a^\alpha \cdots cD_a^\alpha$ (n times composition).

Theorem 5.2 (Taylor series expansion using Riemann–Liouville fractional derivatives [10]). *Let us assume the continuous function $f : \mathbb{R} \rightarrow \mathbb{R}$ has fractional derivatives of order $k\alpha$, for any positive integer k and any α , $0 < \alpha \leq 1$. Then the following equality holds:*

$$f(x+h) = \sum_{k=0}^{+\infty} \frac{h^{\alpha k}}{\Gamma(\alpha k + 1)} D_{a^+}^{\alpha k} f(x), \quad (5.4)$$

where $D_{a^+}^{\alpha k} f(x)$ is the Riemann–Liouville derivative of order αk of $f(x)$.

Also duality theory for left and right fractional derivatives is needed; it is called symmetric duality and was developed by Caputo and Torres in [7]. They used it to relate left and right fractional integrals with left and right Riemann–Liouville and Caputo fractional derivatives. We need the following results for the analysis of the convergence of the fractional iterative methods.

Theorem 5.3 (Lombardero [16]). *Let $\alpha \geq 0$, $n = [\alpha] + 1$, and $\beta \in \mathbb{R}$. Thus, the following identity holds:*

$$D_{a^+}^\alpha (x-a)^\beta = \frac{\Gamma(\beta+1)}{\Gamma(\beta+1-\alpha)} (x-a)^{\beta-\alpha}. \quad (5.5)$$

In addition, the relationship between Caputo and Riemann–Liouville fractional derivatives is explored in the next result from Lombardero.

Theorem 5.4 ([16]). *Let $\alpha \notin \mathbb{N}$ such that $\alpha \geq 0$, $n = [\alpha] + 1$, and let $f \in L^1([a, b])$ be a function whose Caputo and Riemann–Liouville fractional derivatives exist. Thus, the following identity holds:*

$$cD_a^\alpha f(x) = D_{a^+}^\alpha f(x) - \sum_{k=0}^{n-1} \frac{f^{(k)}(a)}{\Gamma(k+1-\alpha)} (x-a)^{k-\alpha}, \quad x > a. \quad (5.6)$$

As a consequence of Theorems 5.3 and 5.4, we have

$${}_cD_{x_0}^\alpha (x - x_0)^k = D_{x_0}^\alpha (x - x_0)^k, \quad k = 1, 2, \dots$$

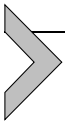
This result allows us to work with the Caputo fractional derivative and conclude that the derived results are also valid for the Riemann–Liouville fractional derivative.

Finally, to prove the order of convergence of some of the designed methods, Newton’s generalized binomial theorem (see [1]) is needed. We have

$$(x + y)^r = \sum_{k=0}^{+\infty} \binom{r}{k} x^{r-k} y^k, \quad k \in \{0\} \cup \mathbb{N}, \quad r \in \mathbb{R}, \quad (5.7)$$

where the generalized binomial coefficient is

$$\binom{r}{k} = \frac{\Gamma(r + 1)}{k! \Gamma(r - k + 1)}.$$



5.3. Design and analysis of iterative methods using fractional derivatives

In this section, we show the main aspects of the design of high-order fractional iterative methods for solving nonlinear equations. Moreover, we state how their order of convergence is proven. They are based on the classical Newton, Chebyshev, and Traub schemes.

Let $f : I \subseteq \mathbb{R} \rightarrow \mathbb{R}$ be a continuous function whose fractional derivative of Caputo type is defined for any order of index α , $0 < \alpha \leq 1$. By using Theorem 5.3, the Taylor development of a function $f(x)$ around its zero $a = \bar{x}$, in terms of fractional derivatives of Caputo type, is

$$f(x) = \frac{{}_cD_{\bar{x}}^\alpha f(\bar{x})}{\Gamma(\alpha + 1)} [(x - \bar{x})^\alpha + C_2(x - \bar{x})^{2\alpha} + C_3(x - \bar{x})^{3\alpha}] + O[(x - \bar{x})^{4\alpha}], \quad (5.8)$$

where $C_j = \frac{\Gamma(\alpha + 1) {}_cD_{\bar{x}}^{j\alpha} f(\bar{x})}{\Gamma(j\alpha + 1) {}_cD_{\bar{x}}^\alpha f(\bar{x})}$ for $j \geq 2$, and the corresponding expansion of the fractional derivative of $f(x)$ around \bar{x} is

$$\begin{aligned} {}_cD_a^\alpha f(x) &= \frac{{}_cD_{\bar{x}}^\alpha f(\bar{x})}{\Gamma(\alpha + 1)} \left[\Gamma(\alpha + 1) + \frac{\Gamma(2\alpha + 1)}{\Gamma(\alpha + 1)} C_2(x - \bar{x})^\alpha \right. \\ &\quad \left. + \frac{\Gamma(3\alpha + 1)}{\Gamma(2\alpha + 1)} C_3(x - \bar{x})^{2\alpha} \right] + O[(x - \bar{x})^{3\alpha}]. \end{aligned} \quad (5.9)$$

Next, the results corresponding to the same iterative schemes but with the fractional derivative Riemann–Liouville are stated without proof.

Newton type methods with fractional derivative

First, we present two types of iterative schemes based on the adaptation of Newton's method

$$x_{k+1} = x_k - \frac{f(x_k)}{f'(x_k)}, \quad k = 0, 1, 2, \dots,$$

with order of convergence 2, to the fractional derivatives of Caputo and Riemann–Liouville. In [2], two fractional variants of Newton's method with convergence order 2α were proposed. They were designed by using, among other elements, fractional derivatives of Caputo and Riemann–Liouville type. In the following results, we present the iterative expressions of the Riemann–Liouville fractional Newton's method and of the Caputo–fractional Newton's method, where $\Gamma(\alpha + 1)$ appears as a damping parameter.

Theorem 5.5. *Let $f : I \subset \mathbb{R} \rightarrow \mathbb{R}$ be a continuous function whose fractional derivatives of order $k\alpha$ are defined for any positive integer k and any α , $0 < \alpha \leq 1$, on the interval I containing the zero \bar{x} of $f(x)$ and let the fractional derivatives of the function $f(x)$ Riemann–Liouville type, $D_{a^+}^{k\alpha}f(x)$, and Caputo type, ${}_cD_{\bar{x}}^{\alpha}f(x)$, be continuous and non-zero at \bar{x} . Also, suppose that x_0 is an initial approximation close enough to \bar{x} . Then the order of local convergence of Newton's fractional methods*

$$x_{k+1} = x_k - \Gamma(\alpha + 1) \frac{f(x_k)}{D_{a^+}^{\alpha}f(x_k)}, \quad k = 0, 1, \dots, \quad (5.10)$$

of the Riemann–Liouville type and

$$x_{k+1} = x_k - \Gamma(\alpha + 1) \frac{f(x_k)}{{}_cD_a^{\alpha}f(x_k)}, \quad k = 0, 1, \dots, \quad (5.11)$$

of Caputo type is at least 2α , where $0 < \alpha \leq 1$, with the error equation

$$e_{k+1} = \frac{\Gamma(2\alpha + 1) - (\Gamma(\alpha + 1))^2}{(\Gamma(\alpha + 1))^3} C_2 e_k^{2\alpha} + O[e_k^{3\alpha}],$$

in both cases, where $C_j = \frac{\Gamma(\alpha + 1) {}_cD_{\bar{x}}^{j\alpha}f(\bar{x})}{\Gamma(j\alpha + 1) {}_cD_{\bar{x}}^{\alpha}f(\bar{x})}$, for $j \geq 2$.

Proof. Let $\{x_k\}_{k \geq 0}$ be a sequence of iterations obtained by (5.10), which approximates the zero \bar{x} of the nonlinear function $f(x)$. Using (5.8) and (5.9) from the Taylor expansion of the nonlinear function and its Caputo derivative at x_k , around \bar{x} , and introducing $e_k = x - \bar{x}$, we obtain

$$\frac{f(x_k)}{{}_cD_a^\alpha f(x_k)} = \frac{1}{\Gamma(\alpha + 1)} e_k^\alpha + \frac{\Gamma(2\alpha + 1) - (\Gamma(\alpha + 1))^2}{(\Gamma(\alpha + 1))^3} C_2 e_k^{2\alpha} + O[e_k^{3\alpha}],$$

expressed in terms of the error in the k th iteration $e_k = x_k - \bar{x}$. Then the error equation turns out to be

$$\begin{aligned} e_{k+1} &= x_{k+1} - \bar{x} = e_k^\alpha - \Gamma(\alpha + 1) \frac{f(x_k)}{{}_cD_a^\alpha f(x_k)} \\ &= \frac{\Gamma(2\alpha + 1) - (\Gamma(\alpha + 1))^2}{(\Gamma(\alpha + 1))^3} C_2 e_k^{2\alpha} + O[e_k^{3\alpha}]. \end{aligned}$$

This concludes the proof. □

We denote the iterative methods (5.10) and (5.11) as R-LFN₁ and CFN₁, respectively. Next, we define the following pair of designed Newton type methods with fractional derivative, proving their order of convergence.

Theorem 5.6. *We consider that $f : I \subset \mathbb{R} \rightarrow \mathbb{R}$ is a continuous function with fractional derivatives of order $k\alpha$ defined for any positive integer k and $\alpha \in (0, 1]$ defined on the open interval I containing the zero \bar{x} of $f(x)$. Additionally, let us suppose that $D_{a+}^{\alpha k} f(x)$ and ${}_cD_a^\alpha f(x)$ are continuous and non-zero at \bar{x} . The order of convergence of the Riemann–Liouville fractional Newton type method (denoted by R-LFN₂) with iterative expression*

$$x_{k+1} = x_k - \left(\Gamma(\alpha + 1) \frac{f(x_k)}{D_{a+}^{\alpha k} f(x_k)} \right)^{1/\alpha}, \quad k = 0, 1, 2, \dots, \tag{5.12}$$

and the Caputo fractional Newton type method (denoted by CFN₂),

$$x_{k+1} = x_k - \left(\Gamma(\alpha + 1) \frac{f(x_k)}{{}_cD_a^\alpha f(x_k)} \right)^{1/\alpha}, \quad k = 0, 1, 2, \dots, \tag{5.13}$$

is at least $\alpha + 1$, and their error equation is

$$e_{k+1} = \frac{\Gamma(2\alpha + 1) - (\Gamma(\alpha + 1))^2}{\alpha(\Gamma(\alpha + 1))^2} C_2 e_k^{\alpha+1} + O[e_k^{2\alpha+1}],$$

in both cases.

Proof. In the same way as in Theorem 5.5, using (5.8) and (5.9), we obtain again

$$\frac{f(x_k)}{cD_a^\alpha f(x_k)} = \frac{1}{\Gamma(\alpha + 1)} e_k^\alpha + \frac{(\Gamma(\alpha + 1))^2 - \Gamma(2\alpha + 1)}{(\Gamma(\alpha + 1))^3} C_2 e_k^{2\alpha} + O[e_k^{3\alpha}],$$

where $C_j = \frac{\Gamma(\alpha + 1) cD_{\bar{x}}^{j\alpha} f(\bar{x})}{\Gamma(j\alpha + 1) cD_{\bar{x}}^j f(\bar{x})}$, for $j \geq 2$.

Multiplying the last expression by the parameter $\Gamma(\alpha + 1)$, we obtain

$$\Gamma(\alpha + 1) \frac{f(x_k)}{cD_a^\alpha f(x_k)} = e_k^\alpha + \frac{(\Gamma(\alpha + 1))^2 - \Gamma(2\alpha + 1)}{(\Gamma(\alpha + 1))^2} C_2 e_k^{2\alpha} + O[e_k^{3\alpha}],$$

and applying expression (5.7) we obtain

$$\begin{aligned} & \left(\Gamma(\alpha + 1) \frac{f(x_k)}{cD_a^\alpha f(x_k)} \right)^{1/\alpha} \\ &= \left(e_k^\alpha + \frac{(\Gamma(\alpha + 1))^2 - \Gamma(2\alpha + 1)}{(\Gamma(\alpha + 1))^2} C_2 e_k^{2\alpha} + O[e_k^{3\alpha}] \right)^{1/\alpha} \\ &= e_k + \frac{\Gamma(\alpha + 1)}{\Gamma(\alpha)} e_k^{1-\alpha} + \frac{(\Gamma(\alpha + 1))^2 - \Gamma(2\alpha + 1)}{(\Gamma(\alpha + 1))^2} C_2 e_k^{2\alpha} + O[e_k^{2\alpha+1}]. \end{aligned}$$

As $\Gamma(1/\alpha + 1) = \frac{1}{\alpha} \Gamma(1/\alpha)$, we can simplify:

$$\left(\Gamma(\alpha + 1) \frac{f(x_k)}{cD_a^\alpha f(x_k)} \right)^{1/\alpha} = e_k + \frac{(\Gamma(\alpha + 1))^2 - \Gamma(2\alpha + 1)}{\alpha(\Gamma(\alpha + 1))^2} C_2 e_k^{\alpha+1} + O[e_k^{2\alpha+1}].$$

Substituting this result in the iterative expression of the method taking into account that $x_{k+1} = e_{k+1} + \bar{x}$ and $x_k = e_k + \bar{x}$, we obtain

$$e_{k+1} + \bar{x} = e_k + \bar{x} - e_k - \frac{\Gamma(2\alpha + 1) - (\Gamma(\alpha + 1))^2}{\alpha(\Gamma(\alpha + 1))^2} C_2 e_k^{\alpha+1} + O[e_k^{2\alpha+1}].$$

Then,

$$e_{k+1} = \frac{\Gamma(2\alpha + 1) - (\Gamma(\alpha + 1))^2}{\alpha(\Gamma(\alpha + 1))^2} C_2 e_k^{\alpha+1} + O[e_k^{2\alpha+1}].$$

This concludes the proof. \square

Chebyshev type methods with fractional derivative

Now, we are going to present the adaptation of the Chebyshev method for fractional derivatives of Caputo and Riemann–Liouville. The scheme of

the classical Chebyshev method for approximating a root of the nonlinear equation $f(x) = 0$ is

$$x_{k+1} = x_k - \left(1 + \frac{1}{2}L_f(x_k)\right) \frac{f(x_k)}{f'(x_k)},$$

where $L_f = \frac{f(x_k)f''(x_k)}{f'(x_k)^2}$ and has order of convergence three. With the purpose of adapting this method to fractional calculus, we define

$$cL_f^\alpha = \frac{f(x)cD_a^{2\alpha}f(x)}{(cD_a^\alpha f(x))^2}$$

and we call this expression the fractional degree of logarithmic convexity of Caputo type. Next we present several variants of the iterative Chebyshev method using the Caputo derivative and we show that its order of convergence is 2α .

Theorem 5.7. *We consider a continuous function $f : I \subset \mathbb{R} \rightarrow \mathbb{R}$ with $k\alpha$ fractional derivatives defined on the interval I for $k \in \mathbb{N}$ and any $\alpha, 0 < \alpha \leq 1$. Let x_0 be an initial approximation close enough to the zero \bar{x} of $f(x)$. Furthermore, we consider that $cD_{\bar{x}}^\alpha f(x)$ is continuous and non-zero in \bar{x} . Then, the iterative Chebyshev fractional method using Caputo type derivatives denoted by:*

1. CFC_1

$$x_{k+1} = x_k - \Gamma(\alpha + 1) \left(1 + \frac{1}{2}cL_f^\alpha(x_k)\right) \frac{f(x_k)}{cD_a^\alpha f(x_k)} \tag{5.14}$$

has local convergence order at least 2α with an error equation

$$e_{k+1}^\alpha = \frac{2(\Gamma(\alpha + 1))^2 - \Gamma(2\alpha + 1)}{2(\Gamma(\alpha + 1))^2} C_2 e_k^{2\alpha} + O[e_k^{3\alpha}];$$

2. CFC_2

$$x_{k+1} = x_k - \Gamma(\alpha + 1) \left(1 + \frac{1}{2} \frac{cD_a^{\alpha+1}f(x_k)f(x_k)}{(cD_a^\alpha f(x_k))^2}\right) \frac{f(x_k)}{cD_a^\alpha f(x_k)} \tag{5.15}$$

has order of convergence at least 2α , where $0 < \alpha < 1$; on the one hand, if $0 < \alpha \leq \frac{2}{3}$, the error equation is

$$e_{k+1}^\alpha = \left(\frac{(\Gamma(\alpha + 1))^2 - \Gamma(2\alpha + 1)}{(\Gamma(\alpha + 1))^3} C_2 + \frac{1}{2} \frac{1}{(\Gamma(\alpha + 1))^2} \frac{cD_{\bar{x}}^{\alpha+1}f(\bar{x})}{cD_a^\alpha f(\bar{x})}\right) e_k^{2\alpha} + O[e_k^{3\alpha}],$$

and on the other hand, if $\frac{2}{3} \leq \alpha < 1$, then

$$e_{k+1}^{\alpha} = \left(\frac{(\Gamma(\alpha + 1))^2 - \Gamma(2\alpha + 1)}{(\Gamma(\alpha + 1))^3} C_2 + \frac{1}{2} \frac{1}{(\Gamma(\alpha + 1))^2} \frac{cD_{\bar{x}}^{\alpha+1} f(\bar{x})}{cD_{\bar{x}}^{\alpha} f(\bar{x})} \right) e_k^{2\alpha} + O[e_k^{3\alpha}];$$

3. CFC₃

$$x_{k+1} = x_k - \Gamma(\alpha + 1) \left(A + BcL_f^{\alpha}(x_k) \right) \frac{f(x_k)}{cD_{\bar{x}}^{\alpha} f(x_k)} \quad (5.16)$$

has order of convergence at least 3α only if $A = 1$ and $B = \frac{\Gamma(2\alpha+1) - (\Gamma(\alpha+1))^2}{\Gamma(2\alpha+1)}$, where $0 < \alpha < 1$, and the error equation has the form

$$e_{k+1} = \left[-\Gamma(2\alpha + 1) \left(1 - \frac{\Gamma(2\alpha + 1)}{(\Gamma(\alpha + 1))^4} \right) C_2 + \frac{B\Gamma(2\alpha + 1)}{(\Gamma(\alpha + 1))^3} \left(2 - 3 \frac{\Gamma(2\alpha + 1)}{(\Gamma(\alpha + 1))^2} \right) C_2^2 + \frac{1}{\Gamma(\alpha + 1)} \left(\frac{B\Gamma(3\alpha + 1)}{(\Gamma(\alpha + 1))^3} - \frac{\Gamma(3\alpha + 1)}{\Gamma(2\alpha + 1)\Gamma(\alpha + 1)} \right) C_3 \right] e_k^{3\alpha} + O[e_k^{4\alpha}],$$

where $e_k = x - \bar{x}$.

Proof. By using Taylor expansion of $cD_{\bar{x}}^{\alpha} f(x_k)$ given with expression (5.9), we obtain

$$cD_{\bar{x}}^{2\alpha} f(x_k) = \frac{cD_{\bar{x}}^{\alpha} f(\bar{x})}{\Gamma(\alpha + 1)} \left[\Gamma(2\alpha + 1) C_2 + \frac{\Gamma(3\alpha + 1)}{\Gamma(\alpha + 1)} C_3 e_k^{\alpha} \right] + O[e_k^{2\alpha}]. \quad (5.17)$$

Expressions (5.8) and (5.17) allow us to calculate the product $f(x_k)cD_{\bar{x}}^{2\alpha}$ and using (5.9) we calculate $(cD_{\bar{x}}^{\alpha} f(x_k))^2$. This allows us to obtain the Taylor expansion of $cL_f^{\alpha}(x_k)$ around \bar{x} :

$$cL_f^{\alpha} = \frac{\Gamma(2\alpha + 1)}{(\Gamma(\alpha + 1))^2} C_2 e_k^{\alpha} + \frac{1}{(\Gamma(\alpha + 1))^2} \left[\Gamma(2\alpha + 1) C_2^2 + \frac{\Gamma(3\alpha + 1)}{\Gamma(\alpha + 1)} C_3 - \frac{2(\Gamma(2\alpha + 1))^2}{(\Gamma(\alpha + 1))^2} C_2^2 \right] e_k^{2\alpha} + O[e_k^{3\alpha}].$$

Thus

$$1 + \frac{1}{2}cL_f^\alpha = 1 + \frac{\Gamma(2\alpha + 1)}{2(\Gamma(\alpha + 1))^2} C_2 e_k^\alpha + \left(\frac{\Gamma(2\alpha + 1)}{2(\Gamma(\alpha + 1))^2} C_2^2 + \frac{\Gamma(3\alpha + 1)}{2(\Gamma(\alpha + 1))^3} C_3 - \frac{2(\Gamma(2\alpha + 1))^2}{2(\Gamma(\alpha + 1))^4} C_2^2 \right) e_k^{2\alpha} + O[e_k^{3\alpha}]$$

and

$$\begin{aligned} & \left(1 + \frac{1}{2}cL_f^\alpha \right) \frac{f(x_k)}{cD_a^\alpha f(x_k)} \\ &= \frac{1}{\Gamma(\alpha + 1)} e_k^\alpha + \frac{2(\Gamma(\alpha + 1))^2 - \Gamma(2\alpha + 1)}{2(\Gamma(\alpha + 1))^3} C_2 e_k^{2\alpha} + O[e_k^{3\alpha}]. \end{aligned}$$

Then, the error equation is

$$e_{k+1} = \frac{\Gamma(2\alpha + 1) - 2(\Gamma(\alpha + 1))^2}{2(\Gamma(\alpha + 1))^2} C_2 e_k^{2\alpha} + O[e_k^{3\alpha}].$$

The proof of the order of convergence of the CFC₂ and CFC₃ methods are omitted, as they are similar to that of CFC₁. □

Traub type methods with fractional derivative

Our starting point is Traub’s multipoint iterative method (see [28]) with order of convergence three:

$$x_{k+1} = \gamma_k - \frac{f(\gamma_k)}{f'(x_k)},$$

where γ_k is a Newton step. When we apply the technique employed in the construction of the CFN₂ and R-LFN₂ methods, we get respective procedures that use fractional derivatives. We call the resulting schemes fractional Traub type methods and denote them by CFT when the Caputo fractional derivative is used and R-LFT when the Riemann–Liouville fractional derivative is employed.

Theorem 5.8. *Let $f : I \subseteq \mathbb{R} \rightarrow \mathbb{R}$ be a continuous function with fractional derivatives of order $k\alpha$, for any positive integer k and $\alpha \in (0, 1]$, in the open interval I holding the zero of $f(x)$, denoted by \bar{x} . Let us suppose $cD_a^\alpha f(x)$ and $D_{a^+}^{k\alpha} f(x)$ are continuous and non-zero at \bar{x} . Additionally, let us consider an initial estimation x_0 , close enough to \bar{x} . Therefore, the local convergence order of CFT*

$$x_{k+1} = \gamma_k - \left(\Gamma(\alpha + 1) \frac{f(\gamma_k)}{cD_a^\alpha f(x_k)} \right)^{1/\alpha}, \quad k = 0, 1, 2, \dots, \tag{5.18}$$

with

$$y_k = x_k - \left(\Gamma(\alpha + 1) \frac{f(x_k)}{cD_a^\alpha f(x_k)} \right)^{1/\alpha}, \quad k = 0, 1, 2, \dots,$$

for $\alpha^2 + 2\alpha + 1 < 3\alpha + 1$, and that of R-LFT

$$x_{k+1} = y_k - \left(\Gamma(\alpha + 1) \frac{f(y_k)}{D_{a^+}^{\alpha k} f(x_k)} \right)^{1/\alpha}, \quad k = 0, 1, 2, \dots, \quad (5.19)$$

with

$$y_k = x_k - \left(\Gamma(\alpha + 1) \frac{f(x_k)}{D_{a^+}^{\alpha k} f(x_k)} \right)^{1/\alpha}, \quad k = 0, 1, 2, \dots,$$

are at least $2\alpha + 1$, and the error equation is

$$e_{k+1} = -\frac{\Gamma(2\alpha + 1)}{\alpha^2 \Gamma^2(\alpha + 1)} AC_2^2 e_k^{2\alpha+1} + O\left(e_k^{\alpha^2+2\alpha+1}\right),$$

where

$$A = \frac{\Gamma^2(\alpha + 1) - \Gamma(2\alpha + 1)}{\Gamma^2(\alpha + 1)},$$

in both cases.

Proof. Let us remark that the first step y_k of scheme CFT is CFN₂. As its order of convergence has already been proven, we omit the calculations and give the error equation with terms enough to be used in this proof:

$$\begin{aligned} y_k - \bar{x} &= -\frac{1}{\alpha} AC_2 e_k^{\alpha+1} + \frac{1}{\alpha} \left[\left(\frac{\Gamma(2\alpha + 1)}{\Gamma^2(\alpha + 1)} + \frac{\alpha - 1}{2\alpha} A \right) AC_2^2 - BC_3 \right] e_k^{2\alpha+1} \\ &\quad + O\left(e_k^{3\alpha+1}\right), \end{aligned}$$

where A has been already defined and

$$B = \frac{\Gamma(\alpha + 1)\Gamma(2\alpha + 1) - \Gamma(3\alpha + 1)}{\Gamma(\alpha + 1)\Gamma(2\alpha + 1)}.$$

We firstly develop $f(y_k)$:

$$f(y_k) = \frac{cD_{\bar{x}}^\alpha f(\bar{x})}{\Gamma(\alpha + 1)} \left[(y_k - \bar{x})^\alpha + C_2 (y_k - \bar{x})^{2\alpha} \right] + O\left(e_k^{3\alpha+1}\right).$$

Now, in order to obtain the expansion of powers such as $(\gamma_k - \bar{x})^\alpha$, we use Newton's generalized binomial theorem,

$$\begin{aligned} & (\gamma_k - \bar{x})^\alpha \\ &= \left(-\frac{1}{\alpha}\right)^\alpha A^\alpha C_2^\alpha e_k^{\alpha^2+\alpha} \\ &+ \left(-\frac{1}{\alpha}\right)^{\alpha-1} A^{\alpha-1} C_2^{\alpha-1} \left[\left(\frac{\Gamma(2\alpha+1)}{\Gamma^2(\alpha+1)} + \frac{\alpha-1}{2\alpha} A\right) AC_2^2 - BC_3 \right] e_k^{\alpha^2+2\alpha} \\ &+ \frac{\alpha^2-\alpha}{2} \left(-\frac{1}{\alpha}\right)^\alpha A^{\alpha-2} C_2^{\alpha-2} \\ &\times \left[\left(\frac{\Gamma(2\alpha+1)}{\Gamma^2(\alpha+1)} + \frac{\alpha-1}{2\alpha} A\right) AC_2^2 - BC_3 \right]^2 e_k^{\alpha^2+3\alpha} + O(e_k^{3\alpha+1}) \end{aligned}$$

and

$$(\gamma_k - \bar{x})^{2\alpha} = \left(-\frac{1}{\alpha}\right)^{2\alpha} A^{2\alpha} C_2^{2\alpha} e_k^{2\alpha^2+2\alpha} + O(e_k^{3\alpha+1}).$$

Also, let us note that $\alpha^2 + 3\alpha < 3\alpha + 1$ for all $\alpha \in (0, 1]$ and also $2\alpha^2 + 2\alpha < 3\alpha + 1$ but $\alpha^2 + 4\alpha > 3\alpha + 1$ and $2\alpha^2 + 3\alpha > 3\alpha + 1$.

Then,

$$\begin{aligned} f(\gamma_k) &= \frac{cD_{\bar{x}}^\alpha f(\bar{x})}{\Gamma(\alpha+1)} \left[\left(-\frac{1}{\alpha}\right)^\alpha A^\alpha C_2^\alpha e_k^{\alpha^2+\alpha} + \left(-\frac{1}{\alpha}\right)^{\alpha-1} D e_k^{\alpha^2+2\alpha} \right. \\ &+ \left. \left(-\frac{1}{\alpha}\right)^{2\alpha} A^{2\alpha} C_2^{2\alpha+1} e_k^{2\alpha^2+2\alpha} + \frac{\alpha-1}{2} \left(-\frac{1}{\alpha}\right)^{\alpha-2} E e_k^{\alpha^2+3\alpha} \right] \\ &+ O(e_k^{3\alpha+1}), \end{aligned}$$

where

$$D = \left(\frac{\Gamma(2\alpha+1)}{\Gamma^2(\alpha+1)} + \frac{\alpha-1}{2\alpha} A\right) A^\alpha C_2^{\alpha+1} - A^{\alpha-1} BC_3 C_2^{\alpha-1}$$

and

$$\begin{aligned} E &= \frac{1}{\alpha} \left(\frac{\Gamma(2\alpha+1)}{\Gamma^2(\alpha+1)} + \frac{\alpha-1}{2\alpha} A\right)^2 A^\alpha C_2^{\alpha+2} + \frac{1}{\alpha} A^{\alpha-2} B^2 C_2^{\alpha-2} C_3^2 \\ &- \frac{2}{\alpha} \left(\frac{\Gamma(2\alpha+1)}{\Gamma^2(\alpha+1)} + \frac{\alpha-1}{2\alpha} A\right) A^{\alpha-1} BC_2^\alpha C_3. \end{aligned}$$

Then, the Taylor development of $\frac{f(y_k)}{{}_cD_a^\alpha f(x_k)}$ is

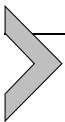
$$\begin{aligned} \frac{f(y_k)}{{}_cD_a^\alpha f(x_k)} &= \frac{1}{\Gamma(\alpha+1)} \left[\left(\frac{-1}{\alpha}\right)^\alpha A^\alpha C_2^\alpha e_k^{\alpha^2+\alpha} \right. \\ &\quad + \left(\frac{-1}{\alpha}\right)^{\alpha-1} \left(D + \frac{\Gamma(2\alpha+1)}{\Gamma(\alpha+1)} \frac{1}{\alpha} A^\alpha C_2^{\alpha+1}\right) e_k^{\alpha^2+2\alpha} \\ &\quad + \left(\frac{-1}{\alpha}\right)^{2\alpha} A^{2\alpha} C_2^{2\alpha+1} e_k^{2\alpha^2+2\alpha} \\ &\quad + \left(\frac{-1}{\alpha}\right)^{\alpha-2} \left(\frac{\alpha-1}{2} E - \frac{\Gamma(3\alpha+1)}{\Gamma(\alpha+1)\Gamma(2\alpha+1)} \frac{1}{\alpha^2} A^\alpha C_2^\alpha C_3 \right. \\ &\quad \left. + \frac{1}{\alpha} \frac{\Gamma(2\alpha+1)}{\Gamma^2(\alpha+1)} DC_2 + \frac{\Gamma^2(2\alpha+1)}{\Gamma^4(\alpha+1)} \frac{1}{\alpha^2} A^\alpha C_2^{\alpha+2}\right) e_k^{\alpha^2+3\alpha} \left. \right] \\ &\quad + O(e_k^{3\alpha+1}). \end{aligned}$$

Moreover, by using again the generalized binomial theorem,

$$\begin{aligned} &\left(\Gamma(\alpha+1) \frac{f(y_k)}{{}_cD_a^\alpha f(x_k)}\right)^{1/\alpha} \\ &= \left(\frac{-1}{\alpha}\right) \left[AC_2 e_k^{\alpha+1} + \left(-\frac{\Gamma(2\alpha+1)}{\Gamma(\alpha+1)} \left(1 + \frac{1}{\alpha}\right) AC_2^2 \right. \right. \\ &\quad \left. \left. - \frac{\alpha-1}{2\alpha} A^2 C_2^2 + BC_3\right) e_k^{2\alpha+1} \right. \\ &\quad \left. - \left(\frac{-1}{\alpha}\right)^{\alpha+1} A^{\alpha+1} C_2^{\alpha+2} e_k^{\alpha^2+2\alpha+1} \right] + O(e_k^{3\alpha+1}). \end{aligned}$$

Finally, after some algebraic manipulations, the resulting error equation is

$$e_{k+1} = -\frac{\Gamma(2\alpha+1)}{\alpha^2 \Gamma^2(\alpha+1)} AC_2^2 e_k^{2\alpha+1} + O(e_k^{\alpha^2+2\alpha+1}). \quad \square$$



5.4. Numerical analysis of the proposed methods

To get the results shown in this section, we have used MATLAB[®] R2018b with double precision arithmetics, $|x_{k+1} - x_k| < 10^{-8}$ or $|f(x_{k+1})| < 10^{-8}$ as stopping criteria, and a maximum of 500 iterations. For the calculation of the Gamma function, $\Gamma(x)$, we have used the program made in [14]. For the Mittag-Leffler function, $E_{\alpha,\beta}(x)$, we use the program provided by

Table 5.1 Fractional Caputo Newton type results for $f_1(x)$ and initial estimation $x_0 = -1.5$.

α	CFN ₁ method				CFN ₂ method			
	\bar{x}	$ x_{k+1} - x_k $	$ f(x_{k+1}) $	iter	\bar{x}	$ x_{k+1} - x_k $	$ f(x_{k+1}) $	iter
0.6	-	0.29821	28.343	500	-	1.7603e-07	0.0035619	500
0.65	-	0.17488	11.329	500	-	4.1154e-08	6.7515e-04	500
0.7	-	0.058499	2.98929	500	\bar{x}_4	9.9926e-09	1.1322e-04	432
0.75	\bar{x}_4	9.6537e-09	4.1645e-07	151	\bar{x}_4	9.8524e-09	4.6756e-05	230
0.8	\bar{x}_4	8.5475e-09	3.0465e-07	50	\bar{x}_4	9.6579e-09	1.8943e-05	124
0.85	\bar{x}_4	9.468e-09	2.606e-07	28	\bar{x}_4	9.9396e-09	7.7541e-06	67
0.9	\bar{x}_4	3.9203e-09	7.3851e-08	19	\bar{x}_4	9.109e-09	2.6706e-06	37
0.95	\bar{x}_4	2.5822e-09	2.4894e-08	13	\bar{x}_4	7.3622e-09	6.4461e-07	20
1	\bar{x}_4	3.0876e-06	8.8694e-10	6	\bar{x}_4	3.0876e-06	8.8694e-10	6

Igor Podlubny in MathWorks. Regarding the precision of these functions, the Gamma function is calculated with 15 digits of accuracy along the real axis and 13 elsewhere in \mathbb{C} ; and *mlf* for computing the Mittag-Leffler function has nine significant digits of precision. Moreover, in all the numerical tests, we used $a = 0$, as in Caputo and as in Riemann–Liouville derivatives.

We are going to test four nonlinear functions in order to make a comparison between the designed methods. It is important to point out that in any case a comparison is being made with the classical methods (when $\alpha = 1$).

Our first test function is $f_1(x) = -12.84x^6 - 25.6x^5 + 16.55x^4 - 2.21x^3 + 26.71x^2 - 4.29x - 15.21$ with roots $\bar{x}_1 = 0.82366 + 0.24769i$, $\bar{x}_2 = 0.82366 - 0.24769i$, $\bar{x}_3 = -2.62297$, $\bar{x}_4 = -0.584$, $\bar{x}_5 = -0.21705 + 0.99911i$, and $\bar{x}_6 = -0.21705 - 0.99911i$.

We can see that Chebyshev type methods (Table 5.2) require fewer iterations to converge than Newton type methods (Table 5.1) with Caputo derivative, for the same value of x_0 and the same values of α . It also can be observed that Newton and Chebyshev type methods require approximately the same values of α to converge.

In Table 5.3, Chebyshev type methods require fewer iterations to converge than the Traub type method with Caputo derivative, for the same value of x_0 and the same values of α , and the Chebyshev type method requires a bit higher values of α to converge.

We also can see that Chebyshev type methods (Table 5.5) require fewer iterations to converge than Newton type methods (Table 5.4) with Riemann–Liouville derivative, for the same value of x_0 and the same values

Table 5.2 Fractional Caputo Chebyshev type results for $f_1(x)$ and initial estimation $x_0 = -1.5$.

α	CFC ₁ method				CFC ₂ method			
	\bar{x}	$ x_{k+1} - x_k $	$ f(x_{k+1}) $	iter	\bar{x}	$ x_{k+1} - x_k $	$ f(x_{k+1}) $	iter
0.6	-	0.57573	70.827	500	-	1.5363	4.0362e+07	500
0.65	-	0.40423	30.825	500	-	0.77071	2.6863e+02	500
0.7	-	0.21083	12.033	500	-	0.41308	43.079	500
0.75	\bar{x}_4	9.3028e-09	4.0131e-07	163	\bar{x}_4	9.3699e-09	4.0421e-07	177
0.8	\bar{x}_4	9.7765e-09	3.4846e-07	51	\bar{x}_4	8.6947e-09	3.099e-07	54
0.85	\bar{x}_4	8.9761e-09	2.4707e-07	28	\bar{x}_4	9.2003e-09	2.5324e-07	29
0.9	\bar{x}_4	6.5715e-09	1.2379e-07	18	\bar{x}_4	3.5407e-09	6.6699e-08	19
0.95	\bar{x}_4	4.5471e-09	4.3837e-08	12	\bar{x}_4	5.6834e-09	5.4792e-08	12
1	\bar{x}_4	3.5714e-04	9.4953e-09	4	\bar{x}_4	3.5713e-04	9.4953e-09	4

Table 5.3 Fractional Caputo CFN₃ and Traub type results for $f_1(x)$ and initial estimation $x_0 = -1.5$.

α	CFN ₃ method				CFT method			
	\bar{x}	$ x_{k+1} - x_k $	$ f(x_{k+1}) $	iter	\bar{x}	$ x_{k+1} - x_k $	$ f(x_{k+1}) $	iter
0.6	-	0.44235	48.853	500	-	6.2898e-08	0.0012681	500
0.65	-	0.29878	21.468	500	-	1.1562e-08	1.8867e-04	500
0.7	-	0.13201	7.1676	500	\bar{x}_4	9.9588e-09	6.9453e-05	268
0.75	\bar{x}_4	9.8478e-09	4.2482e-07	158	\bar{x}_4	9.9889e-09	2.7995e-05	138
0.8	\bar{x}_4	8.7967e-09	3.1353e-07	51	\bar{x}_4	9.5606e-09	1.0693e-05	73
0.85	\bar{x}_4	9.0876e-09	2.5014e-07	28	\bar{x}_4	9.4657e-09	4.0225e-06	39
0.9	\bar{x}_4	6.9558e-09	1.3103e-07	18	\bar{x}_4	6.8084e-09	1.0286e-06	22
0.95	\bar{x}_4	4.8585e-09	4.6839e-08	12	\bar{x}_4	5.2078e-09	1.8928e-07	12
1	\bar{x}_4	3.5714e-04	9.49523e-09	4	\bar{x}_4	2.2023e-10	5.329e-15	5

Table 5.4 Fractional Riemann–Liouville Newton type results for $f_1(x)$ and initial estimation $x_0 = -1.5$.

α	R-LFN ₁ method				R-LFN ₂ method			
	\bar{x}	$ x_{k+1} - x_k $	$ f(x_{k+1}) $	iter	\bar{x}	$ x_{k+1} - x_k $	$ f(x_{k+1}) $	iter
0.6	-	0.31207	24.999	500	-	8.2311e-08	0.001664	500
0.65	-	0.21206	12.298	500	-	2.0291e-08	3.3261e-04	500
0.7	-	0.11720	5.6486	500	\bar{x}_4	9.9746e-09	9.2638e-05	354
0.75	-	0.017984	0.76427	500	\bar{x}_4	9.9858e-09	4.0402e-05	196
0.8	\bar{x}_4	9.8676e-09	3.5368e-07	72	\bar{x}_4	9.6983e-09	1.6881e-05	110
0.85	\bar{x}_4	8.8611e-09	2.4785e-07	32	\bar{x}_4	9.4322e-09	6.8049e-06	62
0.9	\bar{x}_4	4.1273e-09	7.9749e-08	20	\bar{x}_4	8.923e-09	2.4689e-06	35
0.95	\bar{x}_4	3.9835e-09	3.9713e-08	13	\bar{x}_4	9.0322e-09	7.4692e-07	19
1	\bar{x}_4	3.0876e-06	8.8694e-10	6	\bar{x}_4	3.0876e-06	8.8694e-10	6

Table 5.5 Fractional Riemann–Liouville Chebyshev type results for $f_1(x)$ and initial estimation $x_0 = -1.5$.

α	R-LFC ₁ method				R-LFC ₂ method			
	\bar{x}	$ x_{k+1} - x_k $	$ f(x_{k+1}) $	iter	\bar{x}	$ x_{k+1} - x_k $	$ f(x_{k+1}) $	iter
0.6	-	0.57333	54.51	500	-	1.5363	4.0365e+07	500
0.65	-	0.44214	28.188	500	-	0.77657	2.634e+02	500
0.7	-	0.30834	16.006	500	-	0.44709	42.958	500
0.75	-	0.10957	4.8923	500	-	0.19566	10.827	500
0.8	\bar{x}_4	9.8873e-09	3.5439e-07	76	\bar{x}_4	8.0733e-09	2.8937e-07	80
0.85	\bar{x}_4	5.7531e-09	1.60921e-07	33	\bar{x}_4	6.2439e-09	1.7465e-07	34
0.9	\bar{x}_4	7.00145e-09	1.3528e-07	19	\bar{x}_4	4.0498e-09	7.8251e-08	20
0.95	\bar{x}_4	7.2146e-09	7.1926e-08	12	\bar{x}_4	9.0182e-09	8.9907e-08	12
1	\bar{x}_4	3.5714e-04	9.4953e-09	4	\bar{x}_4	3.5714e-04	9.4953e-09	4

Table 5.6 Fractional Riemann–Liouville R-LFC₃ and Traub type results for $f_1(x)$ and initial estimation $x_0 = -1.5$.

α	R-LFC ₃ method				R-LFT method			
	\bar{x}	$ x_{k+1} - x_k $	$ f(x_{k+1}) $	iter	\bar{x}	$ x_{k+1} - x_k $	$ f(x_{k+1}) $	iter
0.6	-	0.45032	39.9	500	-	2.9398e-08	5.9231e-04	500
0.65	-	0.34255	21.246	500	\bar{x}_4	9.9696e-09	1.3359e-04	411
0.7	-	0.22795	11.603	500	\bar{x}_4	9.9316e-09	5.6773e-05	220
0.75	-	0.056339	2.4535	500	\bar{x}_4	9.7458e-09	2.35e-05	119
0.8	\bar{x}_4	9.9718e-09	3.5742e-07	75	\bar{x}_4	9.5628e-09	9.4891e-06	65
0.85	\bar{x}_4	5.7739e-09	1.615e-07	33	\bar{x}_4	9.3134e-09	3.6307e-06	36
0.9	\bar{x}_4	7.4112e-09	1.432e-07	19	\bar{x}_4	9.6151e-09	1.3022e-06	20
0.95	\bar{x}_4	7.725e-09	7.7015e-08	12	\bar{x}_4	3.6166e-09	1.3015e-07	12
1	\bar{x}_4	3.5714e-04	9.4953e-09	4	\bar{x}_4	2.2023e-10	5.329e-15	5

of α . Also, the Chebyshev type method requires a bit higher values of α to converge.

In Table 5.6, Chebyshev type methods require fewer iterations to converge than the Traub type method with Riemann–Liouville derivative, for the same value of x_0 and the same values of α , and Chebyshev type methods require higher values of α to converge.

We can also note that, in general, methods with Caputo derivative (Tables 5.1–5.3) require fewer iterations and lower values of α to converge than methods with Riemann–Liouville derivative (Tables 5.4–5.6).

Our second test function is $f_2(x) = ix^{1.8} - x^{0.9} - 16$ with roots $\bar{x}_1 = 2.90807 - 4.24908i$ and $\bar{x}_2 = -3.85126 + 1.74602i$.

We can see that Chebyshev type methods (Table 5.8) require fewer iterations to converge than Newton type methods (Table 5.7) with Caputo derivative, for the same value of x_0 and the same values of α . It also can

Table 5.7 Fractional Caputo Newton type results for $f_2(x)$ and initial estimation $x_0 = -4.5$.

α	CFN ₁ method				CFN ₂ method			
	\bar{x}	$ x_{k+1} - x_k $	$ f(x_{k+1}) $	iter	\bar{x}	$ x_{k+1} - x_k $	$ f(x_{k+1}) $	iter
0.6	\bar{x}_2	9.6447e-09	9.1533e-08	135	-	1.9397e-06	0.0040584	500
0.65	\bar{x}_2	8.7093e-09	7.1238e-08	83	-	4.5637e-07	7.7439e-04	500
0.7	\bar{x}_2	8.0195e-09	5.5214e-08	57	-	7.0051e-08	9.4467e-05	500
0.75	\bar{x}_2	7.7567e-09	4.3576e-08	41	\bar{x}_2	9.934e-09	8.9604e-06	430
0.8	\bar{x}_2	9.2798e-09	4.0719e-08	30	\bar{x}_2	9.9356e-09	3.2931e-06	207
0.85	\bar{x}_2	5.0655e-09	1.623e-08	23	\bar{x}_2	9.9551e-09	1.1831e-06	100
0.9	\bar{x}_2	4.2584e-09	8.8324e-09	17	\bar{x}_2	9.5415e-09	3.8313e-07	49
0.95	\bar{x}_2	2.6355e-09	2.6468e-09	12	\bar{x}_2	7.6885e-09	8.4483e-08	23
1	\bar{x}_2	5.3275e-06	1.5148e-11	4	\bar{x}_2	5.3275e-06	1.5148e-11	4

Table 5.8 Fractional Caputo Chebyshev type results for $f_2(x)$ and initial estimation $x_0 = -4.5$.

α	CFC ₁ method				CFC ₂ method			
	\bar{x}	$ x_{k+1} - x_k $	$ f(x_{k+1}) $	iter	\bar{x}	$ x_{k+1} - x_k $	$ f(x_{k+1}) $	iter
0.6	\bar{x}_2	9.6784e-09	9.1853e-08	136	-	0.99265	13.691	500
0.65	\bar{x}_2	8.0926e-09	6.6193e-08	83	\bar{x}_2	8.2737e-09	6.7675e-08	83
0.7	\bar{x}_2	8.9322e-09	6.1497e-08	56	\bar{x}_2	9.8633e-09	6.7909e-08	56
0.75	\bar{x}_2	9.8284e-09	5.5214e-08	40	\bar{x}_2	6.4268e-09	3.6104e-08	41
0.8	\bar{x}_2	7.1523e-09	3.1384e-08	30	\bar{x}_2	7.2881e-09	3.198e-08	30
0.85	\bar{x}_2	9.2029e-09	2.9488e-08	22	\bar{x}_2	9.5021e-09	3.0446e-08	22
0.9	\bar{x}_2	2.8734e-09	5.9598e-09	17	\bar{x}_2	3.0885e-09	6.4058e-09	17
0.95	\bar{x}_2	9.6575e-09	9.6987e-09	11	\bar{x}_2	1.6068e-09	1.6137e-09	12
1	\bar{x}_2	1.5968e-05	1.7764e-15	3	\bar{x}_2	1.5968e-05	1.7764e-15	3

be observed that Chebyshev type methods require lower values of α than Newton type methods to converge.

In Table 5.9, Chebyshev type methods require fewer iterations to converge than the Traub type method with Caputo derivative, for the same value of x_0 and the same values of α , and Chebyshev type methods require lower values of α to converge.

We also can see that Chebyshev type methods (Table 5.11) require fewer iterations to converge than Newton type methods (Table 5.10) with Riemann–Liouville derivative, for the same value of x_0 and the same values of α . Also in this case, Chebyshev type methods require lower values of α to converge.

In Table 5.12, Chebyshev type methods require fewer iterations to converge than the Traub type method with Riemann–Liouville derivative, for

Table 5.9 Fractional Caputo CFC₃ and Traub type results for $f_2(x)$ and initial estimation $x_0 = -4.5$.

α	CFC ₃ method				CFT method			
	\bar{x}	$ x_{k+1} - x_k $	$ f(x_{k+1}) $	iter	\bar{x}	$ x_{k+1} - x_k $	$ f(x_{k+1}) $	iter
0.6	\bar{x}_2	8.8419e-09	8.3914e-08	147	-	6.9328e-07	0.0014451	500
0.65	\bar{x}_2	8.8258e-09	7.219e-08	83	-	1.2842e-07	2.1663e-04	500
0.7	\bar{x}_2	9.7327e-09	6.7009e-08	56	-	1.577e-08	2.0497e-05	500
0.75	\bar{x}_2	6.5177e-09	3.6615e-08	41	\bar{x}_1	9.859e-09	5.2033e-06	257
0.8	\bar{x}_2	7.5319e-09	3.3049e-08	30	\bar{x}_2	9.6449e-09	1.8367e-06	120
0.85	\bar{x}_2	9.6136e-09	3.0803e-08	22	\bar{x}_2	9.1797e-09	6.0224e-07	57
0.9	\bar{x}_2	2.9946e-09	6.2112e-09	17	\bar{x}_2	9.1356e-09	1.8638e-07	27
0.95	\bar{x}_2	1.4895e-09	1.4959e-09	12	\bar{x}_2	5.5216e-09	2.6074e-08	13
1	\bar{x}_2	1.5968e-05	1.7764e-15	3	\bar{x}_2	1.1681e-05	3.5527e-15	3

Table 5.10 Fractional Riemann–Liouville Newton type results for $f_2(x)$ and initial estimation $x_0 = -4.5$.

α	R-LFN ₁ method				R-LFN ₂ method			
	\bar{x}	$ x_{k+1} - x_k $	$ f(x_{k+1}) $	iter	\bar{x}	$ x_{k+1} - x_k $	$ f(x_{k+1}) $	iter
0.6	\bar{x}_2	9.8908e-09	7.0198e-08	321	-	7.6079e-07	0.001593	500
0.65	\bar{x}_2	9.5716e-09	6.0692e-08	105	-	1.8874e-07	3.2037e-04	500
0.7	\bar{x}_2	8.3392e-09	4.5994e-08	61	-	2.9902e-08	4.0532e-05	500
0.75	\bar{x}_2	6.5731e-09	3.048e-08	43	\bar{x}_1	9.9785e-09	7.4479e-06	367
0.8	\bar{x}_2	7.592e-09	2.8258e-08	30	\bar{x}_1	9.8775e-09	2.8264e-06	192
0.85	\bar{x}_2	8.3034e-09	2.3137e-08	22	\bar{x}_2	9.4686e-09	1.0137e-06	93
0.9	\bar{x}_2	9.4241e-09	1.7387e-08	16	\bar{x}_2	9.9072e-09	3.6628e-07	45
0.95	\bar{x}_2	1.649e-09	1.5036e-09	12	\bar{x}_2	7.7314e-09	8.0728e-08	22
1	\bar{x}_2	5.3275e-06	1.5148e-11	4	\bar{x}_2	5.3275e-06	1.5148e-11	4

the same value of x_0 and the same values of α , and Chebyshev type methods require lower values of α to converge.

We note that, in general, methods with Caputo derivative (Tables 5.7–5.9) require lower numbers of iterations and a bit higher values of α to converge than methods with Riemann–Liouville derivative (Tables 5.10–5.12).

Our third test function is $f_3(x) = e^x - 1$ with only real root $\bar{x}_1 = 0$. In this case, it is necessary to use a value of α closer to 1 to ensure convergence.

We can see that Newton type methods (Table 5.13) require a bit fewer iterations to converge than Chebyshev type methods (Table 5.14) with Caputo derivative, for the same value of x_0 and the same values of α . We can also observe that Newton type methods require lower values of α to converge.

Table 5.11 Fractional Riemann–Liouville Chebyshev type results for $f_2(x)$ and initial estimation $x_0 = -4.5$.

α	R-LFC ₁ method				R-LFC ₂ method			
	\bar{x}	$ x_{k+1} - x_k $	$ f(x_{k+1}) $	iter	\bar{x}	$ x_{k+1} - x_k $	$ f(x_{k+1}) $	iter
0.6	\bar{x}_2	9.6314e-09	6.8357e-08	335	\bar{x}_2	9.683e-09	6.8723e-08	296
0.65	\bar{x}_2	9.2392e-09	5.8585e-08	109	\bar{x}_2	9.0118e-09	5.7143e-08	107
0.7	\bar{x}_2	9.4967e-09	5.2378e-08	64	\bar{x}_2	9.7264e-09	5.3645e-08	63
0.75	\bar{x}_2	7.50469e-09	3.48e-08	40	\bar{x}_2	8.26e-09	3.8303e-08	43
0.8	\bar{x}_2	8.3924e-09	3.1238e-08	29	\bar{x}_2	6.233e-09	2.32e-08	30
0.85	\bar{x}_2	5.8975e-09	1.6433e-08	22	\bar{x}_2	4.936e-09	1.3754e-08	22
0.9	\bar{x}_2	6.215e-09	1.1466e-08	16	\bar{x}_2	6.298e-09	1.162e-08	16
0.95	\bar{x}_2	6.3727e-09	5.8109e-09	11	\bar{x}_2	7.0039e-09	6.3864e-09	11
1	\bar{x}_2	1.5968e-05	1.7764e-15	3	\bar{x}_2	1.5968e-05	1.7764e-15	3

Table 5.12 Fractional Riemann–Liouville R-LFC₃ and Traub type results for $f_2(x)$ and initial estimation $x_0 = -4.5$.

α	R-LFC ₃ method				R-LFT method			
	\bar{x}	$ x_{k+1} - x_k $	$ f(x_{k+1}) $	iter	\bar{x}	$ x_{k+1} - x_k $	$ f(x_{k+1}) $	iter
0.6	\bar{x}_2	9.8736e-09	7.0076e-08	336	-	2.7288e-07	5.6848e-04	500
0.65	\bar{x}_2	8.5834e-09	5.4427e-08	109	-	5.3251e-08	8.9778e-05	500
0.7	\bar{x}_2	8.7672e-09	4.8355e-08	62	\bar{x}_2	9.9711e-09	1.1573e-05	435
0.75	\bar{x}_2	8.2043e-09	3.8044e-08	41	\bar{x}_2	9.9117e-09	4.3496e-06	215
0.8	\bar{x}_2	8.8048e-09	3.2773e-08	29	\bar{x}_2	9.5765e-09	1.5662e-06	105
0.85	\bar{x}_2	5.8278e-09	1.6239e-08	22	\bar{x}_2	9.7086e-09	5.6297e-07	52
0.9	\bar{x}_2	6.3132e-09	1.1648e-08	16	\bar{x}_2	8.1865e-09	1.5588e-07	25
0.95	\bar{x}_2	6.5338e-09	5.9578e-09	11	\bar{x}_2	8.0857e-09	3.4712e-08	12
1	\bar{x}_2	1.5968e-05	1.7764e-15	3	\bar{x}_2	1.1681e-05	3.5527e-15	3

Table 5.13 Fractional Caputo Newton type results for $f_3(x)$ and initial estimation $x_0 = 0.2$.

α	CFN ₁ method				CFN ₂ method			
	\bar{x}	$ x_{k+1} - x_k $	$ f(x_{k+1}) $	iter	\bar{x}	$ x_{k+1} - x_k $	$ f(x_{k+1}) $	iter
0.9	-	9.2247e-04	4.6835e-04	500	\bar{x}_1	2.5158e-08	2.6106e-09	8
0.91	-	4.1587e-04	2.1047e-04	500	\bar{x}_1	1.351e-08	1.2569e-09	8
0.92	-	1.5472e-04	7.8089e-05	500	\bar{x}_1	8.8464e-08	7.2879e-09	7
0.93	-	4.374e-05	2.2023e-05	500	\bar{x}_1	4.5591e-08	3.2741e-09	7
0.94	-	8.1878e-06	4.1145e-06	500	\bar{x}_1	2.1227e-08	1.3017e-09	7
0.95	-	7.9228e-07	3.975e-07	500	\bar{x}_1	1.7783e-07	9.0542e-09	6
0.96	-	2.4154e-08	1.2102e-08	500	\bar{x}_1	7.3682e-08	2.9901e-09	6
0.97	\bar{x}_1	2.1421e-08	8.6918e-09	17	\bar{x}_1	2.3997e-08	7.2773e-10	6
0.98	\bar{x}_1	2.2259e-08	6.4645e-09	11	\bar{x}_1	2.5831e-07	5.2033e-09	5
0.99	\bar{x}_1	6.6485e-08	9.7837e-09	7	\bar{x}_1	4.0319e-08	4.0463e-10	5
1	\bar{x}_1	1.5194e-08	0	4	\bar{x}_1	1.5194e-08	0	4

Table 5.14 Fractional Caputo Chebyshev type results for $f_3(x)$ and initial estimation $x_0 = 0.2$.

α	CFC ₁ method				CFC ₂ method			
	\bar{x}	$ x_{k+1} - x_k $	$ f(x_{k+1}) $	iter	\bar{x}	$ x_{k+1} - x_k $	$ f(x_{k+1}) $	iter
0.9	-	0.002361	0.0011986	500	-	0.0022881	0.001165	500
0.91	-	0.0010717	5.4235e-04	500	-	0.0010399	5.2739e-04	500
0.92	-	4.0137e-04	2.0257e-04	500	-	3.9006e-04	1.9715e-04	500
0.93	-	1.1420e-04	5.7503e-05	500	-	1.1119e-04	5.6043e-05	500
0.94	-	2.1513e-05	1.0811e-05	500	-	2.0995e-05	1.056e-05	500
0.95	-	2.0945e-06	1.0509e-06	500	-	2.0497e-06	1.0287e-06	500
0.96	-	6.4237e-08	3.2188e-08	500	-	6.3067e-08	3.1606e-08	500
0.97	\bar{x}_1	2.2373e-08	9.4323e-09	19	\bar{x}_1	1.7769e-08	7.521e-09	19
0.98	\bar{x}_1	2.9223e-08	8.7347e-09	11	\bar{x}_1	2.1022e-08	6.2973e-09	11
0.99	\bar{x}_1	2.3787e-08	3.8697e-09	7	\bar{x}_1	5.1375e-08	7.9327e-09	6
1	\bar{x}_1	0.0023015	4.0565e-09	2	\bar{x}_1	0.0023015	4.0565e-09	2

Table 5.15 Fractional Caputo CFC₃ and Traub type results for $f_3(x)$ and initial estimation $x_0 = 0.2$.

α	CFC ₃ method				CFT method			
	\bar{x}	$ x_{k+1} - x_k $	$ f(x_{k+1}) $	iter	\bar{x}	$ x_{k+1} - x_k $	$ f(x_{k+1}) $	iter
0.9	-	0.0021509	0.001092	500	\bar{x}_1	3.1633e-07	9.2854e-09	5
0.91	-	9.8481e-04	4.9839e-04	500	\bar{x}_1	1.7542e-07	4.3293e-09	5
0.92	-	3.7211e-04	1.878e-04	500	\bar{x}_1	9.0552e-08	1.8388e-09	5
0.93	-	1.0683e-04	5.3792e-05	500	\bar{x}_1	4.2699e-08	6.9418e-10	5
0.94	-	2.0309e-05	1.0206e-05	500	\bar{x}_1	1.79e-08	2.2469e-10	5
0.95	-	1.9957e-06	1.0013e-06	500	\bar{x}_1	7.0013e-07	6.4561e-09	4
0.96	-	6.1784e-08	3.0958e-08	500	\bar{x}_1	2.9042e-07	1.8294e-09	4
0.97	\bar{x}_1	2.1482e-08	9.0607e-09	19	\bar{x}_1	9.4541e-08	3.6228e-10	4
0.98	\bar{x}_1	2.7664e-08	8.2823e-09	11	\bar{x}_1	1.9964e-08	3.7599e-11	4
0.99	\bar{x}_1	1.9499e-08	3.203e-09	7	\bar{x}_1	2.7685e-06	1.5139e-09	3
1	\bar{x}_1	0.0023015	4.0565e-09	2	\bar{x}_1	1.7116e-08	0	3

In Table 5.15, the Traub type method requires fewer iterations to converge than Chebyshev type methods with Caputo derivative, for the same value of x_0 and the same values of α , and also requires lower values of α to converge.

We can see that Chebyshev type methods (Table 5.17) require fewer iterations to converge than Newton type methods (Table 5.16) with Riemann–Liouville derivative, for the same value of x_0 and the same values of α . In this case, Chebyshev type methods require the same values of α as Newton type methods to converge.

In Table 5.18, Chebyshev type methods require fewer iterations to converge than the Traub type method with Riemann–Liouville derivative, for

Table 5.16 Fractional Riemann–Liouville Newton type results for $f_3(x)$ and initial estimation $x_0 = 0.2$.

α	R-LFN ₁ method				R-LFN ₂ method			
	\bar{x}	$ x_{k+1} - x_k $	$ f(x_{k+1}) $	iter	\bar{x}	$ x_{k+1} - x_k $	$ f(x_{k+1}) $	iter
0.9	-	2.3837e-07	1.0176e-04	500	-	6.7672e-07	3.7289e-04	500
0.91	-	2.2269e-07	9.7116e-05	500	-	5.7799e-07	3.1534e-04	500
0.92	-	2.0596e-07	9.1637e-05	500	-	4.8744e-07	2.6335e-04	500
0.93	-	1.8797e-07	8.5216e-05	500	-	4.0451e-07	2.1646e-04	500
0.94	-	1.6846e-07	7.7728e-05	500	-	3.2865e-07	1.7423e-04	500
0.95	-	1.4717e-07	6.9027e-05	500	-	2.5931e-07	1.3628e-04	500
0.96	-	1.2373e-07	5.8939e-05	500	-	1.9576e-07	1.0215e-04	500
0.97	-	9.768e-08	4.7242e-05	500	-	1.33e-07	7.036e-05	500
0.98	-	6.3507e-08	3.2418e-05	500	-	9.0754e-08	4.5746e-05	500
0.99	-	3.7563e-08	1.8423e-05	500	-	4.2567e-08	2.1369e-05	500
1	\bar{x}_1	1.5194e-08	0	4	\bar{x}_1	1.5194e-08	0	4

Table 5.17 Fractional Riemann–Liouville Chebyshev type results for $f_3(x)$ and initial estimation $x_0 = 0.2$.

α	R-LFC ₁ method				R-LFC ₂ method			
	\bar{x}	$ x_{k+1} - x_k $	$ f(x_{k+1}) $	iter	\bar{x}	$ x_{k+1} - x_k $	$ f(x_{k+1}) $	iter
0.9	-	2.4356e-07	1.0297e-04	500	-	2.4201e-07	1.0263e-04	500
0.91	-	2.2756e-07	9.8266e-05	500	-	2.2612e-07	9.7948e-05	500
0.92	-	2.1051e-07	9.2731e-05	500	-	2.0915e-07	9.2421e-05	500
0.93	-	1.922e-07	8.625e-05	500	-	1.9089e-07	8.5944e-05	500
0.94	-	1.7236e-07	7.8693e-05	500	-	1.711e-07	7.8392e-05	500
0.95	-	1.507e-07	6.9915e-05	500	-	1.4951e-07	6.9623e-05	500
0.96	-	1.269e-07	5.9744e-05	500	-	1.258e-07	5.9469e-05	500
0.97	-	1.0054e-07	4.7974e-05	500	-	9.9576e-08	4.7729e-05	500
0.98	-	7.1115e-08	3.4351e-05	500	-	7.0357e-08	3.4155e-05	500
0.99	-	3.7955e-08	1.8537e-05	500	-	3.7501e-08	1.8417e-05	500
1	\bar{x}_1	0.0023015	4.0565e-09	2	\bar{x}_1	0.0023015	4.0565e-09	2

the same value of x_0 and the same values of α , and the same values of α to converge.

We also note that, in general, methods with Caputo derivative (Tables 5.13–5.15) require lower values of α to converge than methods with Riemann–Liouville derivative (Tables 5.16–5.18). In this case, iterations are not compared because methods with Riemann–Liouville derivative only converge for classical ones.

Our last test function is $f_4(x) = \sin(10x) - 0.5x + 0.2$ with real roots $\bar{x}_1 = -1.4523$, $\bar{x}_2 = -1.3647$, $\bar{x}_3 = -0.87345$, $\bar{x}_4 = -0.6857$, $\bar{x}_5 = -0.27949$, $\bar{x}_6 = -0.021219$, $\bar{x}_7 = 0.31824$, $\bar{x}_8 = 0.64036$, $\bar{x}_9 = 0.91636$, $\bar{x}_{10} = 1.3035$, $\bar{x}_{11} = 1.5118$, $\bar{x}_{12} = 1.9756$, and $\bar{x}_{13} = 2.0977$.

Table 5.18 Fractional Riemann–Liouville R-LFC₃ and Traub type results for $f_3(x)$ and initial estimation $x_0 = 0.2$.

α	R-LFC ₃ method				R-LFT method			
	\bar{x}	$ x_{k+1} - x_k $	$ f(x_{k+1}) $	iter	\bar{x}	$ x_{k+1} - x_k $	$ f(x_{k+1}) $	iter
0.9	-	2.4304e-07	1.0285e-04	500	-	3.6114e-07	1.993e-04	500
0.91	-	2.2711e-07	9.8161e-05	500	-	3.0667e-07	1.6748e-04	500
0.92	-	2.1014e-07	9.2642e-05	500	-	2.5688e-07	1.3892e-04	500
0.93	-	1.9189e-07	8.6175e-05	500	-	2.1135e-07	1.133e-04	500
0.94	-	1.7211e-07	7.8633e-05	500	-	1.6986e-07	9.0407e-05	500
0.95	-	1.5052e-07	6.9869e-05	500	-	1.3232e-07	7.0024e-05	500
0.96	-	1.2677e-07	5.9712e-05	500	-	9.8323e-08	5.1901e-05	500
0.97	-	1.0046e-07	4.7954e-05	500	-	6.319e-08	3.466e-05	500
0.98	-	7.1075e-08	3.4341e-05	500	-	4.8178e-08	2.3718e-05	500
0.99	-	3.7943e-08	1.8534e-05	500	-	2.2946e-08	1.1127e-05	500
1	\bar{x}_1	0.0023015	4.0565e-09	2	\bar{x}_1	1.7116e-08	0	3

Table 5.19 Fractional Caputo Newton type results for $f_4(x)$ and initial estimation $x_0 = 3$.

α	CFN ₁ method				CFN ₂ method			
	\bar{x}	$ x_{k+1} - x_k $	$ f(x_{k+1}) $	iter	\bar{x}	$ x_{k+1} - x_k $	$ f(x_{k+1}) $	iter
0.6	\bar{x}_{12}	8.408e-09	1.8613e-08	36	-	1.4339e-07	2.6898e-04	500
0.65	\bar{x}_{12}	9.1296e-09	1.6527e-08	24	\bar{x}_{13}	9.8912e-09	5.2792e-06	169
0.7	\bar{x}_{10}	8.4237e-09	3.0203e-08	63	\bar{x}_{13}	9.9073e-09	3.0502e-06	121
0.75	\bar{x}_{12}	4.0708e-09	4.2781e-09	10	\bar{x}_{12}	9.868e-09	4.5063e-06	235
0.8	\bar{x}_{10}	9.976e-09	2.3499e-08	22	\bar{x}_{11}	9.5351e-09	1.7694e-06	76
0.85	\bar{x}_{10}	4.7561e-09	8.2545e-09	18	\bar{x}_9	9.1437e-09	9.5832e-07	51
0.9	\bar{x}_4	4.3677e-09	1.0885e-08	18	\bar{x}_2	9.5876e-09	2.2755e-07	42
0.95	-	0.1703	0.83083	500	\bar{x}_{15}	9.9619e-09	1.3042e-06	81
1	-	0.22037	2.0846	500	-	0.22037	2.0846	500

In some cases, the methods can converge to the root $\bar{x}_{14} = 22.146 + 0.30774i$ or $\bar{x}_{15} = 20.89 + 0.30176i$ or $\bar{x}_{16} = 2.6655 + 0.051224i$, which may be far from the initial estimation used.

We can see that Chebyshev type methods (Table 5.20) do not work for this function with Caputo derivative, while Newton type methods (Table 5.19) work even for lower values of α .

In Table 5.21, we can observe the same behavior of the Chebyshev type method compared with the Traub type method.

The same behavior seen in Tables 5.19–5.21 is observed in Tables 5.22–5.24, respectively.

We note that the number of iterations is not necessarily reduced when α increases, and also that the methods converge to different roots. Let us also remark that in Tables 5.19, 5.21, 5.22, and 5.24, the classical Newton

Table 5.20 Fractional Caputo Chebyshev type results for $f_4(x)$ and initial estimation $x_0 = 3$.

α	CFC ₁ method				CFC ₂ method			
	\bar{x}	$ x_{k+1} - x_k $	$ f(x_{k+1}) $	iter	\bar{x}	$ x_{k+1} - x_k $	$ f(x_{k+1}) $	iter
0.6	-	-	-	-	-	-	-	-
0.65	-	-	-	-	-	-	-	-
0.7	-	-	-	-	-	-	-	-
0.75	\bar{x}_2	9.3632e-09	2.9659e-08	67	-	-	-	-
0.8	-	-	-	-	-	-	-	-
0.85	-	-	-	-	-	-	-	-
0.9	-	-	-	-	-	-	-	-
0.95	-	-	-	-	-	-	-	-
1	-	-	-	-	-	-	-	-

Table 5.21 Fractional Caputo CFC₃ and Traub type results for $f_4(x)$ and initial estimation $x_0 = 3$.

α	CFC ₃ method				CFT method			
	\bar{x}	$ x_{k+1} - x_k $	$ f(x_{k+1}) $	iter	\bar{x}	$ x_{k+1} - x_k $	$ f(x_{k+1}) $	iter
0.6	\bar{x}_{12}	8.0613e-09	1.7846e-08	43	-	5.3605e-08	9.8416e-05	500
0.65	-	1.9874e-05	8.3012e-05	500	-	-	-	-
0.7	-	-	-	-	\bar{x}_4	9.9241e-09	7.4684e-06	224
0.75	-	-	-	-	\bar{x}_{12}	9.7623e-09	2.6495e-06	142
0.8	-	-	-	-	\bar{x}_9	9.7441e-09	1.3325e-06	52
0.85	-	-	-	-	\bar{x}_7	8.3509e-09	5.3216e-07	32
0.9	-	-	-	-	\bar{x}_9	8.5295e-09	1.7466e-07	23
0.95	-	-	-	-	-	-	-	-
1	-	-	-	-	-	0.25782	1.8154	500

Table 5.22 Fractional Riemann–Liouville Newton type results for $f_4(x)$ and initial estimation $x_0 = 3$.

α	R-LFN ₁ method				R-LFN ₂ method			
	\bar{x}	$ x_{k+1} - x_k $	$ f(x_{k+1}) $	iter	\bar{x}	$ x_{k+1} - x_k $	$ f(x_{k+1}) $	iter
0.6	\bar{x}_{12}	7.7242e-09	1.6581e-08	33	-	1.4235e-07	2.7305e-04	500
0.65	\bar{x}_{12}	7.3338e-09	1.2864e-08	23	\bar{x}_{13}	9.8532e-09	4.9292e-06	158
0.7	-	0.18129	6.9714e+07	500	\bar{x}_{13}	9.9595e-09	2.9517e-06	116
0.75	\bar{x}_{12}	3.7455e-09	3.8012e-09	12	\bar{x}_{12}	9.8631e-09	4.5403e-06	238
0.8	-	0.030964	0.15115	500	\bar{x}_{11}	9.9545e-09	1.817e-06	77
0.85	\bar{x}_{11}	6.0787e-09	1.913e-08	32	\bar{x}_9	9.2941e-09	9.6601e-07	51
0.9	\bar{x}_4	4.9751e-09	1.243e-08	15	\bar{x}_2	9.0915e-09	2.162e-07	42
0.95	-	0.28537	2.397	500	\bar{x}_{14}	6.5531e-09	9.4542e-07	51
1	-	0.22037	2.0846	500	-	0.22037	2.0846	500

Table 5.23 Fractional Riemann–Liouville Chebyshev type results for $f_4(x)$ and initial estimation $x_0 = 3$.

α	R-LFC ₁ method				R-LFC ₂ method			
	\bar{x}	$ x_{k+1} - x_k $	$ f(x_{k+1}) $	iter	\bar{x}	$ x_{k+1} - x_k $	$ f(x_{k+1}) $	iter
0.6	-	-	-	-	-	-	-	-
0.65	-	0.31169	37.257	500	-	-	-	-
0.7	\bar{x}_2	9.8807e-09	3.6e-08	476	-	-	-	-
0.75	-	-	-	-	-	-	-	-
0.8	-	-	-	-	-	-	-	-
0.85	-	-	-	-	-	-	-	-
0.9	-	-	-	-	-	-	-	-
0.95	-	-	-	-	-	-	-	-
1	-	-	-	-	-	-	-	-

Table 5.24 Fractional Riemann–Liouville R-LFC₃ and Traub type results for $f_4(x)$ and initial estimation $x_0 = 3$.

α	R-LFC ₃ method				R-LFT method			
	\bar{x}	$ x_{k+1} - x_k $	$ f(x_{k+1}) $	iter	\bar{x}	$ x_{k+1} - x_k $	$ f(x_{k+1}) $	iter
0.6	-	-	-	-	-	-	-	-
0.65	-	0.26732	2.1206e+02	500	\bar{x}_{16}	9.9621e-09	1.2812e-05	450
0.7	-	-	-	-	\bar{x}_{13}	9.8235e-09	1.7922e-06	74
0.75	-	-	-	-	\bar{x}_{12}	9.8996e-09	2.6985e-06	143
0.8	\bar{x}_{12}	1.106e-08	7.6287e-09	13	\bar{x}_9	9.5075e-09	1.2959e-06	52
0.85	-	-	-	-	\bar{x}_3	8.282e-09	3.3276e-07	31
0.9	-	-	-	-	\bar{x}_6	6.3651e-09	9.7585e-08	18
0.95	-	-	-	-	-	-	-	-
1	-	-	-	-	-	0.25782	1.8154	500

and Traub methods ($\alpha = 1$) show the worst performance, as they do not converge to any of the solutions in the maximum number of iterations. On the contrary, proposed methods for $\alpha < 1$ are able to reach different solutions within a reasonable number of iterations.

5.4.1 Dependence on initial estimations

Now, we are going to analyze the dependence on the initial estimation of the Newton, Chebyshev and Traub type methods by using convergence planes defined in [17]. In them (see, for example, Fig. 5.1(a)) the abscissa axis corresponds to the starting guess and the fractional index α appears in the ordinate axis. A mesh of 400×400 points is used. Points that are not painted in black color correspond to those pairs of initial estimations and values of α that converge to one of the roots with a tolerance of 10^{-3} . Different colors mean convergence to different roots. Therefore, when a

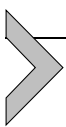
point is painted in black, this shows that no root is found in a maximum of 500 iterations. Moreover, for all convergence planes, the percentage of convergent pairs (x_0, α) is calculated, in order to compare the performance of the methods. The code used is a modification of that presented in [8].

In Fig. 5.1, we can see for $f_1(x)$ that Chebyshev type methods have a bit higher percentage of convergence than Newton and Traub type methods, not only with Caputo derivative, but also with Riemann–Liouville derivative. We can also see that methods with Caputo derivative have a slightly higher percentage of convergence than methods with Riemann–Liouville derivative.

In Fig. 5.2, we can see for $f_2(x)$ that Chebyshev type methods have a higher percentage of convergence than Newton and Traub type methods, not only with Caputo derivative, but also with Riemann–Liouville derivative. We also note that methods with Riemann–Liouville derivative have a bit higher percentage of convergence than methods with Caputo derivative.

In Fig. 5.3, we can see for $f_3(x)$ that Chebyshev type methods have a lower percentage of convergence than Newton and Traub type methods with Caputo derivative. We can also see that methods with Riemann–Liouville derivative have a much lower percentage of convergence than methods with Caputo derivative because these do not work for this function with Riemann–Liouville derivative.

In Fig. 5.4, we can see for $f_4(x)$ that Chebyshev type methods have a similar percentage of convergence to Newton and Traub type methods, not only with Caputo derivative, but also with Riemann–Liouville derivative. We also note that methods with Riemann–Liouville derivative have a similar percentage of convergence to methods with Caputo derivative.



5.5. Concluding remarks

Four fractional Newton type methods, six fractional Chebyshev type methods and two fractional Traub type schemes have been designed by using Caputo and Riemann–Liouville derivatives. The convergence properties of procedures CFN_2 , $R-LFN_2$ and CFT , $R-LFT$ imply always (at least) linear convergence, reaching order $1 + \alpha$ and $1 + 2\alpha$, respectively. Although the interest in this kind of method is mainly theoretical, some numerical tests have been done, and the dependence on the initial estimation has been analyzed.

It can be concluded that Chebyshev type methods show a better behavior for polynomials, whereas Newton and Traub type methods show

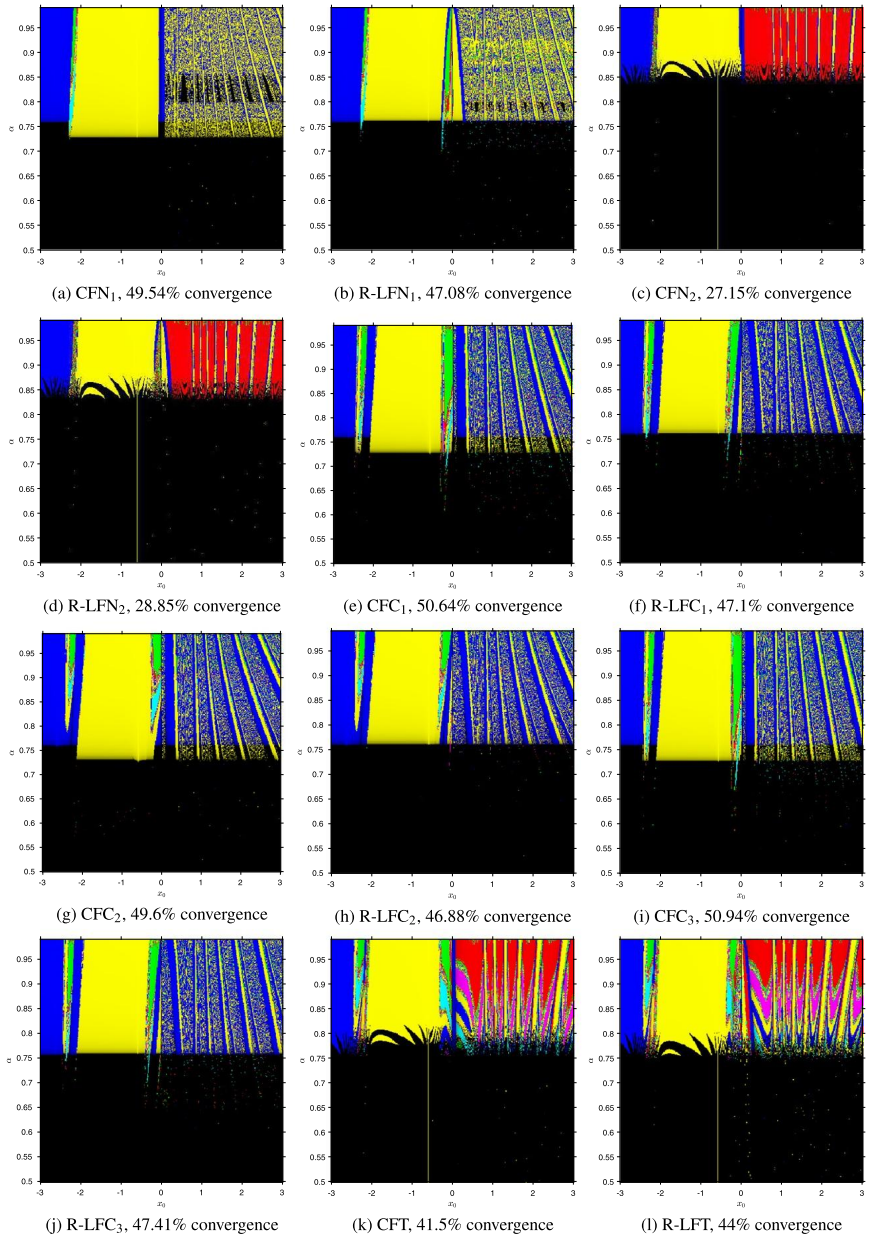


Figure 5.1 Convergence planes of proposed methods on $f_1(x)$ with $-3 \leq x_0 \leq 3$.

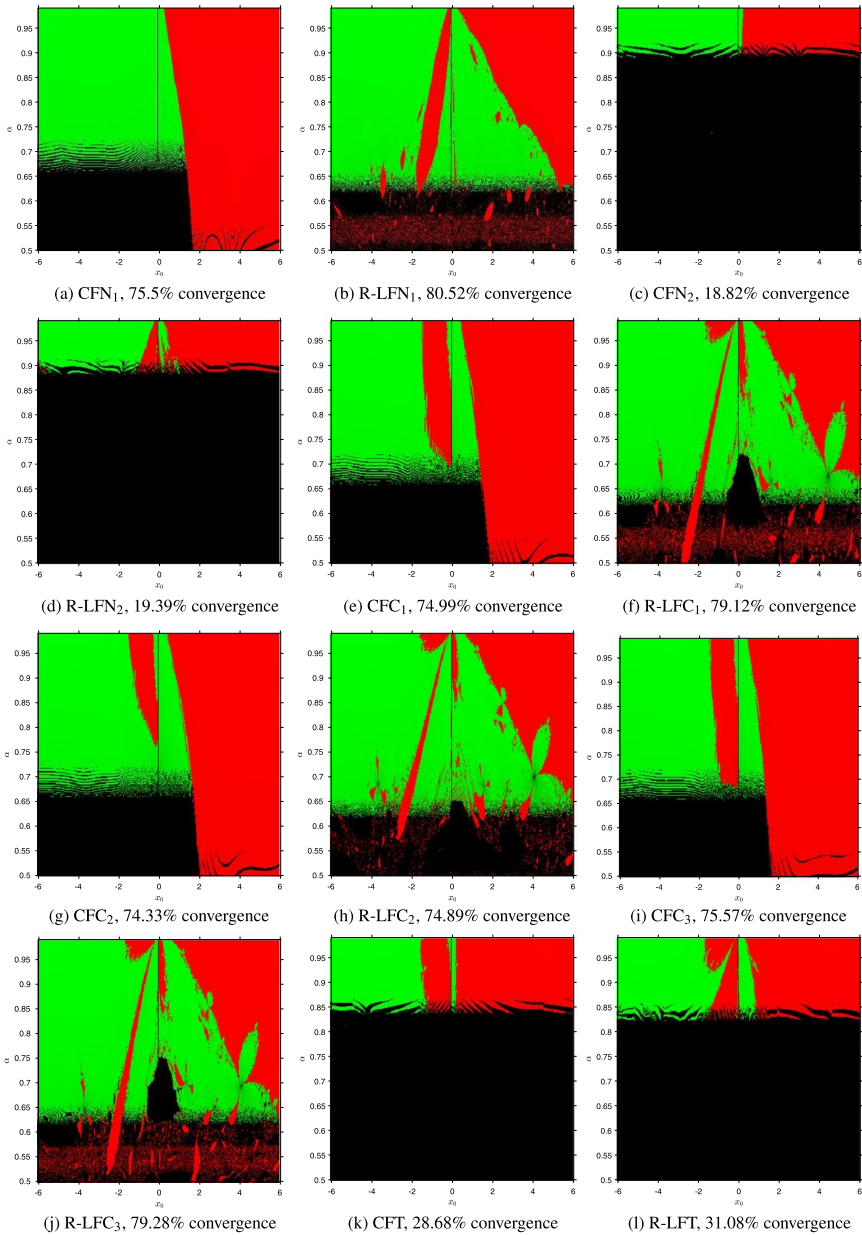


Figure 5.2 Convergence planes of proposed methods on $f_2(x)$ with $-6 \leq x_0 \leq 6$.

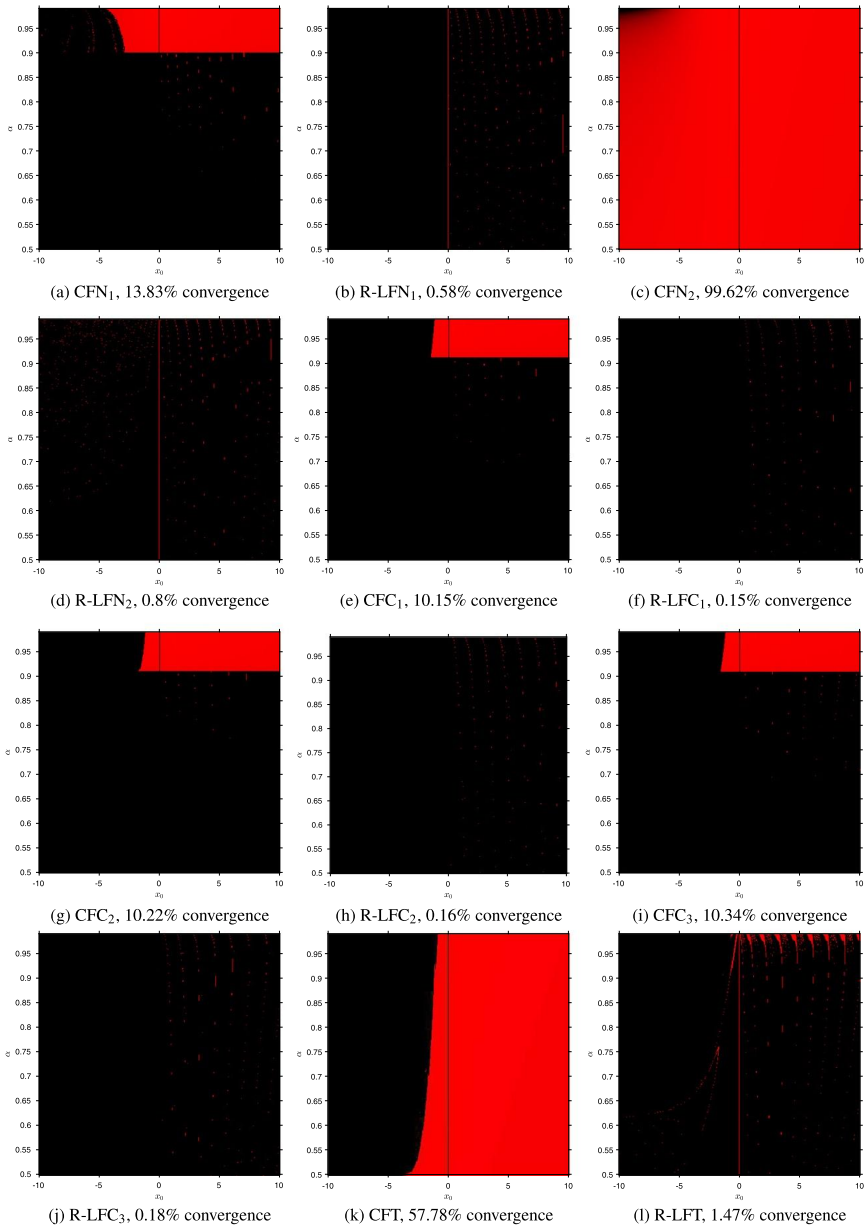


Figure 5.3 Convergence planes of proposed methods on $f_3(x)$ with $-10 \leq x_0 \leq 10$.

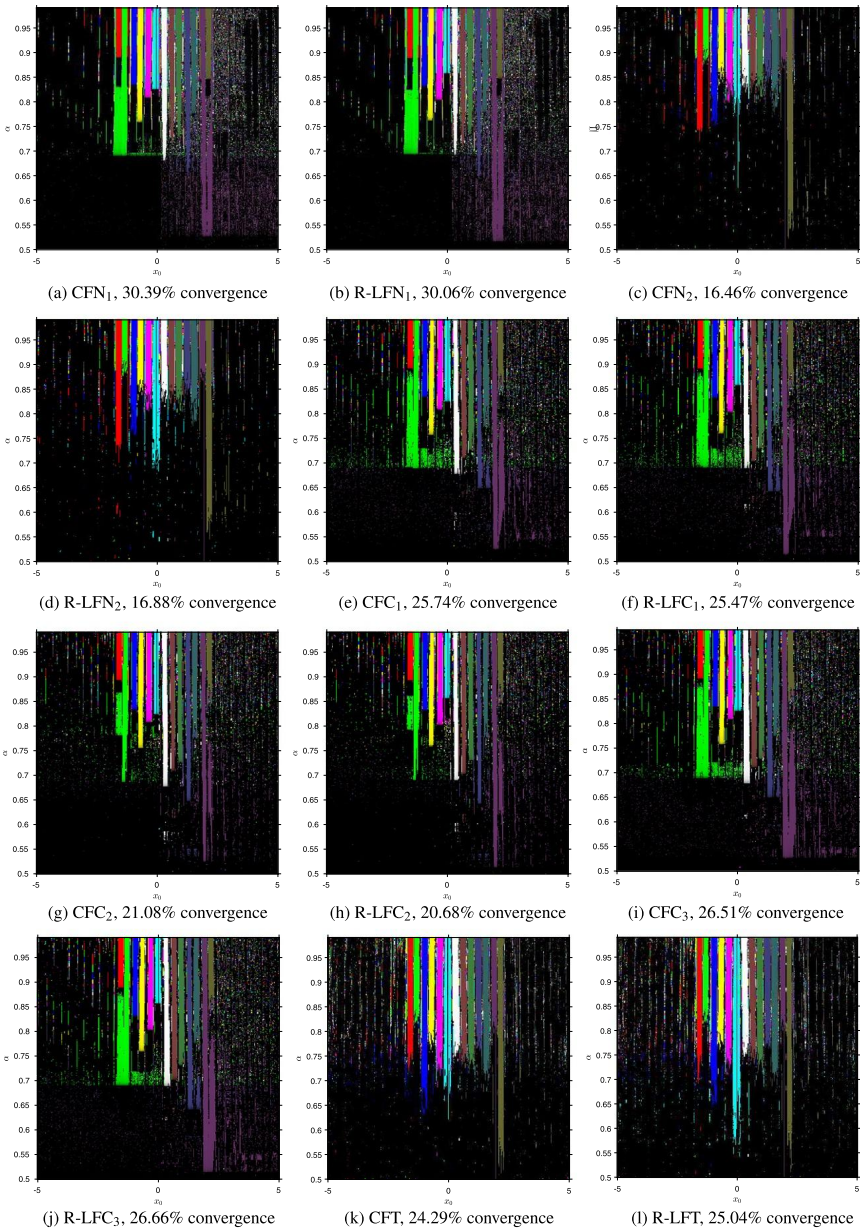


Figure 5.4 Convergence planes of proposed methods on $f_4(x)$ with $-5 \leq x_0 \leq 5$.

a better behavior for transcendent functions. Also, Traub type procedures improve Newton type ones and Chebyshev type methods with order 3α improve those with order 2α , not only because they require fewer iterations, but also because they have higher percentages of convergence. Additionally, a better performance of iterative methods based on Caputo derivatives, with respect to Riemann–Liouville–based schemes, has been observed.

The test shows that, for some problems, the methods using fractional derivatives reach different solutions with the same initial approximation. In addition, in the case of example $f_4(x)$, the fractional iterative schemes work better than the classical Newton and Traub methods ($\alpha = 1$), which do not converge within 500 iterations.

Acknowledgments

This research was supported by the Ministerio de Ciencia, Innovación y Universidades PGC2018-095896-B-C22 (MCIU/AEI/FEDER, UE) and the Ministry of Higher Education Science and Technology of Dominican Republic, FONDOCYT 2018-2019-1D2-140.

References

- [1] M. Abramowitz, I.A. Stegun, Handbook of Mathematical Functions with Formulas, Graphs, and Mathematical Tables, Dover Publications Inc., New York, 1970.
- [2] A. Akgül, A. Cordero, J.R. Torregrosa, A fractional Newton method with 2α th-order of convergence and its stability, Appl. Math. Lett. 98 (2019) 344–351.
- [3] S. Ali, T. Abdeljawad, K. Shah, F. Jarad, M. Arif, Computation of iterative solutions along with stability analysis to a coupled system of fractional order differential equations, Adv. Differ. Equ. 215 (2019), <https://doi.org/10.1186/s13662-019-2151-z>.
- [4] S. Ali, K. Shah, F. Jarad, On stable iterative solutions for a class of boundary value problem of nonlinear fractional order differential equations, Math. Methods Appl. Sci. 42 (2019) 969–981.
- [5] F. Brambila, A. Torres, Fractional Newton–Raphson method, arXiv:1710.07634v3, 2017.
- [6] G. Candelario, A. Cordero, J.R. Torregrosa, Multipoint fractional iterative methods with $(2\alpha + 1)$ th-order of convergence for solving nonlinear problems, Mathematics 8 (2020), <https://www.mdpi.com/2227-7390/8/3/452/htm>.
- [7] M.C. Caputo, D.F.M. Torres, Duality for the left and right fractional derivatives, Signal Process. 107 (2015) 265–271.
- [8] E.I. Chicharro, A. Cordero, J.R. Torregrosa, Drawing dynamical and parameters planes of iterative families and methods, Sci. World J. 2013 (780153) (2013) 1–11.
- [9] A. Cordero, I. Girona, J.R. Torregrosa, A variant of Chebyshev’s method with 3α th-order of convergence by using fractional derivatives, Symmetry 11 (8) (2019), <https://www.mdpi.com/2073-8994/11/8/1017/htm>.
- [10] G. Jumarie, Modified Riemann–Liouville derivative and fractional Taylor series of nondifferentiable functions further results, Comput. Math. Appl. 51 (2006) 1367–1376.
- [11] M.A. Khan, S. Ullah, M. Farhan, The dynamics of Zika virus with Caputo fractional derivative, AIMS Math. 4 (2019) 134–146.

- [12] H. Khan, A. Khan, W. Chen, K. Shah, Stability analysis and a numerical scheme for fractional Klein–Gordon equations, *Math. Methods Appl. Sci.* 42 (2) (2019) 723–732.
- [13] S. Khan, K. Shah, G. Zaman, F. Jarad, Existence theory and numerical solutions to smoking model under Caputo–Fabrizio fractional derivative, *Chaos* 29 (1) (2019) 013128, <https://doi.org/10.1063/1.5079644>.
- [14] C. Lanczos, A precision approximation of the gamma function, *SIAM J. Numer. Anal.* 1 (1964) 86–96.
- [15] H.Y. Liu, J.H. He, *From Leibniz’s Notation for Derivative to the Fractal Derivative, Fractional Derivative and Application in Mongolian Yurt*, De Gruyter, Berlin, 2015.
- [16] A. Lombardero, Cálculo Fraccionario y dinámica newtoniana, *Pensam. Mat. IV* (2014) 77–106.
- [17] Á.A. Magreñán, A new tool to study real dynamics: the convergence plane, *Appl. Math. Comput.* 248 (2014) 215–224.
- [18] A.M. Mathai, H.J. Haubold, *Fractional and Multivariable Calculus, Model Building and Optimization Problems*, Springer, Berlin, 2017.
- [19] K. Miller, B. Ross, *An Introduction to the Fractional Calculus and Fractional Differential Equations*, John Wiley & Sons, New York, 1993.
- [20] F. Mirzaee, S. Alipour, Numerical solution of nonlinear partial quadratic integro-differential equations of fractional order via hybrid of block-pulse and parabolic functions, *Numer. Methods Partial Differ. Equ.* 35 (3) (2019) 1134–1151.
- [21] M. Modanli, A. Akgül, On solutions of fractional order telegraph partial differential equation by Crank–Nicholson finite difference method, *Appl. Math. Nonlinear Sci.* 5 (1) (2020) 163–170.
- [22] Z.M. Odibat, N.T. Shawagfeh, Generalized Taylor’s formula, *Appl. Math. Comput.* 186 (2007) 286–293.
- [23] K.B. Oldham, J. Spanier, *The Fractional Calculus*, Academic Press Inc., California, 1974.
- [24] J.M. Ortega, W.C. Rheinholdt, *Iterative Solution of Nonlinear Equations in Several Variables*, Academic Press Inc., New York, 1970.
- [25] K.M. Owolabi, Robust and adaptive techniques for numerical simulation of nonlinear partial differential equations of fractional order, *Commun. Nonlinear Sci. Numer. Simul.* 44 (2017) 304–317.
- [26] I. Podlubny, *Fractional Differential Equations, Mathematics in Science and Engineering*, vol. 198, Academic Press Inc., San Diego, 1999.
- [27] K. Shah, J. Wang, A numerical scheme based on non-discretization of data for boundary value problems of fractional order differential equations, *Rev. R. Acad. Cienc. Exactas Fís. Nat., Ser. A Mat.* 113 (2019) 2277–2294.
- [28] J.F. Traub, *Iterative Methods for the Solution of Equations*, Chelsea Publishing Company, New York, 1982.
- [29] J.J. Trujillo, M. Rivero, B. Bonilla, On a Riemann–Liouville generalized Taylor’s formula, *J. Math. Anal. Appl.* 231 (1) (1999) 255–265.

Design of fractional-order finite-time sliding mode controllers for quadrotor UAVs subjected to disturbances and uncertainties

Moussa Labbadi^a, Yassine El houm^a, Yassine Boukal^b,
Karima Boudaraia^a, and Mohamed Cherkaoui^a

^aEngineering for Smart and Sustainable Systems Research Center, Mohammadia School of Engineers, Mohammed V University in Rabat, Rabat, Morocco

^bAeronautics, Space & Defense division, ALTRAN, Blagnac, France

6.1. Introduction

6.1.1 Motivation and background

Quadrotors are among the most widespread unmanned aerial vehicles (UAVs) among flying robots thanks to the simple frame design, low-cost development, and relatively simple usage and operation. They are mainly composed from a rigid frame attached to four rotors, mostly chosen as brushless DC motor due to their high torque characteristic. The quadrotor generates lift using four propellers mounted on the motors (two clockwise and two counterclockwise blades).

This system is energized by a lithium polymer battery, sized according to the total weight-to-thrust ratio. The vehicle has enormous capabilities in many areas and disciplines, such as military intervention, where it can autonomously explore hostile areas and gather useful information for real-time human intervention, or even for postanalysis. It can be used also in civil areas such as agriculture, where swarms of drones cooperate to optimize yield production by monitoring and differentiating between healthy and unhealthy plants.

Applications of this platform are expanding continuously, which explains how today's drone industry is worth billions of dollars and expected to grow significantly in the coming years.

In the research area, quadrotors also serve as an essential platform to test different control architectures since they are characterized by non-linear dynamics [14,15], and they are easily affected by disturbances and uncertainties [19,20]. Thus, a robust controller is strongly recommended to achieve desirable performance [21].

This chapter addresses the problem of path following by introducing two fractional-order sliding mode controllers (FOSMCs) to steer the vehicle in a disturbed and uncertain environment [18], where the first controller, FOSMC, uses a new reaching law to stabilize the drone, while the second controller, fractional-order fast terminal SMC (FOFTSMC), targets a robust control convergence and alleviates the chattering problem [22]. In the next subsection we highlight some related work and discuss the control strategy efficacy with respect to what has been cited.

6.1.2 Literature review

A group of researchers propose an architecture derived from adaptive neural networks using a PID SMC and a robust integral signum of error method to stabilize the quadrotor system in [24]. This technique guarantees faster convergence for attitude variables to reach their desirable references, while the RPD-SMC takes care of the problem of position tracking. Since its architectures combine a simple PD with a robust SMC and use RBNNS to approximate arbitrary functions, this technique can be easily implemented in a real quadcopter system. The problem of trajectory tracking of a quadcopter with measurement delay and time-varying disturbances has been addressed in [36]. The work uses a nominal backstepping controller (NBC) with a compensator. Estimated values of disturbances and time measurement delays are used by the NBC to compensate their effects and alleviate the undesirable impact on trajectory tracking performance. A double active disturbance rejection architecture in [37] deals with the nonlinearity problem, coupling, and sensitivity to disturbances. The state observer is implemented to compensate for system uncertainties, which leads to a significant improvement in system response. A control structure of a quadcopter system in the discrete-time domain consists of a state observer and a predictor is studied in [16]. It shows enhanced performance by alleviating the effect of delays (in inputs and outputs) and actively rejecting disturbances by compensation. Using matrix inequalities, the maximum delay is evaluated in order to guarantee system stability. Another controller structure (PPC) is used to stabilize the drone with disturbances coming from

unknown sources such as payloads and wind gust [17]. The outer loop is controlled by the PPC scheme, while the inner loop is stabilized using an adaptive controller. A transformation of the underactuated quadcopter system into a fully actuated one is shown in [25]. To steer the UAV backstepping SMCs are adopted in this case, while a feedforward compensator based on ESO takes care of the rejection of disturbances. A new technique addresses the trajectory tracking problem by applying hyperbolic functions which leads to a better tracking performance [2]. Based on model predictive control (MPC) theory a control scheme is developed to stabilize the UAV [3]. System dynamics are obtained based on a linearized system dynamic for each operating point. Two variants are considered: an integral MPC and a regular MPC, respectively, for translational and attitude subsystems. The clear advantage of this technique is the ability to steer the quadcopter in an uncertain environment with physical constraints. Based on dynamic inversion, a finite-time control structure is applied for the X-Y translational subsystem, while the attitude subsystem is stabilized using a robust variant of the SMC technique [4]. This latter shows strong robustness against model uncertainties and disturbances. A new adaptive controller structure takes into account the presence of external disturbances in [5]. It assumes generally that the geometric center is not aligned with the center of mass (C_g) which suppresses its effect on the closed-loop system performance. The controller takes also into account parameter uncertainties in the model dynamics (for instance C_g). The problem of tracking the trajectory has been validated experimentally using a state feedback adaptation law while the vehicle is subjected to external disturbances [6]. This latter is estimated using a smooth projector operator. Experimental design of a global controller for a quadcopter path following problem in presence of constant wind gust disturbances has been treated in [7]. An adaptive state feedback controller stabilizes altitude and attitude subsystems, ensures global convergence in closed-loop configuration, and guarantees a maximum bound constraint on control input command. This technique leads to a significant control action improvement. A new technique makes use of quantum technology to stabilize a quadcopter UAV in [9]. The controller deals with unknown actuator failures and external disturbances. A hardware validation using a Quanser 3-DOF system is proposed to evaluate system performance. The problem of trajectory tracking using a nonlinear resilient control scheme has been developed using a backstepping approach with the help of a disturbance observer [8]. The resilient controller deals with the problem of

actuator performance degradation. Other researchers investigate the limits of classical design techniques in practice, which can be affected by external disturbances, measurement noise, and time delays [13]. The authors propose a controller based on a modified disturbance rejection in presence of input delays and external disturbances. A dynamical model is identified including input delays at first. A tracking differentiator provides smooth profiles for the references, while an observer copes with state estimation with input delays and a predictor estimates disturbances. The nonlinear PD controller deals with the tracking problem. An integral backstepping (IB) SMC (BS-SMC) has been implemented in order to steer a quadcopter system. The work also claims to suppress the chattering phenomena using this technique. The tracking is tested under constant and unknown stochastic disturbances. An augmented SMC with fault-tolerant feature has been implemented experimentally with faulty actuators and damaged propellers to evaluate tracking performance [23]. Two passive and active variants of the controller are implemented and compared in order to show their pros and cons and application considerations and limitations. A hybrid controller is adopted to stabilize the drone in [26]. The control scheme alleviates the chattering phenomena and guarantees convergence with a prescribed timing. Two controllers coupled with each other are used to steer the attitude subsystem, while an adaptive PID controller takes care of the translational subsystem with major features like lack of chattering and robustness against disturbances. The bound of the unknown disturbances is estimated with an adaptive controller associated with a novel fuzzy adaptive range. A fault detection and isolation technique for second-order integrators studies the formation of a set of drones [29]. The disturbed observer is implemented based on dynamical models. The drones communicate their states to each other, which update the states of the disturbed observer. Based on this information two disturbed observers are designed (fault detection and fault isolation). The controller of each drone is robust against self-faults and other vehicles' faults. An integral predictive controller coupled with a nonlinear structure controls a quadcopter system in [30]. MPC takes care of the position tracking problem, while an H_∞ nonlinear controller controls the attitude subsystem. An integral position error is taken into account in order to ensure a null steady-state error when disturbances are present. The controller guarantees convergence and deals with parametric uncertainties and unmodeled dynamics. A feedback trajectory tracking controller mixed with an extended state observer (ESO) with dynamic surface control (DSC) has been applied to a quadrotor system [31]. The ESO estimates

state variables and disturbances in the inner loop path. The position and attitude controllers are synthesized by the DSC and the estimated signal from the ESO. A robust backstepping trajectory tracking feedback control law is adopted for a quadcopter in an uncertain and disturbed environment [31]. The ESO estimates disturbances and measurable state variables for the inner loop. A sigmoid tracking differentiator (STD) takes care of the computation of the virtual command derivative. The desired performance is achieved using minimal information due to the use of the STD. An attitude subsystem has been described using the modified Rodrigues parameters (MRPs) technique [32]. It divides the system in two subsystems. A backstepping technique with disturbance observer and SMC stabilizes the drone globally k -exponentially/uniformly. A disturbance rejection control scheme for the inner loop subsystem in presence of disturbances and uncertainties (DOB) has been adopted in [33]. The authors use a disturbance observer and a feedback control law. The DOB optimized by H_∞ is used to compensate attitude dynamics by the nominal plant; this latter is used for the feedback controller. The trajectory tracking problem with input saturation is highlighted in [34]. Torque and thrust controllers are implemented to steer the UAV in the desirable trajectory with input saturation constraint. To stabilize the UAV under gust wind, researchers in [35] propose an ADRC framework control for the attitude subsystem coupled with a PD structure for the outer subsystem. Disturbances are estimated by the ESO. An adaptive law based on SMC techniques stabilizes the quadrotor with the problem of thrust constraint and inertial parameter uncertainty [38]. An auxiliary dynamic system is used for the outer loop in the control design phase in order to choose controller parameters with respect to the thrust constraint problem. The tracking trajectory problem using a hierarchical control technique under uncertain inertial parameters has been studied in [39]. The outer loop is designed in a way that the convergence rate of the mass estimation goes to the actual value.

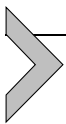
6.1.3 Contributions

Control problems of the UAV system subjected to time-varying disturbances and parametric uncertainties with stability analysis are addressed. This chapter proposes two noninteger controllers using an SMC approach. The proposed sliding mode surfaces for both attitude/position subsystems are developed with the fractional-order operators. The stability of the quadrotor system is ensured using Lyapunov theory. Moreover, new suf-

ficient switching control laws are derived, which can easily compensate for the upper bound of the disturbances affecting each degree of freedom. Two numerical simulations for the quadrotor model using the proposed controllers are studied to show the effectiveness of proposed fractional-order controllers based on the SMC technique.

6.1.4 Chapter organization

The chapter is structured as follows. In Section 6.2, preliminaries on fractional-order derivatives are provided. The UAV plant model is studied in Section 6.3. Section 6.4 is dedicated to the design of the controllers in presence of time-varying disturbances using a Lyapunov function. Section 6.5 demonstrates the effectiveness of the proposed methods. Finally, concluding remarks on the proposed controllers are given in Section 6.6.



6.2. Preliminary results

Two definitions most used for fractional-order derivatives for a given function $\Theta(t)$ are the Riemann–Liouville (RL) definition and the Caputo (C) definition [12,27]. The Riemann–Liouville definition is defined as [12, 27]

$${}^{RL}D_{\tau}^{\beta}\Xi(\tau) = \frac{1}{\Gamma(n-\beta)} \frac{d^n}{d\tau^n} \int_a^{\tau} \frac{\Xi(\rho)}{(\tau-\rho)^{\beta-n+1}} d\tau. \quad (6.1)$$

The Caputo definition is given as [12,28]

$${}^C D_{\tau}^{\beta}\Xi(\tau) = \frac{1}{\Gamma(\beta-n)} \int_a^{\tau} \frac{\Xi^{(n)}(\rho)}{(\tau-\rho)^{\beta-n+1}} d\rho, \quad (6.2)$$

where $n \in \mathbb{N}^*$, β is the order of the derivative with $(n-1) < \beta < n$, and $\Gamma(\cdot)$ represents the Gamma function, defined by

$$\Gamma(z) = \int_0^{\infty} e^{-\tau} \tau^{z-1} d\tau. \quad (6.3)$$

The Riemann–Liouville and Caputo operators are two definitions of the fractional-order derivative. The notation ${}^{RL}D^{\alpha}$ and ${}^C D^{\alpha}$ for Riemann–Liouville and Caputo operators, respectively, are replaced by D^{α} in the rest of the chapter.

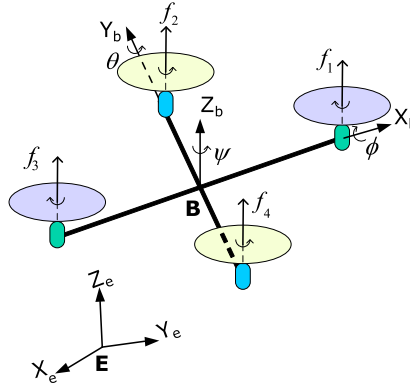


Figure 6.1 Representation of a quadrotor in fixed and body frames.

6.3. Quadrotor system dynamics

Buildup of the UAV dynamical model is addressed using Newton–Euler formalism. Two fixed frames are considered for this purpose: an inertial referential frame $\Xi = [X_{\Xi}, Y_{\Xi}, Z_{\Xi}]$ and frame $\beta = [X_{\beta}, Y_{\beta}, Z_{\beta}]$ (Fig. 6.1). The UAV center of mass is located in the Ξ frame using the vector $\xi = [x, y, z]^T$, while for the body fixed frame the Euler angles are considered $\rho = [\phi, \theta, \psi]^T$. The range for the Euler angles is given by:

The roll angle corresponds to the rotation with respect to the x -axis, $\pm\pi/2$. The pitch angle corresponds to the rotation with respect to the y -axis, $\pm\pi/2$.

The yaw angle corresponds to the rotation with respect to the z -axis, $\pm\pi$.

Some assumptions should be considered before constructing the plant model:

- The center of gravity is aligned with the center of the body mass.
- The quadcopter body axes are considered to be principal axes.
- The ground effect acting on the quadcopter is neglected.
- Drag and thrust are directly related to the velocity of the rotors using square function.
- The quadcopter system is considered as a rigid body.

In order to represent rotational and translational dynamics, a rotation matrix is constructed from three successive rotation matrices for Euler angles

[1] [10]. The transformation is obtained from multiplication of these matrices:

$$R_1 = \begin{bmatrix} 1 & 0 & 0 \\ 0 & c(\phi) & -s(\phi) \\ 0 & s(\phi) & c(\phi) \end{bmatrix}; \quad R_2 = \begin{bmatrix} c(\theta) & 0 & s(\theta) \\ 0 & 1 & 0 \\ -s(\theta) & 0 & c(\theta) \end{bmatrix};$$

$$R_3 = \begin{bmatrix} c(\psi) & -s(\psi) & 0 \\ s(\psi) & c(\psi) & 0 \\ 0 & 0 & 1 \end{bmatrix},$$

where $c(\text{angle})$ and $s(\text{angle})$ refer respectively to $\cos(\text{angle})$ and $\sin(\text{angle})$ functions.

Initially, the body fixed frame is aligned with the referential frame. A rotation around the x -axis followed by a second rotation around the y -axis and a final rotation around z -axis constructs the overall rotation matrix R . Multiplication of elementary rotation in the order $R_3R_2R_1$ results in a rotation matrix describing the overall transformation [11].

Angular velocities are linked to Euler angles by the following equations:

$$\omega = \begin{bmatrix} \dot{\phi} \\ 0 \\ 0 \end{bmatrix} + R_1^T \begin{bmatrix} 0 \\ \dot{\theta} \\ 0 \end{bmatrix} + (R_2R_1)^T \begin{bmatrix} 0 \\ 0 \\ \dot{\psi} \end{bmatrix},$$

$$\omega = \begin{bmatrix} 1 & 0 & -s(\theta) \\ 0 & c(\phi) & -s(\phi)c(\theta) \\ 0 & -s(\phi) & c(\phi)c(\theta) \end{bmatrix} \begin{bmatrix} \dot{\phi} \\ \dot{\theta} \\ \dot{\psi} \end{bmatrix}.$$

The net force considered in the book chapter is divided in the following force elements:

$f_i = b\omega_i^2$ represents the generated thrust due to the motor rotational speed, where i represents the four motors and b represents an aerodynamic constant;

$F_p = d\omega_i^2$ represents the drag force due to the rotation of the propellers, where d is a constant related to the construction of the props;

$F_k = K_{f1}v$ is the drag due to the drone movement in 3D space, where K_{f1} is a constant coefficient.

The net moment can be divided in the following elementary moments:

$M_{roll} = lb(\omega_4^2 - \omega_2^2)$ and $M_{pitch} = lb(\omega_3^2 - \omega_1^2)$ moments come from the difference in forces f_4, f_2 for roll angle and forces f_3, f_1 for pitch angle, where the subscript refers to an index, while the superscript refers to the power; $M_{yaw} = d(\omega_1^2 + \omega_3^2 - \omega_2^2 - \omega_4^2)$ comes from the reaction torque for each propeller; $M_{friction} = K_{f2}\omega^2$ comes from the aerodynamic friction proportional to the vehicle angular velocity.

The gyroscopic effect can be formulated from two sources, one coming from the props rotation and the other from the rotation of the entire drone.

The gyroscopic moment from propellers is given by the following equation:

$$M_{props} = \sum_1^4 \omega \wedge J_r \left[\begin{array}{ccc} 0 & 0 & (-1)^{i+1} \omega_i \end{array} \right]^T,$$

where J_r represents the inertia of the rotors.

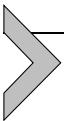
The gyroscopic effect from the drone movement is as follows: $M_{drone} = \omega \wedge I\omega$, where I represents the moment of inertia matrix.

Translational and rotational equations of motion can be obtained using Newton–Euler formalism: $m\ddot{\xi} = \Sigma F_j$, $I\dot{\omega} = -\omega \wedge I\omega + \Sigma M_j$, where F_j and M_j represent respectively the net forces and net moments.

The system dynamics are given as follows:

$$\begin{bmatrix} \ddot{x} \\ \ddot{y} \\ \ddot{z} \\ \ddot{\phi} \\ \ddot{\theta} \\ \ddot{\psi} \end{bmatrix} = \begin{bmatrix} -\frac{K_{f1x}}{m}\dot{x} + \frac{1}{m}u_x\mathcal{U}_1 + \mathcal{D}_x(t) \\ -\frac{K_{f1y}}{m}\dot{y} + \frac{1}{m}u_y\mathcal{U}_1 + \mathcal{D}_y(t) \\ -\frac{K_{f1z}}{m}\dot{z} + \frac{c(\phi)c(\theta)}{m}\mathcal{U}_1 - g + \mathcal{D}_z(t) \\ \frac{I_2-I_3}{I_1}\dot{\theta}\dot{\psi} - \frac{I_r}{I_1}\dot{\theta}\dot{\omega}_r - \frac{K_{f2x}}{I_1}\dot{\phi}^2 + \frac{1}{I_1}\mathcal{U}_2 + \mathcal{D}_\phi(t) \\ \frac{I_3-I_1}{I_2}\dot{\psi}\dot{\phi} - \frac{I_r}{I_2}\dot{\phi}\dot{\omega}_r - \frac{K_{f2y}}{I_2}\dot{\theta}^2 + \frac{1}{I_2}\mathcal{U}_3 + \mathcal{D}_\theta(t) \\ \frac{I_1-I_2}{I_3}\dot{\theta}\dot{\phi} - \frac{K_{f2z}}{I_3}\dot{\psi}^2 + \frac{1}{I_3}\mathcal{U}_4 + \mathcal{D}_\psi(t) \end{bmatrix},$$

where $\mathcal{U}_1 = b\omega_i^2$, for $i = 1, 2, 3, 4$, $\mathcal{U}_2 = (\omega_4^2 - \omega_2^2)bl$, $\mathcal{U}_3 = (\omega_3^2 - \omega_1^2)bl$, $\mathcal{U}_4 = (\omega_1^2 - \omega_2^2 + \omega_3^2 - \omega_4^2)d$, $u_x = c(\phi)c(\psi)s(\theta) + s(\phi)s(\psi)$, and $u_y = c(\phi)s(\psi)s(\theta) - s(\phi)c(\psi)$, where $\mathcal{D}_j(t)$ is an external disturbance acting on the UAV system.



6.4. Fractional-order SMC controllers for quadrotors

Two fractional-order controllers based on SMC and fast SMC are designed for outer and inner loops of a UAV system. The overall schema is illustrated in Fig. 6.2.

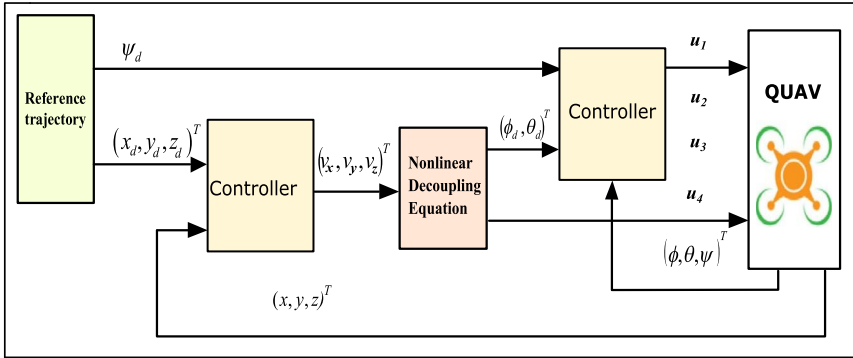


Figure 6.2 Closed-loop control structure for translational and rotational subsystems.

6.4.1 FOSMC-FOFTSMC design mechanism

6.4.1.1 Translational subsystem controller using FOSMC-FOFTSMC

In this part, three fractional-order controllers will be presented for translational subsystems subjected to external disturbances. Signals for the position subsystem are created as follows:

$$\begin{cases} \mathcal{V}_x = \frac{\mathcal{U}_1}{m} (s\theta c\phi c\psi + s\phi s\psi), \\ \mathcal{V}_y = \frac{\mathcal{U}_1}{m} (s\theta c\phi s\psi - s\phi c\psi), \\ \mathcal{V}_z = -g + \frac{\mathcal{U}_1}{m} (c\theta c\phi). \end{cases} \quad (6.4)$$

After a simple calculation from Eq. (6.4), we have

$$\begin{cases} \mathcal{U}_1 = m\sqrt{\mathcal{V}_x^2 + \mathcal{V}_y^2 + (\mathcal{V}_z + g)^2}, \\ \phi_d = \arctan(\cos\theta_d(\frac{\mathcal{V}_x \sin\psi_d - \mathcal{V}_y \cos\psi_d}{\mathcal{V}_z + g})), \\ \theta_d = \arctan(\frac{\mathcal{V}_x \cos\psi_d + \mathcal{V}_y \sin\psi_d}{\mathcal{V}_z + g}). \end{cases} \quad (6.5)$$

The tracking errors are defined as

$$\begin{bmatrix} E_x(t) \\ E_y(t) \\ E_z(t) \end{bmatrix} = \begin{bmatrix} x - x_d \\ y - y_d \\ z - z_d \end{bmatrix}, \quad (6.6)$$

and the time derivatives of these tracking errors are defined as

$$\begin{bmatrix} \dot{E}_x(t) \\ \dot{E}_y(t) \\ \dot{E}_z(t) \end{bmatrix} = \begin{bmatrix} \dot{x} - \dot{x}_d \\ \dot{y} - \dot{y}_d \\ \dot{z} - \dot{z}_d \end{bmatrix}. \quad (6.7)$$

The sliding surfaces for the position are as follows:

$$\begin{bmatrix} \sigma_7(t) \\ \sigma_9(t) \\ \sigma_{11}(t) \end{bmatrix} = \begin{bmatrix} \lambda_x E_x(t) + \dot{E}_x(t) \\ \lambda_y E_y(t) + \dot{E}_y(t) \\ \lambda_z E_z(t) + \dot{E}_z(t) \end{bmatrix}, \quad (6.8)$$

where λ_x , λ_y , and λ_z are positive constants. The derivatives of (6.8) are

$$\begin{bmatrix} \dot{\sigma}_7(t) \\ \dot{\sigma}_9(t) \\ \dot{\sigma}_{11}(t) \end{bmatrix} = \begin{bmatrix} \lambda_x \dot{E}_x(t) + (\ddot{x} - \ddot{x}_d) \\ \lambda_y \dot{E}_y(t) + (\ddot{y} - \ddot{y}_d) \\ \lambda_z \dot{E}_z(t) + (\ddot{z} - \ddot{z}_d) \end{bmatrix}. \quad (6.9)$$

Forcing $\dot{\sigma}_j = 0$ (where $j = 7, 9$, or 11), translational subsystem control signals are formulated as

$$\begin{aligned} \mathcal{V}_{eq\mathcal{X}} &= \frac{K_{f1x}}{m} \dot{x} - \lambda_x \dot{E}_x(t) + \ddot{x}_d, \\ \mathcal{V}_{eq\mathcal{Y}} &= \frac{K_{f1y}}{m} \dot{y} - \lambda_y \dot{E}_y(t) + \ddot{y}_d, \\ \mathcal{V}_{eq\mathcal{Z}} &= \frac{K_{f1z}}{m} \dot{z} + g - \lambda_z \dot{E}_z(t) + \ddot{z}_d. \end{aligned} \quad (6.10)$$

The switching control laws are added to the equivalent control laws to enhance robustness in disturbed and uncertain environments:

$$\begin{aligned} \mathcal{V}_{sw\mathcal{X}} &= -\varepsilon_7 D_t^{\gamma_7} \operatorname{sgn}(\sigma_7(t)) - h_7 \sigma_7(t), \\ \mathcal{V}_{sw\mathcal{Y}} &= -\varepsilon_9 D_t^{\gamma_9} \operatorname{sgn}(\sigma_9(t)) - h_9 \sigma_9(t), \\ \mathcal{V}_{sw\mathcal{Z}} &= -\varepsilon_{11} D_t^{\gamma_{11}} \operatorname{sgn}(\sigma_{11}(t)) - h_{11} \sigma_{11}(t), \end{aligned} \quad (6.11)$$

where ε_j , h_j are nonzero positive coefficients and γ_j is a fractional order satisfying $0 \leq \gamma_j < 1$. Consequently, the ultimate controllers for the position

subsystem are

$$\begin{aligned}
 \mathcal{V}_x &= \frac{K_{f1x}}{m} \dot{x} - \lambda_x \dot{E}_x(t) + \ddot{x}_d - \varepsilon_7 D_t^{\gamma_7} \operatorname{sgn}(\sigma_7(t)) - h_7 \sigma_7(t), \\
 \mathcal{V}_y &= \frac{K_{f1y}}{m} \dot{y} - \lambda_y \dot{E}_y(t) + \ddot{y}_d - \varepsilon_9 D_t^{\gamma_9} \operatorname{sgn}(\sigma_9(t)) - h_9 \sigma_9(t), \\
 \mathcal{V}_z &= \frac{K_{f1z}}{m} \dot{z} + g - \lambda_z \dot{E}_z(t) + \ddot{z}_d - \varepsilon_{11} D_t^{\gamma_{11}} \operatorname{sgn}(\sigma_{11}(t)) - h_{11} \sigma_{11}(t).
 \end{aligned} \tag{6.12}$$

Theorem 6.1. *The translational part with the proposed controllers \mathcal{V}_x , \mathcal{V}_y , and \mathcal{V}_z should be asymptotically stable.*

Proof. We choosing a Lyapunov function as

$$V_p = \frac{1}{2} \sigma_7(t)^2 + \frac{1}{2} \sigma_9(t)^2 + \frac{1}{2} \sigma_{11}(t)^2. \tag{6.13}$$

The derivative of (6.13) is

$$\begin{aligned}
 \dot{V}_p &= \dot{\sigma}_9(t) \sigma_9(t) + \dot{\sigma}_{11}(t) \sigma_{11}(t) + \dot{\sigma}_7(t) \sigma_7(t) \\
 &= (-\ddot{x}_d - \frac{K_{f1x}}{m} \dot{x} + \mathcal{D}_x(t) + \lambda_x \dot{E}_x(t) + \mathcal{V}_x) \sigma_7(t) \\
 &\quad + \sigma_9(t) (-\ddot{y}_d - \frac{K_{f1y}}{m} \dot{y} + \mathcal{D}_y(t) + \lambda_y \dot{E}_y(t) + \mathcal{V}_y) \\
 &\quad + (-K_{f1z} \frac{\dot{z}}{m} - \ddot{z}_d + \mathcal{D}_z(t) + \lambda_z \dot{E}_z(t) + \mathcal{V}_z) \sigma_{11}(t) \\
 &= \sigma_7(t) [-\ddot{x}_d - \frac{K_{f1x}}{m} \dot{x} + \lambda_x \dot{E}_x(t) + \mathcal{D}_x(t) \\
 &\quad + (\frac{K_{f1x}}{m} \dot{x} - \lambda_x \dot{E}_x(t) + \ddot{x}_d - h_7 \sigma_7(t) - \varepsilon_7 D_t^{\gamma_7} \operatorname{sgn}(\sigma_7(t)))] \\
 &\quad + \sigma_9(t) [-\ddot{y}_d - \frac{K_{f1y}}{m} \dot{y} + \lambda_y \dot{E}_y(t) + \mathcal{D}_y(t) \\
 &\quad + (\frac{K_{f1y}}{m} \dot{y} - \lambda_y \dot{E}_y(t) + \ddot{y}_d - \varepsilon_9 D_t^{\gamma_9} \operatorname{sgn}(\sigma_9(t)) - h_9 \sigma_9(t))] \\
 &\quad + \sigma_{11}(t) [-\ddot{z}_d - K_{f1z} \frac{\dot{z}}{m} + \mathcal{D}_z(t) + (K_{f1z} \frac{\dot{z}}{m} + g - \lambda_z \dot{E}_z(t) \\
 &\quad + \ddot{z}_d - h_{11} \sigma_{11}(t)) + \dot{E}_z(t) \lambda_z - \varepsilon_{11} D_t^{\gamma_{11}} \operatorname{sgn}(\sigma_{11}(t))] \\
 &= \sigma_7(t) [-h_7 \sigma_7(t) - \varepsilon_7 D_t^{\gamma_7} \operatorname{sgn}(\sigma_7(t)) + \mathcal{D}_x(t)] + \sigma_9(t) [-h_9 \sigma_9(t) \\
 &\quad - \varepsilon_9 D_t^{\gamma_9} \operatorname{sgn}(\sigma_9(t)) + \mathcal{D}_y(t)] + \sigma_{11}(t) [-h_{11} \sigma_{11}(t) \\
 &\quad - \varepsilon_{11} D_t^{\gamma_{11}} \operatorname{sgn}(\sigma_{11}(t)) + \mathcal{D}_z(t)],
 \end{aligned} \tag{6.14}$$

with

$$\sigma_i(t)\varepsilon_i D_t^{\gamma_i} \text{sgn}(\sigma_i(t)) - \sigma_i(t)\mathcal{D}_{\mathcal{I}}(t) \geq 0. \quad (6.15)$$

From (6.15), and (6.14) it can be simplified to

$$\begin{aligned} \dot{V}_p &\leq -h_9\sigma_9(t)^2 - h_{11}\sigma_{11}(t)^2 - h_7\sigma_7(t)^2 \\ &\leq 0, \end{aligned} \quad (6.16)$$

meaning that the translational path is stable according to the stability analysis. \square

6.4.1.2 Rotational subsystem controller using FOSMC-FOFTSMC

To enhance the response of the UAV attitude, fractional-order FT-SMC surfaces are considered.

We define attitude errors as follows:

$$\begin{bmatrix} E_\psi(t) \\ E_\theta(t) \\ E_\phi(t) \end{bmatrix} = \begin{bmatrix} \psi - \psi_d \\ \theta - \theta_d \\ \phi - \phi_d \end{bmatrix}. \quad (6.17)$$

Using the fractional operators, the sliding mode surfaces of the attitude are

$$\begin{bmatrix} \sigma_1(t) \\ \sigma_3(t) \\ \sigma_5(t) \end{bmatrix} = \begin{bmatrix} D_t^{\alpha_1+1} E_\phi(t) + m_1 E_\phi(t) + n_1 E_\phi(t)^{b_1/a_1} \\ D_t^{\alpha_3+1} E_\theta(t) + m_3 E_\theta(t) + n_3 E_\theta(t)^{b_3/a_3} \\ D_t^{\alpha_5+1} E_\psi(t) + m_5 E_\psi(t) + n_5 E_\psi(t)^{b_5/a_5} \end{bmatrix}, \quad (6.18)$$

where m_1, n_1 are positive parameters. The term α_j is included in the $(0, 1)$ interval. The FOSM time derivative is represented as

$$\begin{bmatrix} \dot{\sigma}_1(t) \\ \dot{\sigma}_3(t) \\ \dot{\sigma}_5(t) \end{bmatrix} = \begin{bmatrix} D_t^{\alpha_1} \ddot{E}_\phi(t) + m_1 \dot{E}_\phi(t) + \frac{n_1 b_1}{a_1} E_\phi(t)^{(1-\frac{b_1}{a_1})} \dot{E}_\phi(t) \\ D_t^{\alpha_3} \ddot{E}_\theta(t) + m_3 \dot{E}_\theta(t) + \frac{n_3 b_3}{a_3} E_\theta(t)^{(1-\frac{b_3}{a_3})} \dot{E}_\theta(t) \\ D_t^{\alpha_5} \ddot{E}_\psi(t) + m_5 \dot{E}_\psi(t) + \frac{n_5 b_5}{a_5} E_\psi(t)^{(1-\frac{b_5}{a_5})} \dot{E}_\psi(t) \end{bmatrix}. \quad (6.19)$$

The control laws are written as follows:

$$\begin{aligned} u_2 = I_1 &[-\{\dot{\theta}\dot{\psi} \frac{(I_2 - I_3)}{I_1} - \frac{I_r}{I_1} \Omega_r \dot{\theta} - \frac{K_{f2x}}{I_1} \dot{\phi}^2\} - D_1 D_t^{\gamma_1} \text{sgn}(\sigma_1(t))] \\ &- D_t^{-\alpha_1} (m_1 \dot{E}_\phi(t) + \frac{n_1 b_1}{a_1} E_\phi(t)^{(1-\frac{b_1}{a_1})} \dot{E}_\phi(t) + h_1 \sigma_1(t)), \end{aligned}$$

$$\begin{aligned}
\mathcal{U}_3 &= I_2[-\{\dot{\phi}\dot{\psi}\frac{(I_3 - I_1)}{I_2} + \frac{I_r}{I_2}\Omega_r\dot{\phi} - \frac{K_{f2y}}{I_2}\dot{\theta}^2\} - D_3D_t^{\gamma_3}\text{sgn}(\sigma_3(t))] \\
&\quad - D_t^{-\alpha_3}(m_3\dot{E}_\theta(t) + \frac{n_3b_3}{a_3}E_\theta(t)^{(1-\frac{b_3}{a_3})}\dot{E}_\theta(t) + h_3\sigma_3(t)), \\
\mathcal{U}_4 &= I_3[-\{\dot{\phi}\dot{\theta}\frac{(I_1 - I_2)}{I_3} - \frac{k_{f2z}}{I_3}\dot{\psi}^2\} - D_5D_t^{\gamma_5}\text{sgn}(\sigma_5(t))] \\
&\quad - D_t^{-\alpha_5}(m_5\dot{E}_\psi(t) + \frac{n_5b_5}{a_5}E_\psi(t)^{(1-\frac{b_5}{a_5})}\dot{E}_\psi(t) + h_5\sigma_5(t)).
\end{aligned} \tag{6.20}$$

Theorem 6.2. *The translational part with the proposed controllers \mathcal{U}_2 , \mathcal{U}_3 , and \mathcal{U}_4 should be asymptotically stable.*

Proof. The Lyapunov function for the attitude subsystem is

$$V_r = \frac{1}{2}\sigma_3(t)^2 + \frac{1}{2}\sigma_5(t)^2 + \frac{1}{2}\sigma_1(t)^2. \tag{6.21}$$

Now, \dot{V}_r can be calculated as

$$\begin{aligned}
\dot{V}_r &= \dot{\sigma}_3(t)\sigma_3(t) + \dot{\sigma}_5(t)\sigma_5(t) + \dot{\sigma}_1(t)\sigma_1(t) \\
&= [D_t^{\alpha_1}(\dot{\psi}\dot{\theta}\frac{(I_2 - I_3)}{I_1} - \frac{I_r}{I_1}\Omega_r\dot{\theta} - \frac{K_{f2x}}{I_1}\dot{\phi}^2 + \frac{1}{I_1}\mathcal{U}_2 \\
&\quad + \mathcal{D}_\phi(t) + m_1\dot{E}_\phi(t) + \frac{n_1b_1}{a_1}E_\phi(t)^{(1-\frac{b_1}{a_1})}\dot{E}_\phi(t)]\sigma_1(t) \\
&\quad + \sigma_9(t)[D_t^{\alpha_3}(\dot{\phi}\dot{\psi}\frac{(I_3 - I_1)}{I_2} + \frac{I_r}{I_2}\Omega_r\dot{\phi} - \frac{K_{f2y}}{I_2}\dot{\theta}^2 + \frac{1}{I_2}\mathcal{U}_3 \\
&\quad + \mathcal{D}_\theta(t) + m_3\dot{E}_\theta(t) + \frac{n_3b_3}{a_3}E_\theta(t)^{(1-\frac{b_3}{a_3})}\dot{E}_\theta(t)] \\
&\quad + \sigma_{11}(t)[D_t^{\alpha_5}(\dot{\theta}\frac{(I_1 - I_2)}{I_3} - \frac{K_{f2z}}{I_3}\dot{\psi}^2 + \frac{1}{I_3}\mathcal{U}_4 + \mathcal{D}_\psi(t) \\
&\quad + m_5\dot{E}_\psi(t) + \frac{n_5b_5}{a_5}E_\psi(t)^{(1-\frac{b_5}{a_5})}\dot{E}_\psi(t)].
\end{aligned} \tag{6.22}$$

Substituting the controllers $[\mathcal{U}_2 \ \mathcal{U}_3 \ \mathcal{U}_4]^T$ into (6.22) and using the condition in (6.23),

$$\sigma_j D_j D_t^{\gamma_j} \text{sgn}(\sigma_j) - \sigma_j \delta_j \geq 0. \tag{6.23}$$

Now, \dot{V}_r is represented in an inequality as

$$\dot{V}_r \leq -h_3\sigma_3(t)^2 - h_5\sigma_5(t)^2 - h_1\sigma_1(t)^2 \leq 0. \tag{6.24}$$

□

6.4.2 IFOSMC design structure for UAV systems

6.4.2.1 IFOSMC control for translational systems

In Section 6.4.1, a fractional-order hybrid control method has been studied for the UAV system. Hence, to improve the trajectory tracking performance of the UAV, an improved fractional-order SMC technique will be presented.

Let us introduce the proportional derivative and its derivatives:

$$\sigma_7(t) = k_x E_x(t) + D^{\beta_x+1} E_x(t), \quad (6.25a)$$

$$\sigma_9(t) = k_y E_y(t) + D^{\beta_y+1} E_y(t), \quad (6.25b)$$

$$\sigma_{11}(t) = k_z E_z(t) + D^{\beta_z+1} E_z(t), \quad (6.25c)$$

where k_x , k_y , and k_z are positive parameters and $0 < \beta_x, \beta_y, \beta_z < 1$. We define the time derivative of Eq. (6.25) as

$$\dot{\sigma}_7(t) = k_x \dot{E}_x(t) + D^{\beta_x} \ddot{E}_x(t), \quad (6.26a)$$

$$\dot{\sigma}_9(t) = k_y \dot{E}_y(t) + D^{\beta_y} \ddot{E}_y(t), \quad (6.26b)$$

$$\dot{\sigma}_{11}(t) = k_z \dot{E}_z(t) + D^{\beta_z} \ddot{E}_z(t). \quad (6.26c)$$

Setting $\dot{\sigma}_j(t) = 0$, the control laws of the position without any disturbances can be obtained:

$$k_x \dot{E}_x(t) + D^{\beta_x} \left[\frac{K_{f1x}}{m} \dot{x} + \mathcal{V}_x - \ddot{x}_d \right] = 0, \quad (6.27a)$$

$$k_y \dot{E}_y(t) + D^{\beta_y} \left[\frac{K_{f1y}}{m} \dot{y} + \mathcal{V}_y - \ddot{y}_d \right] = 0, \quad (6.27b)$$

$$k_z \dot{E}_z(t) + D^{\beta_z} \left[\frac{K_{f1z}}{m} \dot{z} - g + \mathcal{V}_z - \ddot{z}_d \right] = 0. \quad (6.27c)$$

Then, the equivalent controllers of the position are given by

$$\mathcal{V}_{eq\mathcal{X}} = -k_x D^{1-\beta_x} E_x(t) - \frac{K_{f1x}}{m} \dot{x} + \ddot{x}_d, \quad (6.28a)$$

$$\mathcal{V}_{eq\mathcal{Y}} = -k_y D^{1-\beta_y} E_y(t) - \frac{K_{f1y}}{m} \dot{y} + \ddot{y}_d, \quad (6.28b)$$

$$\mathcal{V}_{eq\mathcal{Z}} = -k_z D^{1-\beta_z} E_z(t) - \frac{K_{f1z}}{m} \dot{z} + g + \ddot{z}_d. \quad (6.28c)$$

Assumption 6.1. We assume that the disturbances are bounded, with $|\mathcal{D}_j(t)| \leq \delta_k = a_{j0} + a_{j1} |E|_j + a_{j2} |E|_{j+1}$, where δ_k (k denotes translational and

rotational variables) is the maximum bound of the disturbances and a_{j0} , a_{j1} , and a_{j2} are strictly positive parameters.

Switching control laws are considered as follows:

$$\mathcal{V}_{sw\mathcal{X}} = -K_{x1}\sigma_7(t) - (\delta_x + \eta_x)\text{sgn}(\sigma_7(t)), \quad (6.29a)$$

$$\mathcal{V}_{sw\mathcal{Y}} = -K_{y1}\sigma_9(t) - (\delta_y + \eta_y)\text{sgn}(\sigma_9(t)), \quad (6.29b)$$

$$\mathcal{V}_{sw\mathcal{Z}} = -K_{z1}\sigma_{11}(t) - (\delta_z + \eta_z)\text{sgn}(\sigma_{11}(t)), \quad (6.29c)$$

where for $j = x, y, z$, K_{j1} and η_j are positive parameters. Then, the ultimate control laws are formulated as

$$\mathcal{V}_{\mathcal{X}} = -k_x D^{1-\beta_x} E_x(t) - \frac{K_{f1x}}{m} \dot{x} + \ddot{x}_d - K_{x1}\sigma_7(t) - (\delta_x + \eta_x)\text{sgn}(\sigma_7(t)), \quad (6.30a)$$

$$\mathcal{V}_{\mathcal{Y}} = -k_y D^{1-\beta_y} E_y(t) - \frac{K_{f1y}}{m} \dot{y} + \ddot{y}_d - K_{y1}\sigma_9(t) - (\delta_y + \eta_y)\text{sgn}(\sigma_9(t)), \quad (6.30b)$$

$$\mathcal{V}_{\mathcal{Z}} = -k_z D^{1-\beta_z} E_z(t) - \frac{K_{f1z}}{m} \dot{z} + g + \ddot{z}_d - K_{z1}\sigma_{11}(t) - (\delta_z + \eta_z)\text{sgn}(\sigma_{11}(t)). \quad (6.30c)$$

Theorem 6.3. *Using Assumption 6.1 and considering the x -subsystem with the control command $\mathcal{V}_{\mathcal{X}}$, the position is stable asymptotically.*

Proof. Choosing a Lyapunov function as

$$\mathcal{V}_{\Upsilon} = 0.5\sigma_7(t)^2, \quad (6.31)$$

$\dot{\mathcal{V}}_{\Upsilon}$ is calculated as

$$\dot{\mathcal{V}}_{\Upsilon} = \dot{\sigma}_7(t)\sigma_7(t) = \sigma_7(t)[k_x \dot{E}_x(t) + D^{\beta_x}(\frac{K_{f1x}}{m} \dot{x} + \mathcal{V}_{\mathcal{X}} + \mathcal{D}_x(t) - \ddot{x}_d)]. \quad (6.32)$$

By inserting (6.30a), we have

$$\begin{aligned} \dot{\mathcal{V}}_{\Upsilon} &= \sigma_7(t)[D^{\beta_x}\{\mathcal{D}_x(t) - K_{x1}\sigma_7(t) - (\delta_x + \eta_x)\text{sgn}(\sigma_7(t))\}] \\ &\leq \sigma_7(t)[D^{\beta_x}\{-K_{x1}\sigma_7(t) - \eta_x\text{sgn}(\sigma_7(t))\}] \\ &\leq D^{\beta_x}\{-K_{x1}\sigma_7(t)^2 - \eta_x|\sigma_7(t)|\} \\ &\leq -K_{x1}\sigma_7(t)^2 - \eta_x|\sigma_7(t)|. \end{aligned} \quad (6.33)$$

Now, $\mathcal{V}_\Upsilon(t_s)$ (with $\forall t \geq t_0$, $\mathcal{V}_\Upsilon(t_0) \geq 0$) tends to zero in prescribed time t_s , where t_0 refers to the starting time. To get t_s and finish the proof of Theorem 6.3, inequality (6.33) can be reformulated as

$$\dot{\mathcal{V}}_\Upsilon \leq -2K_{x1}\mathcal{V}_\Upsilon - \sqrt{2}\eta_x\mathcal{V}_\Upsilon^{\frac{1}{2}}. \quad (6.34)$$

Dividing (6.34) by $\mathcal{V}_\Upsilon^{\frac{1}{2}}$, we obtain

$$dt \leq -\frac{\mathcal{V}_\Upsilon^{-\frac{1}{2}}}{2K_{x1}\mathcal{V}_\Upsilon^{\frac{1}{2}} + \sqrt{2}\eta_x} d\mathcal{V}_\Upsilon. \quad (6.35)$$

By integrating (6.35) from t_0 to t_s and after a simple calculation, we get

$$t_s - t_0 \leq -\int_{\mathcal{V}_\Upsilon(t_0)}^0 \frac{\mathcal{V}_\Upsilon^{-\frac{1}{2}}}{2K_{x1}\mathcal{V}_\Upsilon^{\frac{1}{2}} + \sqrt{2}\eta_x} d\mathcal{V}_\Upsilon \quad (6.36)$$

$$= \frac{1}{K_{x1}} \ln \frac{2K_{x1}\mathcal{V}_\Upsilon^{\frac{1}{2}}(t_0) + \sqrt{2}\eta_x}{\sqrt{2}\eta_x}. \quad (6.37)$$

□

6.4.2.2 IFOSMC structure for attitude subsystem

An improved FOSMC will be designed for attitude under disturbances. Using the same technique of the position part studied previously, we can define the sliding surfaces and its derivatives:

$$\sigma_1(t) = k_\phi E_\phi(t) + D^{\beta_\phi+1} E_\phi(t), \quad (6.38a)$$

$$\sigma_3(t) = k_\theta E_\theta(t) + D^{\beta_\theta+1} E_\theta(t), \quad (6.38b)$$

$$\sigma_5(t) = k_\psi E_\psi(t) + D^{\beta_\psi+1} E_\psi(t), \quad (6.38c)$$

where k_ϕ , k_θ , and k_ψ are positive constants and $0 < \beta_\phi, \beta_\theta, \beta_\psi < 1$.

We define sliding surface derivatives with respect to time as

$$\dot{\sigma}_3(t) = k_\theta \dot{E}_\theta(t) + D^{\beta_\theta} \ddot{E}_\theta(t), \quad (6.39a)$$

$$\dot{\sigma}_5(t) = k_\psi \dot{E}_\psi(t) + D^{\beta_\psi} \ddot{E}_\psi(t), \quad (6.39b)$$

$$\dot{\sigma}_1(t) = k_\phi \dot{E}_\phi(t) + D^{\beta_\phi} \ddot{E}_\phi(t). \quad (6.39c)$$

Similarly, the control laws \mathcal{U}_2 , \mathcal{U}_3 , and \mathcal{U}_4 are designed in the same manner presented in the previous subsection.

Control inputs for the translational part can be presented as follows:

$$U_2 = \frac{1}{\varepsilon_1} [-k_\phi D^{1-\beta_\phi} E_\phi(t) - \{\dot{\theta} \dot{\psi} \frac{(I_2 - I_3)}{I_1} - \frac{I_r}{I_1} \Omega_r \dot{\theta} - \frac{K_{f2x}}{I_1} \dot{\phi}^2\} + \ddot{\phi}_d - K_{\phi 1} \sigma_1(t) - (\delta_\phi + \eta_\phi) \text{sgn}(\sigma_1(t))], \quad (6.40a)$$

$$U_3 = \frac{1}{\varepsilon_2} [-k_\theta D^{1-\beta_\theta} E_\theta(t) - \{\dot{\phi} \dot{\psi} \frac{(I_3 - I_1)}{I_2} + \frac{I_r}{I_2} \Omega_r \dot{\phi} - \frac{K_{f2y}}{I_2} \dot{\theta}^2\} + \ddot{\theta}_d - K_{\theta 1} \sigma_3(t) - (\delta_\theta + \eta_\theta) \text{sgn}(\sigma_3(t))], \quad (6.40b)$$

$$U_4 = \frac{1}{\varepsilon_3} [-k_\psi D^{1-\beta_\psi} E_\psi(t) - \{\dot{\phi} \dot{\theta} \frac{(I_1 - I_2)}{I_3} - \frac{k_{f2z}}{I_3} \dot{\psi}^2\} \sigma_5(t) + \ddot{\psi}_d - K_{\psi 1} \sigma_5(t) - (\delta_\psi + \eta_\psi) \text{sgn}(\sigma_5(t))], \quad (6.40c)$$

where k_ϕ , k_θ , k_ψ , $K_{\phi 1}$, $K_{\theta 1}$, and $K_{\psi 1}$ are positive parameters and $0 < \beta_\phi, \beta_\theta, \beta_\psi < 1$.

Theorem 6.4. *The control laws obtained by the proposed FOSMC technique guarantee UAV stability.*

Proof. A Lyapunov function can be considered as

$$\begin{aligned} \mathcal{V}_T &= \frac{1}{2} [\mathcal{V}_x + \mathcal{V}_y + \mathcal{V}_z + \mathcal{V}_\phi + \mathcal{V}_\theta + \mathcal{V}_\psi] \\ &= \frac{1}{2} [\sigma_1(t)^2 + \sigma_3(t)^2 + \sigma_5(t)^2 + \sigma_7(t)^2 + \sigma_9(t)^2 + \sigma_{11}(t)^2]. \end{aligned} \quad (6.41)$$

Then $\dot{\mathcal{V}}_T$ is

$$\dot{\mathcal{V}}_T = \dot{\sigma}_5(t) \sigma_5(t) + \dot{\sigma}_9(t) \sigma_9(t) + \dot{\sigma}_3(t) \sigma_3(t) + \dot{\sigma}_{11}(t) \sigma_{11}(t) + \dot{\sigma}_1(t) \sigma_1(t). \quad (6.42)$$

After a simple calculus and using (6.33), the previous inequality can be rewritten as

$$\begin{aligned} \dot{\mathcal{V}}_T &\leq -K_{x1} \sigma_7(t)^2 - \eta_x |\sigma_7(t)| - K_{y1} \sigma_9(t)^2 - \eta_y |\sigma_9(t)| \\ &\quad - K_{z1} \sigma_{11}(t)^2 - \eta_z |\sigma_{11}(t)| - K_{\phi 1} \sigma_1(t)^2 - \eta_\phi |\sigma_1(t)| \\ &\quad - K_{\theta 1} \sigma_3(t)^2 - \eta_\theta |\sigma_3(t)| - K_{\psi 1} \sigma_5(t)^2 - \eta_\psi |\sigma_5(t)| \\ &\leq 0. \end{aligned} \quad (6.43)$$

As a result $\dot{\mathcal{V}}_T$ is nonincreasing. \square

Table 6.1 Quadrotor model parameters.

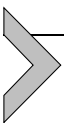
Parameter	Value	Parameter	Value
g (m/s^2)	9.81	K_{f1y} ($N/m/s$)	5.5670e-4
m (kg)	0.486	K_{f1z} ($N/m/s$)	5.5670e-4
I_1 ($kg.m^2$)	3.827e-3	K_{f2x} ($N/rad/s$)	5.5670e-4
I_2 ($kg.m^2$)	3.827e-3	K_{f2y} ($N/rad/s$)	5.5670e-4
I_3 ($kg.m^2$)	7.6566e-3	K_{f2z} ($N/rad/s$)	5.5670e-4
I_r ($kg.m^2$)	2.8385e-5	b ($N.s^2$)	2.9842e-3
K_{f1x} ($N/m/s$)	5.5670e-4	k ($N.m.s^2$)	3.2320e-2

Table 6.2 Parameters of FOSMC-FOFTSMC controller.

Parameter	Value	Parameter	Value
D_j ($j = 1, 3, 5$)	96.14	m_j	6.8
n_j	20.22	b_j	3.85
a_j	3.77	h_j	12.55
γ_j	0.385	α_j	8.86e-4
λ_n ($n = x, y, z$)	4	ε_j	4
h_i ($i = 7, 9, 11$)	1	γ_i	0.02

Table 6.3 Parameters of the IFOSMC controller.

Parameter	Value	Parameter	Value
$a_{\psi,\theta,\phi}$	0.4	$a_{z,y,x}$	0.42
$\beta_{z,y,x}$	0.01	$\beta_{\psi,\theta,\phi}$	0.01
$k_{z,y,x}$	15	$k_{\psi,\theta,\phi}$	22.7146
$K_{z1,y1,x1}$	4	$K_{\phi1,\theta1,\psi1}$	45.8990
η	0.5	-	-



6.5. Simulation results and discussion

Two simulations are conducted in this section using MATLAB[®] software. Robustness of the fractional-order control methods is checked under disturbances and parametric uncertainties. The first simulation is conducted to show the trajectory tracking of the FOFTSMC whereas the second simulation is conducted to compare the performances of the FOFTSMC and IFOSMC methods. Numerical simulations are conducted by using the quadrotor parameters presented in Table 6.1. Controller parameters for FOSMC-FOFTSMC and IFOSMC are presented respectively in Table 6.2 and Table 6.3.

Remark 6.1. To alleviate the chattering, discontinuous term in the fractional-order controllers is replaced by the hyperbolic tangent function.

6.5.1 Simulation 1

The desired yaw and position used in this simulation are given by

$$x_d = \begin{cases} 0.6 \text{ m} & \text{if } t \leq 10 \text{ or } t > 30, \\ 0.3 \text{ m} & \text{otherwise,} \end{cases} \quad (6.44)$$

$$\gamma_d = \begin{cases} 0.6 \text{ m} & \text{if } t \leq 20 \text{ or } t > 40, \\ 0.3 \text{ m} & \text{otherwise,} \end{cases} \quad (6.45)$$

$$z_d = \begin{cases} 0.6 \text{ m} & \text{if } t \leq 50, \\ 0 \text{ m} & \text{otherwise,} \end{cases} \quad \psi_d = 0.1 \text{ rad.} \quad (6.46)$$

The disturbances used in this part are given by

$$\mathcal{D}_\eta(t)|_{\eta=x,y,z} = \begin{cases} \frac{1}{2} \sin(\frac{1}{2}t) + \frac{1}{2} \cos(0.7t) \frac{m}{s^2}, \\ \text{if } t \leq 10 \text{ and } t \leq 50, \\ 0 \frac{m}{s^2} & \text{otherwise,} \end{cases} \quad (6.47)$$

$$\begin{cases} \mathcal{D}_\phi(t) = \frac{1}{2} \cos(0.4t) \frac{rad}{s^2}, \\ \mathcal{D}_\theta(t) = \frac{1}{2} \sin(\frac{1}{2}t) \frac{rad}{s^2}, \\ \mathcal{D}_\psi(t) = \frac{1}{2} \sin(0.7t) \frac{rad}{s^2}. \end{cases} \quad (6.48)$$

The efficiency of FOSMC-FOFTSMC is evaluated by introducing uncertainties in the model. The UAV parameters can vary up to $\pm 50\%$ more than their normal values.

The attitude and position results are shown in Figs. 6.3–6.5. We can observe that the fractional-order controller drives variables to follow desired references under disturbances/uncertainties. From these results, we conclude that the steady-state errors converge to zero in finite time. Moreover, in the case where the environment becomes more disturbed and uncertain, the fractional-order controller steer pitch and yaw and roll angles follow

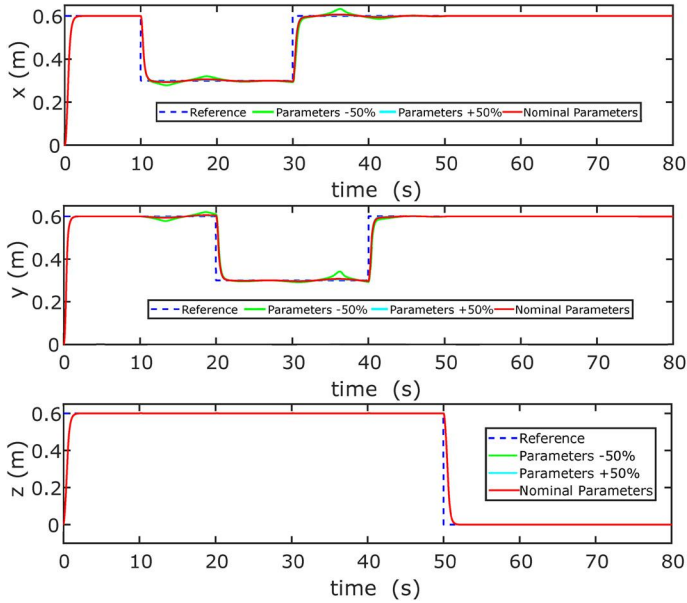


Figure 6.3 Position (x, y, z).

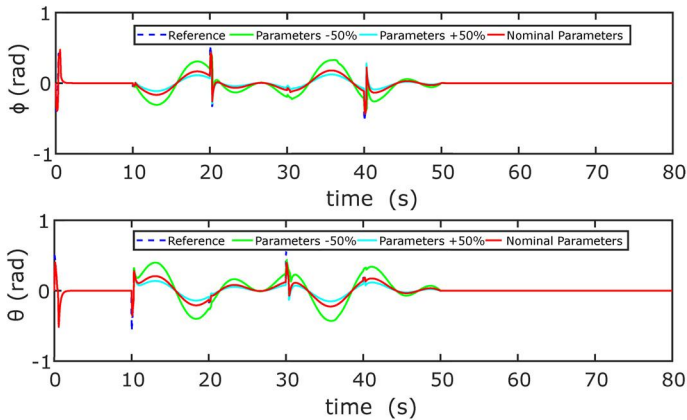


Figure 6.4 Roll and pitch angles.

their angles with excellent tracking performance. The result in 3D space of trajectory tracking is shown in Fig. 6.6. We observe that the fractional-order controller steers the UAV system with high performance.

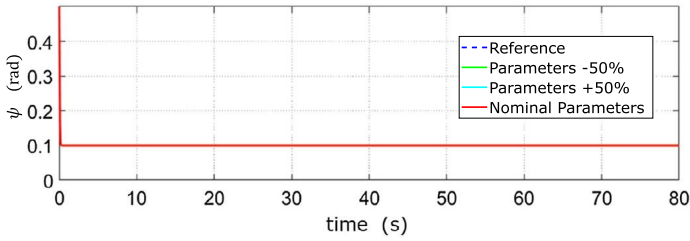


Figure 6.5 Yaw angle.

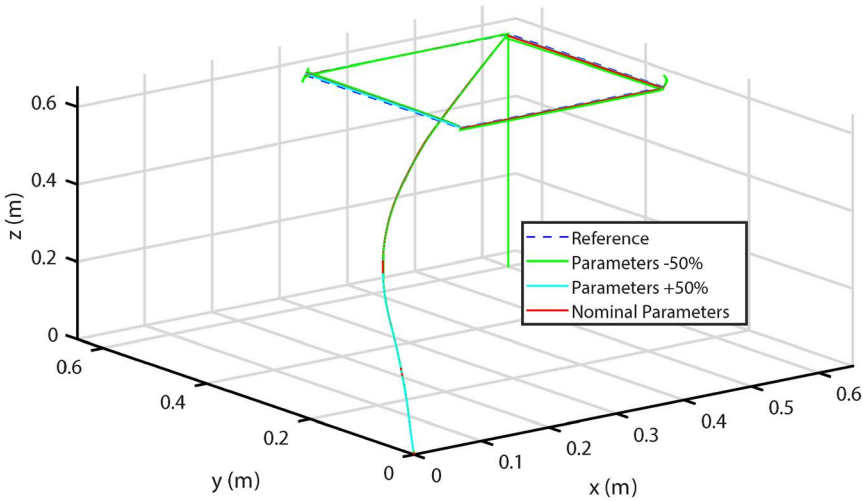


Figure 6.6 3D trajectory plot.

6.5.2 Simulation 2

In this subsection, a second numerical simulation test will be conducted to test the theoretical results obtained from the proposed fractional-order controllers. In the first step, the desired trajectory is the following:

$$x_d = \cos(t)m, \quad y_d = \sin(t)m, \quad z_d = \frac{1}{2}t + \frac{1}{2}m, \quad \psi_d = 0 \text{ rad.} \quad (6.49)$$

Initial conditions of the UAV are given as $[\frac{1}{2}, 0, 0]$ m and $[0, 0, 0.1]$ rad. In the third step, the obtained results will be discussed. The results of the IFOSMC and FOSMC-FOFTSMC are shown in Figs. 6.7–6.11. Fractional-order controllers have been successfully implemented in the system, thus a better performance in term of trajectory tracking has been

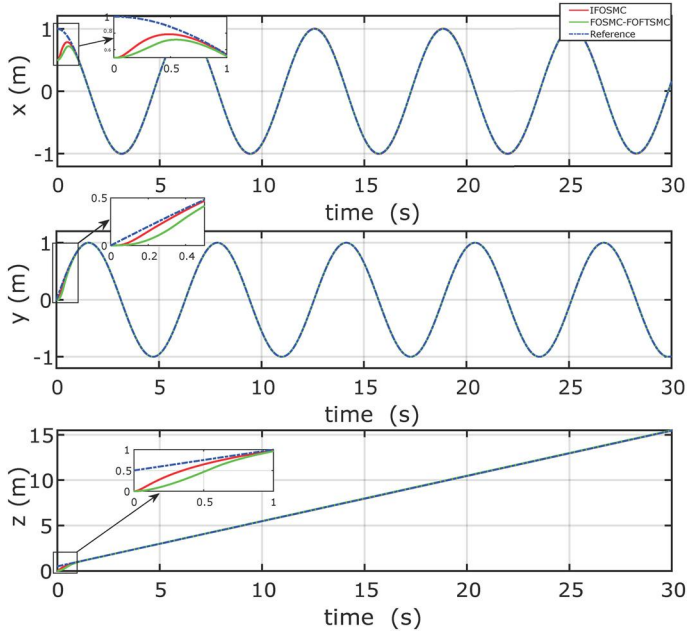


Figure 6.7 Position tracking.

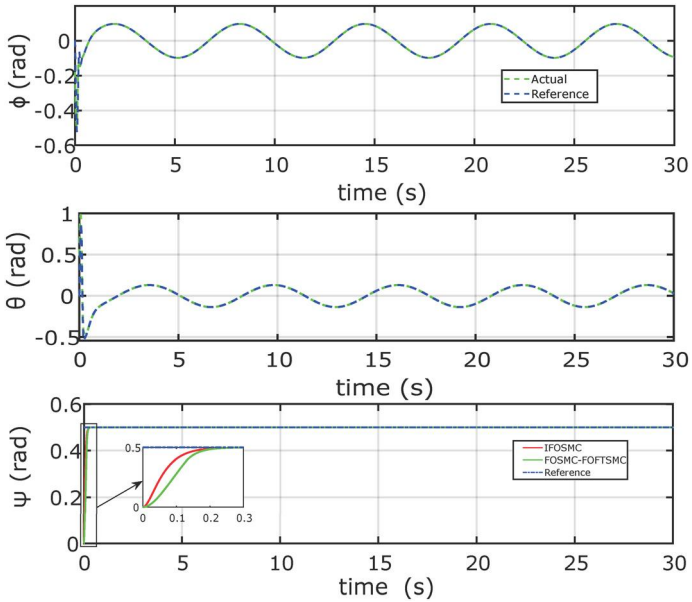


Figure 6.8 Euler angles.

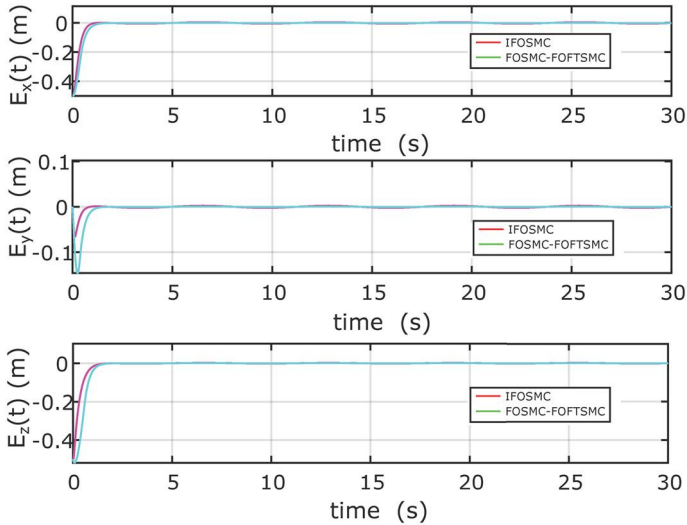
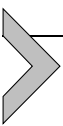


Figure 6.9 Tracking errors.

achieved even in the presence of uncertain disturbances. The responses of the position are plotted in Fig. 6.7. It can be seen that the drone efficiently tracks the reference commands with high accuracy. Fig. 6.8 shows the roll, pitch, and yaw tracking performances. It can be seen from the obtained results of IFOSMC and FOSMC-FOFTSMC presented in Fig. 6.8 that the Euler angles follow their reference values. Fig. 6.9 shows the errors tracking of IFOSMC and FOSMC-FOFTSMC; actually these errors converge to their nominal values despite the effects of disturbances. The signal inputs are plotted in Fig. 6.10. These inputs are smooth and converge to their values.

The result of the flight trajectory in 3D is plotted in Fig. 6.11.

We can capture from these results that the IFOSMC outperforms the FOSMC-FOFTSMC at the startup of the simulation (more perturbations occur during this phase).



6.6. Conclusion

Due to external disturbances/uncertainties being a problem found in control system, in this chapter the design of two fractional-order control laws is proposed for the stabilization of a quadrotor subjected to disturbances/uncertainties. The SMC combined with fractional controller shows

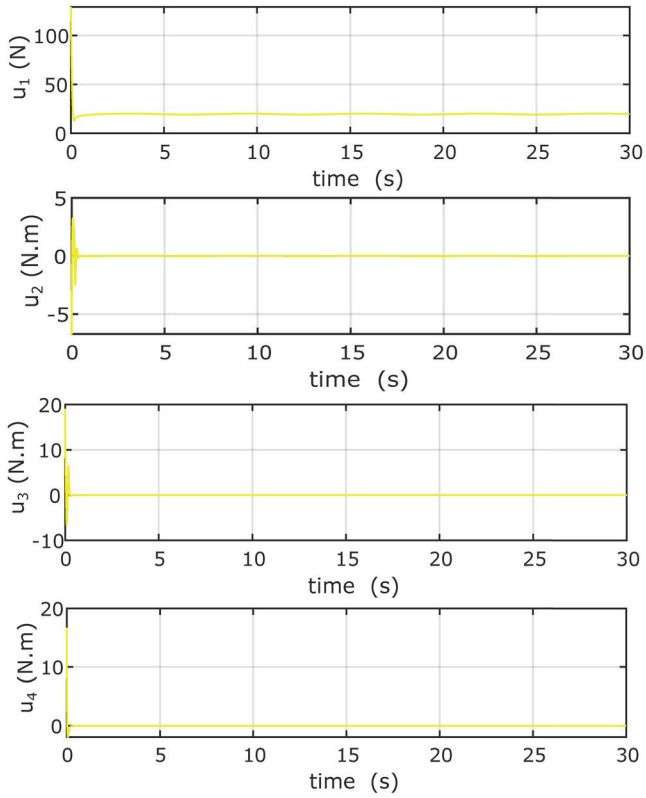


Figure 6.10 Control signals.

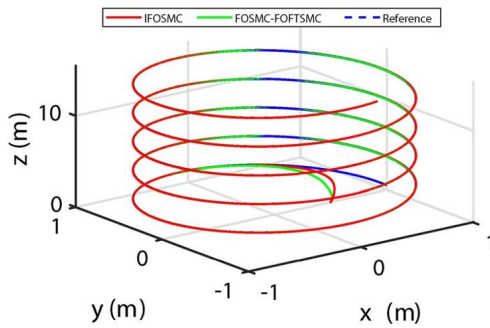


Figure 6.11 Desired 3D trajectory tracking.

a strong response in terms of compensating and rejecting external disturbances. Suitable sliding surfaces based on fractional operators were designed to derive efficient control laws. The obtained results confirm the robustness of the proposed fractional-order controllers, which show that the improved FOSMC with a new switching control law is more robust compared to the FOSMC-FOFTSMC proposed in this chapter.

As a future direction, the implementations of these fractional-order controllers could be considered, to validate controllers in real-time.

References

- [1] S. Abdelhay, A. Zakriti, Modeling of a quadcopter trajectory tracking system using PID controller, *Procedia Manufacturing* 32 (2019) 564–571, <https://doi.org/10.1016/j.promfg.2019.02.253>.
- [2] A. Ailon, S. Arogeti, Closed-form nonlinear tracking controllers for quadrotors with model and input generator uncertainties, *Automatica* 54 (2015) 317–324, <https://doi.org/10.1016/j.automatica.2015.02.020>.
- [3] K. Alexis, G. Nikolakopoulos, A. Tzes, On trajectory tracking model predictive control of an unmanned quadrotor helicopter subject to aerodynamic disturbances, *Asian Journal of Control* 16 (2012) 209–224, <https://doi.org/10.1002/asjc.587>.
- [4] U. Ansari, A.H. Bajodah, M.T. Hamayun, Quadrotor control via robust generalized dynamic inversion and adaptive non-singular terminal sliding mode, *Asian Journal of Control* 21 (2018) 1237–1249, <https://doi.org/10.1002/asjc.1800>.
- [5] G. Antonelli, E. Cataldi, F. Arrichiello, P.R. Giordano, S. Chiaverini, A. Franchi, Adaptive trajectory tracking for quadrotor MAVs in presence of parameter uncertainties and external disturbances, *IEEE Transactions on Control Systems Technology* 26 (2018) 248–254, <https://doi.org/10.1109/tcst.2017.2650679>.
- [6] D. Cabecinhas, R. Cunha, C. Silvestre, A nonlinear quadrotor trajectory tracking controller with disturbance rejection, *Control Engineering Practice* 26 (2014) 1–10, <https://doi.org/10.1016/j.conengprac.2013.12.017>.
- [7] D. Cabecinhas, R. Cunha, C. Silvestre, A globally stabilizing path following controller for rotorcraft with wind disturbance rejection, *IEEE Transactions on Control Systems Technology* 23 (2015) 708–714, <https://doi.org/10.1109/tcst.2014.2326820>.
- [8] F. Chen, W. Lei, K. Zhang, G. Tao, B. Jiang, A novel nonlinear resilient control for a quadrotor UAV via backstepping control and nonlinear disturbance observer, *Nonlinear Dynamics* 85 (2016) 1281–1295, <https://doi.org/10.1007/s11071-016-2760-y>.
- [9] F. Chen, F. Lu, B. Jiang, G. Tao, Adaptive compensation control of the quadrotor helicopter using quantum information technology and disturbance observer, *Journal of the Franklin Institute* 351 (2014) 442–455, <https://doi.org/10.1016/j.jfranklin.2013.09.009>.
- [10] A. Chovancová, T. Fico, L. Chovanec, P. Hubinský, Mathematical modelling and parameter identification of quadrotor (a survey), *Procedia Engineering* 96 (2014) 172–181, <https://doi.org/10.1016/j.proeng.2014.12.139>.
- [11] P. Corke, Representing position and orientation, in: *Robotics, Vision and Control: Fundamental Algorithms in MATLAB®*, Springer Berlin Heidelberg, Berlin, Heidelberg, 2011, pp. 15–41, https://doi.org/10.1007/978-3-642-20144-8_2.
- [12] S. Das, *Functional Fractional Calculus for System Identification and Controls*, Springer-Verlag, Heidelberg, 2008.
- [13] W. Dong, G.-Y. Gu, X. Zhu, H. Ding, A high-performance flight control approach for quadrotors using a modified active disturbance rejection technique, *Robotics and*

- Autonomous Systems 83 (2016) 177–187, <https://doi.org/10.1016/j.robot.2016.05.005>.
- [14] Y. El Houm, A. Abbou, A. Mousmi, Quadcopter modelling, control design and PIL verification based on DSP F28377s, in: 2017 International Renewable and Sustainable Energy Conference (IRSEC), IEEE, 2017, pp. 1–7.
 - [15] Y. El Houm, A. Abbou, A. Mousmi, M. Labbadi, Quadcopter attitude stabilization in a gyroscopic testbench, in: International Conference Europe Middle East & North Africa Information Systems and Technologies to Support Learning, Springer, 2019, pp. 621–630.
 - [16] A. Gonzalez, V. Balaguer, P. Garcia, A. Cuenca, Gain-scheduled predictive extended state observer for time-varying delays systems with mismatched disturbances, ISA Transactions 84 (2019) 206–213, <https://doi.org/10.1016/j.isatra.2018.09.024>.
 - [17] C. Hua, J. Chen, X. Guan, Adaptive prescribed performance control of QUAVs with unknown time-varying payload and wind gust disturbance, Journal of the Franklin Institute 355 (2018) 6323–6338, <https://doi.org/10.1016/j.jfranklin.2018.05.062>.
 - [18] M. Labbadi, Y. Boukal, M. Cherkaoui, Path following control of quadrotor UAV with continuous fractional-order super twisting sliding mode, Journal of Intelligent & Robotic Systems (2020) 1–23.
 - [19] M. Labbadi, M. Cherkaoui, Robust adaptive backstepping fast terminal sliding mode controller for uncertain quadrotor UAV, Aerospace Science and Technology 93 (2019) 105306.
 - [20] M. Labbadi, M. Cherkaoui, Robust adaptive nonsingular fast terminal sliding-mode tracking control for an uncertain quadrotor UAV subjected to disturbances, ISA Transactions 99 (2020) 290–304.
 - [21] M. Labbadi, M. Cherkaoui, Y. El Houm, M. Guisser, A comparative analysis of control strategies for stabilizing a quadrotor, in: International Conference Europe Middle East & North Africa Information Systems and Technologies to Support Learning, Springer, 2018, pp. 625–630.
 - [22] M. Labbadi, M. Cherkaoui, M. Guisser, et al., Modeling and robust integral sliding mode control for a quadrotor unmanned aerial vehicle, in: 2018 6th International Renewable and Sustainable Energy Conference (IRSEC), IEEE, 2018, pp. 1–6.
 - [23] T. Li, Y. Zhang, B.W. Gordon, Passive and active nonlinear fault-tolerant control of a quadrotor unmanned aerial vehicle based on the sliding mode control technique, Proceedings of the Institution of Mechanical Engineers. Part I, Journal of Systems and Control Engineering 227 (2012) 12–23, <https://doi.org/10.1177/0959651812455293>.
 - [24] Z. Li, X. Ma, Y. Li, Robust tracking control strategy for a quadrotor using RPD-SMC and RISE, Neurocomputing 331 (2019) 312–322, <https://doi.org/10.1016/j.neucom.2018.11.070>.
 - [25] D. Ma, Y. Xia, G. Shen, Z. Jia, T. Li, Flatness-based adaptive sliding mode tracking control for a quadrotor with disturbances, Journal of the Franklin Institute 355 (2018) 6300–6322, <https://doi.org/10.1016/j.jfranklin.2018.06.018>.
 - [26] A. Modirrousta, M. Khodabandeh, A novel nonlinear hybrid controller design for an uncertain quadrotor with disturbances, Aerospace Science and Technology 45 (2015) 294–308, <https://doi.org/10.1016/j.ast.2015.05.022>.
 - [27] I. Podlubny, Fractional Differential Equations, Academic, New York, 1999.
 - [28] I. Podlubny, Geometric and physical interpretation of fractional integration and fractional differentiation, Fractional Calculus and Applied Analysis 5 (2002) 367–386.
 - [29] L. Qin, X. He, R. Yan, R. Deng, D. Zhou, Distributed sensor fault diagnosis for a formation of multi-vehicle systems, Journal of the Franklin Institute 356 (2019) 791–818, <https://doi.org/10.1016/j.jfranklin.2017.11.020>.
 - [30] G.V. Raffo, M.G. Ortega, F.R. Rubio, An integral predictive/nonlinear H_∞ control structure for a quadrotor helicopter, Automatica 46 (2010) 29–39.

- [31] X. Shao, N. Liu, J. Liu, H. Wang, Model-assisted extended state observer and dynamic surface control-based trajectory tracking for quadrotors via output-feedback mechanism, *International Journal of Robust and Nonlinear Control* 28 (2018) 2404–2423, <https://doi.org/10.1002/rnc.4023>.
- [32] L. Wang, H. Jia, The trajectory tracking problem of quadrotor UAV: global stability analysis and control design based on the cascade theory, *Asian Journal of Control* 16 (2013) 574–588, <https://doi.org/10.1002/asjc.746>.
- [33] L. Wang, J. Su, Robust disturbance rejection control for attitude tracking of an aircraft, *IEEE Transactions on Control Systems Technology* 23 (2015) 2361–2368, <https://doi.org/10.1109/tcst.2015.2398811>.
- [34] R. Wang, J. Liu, Trajectory tracking control of a 6-DOF quadrotor UAV with input saturation via backstepping, *Journal of the Franklin Institute* 355 (2018) 3288–3309, <https://doi.org/10.1016/j.jfranklin.2018.01.039>.
- [35] H. Yang, L. Cheng, Y. Xia, Y. Yuan, Active disturbance rejection attitude control for a dual closed-loop quadrotor under gust wind, *IEEE Transactions on Control Systems Technology* 26 (2018) 1400–1405, <https://doi.org/10.1109/tcst.2017.2710951>.
- [36] J. Zhang, D. Gu, Z. Ren, B. Wen, Robust trajectory tracking controller for quadrotor helicopter based on a novel composite control scheme, *Aerospace Science and Technology* 85 (2019) 199–215, <https://doi.org/10.1016/j.ast.2018.12.013>.
- [37] Y. Zhang, Z. Chen, X. Zhang, Q. Sun, M. Sun, A novel control scheme for quadrotor UAV based upon active disturbance rejection control, *Aerospace Science and Technology* 79 (2018) 601–609, <https://doi.org/10.1016/j.ast.2018.06.017>.
- [38] Y. Zou, Nonlinear robust adaptive hierarchical sliding mode control approach for quadrotors, *International Journal of Robust and Nonlinear Control* 27 (2016) 925–941, <https://doi.org/10.1002/rnc.3607>.
- [39] Y. Zou, B. Zhu, Adaptive trajectory tracking controller for quadrotor systems subject to parametric uncertainties, *Journal of the Franklin Institute* 354 (2017) 6724–6746, <https://doi.org/10.1016/j.jfranklin.2017.08.027>.

Performance evaluation of fractional character vector control applied for doubly fed induction generator operating in a network-connected wind power system

Abdellatif Kasbi and Abderrafii Rahali

Laboratory of Optics, Information Processing, Mechanics, Energy and Electronics, Faculty of Sciences, Moulay Ismail University, Meknes, Morocco

7.1. Introduction

Wind power is derived by capturing kinetic energy from moving air masses and converting it into electric power, which is one of the alternative renewable energies to the conventional energy that relies on fossil fuels. In accordance with the statistics provided by the Global Wind Energy Council (GWEC) [13], the global cumulative installed capacity for wind-powered electricity has increased exponentially in the recent years; from around 539.7 GW at the end of 2017, this grew by 51.3 GW in 2018 and by 71.97 GW in 2019, which brings the total to 663 GW at the end of 2019, and it will reach a capacity of around 925 GW in 2023.

The growth of the wind energy capacity installed worldwide is due to the technological progress in wind power systems (WPSs) over the past few years. Modern WPSs with a doubly fed induction generator (DFIG) are the most dominant prototype technology in the present wind energy industry because of their many benefits, which include the ability to operate in the variable-speed mode allowing to maximize the output real power for different values of wind speed and consequently reach a higher aerodynamic efficiency, as well as the flexibility concerning reactive power control, including the reduced size of the back-to-back static converters due to the fact that a size with a capacitance of only 30% of the rated generator power is sufficient [1]. This achieves a smoother connec-

tion to the network, allows minimizing the energy losses, and makes the aero-generator cheaper, lighter, and more efficient, offering higher power quality. Moreover, these modern technologies are more controllable where the reactive and real powers can be controlled separately, which makes this aero-generator equipped with DFIG a competitive option in terms of network compatibility [1,4]. Moreover, with an appropriate control scheme, the mechanical stress and aerodynamic noise can be reduced on these variable-speed aero-generators through absorbing the natural fluctuations of wind energy [18]. Therefore, it is very interesting to have a robust and achievable control scheme to control the DFIG in wind power applications.

According to the research literature, vector control is an attractive method gaining popularity for variable-speed aero-generators control because of its advantages such as easy implementation and guaranteed decoupled regulation of reactive and real powers [17,28]. Additionally, it is possible to adopt and combine this control approach with different structure of controllers, from the usual proportional integral (PI) to more advanced modern controllers. Vector control based on PI controllers, also known as classical vector control (CVC), is well known and very commonly applied to control aero-generators equipped with DFIG because of its mere structure and acceptable performance [2,6,11,14]. However, this classical control scheme suffers from performance deterioration and produces a response not desirable in situations where the wind system experiences DFIG machine parameter uncertainties as well as network voltage faults [3,7]. Aiming at overcoming the performance limitations of the CVC scheme, several techniques and methods have been reported in a number of research papers. As discussed in [2], a multiobjective PSO algorithm is suggested for application to the dynamic model of the DFIG WPS. Authors of Ref. [3] have modified the vector control scheme by injecting additional voltage terms to rotor voltage references in order to enhance the transient behavior of the control system intended for a DFIG wind turbine. In [6], the root tree optimization algorithm was used to adjust the gains of the PI controller in order to avoid chattering phenomena in reactive and real powers produced by DFIG. In [15], a robust backstepping control strategy for power flow control of DFIG-based wind turbines in network-connected mode was designed. Maximum power point tracking (MPPT) based on a fuzzy logic approach for the DFIG wind turbine system was reported in [5]. An overall control scheme based on sliding mode for generator side converter and network side converter control to operate a DFIG-based wind turbine was presented in [7,22].

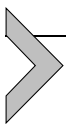
In recent years, the fractional-order control approach has become an interesting research field because it emerged as a very adequate and competent control technique for the installations experiencing parametric uncertainties and outside disturbances [23,26,29]. The main advantage of considering fractional calculus in control system design is that it provides extra degrees of freedom. Hence, fractional-character control systems can be formulated to achieve an optimal dynamic response. Moreover, a higher grade of robustness can appear in the control scheme through considering a broad range of parameter values of the system. In [26], the significant advantages that characterize the application of fractional-order control are briefly illustrated. In this context, the possibility of overcoming the performance limitations of PID controllers through utilizing the theory of fractional calculus has resulted in remarkable interest in fractional-order PID (FO-PID) controllers, denoted with the form $PI^\delta D^\mu$, in which δ and μ are the orders of integration and derivative, which can take any value between 0 and 2.

The new controller family (FO-PID) introduced by Podlubny [25] as a generalization to the integer-order PID controllers is characterized by five dimensions, such as extending the orders of integration and derivative to include fractional numbers instead of being limited to integer ones, i.e., two additional dimensions are created, which gives more flexibility in reaching control goals. Indeed, due to considering the two extra dimensions (δ and μ) in FOPI controller design in comparison with the integer PID controllers, better regulation has been achieved [8–10]. One of the particular FO-PID controllers is fractional-order PI (FOPI), which has been described by the irrational transfer function of $k_p + (k_i/s^\delta)$, where k_p , k_i , δ , and s denote proportional gain, integral gain, the fractional order, and the Laplace variable, respectively.

Due to the flexibility in designing FOPI controllers, several authors have been motivated to study the control of dynamic processes by using these fractional controllers for different applications in industry and engineering around the world [8,19,27]. Recently, FOPI control has been considered in pitch angle regulation loops, which are used to manage the wind speeds higher than that corresponding to the rated power, for enhancing the performance of WPSs at high wind speeds [21]. Most of the previously mentioned researches, which are performed in various fields, confirm that the FOPI controllers outperform the integer-order ones in terms of disturbance rejection, system stabilization, and reference tracking for a vast gamut of parameter values.

In this direction, in this chapter we propose a fractional-character vector control scheme to regulate a network-connected mode DFIG employed in wind power generation. It is an improved vector control scheme based on the use of FOPI controllers in the power and rotor current regulation loops. It results in a more flexible control scheme, using PI controllers which have a fractional character, which allows us to control the DFIG more accurately than the integer-order PI controllers. Different functioning conditions are considered to prove the efficacy and feasibility of the fractional vector control (FVC) scheme. The generator is controlled such that a DFIG wind turbine is able to realize MPPT at each wind speed in order to extract the optimum power from wind energy, even in the presence the uncertainties in the network voltage or in the system parameters. The WPS performance obtained by using FVC is compared to the one obtained using CVC, and simulation results show that the functioning and the productivity of the WPS are better under the proposed fractional-character vector control than under standard vector control.

The chapter is composed from six sections organized as follows. A concise introduction is provided in Section 7.1. Section 7.2 introduces the mathematical modeling of studied variable-speed WPSs, the wind turbine, and the DFIG. It also describes the MPPT scheme that allows the blades to extract maximum power from the wind. Section 7.3 describes the fractional-character vector control based on FOPI controllers. The design of FOPI controllers applied in power and rotor current regulation loops is presented in Section 7.4. In Section 7.5, numerical results will be presented and analyzed to evaluate the performance and validate the efficacy of the proposed scheme compared with the classical scheme. Section 7.6 includes the conclusion.



7.2. Variable-speed wind power system modeling

The studied topology of the WPS equipped with a DFIG in network-connected mode is illustrated in Fig. 7.1, where the rotor shaft of the DFIG is connected to the shaft turbine via a gearbox for multiplying the turbine speed and transmitting it to the generator shaft. Kinetic energy of the air masses is extracted and converted into mechanical power across the turbine blades, and then the DFIG converts it into electrical power. The generated power at the stator circuit level is directly transmitted to the network, whereas the power exchange between the rotor circuit and network is carried out through the electronic component-based static power converter

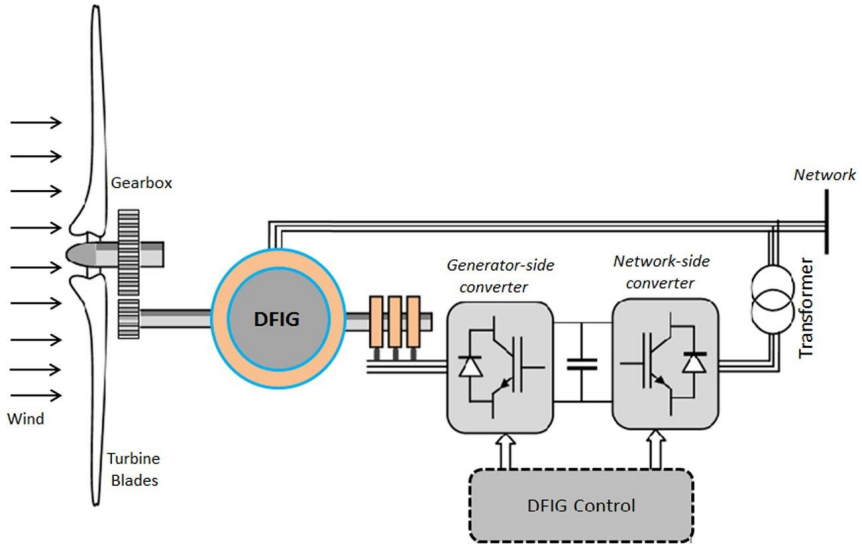


Figure 7.1 Variable-speed wind power system based on DFIG.

block, which consists of a network-side converter and a generator-side converter with a DC link capacitor between them [31].

7.2.1 Wind turbine modeling

The extracted aerodynamic power from the kinetic energy of moving air masses by turbine blades is expressed as follows [4,16]:

$$P_{extracted} = 0.5\rho_{air}\pi R^2 C_p(\lambda, \beta) v^3, \quad (7.1)$$

where ρ_{air} [kg/m³], R [m], v [$\frac{m}{s}$], and $C_p(\lambda, \beta)$ denote respectively air density, blade length, wind speed, and the turbine aerodynamic efficiency, which is a function of the blade pitch angle β [deg] and the tip-speed ratio (TSR) λ . The expression used to describe the turbine efficiency is [16]:

$$\begin{cases} C_p(\lambda, \beta) = 0.5176 \left(\frac{116}{\lambda_i} - 0.4\beta - 5 \right) \exp\left(\frac{21}{\lambda_i}\right) + 0.0068\lambda, \\ \frac{1}{\lambda_i} = \frac{1}{\lambda + 0.08\beta} - \frac{0.035}{\beta^3 + 1}. \end{cases} \quad (7.2)$$

The TSR is defined as the ratio of the blade's extremity's linear speed to the wind speed. It is expressed as follows:

$$\lambda = \frac{\Omega_t \cdot R}{v}. \quad (7.3)$$

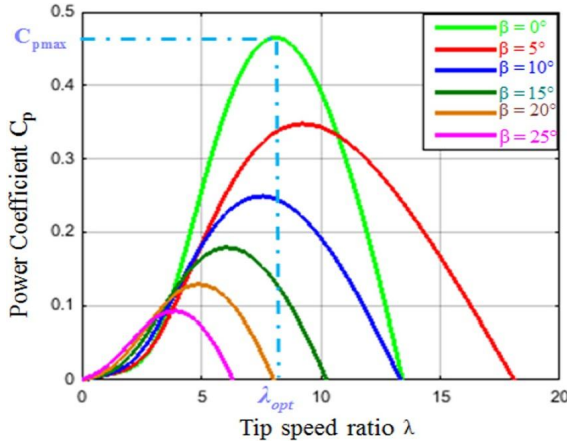


Figure 7.2 Aerodynamic efficiency (C_p) vs. tip-speed ratio (λ).

In (7.3) Ω_t [rad/s] denotes the shaft turbine speed.

The aerodynamic torque exerted on the turbine shaft is expressed as follows:

$$C_{aer} = \frac{P_{extracted}}{\Omega_t} = \frac{0.5\rho_{air}\pi R^3}{\Omega_t} C_p(\lambda, \beta) v^3. \quad (7.4)$$

The turbine characteristic coefficient C_p as a function of the TSR for different values of the pitch angle is illustrated in Fig. 7.2. It can be found that maximum aerodynamic efficiency $C_{p-max} = 0.48$ is obtained at optimal TSR $\lambda_{opt} = 8.1$ when the collective pitch angle equals zero degrees. In subrated functioning conditions, TSR and pitch angle have to be set at their optimal values $\lambda = 8.1$ and $\beta = 0$ degrees, respectively, to operate the variable-speed WPS at maximum power, which corresponds to the maximum value of the aerodynamic efficiency $C_{p-max} = 0.48$. This is achieved by changing the shaft rotor speed appropriately with the wind speed following relationship (7.3).

7.2.2 Dynamic modeling of DFIGs

The machine used in the conversion of wind power is the DFIG. The dynamic model of this generator in a (d, q) mobile reference frame may be expressed by the following equations [1,6,28].

The stator circuit voltages are given as follows:

$$\begin{cases} V_{sd} = R_s I_{sd} + \frac{d\varphi_{sd}}{dt} - \omega_s \varphi_{sq}, \\ V_{sq} = R_s I_{sq} + \frac{d\varphi_{sq}}{dt} + \omega_s \varphi_{sd}. \end{cases} \quad (7.5)$$

The stator circuit fluxes are given as follows:

$$\begin{cases} \varphi_{sd} = L_s I_{sd} + L_m I_{rd}, \\ \varphi_{sq} = L_s I_{sq} + L_m I_{rq}. \end{cases} \quad (7.6)$$

The rotor circuit voltages are given as follows:

$$\begin{cases} V_{rd} = R_r I_{rd} + \frac{d\varphi_{rd}}{dt} - (\omega_s - \omega) \varphi_{rq}, \\ V_{rq} = R_r I_{rq} + \frac{d\varphi_{rq}}{dt} + (\omega_s - \omega) \varphi_{rd}. \end{cases} \quad (7.7)$$

The rotor circuit fluxes are given as follows:

$$\begin{cases} \varphi_{rd} = L_m I_{sd} + L_r I_{rd}, \\ \varphi_{rq} = L_m I_{sq} + L_r I_{rq}. \end{cases} \quad (7.8)$$

The torque produced by the DFIG is defined by the following equation:

$$C_{em} = \frac{3}{2} \frac{pL_m}{L_s} (I_{sq}\varphi_{sd} - I_{sd}\varphi_{sq}). \quad (7.9)$$

By applying the fundamental principle of dynamics to the rotor shaft, one has

$$J \frac{d\Omega_m}{dt} = C_g - C_{em} - f_v \Omega_m. \quad (7.10)$$

The expressions of real and reactive power of the DFIG are written as follows:

$$\begin{cases} P_s = \frac{3}{2} (V_{sd} I_{sd} + V_{sq} I_{sq}), \\ Q_s = \frac{3}{2} (V_{sq} I_{sd} - V_{sd} I_{sq}). \end{cases} \quad (7.11)$$

7.2.3 Maximum power point tracking law

Due to the highly fluctuating and random nature of the wind speed, the utmost power extraction is important in the case of a variable-speed WPS since it increases its energy efficiency. For each wind speed value lower than that corresponding to the nominal power, it is necessary to adjust the shaft speed of the turbine in a linear way with the wind speed so as to

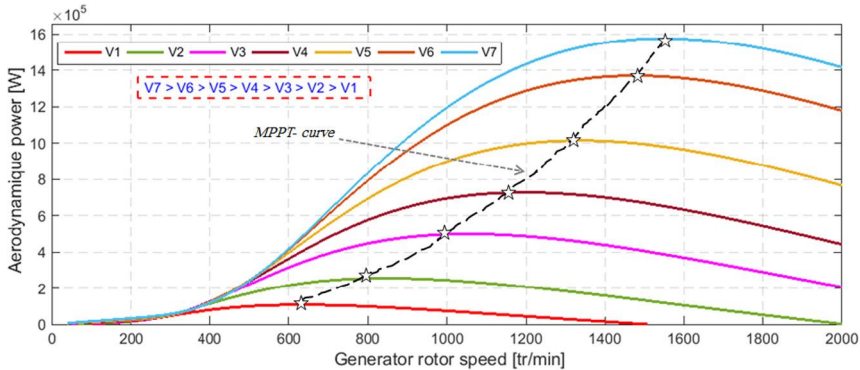


Figure 7.3 Aerodynamic power vs. rotor speed at different wind speeds.

keep TSR at its optimum value. The MPPT control scheme aims to obtain the maximum feasible power from the moving air masses. The idea of the MPPT scheme is to maximize the output electrical power through tracking the reference turbine speed that allows $\lambda = \lambda_{opt}$. As result, the WPS becomes more productive with the MPPT control law that is achieved by adjusting the rotational speed of the turbine for each concerned wind speed [5,18].

By exploiting Fig. 7.3, which shows the aerodynamic power as a function of rotor shaft speed for different given values of wind speed, it can be observed that the maximal power point corresponds to a particular rotor speed for each wind speed. It can be noted also that a small deviation from the reference rotor speed causes a significant decrease in the extracted power. Therefore, the turbine speed must continuously track its optimal value, which corresponds to optimal TSR, $\lambda_{opt} = 8.1$, and maximal aerodynamic efficiency, $C_{p-max} = 0.48$, for a pitch angle $\beta = 0$ degrees.

Wind speed is a significant input variable for WPSs. It is difficult to accurately measure wind speed in the field, but it is possible to obtain it from the estimated turbine speed.

By means of Eq. (7.3), the estimated value of wind speed is expressed as follows:

$$v_{estimated} = \frac{\Omega_t \cdot R}{\lambda_{opt}}. \tag{7.12}$$

Then, the optimal aerodynamic torque can be expressed as

$$C_{aer}^* = \frac{\rho \pi R^2 C_{p-max} v_{estimated}^3}{2 \Omega_t}. \tag{7.13}$$

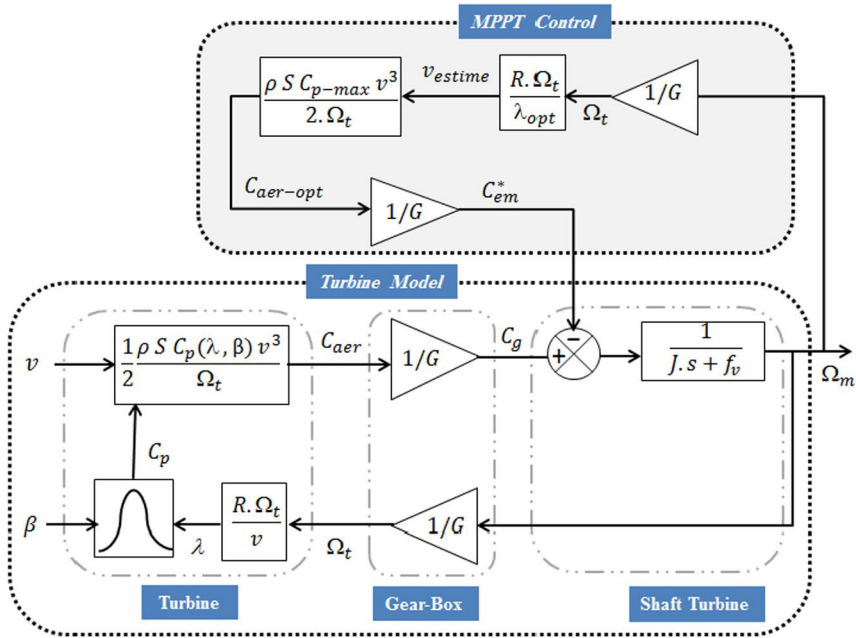


Figure 7.4 MPPT scheme of a wind power system.

Replacing the wind speed v in Eq. (7.13) by its expression given in Eq. (7.12), it is possible to estimate in real time the reference value of the electromagnetic torque from expression (7.14) depending on the optimal TSR (λ_{opt}) and the mechanic rotor speed (Ω_m):

$$C_{em}^* = \frac{\rho \pi R^5}{2} \frac{C_{p-max}}{(G \lambda_{opt})^3} \Omega_m^2. \tag{7.14}$$

Fig. 7.4 illustrates the aerodynamic model of the turbine with the MPPT control scheme.

7.3. Vector control scheme of DFIG using fractional-order PI controllers

This section aims to present a fractional-character vector control scheme based on the use of the FOPI controllers in the d - and q -axis regulation loops. This control structure is investigated as a simple and powerful solution to deal with the DFIG parameter variations and the

network voltage faults which cause bad operation of the system. In the vector control technique-based control scheme proposed to regulate the network-connected WPS, DFIG control includes two regulation loops for each control axis. The inner regulation loop is used to regulate rotor current and the outer regulation loop is employed to control the power.

7.3.1 A brief about fractional calculus

The theory of fractional-order calculus was introduced as an extension or as a generalization of standard integer-order calculus, where the fractional-order integral and derivative are extensions of the integer-order ones. The basic fractional integro-differential operator is represented as follows [24]:

$${}_{\alpha}D_t^{\delta} \cong D^{\delta} = \begin{cases} \frac{d^{\delta}}{dt^{\delta}}, & \text{for } \delta > 0, \\ 1, & \text{for } \delta = 0, \\ \int_{\alpha}^t (d\tau)^{\delta}, & \text{for } \delta < 0. \end{cases} \quad (7.15)$$

In (7.15), δ denotes the fractional order of the integro-differential operator while α and t denote the operation bounds.

Numerous different operators of fractional calculus have been presented. The Riemann–Liouville derivative and integral are the most frequently used of these operators, and they are expressed respectively as

$${}_{\alpha}D_t^{\delta} f(t) = \frac{d^{\delta}}{dt^{\delta}} f(t) = \frac{1}{\Gamma(m-\delta)} \frac{d^m}{dt^m} \int_{\alpha}^t \frac{f(\tau)}{(t-\tau)^{\delta-m+1}} d\tau, \quad (7.16)$$

$${}_{\alpha}D_t^{-\delta} f(t) = I^{\delta} f(t) = \frac{1}{\Gamma(\delta)} \int_{\alpha}^t \frac{f(\tau)}{(t-\tau)^{1-\delta}} d\tau, \quad (7.17)$$

where Γ denotes the Gamma function and m denotes the first integer value larger than δ which satisfies $m-1 \leq \delta < m$.

To execute the fractional-order operators in practical or simulation studies, the literature provides several approximations, in which the Oustaloup approximation is one of the most commonly adopted approximations in continuous time. The approximation method developed by Oustaloup was applied in this chapter, and can be defined as in [12]. We have

$$s^{\delta} \cong G \prod_{k=-N}^N \left[\frac{s + \omega_{z,n}}{s + \omega_{p,n}} \right], \quad (7.18)$$

where G is a gain, $\omega_{z,n}$ are the zeros, and $\omega_{p,n}$ denotes the poles such as

$$G = \omega_h^\delta, \quad \omega_{z,n} = \omega_b \left(\frac{\omega_h}{\omega_b} \right)^{\frac{k+N+\frac{1-\delta}{2}}{2N+1}}, \quad \omega_{p,n} = \omega_b \left(\frac{\omega_h}{\omega_b} \right)^{\frac{k+N+\frac{1+\delta}{2}}{2N+1}}, \quad (7.19)$$

where ω_h and ω_b are the upper and lower limits of the selected frequency range. In this study, the chosen frequency range is $[10^{-5}, 10^5]$ rad/s.

7.3.2 Concept of vector control of DFIG

The principle of the vector control is to achieve a control scheme that allows decoupled control in the d - and q -axes, i.e., between the reactive and real power exchanged with the network. The vector control technology is chosen because of its efficiency and simplicity. The idea of this control method is founded on synchronizing the (d, q) rotor reference frame with the stator flux vector in a way that it has to be aligned with the direct axis. Then, the flux direct component is equal to the total flux ($\varphi_{sd} = \varphi_s$), whereas its quadrature component is null ($\varphi_{sq} = 0$). In addition, consider that the resistance of stator winding is neglected ($R_s \approx 0$) and that the network is steady and powerful, with the voltage and synchronous angular frequency (ω_s) constant, which leads to $\varphi_s \approx cst$ [11,17]. Under such constraints, the electromagnetic torque is expressed as follows:

$$C_{em} = \frac{3}{2} \frac{pL_m}{L_s} I_{sq} \varphi_s. \quad (7.20)$$

Stator voltages given by (7.5) can be simplified as

$$\begin{cases} V_{sd} \approx 0, \\ V_{sq} = V_s \approx \omega_s \varphi_s. \end{cases} \quad (7.21)$$

Also, rotor voltages given by (7.7) are expressed as follows:

$$\begin{cases} V_{rd} = R_r I_{rd} + \sigma L_r \frac{dI_{rd}}{dt} - \sigma L_r g \omega_s I_{rq}, \\ V_{rq} = R_r I_{rq} + \sigma L_r \frac{dI_{rq}}{dt} + \sigma L_r g \omega_s I_{rd} + g \frac{L_m V_s}{L_s}, \end{cases} \quad (7.22)$$

where $\sigma = 1 - L_m^2/L_s L_r$ and $g = (\omega_s - \omega)/\omega_s$.

As a function of the Laplace variable s , (7.22) can be written as the following form:

$$\begin{cases} I_{rd} = \left[\frac{1}{R_r + \sigma L_r s} \right] (V_{rd} + g\sigma L_r \omega_s I_{rq}), \\ I_{rq} = \left[\frac{1}{R_r + \sigma L_r s} \right] (V_{rq} - g\sigma L_r \omega_s I_{rd} - g \frac{L_m V_s}{L_s}) \\ \Leftrightarrow \begin{cases} I_{rd} = [G_r(s)] (V_{rd} + C_{q \rightarrow d}), \\ I_{rq} = [G_r(s)] (V_{rq} + C_{d \rightarrow q} + D). \end{cases} \end{cases} \quad (7.23)$$

From (7.23), it appears that the d - and q -axes are coupled. A decoupling system must be established, by introducing feedforward terms $C_{q \rightarrow d}$ and $C_{d \rightarrow q}$ in which $C_{q \rightarrow d} = g\sigma L_r \omega_s I_{rq}$ and $C_{d \rightarrow q} = -g\sigma L_r \omega_s I_{rd}$.

Also, the disturbance term $D = -gL_m V_s / L_s$ was compensated via introducing a feedforward term.

Fig. 7.5 depicts the proposed control scheme of DFIG using the FOPI controllers, in the current and power regulation loops, for regulating the reactive and real power exchanged between the WPS and the network. The real axis control of DFIG allows the MPPT, which seeks to capture the maximum power from the available wind energy, while the reactive axis is controlled to achieve the reactive power imposed by the network.

The control signals that actually drives the DFIG are the reference voltages V_{rd}^* and V_{rq}^* obtained from the rotor real and reactive current control loops, respectively, as given by the following equations:

$$\begin{cases} V_{rd}^* = k_{pc} (I_{rd}^* - I_{rd}) + k_{ic} D^{-\delta_c} (I_{rd}^* - I_{rd}), \\ V_{rq}^* = k_{pc} (I_{rq}^* - I_{rq}) + k_{ic} D^{-\delta_c} (I_{rq}^* - I_{rq}). \end{cases} \quad (7.24)$$

Also, we use a power regulator with FOPI control for each axis. So, the reactive and real reference currents I_{rd}^* and I_{rq}^* can be expressed as follows:

$$\begin{cases} I_{rd}^* = k_{pp} (Q_s^* - Q_s) + k_{ip} D^{-\delta_p} (Q_s^* - Q_s), \\ I_{rq}^* = k_{pp} (P_s^* - P_s) + k_{ip} D^{-\delta_p} (P_s^* - P_s). \end{cases} \quad (7.25)$$

In (7.24) and (7.25), $k_{pc(p)}$, $k_{ic(p)}$, and $\delta_{c(p)}$ are the FOPI controller dimensions.

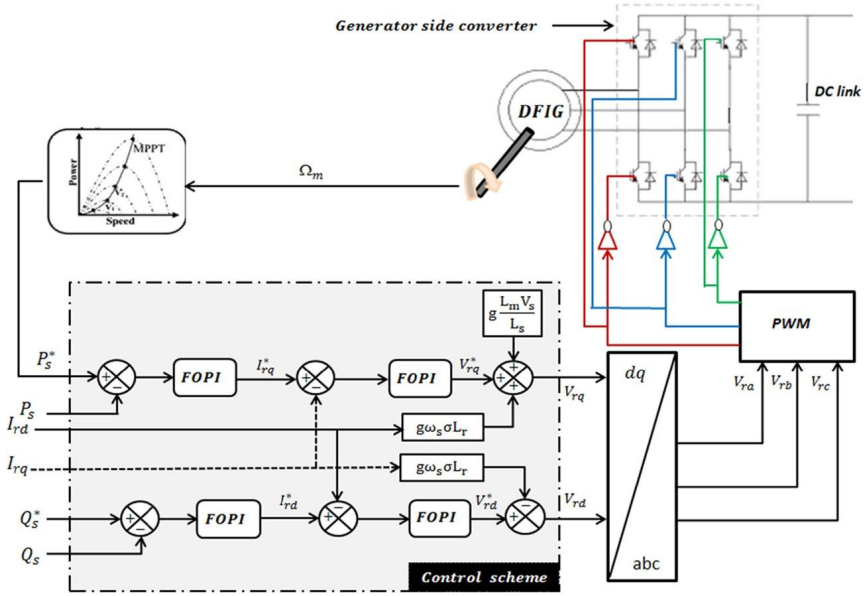


Figure 7.5 Proposed vector control scheme with FOPI controllers.

7.4. Design of FOPI controllers applied in the power and current regulation loops

Design operation of such a fractional-order regulator consists of determining its three dimensions, i.e., proportional and integral gains $k_p, k_i \in R^+$ and the extra order of integration $\delta \in [0, 2]$. The design technique approved in the present work focuses on the extension of a simple practical method proposed by the authors of [20], in which three interesting design specifications to be met by the FOPI regulator are considered. These design requirements are defined in the frequency domain such that depending on the process characteristics $G(s)$, the objective is to find a controller $C(s)$ that ensures the system robustness and stability. To achieve such an objective, the open-loop trigonometric transfer function $H(s) = C(s)G(s)$ would meet the following specifications.

Requirement 1. The gain margin condition at crossover frequency ω_c

$$|H(j\omega)|_{\omega=\omega_{gc}} = |C(j\omega)G(j\omega)|_{\omega=\omega_{gc}} = 1. \quad (7.26)$$

Requirement 2. The phase margin constraint at ω_{gc}

$$\text{Arg}[H(j\omega)]_{\omega=\omega_{gc}} = \text{Arg}[C(j\omega)G(j\omega)]_{\omega=\omega_{gc}} = -\pi + \vartheta_m. \quad (7.27)$$

Requirement 3. So as to ensure the robustness to the gain variation, the phase of the system's open-loop transfer function around the crossover frequency ω_{gc} should remain unchanged:

$$\frac{d}{d\omega} (\text{Arg}[H(j\omega)])|_{\omega=\omega_{gc}} = 0, \quad (7.28)$$

where ω_{gc} and ϑ_m denote the gain crossover frequency and phase margin, respectively.

The FOPI controller provides a control signal $u(t)$ given by

$$u(t) = k_p e(t) + k_i \frac{d^{-\delta}}{dt^{-\delta}} e(t). \quad (7.29)$$

In the Laplace domain, its transfer function is as follows:

$$C(s) = \frac{U(s)}{E(s)} = k_p + \frac{K_i}{s^\delta}. \quad (7.30)$$

The corresponding trigonometric transfer function is

$$C(j\omega) = k_p + K_i \omega^{-\delta} \cos(\delta\pi/2) - jK_i \omega^{-\delta} \sin(\delta\pi/2). \quad (7.31)$$

7.4.1 Design of a fractional-order PI controller as current regulator

In this subsection the proposed fractional-order PI controller is designed to be used as a d - and q -axis rotor current regulator. We consider the rotor current regulation loop for the two axes, shown in Fig. 7.6, with a FOPI controller that is employed as current regulator. The open-loop transfer function of the rotor current regulation loop can be written as

$$H(s) = C(s)G(s) = \left(k_{pc} + \frac{k_{ic}}{s^\delta} \right) \frac{k}{1 + \tau s}, \quad (7.32)$$

where $k = 1/R_r$ and $\tau = L_r \sigma / R_r$.

The open-loop trigonometric transfer function of system $H(j\omega)$ can be expressed as

$$H(j\omega) = \left[k_{pc} + K_{ic}(\omega)^{-\delta_c} \cos\left(\frac{\delta_c\pi}{2}\right) - jK_{ic}(\omega)^{-\delta_c} \sin\left(\frac{\delta_c\pi}{2}\right) \right] \frac{k}{1 + j\tau\omega}. \quad (7.33)$$

To accomplish Requirement 1, the magnitude of the open-loop trigonometric transfer function at ω_{gc} must have a value equal to 1, i.e.,

$$\begin{aligned} |H(j\omega_{gc})| &= \sqrt{\left[k_{pc} + K_{ic}(\omega_{gc})^{-\delta_c} \cos(\delta_c\pi/2) \right]^2 + \left[K_{ic}(\omega_{gc})^{-\delta_c} \sin(\delta_c\pi/2) \right]^2} \\ &\quad \times \frac{k}{\sqrt{1 + [\tau\omega_{gc}]^2}} \\ &= 1. \end{aligned} \quad (7.34)$$

According to Requirement 2, the phase of $H(j\omega)$ at ω_{gc} can be expressed as

$$\text{Arg}[H(j\omega_{gc})] = \text{Arg}[C(j\omega_{gc})] + \text{Arg}[G(j\omega_{gc})] = \vartheta_m - 180^\circ, \quad (7.35)$$

$$- \arctan \frac{K_{ic}(\omega_{gc})^{-\delta_c} \sin(\delta_c\pi/2)}{k_{pc} + K_{ic}(\omega_{gc})^{-\delta_c} \cos(\delta_c\pi/2)} - \arctan(\tau\omega_{gc}) = \vartheta_m - 180^\circ. \quad (7.35a)$$

From expression (7.35a), we can express the ratio $\frac{k_{ic}}{k_{pc}}$ as a function of fractional order δ_c :

$$\frac{k_{ic}}{k_{pc}} = - \frac{\tan[\arctan(\tau\omega_{gc}) + \vartheta_m]}{(\omega_{gc})^{-\delta_c} \sin(\delta_c\pi/2) + \alpha}, \quad (7.35b)$$

where $\alpha = (\omega_{gc})^{-\delta_c} \cos(\delta_c\pi/2) \tan[\arctan(\tau\omega_{gc}) + \vartheta_m]$.

To ensure the robustness of the controller, Requirement 3 has to be fulfilled; therefore,

$$\begin{aligned} &\frac{d}{d\omega} (\text{Arg}[H(j\omega)])|_{\omega=\omega_{gc}} \\ &= \frac{d}{d\omega} (\text{Arg}[C(j\omega)])|_{\omega=\omega_{gc}} + \frac{d}{d\omega} (\text{Arg}[G(j\omega)])|_{\omega=\omega_{gc}} = 0, \end{aligned} \quad (7.36)$$

$$\begin{aligned} & \frac{d}{d\omega} (\text{Arg}[H(j\omega)]) \Big|_{\omega=\omega_{gc}} \\ &= \frac{\frac{k_{ic}}{k_{pc}} \delta_c (\omega_{gc})^{\delta_c-1} \sin(\delta_c \pi / 2)}{(\omega_{gc})^{2\delta_c} + 2 \left(\frac{k_{ic}}{k_{pc}}\right) (\omega_{gc})^{\delta_c} \cos(\delta_c \pi / 2) + \left(\frac{k_{ic}}{k_{pc}}\right)^2} - \frac{\tau}{1 + (\tau \omega_{gc})^2} = 0. \end{aligned} \quad (7.36a)$$

From (7.36a), we can establish another equation regarding the ratio of k_{ic} and k_{pc} in the following form:

$$a \left(\frac{k_{ic}}{k_{pc}}\right)^2 + b \left(\frac{k_{ic}}{k_{pc}}\right) + c = 0, \quad (7.36b)$$

where $a = \frac{\tau}{1 + (\tau \omega_{gc})^2}$, $b = 2a (\omega_{gc})^{\delta_c} \cos(\delta_c \pi / 2) - \delta_c (\omega_{gc})^{\delta_c-1} \sin(\delta_c \pi / 2)$ and $c = a (\omega_{gc})^{2\delta_c}$.

Solution of Eq. (7.36b) gives

$$\left(\frac{k_{ic}}{k_{pc}}\right) = \frac{-b \pm \sqrt{b^2 - 4ac}}{2a}. \quad (7.36c)$$

The design specifications of the rotor current controller have been finalized, and three nonlinear equations of the three variables k_{pc} , k_{ic} , and δ_c are obtained; the two mathematical relations (7.34) and (7.35b) are from the basic specifications of gain and phase at the crossover frequency and the third one (7.36c) is formed to prove the robustness of the controller against the gain variations around ω_{gc} . To progress in the design of the FOPI controller for the rotor current control loop, the open-loop gain crossover frequency and the phase margin are considered as $\omega_{gc} = 250$ rad/s and $\emptyset_m = 50$ degrees. By plotting the ratio K_{ic}/K_{pc} in the function of δ_c for the two Eqs. (7.35b) and (7.36c), the proper values of δ_c and K_{ic}/K_{pc} can be concluded from the coordinates of the intersection point, as shown in Fig. 7.7. After defining the ratio K_{ic}/K_{pc} and fractional order δ_c , the values of K_{pc} and K_{ic} can be calculated from the proper value of K_{ic}/K_{pc} and Eq. (7.34). Hence, the designed FOPI controller for rotor current regulation loop is

$$C(s) = k_{pc} + \frac{k_{ic}}{s^{\delta_c}} = 0.028 + \frac{7.37}{s^{0.857}}. \quad (7.37)$$

The open-loop Bode plot of the trigonometric transfer function of the rotor current regulation loop is shown in Fig. 7.8. It can be observed that

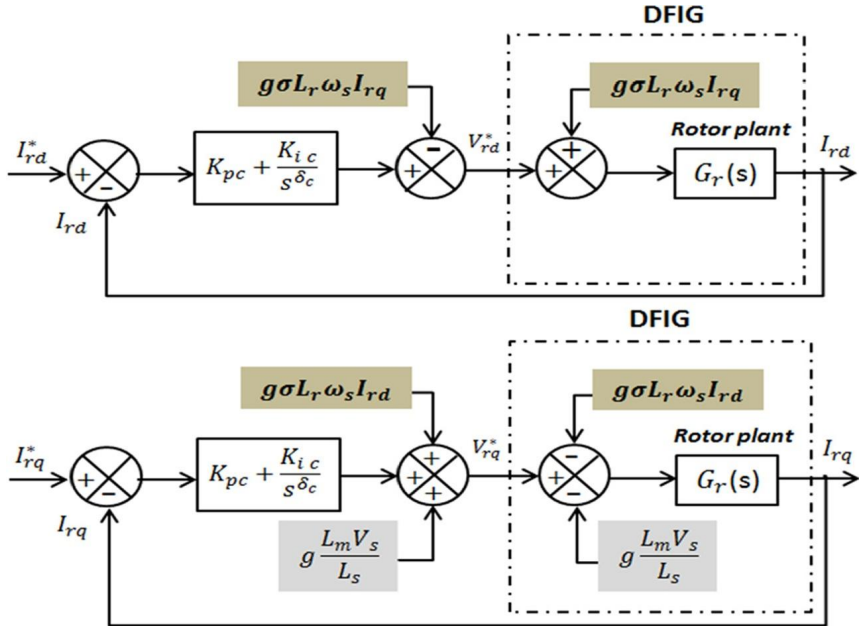


Figure 7.6 *d*- and *q*-axis rotor current regulation loops.

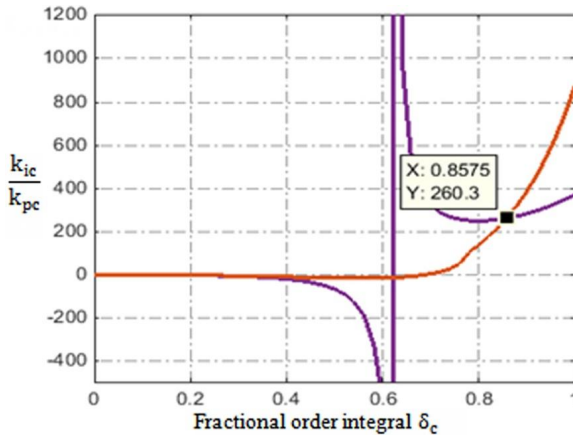


Figure 7.7 Relationship between k_{ic}/k_{pc} and δ_c .

the phase plot is flat around the crossover frequency $[-24.4\%, +28.8\%]\omega_{gc}$ and the set of frequency specifications is confirmed. It means that with the designed FOPI controller, the system is most robust.

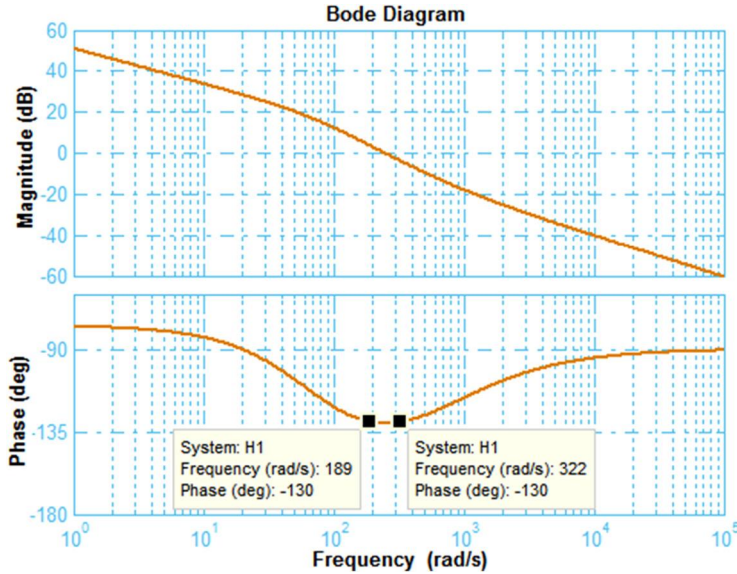


Figure 7.8 Open-loop Bode diagram of the current loop transfer function.

Table 7.1 Stability analysis for rotor current control closed-loop system.

Stability index	Symbol	Value	Unit
Crossover frequency	ω_{gc}	250	rad/s
Phase	$\angle H(j\omega) _{\omega_{gc}}$	-130	deg
Phase margin	PM	50	deg
Gain margin	GM	∞	-

Now the closed-loop stability analysis of the rotor current system with proposed FOPI controller is investigated. Stability is one of the essential indices of control system analysis. Here, the stability of the system with the proposed FOPI controller can be assessed from the Bode diagram which provides quantitative measures for stability in terms of phase and gain margins. It also provides a complete picture of the system dynamics from the low- to high-frequency range. As per reference [30], a closed-loop system is stable if both the phase margin (PM) and the gain margin (GM) are positive. The corresponding values identified from the open-loop frequency response of the system are presented in Table 7.1, and according to the Bode analysis technique, the rotor current closed-loop system is stable.

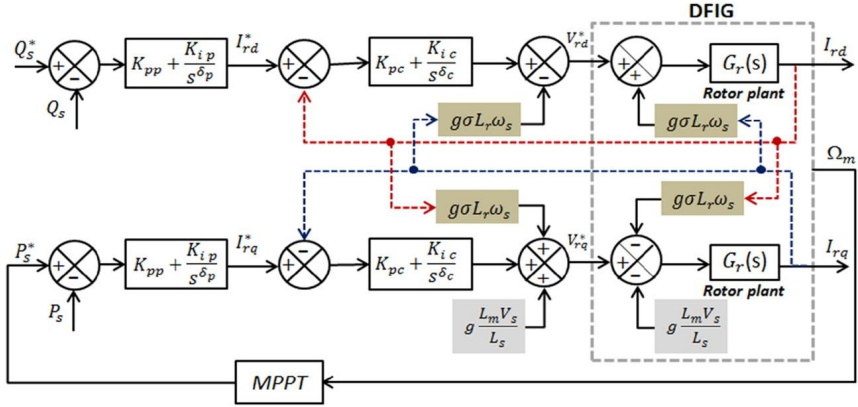


Figure 7.9 Decoupled reactive and real power control of DFIG.

7.4.2 Design of a fractional-order PI controller as power regulator

The simplified scheme of the DFIG power regulation loops based on the FOPI controllers is shown in Fig. 7.9. The FOPI controller used as power regulator will be designed in the same way the rotor current regulator.

The open-loop transfer function $H(s)$ of the DFIG power control system is described by the following equation:

$$H(s) = \left[k_{pp} + \frac{k_{ip}}{s^{\delta_p}} \right] \frac{\left[k_{pc} + \frac{k_{ic}}{s^{\delta_c}} \right]}{\left[k_{pc} + \frac{k_{ic}}{s^{\delta_c}} \right] + \frac{1+\tau s}{k}}, \quad (7.38)$$

we pose $P(s) = k_{pp} + \frac{k_{ip}}{s^{\delta_p}}$, $Q(s) = k_{pc} + \frac{k_{ic}}{s^{\delta_c}}$, and $R(s) = \left[k_{pc} + \frac{k_{ic}}{s^{\delta_c}} \right] + \frac{1+\tau s}{k}$.

The corresponding open-loop trigonometric transfer function $H(j\omega)$ can be expressed as follows:

$$H(j\omega) = P(j\omega) \frac{Q(j\omega)}{R(j\omega)} \Rightarrow H(j\omega) = \left[k_{pp} + K_{ip}(\omega)^{-\delta_p} \cos\left(\frac{\delta_p \pi}{2}\right) - jK_{ip}(\omega)^{-\delta_p} \sin\left(\frac{\delta_p \pi}{2}\right) \right] \times \frac{k_{pc} + K_{ic}(\omega)^{-\delta_c} \cos\left(\frac{\delta_c \pi}{2}\right) - jK_{ic}(\omega)^{-\delta_c} \sin\left(\frac{\delta_c \pi}{2}\right)}{k_{pc} + K_{ic}(\omega)^{-\delta_c} \cos\left(\frac{\delta_c \pi}{2}\right) - jK_{ic}(\omega)^{-\delta_c} \sin\left(\frac{\delta_c \pi}{2}\right) + \frac{1+j\tau\omega}{k}}. \quad (7.39)$$

Requirement 1 concerning the gain limitation constraint at ω_{gc} gives the following equation:

$$|H(j\omega_{gc})| = 1 \Rightarrow |P(j\omega_{gc})| = \frac{|R(j\omega_{gc})|}{|Q(j\omega_{gc})|} \Rightarrow$$

$$\sqrt{\left[k_{pp} + K_{ip} (\omega_{gc})^{-\delta_p} \cos(\delta_p \pi / 2) \right]^2 + \left[K_{ip} (\omega_{gc})^{-\delta_p} \sin(\delta_p \pi / 2) \right]^2}$$

$$= \frac{\sqrt{\left[1 + k k_{pc} + k K_{ic} (\omega_{gc})^{-\delta_c} \cos(\delta_c \pi / 2) \right]^2 + \left[\tau \omega_{gc} - k K_{ic} (\omega_{gc})^{-\delta_c} \sin(\delta_c \pi / 2) \right]^2}}{\sqrt{\left[k k_{p.c} + k K_{ic} (\omega_{gc})^{-\delta_c} \cos(\delta_c \pi / 2) \right]^2 + \left[k K_{ic} (\omega_{gc})^{-\delta_c} \sin(\delta_c \pi / 2) \right]^2}}. \quad (7.40)$$

The phase margin of the open-loop trigonometric transfer function at crossover frequency ω_{gc} should satisfy Requirement 2; therefore,

$$Arg[H(j\omega_{gc})] = Arg[P(\omega_{gc})] + Arg[Q(\omega_{gc})] - Arg[R(\omega_{gc})] = \varphi_m - 180^\circ, \quad (7.41)$$

where

$$Arg[P(\omega_{gc})] = \theta(\omega_{gc}) = -\arctan \frac{K_{ip} (\omega_{gc})^{-\delta_p} \sin(\delta_p \pi / 2)}{k_{pp} + K_{ip} (\omega_{gc})^{-\delta_p} \cos(\delta_p \pi / 2)},$$

$$Arg[Q(\omega_{gc})] = \Psi(\omega_{gc}) = -\arctan \frac{K_{ic} (\omega_{gc})^{-\delta_c} \sin(\delta_c \pi / 2)}{k_{pc} + K_{ic} (\omega_{gc})^{-\delta_c} \cos(\delta_c \pi / 2)},$$

$$Arg[R(\omega_{gc})] = \xi(\omega_{gc}) = \arctan \frac{\tau \omega_{gc} - k K_{ic} (\omega_{gc})^{-\delta_c} \sin(\delta_c \pi / 2)}{1 + k k_{pc} + k K_{ic} (\omega_{gc})^{-\delta_c} \cos(\delta_c \pi / 2)}.$$

Then, expression (7.41) becomes as follows:

$$-\arctan \frac{K_{ip} (\omega_{gc})^{-\delta_p} \sin(\delta_p \pi / 2)}{k_{pp} + K_{ip} (\omega_{gc})^{-\delta_p} \cos(\delta_p \pi / 2)} = \varphi_m - 180^\circ - \Psi + \xi. \quad (7.41a)$$

Following Eq. (7.41a), we can establish the expression of the ratio K_{ip}/K_{pp} in the function of δ_p as

$$\frac{k_{ip}}{k_{pp}} = -\frac{\tan[\varphi_m + \xi - \Psi]}{(\omega_{gc})^{-\delta_p} \sin(\delta_p \pi / 2) + \alpha}, \quad (7.41b)$$

where $\alpha = (\omega_{gc})^{-\delta_p} \cos(\delta_p \pi / 2) \tan[\varphi_m + \xi - \Psi]$.

According to Requirement 3 about the robustness condition, the phase angle gradient of the system open-loop transfer function at crossover frequency ω_{gc} is expressed as follows:

$$\begin{aligned}
 & \frac{d}{d\omega} (\text{Arg}[H(j\omega)])|_{\omega=\omega_{gc}} \\
 &= \frac{d}{d\omega} \theta(\omega)|_{\omega=\omega_{gc}} + \frac{d}{d\omega} \Psi(\omega)|_{\omega=\omega_{gc}} - \frac{d}{d\omega} \xi(\omega)|_{\omega=\omega_{gc}} = 0 \quad \Rightarrow \\
 & \frac{d}{d\omega} \theta(\omega)|_{\omega=\omega_{gc}} = -\frac{d}{d\omega} \Psi(\omega)|_{\omega=\omega_{gc}} + \frac{d}{d\omega} \xi(\omega)|_{\omega=\omega_{gc}} \quad \Rightarrow \\
 & \frac{\frac{k_{ip}}{k_{pp}} \delta_p (\omega_{gc})^{\delta_p-1} \sin(\delta_p \pi / 2)}{(\omega_{gc})^{2\delta_p} + 2 \frac{k_{ip}}{k_{pp}} (\omega_{gc})^{\delta_p} \cos(\delta_p \pi / 2) + \left(\frac{k_{ip}}{k_{pp}}\right)^2} = -\frac{A}{B} + \frac{C}{D}, \quad (7.42)
 \end{aligned}$$

where

$$\begin{aligned}
 A &= \frac{k_{ic}}{k_{pc}} \delta_c (\omega_{gc})^{-\delta_c-1} \sin(\delta_c \pi / 2), \\
 B &= 1 + 2 \frac{k_{ic}}{k_{pc}} (\omega_{gc})^{-\delta_c} \cos(\delta_c \pi / 2) + (\omega_{gc})^{-2\delta_c} \left(\frac{k_{ic}}{k_c}\right)^2, \\
 C &= \tau (1 + k k_{pc}) + \tau k k_{ic} (\omega_{gc})^{-\delta_c} \cos(\delta_c \pi / 2) \\
 &\quad + k (1 + k k_{pc}) k_{i,c} \delta_c (\omega_{gc})^{-\delta_c-1} \sin(\delta_c \pi / 2) \\
 &\quad + \tau k \delta_c k_{ic} (\omega_{gc})^{-\delta_c} \cos(\delta_c \pi / 2), \\
 D &= [1 + k k_{p,c} + k K_{ic} (\omega_{gc})^{-\delta_c} \cos(\delta_c \pi / 2)]^2 \\
 &\quad + [\tau \omega_{gc} - k K_{ic} (\omega_{gc})^{-\delta_c} \sin(\delta_c \pi / 2)]^2.
 \end{aligned}$$

From expression (7.42), we can establish another formula regarding the ratio between k_{ip} and k_{pp} in the following form:

$$\begin{aligned}
 & \frac{\frac{k_{ip}}{k_{pp}} \delta_p (\omega_{gc})^{\delta_p-1} \sin(\delta_p \pi / 2)}{(\omega_{gc})^{2\delta_p} + 2 \frac{k_{ip}}{k_{pp}} (\omega_{gc})^{\delta_p} \cos(\delta_p \pi / 2) + \left(\frac{k_{ip}}{k_{pp}}\right)^2} = a \\
 & \Rightarrow a \left(\frac{k_{ip}}{k_{pp}}\right)^2 + b \left(\frac{k_{ip}}{k_{pp}}\right) + c = 0, \quad (7.42a)
 \end{aligned}$$

where $a = -\frac{A}{B} + \frac{C}{D}$, $b = 2a (\omega_{gc})^{\delta_p} \cos(\delta_p \pi / 2) - \delta_p (\omega_{gc})^{\delta_p-1} \sin(\delta_p \pi / 2)$, and $c = a (\omega_{gc})^{2\delta_p}$.

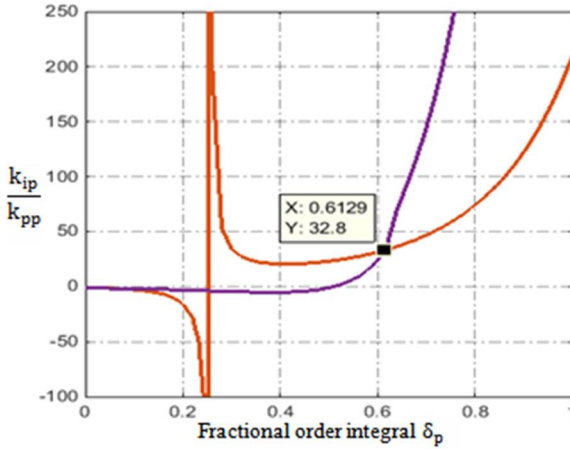


Figure 7.10 Relation curve between k_{ip}/k_{pp} and δ_p .

Solution of Eq. (7.42a) gives

$$\left(\frac{k_{ip}}{k_{pp}}\right) = \frac{-b \pm \sqrt{b^2 - 4ac}}{2a}. \quad (7.42b)$$

Similar to Section 7.4.1, we can solve the equation system (7.40), (7.41b), and (7.42b) in order to get the three parameters which specify the FOPI controller. As exemplified in Fig. 7.10, the intersection point of graphs of Eqs. (7.41b) and (7.42b) defines the proper values of the fractional order δ_p and of the ratio K_{ip}/K_{pp} . From the proper value of K_{ip}/K_{pp} and Eq. (7.40), the values of integral gain and proportional gain can be calculated. Hence, the designed FOPI controller for DFIG power regulation loops is

$$C(s) = k_{pp} + \frac{k_{ip}}{s^{\delta_p}} = 3.57 + \frac{116.62}{s^{0.613}}. \quad (7.43)$$

Fig. 7.11 shows the open-loop Bode plot of the trigonometric transfer function of the DFIG power regulation loop. According to this figure, it can be observed that the phase plot is flat around the gain crossover frequency $[-4.8\%, +61.8\%]\omega_{gc}$ and all frequency domain constraints are satisfied. This means that the system response is more robust with the designed fractional-order controller.

Furthermore, the stability of the whole system with the proposed control scheme is analyzed by applying the Bode analysis technique which is discussed in the previous section, by which we can analyze the stability of

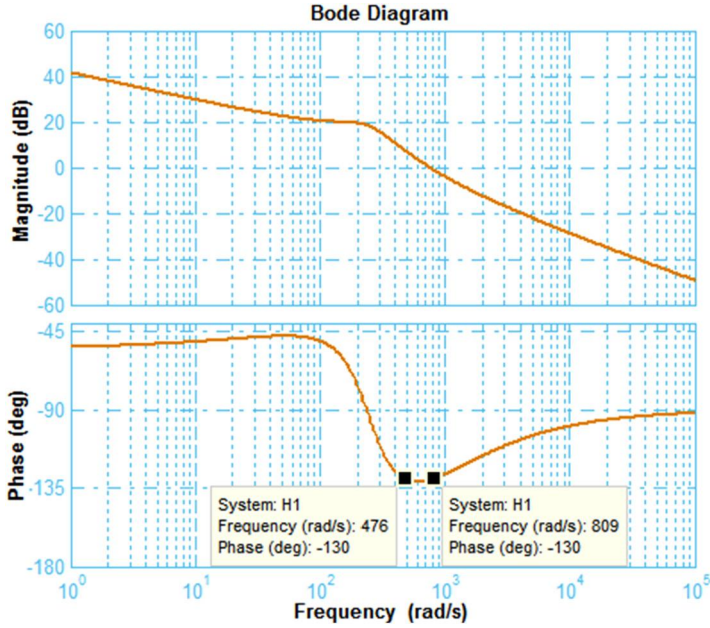
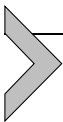


Figure 7.11 Open-loop Bode diagram of the power regulation loop.

the whole system from the open-loop system frequency response by measuring the gain margin and the phase margin, which can determine the stability of the closed-loop system. From Fig. 7.11, the phase margin and gain margin of the open-loop system frequency response are as follows: $PM = 50^\circ$ and $GM = \infty$. This means that the closed-loop system with the proposed control scheme is stable.



7.5. Numerical results and analysis

To assess the effectiveness and superiority of the presented control scheme and for comparison aims, numerical simulations for both FVC and CVC are carried out using MATLAB[®]/Simulink software. The test system which has been considered in this study consists of a network-connected 1.5-MW DFIG, with the corresponding parameters reported in Table 7.2. Concerning the DFIG control strategy, the reactive axis is controlled to operate the WPS at reactive power imposed by the electrical network where a series of three consecutive references of reactive power Q_r are imposed, i.e., 0 VAR, 500000 VAR, -500000 VAR, lasting 7 s, 6 s, and 7 s, respectively,

Table 7.2 DFIG generator and wind turbine parameters.

DFIG	Wind turbine		
Typical peak power (P_n)	1.5 MW	Number of blades	3
Stator voltage (V_s)	398/690 V	Blade radius (R)	30.5 m
Stator frequency (f_s)	50 Hz	Gearbox gain (G)	70
DC-link voltage (U_{DC})	1200 V	Inertia moment (J)	10^3 kg m^2
DC-link capacitor (C_{DC})	16000 μF	Friction coefficient (f_v)	$24 \cdot 10^{-4} \text{ N ms}^{-1}$
Stator inductance (L_s)	0.0137 H	Optimal tip speed ratio (λ_{opt})	8.1
Stator resistance (R_s)	0.012 Ω	Maximal power coefficient (C_{p-max})	0.48
Rotor inductance (L_r)	0.0136 H		
Rotor resistance (R_r)	0.021 Ω		
Mutual inductance (L_m)	0.0135 H		
Number of pole pairs (P)	2		

Table 7.3 Controllers' parameters in the power and current control loops.

	CVC	FVC
Current controller	$k_{pc} = 0.006, k_{ic} = 0.420$	$k_{pc} = 0.028, k_{ic} = 7.37, \delta_c = 0.857$
Power controller	$k_{pp} = 0.333, k_{ip} = 6.667$	$k_{pp} = 3.57, k_{ip} = 116.62, \delta_p = 0.618$

whereas the active-axis control is performed under an MPPT law which forces the wind turbine to extract maximum power from the wind, i.e., it allows the system to function at the optimum power coefficient value of $C_{p-max} = 0.48$. Table 7.3 lists the regulators' parameters in the power and current regulation loops for both control structures.

So as to be close to the real conditions, the DFIG wind turbine was tested with a variable wind speed model to examine the dynamic performance of the proposed control structure; the wind profile applied for simulation purposes is depicted in Fig. 7.12. Moreover, to evaluate the effectiveness and robustness degree of the presented control structure, the DFIG wind turbine was investigated under two major disturbances, which generally affect the productivity and operating of the system:

- **generator parameters variations and**
- **network voltage faults.**

Firstly, to show the dynamic performance of the fractional-character vector control proposed, the WPS is operated under the adopted vari-

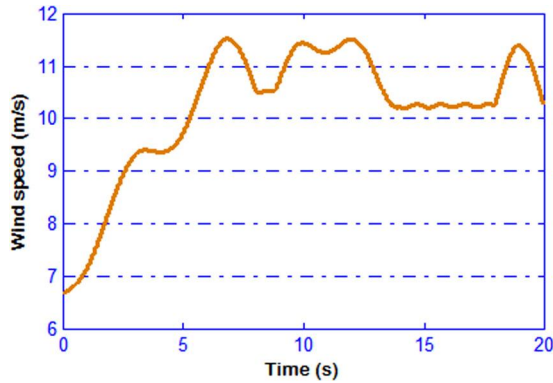


Figure 7.12 Wind speed model.

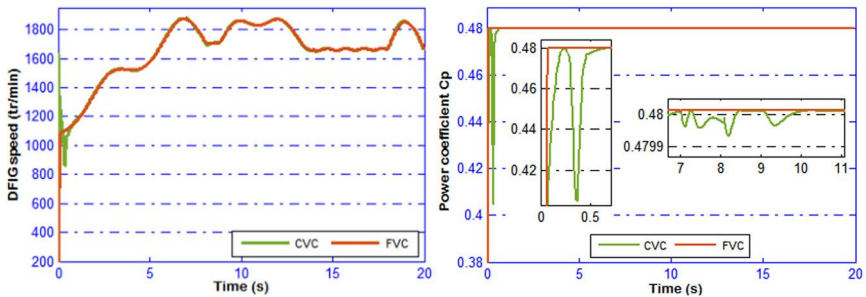


Figure 7.13 Temporal evolution of DFIG rotor speed and power coefficient.

able wind speed without any other disturbance. The control performance for both CVC and FVC in active and reactive axes is demonstrated in Figs. 7.13–7.15, from which one can note that MPPT of the DFIG wind turbine connected to the network is well achieved for both control structures.

Besides, the evolution of the power coefficient C_p , which represents the aerodynamic efficiency of the wind turbine, confirms that a DFIG WPS extracts the optimal wind power under a random variation of the wind speed, because it keeps its optimum value at each given wind speed, as demonstrated by Fig. 7.13. Moreover, one can see that not only the suggested control structure reaches the MPPT more rapidly than the CVC structure, but also more precisely and without oscillations. The DFIG rotor shaft is driven in rotation by the turbine through the gearbox. Fig. 7.13 illustrates that the generator speed evolves in the same shape as the adopted wind

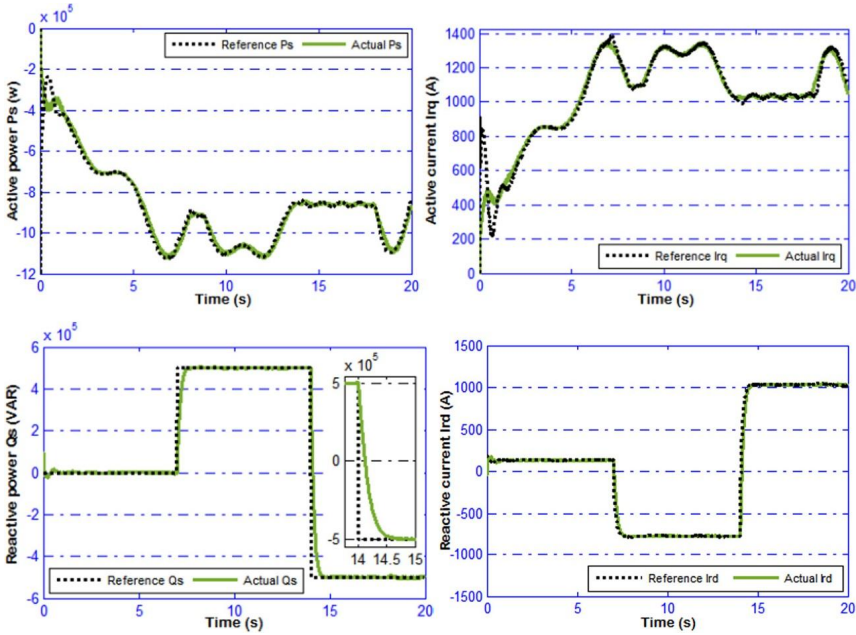


Figure 7.14 Active power P_s , active current I_{qr} , reactive power Q_s , and reactive current I_{dr} tracking performance using the CVC (in the ideal case).

speed model to extract the optimal power according to the MPPT control law.

In such an ideal case without any disturbances, the tracking performance of the current and power control loops, for both active and reactive axes, under CVC and FVC are presented in Figs. 7.14 and 7.15, respectively. The stator real power tracks its reference value that is defined by the maximum power point for each wind speed, while the reactive power tracks its reference value which is imposed by the network. The active component of the rotor current has the same shape as the stator real power, and follows its reference in order to optimize the wind energy extraction, while the reactive component, which corresponds to the power factor, follows its reference to meet the requirement in reactive power. From such numerical results, which illustrate the tracking performance of the CVC and FVC schemes, it can be concluded that the FVC controls the reactive and real powers in a more rapid, accurate, and smooth way compared to the CVC.

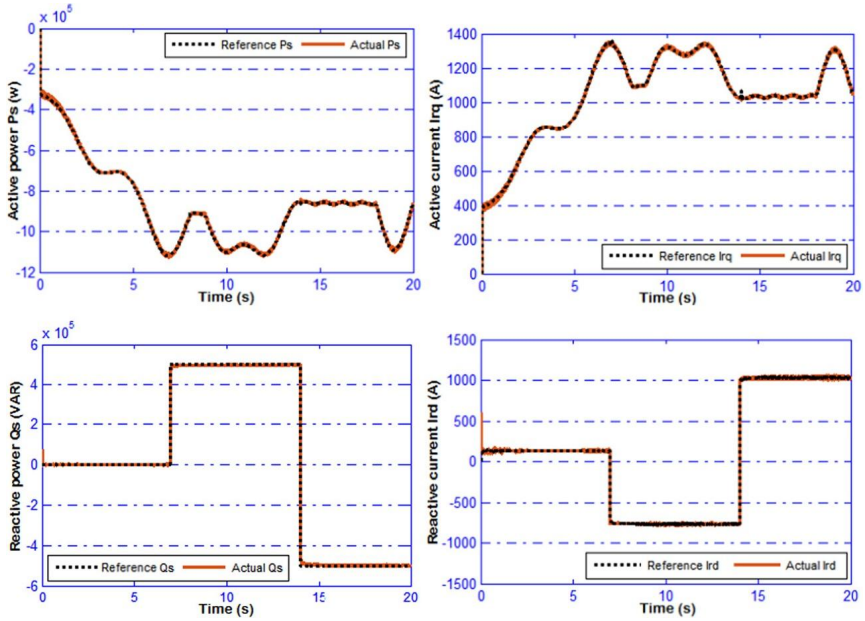


Figure 7.15 Active power P_s , active current I_{q} , reactive power Q_s , and reactive current I_{d} tracking performance using the FVC (in the ideal case).

7.5.1 Robustness evaluation against generator parameter variations

Herein, the robustness performance of FVC and CVC is examined against parameter variation disturbances, produced by the temperature increase in windings of the generator, which is commonly seen over the operation of electrical machines. In order to evaluate the control performance of the proposed control structure under the effect of parameter uncertainties, a 100% variation from their rated values of the rotor inductance L_r and resistance R_r is imposed at $t = 10$ s.

Note that both control structures applied to the DFIG were tested under parameter variations and that the numerical results obtained by each structure were graphically compared to the ones of the ideal case without any uncertainties, as depicted in Fig. 7.16 (CVC) and Fig. 7.17 (FVC). It can be clearly observed from the controlled variable profiles of the current and power regulation loops that the control performance of the CVC scheme deteriorates when the system is subjected to parameter uncertainties, while from the numerical results provided in Fig. 7.17, it can be concluded that the proposed control structure is able to reject such parametric disturbances

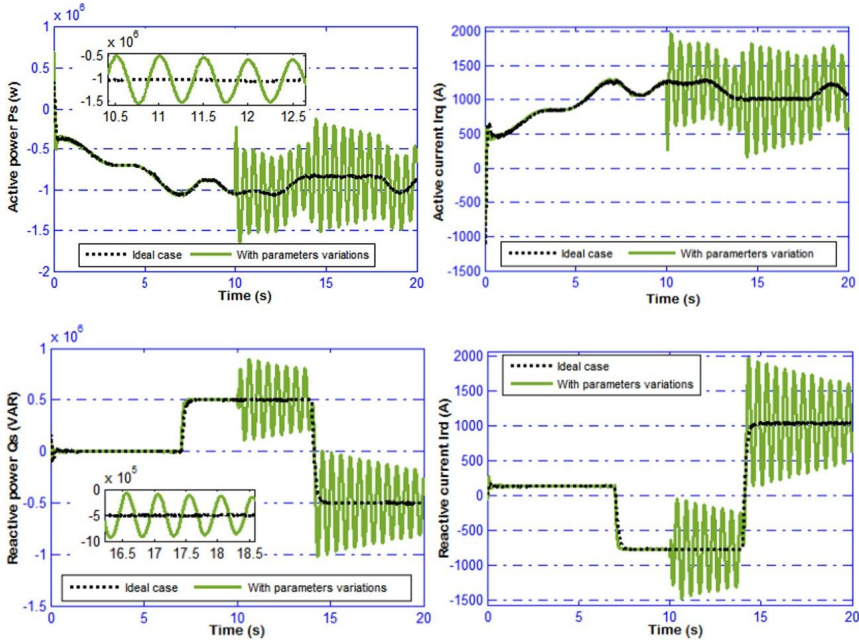


Figure 7.16 Active power P_s , active current I_{cq} , reactive power Q_s , and reactive current I_{dq} profile obtained using CVC (in the ideal case and under parameter variations).

and guarantees a suitable dynamic response, where, except for the peaks appearing at the instant of DFIG parameter variation, the wind system response is almost the same as in the case of normal conditions.

7.5.2 Robustness evaluation against network voltage drop

Due to the high integration of WPSs into the electrical network during the last years, DFIG WPSs are essentially required to have the ability to realize low-voltage ride-through in order to remain safely connected in situations where the power network voltage temporarily reduces due to a fault or a sudden load change. The output powers of the DFIG are sensitive to the network voltage drops because the stator windings of DFIGs are connected directly to the power network. Indeed, the network voltage drops cause a decrease in the stator flux value, which leads to demagnetization of the DFIG, and a change of the flux affects the stator real and reactive power.

To investigate the ability and feasibility of the proposed control structure in the face of network voltage disturbances, which are a common

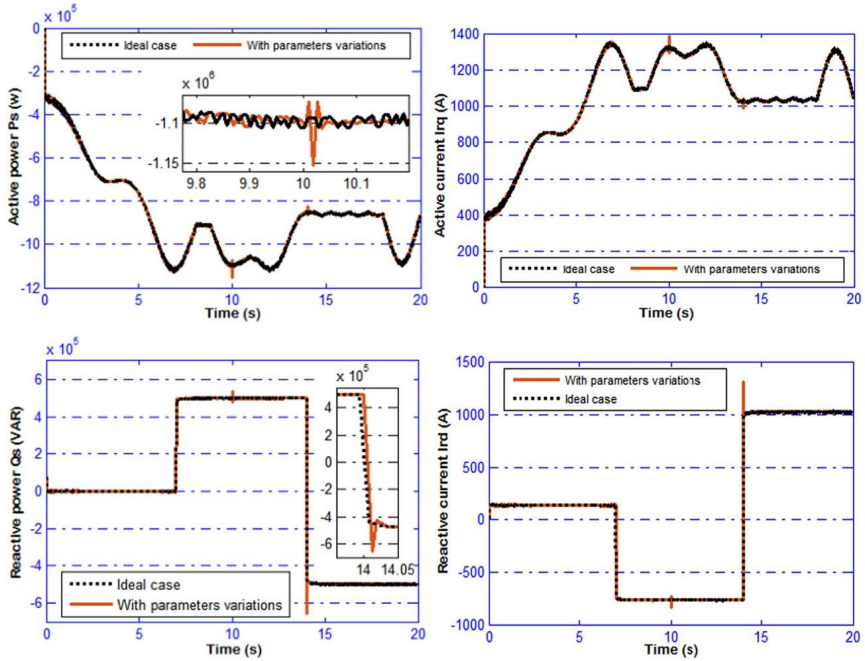


Figure 7.17 Active power P_s , active current $I_{q\prime}$, reactive power Q_s , and reactive current $I_{d\prime}$ profiles obtained using FVC (in the ideal case and under parameter variations).

phenomenon that appears in the power network and affects the performance of its connected WPSs, a 30% symmetrical three-phase voltage drop from the rated value at the electrical network which lasts 1000 ms has been applied at $t = 10$ s. Fig. 7.18 and Fig. 7.19 show the DFIG rotational speed Ω_m , power coefficient C_p , real power P_s , and reactive power Q_s profiles obtained by CVC and FVC structures, respectively. Peaks appear at power network voltage change instances. The superior efficiency of the FVC scheme in comparison with the CVC scheme of the generator side converter is clearly observed, due to a 643 kW peak reduction of the active power, immediately at the occurrence of the voltage drop. Moreover, one can see that the proposed control structure reaches the MPPT more rapidly than the CVC structure, during and after voltage drop. From the simulation results presented, it is concluded that the proposed fractional-character control structure guarantees the highest robust performance regarding the voltage drop disturbance rejection.

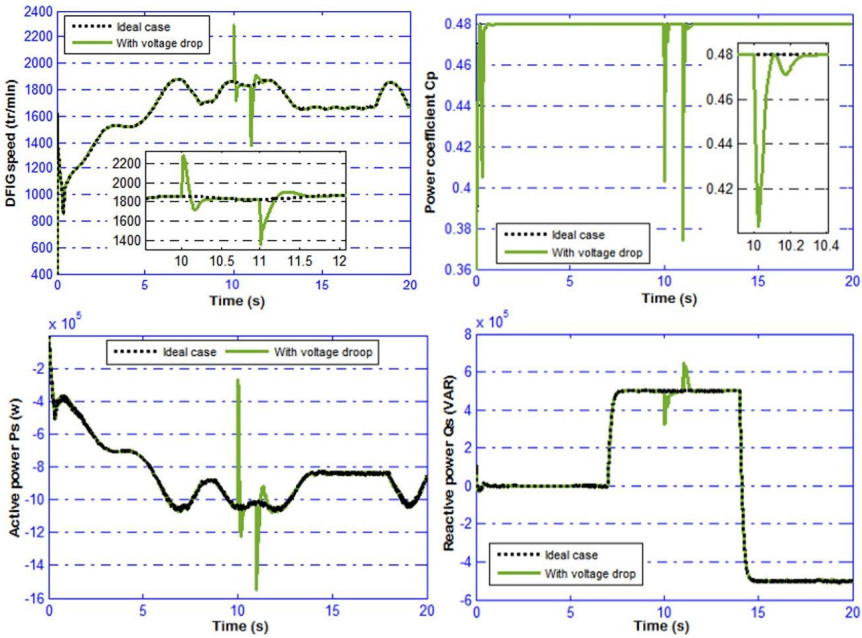


Figure 7.18 DFIG rotational speed Ω_m , power coefficient C_p , real power P_s , and reactive power Q_s profiles obtained using CVC (in the ideal case and under a sudden 30% voltage drop at the power network).

7.5.3 Comparative studies

Table 7.4 presents a quantitative comparison between the two control structures in terms of the percentage of the steady-state error in the ideal conditions without any disturbances. In the operation case under parameter variations or network voltage drop, the comparison is made in terms of the peak value of real power $|P_s|$ and settling time t_s at disturbance occurrence. It is worth noting that the proposed control structure has slightly stronger robustness than that of the CVC due to its fractional mechanism.



7.6. Conclusion

As fractional-order control offers a higher degree of freedom and a number of advantages over integer-order control, this chapter proposes a fractional-character vector control scheme to control a WPS equipped with a DFIG in network-connected mode. The proposed control scheme structure focuses on using the fractional-order PI controllers instead of

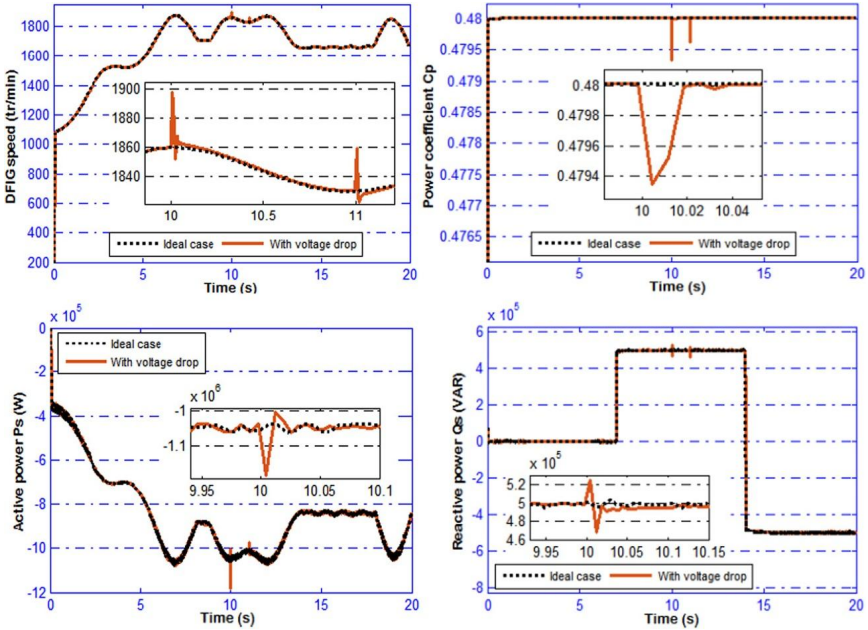


Figure 7.19 DFIG rotational speed Ω_m , power coefficient C_p , real power P_s , and reactive power Q_s profiles obtained using FVC (in the ideal case and under a sudden 30% voltage drop at the power network).

Table 7.4 Control structures comparison.

	Operation under ideal conditions without any disturbances			
	CVC		FVC	
Error [%]	3.32		2.47	
	Operation under parameter variations		Operation under voltage drop	
	CVC	FVC	CVC	FVC
$ P_s $ [%]	77.27	4.55	72.76	13.33
t_s [s]	>10	0.021	0.221	0.025

the integer-order ones in the power and rotor current regulation loops of the generator-side converter according to the stator flux orientation-based control strategy. In this work, the design of the power and current FOPI controllers is made using a frequency-domain method, which is based on the linearized dynamic model of the DFIG generator. The efficiency of the FVC compared to that of the CVC has been examined through simulation

tests performed for a 1.5-MW DFIG WPS. Moreover, the robustness of the new control structure is surveyed against generator parameter uncertainties as well as network voltage faults. The obtained numerical results validate that the FVC is capable to attenuate the effects of the system parameter evolution and network voltage disturbances and improve the WPS response and the performance in wind energy conversion. Future studies will focus on the use of fractional calculus theory to more accurately describe the nonlinear dynamics of a DFIG-based WPS.

References

- [1] A. Abdelbaset, Y.S. Mohamed, A.H.M. El-Sayed, A.E.H.A. Ahmed, Literature review, in: A. Abdelbaset, et al. (Eds.), *Wind Driven Doubly Fed Induction Generator: Grid Synchronization and Control*, Springer International Publishing AG, 2018, pp. 7–20, 2018.
- [2] M.E.B. Aguilar, D.V. Coury, R. Reginatto, R.M. Monaro, Multi-objective PSO applied to PI control of DFIG wind turbine under electrical fault conditions, *Electric Power Systems Research* 180 (2020) 106081.
- [3] M.A.S. Ali, K.K. Mehmood, S. Baloch, C.H. Kim, Modified rotor-side converter control design for improving the LVRT capability of a DFIG-based WECS, *Electric Power Systems Research* 186 (2020) 106403.
- [4] W. Ayrir, Amélioration de la commande directe du couple d'une éolienne à base d'une génératrice asynchrone doublement alimentée par la logique floue, Ph.D. thesis, Université Abdelmalek Essaadi, Morocco, 2019.
- [5] K. Belmokhtar, M.L. Doumbia, K. Agbossou, Novel fuzzy logic based sensorless maximum power point tracking strategy for wind turbine systems driven DFIG (doubly-fed induction generator), *Energy* 76 (2014) 679–693.
- [6] A. Benamor, M.T. Benchouia, K. Srairi, M.E.H. Benbouzid, A new rooted tree optimization algorithm for indirect power control of wind turbine based on a doubly-fed induction generator, *ISA Transactions* 88 (2019) 296–306.
- [7] M. Benbouzid, B. Beltran, Y. Amirat, G. Yao, J. Han, H. Mangel, Second-order sliding mode control for DFIG-based wind turbines fault ride-through capability enhancement, *ISA Transactions* 53 (3) (2014) 827–833.
- [8] Y. Bensafia, K. Khettab, S. Ladaci, Robust DC-motor speed control using a fractional adaptive PI^α regulator, *International Journal of Digital Signals and Smart Systems* 1 (2) (2017) 129–142.
- [9] K. Chen, R. Tang, C. Li, J. Lu, Fractional order PI^λ controller synthesis for steam turbine speed governing systems, *ISA Transactions* 77 (2018) 49–57.
- [10] A. Chevalier, C. Francis, C. Copot, C.M. Ionescu, R. De Keyser, Fractional-order PID design: towards transition from state-of-art to state-of-use, *ISA Transactions* 84 (2019) 178–186.
- [11] L. Fan, Z. Miao, *Modeling and Analysis of Doubly Fed Induction Generator Wind Energy Systems*, Academic Press, 2015.
- [12] Z. Gao, X. Liao, Improved Oustaloup approximation of fractional-order operators using adaptive chaotic particle swarm optimization, *Journal of Systems Engineering and Electronics* 23 (1) (2012) 145–153.
- [13] GWEC, *Global Wind Report 2019 - Annual Market Update*, the Global Wind Energy Council [Online]. Available: <https://gwec.net/global-wind-report-2019/>. (Accessed 1 August 2020).

- [14] M. Jazaeri, A.A. Samadi, Self-tuning fuzzy PI based controller of DFIG wind turbine for transient conditions enhancement, *International Transactions on Electrical Energy Systems* 25 (11) (2015) 2657–2673.
- [15] S. Kammoun, S. Sallem, M.B.A. Kammoun, Backstepping control for low-voltage ride through enhancement of DFIG-based wind turbines, *Arabian Journal for Science and Engineering* 42 (12) (2017) 5083–5099.
- [16] A. Kasbi, A. Rahali, A simple methodology for optimal fuzzy control of DFIG based wind turbine, in: *2020 1st International Conference on Innovative Research in Applied Science, Engineering and Technology (IRASET)*, 16–19 April 2020, IEEE, pp. 1–6.
- [17] K. Kerrouche, A. Mezouar, K. Belgacem, Decoupled control of doubly fed induction generator by vector control for wind energy conversion system, *Energy Procedia* 42 (2013) 239–248.
- [18] A. Khamlichi, B. Ayyat, M. Bezzazi, C. Vivas, Advanced control of wind turbines, in: Rupp Carrievau (Ed.), *Fundamental and Advanced Topics in Wind Power*, IntechOpen, 2011, pp. 291–308.
- [19] R. Lamba, S.K. Singla, S. Sondhi, Fractional order PID controller for power control in perturbed pressurized heavy water reactor, *Nuclear Engineering and Design* 323 (2017) 84–94.
- [20] H. Li, Y. Luo, Y. Chen, A fractional order proportional and derivative (FOPD) motion controller: tuning rule and experiments, *IEEE Transactions on Control Systems Technology* 18 (2) (2009) 516–520.
- [21] H. Mahvash, S.A. Taher, M. Shahidehpour, Fractional order control scheme in pitch control loop of synchronous generator wind turbine type 4 at high wind speed operation in a microgrid, *Journal of Renewable and Sustainable Energy* 11 (1) (2019) 013305.
- [22] A. Merabet, H. Eshaft, A.A. Tanvir, Power-current controller based sliding mode control for DFIG-wind energy conversion system, *IET Renewable Power Generation* 12 (10) (2018) 1155–1163.
- [23] F. Padula, A. Visioli, On the fragility of fractional-order PID controllers for FOPDT processes, *ISA Transactions* 60 (2016) 228–243.
- [24] I. Petráš, *Fractional-Order Nonlinear Systems: Modeling, Analysis and Simulation*, Springer Science & Business Media, 2011.
- [25] I. Podlubny, Fractional-order systems and PID^μ controllers, *IEEE Transactions on Automatic Control* 44 (1) (1999) 208–214.
- [26] S. Sondhi, Y.V. Hote, Fractional order controller and its applications: a review, in: *Proc. of Asia MIC*, 2–4 April 2012, Phuket, Thailand.
- [27] S. Sondhi, Y.V. Hote, Fractional order PID controller for perturbed load frequency control using Kharitonov's theorem, *International Journal of Electrical Power & Energy Systems* 78 (2016) 884–896.
- [28] A. Tamaarat, A. Benakcha, Performance of PI controller for control of active and reactive power in DFIG operating in a grid-connected variable speed wind energy conversion system, *Frontiers in Energy* 8 (3) (2014) 371–378.
- [29] B.M. Vinagre, C.A. Monje, A.J. Calderón, J.I. Suárez, Fractional PID controllers for industry application. A brief introduction, *Journal of Vibration and Control* 13 (9–10) (2007) 1419–1429.
- [30] B. William, Frequency response, in: B. William (Ed.), *Instrumentation and Control Systems*, 2nd edition, Elsevier, 2015, pp. 241–270.
- [31] D. Xu, F. Blaabjerg, W. Chen, N. Zhu, Basics of wind power generation system, in: D. Xu, et al. (Eds.), *Advanced Control of Doubly Fed Induction Generator for Wind Power Systems*, Wiley-IEEE press, 2018, pp. 21–42.

This page intentionally left blank

Finite time synchronization of discontinuous fractional order Cohen–Grossberg memristive neural networks with discrete delays under sliding mode control strategies

Pratap Anbalagan^{a,c}, Raja Ramachandran^b, and Evren Hincal^c

^aDepartment of Mathematics, Alagappa University, Alagappapuram, Tamilnadu, India

^bRamanujan Centre for Higher Mathematics, Alagappa University, Alagappapuram, Tamilnadu, India

^cDepartment of Mathematics, Near East University TRNC, Mersin, Turkey

Chapter points

- The existence of solution in Filippov's sense for FDCGMNNs is obtained.
- A finite time sliding mode controller is designed to guarantee the synchronization of FDCGMNNs for finite time cases.

8.1. Introduction

Around 300 years ago, fractional-order calculus was introduced, and it did not gain further interest for a long time due to its lack of application background and its complexity. The final objective of solving differential systems which are representations of physical phenomena is to understand the real-world problems and provide solutions to the addressed problems with high accuracy [64,65]. Over the past few years, fractional-order differential equations found numerous applications in different types of complex systems from diverse disciplines, for example colored noise, ecology, finance, medicine, turbulence, and statistical distribution theory [2,16,33,39]. Moreover, they have many applications in various branches of science and engineering. One of the most peculiar properties of the fractional differential equation is its ability to trace the motion of an object continuously and instantaneously. Moreover, it possesses the memory of the

system [37,51]. The fractional differential equation penetrates the sciences and allows us to use it as a tool to understand the nature of dynamical systems with more accuracy than in the case of integer-order differential equations [33]. In recent times, fractional calculus became the hub of research among diverse fields of researchers and scientists owing to its aforementioned properties [6,23,28]. Due to these properties, by modeling dynamical systems using fractional orders instead of integer orders, we come up with precise information regarding the system even at every real-order moment, which is a highly valuable tool for analyzing the complex characteristics that are useful to predict the nature of the system more effectively. For recent developments in this theory and applications, we refer the reader to [6–8,21,24–26,55].

The basic idea of Cohen–Grossberg neural networks (CGNNs) was initially coined by Cohen and Grossberg in 1983 [15]. In their model, they demonstrate the implementation of specific CGNNs in which the processing units will converge if the inputs are static and can be used for useful calculations. In dynamical systems, CGNNs have widespread applications in several fields, such as filtering, secure communications, nonlinear optimization problems, image processing, associative memory, and parallel computation [48,73,74]. In addition, the time lags will always occur in the process of transmission and information storage in real neural networks due to the finite switching rate of the amplifiers. As a result, the occurrence of time delay in CGNNs may cause the behavior of a system to exhibit oscillation, divergence, and instability characteristics, which are generally encountered in different engineering, physical, and neural-based systems. With the above details, in the current scenario, CGNNs have become a great topic of intellectual study to check the dynamical behaviors of CGNNs with time delays, attracting the interest of several researchers from all over the world (see [29–31,54] and references cited therein).

By utilizing the symmetry theory concept [14], a memristor was firstly considered by Chua in 1971 as the fourth circuit component after resistor, capacitor, and inductor. The resistor depicts the voltage–current relationship, the capacitor depicts the charge–voltage relationship, and the inductor depicts the flux–current relationship. Chua illustrated the lack of a flux–charge relationship, which he characterized as memristance, which is the value of the memristor. The mathematical linkage between flux (q) and charge (φ) is $M(q) = \frac{d\varphi}{dq}$. The Hewlett-Packard laboratory fabricated a practically working memristor device in 2008 [56,57]. The new circuit has memory characteristics like biological neurons, which are distinctive from

other elements of the circuit, such as resistor and capacitor. A memristor has a number of good features like nanometer size, nonvolatility, and nonlinearity, which make it more suitable for simulating synapse resistors [5,34,41]. By replacing the resistors with memristors in a conventional CGNN model, a new Cohen–Grossberg type memristive neural network model can be constructed. The resulting Cohen–Grossberg type memristive neural networks (CGMNNs) are advantage over the conventional Cohen–Grossberg type neural networks because they require low power with strong scalability and high density. Currently, CGMNNs play a significant role in understanding the neuronal processes in the human brain. They are useful in many areas, including associative memory, optimization, engineering, and signal and image processing. Therefore, in theory and applications, it is necessary and important to study CGMNNs. Several interesting results have been documented in recent literatures [38,50,52,53]. On the other hand, a lot of consideration has been given to fractional-order neural networks in light of their potential applications to different fields such as associative memory, electrical engineering, fluid dynamics, and secure communication. In the circuit implementation of integer-order memristive neural networks, many scholars endeavored to update the ordinary capacitor to a fractional capacitor; at that point fractional-order memristor-based neural networks (FOMBNNs) are formed. In recent years, several outstanding results on the different types of FOMBNNs, especially FOMBNNs with recurrent type [3,40], FOMBNNs with fuzzy type [4,36], FOMBNNs with BAM type [9,49], FOMBNNs with competitive type [44,47], and FOMBNNs with Cohen–Grossberg type [73,74], have been proposed and studied. Currently, an ever-increasing number of specialists talks about FCGNNs and some significant outcomes were accounted [32,48,58,71]. However, there have been few investigations of fractional-order CGMNNs (FCGMNNs), as shown by [73,74].

Over the past few years, synchronization has already emerged as a hot research theme and it has been successfully applied in fluid dynamics, optimal control, control theory, and so on. Several kinds of synchronization have been analyzed in the sense of discontinuous CGNNs represented by delay differential equations and lots of scientific results have been established in the literature [1,35,59,60]. But, these results deal with integer-order cases, and few outcomes are concentrated on fractional-order cases [45]. Different from infinite time synchronization, finite time synchronization requires the master–slave system to remain completely identical after some finite time, which is known as the settling time. For finite time drive–

response synchronization of noninteger-order neural networks, many aspects have been broadly investigated under various control techniques such as adaptive feedback control [11], state feedback control [13], pinning control [45], and impulsive control [74]. The interesting feature of sliding mode control is its fast global convergence and high robustness to outside disturbances. By using the sliding mode control scheme the state trajectories of the considered dynamical system are retained by constructing a preferable sliding surface and designing the suitable control for our sliding mode surface. The prime advantages of sliding mode control include less reaction to the disturbances, quick responses, and implementation simplicity. Similarly, the key feature of control strategies of sliding mode control is their ability to apply the suitable sliding surface based on the input–output behavior of the observed plant. It establishes the stability and robustness of the system in an effective way.

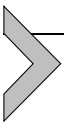
8.1.1 Related works

Chen et al. [12] have examined the sliding mode control problem of projective, complete, and anti-synchronization criteria for time-delayed fractional-order neural networks (FONNs) for different parameters based on Lyapunov stability theory and the Razumikhin approach. Chen et al. [13] have designed the state feedback and adaptive control for several synchronization criteria for discontinuous FONNs by means of some famous inequality techniques, properties of Caputo fractional derivatives, and Lyapunov stability theory. Pratap et al. [45] have established the stability and quasynchronization criteria for discontinuous FCGNNs with time-delay effects by the fractional comparison principle and pinning feedback control. Rajivganthi et al. [48] have investigated the delay-independent stability criteria for FCGNNs with BAM type model for finite time cases based on properties of the Caputo fractional derivative, the contraction mapping principle, some famous inequality scaling skills, and the mean value theorem. Wang et al. [62] have investigated the sliding mode control problem of synchronization criteria of time-delayed memristive FONNs for fixed time cases by Lyapunov stability theory. Wu et al. [68] have derived some sufficient criteria via a matrix element method that ensure the finite time synchronization criteria for FONNs for finite time cases under sliding mode control technology. Zhang et al. [73] have analyzed the finite time and impulsive synchronization criteria for memristive FCGNNs with time-delay effects by state feedback and impulsive control, respectively. Zheng et al. [74] have demonstrated the stability and synchronization criteria for

memristive FCGNNs with time-delay effects by the Gronwall inequality and simple linear feedback control, respectively.

Motivated by the aforementioned publications, the main objective of this chapter is to investigate the sliding model control for finite time synchronization of discontinuous FCGMNNs with discrete delays. The essential theme of this chapter lies in the following aspects. (1) Based on nonsmooth analysis and the growth property, the existence of solutions in Filippov's sense is established and it is improved compared to those in previous works. (2) Based on the theory of sliding mode control, a novel fractional integral sliding mode dynamic surface is designed and an appropriate finite time sliding mode control law is proposed to guarantee the existence of sliding motion. (3) Based on the finite time stability theory and fractional Lyapunov stability theory, we have established the finite time reachability criteria for specified fractional integral sliding mode dynamic surfaces, and some sufficient criteria are derived to ensure finite time synchronization of the addressed model. The remaining structure of this chapter is outlined as follows: Basic tools on fractional-order derivatives, properties of the Mittag-Leffler function, and a system description for FDCGMNNs are formally defined in Section 8.2. Section 8.3 describes the main results of this chapter. In Section 8.4, numerical results and their applications are presented. At last, Section 8.5 ends with conclusions and future directions.

In the following, \mathbb{R}^m refers to the m -dimensional space. The set of all $m \times m$ real matrices is represented by $\mathbb{R}^{m \times m}$. Let us denote $\|R\| = \max_{1 \leq x \leq m} \{\sum_{y=1}^m |r_{xy}|\}$. The symbol $\|\cdot\|$ indicates norm-2; $C([-\mu, 0], \mathbb{R}^m)$ refers to the set of all continuous functions from $[-\mu, 0]$ to \mathbb{R}^m , where $\mu > 0$; $sign(\cdot)$ indicates the signum function; and $BCC(\Omega)$ refers to the set of all nonempty bounded closed and convex subsets of Ω .



8.2. Preliminaries

In this section, some preliminaries, a model description, and some assumptions are introduced.

8.2.1 Basic tools for fractional-order derivatives

There are several fractional derivatives, like the Riemann–Liouville fractional derivative, the Caputo fractional derivative, the Caputo–Fabrizio derivative, the Atangana derivative, and the Hadamard derivative. Compared to the other kinds of fractional-order derivative, the initial values of

the Caputo fractional have a similar form as those of the integer-order differential equation, facilitating understanding of physical significance and extensive practical applications. Furthermore, the Caputo fractional derivative can easily solve the initial value problem of nonlinear fractional dynamical systems, which is broadly applied in the modeling of real-world practical systems. Due to these advantages, the definition of Caputo derivative will be considered in this chapter.

Definition 8.1. [43] The fractional-order integral with order $\lambda > 0$ for a function $u(t)$ is described as follows:

$${}_0D_t^{-\lambda} u(t) = \frac{1}{\Gamma(\lambda)} \int_0^t (t - \varsigma)^{\lambda-1} u(\varsigma) d\varsigma, \quad (8.1)$$

where $\Gamma(\cdot)$ is the gamma function, which is described as

$$\Gamma(\tau) = \int_0^\infty \exp(-t)t^{\vartheta-1} dt, \quad (\text{Re}(\vartheta) > 0), \quad (8.2)$$

where $\text{Re}(\vartheta)$ refers to the real part of ϑ .

Definition 8.2. [43] The Caputo fractional derivative with order $0 < \lambda < 1$ for function $u(t)$ is described as follows:

$${}_0^C D_t^\lambda u(t) = \frac{1}{\Gamma(1 - \lambda)} \int_0^t \frac{u'(\varsigma)}{(t - \varsigma)^\lambda} d\varsigma. \quad (8.3)$$

Furthermore, the following Caputo fractional-order derivative properties are given.

Property (i). Let δ be any scalar. Then ${}_0^C D_t^\gamma \delta = 0$ holds.

Property (ii). For any scalars ω and ϖ , the linearity of the Caputo fractional-order derivative gives

$${}_0^C D_t^\lambda (\omega u_1(t) + \varpi u_2(t)) = \omega {}_0^C D_t^\lambda u_1(t) + \varpi {}_0^C D_t^\lambda u_2(t).$$

Property (iii). Suppose $\xi_1(t)$ and $\xi_2(t)$ and its all derivatives are continuous in the interval $[0, t]$. The Leibniz rule for fractional-order differentiation is

$${}_0^C D_t^\lambda (\xi_1(t)\xi_2(t)) = \sum_{\ell=0}^{+\infty} \frac{\lambda \Gamma(\lambda)}{\ell \Gamma(\ell) \Gamma(\lambda + 1 - \ell)} \xi_1^{(\ell)}(t) {}_0^C D_t^{\lambda-\ell} \xi_2(t),$$

where $\xi_1^{(\ell)}(t)$ indicates the integer-order derivative of function $\xi_1(t)$ with order ℓ and ${}_0^C D_t^{\lambda-\ell} \xi_2(t)$ indicates the fractional-order derivative of function $\xi_2(t)$ with order $\lambda - \ell$.

Property (iv). For $\lambda_1 > 0$, $\lambda_2 > 0$, and $\lambda_1 + \lambda_2 > 1$, the following inequality holds:

$${}_0^C D_t^{\lambda_1} \left({}_0^C D_t^{\lambda_2} u(t) \right) = {}_0^C D_t^{\lambda_1 + \lambda_2} u(t).$$

Property (v). For the Caputo fractional-order derivative, we have

$${}_0^C D_t^\lambda {}_0 D_t^{-\lambda} u(t) = u(t).$$

Property (vi). If $u(t) \in C^m[0, +\infty)$, then

$${}_0 D_t^{-\lambda} {}_0^C D_t^\lambda u(t) = u(t) - \sum_{\ell=1}^{m-1} \frac{t^{(\ell)}}{\ell!} u^{(\ell)}(0), \quad t \geq 0,$$

where $m - 1 < \lambda < m$ and m is a positive integer.

Consider the following delay differential system with fractional order:

$$\begin{cases} {}_0^C D_t^\lambda u(t) = g(t, u(t - \mu)), & t > 0, \\ u(t) = u_0(t), & t \in [-\mu, 0], \end{cases} \quad (8.4)$$

where $0 < \lambda < 1$, $u(t) \in \mathbb{R}^m$, $\mu > 0$, $g: [0, +\infty) \times \mathbb{R}^m \rightarrow \mathbb{R}^m$ is piecewise continuous and its solution can be written as follows:

$$u(t) = u_0(t) + \frac{1}{\Gamma(\lambda)} \int_0^t (t - \ell)^{\lambda-1} g(\ell, u(\ell - \mu)) d\ell. \quad (8.5)$$

Lemma 8.1. [70] Let $\xi(t) \in \mathbb{R}^m$ be a continuously differentiable vector-valued function. Then

$${}_0^C D_t^\lambda \xi^2(t) \leq 2\xi(t) {}_0^C D_t^\lambda \xi(t), \quad \lambda \in (0, 1). \quad (8.6)$$

8.2.2 Mittag-Leffler function

The definition of the Mittag-Leffler function with one and two parameters and its properties are given in this subsection.

Definition 8.3. [43] The Mittag-Leffler function with two parameters $\lambda, \zeta > 0$ is described as follows:

$$M_{\lambda,\zeta}(\varsigma) = \sum_{\ell=0}^{+\infty} \frac{\varsigma^\ell}{\Gamma(\lambda u + \zeta)}, \tag{8.7}$$

where $\varsigma \in \mathbb{R}$. Especially, when $\zeta = 1$,

$$M_{\lambda,1}(\varsigma) =: M_\lambda(\varsigma) = \sum_{\ell=0}^{+\infty} \frac{\varsigma^\ell}{\Gamma(\lambda u + 1)}. \tag{8.8}$$

Definition 8.4. [43] The Laplace transform of the Mittag-Leffler function with two parameters is defined as

$$\mathcal{L}\left\{t^{\gamma-1}M_{\lambda,\gamma}(\alpha t^\lambda)\right\} = \frac{s^{\lambda-\gamma}}{s^\lambda - \alpha}, \quad \left(\operatorname{Re}(s) > \sqrt[\lambda]{|\alpha|}\right),$$

where $\lambda \in (m - 1, m)$ and s and t are variables in the Laplace domain and the time domain, respectively.

Lemma 8.2. [66] Suppose the increasing nonnegative function $u_1(\ell)$ is locally integrable on $\ell \in [0, T)$ and the increasing nonnegative function $u_2(\ell) \leq \Delta$ is described on $\ell \in [0, T)$, where Δ is a positive scalar. . If $v(\ell)$ is nonnegative, locally integrable and satisfies

$$v(\ell) \leq u_1(\ell) + u_2(\ell) \int_0^\ell (\ell - t)^{\lambda-1} v(t) dt, \quad \ell \in [0, T), \tag{8.9}$$

we have

$$v(\ell) \leq u_1(\ell)M_\lambda\left(u_2(\ell)\Gamma(\lambda)\ell^\lambda\right), \tag{8.10}$$

where λ is a positive scalar. This inequality is called as the generalized Gronwall inequality.

Lemma 8.3. [69] For $0 < \lambda < 1$ and $|\arg t| < \frac{\pi}{2}$, we have

$$M_\lambda(t) = \frac{1}{\lambda} \exp t^{\frac{1}{\lambda}} - \sum_{\ell=1}^v \frac{1}{t^\ell \Gamma(1 - \lambda \ell)} + \mathcal{O}\left(\frac{1}{t^{v+1}}\right), \quad 0 \neq t \in \mathbb{R}, \quad |t| \rightarrow +\infty, \tag{8.11}$$

where $v > 1$ is a scalar.

8.2.3 Model formulation

In this chapter, the dynamics of fractional-order discontinuous CGMNNs (FDCGMNNs) can be described by the fractional-order delay differential equations:

$$\begin{aligned}
 {}_0^C D_t^\lambda u_x(t) = & -p_x(u_x(t)) \left[q_x(u_x(t)) - \sum_{y=1}^m r_{xy}(u_y(t))g_y(u_y(t)) \right. \\
 & \left. - \sum_{y=1}^m s_{xy}(u_y(t))g_y(u_y(t-\mu)) - F_x \right], \tag{8.12}
 \end{aligned}$$

and the vector form is

$${}_0^C D_t^\lambda u(t) = -P(u(t)) \left[Q(u(t)) - R(u(t))g(u(t)) - S(u(t))g(u(t-\mu)) - F \right], \tag{8.13}$$

where $x = 1, 2, \dots, m$, ${}_0^C D_t^\lambda$ refers to the Caputo fractional derivative of order $0 < \lambda < 1$, $u(t) = (u_1(t), \dots, u_m(t))^T \in \mathbb{R}^m$ are the state variables at time t , $P(u(t)) = \text{diag}(p_1(u_1(t)), \dots, p_m(u_m(t)))$ and $Q(u(t)) = \text{diag}(q_1(u_1(t)), \dots, q_m(u_m(t)))$ indicate an amplification function and a well-behaved function, $g(u(t)) = [g_1(u_1(t)), \dots, g_m(u_m(t))]^T$ signifies the neuron activations at time t , constant $\mu > 0$ refers to the time lag, and $F = (F_1, \dots, F_m)^T$ is an external input.

Based on the memristive properties of current-voltage, the model of memristive connection weights can be described as $R(u(t)) = [r_{xy}(u_x(t))]_{m \times m}$, $S(u(t)) = [s_{xy}(u_x(t))]_{m \times m}$, where

$$r_{xy}(u_y(t)) = \begin{cases} \acute{r}_{xy}, & |u_y(t)| \leq \Pi_x, \\ \grave{r}_{xy}, & |u_y(t)| > \Pi_x, \\ \acute{r}_{xy} \text{ or } \grave{r}_{xy}, & |u_y(t)| = \Pi_x \end{cases}$$

and

$$s_{xy}(u_y(t)) = \begin{cases} \acute{s}_{xy}, & |u_y(t)| \leq \Pi_x, \\ \grave{s}_{xy}, & |u_y(t)| > \Pi_x, \\ \acute{s}_{xy} \text{ or } \grave{s}_{xy}, & |u_y(t)| = \Pi_x, \end{cases}$$

where Π_x are switching jumps, \acute{r}_{xy} , \grave{r}_{xy} , \acute{s}_{xy} , and \grave{s}_{xy} are all constants, and $x, y \in \mathbb{N}$. Let $r_{xy}^- = \min\{\acute{r}_{xy}, \grave{r}_{xy}\}$, $r_{xy}^+ = \max\{\acute{r}_{xy}, \grave{r}_{xy}\}$, $s_{xy}^- = \min\{\acute{s}_{xy}, \grave{s}_{xy}\}$, and

$s_{xy}^+ = \max\{\dot{s}_{xy}, \check{s}_{xy}\}$. The initial values of fractional system (8.12) are $u(\ell) = v(\ell) = (v_1(\ell), \dots, v_m(\ell))^T \in \mathbb{R}^m$ and the norm is described as

$$\|v\| = \sup_{\ell \in [-\mu, 0]} \|v(\ell)\|.$$

In this chapter, the neuron activations are not continuous. Based on the classical definition, the solution of the FDCGMNNs (8.12) does not exist. Therefore, we can recommend the theory of Filippov solution [22].

Definition 8.5. Consider the differential system with fractional order

$$\begin{cases} {}^C_0 D_t^\lambda u(t) = g(t, u), & t > 0, \\ u(0) = u_0, & u \in \mathbb{R}^m, \end{cases} \tag{8.14}$$

where $g(t, u)$ is discontinuous in u . The set-valued map $\mathcal{G} : \mathbb{R}^m \rightarrow 2^{\mathbb{R}^m}$ is described as

$$\mathcal{G}(t, u) = \bigcap_{\tau > 0} \bigcap_{\sigma(\mathcal{J})=0} \overline{\text{co}} \left[g(t, \mathbb{B}(u, \tau) \setminus \mathcal{K}) \right],$$

where $\mathbb{B}(u, \tau) = \{\check{u}; \|\check{u} - u\| \leq \tau\}$, $\mathcal{J} \subseteq \mathbb{R}^m$. The Lebesgue measurable of set \mathcal{K} is denoted as $\sigma(\mathcal{K})$. A vector function $u(t)$ defined on $\mathcal{M} \subseteq \mathbb{R}$ is said to be a Filippov solution of fractional differential system (8.14) if it is absolutely continuous on any subinterval of a nondegenerate interval $[t_1, t_2]$ of \mathcal{M} , for a.a. $t \in \mathcal{M}$, $u(t)$ satisfies the following differential inclusion

$${}^C_0 D_t^\lambda u(t) \in \mathcal{G}(t, u).$$

Via the above theory of differential inclusion, the FDCGMNNs (8.12) can be obtained as follows:

$$\begin{aligned} {}^C_0 D_t^\lambda u_x(t) \in & -p_x(u_x(t)) \left[q_x(u_x(t)) - \sum_{\gamma=1}^m \mathcal{G}(r_{xy}(u_\gamma(t))) \mathcal{G}[g_\gamma(u_\gamma(t))] \right. \\ & \left. - \sum_{\gamma=1}^m \mathcal{G}(s_{xy}(u_\gamma(t))) \mathcal{G}[g_\gamma(u_\gamma(t - \mu))] - F_x \right], \end{aligned} \tag{8.15}$$

for $x = 1, 2, \dots, m$, a.a. $t \geq 0$, where the Filippov set-valued maps are

$$\mathcal{G}[g_\gamma(u_\gamma)] = \left\{ \min\{g_\gamma^-(u_\gamma), g_\gamma^+(u_\gamma)\}, \max\{g_\gamma^-(u_\gamma), g_\gamma^+(u_\gamma)\} \right\}$$

and

$$\mathcal{G}\left(r_{xy}(u_y(t))\right) = \begin{cases} \dot{r}_{xy}, & |u_y(t)| \leq \Pi_x, \\ \check{r}_{xy}, & |u_y(t)| > \Pi_x, \\ [r_{xy}^-, r_{xy}^+], & |u_y(t)| = \Pi_x, \end{cases}$$

$$\mathcal{G}\left(s_{xy}(u_y(t))\right) = \begin{cases} \dot{s}_{xy}, & |u_y(t)| \leq \Pi_x, \\ \check{s}_{xy}, & |u_y(t)| > \Pi_x, \\ [s_{xy}^-, s_{xy}^+], & |u_y(t)| = \Pi_x, \end{cases}$$

or there exist measurable functions $\check{r}_{xy} \in \mathcal{G}\left(r_{xy}(u_y(t))\right)$, $\check{s}_{xy} \in \mathcal{G}\left(s_{xy}(u_y(t))\right)$, and $\beta_y(t) \in \mathcal{G}\left[g_y(u_y(t))\right]$ such that

$${}_0^C D_t^\lambda u_x(t) = -p_x(u_x(t)) \left[q_x(u_x(t)) - \sum_{\gamma=1}^m \check{r}_{xy} \beta_\gamma(t) - \sum_{\gamma=1}^m \check{s}_{xy} \beta_\gamma(t - \mu) - F_x \right]. \quad (8.16)$$

Throughout this chapter, the corresponding response system is described as

$${}_0^C D_t^\lambda v_x(t) = -p_x(v_x(t)) \left[q_x(v_x(t)) - \sum_{\gamma=1}^m r_{xy}(v_y(t)) g_\gamma(v_y(t)) - \sum_{\gamma=1}^m s_{xy}(v_y(t)) g_\gamma(v_y(t - \mu)) - F_x \right] + z_x(t), \quad (8.17)$$

and the vector form is

$${}_0^C D_t^\lambda v(t) = -P(v(t)) \left[Q(v(t)) - R(v(t))g(v(t)) - S(v(t))g(v(t - \mu)) - F \right] + z(t), \quad (8.18)$$

where $x = 1, 2, \dots, m$, $v(t) = (v_1(t), \dots, v_m(t))^T \in \mathbb{R}^m$ are the state variables of system (8.18) at time t , and $z(t) = (z_1(t), \dots, z_m(t))^T \in \mathbb{R}^m$ are suitable control inputs. The model of memristive connection weights of system (8.18) can be described as $R(v(t)) = [r_{xy}(v_x(t))]_{m \times m}$, $S(v(t)) = [s_{xy}(v_x(t))]_{m \times m}$,

where

$$r_{xy}(v_y(t)) = \begin{cases} \hat{r}_{xy}, & |v_y(t)| \leq \Pi_x, \\ \check{r}_{xy}, & |v_y(t)| > \Pi_x, \\ \hat{r}_{xy} \text{ OR } \check{r}_{xy}, & |v_y(t)| = \Pi_x \end{cases}$$

and

$$s_{xy}(v_y(t)) = \begin{cases} \acute{s}_{xy}, & |v_y(t)| \leq \Pi_x, \\ \grave{s}_{xy}, & |v_y(t)| > \Pi_x, \\ \acute{s}_{xy} \text{ OR } \grave{s}_{xy}, & |v_y(t)| = \Pi_x. \end{cases}$$

Via the above theory of differential inclusion, the FDCGMNNs (8.18) can be obtained as follows:

$$\begin{aligned} {}^C_0D_t^\lambda v_x(t) \in & -p_x(v_x(t)) \left[q_x(v_x(t)) - \sum_{y=1}^m \mathcal{G}(r_{xy}(v_y(t))) \mathcal{G}[g_y(v_y(t))] \right. \\ & \left. - \sum_{y=1}^m \mathcal{G}(s_{xy}(v_y(t))) \mathcal{G}[g_y(v_y(t-\mu))] - F_x \right] + z_x(t), \end{aligned} \tag{8.19}$$

for $x = 1, 2, \dots, m$, a.a. $t \geq 0$, where the Filippov set-valued maps are

$$\mathcal{G}[g_y(v_y)] = \left\{ \min\{g_y^-(v_y), g_y^+(v_y)\}, \max\{g_y^-(v_y), g_y^+(v_y)\} \right\}$$

and

$$\begin{aligned} \mathcal{G}(r_{xy}(v_y(t))) &= \begin{cases} \hat{r}_{xy}, & |v_y(t)| \leq \Pi_x, \\ \check{r}_{xy}, & |v_y(t)| > \Pi_x, \\ [r_{xy}^-, r_{xy}^+], & |v_y(t)| = \Pi_x, \end{cases} \\ \mathcal{G}(s_{xy}(v_y(t))) &= \begin{cases} \acute{s}_{xy}, & |v_y(t)| \leq \Pi_x, \\ \grave{s}_{xy}, & |v_y(t)| > \Pi_x, \\ [s_{xy}^-, s_{xy}^+], & |v_y(t)| = \Pi_x, \end{cases} \end{aligned}$$

or there exist measurable functions $\hat{r}_{xy} \in \mathcal{G}(r_{xy}(v_y(t)))$, $\hat{s}_{xy} \in \mathcal{G}(s_{xy}(v_y(t)))$, and $\gamma_y(t) \in \mathcal{G}[g_y(v_y(t))]$ such that

$$\begin{aligned}
{}_0^C D_t^\lambda v_x(t) = & -p_x(v_x(t)) \left[q_x(v_x(t)) - \sum_{\gamma=1}^m \hat{r}_{xy} \gamma_\gamma(t) - \sum_{\gamma=1}^m \hat{s}_{xy} \gamma_\gamma(t - \mu) - F_x \right] \\
& + z_x(t). \tag{8.20}
\end{aligned}$$

Let $w_x(t) = v_x(t) - u_x(t)$. Then based on (8.16) and (8.20), the synchronization error dynamic is described as

$$\begin{aligned}
& {}_0^C D_t^\lambda w_x(t) \\
& = -p_x(v_x(t)) \left[q_x(v_x(t)) - \sum_{\gamma=1}^m \hat{r}_{xy} \gamma_\gamma(t) - \sum_{\gamma=1}^m \hat{s}_{xy} \gamma_\gamma(t - \mu) - F_x \right] \\
& \quad + z_x(t) + p_x(u_x(t)) \left[q_x(u_x(t)) - \sum_{\gamma=1}^m \check{r}_{xy} \beta_\gamma(t) - \sum_{\gamma=1}^m \check{s}_{xy} \beta_\gamma(t - \mu) - F_x \right] \\
& = -\left(p_x(v_x(t)) q_x(v_x(t)) - p_x(u_x(t)) q_x(u_x(t)) \right) + \left(p_x(v_x(t)) - p_x(u_x(t)) \right) F_x \\
& \quad + \sum_{\gamma=1}^m p_x(v_x(t)) \hat{r}_{xy} (\gamma_\gamma(t) - \beta_\gamma(t)) + \sum_{\gamma=1}^m p_x(v_x(t)) \hat{s}_{xy} (\gamma_\gamma(t - \mu) - \beta_\gamma(t - \mu)) \\
& \quad + \sum_{\gamma=1}^m p_x(v_x(t)) \hat{r}_{xy} \beta_\gamma(t) - \sum_{\gamma=1}^m p_x(u_x(t)) \check{r}_{xy} \beta_\gamma(t) + \sum_{\gamma=1}^m p_x(v_x(t)) \hat{s}_{xy} \beta_\gamma(t - \mu) \\
& \quad - \sum_{\gamma=1}^m p_x(u_x(t)) \check{s}_{xy} \beta_\gamma(t - \mu) + z_x(t). \tag{8.21}
\end{aligned}$$

Throughout this chapter, the following assumptions are very important to solve the synchronization problem of FDCGMNNs (8.12) and FDCGMNNs (8.16), respectively.

Assumption 8.1. Suppose there exist positive scalars $\eta_\gamma > 0$ and $\theta_\gamma > 0$ such that

$$|\mathcal{G}[g_\gamma(u_\gamma(t))]| = \sup_{\alpha \in \mathcal{G}[g_\gamma(u_\gamma(t))]} |\alpha| \leq \eta_\gamma |u_\gamma(t)| + \theta_\gamma,$$

for $\gamma = 1, 2, \dots, m$.

Assumption 8.2. In every bounded interval, the bounded nonlinear function $(|g_\gamma(\cdot)| \leq \varpi_\gamma)$ is a continuous function except for a finite number of isolated points σ_k^j . Furthermore, there exist right and left limits $g_\gamma^+(\sigma_j^j)$ and $g_\gamma^-(\sigma_j^j)$, respectively.

Assumption 8.3. For each $x = 1, 2, \dots, m$, there exist positive scalars $\check{\eta}_y > 0$ and $\check{\theta}_y > 0$ such that

$$|\gamma_y(t) - \beta_y(t)| \leq \check{\eta}_y |v_y(t) - u_y(t)| + \check{\theta}_y,$$

where $\gamma_y(t) \in \mathcal{G}[g_y(v_y(t))]$ and $\beta_y(t) \in \mathcal{G}[g_y(u_y(t))]$.

Assumption 8.4. For every $x = 1, 2, \dots, m$, there exist scalars $p_x^* > 0$, $p_x^{**} > 0$, $q_x^* > 0$, $q_x^{**} > 0$, and \check{p}_x such that the amplification function and the behavior function fulfill the following relationship:

$$0 \leq p_x^* \leq p_x(u_x) \leq p_x^{**} < \infty, \quad 0 \leq q_x^* \leq q_x(u_x) \leq q_x^{**} < \infty, \\ |p_x(v) - p_x(u)| \leq \check{p}_x |v - u|, \quad u, v \in \mathbb{R}.$$

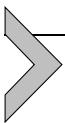
Assumption 8.5. For every $x = 1, 2, \dots, m$, there exist scalars $\varphi_x > 0$ such that the following relationship holds:

$$\frac{p_x(v)q_x(v) - p_x(u)q_x(u)}{v - u} \geq \varphi_x,$$

for all $u, v \in \mathbb{R}$, $u \neq v$.

To derive the existence of Filippov solutions for the FDCGMNNs (8.12), we need to provide the following lemma.

Lemma 8.4. Suppose the set $\Phi = \left\{ u \in \Omega : \varsigma u \in \varsigma \mathbb{G}(u), \varsigma > 1 \right\}$ is bounded. Then the set Φ is a fixed point, where $\mathbb{G} : \Omega \rightarrow BCC(\Omega)$ is a condensing map and Ω is a Banach space.



8.3. Main results

In this part, we will derive the existence of solutions in the Filippov sense. Then, a novel fractional integral sliding mode dynamic surface and finite time sliding model control will be incorporated into the proposed synchronization problem of FDCGMNNs with time delays.

8.3.1 Existence of Filippov solutions

Theorem 8.1. When Assumption 8.1 and Assumption 8.2 hold, then there exist at least one solution $\tilde{u}(t)$ of FDCGMNNs (8.12) on a positive interval in view of FDCGMNNs (8.15).

Proof. A set-valued map

$$u(t) \hookrightarrow -P(u(t)) \left[Q(u(t)) - R(u(t))g(u(t)) - S(u(t))g(u(t - \mu)) - F \right]$$

has nonempty bounded closed convex values and is upper semicontinuous.

Construct a map $\mathbb{G} : C([- \delta, T], \mathbb{R}^m) \rightarrow C([- \delta, T], \mathbb{R}^m)$ based on the solution of FDCGMNNs. We have

$$\mathbb{G} : u(t) = u(0) + \frac{1}{\Gamma(\lambda)} \int_0^t (t - \ell)^{\lambda-1} \left\{ -P(u(\ell)) \left[Q(u(\ell)) - R(u(\ell))g(u(\ell)) - S(u(\ell))g(u(\ell - \mu)) - F \right] \right\} d\ell.$$

Then, we will prove that the set Φ is bounded, where

$$\Phi = \left\{ u \in C([- \delta, T], \mathbb{R}^m) : \varsigma u \in \mathbb{G}(u), \varsigma > 1 \right\}.$$

Thus,

$$u(t) = \frac{1}{\varsigma} \left\{ u(0) + \frac{1}{\Gamma(\lambda)} \int_0^t (t - \ell)^{\lambda-1} \left\{ -P(u(\ell)) \left[Q(u(\ell)) - R(u(\ell))g(u(\ell)) - S(u(\ell))g(u(\ell - \mu)) - F \right] \right\} d\ell \right\}.$$

From Assumption 8.1 and Assumption 8.2, we have

$$\begin{aligned} \|u(t)\| &\leq \|u(0)\| + \left\| \frac{1}{\Gamma(\lambda)} \int_0^t (t - \ell)^{\lambda-1} \left\{ -P(u(\ell)) \left[Q(u(\ell)) - R(u(\ell))g(u(\ell)) - S(u(\ell))g(u(\ell - \mu)) - F \right] \right\} d\ell \right\| \\ &\leq \|u(0)\| + \frac{1}{\Gamma(\lambda)} \int_0^t (t - \ell)^{\lambda-1} \left\{ \|\tilde{P}\| \|\tilde{Q}\| \|u(\ell)\| + \|\tilde{P}\| \|\tilde{R}\| \|g(u(\ell))\| \right. \\ &\quad \left. + \|\tilde{P}\| \|\tilde{S}\| \|g(u(\ell - \mu))\| + \|\tilde{P}\| \|F\| \right\} d\ell \\ &\leq \|u(0)\| + \frac{1}{\Gamma(\lambda)} \int_0^t (t - \ell)^{\lambda-1} \left\{ \|\tilde{P}\| \|\tilde{Q}\| \|u(\ell)\| \right. \\ &\quad \left. + \|\tilde{P}\| \|\tilde{R}\| \left[E \|u(\ell)\| + \Psi \right] \right\} d\ell \end{aligned}$$

$$\begin{aligned}
& + \|\tilde{P}\| \|\tilde{S}\| \left[E\|u(\ell - \mu)\| + \Psi \right] + \|\tilde{P}\| \|F\} \} d\ell \\
= & \|u(0)\| + \frac{1}{\Gamma(\lambda)} \int_0^t (t - \ell)^{\lambda-1} \|\tilde{P}\| \|\tilde{Q}\| \|u(\ell)\| d\ell \\
& + \frac{1}{\Gamma(\lambda)} \int_0^t (t - \ell)^{\lambda-1} \|\tilde{P}\| \|\tilde{R}\| \left[E\|u(\ell)\| + \Psi \right] d\ell \\
& + \frac{1}{\Gamma(\lambda)} \int_0^t (t - \ell)^{\lambda-1} \|\tilde{P}\| \|\tilde{S}\| \left[E\|u(\ell - \mu)\| + \Psi \right] + \|\tilde{P}\| \|F\| d\ell,
\end{aligned}$$

where

$$\begin{aligned}
E &= \max\{\eta_1, \dots, \eta_m\}, \quad \Psi = \max\{\theta_1, \dots, \theta_m\}, \\
\tilde{P} &= \text{diag}\{p_1^{**}, \dots, p_m^{**}\}, \quad \tilde{Q} = \text{diag}\{q_1^{**}, \dots, q_m^{**}\}, \\
\tilde{R} &= (r_{xy})_{m \times m}, \quad r_{xy} = \max\{|\dot{r}_{xy}|, |\dot{s}_{xy}|\}, \\
\tilde{S} &= (s_{xy})_{m \times m}, \quad s_{xy} = \max\{|\dot{s}_{xy}|, |\dot{\delta}_{xy}|\}.
\end{aligned}$$

It is notable that

$$\begin{aligned}
\|u(t - \mu)\| &\leq \sup_{\ell \in [-\mu, t]} \|u(\ell)\| \\
&= \sup_{\ell \in [-\mu, 0]} \|u(\ell)\| + \sup_{\ell \in [0, t]} \|u(\ell)\| \\
&= \|\nu\| + \|u(t)\|.
\end{aligned}$$

From the above inequality, we have

$$\begin{aligned}
\|u(t)\| &\leq \|u(0)\| + \frac{1}{\Gamma(\lambda)} \int_0^t (t - \ell)^{\lambda-1} \|\tilde{P}\| \|\tilde{Q}\| \|u(\ell)\| d\ell \\
&+ \frac{1}{\Gamma(\lambda)} \int_0^t (t - \ell)^{\lambda-1} \|\tilde{P}\| \|\tilde{R}\| \left[E\|u(\ell)\| + \Psi \right] d\ell \\
&+ \frac{1}{\Gamma(\lambda)} \int_0^t (t - \ell)^{\lambda-1} \|\tilde{P}\| \|\tilde{S}\| \left[E(\|u(\ell)\| + \|\nu\|) + \Psi \right] \\
&+ \frac{\|\tilde{P}\| \|F\|}{\Gamma(\lambda)} \int_0^t (t - \ell)^{\lambda-1} d\ell \\
&\leq \|\nu\| + \frac{1}{\Gamma(\lambda)} \int_0^t (t - \ell)^{\lambda-1} \|\tilde{P}\| \|\tilde{Q}\| \|u(\ell)\| d\ell \\
&+ \frac{1}{\Gamma(\lambda)} \int_0^t (t - \ell)^{\lambda-1} \|\tilde{P}\| \|\tilde{R}\| E\|u(\ell)\| d\ell \\
&+ \frac{1}{\Gamma(\lambda)} \int_0^t (t - \ell)^{\lambda-1} \|\tilde{P}\| \|\tilde{R}\| \Psi d\ell
\end{aligned}$$

$$\begin{aligned}
& + \frac{1}{\Gamma(\lambda)} \int_0^t (t-\ell)^{\lambda-1} \|\tilde{P}\| \|\tilde{S}\| E \|u(\ell)\| d\ell \\
& + \frac{1}{\Gamma(\lambda)} \int_0^t (t-\ell)^{\lambda-1} \|\tilde{P}\| \|\tilde{S}\| E \|v\| d\ell \\
& + \frac{1}{\Gamma(\lambda)} \int_0^t (t-\ell)^{\lambda-1} \|\tilde{P}\| \|\tilde{S}\| \Psi d\ell + \frac{1}{\Gamma(\lambda)} \int_0^t (t-\ell)^{\lambda-1} \|\tilde{P}\| \|\tilde{F}\| d\ell \\
= & \|v\| + \frac{\|\tilde{P}\| \|\tilde{S}\| E}{\Gamma(\lambda)} \int_0^t (t-\ell)^{\lambda-1} \|v\| d\ell \\
& + \frac{\left\{ \|\tilde{P}\| \|\tilde{R}\| \Psi + \|\tilde{P}\| \|\tilde{S}\| \Psi + \|\tilde{P}\| \|F\| \right\}}{\Gamma(\lambda)} \int_0^t (t-\ell)^{\lambda-1} d\ell \\
& + \frac{\left\{ \|\tilde{P}\| \|\tilde{Q}\| + \|\tilde{P}\| \|\tilde{R}\| E + \|\tilde{P}\| \|\tilde{S}\| E \right\}}{\Gamma(\lambda)} \int_0^t (t-\ell)^{\lambda-1} \|u(\ell)\| d\ell \\
= & \left[1 + \frac{\|\tilde{P}\| \|\tilde{S}\| E t^\lambda}{\lambda \Gamma(\lambda)} \right] \|v\| \\
& + \frac{1}{\Gamma(\lambda)} \int_0^t (t-\ell)^{\lambda-1} \left\{ \|\tilde{P}\| \|\tilde{R}\| \Psi + \|\tilde{P}\| \|\tilde{S}\| \Psi + \|\tilde{P}\| \|F\| \right\} d\ell \\
& + \frac{1}{\Gamma(\lambda)} \int_0^t (t-\ell)^{\lambda-1} \left\{ \|\tilde{P}\| \|\tilde{Q}\| + \|\tilde{P}\| \|\tilde{R}\| E + \|\tilde{P}\| \|\tilde{S}\| E \right\} \|u(\ell)\| d\ell \\
= &: \Lambda_1(t) + \frac{\Lambda_2(t)}{\Gamma(\lambda)} \int_0^t (t-\ell)^{\lambda-1} \|u(\ell)\| d\ell,
\end{aligned}$$

where

$$\begin{aligned}
\Lambda_1(t) &= \|\tilde{P}\| \left[\left(\|\tilde{R}\| + \|\tilde{S}\| \right) \Psi + \|F\| \right] \frac{t^\lambda}{\Gamma(\lambda+1)} + \left[1 + \frac{\|\tilde{P}\| \|\tilde{S}\| E t^\lambda}{\Gamma(\lambda+1)} \right] \|v\|, \\
\Lambda_2(t) &= \|\tilde{P}\| \left(\|\tilde{Q}\| + \left(\|\tilde{R}\| + \|\tilde{S}\| \right) E \right).
\end{aligned}$$

In view of the famous generalized Gronwall inequality (Lemma 8.2), we have

$$\|u(t)\| \leq \Lambda_1(t) M_{\lambda,1} \left(\Lambda_2(t) t^\lambda \right),$$

which means that Φ is bounded for any positive interval. Based on Lemma 8.4, we conclude that \mathbb{G} has a unique fixed point \tilde{u} , which is a solution of FDCGMNNs (8.15). The proof is completed. \square

8.3.2 Finite time stability criteria for the sliding motion

In view of synchronization error dynamic (8.21), we design the following fractional-order integral sliding surface:

$$\Upsilon_x(t) = w_x(t) + {}_0 D_t^{-\lambda} \left\{ \xi_x w_x(t) + \frac{\sigma_x \operatorname{sign}(w_x(t))}{|w_x(t)|} \right\}, \quad (8.22)$$

where $\xi_x, \sigma_x > 0$, $x = 1, 2, \dots, m$.

By means of the theory of sliding mode, the sliding surface and its derivative must hold:

$$\begin{cases} \Upsilon_x(t) = 0, \\ \dot{\Upsilon}_x(t) = 0. \end{cases} \quad (8.23)$$

Furthermore, one can obtain

$$\dot{\Upsilon}_x(t) = {}_0^C D_t^{1-\lambda} \left\{ {}_0^C D_t^\lambda \Upsilon_x(t) \right\},$$

where Property (iv) and Property (v) have been used. So

$$\dot{\Upsilon}_x(t) = 0,$$

which leads to

$${}_0^C D_t^\lambda \Upsilon_x(t) = 0.$$

Then, combined with (8.22) and (8.23), we sustain that

$${}_0^C D_t^\lambda \Upsilon_x(t) = {}_0^C D_t^\lambda w_x(t) + \xi_x w_x(t) + \frac{\sigma_x \operatorname{sign}(w_x(t))}{|w_x(t)|},$$

which leads to

$${}_0^C D_t^\lambda w_x(t) = -\xi_x w_x(t) - \frac{\sigma_x \operatorname{sign}(w_x(t))}{|w_x(t)|}. \quad (8.24)$$

It is notable that $w = 0$ is an equilibrium point of the system (8.24).

Theorem 8.2. *If $0 < \lambda < 1$, then the sliding mode dynamic (8.24) is stable in a finite time t , where*

$$t \leq \sqrt[\lambda]{\frac{\sum_{x=1}^m w_x^2(0) \Gamma(\lambda + 1)}{\sum_{x=1}^m 2\sigma_x}}.$$

Proof. Construct the following Lyapunov functional:

$$L_1(t) = \sum_{x=1}^m w_x^2(t).$$

According to Lemma 8.1, we have

$$\begin{aligned} {}_0^C D_t^\lambda L_1(t) &\leq 2 \sum_{x=1}^m w_x(t) {}_0^C D_t^\lambda w_x(t) \\ &= 2 \sum_{x=1}^m w_x(t) \left[-\xi_x w_x(t) - \frac{\sigma_x \operatorname{sign}(w_x(t))}{|w_x(t)|} \right] \\ &\leq -\min_{1 \leq x \leq m} \{2\xi_x\} L_1(t) - \sum_{x=1}^m 2\sigma_x \\ &\leq -\rho_1 L_1(t) - \sum_{x=1}^m 2\sigma_x \\ &\leq -\rho_1 L_1(t). \end{aligned} \tag{8.25}$$

From (8.25), there exists a nonnegative function $\Xi(t)$ for which

$${}_0^C D_t^\lambda L_1(t) + \Xi(t) = -\rho L_1(t). \tag{8.26}$$

Applying Laplace transform to (8.26), we obtain

$$s^\lambda L_1(s) - s^{\lambda-1} L_1(0) + \Xi(s) = -\rho L_1(s), \quad t \geq 0,$$

where $L_1(s) = \mathcal{L}\{L_1(t)\}$ and $\Xi(s) = \mathcal{L}\{\Xi(t)\}$. Thus, we have

$$L_1(s) = \frac{L_1(0)s^{\lambda-1} - \Xi(s)}{s^\lambda + \rho}. \tag{8.27}$$

Applying the inverse Laplace transform to (8.27), we receive

$$L_1(t) \leq L_1(0)M_{\lambda,1}(-\lambda t^\lambda) - \Xi(t) * [t^{\lambda-1}M_{\lambda,\lambda}(-\rho t^\lambda)],$$

where $*$ is a convolution operator. On the other hand, $\Xi(t)$, $t^{\lambda-1}$ and $M_{\lambda,\lambda}(-\rho t^\lambda)$ are nonnegative functions, thus we have

$$\Xi(t) * [t^{\lambda-1}M_{\lambda,\lambda}(-\rho t^\lambda)] \geq 0.$$

Hence, we have

$$L_1(t) \leq L_1(0)M_{\lambda,1}(-\rho t^\lambda). \tag{8.28}$$

Based on Lemma 8.3, we have

$$M_{\lambda,1}(t) = \frac{1}{\lambda} e^{t^{\frac{1}{\lambda}}} - \sum_{\ell=1}^{\nu} \frac{1}{t^\ell \Gamma(1-\lambda\ell)} + O\left(\frac{1}{t^{\nu+1}}\right), \quad |t| \rightarrow \infty,$$

where $O\left(\frac{1}{t^{\nu+1}}\right) = 0$. Thus we have

$$\lim_{t \rightarrow +\infty} \left[\frac{\frac{1}{\lambda} e^{t^{\frac{1}{\lambda}}} - \sum_{\ell=1}^{\nu} \frac{1}{t^\ell \Gamma(1-\lambda\ell)} + O\left(\frac{1}{t^{\nu+1}}\right)}{\frac{1}{\lambda} e^{t^{\frac{1}{\lambda}}} - \sum_{\ell=1}^{\nu} \frac{1}{t^\ell \Gamma(1-\lambda\ell)}} \right] = 1.$$

Therefore

$$M_{\lambda,1} \sim \frac{1}{\lambda} e^{t^{\frac{1}{\lambda}}} - \sum_{\ell=1}^{\nu} \frac{1}{t^\ell \Gamma(1-\lambda\ell)}, \quad \text{as } t \rightarrow +\infty.$$

Since $\sum_{\ell=1}^{\nu} \frac{1}{t^\ell \Gamma(1-\lambda\ell)} \geq 0$, one has

$$M_{\lambda,1} \leq \frac{1}{\lambda} e^{t^{\frac{1}{\lambda}}}, \quad \text{as } t \rightarrow +\infty.$$

By thinking of limit function axioms, there exists $t_0 > 0$ such that

$$M_{\lambda,1} \leq \frac{1}{\lambda} e^{t^{\frac{1}{\lambda}}}, \quad t > t_0 > 0.$$

Therefore

$$M_{\lambda,1}(-\lambda(t-t_0)^\lambda) \leq \frac{1}{\lambda} e^{-[\lambda(t-t_0)^\lambda]^{\frac{1}{\lambda}}}, \quad t > t_0 > 0. \tag{8.29}$$

By utilizing inequality (8.28), Eq. (8.29) becomes

$$L_1(t) \leq L_1(0) \left[\frac{1}{\lambda} e^{-[\lambda(t-t_0)^\lambda]^{\frac{1}{\lambda}}} \right], \quad t > t_0 > 0.$$

That is,

$$\sum_{x=1}^m w_x^2(t) \leq \sum_{x=1}^m w_x^2(0) \left[\frac{1}{\lambda} e^{-[\lambda(t-t_0)^\lambda]^{\frac{1}{\lambda}}} \right], \quad t > t_0 > 0.$$

Then

$$\left(\sum_{x=1}^m w_x^2(t) \right)^{\frac{1}{2}} \leq \left(\sum_{x=1}^m w_x^2(0) \right)^{\frac{1}{2}} \left[\frac{1}{\lambda} e^{-[\lambda(t-t_0)]^{\frac{1}{\lambda}}} \right]^{\frac{1}{2}}, \quad t > t_0 > 0.$$

Therefore $\|w(t)\| \rightarrow 0$ as $t \rightarrow +\infty$, which means the sliding mode dynamic (8.24) converges to zero asymptotically, and hence the sliding mode dynamic (8.24) is globally asymptotic stable.

Furthermore, we will deduce that the sliding mode dynamic (8.24) is stable in a finite time. From (8.25), we have

$$\begin{aligned} {}_0^C D_t^\lambda L_1(t) &\leq - \sum_{x=1}^m 2\sigma_x \\ &= -\vartheta. \end{aligned}$$

There exists a function $H(t) \geq 0$ such that the following condition holds:

$${}_0^C D_t^\lambda L_1(t) + H(t) = -\vartheta. \quad (8.30)$$

Taking the fractional integral on each side of (8.30) from 0 to t , we obtain

$$L_1(t) - L_1(0) + {}_0 D_t^{-\lambda} H(t) = {}_0 D_t^{-\lambda} (-\vartheta), \quad (8.31)$$

where

$${}_0 D_t^{-\lambda} H(t) = \frac{1}{\Gamma(\lambda)} \int_0^t (t-\varsigma)^{\lambda-1} H(\varsigma) d\varsigma \geq 0,$$

since $\Gamma(\lambda) > 0$ and $(t-\varsigma)^{\lambda-1} H(\varsigma) > 0$ for $0 \leq \varsigma \leq t$.

Furthermore,

$$\begin{aligned} {}_0 D_t^{-\lambda} (-\vartheta) &= -\frac{\vartheta}{\Gamma(\lambda)} \int_0^t (t-\varsigma)^{\lambda-1} d\varsigma \\ &= \frac{-\vartheta t^\lambda}{\Gamma(\lambda+1)}. \end{aligned} \quad (8.32)$$

In view of inequalities (8.31) and (8.32), one gets

$$-L_1(0) \leq L_1(t) - L_1(0) + {}_0 D_t^{-\lambda} H(t) = \frac{-\vartheta t^\lambda}{\Gamma(\lambda+1)}.$$

Then we get

$$\begin{aligned}
 t &\leq \sqrt[\lambda]{\frac{L_1(0)\Gamma(\lambda + 1)}{\vartheta}} \\
 &= \sqrt[\lambda]{\frac{\sum_{x=1}^m w_x^2(0)\Gamma(\lambda + 1)}{\vartheta}}.
 \end{aligned}$$

Thus, the sliding mode dynamic (8.24) is stable in a finite time. This completes the proof. \square

8.3.3 Reachability criteria

In order to guarantee the existence of the sliding motion, that is to say, in order to ensure that the error trajectories $w_x(t)$ tends to the sliding surface $\Upsilon(t) = 0$, we design an appropriate sliding control technique to force the error trajectories (8.21) go on to the sliding surface within a finite time and remain on it forever. The finite-time sliding mode control strategy is designed as follows:

$$\begin{aligned}
 z_x(t) &= \left(\varphi_x - F_x \check{p}_x - \sum_{y=1}^m \check{p}_x \varpi_y (r_{xy} + s_{xy}) - \sum_{y=1}^m p_y^{**} |\hat{r}_{yx}| \check{\eta}_x \right) |w_x(t)| \\
 &\quad - \sum_{y=1}^m p_y^{**} |\hat{s}_{yx}| \check{\eta}_x |w_x(t - \mu)| - \sum_{y=1}^m p_x^{**} (|\hat{r}_{xy}| + |\hat{s}_{xy}|) \check{\theta}_y \\
 &\quad - \xi_x w_x(t) - \frac{\sigma_x \text{sign}(w_x(t))}{|w_x(t)|} \\
 &\quad - \check{\xi}_x \Upsilon_x(t) - \frac{\check{\sigma}_x \text{sign}(\Upsilon_x(t))}{|\Upsilon_x(t)|} - \zeta \text{sign}(\Upsilon_x(t)), \tag{8.33}
 \end{aligned}$$

where $\xi_x, \sigma_x, \check{\xi}_x, \check{\sigma}_x, \zeta > 0$ are the control gains, $r_{xy} = \max\{|\hat{r}_{xy}|, |\check{r}_{xy}|\}$, and $s_{xy} = \max\{|\hat{s}_{xy}|, |\check{s}_{xy}|\}$.

Here, the following condition is significant.

Assumption 8.6. If $\varepsilon < \zeta$, then the following inequality holds:

$$\left| \sum_{\ell=0}^{+\infty} \frac{\lambda \Gamma(\lambda)}{\ell \Gamma(\ell) \Gamma(\lambda + 1 - \ell)} \Upsilon^{(\ell)}(t)_0^C D_t^{\lambda - \ell} \Upsilon(t) \right| \leq \varepsilon \|\Upsilon(t)\|,$$

where $\Upsilon(t)$ indicates the sliding surface, which is defined in (8.22).

Theorem 8.3. *If Assumptions 8.2–8.6 hold, the trajectories of the synchronization error system (8.21) can be reached onto the sliding surface in a finite time under the designed sliding model control strategy (8.33).*

Proof. Construct the following Lyapunov functional:

$$L_2(t) = \Upsilon^2(t). \tag{8.34}$$

Based on Property (iii), we have

$$\begin{aligned} {}^C_0 D_t^\lambda L_2(t) &= \Upsilon(t) {}^C_0 D_t^\lambda \Upsilon(t) + \sum_{\ell=0}^{+\infty} \frac{\lambda \Gamma(\lambda)}{\ell \Gamma(\ell) \Gamma(\lambda + 1 - \ell)} \Upsilon^{(\ell)}(t) {}^C_0 D_t^{\lambda - \ell} \Upsilon(t) \\ &\leq \Upsilon(t) {}^C_0 D_t^\lambda \Upsilon(t) + \varepsilon \|\Upsilon(t)\| \\ &= \sum_{x=1}^m \Upsilon_x(t) {}^C_0 D_t^\lambda \Upsilon_x(t) + \varepsilon \|\Upsilon(t)\| \\ &= \sum_{x=1}^m \Upsilon_x(t) \left\{ {}^C_0 D_t^\lambda w_x(t) + \xi_x w_x(t) + \frac{\sigma_x \operatorname{sign}(w_x(t))}{|w_x(t)|} \right\} + \varepsilon \|\Upsilon(t)\| \\ &= \sum_{x=1}^m \Upsilon_x(t) \left\{ -\left(p_x(v_x(t)) q_x(v_x(t)) - p_x(u_x(t)) q_x(u_x(t)) \right) \right. \\ &\quad + \left(p_x(v_x(t)) - p_x(u_x(t)) \right) F_x + \sum_{y=1}^m p_x(v_x(t)) \hat{r}_{xy} \left(\gamma_y(t) - \beta_y(t) \right) \\ &\quad + \sum_{y=1}^m p_x(v_x(t)) \hat{s}_{xy} \left(\gamma_y(t - \mu) - \beta_y(t - \mu) \right) \\ &\quad + \sum_{y=1}^m p_x(v_x(t)) \hat{r}_{xy} \beta_y(t) - \sum_{y=1}^m p_x(u_x(t)) \check{r}_{xy} \beta_y(t) \\ &\quad + \sum_{y=1}^m p_x(v_x(t)) \hat{s}_{xy} \beta_y(t - \mu) - \sum_{y=1}^m p_x(u_x(t)) \check{s}_{xy} \beta_y(t - \mu) \\ &\quad + \left(\varphi_x - F_x \check{p}_x - \sum_{y=1}^m \check{p}_x \varpi_y \left(r_{xy} + s_{xy} \right) - \sum_{y=1}^m p_y^{**} |\hat{r}_{yx}| \check{\eta}_x \right) |w_x(t)| \\ &\quad - \sum_{y=1}^m p_y^{**} |\hat{s}_{yx}| \check{\eta}_x |w_x(t - \mu)| - \sum_{y=1}^m p_x^{**} \left(|\hat{r}_{xy}| + |\hat{s}_{xy}| \right) \check{\theta}_y \\ &\quad \left. - \xi_x w_x(t) - \frac{\sigma_x \operatorname{sign}(w_x(t))}{|w_x(t)|} - \check{\xi}_x \Upsilon_x(t) - \frac{\check{\sigma}_x \operatorname{sign}(\Upsilon_x(t))}{|\Upsilon_x(t)|} \right\} \end{aligned}$$

$$\begin{aligned}
 & \left. - \zeta \operatorname{sign}(\Upsilon_x(t)) + \xi_x w_x(t) + \frac{\sigma_x \operatorname{sign}(w_x(t))}{|w_x(t)|} \right\} + \varepsilon \|\Upsilon(t)\| \\
 \leq & - \sum_{x=1}^m \check{\xi}_x \Upsilon_x^2(t) - \sum_{x=1}^m \check{\sigma}_x \Upsilon_x(t) \frac{\operatorname{sign}(\Upsilon_x(t))}{|\Upsilon_x(t)|} \\
 & - \sum_{x=1}^m \zeta \Upsilon_x(t) \operatorname{sign}(\Upsilon_x(t)) + \varepsilon \|\Upsilon(t)\| \\
 \leq & -(\zeta - \varepsilon)\varepsilon \|\Upsilon(t)\| - \sum_{x=1}^m \check{\xi}_x \Upsilon_x^2(t) - \sum_{x=1}^m \check{\sigma}_x. \tag{8.35}
 \end{aligned}$$

As $\zeta - \varepsilon > 0$, the synchronization error system will realize the sliding surface $\Upsilon(t) = 0$ asymptotically based on the designed sliding model control strategy (8.33).

Now we prove that the synchronization error system (8.21) can be reached on the sliding surface in a finite time.

From (8.35), we have

$${}^C_0 D_t^\lambda L_2(t) \leq - \sum_{x=1}^m \check{\sigma}_x. \tag{8.36}$$

By a procedure similar to that in Theorem 8.2, it is easy to get

$$t \leq \sqrt[\lambda]{\frac{\Upsilon^2(0)\Gamma(\lambda + 1)}{\sum_{x=1}^m \check{\sigma}_x}}.$$

Therefore, the trajectories of the synchronization error system (8.21) will tend to the sliding surface in a finite time. The proof is completed. \square

If the activation function of FDCGMNNs (8.12) is continuous, then the following assumption is very important to establish the finite time synchronization problem of FDCGMNNs.

Assumption 8.7. For each $x = 1, 2, \dots, m$, there exist positive scalars $\check{\eta}_y > 0$ such that

$$|g_y(v) - g_y(u)| \leq \check{\eta}_y |v - u|, \quad |g_y(v)| \leq \varpi_y, \quad \forall u, v \in \mathbb{R}, \quad y = 1, 2, \dots, m.$$

The fractional-order integral sliding surface (8.22) is the same as FDCGMNNs with a continuous activation function. The finite time sliding model control strategy is designed for FDCGMNNs with continuous

activation function as follows:

$$\begin{aligned}
 z_x(t) = & \left(\varphi_x - F_x \check{p}_x - \sum_{y=1}^m \check{p}_x \check{\omega}_y (r_{xy} + s_{xy}) - \sum_{y=1}^m p_y^{**} |\hat{r}_{yx}| \check{\eta}_x \right) |w_x(t)| \\
 & - \sum_{y=1}^m p_y^{**} |\hat{s}_{yx}| \check{\eta}_x |w_x(t - \mu)| - \xi_x w_x(t) - \frac{\sigma_x \operatorname{sign}(w_x(t))}{|w_x(t)|} \\
 & - \check{\xi}_x \Upsilon_x(t) - \frac{\check{\sigma}_x \operatorname{sign}(\Upsilon_x(t))}{|\Upsilon_x(t)|} - \zeta \operatorname{sign}(\Upsilon_x(t)), \quad (8.37)
 \end{aligned}$$

where ξ_x , σ_x , $\check{\xi}_x$, $\check{\sigma}_x$, $\zeta > 0$ are the control gains, $r_{xy} = \max\{|\hat{r}_{xy}|, |\check{r}_{xy}|\}$, and $s_{xy} = \max\{|\hat{s}_{xy}|, |\check{s}_{xy}|\}$.

Suppose that $u(t) = (u_1(t), \dots, u_m(t))^T \in \mathbb{R}^m$ and $v(t) = (v_1(t), \dots, v_m(t))^T \in \mathbb{R}^m$ are any two solutions of (8.12) and (8.17). Let $w_x(t) = v_x(t) - u_x(t)$. The synchronization error dynamic is described as

$$\begin{aligned}
 {}_0^C D_t^\lambda w_x(t) = & -p_x(v_x(t)) \left[q_x(v_x(t)) - \sum_{y=1}^m r_{xy}(v_y(t)) g_y(v_y(t)) \right. \\
 & \left. - \sum_{y=1}^m s_{xy}(u_y(t)) g_y(v_y(t - \mu)) - F_x \right] \\
 & + p_x(u_x(t)) \left[q_x(u_x(t)) - \sum_{y=1}^m r_{xy}(u_y(t)) g_y(u_y(t)) \right. \\
 & \left. - \sum_{y=1}^m s_{xy}(u_y(t)) g_y(u_y(t - \mu)) - F_x \right] + z_x(t) \\
 = & - \left(p_x(v_x(t)) q_x(v_x(t)) - p_x(u_x(t)) q_x(u_x(t)) \right) \\
 & + \left(p_x(v_x(t)) - p_x(u_x(t)) \right) F_x + \sum_{y=1}^m p_x(v_x(t)) \hat{r}_{xy} g_y(w_y(t)) \\
 & + \sum_{y=1}^m p_x(v_x(t)) \hat{s}_{xy} g_y(w_y(t - \mu)) + \sum_{y=1}^m p_x(v_x(t)) \check{r}_{xy} g_y(u_y(t)) \\
 & - \sum_{y=1}^m p_x(u_x(t)) \check{r}_{xy} g_y(u_y(t)) + \sum_{y=1}^m p_x(v_x(t)) \hat{s}_{xy} g_y(u_y(t - \mu)) \\
 & - \sum_{y=1}^m p_x(u_x(t)) \check{s}_{xy} g_y(u_y(t - \mu)) + z_x(t), \quad (8.38)
 \end{aligned}$$

where $g_y(w_y(t)) = g_y(v_y(t)) - g_y(u_y(t))$.

Corollary 8.1 is straightforwardly obtained from Theorem 8.2 and Theorem 8.3.

Corollary 8.1. *If Assumptions 8.4–8.7 hold, the trajectories of the synchronization error system (8.38) can be reached on the sliding surface in a finite time under the designed sliding model control strategy (8.37).*

Remark 8.1. This study constitutes the first attempt on the finite time synchronization criteria for the sliding mode control technique to FODGRNs with time delays. This research takes into account the fractional order, time delays, memristive synaptic connection weights, sliding mode control theory, and two-norm methods. Their results are not easy to calculate and they are very complicated. This key innovation of this chapter is to overcome that complication.

Remark 8.2. In the past few years, CGMNNs with fractional-order derivative [73,74] and memristive discontinuous neural networks with fractional-order derivative [17–19,42] have been broadly researched. However, there is no discussion on the dynamics of fractional-order memristive Cohen–Grossberg delayed neural networks with discontinuous activations.

Remark 8.3. When the memristive connection weights of a memristor $\dot{r}_{xy} = \dot{r}_{xy}$ and $\dot{s}_{xy} = \dot{s}_{xy}$, which means the connection weights are implemented only by a resistor, then the proposed results are still valid for finite-time synchronization criteria for the sliding mode control technique to fractional-order general Cohen–Grossberg delayed neural networks with discontinuous activations, while these conservatism results have not been reported anywhere else in the existing literature.

Remark 8.4. When $\lambda = 1$, the FODGRN model (8.22) reduces into finite time synchronization criteria for the sliding mode control technique to integer-order general Cohen–Grossberg delayed neural networks with discontinuous activations, and the results of synchronization criteria are not discussed in the literature.

Remark 8.5. The novel technique to various kinds of synchronization results in this chapter can be easily generalized to different dynamical behaviors like stability, stabilization, passivity, dissipativity, and state estimation for fractional-order Hopfield type neural networks, fractional-order competitive neural networks, fractional-order cellular type neural networks, fractional-order MAM type neural networks, fractional-order

BAM type neural networks, fractional-order Cohen–Grossberg type neural networks, fractional-order complex-valued CGNNs, fractional-order quaternion-valued CGNNs, and other networks. Therefore, the proposed synchronization results and models are more general.



8.4. A numerical example

This section provides an example to justify the superiority and advantages of obtaining finite time synchronization criteria. In the existing literature [20,27,46,49,61,63,67,72], several scientific results have been presented on fractional-order nonlinear time delay systems, and these numerical results can be solved by the Adams–Bashforth–Moulton predictor–corrector algorithm [10]. Inspired by the abovementioned works, the Adams–Bashforth–Moulton predictor–corrector algorithm is applied to numerically solve the fractional-order discontinuous time-delayed CGNNs in the following simulations with step length 0.01. Consider a class of 2D FDCGMNNs with time delays:

$${}^C_0 D_t^{0.998} u(t) = -P(u(t)) \left[Q(u(t)) - R(u(t))g(u(t)) - S(u(t))g(u(t-3)) - F \right], \quad (8.39)$$

where $u(t) = (u_1(t), u_2(t))^T$, $P(u(t)) = \text{diag}(p_1(u_1(t)), p_2(u_2(t)))$, $Q(u(t)) = \text{diag}(q_1(u_1(t)), q_2(u_2(t)))$, $p_1(u) = p_2(u) = 1 + \frac{2.2}{1+u^2}$, $q_1(u) = q_2(u) = 0.5u + \tanh(u)$, $g(u) = 0.005u + 0.08 \text{sign}(u)$, $F_1 = F_2 = 0.1$, and

$$\begin{aligned} r_{11}(u_1(t)) &= \begin{cases} -1.2, & |u_1(t)| \leq 1, \\ -1.7, & |u_1(t)| > 1, \end{cases} \\ r_{12}(u_2(t)) &= \begin{cases} -1.3, & |u_2(t)| \leq 1, \\ -1.1, & |u_2(t)| > 1, \end{cases} \\ r_{21}(u_1(t)) &= \begin{cases} 1.6, & |u_1(t)| \leq 1, \\ 2, & |u_1(t)| > 1, \end{cases} \\ r_{22}(u_2(t)) &= \begin{cases} 1.4, & |u_2(t)| \leq 1, \\ 1.45, & |u_2(t)| > 1, \end{cases} \\ s_{11}(u_1(t)) &= \begin{cases} -3.12, & |u_1(t)| \leq 1, \\ -2.8, & |u_1(t)| > 1, \end{cases} \end{aligned}$$

$$\begin{aligned}
 s_{12}(u_2(t)) &= \begin{cases} 2.4, & |u_2(t)| \leq 1, \\ 2.8, & |u_2(t)| > 1, \end{cases} \\
 s_{21}(u_1(t)) &= \begin{cases} 2.8, & |u_1(t)| \leq 1, \\ 1.9, & |u_1(t)| > 1, \end{cases} \\
 s_{22}(u_2(t)) &= \begin{cases} 3.5, & |u_2(t)| \leq 1, \\ 2.3, & |u_2(t)| > 1. \end{cases}
 \end{aligned}$$

The corresponding 3D response system is described as follows:

$$\begin{aligned}
 {}^C_0D_t^{0.998}v(t) &= -P(v(t))\left[Q(v(t)) - R(v(t))g(v(t)) - S(v(t))g(v(t-3)) - F\right] \\
 &+ z(t), \tag{8.40}
 \end{aligned}$$

where $v(t) = (v_1(t), v_2(t))^T$, $P(v(t)) = \text{diag}(p_1(v_1(t)), p_2(v_2(t)))$, $Q(u(t)) = \text{diag}(q_1(v_1(t)), q_2(v_2(t)))$, $z(t)$ is the control input, and others are the same as for the FDCGMNNs (8.39). The initial conditions are chosen as $u(t) = (-0.2, -0.1)^T$ and $v(t) = (0.2, -0.8)^T$. When the control is not applied, the state trajectories of FDCGMNNs (8.38) and FDCGMNNs (8.39) are shown in Fig. 8.1. Fig. 8.2 depicts the synchronization error trajectories of FDCGMNNs (8.38) and FDCGMNNs (8.39), without applying any control inputs.

One simply verifies that Assumptions 8.2–8.6 hold with $\varpi_1 = \varpi_2 = 0.01$, $\check{\eta}_1 = \check{\eta}_2 = 1$, $\check{\theta}_1 = \check{\theta}_2 = 0.5$, $p_1^* = p_2^* = 0.03$, $\check{p}_1 = \check{p}_2 = 0.6$, and $\varphi_1 = \varphi_2 = 0.075$. In the finite time sliding model control strategy (8.33), we select the control gain parameters $\xi_1 = \xi_2 = 7.5$, $\sigma_1 = \sigma_2 = 0.009$, $\check{\xi}_1 = \check{\xi}_2 = 0.01$, $\check{\sigma}_1 = \check{\sigma}_2 = 0.03$, and $\zeta = 0.2$. The initial value of the sliding mode surface is $\Upsilon(0) = (0.2, 0.4)^T$. Based on Theorem 8.2, the sliding mode dynamic (8.24) is stable in a finite time and the finite time settling time T is less than 18.052.

Based on the finite time sliding model control $z(t)$, the state trajectories of FDCGMNNs (8.38) and FDCGMNNs (8.39) are exhibited in Fig. 8.3. In Fig. 8.4, the synchronization error trajectory tends to zero, which guarantees the global asymptotic synchronization between FDCGMNNs (8.38) and FDCGMNNs (8.39), respectively. Furthermore, based on Theorem 8.3, the obtained finite time settling time T is less than 3.326. In Fig. 8.5, the time behaviors of the sliding dynamic surface (8.22) are shown. Synchronization error norms and sliding dynamic surface norms are displayed in Fig. 8.6.

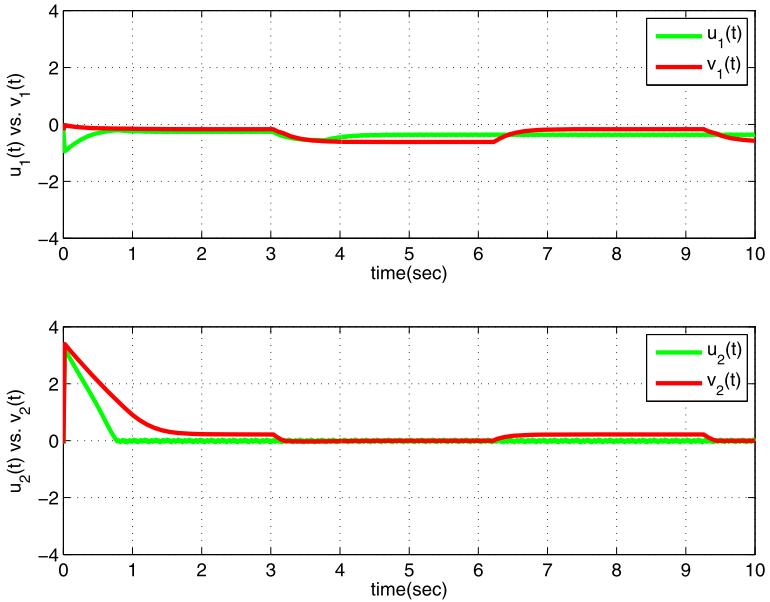


Figure 8.1 The time response of the state variables $u(t)$ and $v(t)$ for the drive system (8.38) and response system (8.39) without control.

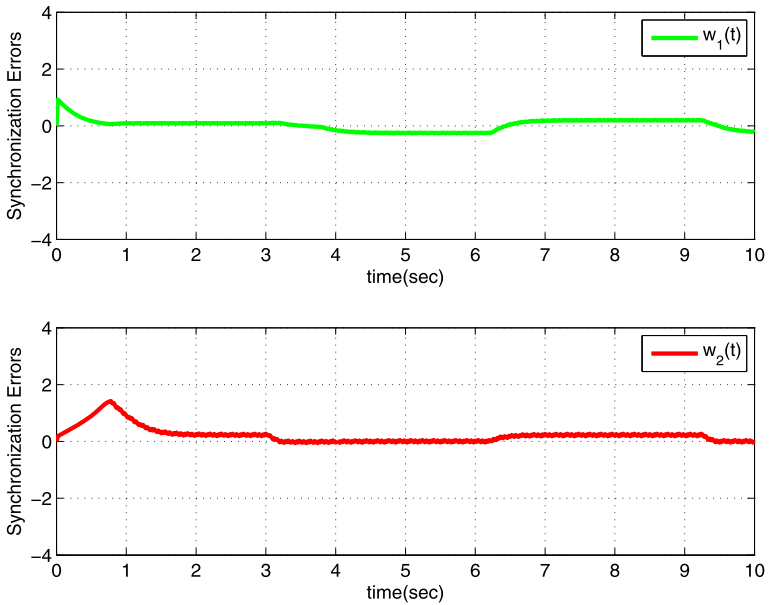


Figure 8.2 Time responses of the synchronization error variables $w(t)$ between drive system (8.38) and response system (8.39) without control.

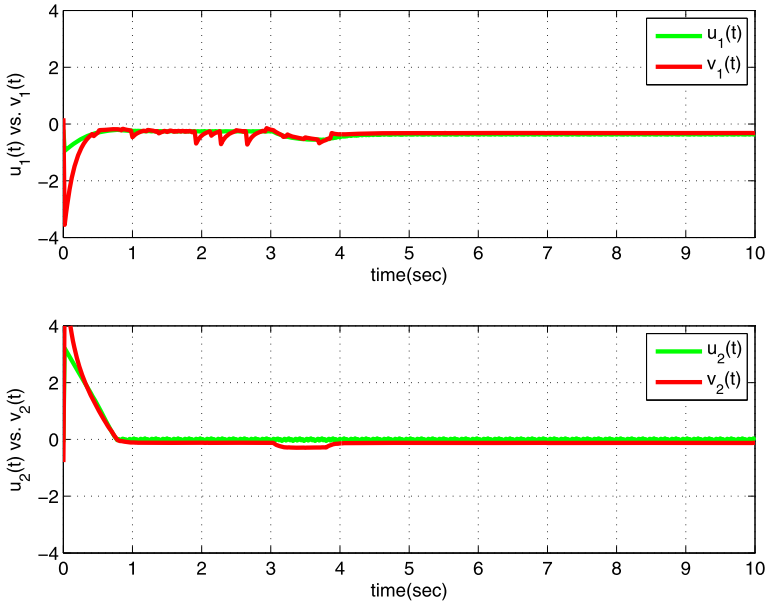


Figure 8.3 The time response of the state variables $u(t)$ and $v(t)$ for drive system (8.38) and response system (8.39) with control.

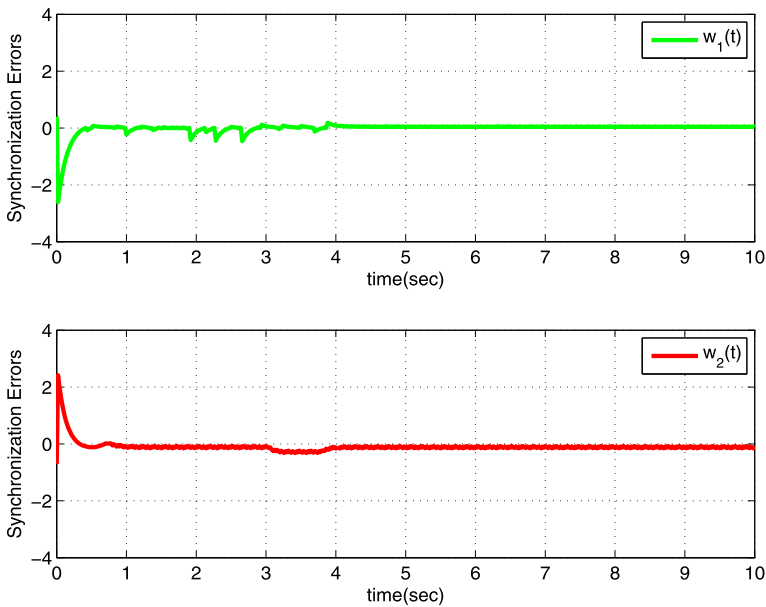


Figure 8.4 Time responses of the synchronization error variables $w(t)$ between drive system (8.38) and response system (8.39) with control.

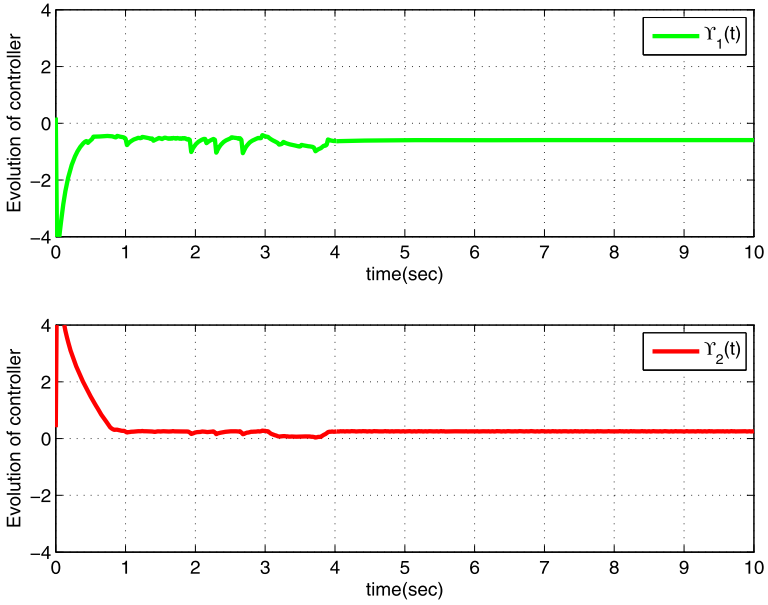


Figure 8.5 The convergence behavior of the sliding dynamic surface (8.22).

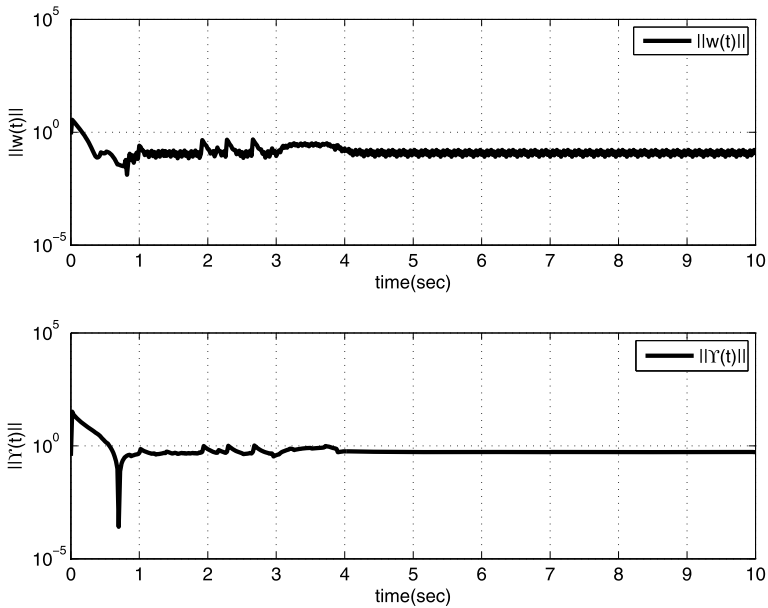
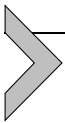


Figure 8.6 The convergence behavior of the norm of synchronization error state variables $w(t)$ with control input and norm of the control evaluation $\|\Upsilon(t)\|$.



8.5. Conclusions

In this chapter, we have analyzed the dynamics of FDCGMNNs with time delay. Based on the nonsmooth analysis, the growth property, and the generalized Gronwall inequality, the existence of Filippov solutions was derived. Then, a novel sliding mode dynamic surface and an effective finite-time sliding mode controller were designed to ensure the finite-time synchronization for addressing FDCGMNNs based on the fractional-order Lyapunov direct approach, sliding mode control theory, and some properties of Caputo fractional-order derivatives. Our future work will be generalized to the adaptive sliding mode controller design for fractional-order discontinuous memristive BAM neural networks with both leakage and mixed time delays.

Acknowledgments

The first and second authors would like to thank the RUSA-Phase 2.0 grant sanctioned vide letter No.F 24-51/2014-U, Policy (TN Multi-Gen), Dept. of Edn. Govt. of India.

References

- [1] A. Abdurrahman, H. Jiang, C. Hu, General decay synchronization of memristor-based Cohen-Grossberg neural networks with mixed time-delays and discontinuous activations, *Journal of the Franklin Institute* 354 (15) (2017) 7028–7052.
- [2] A. Ahmeda, A. Elgazzar, On fractional order differential equations model for nonlocal epidemics, *Physica A* 379 (2007) 607–614.
- [3] M.S. Ali, M. Hymavathi, S. Senan, V. Shekher, S. Arik, Global asymptotic synchronization of impulsive fractional order complex valued memristive based neural networks with time delays, *Communications in Nonlinear Science and Numerical Simulation* 78 (2019) 104869.
- [4] M.S. Ali, G. Narayanan, V. Shekher, H. Alsulami, T. Saeed, Dynamic stability analysis of stochastic fractional-order memristor fuzzy BAM neural networks with delay and leakage terms, *Applied Mathematics and Computation* 369 (2020) 124896.
- [5] F. Alibart, L. Gao, H.D. Hoskins, D.B. Strukov, High precision tuning of state for memristive devices by adaptable variation-tolerant algorithm, *Nanotechnology* 23 (7) (2012) 075201.
- [6] E.G. Bajlekova, *Fractional Evolution Equations in Banach spaces*, University Press Facilities, Eindhoven University of Technology, Eindhoven, 2001.
- [7] O. Baghani, On Fractional Langevin equations involving two fractional orders, *Communications in Nonlinear Science and Numerical Simulation* 42 (2017) 675–681.
- [8] D. Baleanu, A. Jajarmi, H. Mohammadi, S. Rezapour, A new study on the mathematical modelling of human liver with Caputo-Fabrizio fractional derivative, *Chaos, Solitons and Fractals* 134 (2020) 109705.
- [9] H. Bao, J.H. Park, J. Cao, Non-fragile state estimation for fractional-order delayed memristive BAM neural networks, *Neural Networks* 119 (2019) 190–199.
- [10] S. Bhalekar, V. Daftardar-Gejji, A predictor-corrector scheme for solving nonlinear delay differential equations of fractional order, *Journal of Fractional Calculus and Applications* 1 (5) (2011) 1–9.

- [11] C. Chen, L. Li, H. Peng, Y. Yang, Adaptive synchronization of memristor-based BAM neural networks with mixed delays, *Applied Mathematics and Computation* 322 (2018) 100–110.
- [12] J. Chen, C. Li, Z. Wang, X. Yang, Global Mittag-Leffler projective synchronization of nonidentical fractional-order neural networks with delay via sliding mode control, *Neurocomputing* 313 (2018) 324–332.
- [13] J. Chen, B. Chen, Z. Zeng, $O(t^{-\alpha})$ -synchronization and Mittag-Leffler synchronization for the fractional-order memristive neural networks with delays and discontinuous neuron activations, *Neural Networks* 100 (2018) 10–24.
- [14] L.Q. Chua, Memristor—the missing circuit element, *IEEE Transactions on Circuit Theory* 18 (1971) 507–519.
- [15] M.A. Cohen, S. Grossberg, Absolute stability of global pattern formation and parallel memory storage by competitive neural networks, *IEEE Transactions on Systems, Man and Cybernetics* 5 (1983) 815–826.
- [16] G. Cottone, M. Paola, R. Santoro, A novel exact representation of stationary colored Gaussian processes (fractional differential approach), *Journal of Physics A: Mathematical and Theoretical* 43 (8) (2010) 085002.
- [17] X. Ding, Y. Shen, Global dissipativity of fractional-order neural networks with time delays and discontinuous activations, *Neurocomputing* 196 (2016) 159–166.
- [18] X. Ding, Z. Zeng, L. Wang, Robust finite-time stabilization of fractional-order neural networks with discontinuous and continuous activation functions under uncertainty, *IEEE Transactions on Neural Networks and Learning Systems* 29 (5) (2018) 1477–1490.
- [19] Z. Ding, Y. Shen, L. Wang, Global Mittag-Leffler synchronization of fractional order neural networks with discontinuous activations, *Neural Networks* 73 (2016) 77–85.
- [20] F. Du, J.G. Lu, Finite-time stability of neutral fractional order time delay systems with Lipschitz nonlinearities, *Applied Mathematics and Computation* 375 (2020) 125079.
- [21] M.A. Duarte-Mermoud, N. Aguila-Camacho, J.A. Gallegos, R. Castro-Linares, Using general quadratic Lyapunov functions to prove Lyapunov uniform stability for fractional order systems, *Communications in Nonlinear Science and Numerical Simulation* 22 (1) (2015) 650–659.
- [22] A. Filippov, *Differential Equations With Discontinuous Right-Hand Sides*, Kluwer, Dordrecht, 1988.
- [23] B. Ghanbari, J.F. Gomez-Aguilar, Analysis of two avian influenza epidemic models involving fractal-fractional derivative with power and Mittag-Leffler memories, *Chaos: An Interdisciplinary Journal of Nonlinear Science* 29 (12) (2019) 123113.
- [24] V. Govindaraj, Raju K. George, Trajectory controllability of fractional integro-differential systems in Hilbert spaces, *Asian Journal of Control* 20 (6) (2018) 1–11.
- [25] P. Guo, C. Zeng, C. Li, Y. Chen, Numerics for the fractional Langevin equation driven by the fractional Brownian motion, *Fractional Calculus and Applied Analysis* 16 (2013) 123–141.
- [26] C. Huang, J. Cao, M. Xiao, Hybrid control on bifurcation for a delayed fractional gene regulatory network, *Chaos, Solitons and Fractals* 87 (2016) 19–29.
- [27] X. Huang, J. Jia, Y. Fan, Z. Wang, J. Xia, Interval matrix method based synchronization criteria for fractional-order memristive neural networks with multiple time-varying delays, *Journal of the Franklin Institute* 357 (3) (2020) 1707–1733.
- [28] A. Jajarmi, S. Arshad, D. Baleanu, A new fractional modelling and control strategy for the outbreak for dengue fever, *Physica A* 553 (2019) 122524.
- [29] J. Jian, Z. Zhao, Global stability in Lagrange sense for BAM-type Cohen–Grossberg neural networks with time-varying delays, *Systems Science & Control Engineering: An Open Access Journal* 3 (2015) 1–7.

- [30] Y. Kao, C. Wang, L. Zhang, Delay-dependent robust exponential stability of impulsive Markovian jumping reaction diffusion Cohen–Grossberg neural networks, *Neural Processing Letters* 38 (3) (2013) 321–346.
- [31] Y. Ke, C. Miao, Stability analysis of inertial Cohen–Grossberg-type neural networks with time delays, *Neurocomputing* 117 (2013) 196–205.
- [32] Y. Ke, C. Miao, Stability analysis of fractional-order Cohen–Grossberg neural networks with time delay, *International Journal of Computer Mathematics* 92 (6) (2015) 1102–1113.
- [33] A. Kilbas, H. Srivastava, J.J. Trujillo, *Theory and Applications of Fractional Differential Equations*, Elsevier, Amsterdam, 2006.
- [34] S. Kvaterny, E.G. Friedman, A. Kolodny, U.C. Weiser, TEAM: threshold adaptive memristor model, *IEEE Transactions on Circuits and Systems I* 60 (1) (2013) 211–221.
- [35] J. Li, H. Jiang, C. Hu, Z. Yu, Multiple types of synchronization analysis for discontinuous Cohen–Grossberg neural networks with time-varying delays, *Neural Networks* 99 (2018) 101–113.
- [36] R. Li, X. Gao, J. Cao, Quasi-state estimation and quasi-synchronization control of quaternion-valued fractional-order fuzzy memristive neural networks: Vector ordering approach, *Applied Mathematics and Computation* 362 (2019) 124572.
- [37] K.S. Miller, B. Ross, *An Introduction to the Fractional Calculus and Fractional Differential Equations*, Wiley, New York, 1993.
- [38] X. Nie, W.X. Zheng, J. Cao, Multistability of memristive Cohen–Grossberg neural networks with non-monotonic piecewise linear activation functions and time-varying delays, *Neural Networks* 71 (2015) 27–36.
- [39] N. Ozalp, E. Demirci, A fractional order SEIR model with vertical transmission, *Mathematical and Computer Modelling* 54 (1) (2011) 1–6.
- [40] S.M. Abedi Pahnehkolaei, A. Alfi, J.A. Tenreiro Machado, Delay-dependent stability analysis of the QUAD vector field fractional order quaternion-valued memristive uncertain neutral type leaky integrator echo state neural networks, *Neural Networks* 117 (2019) 307–327.
- [41] M.D. Pickett, D.B. Strukov, J.L. Borghetti, J.J. Yang, G.S. Snider, D.R. Stewart, R.S. Williams, Switching dynamics in titanium dioxide memristive devices, *Journal of Applied Physics* 106 (7) (2009) 074508.
- [42] X. Peng, H. Wu, Robust Mittag-Leffler synchronization for uncertain fractional-order discontinuous neural networks via non-fragile control strategy, *Neural Processing Letters* 48 (3) (2018) 1521–1542.
- [43] I. Podlubny, *Fractional Differential Equations*, Academic Press, San Diego, California, 1999.
- [44] A. Pratap, R. Raja, J. Cao, G. Rajchakit, F.E. Alsaadie, Further synchronization in finite time analysis for time-varying delayed fractional order memristive competitive neural networks with leakage delay, *Neurocomputing* 317 (2018) 110–126.
- [45] A. Pratap, R. Raja, J. Cao, C.P. Lim, O. Bagdasar, Stability and pinning synchronization analysis of fractional order delayed Cohen–Grossberg neural networks with discontinuous activations, *Applied Mathematics and Computation* 359 (2019) 241–260.
- [46] Y. Qiao, H. Yan, L. Duan, J. Miao, Finite-time synchronization of fractional-order gene regulatory networks with time delay, *Neural Networks* 126 (2020) 1–10.
- [47] G. Rajchakit, P. Chanthorn, M. Niezabitowski, R. Raja, D. Baleanu, A. Pratap, Impulsive effects on stability and passivity analysis of memristor-based fractional-order competitive neural networks, *Neurocomputing* 417 (2020) 290–301.
- [48] C. Rajivganthi, F.A. Rihan, S. Lakshmanan, P. Muthukumar, Finite-time stability analysis for fractional-order Cohen Grossberg BAM neural networks with time delays, *Neural Computing & Applications* 29 (12) (2018) 1309–1320.

- [49] C. Rajivganthi, F. Rihan, S. Lakshmanan, R. Rakkiappan, P. Muthuumar, Synchronization of memristor-based delayed BAM neural networks with fractional-order derivatives, *Complexity* 21 (2016) 412–426.
- [50] F. Ren, M. Jiang, H. Xu, M. Li, Quasi fixed-time synchronization of memristive Cohen–Grossberg neural networks with reaction–diffusion, *Neurocomputing* 415 (2020) 74–83.
- [51] J. Sabatier, R.P. Agrawal, J. Machado, *Theoretical Developments and Applications in Physics and Engineering, Advance in Fractional Calculus*, Springer, Berlin, 2007.
- [52] Y. Shi, J. Cao, Finite-time synchronization of memristive Cohen–Grossberg neural networks with time delays, *Neurocomputing* 377 (2020) 159–167.
- [53] Y. Shi, J. Cao, Input-to-state stability analysis for memristive Cohen–Grossberg-type neural networks with variable time delays, *Chaos, Solitons and Fractals* 114 (2018) 364–369.
- [54] Q. Shuihan, H. Yanli, R. Shunyan, Finite-time synchronization of coupled Cohen–Grossberg neural networks with and without coupling delays, *Journal of the Franklin Institute* 355 (10) (2018) 4379–4403.
- [55] I. Stamova, *Stability of Impulsive Fractional Differential Equations*, Walter de Gruyter, Berlin, 2009.
- [56] D.B. Strukov, G.S. Snider, D.R. Stewart, R.S. Williams, The missing memristor found, *Nature* 453 (2008) 80–83.
- [57] J.M. Tour, T. He, Electronics: the fourth element, *Nature* 453 (2008) 42–43.
- [58] L. Wan, A. Wu, Mittag–Leffler stability analysis of fractional-order fuzzy Cohen–Grossberg neural networks with deviating argument, *Advances in Difference Equations* 2017 (2017) 308, <https://doi.org/10.1186/s13662-017-1368-y>.
- [59] D. Wang, L. Huang, Robust synchronization of discontinuous Cohen–Grossberg neural networks: pinning control approach, *Journal of the Franklin Institute* 355 (13) (2018) 5866–5892.
- [60] D. Wang, L. Huang, L. Tang, L. Zhuang, Generalized pinning synchronization of delayed Cohen–Grossberg neural networks with discontinuous activations, *Neural Networks* 104 (2018) 80–92.
- [61] F. Wang, T.Q. Yang, M.F. Hu, Asymptotic stability of delayed fractional-order neural networks with impulsive effects, *Neurocomputing* 154 (2015) 239–244.
- [62] W. Wang, X. Jia, Z. Wang, X. Luo, L. Lixiang, J. Kurths, M. Yuan, Fixed-time synchronization of fractional order memristive MAM neural networks by sliding mode control, *Neurocomputing* 401 (2020) 364–376.
- [63] C. Wenting, Z. Song, L. Jinyu, S. Kaili, Global Mittag–Leffler stabilization of fractional-order complex-valued memristive neural networks, *Applied Mathematics and Computation* 338 (2018) 346–362.
- [64] S. Westerlund, Dead matter has memory, *Physica Scripta* 43 (2) (1991) 174–179.
- [65] S. Westerlund, L. Ekstam, Capacitor theory, *IEEE Transactions on Dielectrics* 1 (5) (1994) 826–839.
- [66] R. Wong, Y. Zhao, Exponential asymptotics of the Mittag–Leffler function, *Constructive Approximation* 18 (3) (2002) 355–385.
- [67] A. Wu, Z. Zeng, X. Song, Global Mittag–Leffler stabilization of fractional-order bidirectional associative memory neural networks, *Neurocomputing* 177 (12) (2016) 489–496.
- [68] H. Wu, L. Wang, P. Niu, Y. Wang, Global projective synchronization in finite time of nonidentical fractional-order neural networks based on sliding mode control strategy, *Neurocomputing* 235 (2017) 264–273.
- [69] H.P. Ye, J.D. Gao, Y.S. Ding, A generalized Gronwall inequality and its application to a fractional differential equation, *Journal of Mathematical Analysis and Applications* 328 (2007) 1075–1081.

- [70] J. Yu, C. Hu, H. Jiang, Corrigendum to projective synchronization for fractional neural networks, *Neural Networks* 67 (2015) 152–154.
- [71] F. Zhang, Z. Zheng, Multiple Mittag-Leffler stability of delayed fractional-order Cohen–Grossberg neural networks via mixed monotone operator pair, *IEEE Transactions on Cybernetics* (2020), <https://doi.org/10.1109/TCYB.2019.2963034>.
- [72] L. Zhang, Y. Yang, Different impulsive effects on synchronization of fractional-order memristive BAM neural networks, *Nonlinear Dynamics* 93 (2) (2018) 233–250.
- [73] L. Zhang, Y. Yang, X. Xu, Synchronization analysis for fractional order memristive Cohen–Grossberg neural networks with state feedback and impulsive control, *Physica A* 506 (2018) 644–660.
- [74] M. Zheng, L. Li, H. Peng, J. Xiao, Y. Yang, H. Zhao, Finite-time stability and synchronization for memristor-based fractional-order Cohen–Grossberg neural network, *The European Physical Journal B: Condensed Matter and Complex Systems* 89 (9) (2016) 1–11.

Variable-order control systems: a steady-state error analysis

Hamidreza Ghazisaeedi and Mohammad Saleh Tavazoei

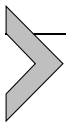
Electrical Engineering Department, Sharif University of Technology, Tehran, Iran

9.1. Introduction

In the past decade, fractional-order systems have received much attention and have been considerably applied for modeling and control of a wide range of real-world plants [1,2,6,10,22,23,25]. The important characteristic associated with fractional calculus is to extend the concept of integration and differentiation to any real or imaginary order. This characteristic leads to the proposal of the concept of variable-order operators as a generalization of constant-order integrals and derivatives [8,22,23]. In this case, the order of operators is a multivariable function. This function is called the order function. Also, the dynamical systems described by variable-order operators are called variable-order systems (some applications of variable-order systems and operators can be found in [3,9,17,18,21]). Moreover, fractional variable-order controllers are the extended controllers resulting from the use of variable-order operators. For instance, fractional variable-order proportional integral derivative (FVOPID) controllers have been applied for satisfying complicated control objectives in design of control systems [4,7,11,12,20,26].

There are three common definitions for variable operators which have been thoroughly studied in [8] and [22,23]. In this chapter, our focus is on the third definition, which is in a convolution form. The convolution form of the third definition of variable-order integral connects it to time-invariant variable-order systems. The main purpose of this chapter is to present some results on the type number concept in variable-order systems. To this end, first of all the concept of type number in fractional systems [24] is restated. Then, some theorems are presented for determining the type number in an intensive range of variable-order systems (it is worth noting that in [5] and [27] powerful numerical methods have been presented which can be used for simulation of variable-order systems).

This chapter is organized as follows. Section 9.2 presents definitions of variable-order integrators. Also, in this section a notation for representation of variable-order integrators in the Laplace domain is offered which is used in the rest of the chapter. In Section 9.3, some results are presented for determination of the type number in a wide range of variable-order systems. A numerical method for simulation of a class of fractional variable-order systems is presented in Section 9.4. In Section 9.5, the obtained results are verified by some numerical examples on variable-order systems and circuits. Finally, this chapter is concluded in Section 9.6.



9.2. Variable-order operators

In this section, the definition of fractional variable-order operators is briefly reviewed, and a notation is offered for Laplace transform of integral types of variable-order operators.

Definition 9.1. [8] Assume that $q(t) > 0$ for all $t > 0$. The integral of function $f(t)$ with variable-order function $q(t)$ is defined as follows:

$${}_0D_t^{-q(t)}f(t) = \int_0^t \frac{(t-\tau)^{q(t-\tau)-1}}{\Gamma(q(t-\tau))}f(\tau)d\tau. \quad (9.1)$$

Now, we suggest the notation $I^{q(t)}(s)$ for describing the variable-order integrators of order $q(t)$ in the Laplace domain. Considering (9.1), $I^{q(t)}(s)$ is defined as follows:

$$I^{q(t)}(s) = \int_0^\infty e^{-st} \frac{t^{q(t)-1}}{\Gamma(q(t))} dt. \quad (9.2)$$

For example, if

$$q(t) = \begin{cases} 1, & t \leq 1, \\ 2, & t > 1, \end{cases} \quad (9.3)$$

then

$$I^{q(t)}(s) = \frac{s + e^{-s}}{s^2}. \quad (9.4)$$

Definition 9.2. [20] Considering the order function $\alpha(t) > 0$, the fractional variable-order derivative operators of types A, B, and C are defined as follows.

The variable-order derivative of type A is defined as

$${}_0^A D_t^{\alpha(t)} = \lim_{h \rightarrow 0} \sum_{r=0}^n \frac{(-1)^r}{h^{\alpha(t)}} \binom{\alpha(t)}{r} f(t - rh). \quad (9.5)$$

The variable-order derivative of type B is defined as

$${}_0^B D_t^{\alpha(t)} = \lim_{h \rightarrow 0} \sum_{r=0}^n \frac{(-1)^r}{h^{\alpha(t-rh)}} \binom{\alpha(t-rh)}{r} f(t - rh). \quad (9.6)$$

The variable-order derivative of type C is defined as

$${}_0^C D_t^{\alpha(t)} = \lim_{h \rightarrow 0} \sum_{r=0}^n \frac{(-1)^r}{h^{\alpha(rh)}} \binom{\alpha(rh)}{r} f(t - rh). \quad (9.7)$$

In Eqs. (9.5)–(9.7),

$$n = \left\lfloor \frac{t}{h} \right\rfloor \quad \text{and} \quad \binom{a}{b} = \frac{\Gamma(a+1)}{\Gamma(b+1)\Gamma(a-b+1)}. \quad (9.8)$$

Variable-order operators can be effectively applied in modeling of physical processes containing elements with variable behaviors. For example, in heterogeneous media fractional-order operators have been widely used for modeling the heat transfer process [14]. But in the cases that some elements inside the process change over time, the use of variable-order operators can provide a more precise model for describing the behavior of the process [16].



9.3. Main results

This section is dedicated to presenting some theorems which are useful in determining the type number of variable-order systems. First of all, the definition of type number is restated.

Definition 9.3. [24] An asymptotically stable system with input $r(t)$ and output $y(t)$ is of type number $\gamma \in \mathbb{R}^{\geq 0}$ if for inputs in the form $r(t) = t^\lambda$, $\lim_{t \rightarrow \infty} (r(t) - y(t))$ is zero where $0 < \lambda < \gamma$ and infinite where $\lambda > \gamma$.

In [24] it is shown that the type number of an asymptotically stable closed-loop fractional-order system in the unity feedback structure

equals γ , if its open-loop transfer function has the form $G_{ol}(s) = G(s)/s^\gamma$, where $G(0) \neq 0, \infty$ and

$$G(s) = \frac{b_r s^{\beta_r} + b_{r-1} s^{\beta_{r-1}} + \dots + b_0}{s^{\alpha_n} + a_{n-1} s^{\alpha_{n-1}} + \dots + a_0}. \tag{9.9}$$

Here, the aim is to extend the abovementioned result for a more general case, i.e., the case that the fractional integral is replaced by a variable-order one. To this end, at first consider the following lemma.

Lemma 9.1. *If $0 < b < q(t) < m$ for $t > 0$, where b and m are two constants, then*

$$\lim_{s \rightarrow 0^+} s^\lambda \int_0^l e^{-st} \frac{t^{q(t)-1}}{\Gamma(q(t))} dt = 0, \tag{9.10}$$

for $\lambda > 0$ and $0 \leq l < \infty$.

Proof. It is clear that

$$x_1 < x_2 \rightarrow \begin{cases} a^{x_2} < a^{x_1}, & a < 1, \\ a^{x_1} < a^{x_2}, & a > 1. \end{cases} \tag{9.11}$$

A straightforward result of (9.11) is

$$\begin{cases} t^{m-1} < t^{q(t)-1} < t^{b-1}, & 0 < t < 1, \\ t^{b-1} < t^{q(t)-1} < t^{m-1}, & t > 1. \end{cases} \tag{9.12}$$

The integral in Lemma 9.1 can be split into two integrals as follows:

$$\int_0^l e^{-st} \frac{t^{q(t)-1}}{\Gamma(q(t))} dt = \int_0^a e^{-st} \frac{t^{q(t)-1}}{\Gamma(q(t))} dt + \int_a^l e^{-st} \frac{t^{q(t)-1}}{\Gamma(q(t))} dt. \tag{9.13}$$

Assume that $0 < a < 1$. Now, it is shown that (9.13) is finite. Note that the second integral in the right-hand side of (9.13) is finite because the integral function is finite for $a < t < l$ and $0 < b < q(t) < m$. Therefore, it should be proved that the first integral in the right-hand side of (9.13) is also finite. From (9.12),

$$t^{q(t)-1} < t^{b-1}, \tag{9.14}$$

where $0 < t < a < 1$. Also, since $q(t) > b > 0$, $1/\Gamma(q(t))$ is finite, i.e.,

$$\frac{1}{\Gamma(q(t))} < L, \tag{9.15}$$

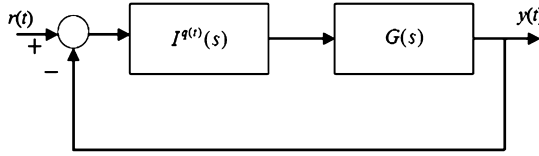


Figure 9.1 A unity negative feedback control system.

where L is a constant. From (9.14) and (9.15), it is obtained that

$$e^{-st} \frac{t^{q(t)-1}}{\Gamma(q(t))} < L e^{-st} t^{b-1}, \quad (9.16)$$

where $0 < t < a < 1$. By integrating of (9.16) from 0 to a ,

$$\int_0^a e^{-st} \frac{t^{q(t)-1}}{\Gamma(q(t))} dt < \int_0^a L e^{-st} t^{b-1} dt. \quad (9.17)$$

The integral in the right-hand side of (9.17) is finite. Hence, the integral in the left-hand side of (9.13) is finite, and consequently Lemma 9.1 is concluded. \square

We are now in a position to state Theorem 9.1, which can be used for determining the type number of an asymptotically stable system whose open-loop transfer function is in the form of $G_{ol}(s) = I^{q(t)}(s)G(s)$, where $G(0) \neq 0, \infty$ and the limit of order function at infinity is available.

Theorem 9.1. *In the control system of Fig. 9.1, assume that $0 < b < q(t) < M$ for $t > 0$, where b and M are two constants. Also, suppose that this control system is asymptotically stable, $G(0) \neq 0$ & ∞ , and $\lim_{t \rightarrow \infty} q(t) = \alpha < \infty$. In this case, the type number of the control system equals α .*

Proof. Assume that $e_\lambda(t) = t^\lambda - y(t)$ is the error of the control system of Fig. 9.1 to input $r(t) = t^\lambda$ where $\lambda > 0$. The Laplace transform of error signal $e_\lambda(t)$ is given as follows:

$$E_\lambda(s) = \frac{\Gamma(\lambda + 1)}{s^{\lambda+1} + s^{\lambda+1} I^{q(t)}(s)G(s)}. \quad (9.18)$$

Using the final value theorem, we obtain

$$e_\lambda(\infty) = \lim_{s \rightarrow 0^+} \frac{\Gamma(\lambda + 1)}{s^\lambda I^{q(t)}(s)G(s)}. \quad (9.19)$$

The control system of Fig. 9.1 is of type number α if

$$\lim_{s \rightarrow 0^+} s^\lambda I^{q(t)}(s)G(s) = \begin{cases} \infty, & \lambda < \alpha, \\ 0, & \lambda > \alpha. \end{cases} \tag{9.20}$$

Since $G(0) \neq 0, \infty$, (9.20) is equivalent to

$$\lim_{s \rightarrow 0^+} s^\lambda I^{q(t)}(s) = \begin{cases} \infty, & \lambda < \alpha, \\ 0, & \lambda > \alpha. \end{cases} \tag{9.21}$$

Note that

$$\lim_{t \rightarrow \infty} q(t) = \alpha \rightarrow \forall \varepsilon > 0 \exists l, t > l \rightarrow |q(t) - \alpha| < \varepsilon. \tag{9.22}$$

Also, let ε in (9.22) be chosen small enough such that $l > 1$. In this case, from (9.22) and (9.12), we obtain for $t > l$

$$t^{\alpha-\varepsilon-1} < t^{q(t)-1} < t^{\alpha+\varepsilon-1}. \tag{9.23}$$

According to the result obtained in (9.15),

$$p < \frac{1}{\Gamma(q(t))} < L, \tag{9.24}$$

where p is a constant. From (9.23) and (9.24), it is concluded that

$$pt^{\alpha-\varepsilon-1} < \frac{t^{q(t)-1}}{\Gamma(q(t))} < Lt^{\alpha+\varepsilon-1}, \quad 1 < l < t. \tag{9.25}$$

Multiplying (9.25) in e^{-st} (in the remainder, we assume that it is a real positive value) and integrating resulting inequalities, we find

$$\int_l^\infty pe^{-st}t^{\alpha-\varepsilon-1} dt < \int_l^\infty e^{-st} \frac{t^{q(t)-1}}{\Gamma(q(t))} dt < \int_l^\infty Le^{-st}t^{\alpha+\varepsilon-1} dt. \tag{9.26}$$

If we add the term $\int_0^l e^{-st} \frac{t^{q(t)-1}}{\Gamma(q(t))} dt$ to the above inequalities, the center part of (9.26) will be the Laplace transform of a variable-order integrator, i.e.,

$$\begin{aligned} \int_0^l e^{-st} \frac{t^{q(t)-1}}{\Gamma(q(t))} dt + \int_l^\infty pe^{-st}t^{\alpha-\varepsilon-1} dt < I^{q(t)}(s) < \\ \int_0^l e^{-st} \frac{t^{q(t)-1}}{\Gamma(q(t))} dt + \int_l^\infty Le^{-st}t^{\alpha+\varepsilon-1} dt. \end{aligned} \tag{9.27}$$

Suppose that λ is a positive number. From (9.27),

$$s^\lambda \left(\int_0^l e^{-st} \frac{t^{q(t)-1}}{\Gamma(q(t))} dt + \int_l^\infty p e^{-st} t^{\alpha-\varepsilon-1} dt \right) < s^\lambda I^{q(t)}(s) < s^\lambda \left(\int_0^l e^{-st} \frac{t^{q(t)-1}}{\Gamma(q(t))} dt + \int_l^\infty L e^{-st} t^{\alpha+\varepsilon-1} dt \right). \tag{9.28}$$

Consider $\lambda = \alpha + 2\varepsilon$. Now, we calculate the limit of the right- and left-hand sides of the above inequalities as $s \rightarrow 0$. The limit of the right-hand side of (9.28) is rewritten as

$$\lim_{s \rightarrow 0^+} s^{\alpha+2\varepsilon} \left(\int_0^l e^{-st} \frac{t^{q(t)-1}}{\Gamma(q(t))} dt + \int_l^\infty L e^{-st} t^{\alpha+\varepsilon-1} dt \right) = \lim_{s \rightarrow 0^+} s^{\alpha+2\varepsilon} \int_l^\infty L e^{-st} t^{\alpha+\varepsilon-1} dt. \tag{9.29}$$

The first part of the left-hand side of (9.29) is zero (see Lemma 9.1). Also,

$$\lim_{s \rightarrow 0^+} s^{\alpha+2\varepsilon} \int_l^\infty L e^{-st} t^{\alpha+\varepsilon-1} dt = \lim_{s \rightarrow 0^+} s^{\alpha+2\varepsilon} \left(\int_0^l L e^{-st} t^{\alpha+\varepsilon-1} dt + \int_l^\infty L e^{-st} t^{\alpha+\varepsilon-1} dt \right). \tag{9.30}$$

The right-hand side of (9.30) is the Laplace transform of $L t^{\alpha+\varepsilon-1}$. Hence, we have

$$\lim_{s \rightarrow 0^+} s^{\alpha+2\varepsilon} \int_l^\infty L e^{-st} t^{\alpha+\varepsilon-1} dt = \lim_{s \rightarrow 0^+} s^{\alpha+2\varepsilon} \frac{L \Gamma(\alpha + \varepsilon)}{s^{\alpha+\varepsilon}} = 0. \tag{9.31}$$

Eqs. (9.29) and (9.31) result in

$$\lim_{s \rightarrow 0^+} s^{\alpha+2\varepsilon} \left(\int_0^l e^{-st} \frac{t^{q(t)-1}}{\Gamma(q(t))} dt + \int_l^\infty L e^{-st} t^{\alpha+\varepsilon-1} dt \right) = 0. \tag{9.32}$$

By repeating the same idea for the left-hand side of Eq. (9.28), it is found that

$$\lim_{s \rightarrow 0^+} s^{\alpha+2\varepsilon} \left(\int_0^l e^{-st} \frac{t^{q(t)-1}}{\Gamma(q(t))} dt + \int_l^\infty p e^{-st} t^{\alpha-\varepsilon-1} dt \right) = 0. \tag{9.33}$$

Considering (9.28), (9.32), and (9.33) and using the pinching theorem [15], we obtain

$$\lim_{s \rightarrow 0^+} s^{\alpha+2\varepsilon} I^{q(t)}(s) = 0. \tag{9.34}$$

By assuming $\lambda = \alpha - 2\varepsilon > 0$ and following a similar procedure, from (9.28) it can be concluded that

$$\lim_{s \rightarrow 0^+} s^{\alpha-2\varepsilon} I^{q(t)}(s) = \infty. \tag{9.35}$$

Eqs. (9.34) and (9.35) result in (9.21), or equivalently (9.20), and the proof is completed. \square

Theorem 9.1 is of great benefit for determining the type number in some classes of variable-order systems. The following lemma can be used for finding the steady-state error of these systems to reference input $r(t) = t^\alpha$, where α is the system type number.

Lemma 9.2. *If $0 < b < q(t) < M$, where b and M are two positive constants and $\lim_{t \rightarrow \infty} q(t) = \alpha$, then*

$$\lim_{s \rightarrow 0^+} s^\alpha I^{q(t)}(s) = 1. \tag{9.36}$$

Proof. Suppose that $f(t) = \frac{t^{q(t)-1}}{\Gamma(q(t))} - \frac{t^{\alpha-1}}{\Gamma(\alpha)}$. It is clear that

$$\lim_{t \rightarrow \infty} f(t) = 0. \tag{9.37}$$

From (9.37) and the final value theorem,

$$\lim_{s \rightarrow 0^+} sF(s) = 0, \tag{9.38}$$

where $F(s) = I^{q(t)}(s) - \frac{1}{s^\alpha}$ is the Laplace transform of $f(t)$. If $\alpha > 1$,

$$\lim_{s \rightarrow 0^+} s^{1-\alpha} (s^\alpha I^{q(t)}(s) - 1) = 0. \tag{9.39}$$

It is obvious that $\lim_{s \rightarrow 0^+} s^{1-\alpha} = \infty$ where $\alpha > 1$. Hence, (9.36) is deduced from (9.39) for the case $\alpha > 1$. Now, assume that $\alpha \leq 1$. In this case, from the obtained result we find

$$\lim_{s \rightarrow 0^+} s^{\alpha+1} I^{q(t)+1}(s) = 1. \tag{9.40}$$

Define $g(t) = \frac{t^{q(t)}}{\Gamma(q(t))} - \frac{\alpha t^{q(t)}}{\Gamma(q(t)+1)}$ and note that $\lim_{t \rightarrow \infty} g(t) = 0$. Using properties of the Laplace transform, it can be easily shown that

$$G(s) = -(I^{q(t)}(s))' - \alpha I^{q(t)+1}(s), \tag{9.41}$$

where $G(s)$ is the Laplace transform of $g(t)$. If the final value theorem is applied, $\lim_{t \rightarrow \infty} g(t) = 0$ results in

$$\lim_{s \rightarrow 0^+} sG(s) = 0. \quad (9.42)$$

From (9.41) and (9.42), it can be concluded that

$$\lim_{s \rightarrow 0^+} s(- (I^{q(t)}(s))' - \alpha I^{q(t)+1}(s)) = 0. \quad (9.43)$$

By using the l'Hopital rule,

$$\lim_{s \rightarrow 0^+} \frac{I^{q(t)}(s)}{s^{-\alpha}} = \lim_{s \rightarrow 0^+} \frac{(I^{q(t)}(s))'}{-\alpha s^{-\alpha-1}}. \quad (9.44)$$

Multiplying the nominator and denominator in the right-hand side of (9.44) to $I^{q(t)+1}(s)$ yields

$$\lim_{s \rightarrow 0^+} \frac{I^{q(t)}(s)}{s^{-\alpha}} = \lim_{s \rightarrow 0^+} \frac{(I^{q(t)}(s))' I^{q(t)+1}(s) s^{\alpha+1}}{-\alpha I^{q(t)+1}(s)}. \quad (9.45)$$

From (9.40) and (9.45), it is deduced that

$$\lim_{s \rightarrow 0^+} \frac{I^{q(t)}(s)}{s^{-\alpha}} = \lim_{s \rightarrow 0^+} \frac{(I^{q(t)}(s))'}{-\alpha I^{q(t)+1}(s)}. \quad (9.46)$$

The right-hand side of (9.46) can be rewritten as

$$\lim_{s \rightarrow 0^+} \frac{(I^{q(t)}(s))'}{-\alpha I^{q(t)+1}(s)} = \lim_{s \rightarrow 0^+} \frac{s(- (I^{q(t)}(s))' - \alpha I^{q(t)+1}(s))}{s(\alpha I^{q(t)+1}(s))} + 1. \quad (9.47)$$

According to (9.21), (9.43), and (9.47), (9.36) is derived. \square

As an example, consider the order function (9.3). For this order function, from (9.4) we have $\lim_{s \rightarrow 0} s^2 I^{q(t)}(s) = 1$, which is verified by Lemma 9.2. The following theorem deals with finding the type number in a more general form of variable-order systems.

Theorem 9.2. Consider an asymptotically stable system described by the following transfer function:

$$T(s) = \frac{\sum_{j=1}^n b_j I^{q_j(t)}(s)}{1 + \sum_{i=1}^n a_i I^{q_i(t)}(s)}, \quad (9.48)$$

where $\alpha_j = \lim_{t \rightarrow \infty} q_j(t)$ and $\alpha_n > \alpha_{n-1} > \dots > \alpha_1$. This system is of type number $\alpha_n - \beta$, where β is defined as

$$\beta = \{\max_i \alpha_i | a_i \neq b_i\}. \tag{9.49}$$

Proof. Define $K^{q_i(t)}(s) = s^{\alpha_i} I^{q_i(t)}(s)$. By this definition, (9.48) can be rewritten as

$$T(s) = \frac{\sum_{j=1}^n b_j s^{-\alpha_j} K^{q_j(t)}(s)}{1 + \sum_{i=1}^n a_i s^{-\alpha_i} K^{q_i(t)}(s)}. \tag{9.50}$$

From Lemma 9.2, it can be concluded that $\lim_{s \rightarrow 0} K^{q_i(t)}(s) = 1$. Assume that the Laplace transform of system error for input $r(t) = t^\lambda$ is denoted by $E_\lambda(s)$ as the Laplace transform of $e_\lambda(t)$. It can be easily shown that

$$E_\lambda(s) = \frac{\Gamma(\lambda + 1)}{s^{\lambda+1}} \frac{1 + \sum_{i=1}^n a_i s^{-\alpha_i} K^{q_i(t)}(s) - \sum_{j=1}^n b_j s^{-\alpha_j} K^{q_j(t)}(s)}{1 + \sum_{i=1}^n a_i s^{-\alpha_i} K^{q_i(t)}(s)}. \tag{9.51}$$

By multiplying the numerator and denominator in the right-hand side of (9.51) with s^{α_n} and using the final value theorem, it can be shown that

$$e_\lambda(\infty) = \lim_{s \rightarrow 0^+} \frac{\Gamma(\lambda + 1)}{s^\lambda} \frac{s^{\alpha_n} + \sum_{i=1}^n a_i s^{\alpha_n - \alpha_i} K^{q_i(t)}(s) - \sum_{j=1}^n b_j s^{\alpha_n - \alpha_j} K^{q_j(t)}(s)}{s^{\alpha_n} + \sum_{i=1}^n a_i s^{\alpha_n - \alpha_i} K^{q_i(t)}(s)}. \tag{9.52}$$

Note that

$$s^{\alpha_n} + \sum_{i=1}^n a_i s^{\alpha_n - \alpha_i} K^{q_i(t)}(s) \simeq a_n, \quad \text{as } s \rightarrow 0^+, \tag{9.53}$$

$$s^{\alpha_n} + \sum_{i=1}^n a_i s^{\alpha_n - \alpha_i} K^{q_i(t)}(s) - \sum_{j=1}^n b_j s^{\alpha_n - \alpha_j} K^{q_j(t)}(s) \simeq (a - b) s^{\alpha_n - \beta}, \quad \text{as } s \rightarrow 0^+, \tag{9.54}$$

where a and b are defined as follows:

$$\begin{cases} a = \{a_i | \alpha_i = \beta\}, \\ b = \{b_i | \alpha_i = \beta\}. \end{cases} \tag{9.55}$$

From (9.52), (9.53), and (9.54), we obtain

$$e_\lambda(\infty) = \lim_{s \rightarrow 0^+} \frac{\Gamma(\lambda + 1)}{s^\lambda} \frac{(a - b)s^{\alpha_n - \beta}}{a_n}. \quad (9.56)$$

Eq. (9.56) confirms that the closed-loop system is of type number $\alpha_n - \beta$, and its steady-state error to input $t^{\alpha_n - \beta}$ is

$$e_{\alpha_n - \beta}(\infty) = \frac{(a - b)\Gamma(\alpha_n - \beta + 1)}{a_n}. \quad (9.57)$$

□



9.4. A method for numerical simulation

In this section, a method for simulation of a class of fractional variable-order systems based on the Adams predictor method [5] is proposed.

Assume that $T(s)$ as the transfer function of a closed-loop system is described by

$$T(s) = \frac{Y(s)}{R(s)} = \frac{\sum_j b_j F^{n_j(t)}(s)}{1 + \sum_i a_i F^{d_i(t)}(s)}, \quad (9.58)$$

where $Y(s)$ and $R(s)$ are the Laplace transform of the output of system ($y(t)$) and the input of system ($r(t)$), respectively. Eq. (9.58) in the time domain can be rewritten as

$$y(t) = \int_0^t \sum_j b_j \frac{(t - \tau)^{n_j(t - \tau) - 1}}{\Gamma(n_j(t - \tau))} r(\tau) d\tau - \int_0^t \sum_i a_i \frac{(t - \tau)^{d_i(t - \tau) - 1}}{\Gamma(d_i(t - \tau))} y(\tau) d\tau. \quad (9.59)$$

The aim of the proposed algorithm is to find the output value at times $t_n = nh$, where h is the sample time of simulation. According to (9.59), we have

$$y(t_n) = \int_0^{t_n} \sum_j b_j \frac{(t_n - \tau)^{n_j(t_n - \tau) - 1}}{\Gamma(n_j(t_n - \tau))} r(\tau) d\tau - \int_0^{t_n} \sum_i a_i \frac{(t_n - \tau)^{d_i(t_n - \tau) - 1}}{\Gamma(d_i(t_n - \tau))} y(\tau) d\tau. \quad (9.60)$$

By splitting the interval $[t_0, t_n]$ in the above integral to n successive intervals, we obtain

$$\begin{aligned} \gamma(t_n) = & \sum_{k=0}^{n-1} \int_{t_k}^{t_{k+1}} \sum_j b_j \frac{(t_n - \tau)^{n_j(t_n - \tau) - 1}}{\Gamma(n_j(t_n - \tau))} r(t_k) d\tau \\ & - \sum_{k=0}^{n-1} \int_{t_k}^{t_{k+1}} \sum_i a_i \frac{(t_n - \tau)^{d_i(t_n - \tau) - 1}}{\Gamma(d_i(t_n - \tau))} \gamma(t_k) d\tau. \end{aligned} \tag{9.61}$$

Choosing h enough small, we can use the following approximations for $n_j(t_n - \tau)$ and $d_i(t_n - \tau)$ in interval $[t_k, t_{k+1}]$:

$$n_j(t_n - \tau) \approx n_j((n - k - 0.5)h), \quad d_i(t_n - \tau) \approx d_i((n - k - 0.5)h). \tag{9.62}$$

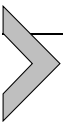
Define

$$\alpha(n, k, j) = n_j((n - k - 0.5)h), \quad \beta(n, k, i) = d_i((n - k - 0.5)h). \tag{9.63}$$

According to (9.61), (9.62), and (9.63) and benefiting from the Adams predictor method [5], we have

$$\begin{aligned} \gamma(t_n) = & \sum_j b_j \sum_{k=0}^{n-1} \frac{h^{\alpha(n,k,j)}}{\Gamma(\alpha(n, k, j) + 1)} ((n - k)^{\alpha(n,k,j)} - (n - k - 1)^{\alpha(n,k,j)}) r(kh) \\ & - \sum_i a_j \sum_{k=0}^{n-1} \frac{h^{\beta(n,k,i)}}{\Gamma(\beta(n, k, i) + 1)} ((n - k)^{\beta(n,k,i)} - (n - k - 1)^{\beta(n,k,i)}) \gamma(kh). \end{aligned} \tag{9.64}$$

Eq. (9.64) can be applied in numerical simulations of a variable-order system described by transfer function (9.58).



9.5. Numerical examples

In this section, three numerical examples are presented to verify the usefulness of the obtained results in behavior analysis of variable-order systems and circuits.

Example 9.1. Consider an asymptotically stable system defined by transfer function

$$T(s) = \frac{s^{-\alpha}}{1 + Iq(t)(s)}, \tag{9.65}$$

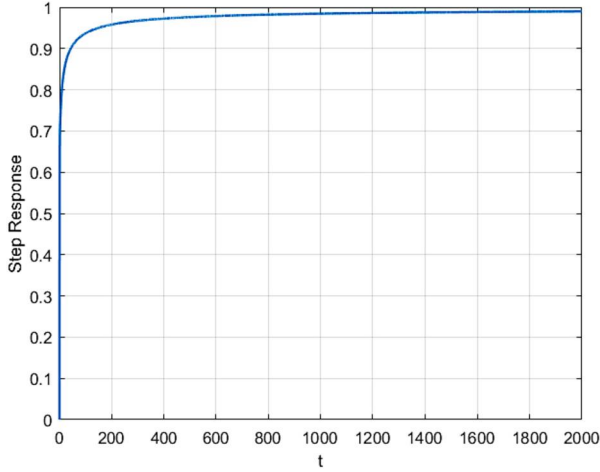


Figure 9.2 Unit step response of system (9.65) for $q(t) = \frac{0.65t+1}{t+1}$.

where $\lim_{t \rightarrow \infty} q(t) = \alpha$. Assume that $y(t)$ denotes the unit step response of this system. Using the final value theorem results in

$$\lim_{s \rightarrow 0^+} s^\alpha I^{q(t)}(s) = \frac{1}{y(\infty)}. \quad (9.66)$$

Considering Lemma 9.2 and (9.66), the final value of the unit step response of system (9.65) should be 1. This result is confirmed by the unit step response of system (9.65) for the sample order function $q(t) = \frac{0.65t+1}{t+1}$ which is numerically plotted in Fig. 9.2 (the Adams predictor method [5] with some modifications is used for numerical simulation of system (9.65)).

Example 9.2. Suppose that an asymptotically stable system is described by transfer function

$$T(s) = \frac{I^{q_2(t)}(s)}{1 + 2I^{q_1(t)}(s) + I^{q_2(t)}(s)}, \quad (9.67)$$

where $q_2(t) = 1.3$ and $q_1(t) = 0.5 + \frac{\sin(0.5t+0.3)}{1+2t}$. According to Theorem 9.2, this system should be of type number $1.3 - 0.5 = 0.8$ and its steady-state error to input $r(t) = t^{0.8}$ is $2\Gamma(1.8) = 1.86$. The error of this system in tracking input $r(t) = t^{0.8}$, which is obtained by the method mentioned in the previous example and plotted in Fig. 9.3, confirms this result.

Example 9.3. In [13], the equivalent electrical circuit for a pickup (a transducer capturing mechanical vibrations in stringed instruments like guitars

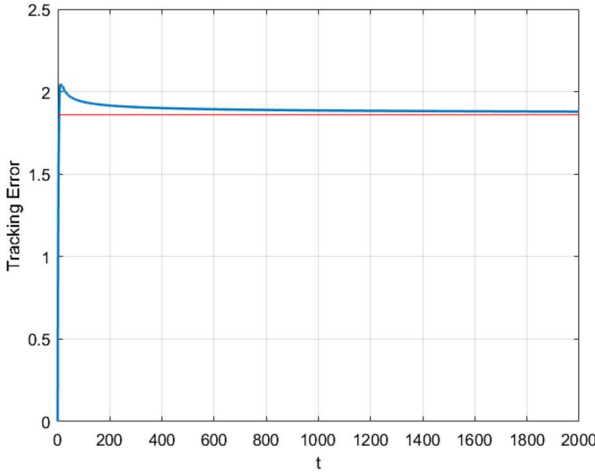


Figure 9.3 The error of system (9.67) in tracking reference input $r(t) = t^{0.8}$.

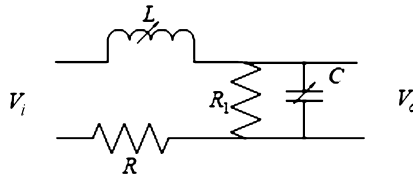


Figure 9.4 Equivalent circuit for pickup as a voltage divider.

and converting them into electrical signals) has been given as a passive network consisting of two resistors, a capacitor, and an inductor. Assume that in this electrical circuit (Fig. 9.4), the capacitor and inductor are variable-order ones [19] with the same order function $q(t)$ tending to the positive value α . In this case, the transfer function $H(s) = V_o(s)/V_i(s)$ has the following form:

$$H(s) = \frac{(I^{q(t)}(s))^2}{(1 + \frac{R}{R_1})(I^{q(t)}(s))^2 + (\frac{L}{R_1} + RC)I^{q(t)}(s) + LC}. \tag{9.68}$$

From Lemma 9.2, it is easy to show that if $v_i(t)$ is a unit step signal, then

$$v_o(\infty) = \lim_{s \rightarrow 0} \frac{(s^\alpha I^{q(t)}(s))^2}{(1 + \frac{R}{R_1})(s^\alpha I^{q(t)}(s))^2 + (\frac{L}{R_1} + RC)s^{2\alpha} I^{q(t)}(s) + LCs^{2\alpha}} = \frac{R_1}{R_1 + R}. \tag{9.69}$$

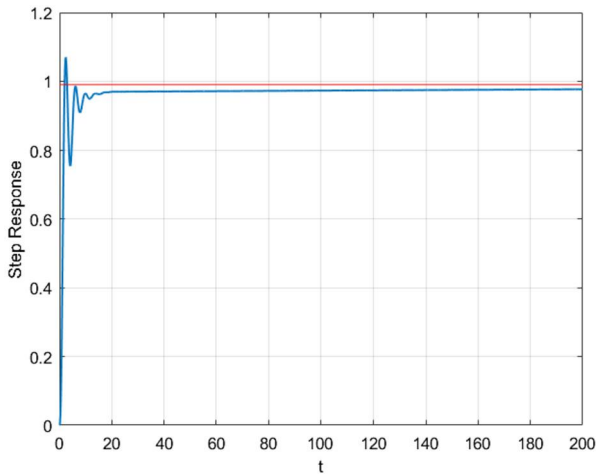


Figure 9.5 The unit step response of the variable-order circuit of Example 9.3 where $L = 2$, $R = 10^4$, $R_1 = 10^6$, $C = 5 \times 10^{-11}$, and $q(t) = 0.4 + e^{-t} \sin(t + 1)$ (as expected from (9.69), this response tends to $v_o(\infty) = 0.99$).

Consequently, if $R \neq 0$, the type number of the described electrical circuit, as a dynamical system, is zero. This result is consistent with the integer-order counterpart of this circuit which acts as a voltage divider in the steady state (the unit step response of the system described by (9.68) is plotted in Fig. 9.5 to confirm this point).

Example 9.4. Consider a system described by transfer function $G(s) = \frac{3.13e^{-50s}}{433.33s+1}$ (see [10]). Assume that the aim is to design a controller (denoted by $C(s)$) for control of this system (in a unity negative feedback structure) such that the following objectives are satisfied.

- 1) The steady-state error of the closed-loop system to ramp inputs should be constant.
- 2) The gain crossover frequency should be equal to $\omega_{cg} = 0.008$ rad/s.
- 3) The phase margin should be $\frac{\pi}{3}$ rad.
- 4) The sensitivity function $S(s) = 1/(1 + C(s)G(s))$ should satisfy $|S(j\omega)| \leq -20\text{db}$ for $\omega \leq 0.001$ (for effective rejection of low-frequency disturbances).
- 5) The closed-loop transfer function $T(s) = C(s)G(s)/(1 + C(s)G(s))$ should satisfy $|T(j\omega)| \leq -20\text{db}$ for $\omega \geq 10$ (for attenuating the high-frequency noises).

- 6) The derivative of the phase of the loop transfer function with respect to the frequency at the gain crossover frequency should be near zero, i.e., $\left. \frac{d}{d\omega}(\arg(C(j\omega)G(j\omega))) \right|_{\omega=\omega_{cg}} \simeq 0$ (for robustness in the overshoot value of the step response of the closed-loop system in the presence of the gain variation).

For more details about control objectives 2–7, see [10].

The controller considered in this example to meet the aforementioned objectives is a fractional variable-order fractional proportional integral derivative (FVOPID) one, which is of the following form:

$$C(s) = k_p + k_I I^{q(t)}(s) + k_d s^\mu, \quad (9.70)$$

where

$$q(t) = \begin{cases} \alpha_2, & t \leq l, \\ \alpha_1, & t > l \end{cases} \quad (9.71)$$

and l is a tunable constant. In order to satisfy the steady-state error-based objective (objective 1), the type number of the control system should be greater than 1. Consequently, according to Theorem 9.1, to satisfy the mentioned objective, we should have $\alpha_2 \geq 1$. Let us choose $\alpha_2 = 1$. Now by substituting $s = j\omega$ in $I^{q(t)}(s)$ and assuming $\alpha_2 = 1$, we obtain

$$I^{q(t)}(j\omega) = \frac{e^{-j\omega l}}{j\omega} + \frac{l^{\alpha_1}}{\Gamma(\alpha_1)} \sum_{k=0}^{\infty} \frac{(-j\omega l)^k}{k!(k + \alpha_1)}. \quad (9.72)$$

Objectives 2 and 3 yield

$$C(j\omega_{cg})G(j\omega_{cg}) = e^{-j2\pi/3}. \quad (9.73)$$

From (9.72) and (9.73), we have

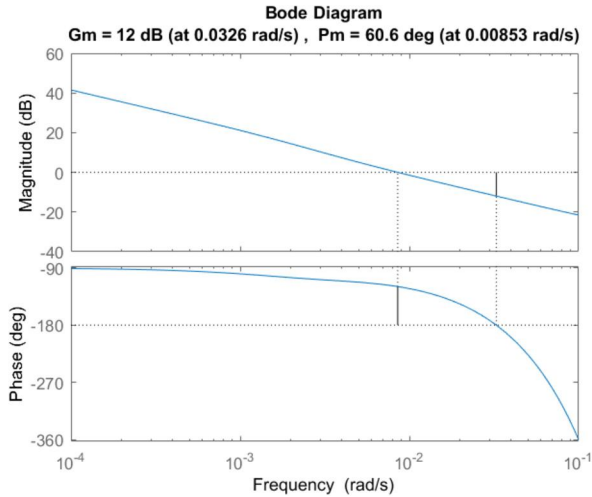
$$\frac{e^{-j\omega_{cg}l}}{j\omega_{cg}} + \frac{l^{\alpha_1}}{\Gamma(\alpha_1)} \sum_{k=0}^{\infty} \frac{(-j\omega_{cg}l)^k}{k!(k + \alpha_1)} = \frac{e^{-2j\pi/3}}{G(j\omega_{cg})}. \quad (9.74)$$

Also, objectives 4 and 5 can be formulated as

$$\begin{aligned} \left| \frac{1}{1 + C(j0.001)G(j0.001)} \right| &= -20db, \\ \left| \frac{C(j10)G(j10)}{1 + C(j10)G(j10)} \right| &= -20db. \end{aligned} \quad (9.75)$$

Table 9.1 The parameters of controller (9.70) in Example 9.4.

k_p	k_I	k_d	l	α_1	α_2	μ
1.1508	0.0038	3.9867	0.7537	0.5521	1	1.06226

**Figure 9.6** Bode diagram of the loop transfer function in Example 9.4.

Solving Eqs. (9.74) and (9.75) and considering the objective

$$\frac{d}{d\omega}(\arg(C(j\omega)G(j\omega))) \Big|_{\omega=\omega_{\text{gc}}} \simeq 0,$$

the controller parameters can be tuned as specified in Table 9.1.

To verify that objectives 2 and 3 are met by the proposed controller, the Bode diagram of the loop transfer function is plotted in Fig. 9.6. Also the steady-state error of the control system to ramp input $r(t)$ can be computed as

$$e(\infty) = \lim_{s \rightarrow 0} \frac{\Gamma(2)}{s(1 + C(s)G(s))} = \frac{\Gamma(2)}{0.0038 \times 3.13} = 84.076, \quad (9.76)$$

which is confirmed by the time-domain numerical simulation results presented in Fig. 9.7. Moreover, since the type number of the control system is 1, this system tracks the step inputs with zero steady-state error. This point is confirmed by the simulation results of Fig. 9.8.

Finally, the frequency response of the closed-loop system and the sensitivity transfer function are plotted in Fig. 9.9 and Fig. 9.10, respectively, in order to verify that objectives 5 and 4 are satisfied.

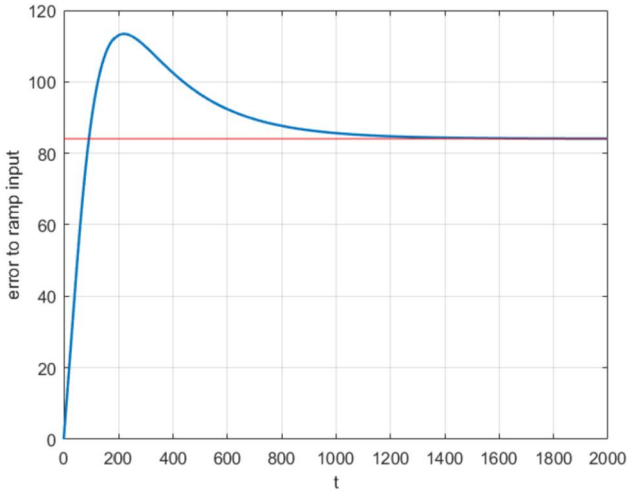


Figure 9.7 The error signal of the closed-loop system in tracking the reference input $r(t) = t$ in Example 9.4.

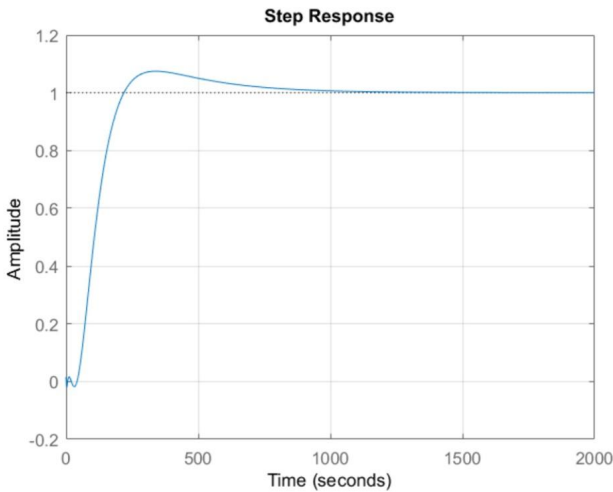
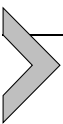


Figure 9.8 The unit step response of the closed-loop system in Example 9.4.



9.6. Conclusion

In this chapter, some useful results were presented for determining the type number in variable-order systems. These results revealed that the

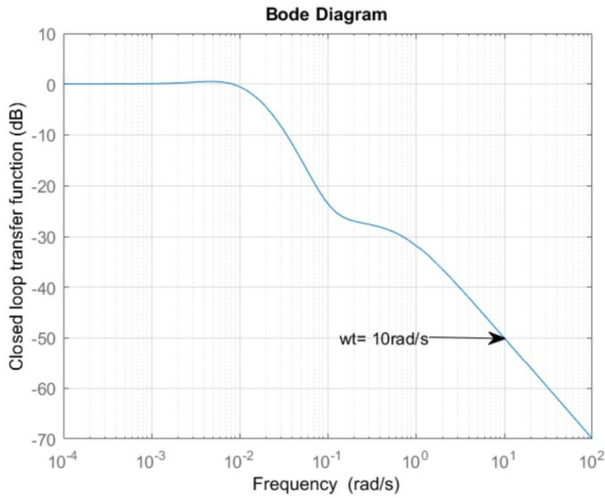


Figure 9.9 Frequency response of the closed-loop transfer function in Example 9.4.

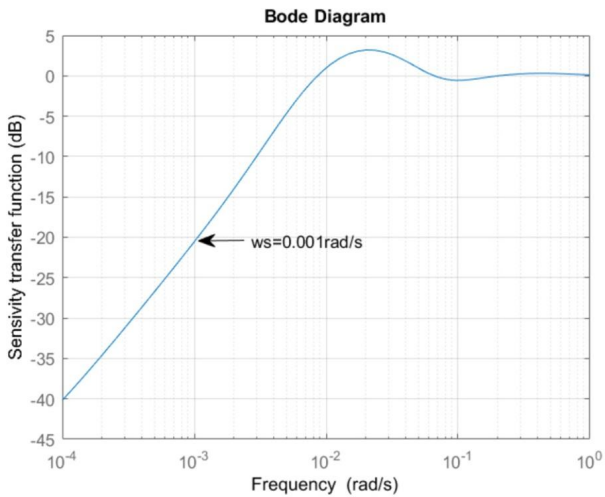


Figure 9.10 Frequency response of the sensitivity transfer function in Example 9.4.

type number of an asymptotically stable variable system is related to the limit of the order functions of the involved operators at infinity. Finally, the obtained results were verified by numerical examples on variable-order systems and circuits.

References

- [1] H. Askari, A. Ansari, Fractional calculus of variations with a generalized fractional derivative, *Fractional Differential Calculus* 6 (1) (2016) 57–72.
- [2] R. Caponetto, G. Dongola, L. Fortuna, I. Petras, *Fractional Order Systems: Modeling and Control Applications*, World Scientific, Singapore, 2010.
- [3] A. Charef, T. Bensouici, Design of digital FIR variable fractional order integrator and differentiator, *Signal, Image and Video Processing* 6 (4) (2012) 679–689.
- [4] A. Dabiri, P.B. Moghaddam, J.A. Machado, Optimal variable-order fractional PID controllers for dynamical systems, *Journal of Computational and Applied Mathematics* 339 (2018) 40–48.
- [5] K. Diethelm, N.J. Ford, A.D. Freed, A predictor corrector approach for the numerical solution of fractional differential equations, *Nonlinear Dynamics* 29 (1) (2002) 3–22.
- [6] R.K.H. Galvao, S. Hadjiloucas, K.H. Kienitz, R.J.M. Afonso, Fractional order modeling of large three-dimensional RC networks, *IEEE Transactions on Circuits and Systems. I, Regular Papers* 60 (3) (2013) 624–637.
- [7] L. Liu, F. Pan, D. Xue, Variable-order fuzzy fractional PID controller, *ISA Transactions* 55 (2015) 227–233.
- [8] C.F. Lorenzo, T.T. Hartley, Variable order and distributed order fractional operators, *Nonlinear Dynamics* 29 (1) (2002) 57–98.
- [9] L. Mescia, P. Bia, D. Caratelli, Fractional derivative based FDTD modeling of transient wave propagation in Havriliak–Negami media, *IEEE Transactions on Microwave Theory and Techniques* 62 (9) (2014) 1920–1929.
- [10] C.A. Monje, Y.Q. Chen, B. Vinagre, M.D. Xue, V. Feliu-Battle, *Fractional-Order Systems and Controls. Fundamentals and Applications*, Advanced Industrial Control Series, Springer-Verlag, London, UK, 2010.
- [11] D. Mozyrska, P. Oziabło, M. Wyrwas, Fractional-, variable-order PID controller implementation based on two discrete-time fractional order operators, in: 2019 7th International Conference on Control, Mechatronics and Automation (ICCMA), 2019, pp. 26–32.
- [12] P.V. Ostalczyk, T. Rybicki, Variable-fractional-order dead-beat control of an electromagnetic - part II, *IFAC Proceedings Volumes* 39 (11) (2008) 101–106.
- [13] R.C.D. Paiva, J. Pakarinen, V. Valimaki, Acoustics and modeling of pickups, *Journal of the Audio Engineering Society* 60 (10) (2012) 768–782.
- [14] P. Sakrajda, M.S. Wiraszka, Fractional variable-order model of heat transfer in time-varying fractal media, in: 19th International Carpathian Control Conference (ICCC), 2018, pp. 548–552.
- [15] S.L. Salas, E. Hile, G.J. Etgen, *Calculus (One and Several Variables)*, John Wiley & Sons, United State of America, 2007.
- [16] P. Sakrajda, D. Sierociuk, Modeling heat transfer process in grid-holes structure changed in time using fractional variable order calculus, in: *Theory and Applications of Non-integer Order Systems*, Springer, 2017, pp. 297–306.
- [17] H. Sheng, H. Sun, Y.Q. Chen, T. Qiu, Synthesis of multifractional Gaussian noises based on variable-order fractional operators, *Signal Processing* 91 (7) (2011) 1645–1650.
- [18] J. Shyu, S.C. Pei, C.H. Chan, An iterative method for the design of variable fractional-order FIR differintegrators, *Signal Processing* 89 (3) (2009) 320–327.
- [19] D. Sierociuk, I. Podlubny, I. Petras, Experimental evidence of variable-order behavior of ladders and nested, *IEEE Transactions on Control Systems Technology* 21 (2) (2013) 459–466.
- [20] D. Sierociuk, M. Macias, Comparison of variable fractional order PID controller for different types of variable order derivatives, in: *Proceedings of the 14th International Carpathian Control Conference (ICCC)*, 2013, pp. 334–339.

- [21] H.G. Sun, W. Chen, Y.Q. Chen, Variable-order fractional differential operators in anomalous diffusion modeling, *Physica A: Statistical Mechanics and its Applications* 388 (21) (2009) 4586–4592.
- [22] D. Tavares, R. Almeida, D.F.M. Torres, Combined fractional variational problems of variable order and some computational aspects, *Journal of Computational and Applied Mathematics* 339 (2018) 374–388.
- [23] D. Tavares, R. Almeida, D.F.M. Torres, Fractional Herglotz variational problem of variable order, *Discrete and Continuous Dynamical Systems* 11 (1) (2018) 143–154.
- [24] M.S. Tavazoei, On type number concept in fractional-order systems, *Automatica* 49 (1) (2013) 301–304.
- [25] M.S. Tavazoei, M. Haeri, S. Jafari, S. Bolouki, M. Siami, Some applications of fractional calculus in suppression of chaotic oscillations, *IEEE Transactions on Industrial Electronics* 55 (11) (2008) 4094–4101.
- [26] C.-C. Tseng, S.-L. Lee, Design of variable fractional order differentiator using infinite product expansion, in: *Proceedings of 20th European Conference on Circuit Theory and Design (ECCTD)*, 2011, pp. 17–20.
- [27] D. Valerio, J.S.D. Costa, Variable-order fractional derivatives and their numerical approximations, *Signal Processing* 91 (3) (2011) 470–483.

This page intentionally left blank

Theoretical study in conformal thermal antennas optimized by a fractional energy[☆]

Rabha W. Ibrahim

IEEE: 94086547, Kuala Lumpur, Malaysia

10.1. Introduction

A conformal map (CM) is a function that locally reserves angles, but not fundamentally sizes. It reserves both angles and the characters (figures) of minor statistics, but not definitely their magnitude, size, or curve. The conformal possessions can be designated in terms of the Jacobian derivative matrix of an established transformation. The transformation is conformal when the Jacobian at each point is a positive scalar time of an alternation matrix (orthogonal matrix satisfying that the determinant is equivalent to one). Several investigators have described CM to cover orientation-reversing mappings whose Jacobians can be carved as some scalar times of an orthogonal matrix. In the complex plane, CM is analytic univalent (one-to-one) on the open unit disk. Moreover, it normalizes to confirm the geometric representation of any formal involving it. Most of these formals includes derivatives of CMs (see [1,2]).

A thermal antenna is an electromagnetic foundation that produces in its neighborhood a spatially clear field in the electromagnetic frequency array. Generally, its production pattern alternates with the wavelength so that the heat flux it emits is guiding. Usually, the production angle of the thermal antenna expressively transforms to the wavelength during the Planck window. Consequently, the heat flux from the spectral assimilation which is slanted by the Planck distribution function is not markedly directional. Nowadays, the improvement of broadband angular discerning sources in the infrared array remains a stimulating difficulty (see [3]).

Conformal antennas (CAs) are gaining attention in numerous aspects from sensor and movable communication structures. Array antennas, whose

[☆] Theoretical study in conformal thermal antennas optimized by a fractional energy.

components are placed on a curved surface, may display some compensations, not only from the aerodynamic point of view, since they can survey the surface of pitchers or airliners, but also from the electrical one. In information, they can emit matching concentrating designs within higher angular areas, as necessary in some investigations (see [4–8]). Specifically, the diagnostics of CAs are necessary to resolve an inverse source problem on the energy field. Its result totals to capsizing a linear integral operator. Actually, the energy source Σ and the energy field Ξ are associated with the integral operator $\Lambda : \Sigma \in X \rightarrow \Xi \in Y$, and in order to properly overcome the problem, not only the energy operator Λ but also the source and field functional spaces X and Y need to be detailed. In applying an antenna scheme, full power transmission will happen when the antenna's response, impedance, is used to a conjugate impedance equal to the individual impedance of the communication line. Consequently, CA optimization would contain not only the energy properties, but also the impedance appearances.

The conformal thermal antenna (CTA) has the attention of many researchers. Aziz et al. [9] presented a system of CTAs using conductive ink which normally requires thermal treatment for removal of binder and solvent, which is not suitable for a thermally sensitive substrate. Mohamadzade et al. [10] reviewed the notion of CTA and its applications in different fields. Song [11] suggested CTA for microwave-induced thermal ablation. A novel CTA system is proposed by Goa et al. [12] using a coverage method based on bipolar-angle mapping that determines whether a liver tumor is completely encompassed by thermal coagulation zones. Singh et al. [13] utilized a thermal simulation in a compact CTA. The engineered coefficient of thermal expansion is used to design CTAs given by Yuxiao and Papapolymerou [14]. The antenna radome and the thermal-protective coating layer outside of the carrier are considered in the design given by Yinusa [15]. Striker et al. [16] presented a multimaterial technique for directly 3D printing Electrify and Ninja Flex together, in a single print job, on a single-extruded printer. The antenna and substrate layers are thermally bonded to one another, during the printing process, with no adhesives added. Simulated temperature profiles and overlaid thermal damage contours without blood perfusion are assumed in the CTA formulation by Fallahi [17]. Biswas and Mirotznik [18] considered the thermal processing to design and embed the antenna elements conformally. Design, optimization, and simulation of CTAs using hyperthermia technology is considered by Rajabi et al. [19]. A low-cost textile CTA utilizing thermal-transfer printing is suggested by

Pulanthran et al. [20]. A hybrid 3D printing process involving a thermal wire-mesh embedding method for conductors of CTA is formulated by Wang et al. [21]. A similar study was conducted by Zhao et al. [22]

Here, we combine the CA and TA to organize the CTA. The geometric representation is considered to be the shell shape by using geometric function theory, such that the antenna is indicated on the cylinder. We shall deal with the frequency, accuracy, and gain of the model, including comparisons with recent works. To complete our investigation, we present the fractional energy operator of the system with analytic presentations.

The chapter is organized as follows. Section 10.2 deals with the definition of the conformal mapping notion, Section 10.3 discusses the thermal optimization method, Section 10.4 discusses CTA optimization, and Section 10.5 presents the conformal fractional energy.



10.2. Conformal mapping

A function $\varphi : X \rightarrow Y$ is titled conformal (or angle preserving) at a point $x_0 \in X$ if it preserves angles between directed curves through x_0 , as well as preserving orientation. Conformal maps preserve shapes, angles, and the small figures, but fail to preserve size or curvature. In this effort, we present a conformal mapping based on geometric function theory (see [23] and [24]).

Suppose that \wedge is the set of all analytic functions $\Upsilon \in \mathcal{U}$, $\mathcal{U} := \{\xi : |\xi| < 1\}$ (the open unit disk) and normalized by the conditions $\Upsilon(0) = 0$ and $\Upsilon'(0) = 1$, expanded by

$$\Upsilon(\xi) = \xi + \sum_{n=2}^{\infty} \gamma_n \xi^n, \quad \xi \in \mathcal{U}. \quad (10.1)$$

A subclass of \wedge is the univalent functions (one-to-one) indicated by (\textcircled{S}) . Moreover, a function $\Upsilon \in \wedge$ is known as starlike in \mathcal{U} , represented by \textcircled{S}^* , if and only if

$$\Re \left(\frac{\xi \Upsilon'(\xi)}{\Upsilon(\xi)} \right) > 0, \quad \xi \in \mathcal{U}.$$

A function $\Upsilon \in \wedge$ is convex in \mathcal{U} , represented by \textcircled{C} , if and only if

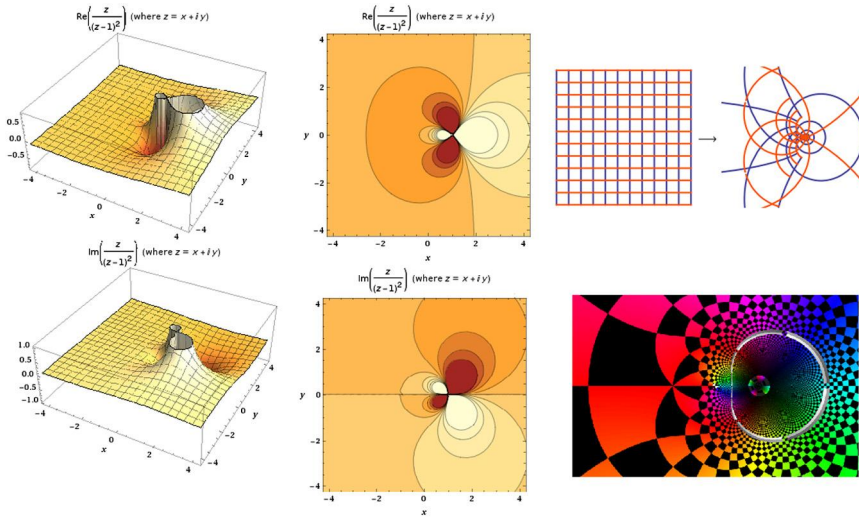


Figure 10.1 Plot of the Koebe function $(\xi/(1 - \xi)^2)$.

$$1 + \Re \left(\frac{\xi \Upsilon''(\xi)}{\Upsilon'(\xi)} \right) > 0, \quad \xi \in \mathbb{U}.$$

The category of univalent functions is classified as a set of special conformal mappings in the open unit disk (for details see [23]). We introduce different types of examples such as the Koebe functions and others.

Example 10.1. We have the following constructions.

Consider the Koebe function of second order (see Fig. 10.1) which represents the extreme starlike function in \mathbb{U}

$$\begin{aligned} \lambda(\xi) &= \frac{\xi}{(1 - \xi)^2} \\ &= \xi + \sum_{n=2}^{\infty} n\xi^n. \end{aligned} \tag{10.2}$$

Next, we consider the Koebe function of first order (see Fig. 10.2), which indicates the extreme convex univalent function in \mathbb{U} (also starlike)

$$\begin{aligned} \Upsilon(\xi) &= \frac{\xi}{1 - \xi} \\ &= \xi + \sum_{n=2}^{\infty} \xi^n. \end{aligned} \tag{10.3}$$

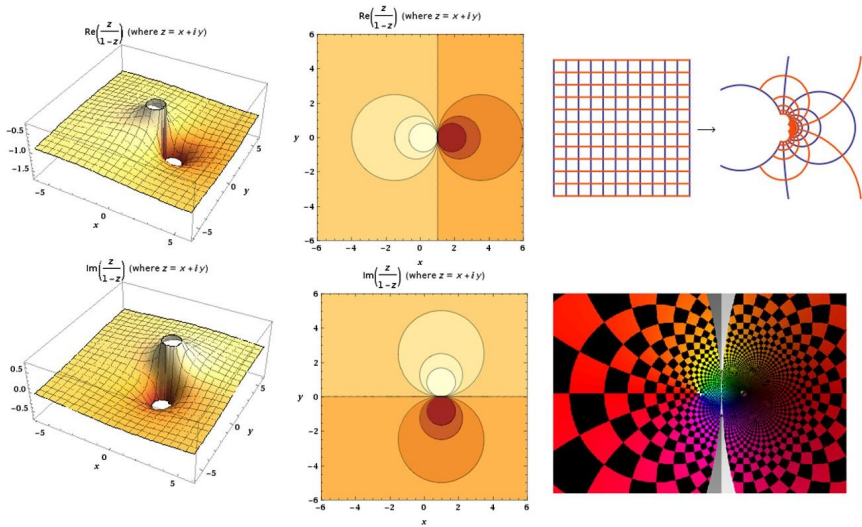


Figure 10.2 Plot of the Koebe function of first order ($\xi/(1 - \xi)$).

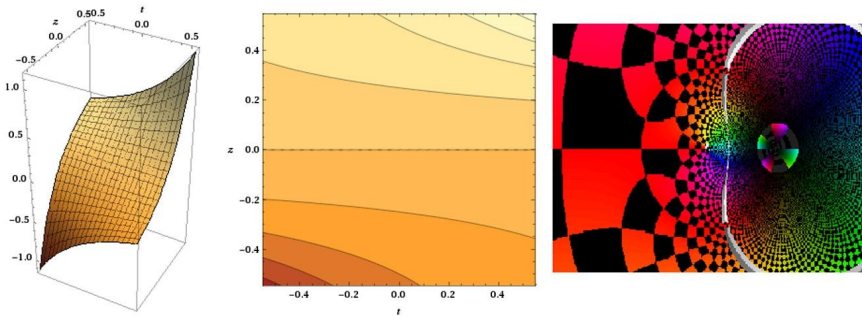


Figure 10.3 The parametric Koebe function of first order $0 < t < 1$.

As a special case of the Koebe function is the parametric Koebe function of first order (see Fig. 10.3),

$$\begin{aligned} \Upsilon_t(\xi) &= \frac{\xi}{1 - t\xi} \\ &= \xi + \sum_{n=2}^{\infty} t^{n-1} \xi^n. \end{aligned} \tag{10.4}$$

In addition, the rotated Koebe function of first order has the formula (see

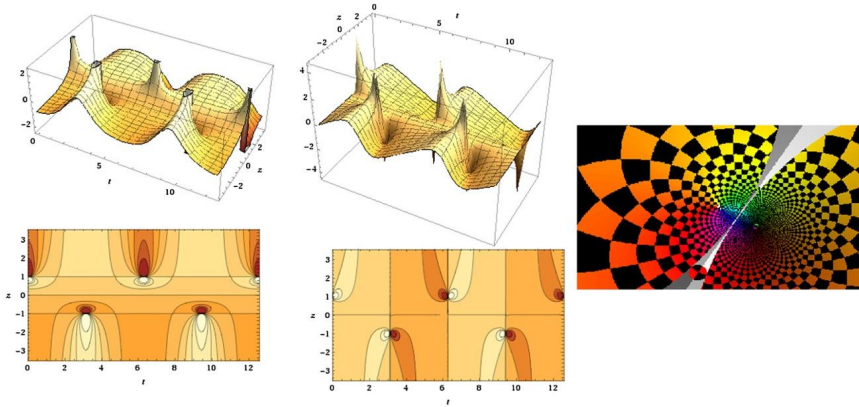
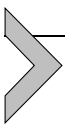


Figure 10.4 The rotated Koebe function; shown are 3D real and imaginary parts, contour plots, and the radiation distribution plot.

Fig. 10.4)

$$\begin{aligned} \chi_t(\xi) &= \frac{\xi}{1 - e^{it} \xi} & (10.5) \\ &= \xi + \sum_{n=2}^{\infty} e^{(n-1)it} \xi^n. \end{aligned}$$

In our discussion, we shall consider the parameters and the rotated Koebe function of first order because they are convex functions (the convexity represents the shell of the antenna).



10.3. Thermal optimization approach

Our approach is based on the class of heat equations of complex variables taking the formula

$$\partial_t \gamma_t(\xi) - \partial_{\xi}^2 \gamma_t(\xi) = E_t(\xi), \quad \xi \in \cup, \quad (10.6)$$

where $E(\xi)$ represents the error function (Fig. 10.5), which is convex in \cup , satisfying

$$E(0) = \gamma(0) = 0, \quad \gamma_t(\xi) \in \wedge,$$

and indicates the optimal coarse model design and t is the temperature mode. Also, we have the following class:

$$\partial_t \chi_t(\xi) - \partial_\xi^2 \chi_t(\xi) = \Lambda_t(\xi), \quad \xi \in \cup, \quad (10.7)$$

where

$$\Lambda_t(\xi) := E_n(\xi) = \frac{1}{\sqrt{\pi}} \Gamma(n) \left(\Gamma\left(\frac{1}{n}\right) - \Gamma\left(\frac{1}{n}, \xi^n\right) \right).$$

The iteration formula becomes

$$E_{t;i+1}(\xi) = (\partial_t \gamma_t(\xi) - \partial_\xi^2 \gamma_t(\xi))_i, \quad i = 1, 2, 3, \dots, \quad (10.8)$$

and

$$\Lambda_{t;i+1}(\xi) = (\partial_t \chi_t(\xi) - \partial_\xi^2 \chi_t(\xi))_i, \quad i = 1, 2, 3, \dots \quad (10.9)$$

The process is dismissed if $|E_{t;i+1}(\xi)|$ converts adequately slightly or the scheme qualifications are fulfilled (see Algorithm 10.1).

Result: Minimize the value of $E_{t;i+1}(\xi)$ or $\Lambda_{t;i+1}(\xi)$

initialization : $i, \gamma_t(\xi)$

while $\xi \in \cup; |\xi| < 1$ **do**

$(\partial_t \gamma_t(\xi) - \partial_\xi^2 \gamma_t(\xi))_i;$	
if $\partial_t \gamma_t(\xi) - \partial_\xi^2 \gamma_t(\xi) \approx 0$ then	
$ E_{t;i+1}(\xi) ;$	
else	
$ E_{t;i+1}(\xi) \approx 0;$	
end	

end

Algorithm 10.1: Optimization algorithm for conformal mapping.

Similarly for $\Lambda_{t;i+1}$.

Example 10.2. Consider the following function:

$$\begin{aligned} \gamma_t(\xi) &= \frac{\xi}{1 - t\xi} \\ &= \xi + \sum_{n=2}^{\infty} t^{n-1} \xi^n. \end{aligned}$$

Then, we obtain

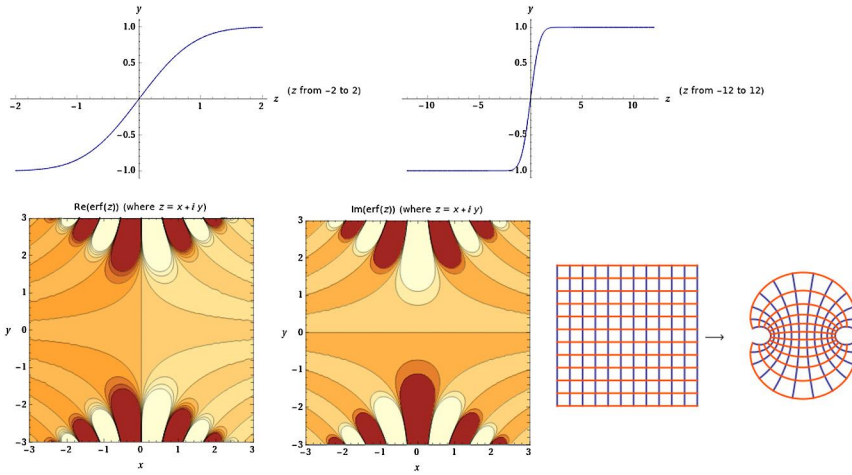


Figure 10.5 The plot of the error function.

$$\begin{aligned} \partial_t \Upsilon_t(\xi) - \partial_\xi^2 \Upsilon_t(\xi) &= E_t(\xi) \Rightarrow \\ \frac{(t(\xi^3 + 2) - \xi^2)}{(t\xi - 1)^3} &= E_t(\xi) \Rightarrow \\ \frac{(t(\xi^3 + 2) - \xi^2)}{(t\xi - 1)^3} &= \frac{(2t\xi)}{\sqrt{(\pi)}} - \frac{(2t^3\xi^3)}{(3\sqrt{(\pi)})} + \frac{(t^5\xi^5)}{(5\sqrt{(\pi)})} + O(\xi^7). \end{aligned}$$

Solving the above equation for ξ , we arrive at $|\xi| = 1$ when $t = 1$ and $|\xi| < \frac{1}{t}$ when $t > 0$. Now consider the function

$$\begin{aligned} \chi_t(\xi) &= \frac{\xi}{1 - e^{it}\xi} \\ &= \xi + \sum_{n=2}^{\infty} e^{(n-1)it} \xi^n. \end{aligned}$$

Then a computation implies that

$$\begin{aligned} \partial_t \chi_t(\xi) - \partial_\xi^2 \chi_t(\xi) &= \Lambda_t(\xi) \Rightarrow \\ \frac{(e^{(it)}(ie^{(it)}\xi^3 - i\xi^2 + 2))}{(-1 + e^{(it)}\xi)^3} &= \Lambda_t(\xi) \Rightarrow \\ \frac{(e^{(it)}(ie^{(it)}\xi^3 - i\xi^2 + 2))}{(-1 + e^{(it)}\xi)^3} &\approx 1. \end{aligned}$$

Solving for ξ , we get

$$\begin{aligned} |\xi| &\leq \left| \frac{(e^{-it})(\sqrt{-e^{it}(e^{it} - 2i)} + e^{it}))}{(e^{it} - i)} \right|, \quad e^{it} \neq i, \\ &\leq \frac{3}{4}, \quad t = \frac{1}{2}(4\pi n + \pi - 2\log(2)). \end{aligned}$$

From the above, we conclude that the thermal optimization appears near the boundary of the disk. Next, we introduce a wavelet conformal function as follows.

Example 10.3. Consider the following function:

$$\begin{aligned} \Upsilon_t(\xi) &= \frac{\sin(t\xi)}{t}, \quad t > 0, \xi \in \mathbb{U} \\ &= \xi - \frac{(t^2\xi^3)}{6} + \frac{(t^4\xi^5)}{120} + O(\xi^7). \end{aligned} \quad (10.10)$$

Then, we obtain

$$\begin{aligned} \partial_t \Upsilon_t(\xi) - \partial_\xi^2 \Upsilon_t(\xi) &= E_t(\xi) \Rightarrow \\ &\frac{(t\xi \cos(t\xi) - \sin(t\xi))}{t^2} + t \sin(t\xi) \\ &= \frac{(2t\xi)}{\sqrt{\pi}} - \frac{(2t^3\xi^3)}{(3\sqrt{\pi})} + \frac{(t^5\xi^5)}{(5\sqrt{\pi})} + O(\xi^7) \Rightarrow \\ t^2\xi - \frac{1}{6}(t(t^3 + 2))\xi^3 + \frac{1}{120}t^3(t^3 + 4)\xi^5 + O(\xi^7) \\ &= \frac{(2t\xi)}{\sqrt{\pi}} - \frac{(2t^3\xi^3)}{(3\sqrt{\pi})} + \frac{(t^5\xi^5)}{(5\sqrt{\pi})} + O(\xi^7). \end{aligned}$$

A comparison between the coefficients implies that we find the optimal solution when $t = \frac{2}{\sqrt{\pi}}$. Fig. 10.6 shows the behavior of the solution when the heat equation is optimized by the error function.

Example 10.4. Consider the following function:

$$\begin{aligned} \Upsilon_t(\xi) &= \frac{e^{(t\xi)}}{t}, \quad t > 0, \xi \in \mathbb{U} \\ &= \xi + \frac{(t\xi^2)}{2} + \frac{(t^2\xi^3)}{6} + \frac{(t^3\xi^4)}{24} + \frac{(t^4\xi^5)}{120} + \frac{(t^5\xi^6)}{720} + O(\xi^7). \end{aligned} \quad (10.11)$$

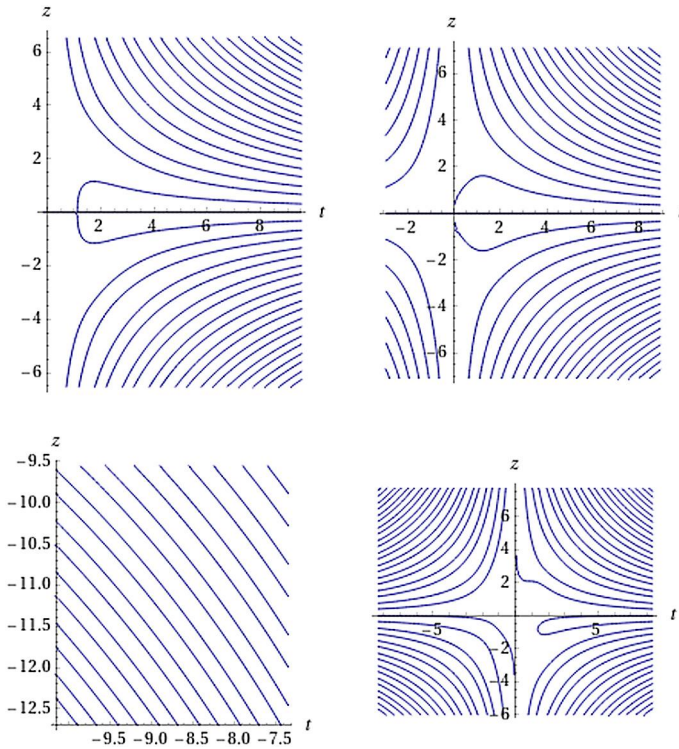


Figure 10.6 The behavior of solutions of the heat equation indicated by function (10.10) optimized by the error function near the origin in the first row and the behavior of the solutions at the boundary $(-1, 1)$ in the second row.

Then, we have

$$\begin{aligned}
 \partial_t \gamma_t(\xi) - \partial_\xi^2 \gamma_t(\xi) &= E_t(\xi) \Rightarrow \\
 \frac{(e^{t\xi})(t\xi - 1) + 1}{t^2 - te^{t\xi}} &= \frac{(2t\xi)}{\sqrt{\pi}} - \frac{(2t^3\xi^3)}{(3\sqrt{\pi})} + \frac{(t^5\xi^5)}{(5\sqrt{\pi})} + O(\xi^7) \Rightarrow \\
 -t - t^2\xi + \frac{1}{2}(1 - t^3)\xi^2 - \frac{1}{6}(t(t^3 - 2))\xi^3 & \\
 - \frac{1}{24}(t^2(t^3 - 3))\xi^4 - \frac{1}{120}(t^3(t^3 - 4))\xi^5 + O(\xi^6) & \\
 = \frac{(2t\xi)}{\sqrt{\pi}} - \frac{(2t^3\xi^3)}{(3\sqrt{\pi})} + \frac{(t^5\xi^5)}{(5\sqrt{\pi})} + O(\xi^7). &
 \end{aligned}$$

The behavior solution at the origin $\partial_t \gamma_t(\xi) - \partial_\xi^2 \gamma_t(\xi) = 0$ satisfies the following formula:

$$t \neq 0, \quad \xi = \frac{(W_n(-e^{(-t^3-1)}) + t^3 + 1)}{t}, \quad n \in \mathbb{Z},$$

where W_n is the analytic omega function (Lambert W function). And the real solution is given by the formula

$$\Re(\xi) = \frac{W(-e^{(-t^3-1)}) + t^3 + 1}{t} \\ \approx \frac{(W(-2.71828^{(-t^3-1)}) + t^3 + 1)}{t}.$$

Moreover, the solution for $\partial_t \gamma_t(\xi) - \partial_\xi^2 \gamma_t(\xi) = 1$ is given by the formula

$$\xi = \frac{W\left(e^{(-t^3-1)}(t^2 - 1)\right) + t^3 + 1}{t}, \quad t \neq 0.$$

The solution for the equation $\partial_t \gamma_t(\xi) - \partial_\xi^2 \gamma_t(\xi) = -1$ is formulated as follows:

$$t \neq 0, \quad \xi = \frac{W_n\left(e^{(-t^3-1)}(-t^2 - 1)\right) + t^3 + 1}{t}, \quad n \in \mathbb{Z},$$

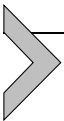
with

$$\Re(\xi) = \frac{\left(W(-e^{(-t^3-1)}(t^2 + 1))\right) + t^3 + 1}{t}.$$

Note that the Taylor series of W around 0 can be expanded by the formula

$$W(\xi) = \sum_{n=1}^{\infty} \frac{(-n)^{n-1}}{n!} \xi^n \\ = \xi - \xi^2 + \frac{3}{2}\xi^3 - \frac{8}{3}\xi^4 + \frac{125}{24}\xi^5 - \dots.$$

Fig. 10.7 shows the behavior of the solution when the heat equation is optimized by the error function.



10.4. CTA optimization

This section deals with the conformal thermal antenna shaped by the shell conformal mapping graph. We consider the cylindrical conformal antenna and the quasicylindrical conformal antenna (see Fig. 10.8).

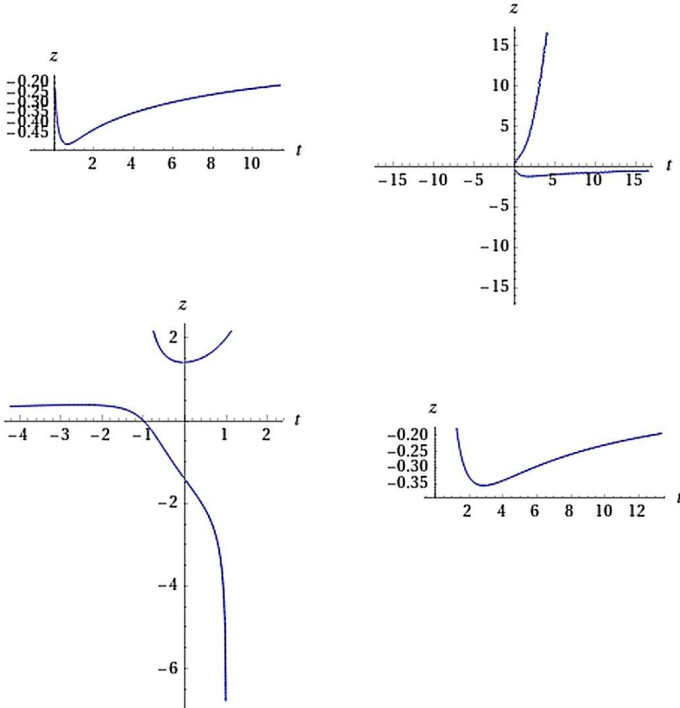


Figure 10.7 The behavior of solutions of the heat equation given by function (10.11) optimized by the error function near the origin in the first row and the behavior of the solutions at the boundary $(-1, 1)$ in the second row.

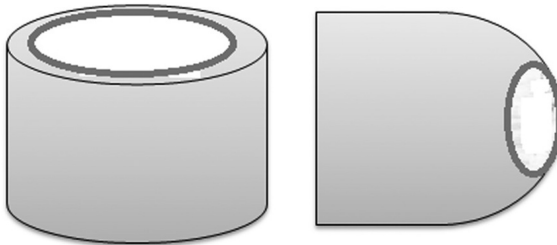


Figure 10.8 Shell conformal thermal antennas placed on the cylinder and quasicylinder.

10.4.1 Cylindrical CTA

The design of starlike-shaped antennas is produced on a reproduced circuit board with $r < 1$, $h = 1.5$ mm. The restriction request to be optimized is the half-length of the reverberation edges (each one). The surface of

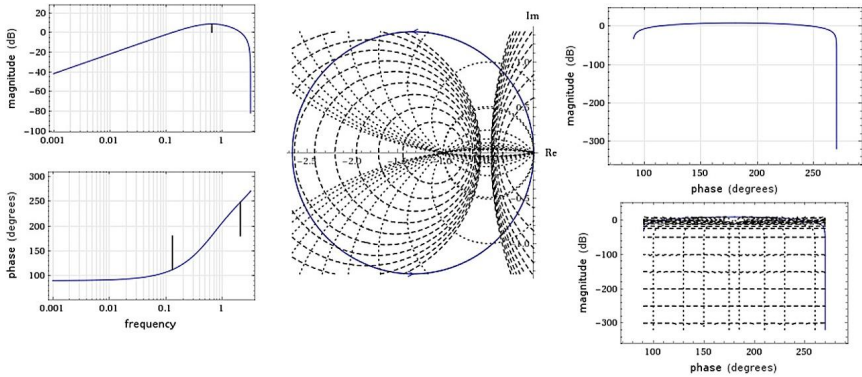


Figure 10.9 Frequency, phase, and magnitude of $E_t(\xi)$ when $t = 0.5$. The stability of the magnitude and the phase at the boundary of \cup .

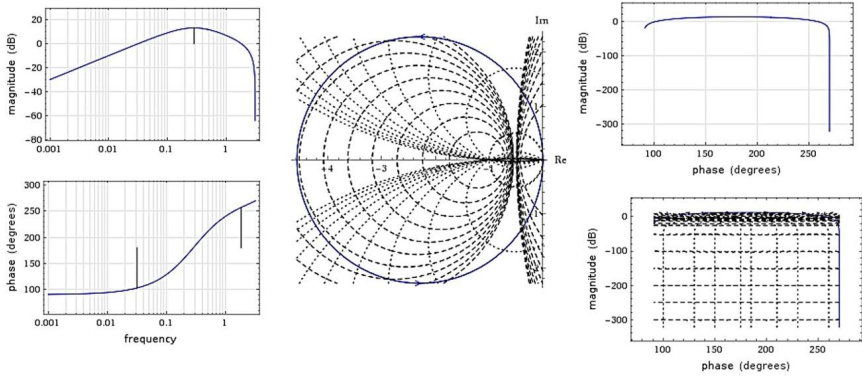


Figure 10.10 Frequency, phase, and magnitude of $E_t(\xi)$ when $t = 0.75$. The stability of the magnitude and the phase at the boundary of \cup .

a cylinder platform has the following data: the radius is 10 mm and the cylinder height is 20 mm. The CA is published on the same substrate, and the optimal construction is given by the conformal convex combination $\Upsilon_t(\xi)$ where

$$\Re\left(1 + \frac{\xi \Upsilon_t''(\xi)}{\Upsilon_t(\xi)}\right) > 0.$$

The properties of $E_t(\xi)$ show that convergence to the equilibrium point occurs when $|\xi| \in \partial\cup$ (see Figs. 10.9–10.11 for different values of t). Thus, we confirm that the edges are minimized. We indicate that one can reduce

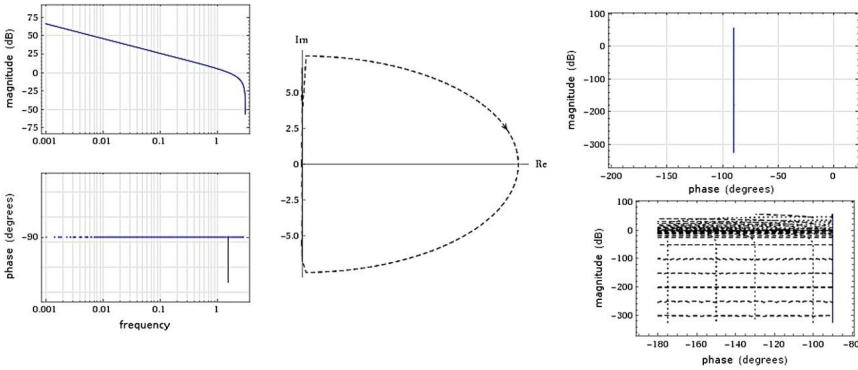


Figure 10.11 Frequency, phase, and magnitude of $E_t(\xi)$ when $t = 1$. The stability of the magnitude and the phase at the boundary of \cup .

or increase the high h and get the same result. We note that the iteration in this case is only two to converge to the optimal value.

10.4.2 Quasicylindrical CTA

For this type of antennas, we consider the conformal mapping

$$\chi_t(\xi) = \frac{\xi}{1 - e^{it} \xi}.$$

In the same manner of the cylindrical conformal antenna, $|\xi| \in \partial\cup$ minimizes the edges of the quasicylindrical conformal antenna after three iterations. Figs. 10.12–10.14 indicate the properties of $\Lambda_t(\xi)$ (error function) in Example 10.2 for different values of t .



10.5. Conformal fractional energy

The required fluctuation wavelengths of the arbitrary outcomes are their assorted kernels that are selected to fit the requirements of different arrangements. As applied, the central variations between Caputo fractional calculus, Caputo–Fabrizio calculus [25], and others are that Caputo calculus is expressed exploiting a control rule and Caputo–Fabrizio calculus is presented employing an exponential function as follows.

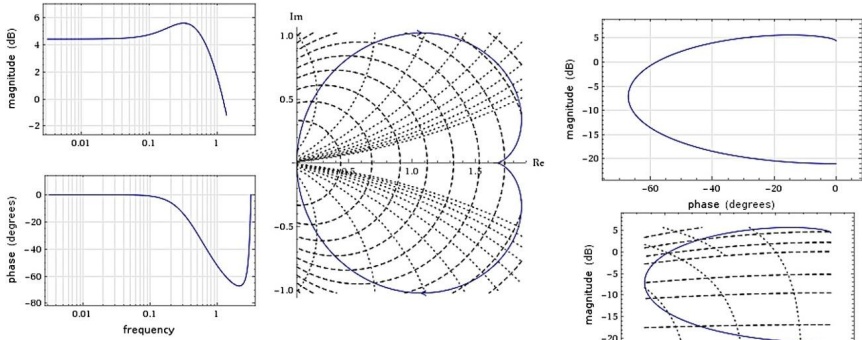


Figure 10.12 Frequency, phase, and magnitude of $\Lambda_t(\xi)$ when $t = 0.5$. The stability of the magnitude and the phase at the boundary of \cup .

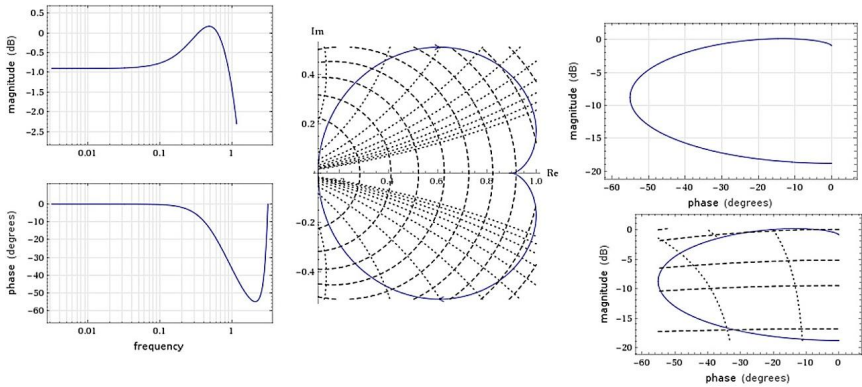


Figure 10.13 Frequency, phase, and magnitude of $\Lambda_t(\xi)$ when $t = 0.75$. The stability of the magnitude and the phase at the boundary of \cup .

Definition 10.1 (CFD). A differential operator Δ^ν , $\nu \in (0, 1)$, is titled CFD of order ν of a function g if and only if Δ^ν fulfills

$$\Delta^\nu g(t) = \frac{1}{1-\nu} \int_0^t g'(\tau) \exp\left(\frac{-\nu}{1-\nu}(t-\tau)\right) d\tau, \quad t \in [0, \infty).$$

The analogical integral is expressed by the formal

$$I^\nu g(t) = (1-\nu)g(t) + \nu \int_0^t g(\tau) d\tau. \tag{10.12}$$

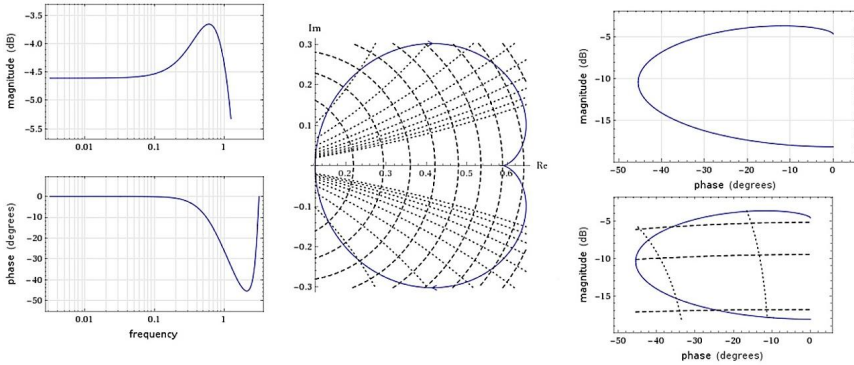


Figure 10.14 Frequency, phase, and magnitude of $\Lambda_t(\xi)$ when $t = 1$. The stability of the magnitude and the phase at the boundary of \cup .

In this section, we formulate our planned strategy for the open unit disk conformal characterizations by using the fractional integral with respect to the time variable (10.12) for the fractional value $\nu \in (0, 1)$. The disk conformal characterizations are achieved thanks to the existence of an effective iterative algorithm. The major objective of the iterative system is to progress the conformal distortions adjacent to the edges step by step. Note that the conformity distortion near the edges is small. Founded by the above conclusion and by utilizing the concept of the shell structure of the normalized function $\gamma \in \Lambda$, we indicate the harmonic energy (minimization of the Dirichlet energy) of γ as follows:

$$\mathcal{E}_\nu(\gamma_t)(\xi) = \frac{(1 - \nu)}{2} \int_\xi (E_t(\xi))^2 d\xi + \frac{\nu}{2} \int_0^t \int_\xi (E_\tau(\xi))^2 d\xi d\tau, \quad (10.13)$$

where t represents the temperature and

$$\mathcal{D}_\nu(\chi_t)(\xi) = \frac{(1 - \nu)}{2} \int_\xi (\Lambda_t(\xi))^2 d\xi + \frac{\nu}{2} \int_0^t \int_\xi (\Lambda_\tau(\xi))^2 d\xi d\tau. \quad (10.14)$$

Note that the energy is a magnitude of how much the smooth function changes over the disk. Mathematically, the condition that h is a harmonic function yields that for all functions $p \in \partial\cup$, we have

$$\lim_{\varepsilon \rightarrow 0} \frac{\mathcal{E}(h + \varepsilon p) - \mathcal{E}h}{\varepsilon} = 0.$$

Fig. 10.15 shows the steps of the proposed method.

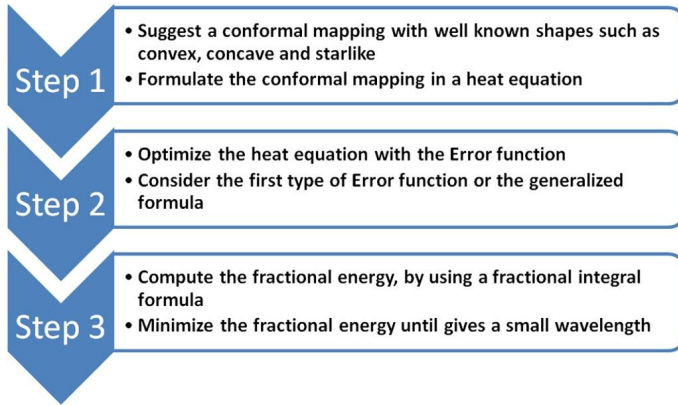


Figure 10.15 The steps of the proposed method.

Example 10.5. Consider the following function:

$$\Upsilon_t(\xi) = \frac{\xi}{1-t\xi} = \xi + \sum_{n=2}^{\infty} t^{n-1} \xi^n.$$

Then, we obtain

$$\begin{aligned} \mathcal{E}_\nu(\Upsilon_t)(\xi) &= \frac{(1-\nu)}{2} \int_{\xi} (\partial_t \Upsilon_t(\xi) - \partial_{\xi}^2 \Upsilon_t(\xi))^2 d\xi \\ &\quad + \frac{\nu}{2} \int_t \int_{\xi} (\partial_t \Upsilon_t(\xi) - \partial_{\xi}^2 \Upsilon_t(\xi))^2 d\xi dt \\ &= \frac{(1-\nu)}{2} \int_{\xi} \left(\frac{\xi^2 - 1}{(1-t\xi)^2} \right)^2 d\xi + \frac{\nu}{2} \int_t \int_{\xi} \left(\frac{\xi^2 - 1}{(1-t\xi)^2} \right)^2 d\xi dt \\ &= (t^4 - 2t^2 + 13)/(6t^5) + \xi + t\xi^2 + 2/6(5t^2 - 1)\xi^3 \\ &\quad + t/2(5t^2 - 2)\xi^4 + O(\xi^5), \end{aligned} \quad (10.15)$$

provided $\nu \rightarrow 0$ (because the second integral does not converge) (see Fig. 10.16). But the real root of $t^4 - 2t^2 + 13 = 0$ is $t \approx 3.6055$. Then we have

$$\mathcal{E}_\nu(\Upsilon_t)(\xi) \approx \xi + 3.605\xi^2 + 21.3\xi^3 + 31.4\xi^4 + O(\xi^5).$$

Consequently, we have

$$\min \mathcal{E}_\nu(\Upsilon_t)(\xi) = \min \left(\xi + 3.605\xi^2 + 21.3\xi^3 + 31.4\xi^4 + O(\xi^5) \right),$$

which yields $\mathfrak{R}(\xi) = -\frac{853}{5032} \approx -0.4$.

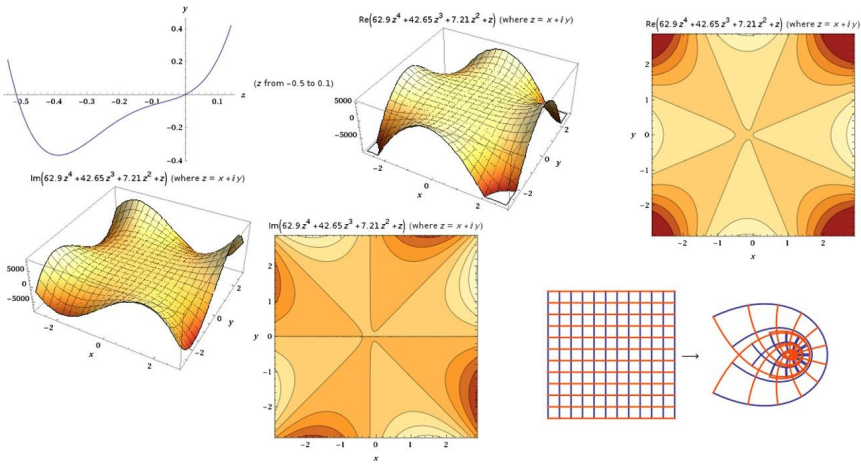


Figure 10.16 Minimization of the energy $\mathcal{E}_\nu(\Upsilon_t)(\xi)$ when $\nu \rightarrow 0$.

Example 10.6. Consider the following function:

$$\begin{aligned} \chi_t(\xi) &= \frac{\xi}{1 - e^{it}\xi} \\ &= \xi + \sum_{n=2}^{\infty} t^{n-1}\xi^n, \quad \xi \in \cup. \end{aligned}$$

Then, we obtain (see Fig. 10.17)

$$\begin{aligned} \mathcal{D}_\nu(\chi_t)(\xi) &= \frac{(1 - \nu)}{2} \int_{\xi} (\Lambda_t(\xi))^2 d\xi + \frac{\nu}{2} \int_t \int_{\xi} (\Lambda_t(\xi))^2 d\xi dt \\ &= \frac{1 - \nu}{2} \int_{\xi} \left(\frac{(ie^{(it)}\xi^2) - 1}{(1 - e^{(it)}\xi)^2} \right)^2 d\xi + \frac{\nu}{2} \int_t \int_{\xi} \left(\frac{(ie^{(it)}\xi^2) - 1}{(1 - e^{(it)}\xi)^2} \right)^2 d\xi dt \\ &= 1/6e^{(-3it)}(-2ie^{(it)} + e^{(2it)} - 13) + \xi + e^{(it)}\xi^2 + 2/6e^{(it)}(5e^{(it)} - i)\xi^3 \\ &\quad + e^{(2it)}(5e^{(it)} - 2i)/2\xi^4 + O(\xi^5) \\ &\approx \xi + \xi^2 + \xi^3 + \xi^4 + O(\xi^5) \\ &= \frac{\xi}{1 - \xi}. \end{aligned} \tag{10.16}$$

The solution of $1/6e^{(-3it)}(-2ie^{(it)} + e^{(2it)} - 13)$ is $t \approx 9.2$, and consequently $\mathcal{D}_\nu \approx \xi/(1 - \xi)$, that is, the energy is minimized at the boundary of \cup .

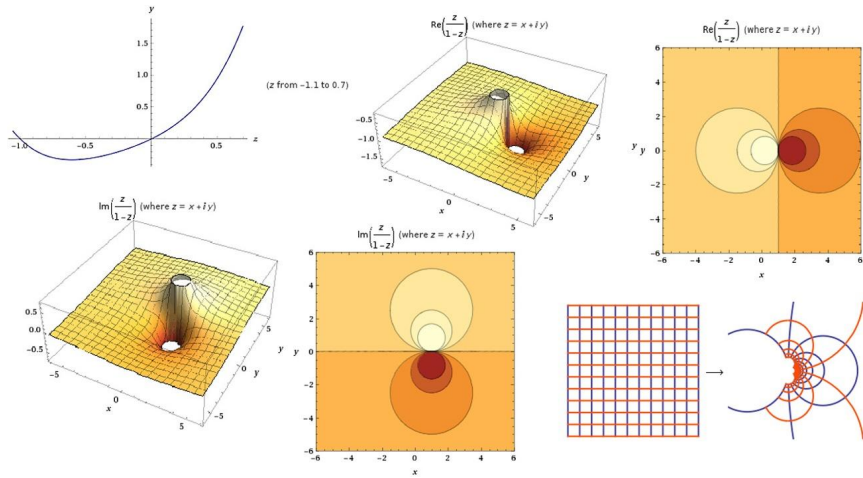


Figure 10.17 Minimization of the energy $D_v(\chi_t)(\xi)$ when $\nu \rightarrow 0$.

10.6. Conclusion

From the above construction, we gave a theoretical study of CTAs. The suggested CTA is considered by a conformal mapping in the open unit disk. The class of the conformal mappings is picked from univalent function theory (injective function). This class confirms a geometric representation in the open unit disk. Then, the conformal mapping is formulated by a heat equation and the error function. Accordingly, we suggested a fractional energy formula utilizing the Caputo–Fabrizio integral operator. We indicated that the fractional energy around the normal frequency remains a stimulating property. As the thinness of the production design is disturbed, it is closely associated to the preoccupation of the construction of the boundary of the shell. In our previous discussion, we did not take angle or rotation into account, because the shell conformal mapping preserves the angles. In the future, one may consider different conformal mapping shapes, such as close to convex (semishell) or starlike conformal mappings.

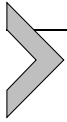
References

- [1] R.W. Ibrahim, Arched foot based on conformal complex neural network testing, *Mathematics and Computers in Simulation* 174 (2020) 175–182.
- [2] R.W. Ibrahim, Conformal geometry of the turtle shell, *Journal of King Saud University – Science* 32 (2020) 2202–2206.
- [3] G. Barbillon, E. Sakat, J.-P. Hugonin, S.-A. Biehs, P. Ben-Abdallah, True thermal antenna with hyperbolic metamaterials, *Optics Express* 25 (19) (2017) 23356–23363.

- [4] L. Josefsson, P. Persson, *Conformal Array Antenna Theory and Design*, vol. 29, John Wiley & Sons, 2006.
- [5] J. Ouyang, F. Yang, H. Zhou, Z. Nie, Z. Zhao, Conformal antenna optimization with space mapping, *Journal of Electromagnetic Waves and Applications* 24 (2–3) (2010) 251–260.
- [6] V. Semkin, F. Ferrero, A. Bisognin, J. Ala-Laurinaho, C. Luxey, F. Devillers, A. Räsänen, Beam switching conformal antenna array for mm-wave communications, *IEEE Antennas and Wireless Propagation Letters* 15 (2015) 28–31.
- [7] Z. Wang, P.S. Hall, J.R. Kelly, P. Gardner, Wideband frequency-domain and space-domain pattern reconfigurable circular antenna array, *IEEE Transactions on Antennas and Propagation* 65 (10) (2017) 5179–5189.
- [8] G. Leone, F. Munno, R. Pierrri, Radiation properties of conformal antennas: the elliptical source, *Electronics* 8 (5) (2019) 531, pp. 1–17.
- [9] A. Aziz, A.T. Abdel-Motagaly, A.A. Ibrahim, W.M. El Rouby, M.A. Abdalla, A printed expanded graphite paper based dual band antenna for conformal wireless applications, *AEÜ. International Journal of Electronics and Communications* 110 (2019) 1–7.
- [10] B. Mohamadzade, R.B. Simorangkir, S. Maric, A. Lalbakhsh, K.P. Esselle, R.M. Hashmi, Recent developments and state of the art in flexible and conformal reconfigurable antennas, *Electronics* 9 (9) (2020) 1–26.
- [11] L. Song, Reconfigurable and conformal antennas based on the emerging liquid metal and electro-textile materials, Ph.D. thesis, UCLA, 2020.
- [12] H. Gao, X. Wang, S. Wu, Z. Zhou, Y. Bai, W. Wu, Conformal coverage of liver tumors by the thermal coagulation zone in 2450-mHz microwave ablation, *International Journal of Hyperthermia* 36 (1) (2019) 590–604.
- [13] S. Singh, S. Singh, D. Singh, Compact conformal multilayer slot antenna for hyperthermia, in: 2019 URSI Asia-Pacific Radio Science Conference (AP-RASC), IEEE, 2019, pp. 1–4.
- [14] Y. He, J. Papapolymerou, Conformal antipodal Vivaldi antenna with parasitic elements for 5G millimeter wave applications, in: 2019 IEEE International Symposium on Antennas and Propagation and USNC-URSI Radio Science Meeting, IEEE, 2019, pp. 271–272.
- [15] K.A. Yinusa, A dual-band conformal antenna for GNSS applications in small cylindrical structures, *IEEE Antennas and Wireless Propagation Letters* 17 (6) (2018) 1056–1059.
- [16] R. Striker, D. Mitra, B.D. Braaten, K.S. Kabir, S. Roy, On the manufacturing process of a single-step fully 3D printed conformal patch antenna, in: 2020 IEEE International Conference on Electro Information Technology (EIT), IEEE, 2020, pp. 288–292.
- [17] H. Fallahi, Antenna and system design for controlled delivery of microwave thermal ablation, Ph.D. thesis, Kansas State University, 2020.
- [18] S. Biswas, M. Mirotznik, Additively manufactured conformal load-bearing antenna structure (CLAS), *IEEE Transactions on Components, Packaging and Manufacturing Technology* 2156 (2) (2020) 1–8.
- [19] S. Rajabi, R.A. Asbagh, F. Askarizadegan, Design, optimization and simulation of knee pain relief device using hyperthermia technology, *American Journal of Electromagnetics and Applications* 8 (2) (2020) 40–45.
- [20] K. Pulanthran, N.M. Jizat, M.S. Islam, A low-cost textile antenna using thermal-transfer printing, in: 2020 16th IEEE International Colloquium on Signal Processing & Its Applications (CSPA), IEEE, 2020, pp. 162–165.
- [21] C. Wang, P. Li, Z. Ren, F. Meng, Effect and experiment of curvature radius of 3-D printed conformal load-bearing antenna array on em performance, *International Journal of RF and Microwave Computer-Aided Engineering* 30 (4) (2020) e22130.

- [22] P. Zhao, J. Huang, Y. Yang, J. Wang, F. Meng, 3D printing technology of the conformal load bearing antenna structure, in: Proceedings of the Seventh Asia International Symposium on Mechatronics, Springer, 2020, pp. 839–847.
- [23] P.L. Duren, Univalent Functions, vol. 259, Springer Science & Business Media, 2001.
- [24] S.S. Miller, P.T. Mocanu, Differential Subordinations: Theory and Applications, CRC Press, 2000.
- [25] M. Caputo, M. Fabrizio, A new definition of fractional derivative without singular kernel, Progress in Fractional Differentiation and Applications 1 (2) (2015) 1–13.

This page intentionally left blank



Optimal design of fractional-order Butterworth filter with improved accuracy and stability margin

Shibendu Mahata, Rajib Kar, and Durbadal Mandal

National Institute of Technology Durgapur, Department of Electronics and Communication Engineering, Durgapur, West Bengal, India

Chapter points

- The proposed technique uses the ideal $(1 + \alpha)$ -order Butterworth magnitude characteristic considered for six decades of frequency in the fitness function.
- It achieves superior accuracy and a better margin of stability compared to the reported literature.
- It demonstrates applicability of the flower pollination algorithm for FOBF design.



11.1. Introduction

The interdisciplinary nature of research concerning the domain of fractional calculus ([11]) has led to significant interest among scholars in recent years ([58]). The fields of science and engineering where the theoretical concepts of fractional calculus are practically applied include control systems ([68]), signal processing ([59]), circuit theory ([46]), and biomedicine ([14], [6]).

The difference between an integer-order system (IOS) and a fractional-order system (FOS) may be understood from their transfer function representations, as given by (11.1) and (11.2), respectively:

$$G_I(s) = \frac{b_m s^m + b_{m-1} s^{m-1} + \dots + b_0}{a_n s^n + a_{n-1} s^{n-1} + \dots + a_0}, \quad (11.1)$$

$$G_F(s) = \frac{b_m s^{\alpha_m} + b_{m-1} s^{\alpha_{m-1}} + \dots + b_0 s^{\alpha_0}}{a_n s^{\beta_n} + a_{n-1} s^{\beta_{n-1}} + \dots + a_0 s^{\beta_0}}, \quad (11.2)$$

where α_j ($j = 0, 1, \dots, m$) and β_j ($j = 0, 1, \dots, n$) can be integer or noninteger numbers; b_j ($j = 0, 1, \dots, m$) and a_j ($j = 0, 1, \dots, n$) represent the coefficients

of the numerator and the denominator polynomials, respectively, of the transfer function.

From (11.1) and (11.2), it follows that an FOS is a superset of an IOS. Also, the well-known Laplacian operator s in an IOS may be generalized to the fractional-order Laplacian operator s^α in case of an FOS. For the particular case when $\alpha = 1$, we have $s^\alpha = s$. The function $Z(s) = s^\alpha$ is expressed in the frequency domain as $Z(j\omega) = \omega^\alpha \{\cos(0.5\alpha\pi) + j\sin(0.5\alpha\pi)\}$. The concept of the s^α operator has led to many exciting developments in the field of circuits and systems:

(i) The impedances of an integer-order inductor and capacitor are given by sL and $1/sC$, respectively, where the inductance L and the capacitance C are expressed in Henry (H) and Farad (F), respectively. The impedances of the fractance elements, such as the fractional-order inductor and the fractional-order capacitor of order α , are defined by $s^\alpha L_\alpha$ and $1/s^\alpha C_\alpha$, respectively; L_α and C_α are known as the pseudoinductance and the pseudocapacitance, respectively, with units of $\text{H}/\text{second}^{1-\alpha}$ ($\text{H}/s^{1-\alpha}$) and $\text{F}/\text{second}^{1-\alpha}$ ($\text{F}/s^{1-\alpha}$), respectively. These new circuit elements are also known as constant phase elements (CPE) since they exhibit a phase response which is frequency-independent ([9]). While no commercial CPE exists in the market as yet, research results indicate a promising future ([52]). To emulate the impedance characteristics of the fractional-order capacitors, researchers have also reported various R-C ladder networks such as the Foster and Cauer structures ([60], [4]).

(ii) An integer-order low-pass filter of order n exhibits a roll-off of $-20n$ dB/dec. This implies that only step changes in the roll-off rate are possible with such filters. A fractional-order low-pass filter of order $(n + \alpha)$ may, however, exhibit a roll-off of $-20(n + \alpha)$ dB/dec. Generalizations of the first-order and second-order filters to the fractional-order domain have been reported in two seminal papers ([50], [47]).

Numerical and stochastic optimization techniques have been exploited in recent years to develop optimal fractional-order filter models. Although the metaheuristics do not provide any proof of convergence to the global optima, their primary advantage lies in the simplicity of implementation. Unlike the numerical optimization methods, the metaheuristics are generally inspired by nature, do not require any derivative information, and use multiple search agents. These algorithms employ a combination of stochastic and deterministic rules to update the position of the agents from the exploration in the initial stages to the exploitation of the search space at

the later stages of the execution. The nature-inspired algorithms require appropriate tuning of the control parameters, which is time consuming; consequently, recent research efforts in the field of evolutionary computation are directed towards the development of adaptive algorithms ([10]).

Both classical and nonclassical optimization techniques have been explored for the optimal modeling of fractional-order filters. The particle swarm optimization (PSO) algorithm, which is inspired by the personal and social intelligence sharing during the movement of birds, fish, etc., was used to model the fractional-order differentiator (FOD) using pole-zero optimization ([43]). An adaptive chaotic PSO algorithm was employed to approximate the frequency-domain behavior of the FOD based on a third-order model ([19]). A hybridization of PSO and the gravitational search algorithm (GSA), which uses adaptive acceleration coefficients and achieves an improved exploitation characteristic, has been used for the design of infinite impulse response (IIR) FOD by [37]. Analog and digital approximations of the FOD were proposed using the flower pollination algorithm (FPA) ([1], [40]). Performance comparisons among different swarm intelligence (SI) techniques, such as ant lion optimization, whale optimization (WO), multiverse optimization, the cuckoo search algorithm (CSA), and FPA were investigated for the rational approximation of the FOD using a weighted sum of first-order high-pass filters by [65]. A physics-inspired internal parameter-free algorithm, namely colliding bodies optimization (CBO), which draws inspiration from the Newtonian laws of collision among gravitational objects, was employed for the design of an IIR fractional-order integrator (FOI) in [36]. A bio-inspired algorithm called symbiotic organisms search (SOS), which mimics the symbiotic relationship among the organisms in the ecosystem, was employed along with a curve fitting technique to determine the analytical expressions of the model coefficients pertaining to an IIR FOI ([42]). The optimal modeling of fractional-order RLC circuits in [48] and filters of the form $1/(1+s)^\alpha$ in [20] were demonstrated using the classical optimization methods. CBO-optimized generalized fractional-order filters of orders α and $\alpha + \beta$ of low-pass, high-pass, and band-pass characteristics were approximated using an integer-order transfer function (IOTF) ([39], [35]). Applicability of the real-coded genetic algorithm (GA) for quality factor maximization of fractional-order band-reject and band-pass filters was reported in [45]. A nonlinear least-squares fitting routine based on the MATLAB[®] function *lsqcurvefit* was used to approximate the fractional-order Chebyshev ([13]), inverse Chebyshev ([16]), elliptic ([17]), and $(1 + \alpha)$ -order low-pass filters

exhibiting an arbitrary quality factor ([25]). A multiobjective optimization framework was developed to model fractional-order filters based on different specifications, namely the stop band gain, the transition bandwidth, and the highest permissible peak in the pass band ([51]). Fractional-order Darwinian PSO, which incorporates a fractional-order velocity expression, was employed to obtain the optimal discrete-time models of fractional-order filters in [7]. The design conditions for a grounded fractional-order inductor designed using the generalized impedance converter were optimally derived and also practically demonstrated by [3]. Fractional-order low-pass Chebyshev filters were optimally modeled using the simulated annealing (SA) algorithm, the nonlinear least-squares method, and the interior search algorithm (ISA) in [56]. ISA was also employed to design the fractional-order low-pass Bessel filter ([55]). Optimal selection of passive components from the industrial series to approximate the impedance profile of the fractional-order elements using the GA was demonstrated in [21]. A comparative study of various SI algorithms such as WO, gray wolf optimization, FPA, moth flame optimization (MFO), and grasshopper optimization was carried out to determine the human eardrum fractional-order model parameters in [8]. GA-based synthesis of capacitive type fractional-order impedance based on the homogeneous distributed R–C structures has been proposed and validated using the thin-film technology in [62]. FPA-optimized programmable CPE implementations using resistive crossbar arrays have also been reported recently ([12]).

A fractional-order Butterworth filter (FOBF) of order $(1 + \alpha)$ is characterized by the magnitude–frequency response, as defined by

$$|T^{1+\alpha}(j\omega)| = \frac{1}{\sqrt{1 + \left(\frac{\omega}{\omega_c}\right)^{2(1+\alpha)}}, \quad (11.3)$$

where the cut-off frequency (in rad/s) of the filter is denoted by ω_c . From (11.3), it follows that (i) $|T^{1+\alpha}(j0)| = 0$ dB and (ii) $|T^{1+\alpha}(j\omega_c)| = -3.01$ dB. An integer-order Butterworth filter also exhibits both these properties. However, the stop band attenuation of the $(1 + \alpha)$ order FOBF is $-20(1 + \alpha)$ dB/dec, which allows the transition band slope to be precisely controlled. Fig. 11.1 shows the magnitude–frequency response of an ideal FOBF for $\alpha = 0.5$, which illustrates that its roll-off rate lies exactly in-between the first-order and second-order Butterworth filters.

Analysis and design procedures using two fractional elements of the same and different orders by considering the Butterworth filter cut-off

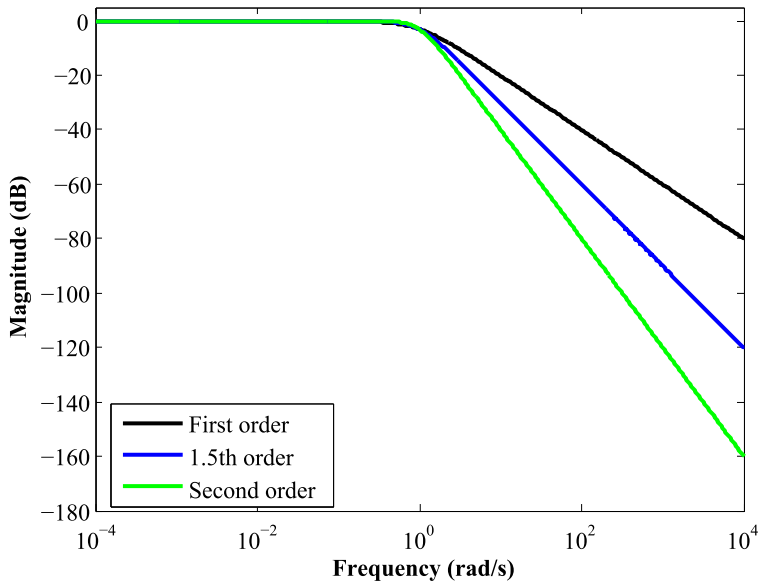


Figure 11.1 Magnitude plots of the first-, second-, and 1.5th-order Butterworth filters.

frequency and magnitude conditions were reported by [53]. Numerical method-based fractional-order transfer function (FOTF) approximants of the FOBF were realized using the passive and active components in [5]. The transformation from the complex s -plane to the complex W -plane, followed by retrofitting to the s -domain, was used to model the FOBF in [2]. SA ([24]), GA ([61], [54]), PSO ([23]), CSA ([57]), ISA ([57]), and the speed-enhanced series combination of CSA and ISA, namely CSA \rightarrow ISA ([57]), were employed to obtain the optimal coefficients of the FOBF which minimize the magnitude error relative to the second-order Butterworth filter model. FOBFs of low-pass and high-pass behavior for orders such as 1.2, 1.4, and 1.8 were reported by [22]. A comparative study between three $(1 + \alpha)$ -order FOTF models to approximate the magnitude–frequency response of the first-order Butterworth filter using a nonlinear curve fitting technique was reported in [15]. Various FOTFs based on the frequency transformation of low-pass FOBF models were presented to approximate the characteristics of the high-pass and band-pass FOBFs ([26]). SOS-optimized FOTF-based high-pass FOBF models were proposed and implemented using the current-mode second-generation current conveyors by [28]. FOTF-based approximation of the FOBF using the numerical

search method was reported in [18]. The corresponding IOTF model was then obtained by substitution of the s^α operator with the biquadratic CFE approximant. Differential voltage–current conveyor–based realization of FOBF was demonstrated by considering a double fractance–based model in [44]. Direct frequency–domain error minimization of the FOBF was carried out in an optimal manner using GSA ([41]). A CBO–based constrained optimization technique was developed to obtain the IOTF approximants of the FOBF in [38]. A two–step, unconstrained optimization method was proposed for the rational approximation of the FOBF with a bandwidth of 10^{-2} to 10^2 rad/s. In the first step, the squared–magnitude function of the IOTF which matches the corresponding ideal response was determined using the GA. In the second step, an optimal third–order FOBF model was achieved by using the GA–based stable approximant as the initial point for Powell’s algorithm ([27]). An extensive comparative study involving five advanced variants of the differential evolution (DE) algorithm (CoDE, EDEV, EFADE, EPSDE, JADE), three state–of–the–art PSO algorithms (AGGSA, EPSO, HCLPSO), and an evolutionary strategy method (CMA–ES–RIS) was conducted for the fifth–order approximation of FOBFs using the death penalty method ([29]). This work also demonstrated for the first time the design of $(2 + \alpha)$ –order FOBFs without using the cascade of $(1 + \alpha)$ –order FOBFs with the first–order Butterworth model. Experiments showed that EFADE achieved the most robust performance among the nine algorithms. In [32], a biquadratic approximant of the CFE pertaining to the s^α operator was substituted in one of the FOTF models reported by [15]. This integer–order model is then used as an initial point for a constrained optimization routine. Results showed that the optimal third–order FOBF approximant achieved good agreement with the theoretical magnitude–frequency relation for six decades of bandwidth. Optimal design of band–pass FOBFs exhibiting symmetric attenuation characteristics was reported using MFO, SOS, FPA, and two variants of PSO ([33]). A computationally efficient optimal method to approximate the asymmetric band–pass FOBF was also recently reported in [31]. Optimal design of digital IIR FOBFs using the direct determination of the z –domain transfer function was reported in [30]. The computationally efficient lattice–wave digital filter was optimally modeled to realize the magnitude–frequency characteristics of the FOBF in [34].

This chapter presents the optimal FOTF approximation of the FOBF by introducing two simple yet effective modifications to the existing approaches. The contributions of the chapter are outlined below.

(i) The proposed cost function uses the ideal FOBF transfer function instead of the first-order or the second-order Butterworth response. It can be intuitively realized that employing the exact theoretical magnitude–frequency characteristic in the cost function may lead to a more accurate approximant.

(ii) The design frequency range of the proposed normalized FOBF is considered over six decades (10^{-3} to 10^3 rad/s). This is in contrast to the reported optimization techniques where lower bandwidths are used; namely 10^{-2} to 1 rad/s ([15]) and 10^{-5} to 1.5 rad/s ([57]). It may be emphasized that the fundamental reason why the reported works used lower or no stop band frequency range for the FOBF modeling is due to their incorporation of the integer-order (first- or second-order) Butterworth magnitude function in the cost function. The optimizer tries to minimize the modeling error throughout the considered frequency range. If a higher stop band frequency (such as up to 1000 rad/s as proposed in this work) was employed, the magnitude–frequency response of the resultant model will track the stop band attenuation behavior of the integer-order filter, thus losing its fractional step characteristic. In contrast, since the proposed work uses the ideal magnitude response of the $(1 + \alpha)$ -order FOBF in the fitness function, the stop band frequency range in the cost function can be extended up to three decades beyond the cut-off frequency. Thus, the proposed method provides an equal emphasis in minimizing the errors in both the pass band and the stop band.

(iii) The applicability of a state-of-the-art metaheuristic global optimization technique, such as FPA, for the design of FOBFs is demonstrated. FPA is a population-based nature-inspired algorithm which mimics the pollination process in flowering plants. This algorithm has recently been employed in several fractional-order filter design applications, demonstrating an efficient performance ([1], [40]). Generalized equations of the coefficients for the proposed model are obtained by employing curve fitting on the FPA-optimized coefficients. The differences between the proposed FOBF design approach and those based on the various optimal techniques reported in the literature are shown in Table 11.1. Modeling accuracy and design stability margin comparisons are conducted to justify the efficacy of the proposed approach over the state-of-the-art.

(iv) In [24], [15], and [57], a three-operational amplifier (Op-Amp) configuration-based FOBF implementation was shown. In this chapter, a single Op-Amp filter topology is used for the same purpose, which further reduces the circuit complexity. Simulations are conducted in OrCAD

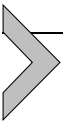
Table 11.1 Comparisons between the different optimal FOBF design techniques.

Reference	Optimization algorithm	Targeted Butterworth filter	Orders considered	Bandwidth (rad/s)
[24]	SA	2nd order	1.1, 1.5, 1.9	NR ^a
[23]	PSO	2nd order	1.3, 1.5, 1.6	NR
[61]	GA	2nd order	1.3, 1.5, 1.6	NR
[15]	<i>lsqcurvefit</i>	1st order	1.01 to 1.99	10 ⁻² to 1
[54]	GA	2nd order	1.1, 1.2, ..., 1.9	10 ⁻⁵ to 1
[57]	CSA, ISA, CSA → ISA	2nd order	1.1, 1.2, ..., 1.9	10 ⁻⁵ to 1.5
Present work	FPA	(1 + α) order	1.01 to 1.99	10 ⁻³ to 10 ³

^a NR: Not reported.

PSpice to justify the practical effectiveness of the proposed model. Monte Carlo analysis is also performed to study the sensitivity to device tolerances for the designed circuit.

The rest of the chapter is structured as follows. Section 11.2 presents the procedure to determine the proposed FOBF model. Simulation results are shown in Section 11.3. In Section 11.4, the main conclusions and future research directions are highlighted.



11.2. Proposed technique

Consider the FOTF model given by

$$H^{1+\alpha}(s) = \frac{c}{s^{1+\alpha} + as^\alpha + b}, \quad (11.4)$$

where a , b , and c are the coefficients of the approximant.

The cost function for the proposed two-variable optimization (minimization) problem is formulated by

$$f = \sum_{i=1}^{10^5} (|T^{1+\alpha}(j\omega_i)| - |H^{1+\alpha}(j\omega_i, X)|)^2, \quad (11.5)$$

where $c = 1$, $\omega \in [10^{-3}, 10^3]$ rad/s, $\omega_c = 1$ rad/s, $|H^{1+\alpha}(j\omega)|$ is the magnitude of the proposed FOBF, and the decision variables vector is denoted by $X = [a \ b]$. The sampled frequency points are linearly spaced in the design

bandwidth. The purpose of the optimization process is to determine the optimal value of X which produces the least error. To obtain the FOBF model for any $\alpha \in (0, 1)$, the following two-step design procedure is used:

- (i) the optimal coefficients for the proposed FOBF, with α varying from 0.01 to 0.99 in steps of 0.01, are generated using FPA; and
- (ii) polynomial fitting is applied on the optimized coefficients to determine the α -dependent expressions of a and b for the proposed FOBF model.

The design technique is discussed in detail below.

11.2.1 Determination of optimal coefficients using FPA

FPA is a bio-inspired optimization algorithm inspired by the pollination process in flowering plants ([63]). The rules used by FPA to imitate the process of pollination are as follows. (i) Cross-pollination leads to global pollination. A Lévy distribution is maintained during the flying movements of the pollinators such as birds and bees. (ii) Self-pollination may be regarded as local pollination since no pollinating agents are required. (iii) Flower constancy is a measure of the reproduction probability. (iv) A control parameter called switch probability (p) provides a choice between carrying out either global or local pollination. The modeling equations of FPA are based on the application of these four rules to attain local and global search processes efficiently. It may be noted that while this work uses the basic FPA as proposed by [63], the local search capability of the algorithm has been enhanced using the concept of fractional-order calculus in [64]. The reported algorithm, called fractional-order FPA (FO-FPA), demonstrated efficient performance in solving the image segmentation problem. The fractional-order chaos maps were incorporated with the basic FPA to adaptively tune the control parameters of the algorithm in [66]. The proposed algorithm, known as fractional-chaotic FPA (FC-FPA), was employed to identify the system parameters for the chaotic characteristic in brushless DC motors. FC-FPA was also applied to obtain the maximum power point tracking for solar photovoltaic systems in a robust and optimal manner in [67].

The search agents of FPA are called flowers. The FOBF is designed using FPA as per the steps outlined below.

Step 1. Randomly distribute all the flowers in the range $[0, 2]$ in the search space.

Step 2. Initialize the control parameters: population size = 50; step size (h) = 1.25; Lévy distribution factor (λ) = 1.5; scaling factor (γ) = 0.12; switch

probability (p) = 0.8; termination condition = 20,000 function evaluations (FEs).

Step 3. Find out the fitness of flowers based on evaluation of (11.5). Identify the global-best solution X^* .

Step 4. Generate a random number $rand$, $0 \leq rand \leq 1$, for each flower. Depending on whether $rand$ exceeds p or not, perform a local search based on (11.6) or the global search according to (11.7), respectively:

$$x_i^{t+1} = x_i^t + \gamma L(\lambda)(X^* - x_i^t), \quad (11.6)$$

where $\Gamma(\cdot)$ denotes the standard Gamma function and $L(\lambda) \sim \frac{\lambda \Gamma(\lambda) \frac{\sin(\pi \lambda)}{2}}{\pi i^{1+\lambda}}$,

$$x_i^{t+1} = x_i^t + \varepsilon(x_j^t - x_k^t). \quad (11.7)$$

The i th flower at the t th and $(t + 1)$ th iterations is represented by x_i^t and x_i^{t+1} , respectively, and $0 \leq \varepsilon \leq 1$ is obtained from a uniform distribution.

Step 5. Find out the fitness of flowers by evaluating (11.5).

Step 6. Identify X^* from the new population if it is superior to the previous X^* .

Step 7. Repeat from Step 4 until the algorithm terminates.

Step 8. Declare X^* as the near-global optimal solution which contains the optimal values of a and b .

The above steps are employed for each design order by performing 20 independent runs of the algorithm. The best solution for each design order is considered as the FPA-optimized solution. The design configuration using the FPA optimizer is shown in Fig. 11.2.

11.2.2 Polynomial fitting

An expression for a and b in terms of α is derived (using the MATLAB function *polyfit*) by fitting the FPA-optimized coefficients in terms of a fourth-degree polynomial. Figs. 11.3 and 11.4 show the polynomial fitting of a and b , respectively, along with their residuals in the corresponding subplots. The norm of residuals obtained for a and b are 0.00449 and 0.0025085, respectively. The expressions of a and b for the proposed FOBF

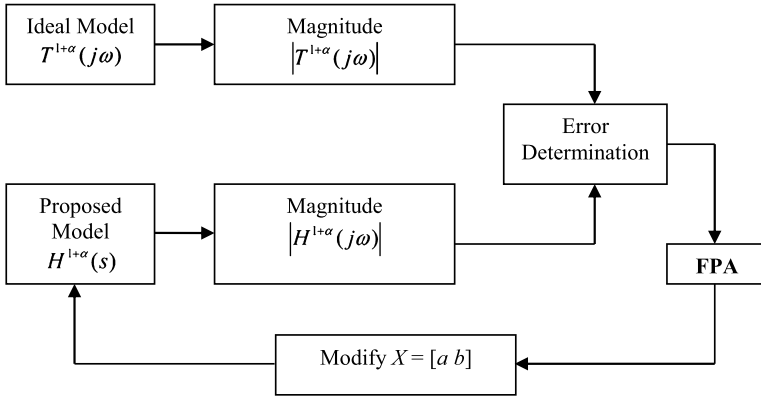


Figure 11.2 FPA-based optimal FOBF design configuration.

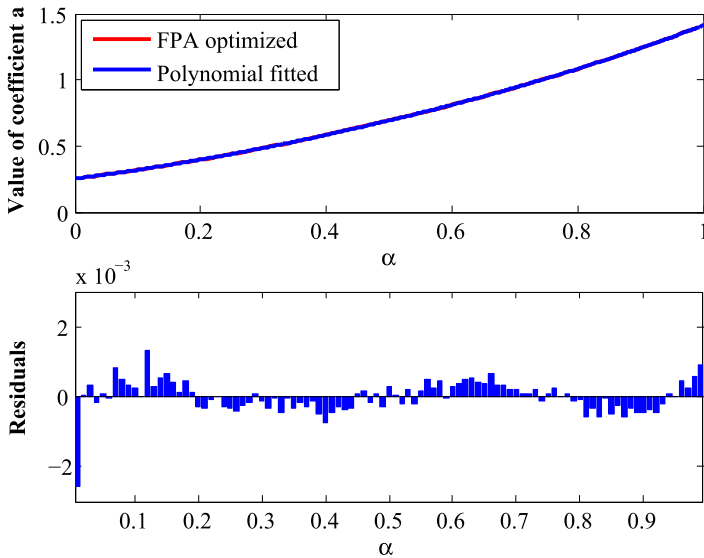


Figure 11.3 Coefficient a and the corresponding residual plot.

model are presented as follows:

$$a = 0.21846\alpha^4 - 0.34684\alpha^3 + 0.70257\alpha^2 + 0.58429\alpha + 0.25448, \quad (11.8)$$

$$b = 0.059107\alpha^4 + 0.025084\alpha^3 - 0.045725\alpha^2 + 0.21474\alpha + 0.74668. \quad (11.9)$$

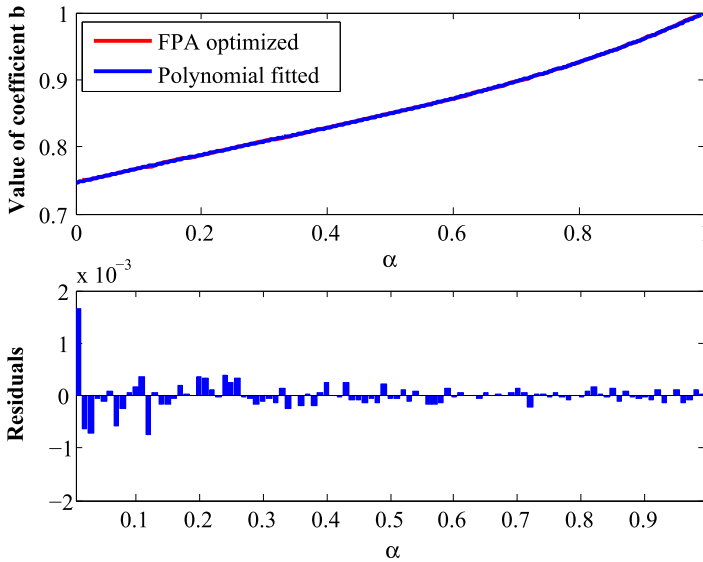


Figure 11.4 Coefficient b and the corresponding residual plot.

It is worth emphasizing that the norm of residuals for both the coefficients are extremely small, which implies that the values of the curve-fitted coefficients are nearly the same as that of the optimal one. This results in the superimposition of the polynomial fitted values with those of the FPA-optimized coefficient curves in these two figures.



11.3. Simulation results and discussion

11.3.1 Design accuracy

The total error (TE), as given by (11.10), is used to compare the accuracy of the proposed FOBFs with the reported ones:

$$TE = 20 \log_{10}(f) dB. \quad (11.10)$$

The FPA-optimized coefficients and the TE values for α ranging from 0.01 to 0.99 are presented in Tables 11.2–11.4. From Fig. 11.5, it can be seen that the TE responses for the models before and after the curve fitting are similar. The magnitude responses of the proposed polynomial-fitted $(1 + \alpha)$ -order FOBFs, with α varying from 0.1 to 0.9 in steps of 0.1,

Table 11.2 FPA-optimized coefficients for $\alpha = 0.01$ to 0.33 .

α	a	b	TE (dB)
0.01	0.257835	0.750481	-65.03
0.02	0.266509	0.750322	-53.20
0.03	0.272983	0.752376	-46.29
0.04	0.278803	0.755138	-41.40
0.05	0.285476	0.757207	-37.66
0.06	0.291964	0.759492	-34.63
0.07	0.299552	0.760917	-32.12
0.08	0.306066	0.763328	-29.93
0.09	0.312836	0.765726	-28.03
0.10	0.319844	0.767906	-26.34
0.11	0.326809	0.770147	-24.83
0.12	0.335503	0.771112	-23.52
0.13	0.341900	0.773954	-22.25
0.14	0.349707	0.775765	-21.14
0.15	0.357533	0.777825	-20.11
0.16	0.365111	0.779968	-19.15
0.17	0.372714	0.782231	-18.26
0.18	0.381070	0.784084	-17.45
0.19	0.388881	0.786072	-16.69
0.20	0.396748	0.788460	-15.97
0.21	0.405045	0.790451	-15.30
0.22	0.413776	0.792240	-14.70
0.23	0.422412	0.794098	-14.12
0.24	0.430832	0.796515	-13.56
0.25	0.439550	0.798367	-13.06
0.26	0.448364	0.800458	-12.58
0.27	0.457540	0.802098	-12.14
0.28	0.466719	0.804086	-11.72
0.29	0.476183	0.805967	-11.34
0.30	0.485287	0.808022	-10.97
0.31	0.494482	0.810101	-10.61
0.32	0.504303	0.812024	-10.30
0.33	0.513499	0.814295	-9.98

Table 11.3 FPA-optimized coefficients for $\alpha = 0.34$ to 0.66 .

α	a	b	TE (dB)
0.34	0.523618	0.815933	-9.71
0.35	0.533114	0.818188	-9.44
0.36	0.543183	0.820044	-9.20
0.37	0.553074	0.822276	-8.97
0.38	0.563351	0.824099	-8.77
0.39	0.573187	0.826389	-8.56
0.40	0.583251	0.828622	-8.38
0.41	0.593964	0.830429	-8.23
0.42	0.604649	0.832465	-8.10
0.43	0.615171	0.834836	-7.96
0.44	0.625904	0.836589	-7.85
0.45	0.637123	0.838673	-7.76
0.46	0.648106	0.840734	-7.68
0.47	0.658766	0.842941	-7.60
0.48	0.670115	0.844995	-7.56
0.49	0.680957	0.847512	-7.50
0.50	0.692839	0.849395	-7.50
0.51	0.704012	0.851582	-7.47
0.52	0.715305	0.853946	-7.47
0.53	0.727327	0.855950	-7.50
0.54	0.738619	0.858362	-7.52
0.55	0.750820	0.860540	-7.57
0.56	0.763071	0.862650	-7.64
0.57	0.774888	0.864945	-7.71
0.58	0.787211	0.867285	-7.80
0.59	0.798972	0.869915	-7.89
0.60	0.811681	0.872122	-8.02
0.61	0.824217	0.874580	-8.15
0.62	0.836939	0.876954	-8.31
0.63	0.849660	0.879404	-8.48
0.64	0.862337	0.881822	-8.66
0.65	0.875244	0.884446	-8.86
0.66	0.888568	0.886922	-9.09

Table 11.4 FPA-optimized coefficients for $\alpha = 0.67$ to 0.99 .

α	a	b	TE (dB)
0.67	0.901390	0.889515	-9.32
0.68	0.914639	0.892083	-9.58
0.69	0.927924	0.894774	-9.86
0.70	0.941452	0.897517	-10.16
0.71	0.954956	0.900146	-10.49
0.72	0.968709	0.902627	-10.85
0.73	0.982742	0.905651	-11.21
0.74	0.996435	0.908478	-11.61
0.75	1.010780	0.911263	-12.05
0.76	1.025210	0.914251	-12.51
0.77	1.039400	0.917131	-13.00
0.78	1.054020	0.920050	-13.54
0.79	1.068520	0.923175	-14.10
0.80	1.083370	0.926242	-14.71
0.81	1.097830	0.929481	-15.34
0.82	1.113190	0.932736	-16.05
0.83	1.128210	0.935840	-16.82
0.84	1.144150	0.939073	-17.66
0.85	1.159270	0.942569	-18.53
0.86	1.175220	0.945701	-19.54
0.87	1.190760	0.949351	-20.57
0.88	1.207050	0.952766	-21.76
0.89	1.223110	0.956306	-23.05
0.90	1.239440	0.959950	-24.48
0.91	1.256050	0.963584	-26.11
0.92	1.272670	0.967524	-27.91
0.93	1.289750	0.971107	-30.06
0.94	1.307080	0.975116	-32.52
0.95	1.324190	0.979174	-35.44
0.96	1.342020	0.982941	-39.20
0.97	1.359380	0.987080	-43.94
0.98	1.377480	0.991445	-50.72
0.99	1.395720	0.995592	-62.64

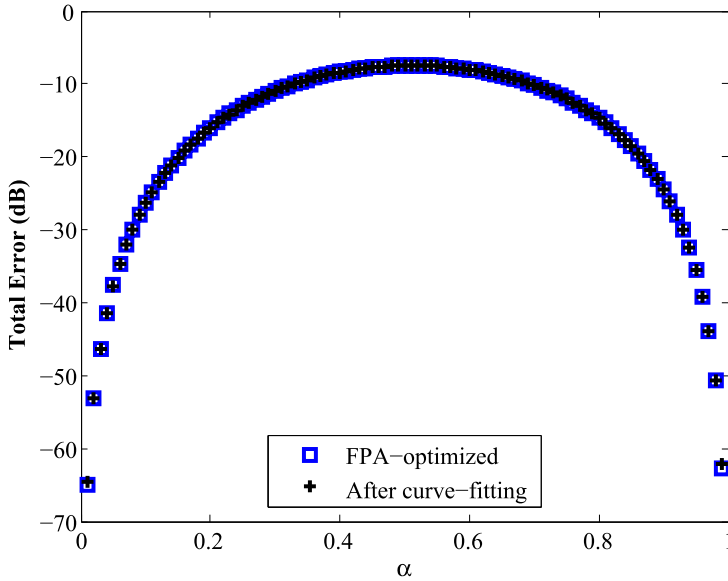


Figure 11.5 Comparison of TE plots between the FPA-based and the curve-fitted FOBF models.

are shown in Fig. 11.6, which illustrates the fractional stepping in the stop band.

The comparison regarding the TE metric with the FOTF model reported in (1) of [15] is shown in Fig. 11.7. It may be observed that the proposed model achieves a lower error throughout the entire design range. Comparisons are also carried out with the FOBF approximants based on different optimization techniques published in the cited literature. Results presented in Table 11.5 show that the proposed technique significantly outperforms all the reported designs in terms of the TE index. Thus, the simple modifications incorporated in the suggested design scheme lead to improved modeling accuracy.

11.3.2 Stability margin

Stability margin is defined as the margin between the region of instability and the nearest pole angle ([15]). A higher margin of stability is a desirable characteristic for any fractional-order filter. The stability of the proposed FOBFs is investigated by employing the W -plane stability analysis method reported in [49]. The steps are outlined below.

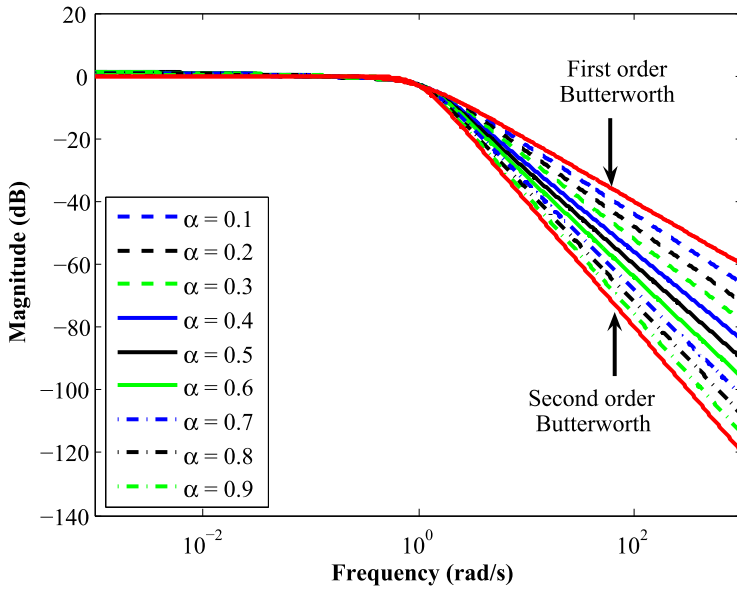


Figure 11.6 Magnitude plots for the proposed FOBF.

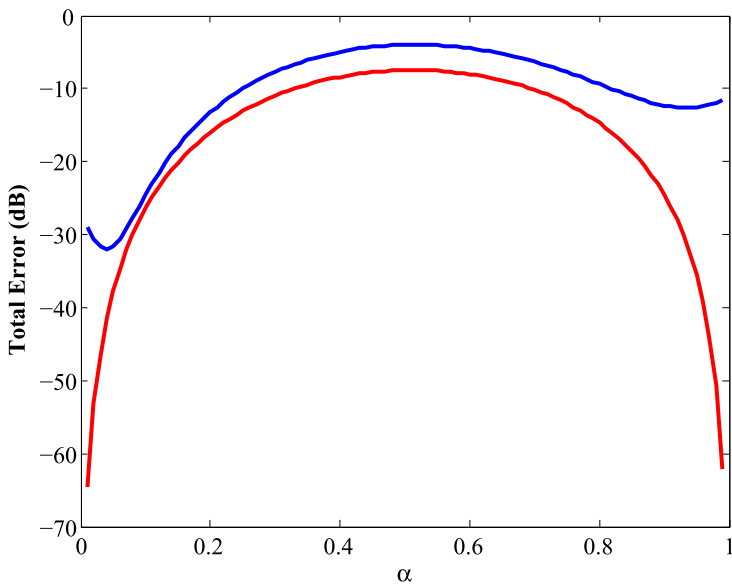


Figure 11.7 Comparison of the proposed FOBF (red; light gray in print version) with the model reported in (1) of [15] (blue; dark gray in print version) regarding the TE metric.

Table 11.5 Comparison with the literature regarding the TE (dB) metric.

Reference	$\alpha = 0.1$	$\alpha = 0.2$	$\alpha = 0.3$	$\alpha = 0.4$	$\alpha = 0.5$	$\alpha = 0.6$	$\alpha = 0.7$	$\alpha = 0.8$	$\alpha = 0.9$
[24]	9.80	NA ^a	NA	NA	4.33	NA	NA	NA	7.75
[23]	NA	NA	-3.42	NA	4.33	0.89	NA	NA	NA
[22]	NA	-10.84	NA	-2.80	NA	NA	NA	-9.16	NA
[61]	NA	NA	5.52	NA	1.42	-0.39	NA	NA	NA
[54]	35.15	39.53	41.36	30.93	31.39	39.90	31.38	40.02	34.27
[57] (CSA)	28.87	28.33	26.92	28.31	28.38	28.00	28.07	30.63	28.62
[57] (ISA)	30.83	33.52	41.16	38.79	36.11	33.79	35.66	30.42	29.46
[57] (CSA \rightarrow ISA)	31.92	31.12	30.99	30.60	30.19	29.73	29.43	29.22	29.07
Present work	-26.34	-15.98	-10.96	-8.40	-7.49	-8.01	-10.16	-14.71	-24.51

^a NA: Not Available.

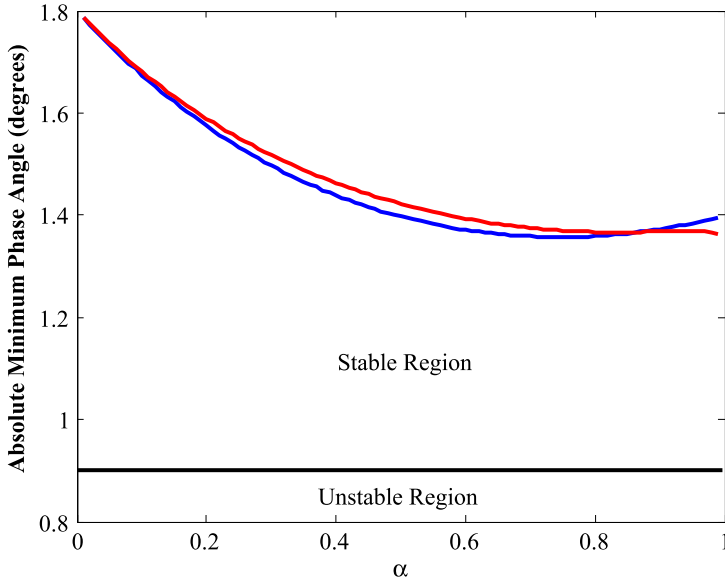


Figure 11.8 Comparison of the proposed FOBF (red; light gray in print version) with the model reported in (1) of [15] (blue; dark gray in print version) regarding the absolute minimum pole angle.

- (i) Set $s = W^m$ and $\alpha = k/m$.
- (ii) Choose k and m corresponding to a particular value of α . In this work, $m = 100$ and k is varied from 1 to 99 in steps of unity.
- (iii) To determine the root angles in the W -plane, solve the characteristic equation as defined by

$$W^{m+k} + aW^k + b = 0. \quad (11.11)$$

- (iv) Determine the absolute root (pole) angles. The FOTF model is stable if and only if all the root angles are greater than $\frac{180}{2m}$ degrees. Thus, for the stability of the proposed model, the root angles must be greater than 0.9 degrees.

The absolute minimum root angle, $|\theta_m(\omega)|$, for the proposed models, is presented in Fig. 11.8. All the proposed designs are stable, and hence physically realizable, since $|\theta_m(\omega)| > 0.9$ degrees for all values of α . The minimum absolute pole angle in the W -plane attained by the reported model given by (1) in [15] is also shown in Fig. 11.8. It is revealed that the proposed model achieves a better margin of stability as compared to the cited literature for $0.01 \leq \alpha \leq 0.87$.

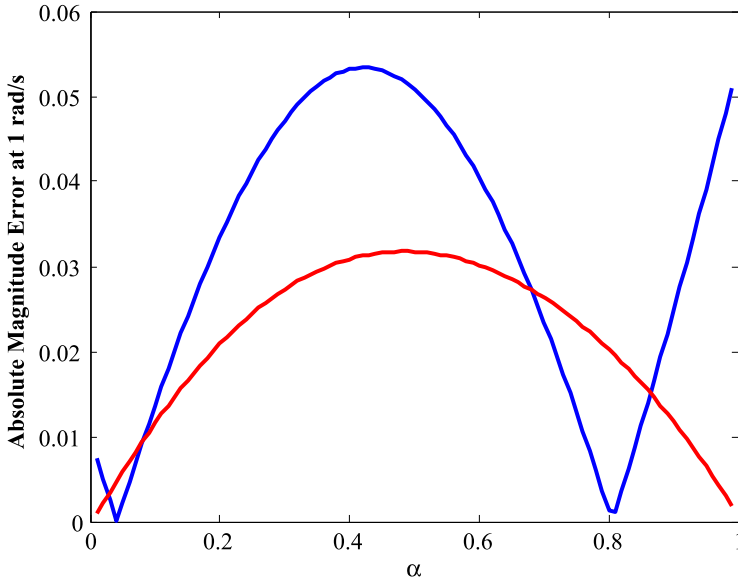


Figure 11.9 Comparison of the proposed FOBF (red; light gray in print version) with the model reported in (1) of [15] (blue; dark gray in print version) regarding the absolute magnitude error at the cut-off frequency.

11.3.3 Cut-off frequency

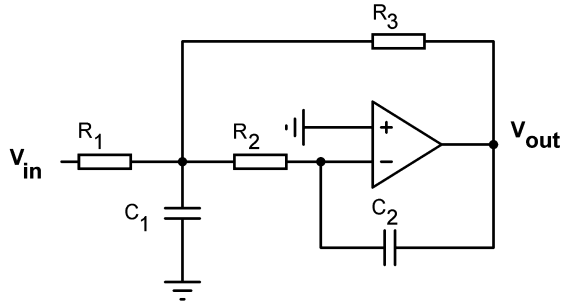
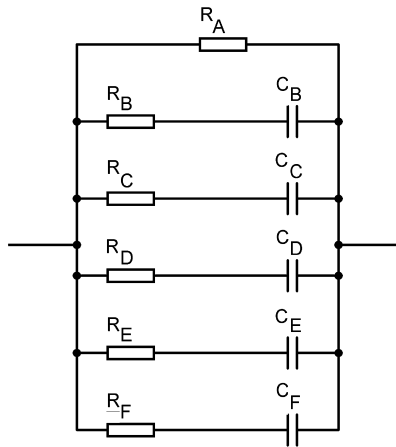
The absolute magnitude errors at the cut-off frequency of 1 rad/s achieved by the reported model in [15] and the proposed FOBF are compared in Fig. 11.9. The proposed model achieves a smaller error than that of the reported one for $0.08 \leq \alpha \leq 0.68$ and $\alpha \geq 0.86$, i.e., for nearly 75% of the design range.

11.3.4 Circuit realization

A single Op-Amp-based biquadratic filter topology is shown in Fig. 11.10, where V_{out} designates the terminal from where a low-pass filter response can be obtained ([15]). The design equations for the circuit topology relative to the FOTF model defined by (11.4) are presented in Table 11.6. The component values (with the magnitude and frequency scaling factors taken as 1000 and 1 kHz, respectively) to realize the proposed 1.5th-order FOBF are $R_1 = 0.85 \text{ k}\Omega$, $R_2 = 1 \text{ k}\Omega$, $R_3 = 1 \text{ k}\Omega$, $C_1 = 708 \text{ nF}$, and $C_{2,\alpha} = 3.34 \times 10^{-6} \text{ F/s}^{0.5}$. It may be noted that $C_{2,\alpha}$ is employed as a fractional-order capacitor. However, the model for a fractional capacitor is unavailable in OrCAD PSpice. Hence, an R-C ladder network such as the well-known

Table 11.6 Relationship between the FOTF and the biquadratic filter transfer function.

FOTF coefficient	c	a	b
Biquad filter coefficient	$\frac{1}{R_1 R_2 C_1 C_{2,\alpha}}$	$\frac{R_1 R_2 + R_2 R_3 + R_3 R_1}{R_1 R_2 R_3 C_1}$	$\frac{1}{R_2 R_3 C_1 C_{2,\alpha}}$

**Figure 11.10** Biquad filter to realize the proposed FOBF.**Figure 11.11** Foster II structure to emulate the fractional-order capacitor.

Foster II structure (refer to Fig. 11.11) is used to emulate the impedance characteristics of the fractional capacitor.

A continued fraction expansion (CFE)-based fifth-order truncation is used to determine the component values of the Foster II network pertaining to $C_{2,\alpha}$. A MATLAB program for this purpose is available from [60]. The center frequency is shifted to 1 kHz. Table 11.7 shows the component values of the Foster structure for the approximation of C_2 . The PSpice-simulated magnitude plot for the implemented 1.5th-order FOBF, with

Table 11.7 Components of the Foster network for the realization of $C_{2,0.5}$.

R_A (k Ω)	R_B (k Ω)	R_C (k Ω)	R_D (k Ω)	R_E (k Ω)	R_F (k Ω)	C_B (nF)	C_C (nF)	C_D (nF)	C_E (nF)	C_F (nF)
41.57	0.421	3.59	8.91	14.71	19.13	7.81	9.25	13.40	26.19	96.46

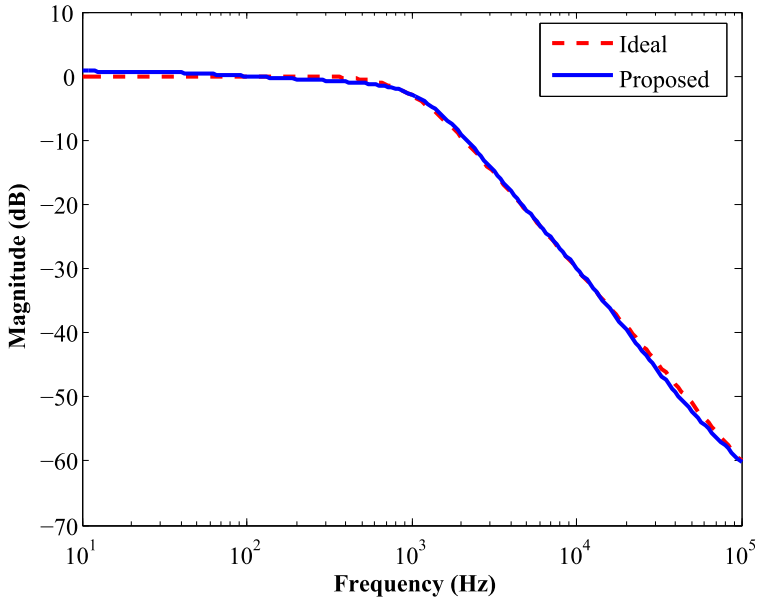
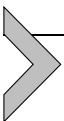


Figure 11.12 PSpice-simulated magnitude plot of the proposed 1.5th-order FOBF as compared to the theoretical one.

MC1458 Op-Amp used as the active element, is shown in Fig. 11.12. It can be observed that the magnitude responses of the theoretical and the designed filter demonstrate a close match.

To determine the sensitivity to component tolerances for the designed circuit, Monte Carlo simulations are performed using the Advanced Analysis Tool in OrCAD PSpice. Component deviations at 5% (chosen from a uniform distribution) for all the resistors and capacitors are considered. The magnitude plots for 100 Monte Carlo simulation runs, as compared to the theoretical response, are shown in Fig. 11.13, which highlights good agreement. The maximum, minimum, mean, and standard deviation indices for the magnitude (dB) at the cut-off frequency of 1 kHz for the designed biquad filter are $(-2.302, -3.606, -2.887, 0.2662)$. The corresponding Monte Carlo histogram is presented in Fig. 11.14.



11.4. Conclusions

This chapter presents the optimal approximation of the $(1 + \alpha)$ -order Butterworth filter by incorporating two simple modifications into

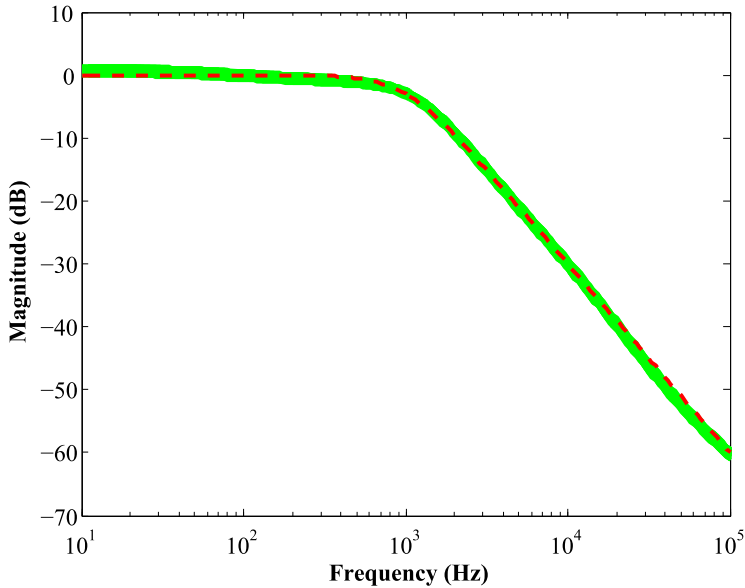


Figure 11.13 Magnitude plots of the proposed 1.5th-order FOBF based on Monte Carlo simulations (*solid green*; light gray in print version) as compared to the theoretical characteristic (*dashed red*; dark gray in print version).

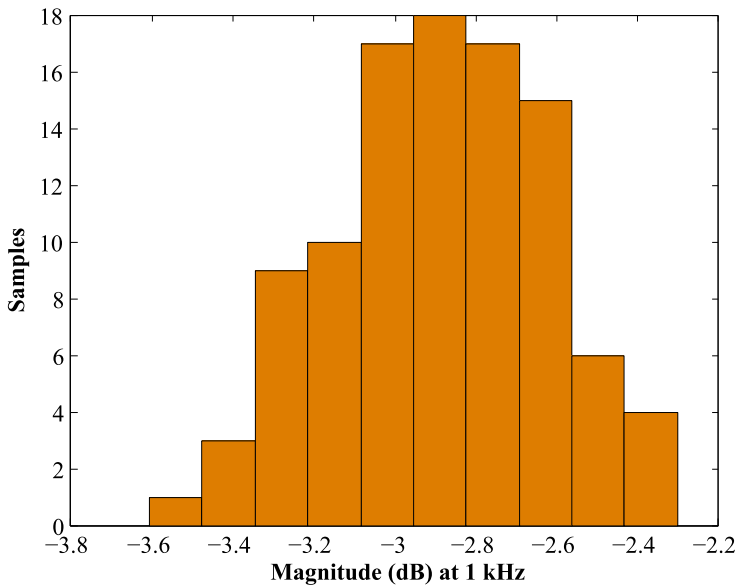


Figure 11.14 Monte Carlo histogram of the proposed 1.5th-order FOBF concerning the magnitude at a cut-off frequency of 1 kHz.

the existing approaches. The proposed technique shows that employing the theoretical FOBF response (instead of the first-order or the second-order Butterworth filter magnitude–frequency characteristic) in the objective function, along with a larger approximation bandwidth, can significantly improve the accuracy as well as the stability margin. The applicability of FPA as an effective optimization tool in fractional-order filter design is also demonstrated. Implementation of the 1.5th-order FOBF using a single Op-Amp biquad filter topology is presented along with PSpice simulations. Monte Carlo simulations are conducted to determine the design sensitivity to the variations in the component tolerances. Future research may explore the design of FOBFs from the perspective of multiobjective optimization which can allow the generation of Pareto-optimal solutions, thus providing greater flexibility in circuit implementation.

References

- [1] A.M. AbdelAty, A.S. Elwakil, A.G. Radwan, C. Psychalinos, B. Maundy, Approximation of the fractional-order Laplacian s^α as a weighted sum of first-order high-pass filters, *IEEE Transactions on Circuits and Systems. II, Express Briefs* 65 (8) (2018) 1114–1118.
- [2] A. Acharya, S. Das, I. Pan, S. Das, Extending the concept of analog Butterworth filter for fractional order systems, *Signal Processing* 94 (2014) 409–420.
- [3] A. Adhikary, S. Choudhary, S. Sen, Optimal design for realizing a grounded fractional order inductor using GIC, *IEEE Transactions on Circuits and Systems. I, Regular Papers* 65 (8) (2018) 2411–2421.
- [4] A. Adhikary, A. Shil, K. Biswas, Realization of foster structure-based ladder fractor with phase band specification, *Circuits, Systems, and Signal Processing* 39 (5) (2020) 2272–2292.
- [5] A.S. Ali, A.G. Radwan, A.M. Soliman, Fractional order Butterworth filter: active and passive realizations, *IEEE Journal on Emerging and Selected Topics in Circuits and Systems* 3 (3) (2013) 346–354.
- [6] I. Assadi, A. Charef, D. Copot, R. De Keyser, T. Bensouici, C. Ionescu, Evaluation of respiratory properties by means of fractional order models, *Biomedical Signal Processing and Control* 34 (2017) 206–213.
- [7] A. Ates, B.B. Alagoz, G. Kavuran, C. Yeroglu, Implementation of fractional order filters discretized by modified fractional order Darwinian particle swarm optimization, *Measurement* 107 (2017) 153–164.
- [8] P. Bertsias, M. Mohsen, L.A. Said, A.S. Elwakil, C. Psychalinos, A.G. Radwan, Design and implementation of an optimized artificial human eardrum model, *Circuits, Systems, and Signal Processing* 39 (6) (2020) 3219–3233.
- [9] K. Biswas, G. Bohannan, R. Caponetto, A.M. Lopes, J.A.T. Machado, *Fractional-Order Devices*, Springer, 2017.
- [10] J. Del Ser, E. Osaba, D. Molina, X.-S. Yang, S. Salcedo-Sanz, D. Camacho, S. Das, P.N. Suganthan, C.A.C. Coello, F. Herrera, Bio-inspired computation: where we stand and what's next, *Swarm and Evolutionary Computation* 48 (2019) 220–250.
- [11] A.S. Elwakil, Fractional-order circuits and systems: an emerging interdisciplinary research area, *IEEE Circuits and Systems Magazine* 10 (4) (2010) 40–50.

- [12] M. Fouda, A. AbdelAty, A. Elwakil, A. Radwan, A. Eltawil, Programmable constant phase element realization with crossbar arrays, *Journal of Advanced Research* 29 (2021) 137–145, <https://doi.org/10.1016/j.jare.2020.08.007>.
- [13] T. Freeborn, B. Maundy, A.S. Elwakil, Approximated fractional order Chebyshev lowpass filters, *Mathematical Problems in Engineering* 2015 (2015) 832468, <https://doi.org/10.1155/2015/832468>.
- [14] T.J. Freeborn, A survey of fractional-order circuit models for biology and biomedicine, *IEEE Journal on Emerging and Selected Topics in Circuits and Systems* 3 (3) (2013) 416–424.
- [15] T.J. Freeborn, Comparison of fractional-order transfer functions to approximate low-pass Butterworth magnitude responses, *Circuits, Systems, and Signal Processing* 35 (6) (2016) 1983–2002.
- [16] T.J. Freeborn, A.S. Elwakil, B. Maundy, Approximated fractional-order inverse Chebyshev lowpass filters, *Circuits, Systems, and Signal Processing* 35 (6) (2016) 1973–1982.
- [17] T.J. Freeborn, D. Kubanek, J. Koton, J. Dvorak, Fractional-order lowpass elliptic responses of $(1 + \alpha)$ -order transfer functions, in: 2018 41st International Conference on Telecommunications and Signal Processing (TSP), IEEE, 2018, pp. 1–5.
- [18] T.J. Freeborn, B. Maundy, A.S. Elwakil, Field programmable analogue array implementation of fractional step filters, *IET Circuits, Devices & Systems* 4 (6) (2010) 514–524.
- [19] Z. Gao, X. Liao, Rational approximation for fractional-order system by particle swarm optimization, *Nonlinear Dynamics* 67 (2) (2012) 1387–1395.
- [20] T. Hélie, Simulation of fractional-order low-pass filters, *IEEE/ACM Transactions on Audio, Speech and Language Processing* 22 (11) (2014) 1636–1647.
- [21] A. Kartci, A. Agambayev, M. Farhat, N. Herencsar, L. Brancik, H. Bagci, K.N. Salama, Synthesis and optimization of fractional-order elements using a genetic algorithm, *IEEE Access* 7 (2019) 80233–80246.
- [22] T. Khanna, D.K. Upadhyay, Design and analysis of higher order fractional step Butterworth filters, in: 2015 International Conference on Soft Computing Techniques and Implementations (ICSCITI), IEEE, 2015, pp. 77–82.
- [23] T. Khanna, D.K. Upadhyay, Design and analysis of improved fractional order Butterworth filters, in: 2015 Annual IEEE India Conference (INDICON), IEEE, 2015, pp. 1–6.
- [24] T. Khanna, D.K. Upadhyay, Design and realization of fractional order Butterworth low pass filters, in: 2015 International Conference on Signal Processing, Computing and Control (ISPCC), IEEE, 2015, pp. 356–361.
- [25] D. Kubanek, T. Freeborn, $(1 + \alpha)$ fractional-order transfer functions to approximate low-pass magnitude responses with arbitrary quality factor, *AEÜ. International Journal of Electronics and Communications* 83 (2018) 570–578.
- [26] D. Kubanek, T. Freeborn, J. Koton, N. Herencsar, Evaluation of $(1 + \alpha)$ fractional-order approximated Butterworth high-pass and band-pass filter transfer functions, *Elektronika Ir Elektrotechnika* 24 (2) (2018) 37–41.
- [27] S. Mahata, S. Banerjee, R. Kar, D. Mandal, Revisiting the use of squared magnitude function for the optimal approximation of $(1 + \alpha)$ -order Butterworth filter, *AEÜ. International Journal of Electronics and Communications* 110 (2019) 152826, <https://doi.org/10.1016/j.aeue.2019.152826>.
- [28] S. Mahata, R. Kar, D. Mandal, Optimal fractional-order highpass Butterworth magnitude characteristics realization using current-mode filter, *AEÜ. International Journal of Electronics and Communications* 102 (2019) 78–89.
- [29] S. Mahata, R. Kar, D. Mandal, Comparative study of nature-inspired algorithms to design $(1 + \alpha)$ and $(2 + \alpha)$ -order filters using a frequency-domain approach, *Swarm and Evolutionary Computation* 55 (2020) 100685, <https://doi.org/10.1016/j.swevo.2020.100685>.

- [30] S. Mahata, R. Kar, D. Mandal, Direct digital fractional-order Butterworth filter design using constrained optimization, *AEÜ. International Journal of Electronics and Communications* 128 (2020) 153511, <https://doi.org/10.1016/j.aeue.2020.153511>.
- [31] S. Mahata, R. Kar, D. Mandal, Optimal approximation of asymmetric type fractional-order bandpass Butterworth filter using decomposition technique, *International Journal of Circuit Theory and Applications* 48 (9) (2020) 1554–1560.
- [32] S. Mahata, R. Kar, D. Mandal, Optimal modelling of $(1 + \alpha)$ order Butterworth filter under the CFE framework, *Fractal and Fractional* 4 (4) (2020) 55, <https://doi.org/10.3390/fractalfract4040055>.
- [33] S. Mahata, R. Kar, D. Mandal, Optimal rational approximation of bandpass Butterworth filter with symmetric fractional-order roll-off, *AEÜ. International Journal of Electronics and Communications* 117 (2020) 153106, <https://doi.org/10.1016/j.aeue.2020.153106>.
- [34] S. Mahata, R. Kar, D. Mandal, Optimal design of lattice wave digital fractional-order Butterworth filter, *International Journal of Circuit Theory and Applications* 49 (1) (2021) 213–220.
- [35] S. Mahata, S. Saha, R. Kar, D. Mandal, Optimal integer-order rational approximation of α and $\alpha + \beta$ fractional-order generalised analogue filters, *IET Signal Processing* 13 (5) (2019) 516–527.
- [36] S. Mahata, S.K. Saha, R. Kar, D. Mandal, Optimal design of wideband infinite impulse response fractional order digital integrators using colliding bodies optimisation algorithm, *IET Signal Processing* 10 (9) (2016) 1135–1156.
- [37] S. Mahata, S.K. Saha, R. Kar, D. Mandal, Optimal and accurate design of fractional-order digital differentiator—an evolutionary approach, *IET Signal Processing* 11 (2) (2017) 181–196.
- [38] S. Mahata, S.K. Saha, R. Kar, D. Mandal, Accurate integer-order rational approximation of fractional-order low-pass Butterworth filter using a metaheuristic optimisation approach, *IET Signal Processing* 12 (5) (2018) 581–589.
- [39] S. Mahata, S.K. Saha, R. Kar, D. Mandal, Approximation of fractional-order low-pass filter, *IET Signal Processing* 13 (1) (2018) 112–124.
- [40] S. Mahata, S.K. Saha, R. Kar, D. Mandal, Optimal design of fractional-order digital differentiator using flower pollination algorithm, *Journal of Circuits, Systems, and Computers* 27 (08) (2018) 1850129, <https://doi.org/10.1142/S0218126618501293>.
- [41] S. Mahata, S.K. Saha, R. Kar, D. Mandal, Optimal design of fractional order low pass Butterworth filter with accurate magnitude response, *Digital Signal Processing* 72 (2018) 96–114.
- [42] S. Mahata, S.K. Saha, R. Kar, D. Mandal, Optimal design of wideband fractional order digital integrator using symbiotic organisms search algorithm, *IET Circuits, Devices & Systems* 12 (4) (2018) 362–373.
- [43] G. Maione, R. Caponetto, A. Pisano, Optimization of zero-pole interlacing for indirect discrete approximations of noninteger order operators, *Computers & Mathematics with Applications* 66 (5) (2013) 746–754.
- [44] S.K. Mishra, M. Gupta, D.K. Upadhyay, Active realization of fractional order Butterworth lowpass filter using DVCC, *Journal of King Saud University. Engineering Sciences* 32 (2) (2020) 158–165.
- [45] A. Pakhira, S. Das, A. Acharya, I. Pan, S. Saha, Optimized quality factor of fractional order analog filters with band-pass and band-stop characteristics, in: 2012 Third International Conference on Computing, Communication and Networking Technologies (ICCCNT'12), IEEE, 2012, pp. 1–6.
- [46] Y.-F. Pu, X. Yuan, B. Yu, Analog circuit implementation of fractional-order memristor: arbitrary-order lattice scaling fracmemristor, *IEEE Transactions on Circuits and Systems. I, Regular Papers* 65 (9) (2018) 2903–2916.

- [47] A.G. Radwan, A.S. Elwakil, A.M. Soliman, On the generalization of second-order filters to the fractional-order domain, *Journal of Circuits, Systems, and Computers* 18 (02) (2009) 361–386.
- [48] A.G. Radwan, M.E. Fouda, Optimization of fractional-order RLC filters, *Circuits, Systems, and Signal Processing* 32 (5) (2013) 2097–2118.
- [49] A.G. Radwan, A. Soliman, A.S. Elwakil, A. Sedeek, On the stability of linear systems with fractional-order elements, *Chaos, Solitons and Fractals* 40 (5) (2009) 2317–2328.
- [50] A.G. Radwan, A.M. Soliman, A.S. Elwakil, First-order filters generalized to the fractional domain, *Journal of Circuits, Systems, and Computers* 17 (01) (2008) 55–66.
- [51] L.A. Said, S.M. Ismail, A.G. Radwan, A.H. Madian, M.F.A. El-Yazeed, A.M. Soliman, On the optimization of fractional order low-pass filters, *Circuits, Systems, and Signal Processing* 35 (6) (2016) 2017–2039.
- [52] Z.M. Shah, M.Y. Kathjoo, F.A. Khanday, K. Biswas, C. Psychalinos, A survey of single and multi-component fractional-order elements (FOEs) and their applications, *Microelectronics Journal* 84 (2019) 9–25.
- [53] A. Soltan, A.G. Radwan, A.M. Soliman, Butterworth passive filter in the fractional-order, in: *ICM 2011 Proceeding*, IEEE, 2011, pp. 1–5.
- [54] A. Soni, M. Gupta, Design of fractional order Butterworth filter using genetic algorithm, in: *2018 2nd IEEE International Conference on Power Electronics, Intelligent Control and Energy Systems (ICPEICES)*, IEEE, 2018, pp. 1052–1055.
- [55] A. Soni, M. Gupta, Analysis and design of optimized fractional order low pass Bessel filter, *Journal of Circuits, Systems, and Computers* 30 (2021) 2150035, <https://doi.org/10.1142/S0218126621500353>.
- [56] A. Soni, M. Gupta, Performance evaluation of different order fractional Chebyshev filter using optimisation techniques, *International Journal of Electronics Letters* 8 (2) (2020) 205–222.
- [57] A. Soni, N. Sreejeth, V. Saxena, M. Gupta, Series optimized fractional order low pass Butterworth filter, *Arabian Journal for Science and Engineering* 45 (3) (2020) 1733–1747.
- [58] H. Sun, Y. Zhang, D. Baleanu, W. Chen, Y. Chen, A new collection of real world applications of fractional calculus in science and engineering, *Communications in Nonlinear Science and Numerical Simulation* 64 (2018) 213–231.
- [59] C.-C. Tseng, S.-L. Lee, Design of digital feller fractional order integrator, *Signal Processing* 102 (2014) 16–31.
- [60] G. Tsirimokou, A systematic procedure for deriving RC networks of fractional-order elements emulators using MATLAB, *AEÜ. International Journal of Electronics and Communications* 78 (2017) 7–14.
- [61] D.K. Upadhyay, T. Khanna, Design and analysis of improved fractional order Butterworth lowpass filters, in: *2015 IEEE International Conference on Electronics, Computing and Communication Technologies (CONECCT)*, IEEE, 2015, pp. 1–6.
- [62] P.A. Ushakov, K.O. Maksimov, S. Stoychev, V. Gravshin, D. Kubanek, J. Koton, Synthesis of elements with fractional-order impedance based on homogenous distributed resistive-capacitive structures and genetic algorithm, *Journal of Advanced Research* 25 (2020) 275–283, <https://doi.org/10.1016/j.jare.2020.06.021>.
- [63] X.-S. Yang, Flower pollination algorithm for global optimization, in: *International Conference on Unconventional Computing and Natural Computation*, Springer, 2012, pp. 240–249.
- [64] D. Yousri, M. Abd Elaziz, S. Mirjalili, Fractional-order calculus-based flower pollination algorithm with local search for global optimization and image segmentation, *Knowledge-Based Systems* 197 (2020) 105889, <https://doi.org/10.1016/j.knsys.2020.105889>.

- [65] D. Yousri, A.M. AbdelAty, A.G. Radwan, A.S. Elwakil, C. Psychalinos, Comprehensive comparison based on meta-heuristic algorithms for approximation of the fractional-order Laplacian s^α as a weighted sum of first-order high-pass filters, *Microelectronics Journal* 87 (2019) 110–120.
- [66] D. Yousri, D. Allam, T.S. Babu, A.M. AbdelAty, A.G. Radwan, V.K. Ramachandaramurthy, M. Eteiba, Fractional chaos maps with flower pollination algorithm for chaotic systems' parameters identification, *Neural Computing & Applications* 32 (2020) 16291–16327, <https://doi.org/10.1007/s00521-020-04906-7>.
- [67] D. Yousri, T.S. Babu, D. Allam, V. Ramachandaramurthy, E. Beshr, M. Eteiba, et al., Fractional chaos maps with flower pollination algorithm for partial shading mitigation of photovoltaic systems, *Energies* 12 (18) (2019) 3548, <https://doi.org/10.3390/en12183548>.
- [68] W. Zheng, Y. Luo, Y. Pi, Y. Chen, Improved frequency-domain design method for the fractional order proportional–integral–derivative controller optimal design: a case study of permanent magnet synchronous motor speed control, *IET Control Theory & Applications* 12 (18) (2018) 2478–2487.

This page intentionally left blank

Pseudospectral methods for the Riesz space-fractional Schrödinger equation

Mahmoud A. Zaky^{a,b}, Mohamed A. Abdelkawy^{c,d},
Samer S. Ezz-Eldien^e, and Eid H. Doha^f

^aNational Research Centre, Department of Applied Mathematics, Cairo, Egypt

^bDepartment of Mathematics, Nazarbayev University, Nur-Sultan, Kazakhstan

^cDepartment of Mathematics, Faculty of Science, Beni-Suef University, Beni-Suef, Egypt

^dDepartment of Mathematics and Statistics, College of Science, Imam Mohammad Ibn Saud Islamic University (IMSIU), Riyadh, Saudi Arabia

^eDepartment of Mathematics, Faculty of Science, New Valley University, El-Kharga, Egypt

^fDepartment of Mathematics, Faculty of Science, Cairo University, Giza, Egypt

Chapter points

- Combined Runge–Kutta/Gegenbauer-based pseudospectral collocation schemes for the space-fractional coupled nonlinear Schrödinger equations are constructed.
- The pseudospectral method is utilized to approximate the fractional Laplacian operator.
- The Runge–Kutta scheme is employed in temporal discretization.
- Numerical examples are listed to confirm the validity and high accuracy of the schemes.
- The effect of the fractional index on the pattern formations of the Riesz space-fractional coupled Schrödinger equations is discussed.

12.1. Introduction

In spite of the fact that the linear Schrödinger equation works well for a wide range of nonrelativistic quantum mechanical problems, there is often evidence in favor of nonlinear Schrödinger equations [1]. The nonlinear Schrödinger equation has been considered as one of the cornerstones of quantum physics in the last century, which describes the state function or wave function of a quantum mechanical system [2]. Nowadays applications of the nonlinear Schrödinger's equation are too numerous to list, not only in the quantum field, but also in chemistry, optoelectronics, neural networks, spectroscopy, etc. [3]. Signals in nonlinear acoustic media, interactions between pulses in nonlinear optics, Bose–Einstein condensates, and

a wide variety of phenomena have been uncovered using models involving a nonlinear coupled system of Schrödinger equations [4].

Over the past decades, considerable attention has been paid to applications of fractional calculus. A prominent example of such applications is given by the spatial fractional anomalous diffusion equation. The similarity between the classical diffusion equation and the Schrödinger equation motivated the generalization of the nonlinear Schrödinger equation and the coupled system of Schrödinger equations in the light of non-Brownian motion in the path integral formulation. This generalization leads to the space-fractional, the time-fractional, and the time-space-fractional Schrödinger equations (FSEs). The Riesz space FSE has been introduced by Laskin in quantum physics by replacing the Brownian paths in the Feynman path integrals by Lévy flights [5]. Similar to the conventional Schrödinger equation, the Riesz space FSE satisfies the Markovian evolution law. Stickler [6] discussed the Lévy crystal in a condensed matter environment as a possible realization of the space-fractional quantum mechanics by introducing a tight binding infinite-range chain. Longhi [7] discussed an optical realization of the space FSE based on transverse light dynamics in a cavity by exploiting the Fourier optics properties. Other physical applications of the Riesz space FSE have been discussed by Guo and Xu [8] and its solution for a free particle and an infinite square potential well has also been introduced. The existence and uniqueness of the solution to the space FSE have been investigated by Guo et al. [9] using the energy method. Moreover, the existence and uniqueness of the solution to systems of the space FSEs have been proved by Hu et al. [10] using the Faedo–Galerkin method. Cho et al. [11] studied the low-regularity well-posedness of the space FSE with cubic nonlinearity in periodic and nonperiodic settings. Following Laskin and similar to deriving the time-fractional diffusion equation by considering non-Markovian evolution [12], Naber [13] used the Caputo temporal fractional derivative [14] as a generalization of the integer-order derivative in the conventional Schrödinger equation to study non-Markovian evolution in quantum mechanics and constructed the temporal FSE. More recently, Dong and Xu [15] and Wang and Xu [16] combined Laskin's work with Naber's work to construct space-time FSEs.

In most cases, it is difficult to give explicit analytical solutions of space-and/or time-fractional differential equations [17–25], and hence the construction of efficient numerical schemes is a very important demand. For example, Bhrawy and Zaky [26–28] developed efficient spectral collocation schemes for variable-order FSEs in multiple dimensions using the variable-

order fractional differentiation matrices. The authors in [29–31] developed and extended a full collocation scheme for solving 1D and 2D time FSEs with Dirichlet boundary and nonlocal conditions. Nonstandard discretizations were discussed in [32–34]. Bhrawy et al. [35] constructed a spectral Jacobi collocation scheme using the fractional differentiation matrices for the numerical solution of FSEs involving time- and space-fractional derivatives. A combination between the L1 scheme and the Legendre spectral Galerkin method for nonlinear time-space FSEs with both smooth and nonsmooth solutions was proposed by Hendy et al. [36–38]. Meanwhile, they discussed the well-posedness of the numerical approximation. Li et al. [39] constructed a Crank–Nicolson/Galerkin finite element scheme for a class of nonlinear Riesz space FSEs. Wang et al. [40] proposed a Crank–Nicolson difference scheme and other linearly implicit conservative difference schemes for the coupled nonlinear Riesz space FSEs. Zhang and Jiang [41] considered a Legendre spectral scheme for the space-fractional coupled nonlinear FSEs. Ran and Zhang [42] analyzed an implicit difference scheme for solving the strongly coupled nonlinear space FSEs.

Nowadays there is a wide and constantly increasing range of spectral methods and there has been significant growth in fractional differential and integral equations [43–46] due to their high-order accuracy. Compared to the effort put into the analysis of finite difference schemes in the literature for solving the coupled nonlinear FSEs, little work has been put into the development and analysis of global spectral schemes. Although the Riesz space-fractional derivative is used widely, its nonlocal property makes its approximation difficult to handle. It is not easy to extend the existing numerical schemes for standard differential equations to their corresponding noninteger-order differential counterparts. The fundamental difficulty in designing an efficient numerical method for approximating the solution of the nonlinear FSEs is how to discretize the Riesz fractional derivative. Motivated by these considerations, we develop an efficient Runge–Kutta/Gegenbauer spectral collocation scheme to solve the coupled nonlinear FSE with the Riesz space-fractional derivative.

The rest of this chapter is organized as follows. In the next section, the coupled system of space FSEs is introduced. In Section 12.3, we collect some useful properties of the Gegenbauer polynomial. In Section 12.4, the spectral collocation discretization to the Riesz space-fractional operator is introduced, and the Runge–Kutta/Gegenbauer spectral collocation scheme is constructed to solve the coupled nonlinear FSEs. In Section 12.5, some

numerical simulations are discussed to illustrate the robustness of the proposed approach. Some concluding remarks are given in the last section.



12.2. Space-fractional couplers

The growing number of fractional differential operator applications in various fields of engineering and science indicates that there are important demands for the mathematical models of real objects. They are used for describing space–time nonlinear optical propagation in disordered media such as in the photon Lévy flight in atomic vapors and colloids [47] or in soft matter. In these models, the fractional derivative arises from the fractal dimension of colloidal aggregates [48]. So far, nonlinear space FSEs have been applied to different fields of physics such as dynamics of waves in a system with a PT-symmetric potential [49], propagation of a chirped Gaussian beam in the system with a harmonic potential [50], light propagation in honeycomb lattices [51], systems with a linear potential [52], the condensed–matter realization of Levy crystals [6], Shannon information entropies of multiple quantum well systems [53], etc.

Here, we introduce some properties of the fractional operators. The left-sided and the right-sided fractional derivatives of Riemann–Liouville type of order β ($n - 1 < \beta < n$) are defined as

$$\begin{aligned} {}_{-\infty}D_{\xi}^{\beta}\psi(\xi, \tau) &= \frac{1}{\gamma(n - \beta)} \frac{\partial^n}{\partial \xi^n} \int_{-\infty}^{\xi} (\xi - z)^{n-1-\beta} \psi(z, \tau) dz, \\ {}_{\xi}D_{+\infty}^{\beta}\psi(\xi, \tau) &= \frac{(-1)^n}{\gamma(n - \beta)} \frac{\partial^n}{\partial \xi^n} \int_{\xi}^{+\infty} (z - \xi)^{n-1-\beta} \psi(z, \tau) dz. \end{aligned} \tag{12.1}$$

The Riesz fractional derivative is defined as

$$\frac{\partial^{\beta}}{\partial |\xi|^{\beta}} \psi(\xi, \tau) = -(-\Delta)^{\frac{\beta}{2}} \psi(\xi, \tau) = c_{\beta} \left[{}_{-\infty}D_{\xi}^{\beta} \psi(\xi, \tau) + {}_{\xi}D_{+\infty}^{\beta} \psi(\xi, \tau) \right], \tag{12.2}$$

where $c_{\beta} = -\frac{1}{2 \cos(\frac{\pi\beta}{2})}$. The fractional Laplacian operator in (12.2) can be represented in the following equivalent Fourier form on the spatial variable ξ :

$$-(-\Delta)^{\frac{\beta}{2}} \psi(\xi, \tau) = -\mathcal{F}^{-1} (|\xi|^{\beta} \mathcal{F}(\psi(\xi, \tau))). \tag{12.3}$$

If ψ is defined on $[A, B]$ and satisfies $\psi(A, \tau) = \psi(B, \tau) = 0$, then the function can be extended by taking $\psi(\xi, \tau) \equiv 0$ for $x \ll a$ and $x \gg b$. Moreover, as shown in [54], if $\psi_{\xi}(A, \tau) = \psi_{\xi}(B, \tau) = 0$, then the Riesz fractional

derivative can be written as

$$\begin{aligned} \frac{\partial^\beta}{\partial |\xi|^\beta} \psi(\xi, \tau) &= -(-\Delta)^{\frac{\beta}{2}} \psi(\xi, \tau) \\ &= -\frac{1}{2 \cos(\frac{\pi\beta}{2})} \left[{}_a D_\xi^\beta \psi(\xi, \tau) + {}_\xi D_b^\beta \psi(\xi, \tau) \right]. \end{aligned} \quad (12.4)$$

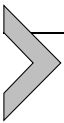
The issue we address this chapter is the numerical simulation of the following nonlinear coupled Riesz space FSE:

$$\begin{aligned} i \frac{\partial \psi}{\partial \tau} - \gamma (-\Delta)^{\beta/2} \psi + \rho (|\psi|^2 + \varrho |\varphi|^2) \psi &= 0, \quad \gamma \in \mathbb{R}, \quad 0 < \tau \leq \tau_{end}, \\ i \frac{\partial \varphi}{\partial \tau} - \gamma (-\Delta)^{\beta/2} \varphi + \rho (|\varphi|^2 + \varrho |\psi|^2) \varphi &= 0, \quad \gamma \in \mathbb{R}, \quad 0 < \tau \leq \tau_{end}, \end{aligned} \quad (12.5)$$

with the initial conditions

$$\psi(\gamma, 0) = \psi_0(\gamma), \quad \varphi(\gamma, 0) = \varphi_0(\gamma), \quad (12.6)$$

where $i = \sqrt{-1}$, $\beta \in (1, 2)$, ρ defines the self-focusing of a signal for the pulses in the birefringent media, $\gamma > 0$ is the group velocity dispersion, and ϱ is the cross-phase modulation which defines the integrability of the system (12.5) and (12.6). When $\varrho = 0$, the system (12.5) is decoupled and becomes a single nonlinear Schrödinger equation with the Riesz space-fractional derivative. The functions $\psi_0(\xi)$ and $\varphi_0(\xi)$ are both smooth complex-valued functions vanishing in $\mathbb{R} \setminus [\mathcal{A}, \mathcal{B}]$ for $\mathcal{A} \ll 0$ and $\mathcal{B} \gg 0$. This system often arises in many areas of science and engineering, including nonlinear optics, quantum physics, fluid mechanics, etc.



12.3. Gegenbauer polynomials and their properties

Here, we make necessary preparations for the scheme development in the forthcoming sections. More precisely, we review some relevant properties of the Gegenbauer polynomials. The Gegenbauer polynomial $C_k^\theta(\xi)$ ($k \geq 0$, $\theta > -1/2$) generalizes the Legendre polynomial $L_k(\xi)$ (coincides when $\theta = 1/2$) and is defined by the coefficient of t^k in the generating function

$$(1 - 2\xi t + t^2)^{-\theta} = \sum_{k=0}^{\infty} C_k^\theta(\xi) t^k. \quad (12.7)$$

The Gegenbauer polynomials satisfy the second-order homogeneous differential equation

$$(1 - \xi^2) \frac{d^2 \gamma}{d\xi^2} - (2\theta + 1)\xi \frac{d\gamma}{d\xi} + k(k + 2\theta)\gamma = 0. \quad (12.8)$$

For $\theta > -1/2$ they have a nice truncated series representation resulting from the series solution to the differential equation (12.8) in the form

$$C_k^\theta(\xi) = \sum_{0 \leq i \leq \frac{k}{2}} (-1)^i \frac{\gamma(k - i + \theta)}{\gamma(\theta) i! (k - 2i)!} (2\xi)^{k-2i}, \quad (12.9)$$

with the derivatives satisfying the recursive relation

$$\frac{d^q}{d\xi^q} C_k^\theta(\xi) = 2^q \frac{\gamma(\theta + q)}{\gamma(\theta)} C_{k-q}^{\theta+q}(\xi). \quad (12.10)$$

The analytical form of the Gegenbauer polynomial can also be written as

$$\begin{aligned} C_j^\theta(\xi) &= \frac{\Gamma(\theta + 0.5)}{\Gamma(2\theta)} \sum_{k=0}^j \frac{\Gamma(2\theta + k + j)}{(j - k)! k! \Gamma(k + \theta + 0.5)} \left(\frac{\xi - 1}{2}\right)^k \\ &= \frac{\Gamma(\theta + 0.5)}{\Gamma(2\theta)} \sum_{k=0}^j (-1)^{j+k} \frac{\Gamma(2\theta + k + j)}{k! (j - k)! \Gamma(k + \theta + 0.5)} \left(\frac{\xi + 1}{2}\right)^k. \end{aligned} \quad (12.11)$$

They are also defined by the three-term recurrence relation

$$\begin{aligned} k C_k^\theta(\xi) &= 2\xi(k + \theta - 1) C_{k-1}^\theta(\xi) - (k + 2\theta - 2) C_{k-2}^\theta(\xi), \quad k \geq 2, \\ C_0^\theta(\xi) &= 1, \quad C_1^\theta(\xi) = 2\theta\xi, \end{aligned} \quad (12.12)$$

and can be expressed by the Rodrigues formula

$$C_k^\theta(\xi) = \frac{(-1)^k \Gamma(\frac{1+2\theta}{2}) \Gamma(k + 2\theta) (1 - \xi^2)^{\frac{1}{2}-\theta}}{2^k k! \Gamma(2\theta) \Gamma(\frac{2\theta+1}{2} + k)} \frac{d^k}{d\xi^k} (1 - \xi^2)^{k+\theta-\frac{1}{2}}. \quad (12.13)$$

They are orthogonal with respect to the weight function $\omega^\theta(\xi) = (1 - \xi^2)^{\theta-1/2}$,

$$\begin{aligned} (C_k^\theta, C_l^\theta)_{\omega^\theta} &= \int_{-1}^1 C_k^\theta(\xi) C_l^\theta(\xi) \omega^\theta(\xi) dx = h_k^\theta \delta_{k,l}, \\ h_k^\theta &= \frac{\pi 2^{1-2\theta} \Gamma(2\theta + 1)}{l!(l + \theta) \Gamma(\theta)^2} \delta_{kl}, \quad k, l \geq 0, \end{aligned} \tag{12.14}$$

and satisfy the pointwise value identities

$$C_k^\theta(1) = \frac{(2\theta)_k}{k!}, \quad C_k^\theta(-x) = (-1)^k C_k^\theta(\xi), \tag{12.15}$$

where $(\xi)_k = \Gamma(x + k) / \Gamma(\xi)$.

Remark 12.1. Note that when $\theta = 0$, we realize the classical Chebyshev polynomials in the sense of

$$T_k(\xi) = \frac{k}{2} \lim_{\theta \rightarrow 0} \frac{C_k^\theta(\xi)}{\theta}, \quad k \geq 1. \tag{12.16}$$

Here, we denote $T_k(\xi) := C_k^0(\xi)$.

Recall the interpolatory Gegenbauer–Gauss–Lobatto quadrature formula:

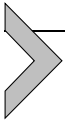
$$\int_{-1}^1 f(\xi) \omega^\theta(\xi) dx = \sum_{j=0}^N f(\xi_j^\theta) \varpi_j^\theta, \quad \forall f \in \mathcal{P}_{2N-1}, \tag{12.17}$$

where $\{\xi_j^\theta\}_{j=0}^N$ are the Gauss–Lobatto–Gegenbauer nodes (i.e., zeros of $(1 - \xi^2) C_{N-1}^{\theta+1}(\xi)$), the related quadrature weights $\{\varpi_j^\theta\}_{j=0}^N$ are represented by the Lagrange basis polynomials (see, e.g., [55]), and \mathcal{P}_N is the set of all polynomials of degree less than or equal to N .

The left and right Riemann–Liouville fractional derivatives of the Gegenbauer polynomial are given by

$$\begin{aligned} & {}_{-1}D_\xi^\beta C_k^\theta(\xi) \\ &= C_k^{\theta, \beta-}(\xi) \\ &= \frac{\Gamma(\theta + 0.5)}{\Gamma(2\theta)} \sum_{k=0}^j \frac{(-1)^{k+j} \Gamma(2\theta + k + j)}{(j - k)! \Gamma(\theta + k + 0.5) 2^k \Gamma(k - \beta + 1)} (\xi + 1)^{k-\beta}, \end{aligned}$$

$$\begin{aligned}
& {}_{\xi} D_1^{\beta} C_k^{\theta}(\xi) \\
&= C_k^{\theta, \beta+}(\xi) \\
&= \frac{\Gamma(\theta + 0.5)}{\Gamma(2\theta)} \sum_{k=0}^j \frac{(-1)^k \Gamma(2\theta + k + j)}{(j - k)! \Gamma(\theta + k + 0.5) 2^k \Gamma(k - \beta + 1)} (1 - \xi)^{k - \beta}.
\end{aligned} \tag{12.18}$$



12.4. Numerical schemes

In spectral methods [56–59], one converts the original partial differential equation into a system of ordinary differential equations (SODE) by assuming a functional dependence on the spatial part of the equation. Along these lines, a number of related methods has been proposed for solving related equations [60,61].

The solutions $u(\xi, \tau)$ of such equations are approximated as $u_{Approx}(\xi, t)$ formulated as a truncated series of orthogonal polynomials for the spatial discretization, which enables us to estimate the related quantities at some chosen points. This discretization leads us to a SODE, which will be solved by using an implicit Runge–Kutta (IRK) scheme.

12.4.1 Spatial discretization

In this subsection, we construct two algorithms for the spatial discretization of single and coupled systems of Riesz space FSEs based on the Gegenbauer–Gauss–Lobatto collocation method.

12.4.1.1 Nonlinear fractional Riesz space Schrödinger equations

In this subsection, we treat the nonlinear Riesz space FSE

$$i \frac{\partial \psi}{\partial \tau} - \gamma (-\Delta)^{\beta/2} \psi + \rho |\psi|^2 \psi = 0, \quad \gamma \in (\mathcal{A}, \mathcal{B}), \quad 0 < \tau \leq \tau_{end}, \tag{12.19}$$

with the following conditions:

$$\psi(\gamma, 0) = \psi_0(\gamma), \tag{12.20}$$

$$\psi(\mathcal{A}, \tau) = \psi(\mathcal{B}, \tau) = 0. \tag{12.21}$$

For a straightforward application of the Gegenbauer-based spectral collocation scheme on $(-1, 1)$, we consider the change of variables $\gamma = \frac{2}{\mathcal{B}-\mathcal{A}}\xi + \frac{\mathcal{A}+\mathcal{B}}{\mathcal{B}-\mathcal{A}}$ and $\psi(\gamma, \tau) = \chi(\xi, \tau)$. This will convert problem (12.19)–(12.21) into

the following equivalent equation, where the spatial domain is defined on $(-1, 1)$:

$$i \frac{\partial \chi}{\partial \tau} - \gamma \left(\frac{2}{\mathcal{B} - \mathcal{A}} \right)^\beta (-\Delta)^{\beta/2} \chi + \rho |\chi|^2 \chi = 0, \quad \xi \in (-1, 1), \quad 0 < \tau \leq \tau_{end}, \quad (12.22)$$

with the following conditions:

$$\chi(\xi, 0) = \chi_0(\xi), \quad (12.23)$$

$$\chi(-1, \tau) = \chi(1, \tau) = 0. \quad (12.24)$$

We now split the complex function $\chi(\xi, \tau)$ into two real functions $\mathcal{P}(\xi, \tau)$ and $\mathcal{Q}(\xi, \tau)$ as

$$\chi(\xi, \tau) = \mathcal{P}(\xi, \tau) + i \mathcal{Q}(\xi, \tau). \quad (12.25)$$

Based on the previous mapping, we deduce that

$$\begin{aligned} & \frac{\partial \mathcal{P}(\xi, \tau)}{\partial \tau} - \gamma \left(\frac{2}{\mathcal{B} - \mathcal{A}} \right)^\beta (-\Delta)^{\beta/2} \mathcal{Q}(\xi, \tau) \\ & + \rho (|\mathcal{P}(\xi, \tau)|^2 + |\mathcal{Q}(\xi, \tau)|^2) \mathcal{Q}(\xi, \tau) = 0, \\ & - \frac{\partial \mathcal{Q}(\xi, \tau)}{\partial \tau} - \gamma \left(\frac{2}{\mathcal{B} - \mathcal{A}} \right)^\beta (-\Delta)^{\beta/2} \mathcal{P}(\xi, \tau) \\ & + \rho (|\mathcal{P}(\xi, \tau)|^2 + |\mathcal{Q}(\xi, \tau)|^2) \mathcal{P}(\xi, \tau) = 0, \end{aligned} \quad (12.26)$$

with the following conditions:

$$\begin{aligned} \mathcal{P}(-1, \tau) &= 0, \quad \mathcal{P}(1, \tau) = 0, \quad \tau \in (0, \tau_{end}], \\ \mathcal{Q}(-1, \tau) &= 0, \quad \mathcal{Q}(1, \tau) = 0, \quad \tau \in (0, \tau_{end}], \\ \mathcal{P}(\xi, 0) &= \mathcal{P}_0(\xi), \quad \mathcal{Q}(\xi, 0) = \mathcal{Q}_0(\xi), \quad \xi \in (-1, 1). \end{aligned} \quad (12.27)$$

The distribution of Gegenbauer–Gauss–Lobatto nodes in $(-1, 1)$ is the major reason for considering them in our discretization. Here, we list the main steps of implementing our Gegenbauer–Gauss–Lobatto collocation scheme for converting the nonlinear system (12.26)–(12.27) into a temporal ordinary differential system.

The spectral approximations of $\mathcal{P}(\xi, \tau)$ and $\mathcal{Q}(\xi, \tau)$ are given by

$$\mathcal{P}(\xi, \tau) \approx \sum_{j=0}^{\mathcal{K}} \epsilon_j(\tau) C_j^\theta(\xi), \quad \mathcal{Q}(\xi, \tau) \approx \sum_{j=0}^{\mathcal{K}} \epsilon_j(\tau) C_j^\theta(\xi). \quad (12.28)$$

The orthogonal property and the discrete inner product permit the following:

$$\begin{aligned}\epsilon_j(\tau) &= \frac{1}{h_j^\theta} \sum_{i=0}^{\mathcal{K}} C_j^\theta(\xi_i^\theta) \varpi_i^\theta \mathcal{P}(\xi_i^\theta, \tau), \\ \varepsilon_j(\tau) &= \frac{1}{h_j^\theta} \sum_{i=0}^{\mathcal{K}} C_j^\theta(\xi_i^\theta) \varpi_i^\theta \mathcal{Q}(\xi_i^\theta, \tau).\end{aligned}\tag{12.29}$$

Hence, the approximate solutions (12.28) take the form

$$\begin{aligned}\mathcal{P}(\xi, \tau) &= \sum_{i,j=0,\dots,\mathcal{K}} \frac{1}{h_j^\theta} C_j^\theta(\xi_i^\theta) C_j^\theta(\xi) \varpi_i^\theta \mathcal{P}(\xi_i^\theta, \tau), \\ \mathcal{Q}(\xi, \tau) &= \sum_{i,j=0,\dots,\mathcal{K}} \frac{1}{h_j^\theta} C_j^\theta(\xi_i^\theta) C_j^\theta(\xi) \varpi_i^\theta \mathcal{Q}(\xi_i^\theta, \tau).\end{aligned}\tag{12.30}$$

The left fractional Riemann–Liouville spatial derivative of order β can be written as

$$\begin{aligned}-_1\mathcal{D}_\xi^\beta \mathcal{P}(\xi, \tau) \Big|_{\xi=\xi_n^\theta} &= \sum_{i=0}^{\mathcal{K}} \wp_{n,i} \mathcal{P}(\xi_i^\theta, \tau), \quad -_1\mathcal{D}_\xi^\beta \mathcal{Q}(\xi, \tau) \Big|_{\xi=\xi_n^\theta} = \sum_{i=0}^{\mathcal{K}} \wp_{n,i} \mathcal{Q}(\xi_i^\theta, \tau), \\ n &= 0, 1, \dots, \end{aligned}\tag{12.31}$$

where

$$\wp_{n,i} = \sum_{j=0}^{\mathcal{K}} \frac{\varpi_i^\theta}{h_j^\theta} C_j^\theta(\xi_i^\theta) C_j^{\theta, \beta-}(\xi_n^\theta).\tag{12.32}$$

Similarly, the right fractional Riemann–Liouville spatial derivative of order β can be written as

$$\begin{aligned}_\xi \mathcal{D}_1^\beta \mathcal{P}(\xi, \tau) \Big|_{\xi=\xi_n^\theta} &= \sum_{i=0}^{\mathcal{K}} \ell_{n,i} \mathcal{P}(\xi_i^\theta, \tau), \quad \xi \mathcal{D}_1^\beta \mathcal{Q}(\xi, \tau) \Big|_{\xi=\xi_n^\theta} = \sum_{i=0}^{\mathcal{K}} \ell_{n,i} \mathcal{Q}(\xi_i^\theta, \tau), \\ n &= 0, 1, \dots, \mathcal{K},\end{aligned}\tag{12.33}$$

where

$$\ell_{n,i} = \sum_{j=0}^{\mathcal{K}} \frac{\varpi_i^\theta}{h_j^\theta} C_j^\theta(\xi_i^\theta) C_j^{\theta, \beta+}(\xi_n^\theta).\tag{12.34}$$

Let us denote

$$\mathcal{P}_n(\tau) = \mathcal{P}(\xi_n^\theta, \tau), \quad \mathcal{Q}_n(\tau) = \mathcal{Q}_n(\xi_n^\theta, \tau).$$

For the spectral Gegenbauer–Gauss–Lobatto collocation technique, Eq. (12.26) is enforced to be zero at the $(\mathcal{K} - 1)$ points. Thus, we obtain

$$\begin{aligned} \dot{\mathcal{P}}_n(\tau) - \gamma \left(\frac{2}{\mathcal{B} - \mathcal{A}} \right)^\beta \frac{1}{2 \cos\left(\frac{\pi\beta}{2}\right)} \sum_{i=1}^{\mathcal{K}-1} (\wp_{n,i} + \ell_{n,i}) \mathcal{Q}_i(\tau) \\ + \rho (\mathcal{P}_n^2(\tau) + \mathcal{Q}_n^2(\tau)) \mathcal{Q}_n(\tau) = 0, \\ -\dot{\mathcal{Q}}_n(\tau) - \gamma \left(\frac{2}{\mathcal{B} - \mathcal{A}} \right)^\beta \frac{1}{2 \cos\left(\frac{\pi\beta}{2}\right)} \sum_{i=1}^{\mathcal{K}-1} (\wp_{n,i} + \ell_{n,i}) \mathcal{P}_i(\tau) \\ + \rho (\mathcal{P}_n^2(\tau) + \mathcal{Q}_n^2(\tau)) \mathcal{P}_n(\tau) = 0, \\ n = 1, 2, \dots, \mathcal{K} - 1, \end{aligned} \tag{12.35}$$

with the initial values

$$\mathcal{P}_n(0) = \mathcal{P}(\xi_n^\theta, 0), \quad \mathcal{Q}_n(0) = \mathcal{Q}(\xi_n^\theta, 0), \quad n = 1, \dots, \mathcal{K} - 1. \tag{12.36}$$

12.4.1.2 Coupled nonlinear fractional Riesz space Schrödinger equations

In this subsection, we treat the following coupled nonlinear Riesz space FSE:

$$\begin{aligned} i \frac{\partial \psi}{\partial \tau} - \gamma (-\Delta)^{\beta/2} \psi + \rho (|\psi|^2 + \varrho |\varphi|^2) \psi = 0, \quad \gamma \in (\mathcal{A}, \mathcal{B}), \quad 0 < \tau \leq \tau_{end}, \\ i \frac{\partial \varphi}{\partial \tau} - \gamma (-\Delta)^{\beta/2} \varphi + \rho (|\varphi|^2 + \varrho |\psi|^2) \varphi = 0, \quad \gamma \in (\mathcal{A}, \mathcal{B}), \quad 0 < \tau \leq \tau_{end}, \end{aligned} \tag{12.37}$$

with the following conditions:

$$\psi(\gamma, 0) = \psi_0(\gamma), \quad \varphi(\gamma, 0) = \varphi_0(\gamma), \tag{12.38}$$

$$\psi(\mathcal{A}, \tau) = 0, \quad \psi(\mathcal{B}, \tau) = 0, \quad \varphi(\mathcal{A}, \tau) = 0, \quad \varphi(\mathcal{B}, \tau) = 0. \tag{12.39}$$

Again we consider the change of variables $\gamma = \frac{2}{\mathcal{B} - \mathcal{A}} \xi + \frac{\mathcal{A} + \mathcal{B}}{\mathcal{B} - \mathcal{A}}$ and $\psi(\gamma, \tau) = \chi(\xi, \tau)$. This will convert problem (12.37)–(12.39) into another one in the

spatial domain $(-1, 1)$, namely,

$$\begin{aligned}
 i \frac{\partial \chi}{\partial \tau} - \gamma \left(\frac{2}{\mathcal{B} - \mathcal{A}} \right)^\beta (-\Delta)^{\beta/2} \chi + \rho (|\chi|^2 + \varrho |\phi|^2) \chi &= 0, \\
 \xi \in (-1, 1), \quad 0 < \tau \leq \tau_{end}, & \\
 i \frac{\partial \phi}{\partial \tau} - \gamma \left(\frac{2}{\mathcal{B} - \mathcal{A}} \right)^\beta (-\Delta)^{\beta/2} \phi + \rho (|\phi|^2 + \varrho |\chi|^2) \phi &= 0, \\
 \xi \in (-1, 1), \quad 0 < \tau \leq \tau_{end}, &
 \end{aligned} \tag{12.40}$$

with the following conditions:

$$\chi(\xi, 0) = \chi_0(\xi), \quad \phi(\xi, 0) = \phi_0(\xi), \tag{12.41}$$

$$\chi(-1, \tau) = \chi(1, \tau) = \phi(-1, \tau) = \phi(1, \tau) = 0. \tag{12.42}$$

We now split the complex functions $(\chi(\xi, \tau)$ and $\phi(\xi, \tau))$ into real functions as

$$\chi(\xi, \tau) = \mathcal{P}(\xi, \tau) + i \mathcal{Q}(\xi, \tau), \quad \phi(\xi, \tau) = \mathcal{R}(\xi, \tau) + i \mathcal{S}(\xi, \tau), \tag{12.43}$$

where $\mathcal{P}(\xi, \tau)$, $\mathcal{Q}(\xi, \tau)$, $\mathcal{R}(\xi, \tau)$, and $\mathcal{S}(\xi, \tau)$ are real functions. Based on the previous mapping, we get

$$\begin{aligned}
 \frac{\partial \mathcal{P}(\xi, \tau)}{\partial \tau} - \gamma \left(\frac{2}{\mathcal{B} - \mathcal{A}} \right)^\beta (-\Delta)^{\beta/2} \mathcal{Q}(\xi, \tau) \\
 + \rho (|\mathcal{P}(\xi, \tau)|^2 + |\mathcal{Q}(\xi, \tau)|^2 + \varrho |\mathcal{R}(\xi, \tau)|^2 + \varrho |\mathcal{S}(\xi, \tau)|^2) \mathcal{Q}(\xi, \tau) &= 0, \\
 -\frac{\partial \mathcal{Q}(\xi, \tau)}{\partial \tau} - \gamma \left(\frac{2}{\mathcal{B} - \mathcal{A}} \right)^\beta (-\Delta)^{\beta/2} \mathcal{P}(\xi, \tau) \\
 + \rho (|\mathcal{P}(\xi, \tau)|^2 + |\mathcal{Q}(\xi, \tau)|^2 + \varrho |\mathcal{R}(\xi, \tau)|^2 + \varrho |\mathcal{S}(\xi, \tau)|^2) \mathcal{P}(\xi, \tau) &= 0, \\
 \frac{\partial \mathcal{R}(\xi, \tau)}{\partial \tau} - \gamma \left(\frac{2}{\mathcal{B} - \mathcal{A}} \right)^\beta (-\Delta)^{\beta/2} \mathcal{S}(\xi, \tau) \\
 + \rho (\varrho |\mathcal{P}(\xi, \tau)|^2 + \varrho |\mathcal{Q}(\xi, \tau)|^2 + |\mathcal{R}(\xi, \tau)|^2 + |\mathcal{S}(\xi, \tau)|^2) \mathcal{S}(\xi, \tau) &= 0, \\
 -\frac{\partial \mathcal{S}(\xi, \tau)}{\partial \tau} - \gamma \left(\frac{2}{\mathcal{B} - \mathcal{A}} \right)^\beta (-\Delta)^{\beta/2} \mathcal{R}(\xi, \tau) \\
 + \rho (\varrho |\mathcal{P}(\xi, \tau)|^2 + \varrho |\mathcal{Q}(\xi, \tau)|^2 + |\mathcal{R}(\xi, \tau)|^2 + |\mathcal{S}(\xi, \tau)|^2) \mathcal{R}(\xi, \tau) &= 0,
 \end{aligned} \tag{12.44}$$

with the following conditions:

$$\begin{aligned}
 \mathcal{P}(-1, \tau) &= 0, & \mathcal{P}(1, \tau) &= 0, & \tau &\in (0, \tau_{end}], \\
 \mathcal{Q}(-1, \tau) &= 0, & \mathcal{Q}(1, \tau) &= 0, & \tau &\in (0, \tau_{end}], \\
 \mathcal{R}(-1, \tau) &= 0, & \mathcal{R}(1, \tau) &= 0, & \tau &\in (0, \tau_{end}], \\
 \mathcal{S}(-1, \tau) &= 0, & \mathcal{S}(1, \tau) &= 0, & \tau &\in (0, \tau_{end}], \\
 \mathcal{P}(\xi, 0) &= \mathcal{P}_0(\xi), & \mathcal{Q}(\xi, 0) &= \mathcal{Q}_0(\xi), & \xi &\in (-1, 1), \\
 \mathcal{R}(\xi, 0) &= \mathcal{R}_0(\xi), & \mathcal{S}(\xi, 0) &= \mathcal{S}_0(\xi), & \xi &\in (-1, 1).
 \end{aligned}
 \tag{12.45}$$

Then, $\mathcal{P}(\xi, \tau)$, $\mathcal{Q}(\xi, \tau)$, $\mathcal{R}(\xi, \tau)$, and $\mathcal{S}(\xi, \tau)$ can be approximated as

$$\begin{aligned}
 \mathcal{P}_{\mathcal{K}}(\xi, \tau) &= \sum_{j=0}^{\mathcal{K}} \epsilon_j(\tau) C_j^\theta(\xi), & \mathcal{Q}_{\mathcal{K}}(\xi, \tau) &= \sum_{j=0}^{\mathcal{K}} \varepsilon_j(\tau) C_j^\theta(\xi), \\
 \mathcal{R}_{\mathcal{K}}(\xi, \tau) &= \sum_{j=0}^{\mathcal{K}} \zeta_j(\tau) C_j^\theta(\xi), & \mathcal{S}_{\mathcal{K}}(\xi, \tau) &= \sum_{j=0}^{\mathcal{K}} \eta_j(\tau) C_j^\theta(\xi).
 \end{aligned}
 \tag{12.46}$$

Using the orthogonal property and the discrete inner product, we obtain the following approximations:

$$\begin{aligned}
 \epsilon_j(\tau) &= \frac{1}{h_j^\theta} \sum_{i=0}^{\mathcal{K}} C_j^\theta(\xi_i^\theta) \varpi_i^\theta \mathcal{P}(\xi_i^\theta, \tau), & \varepsilon_j(\tau) &= \frac{1}{h_j^\theta} \sum_{i=0}^{\mathcal{K}} C_j^\theta(\xi_i^\theta) \varpi_i^\theta \mathcal{Q}(\xi_i^\theta, \tau), \\
 \zeta_j(\tau) &= \frac{1}{h_j^\theta} \sum_{i=0}^{\mathcal{K}} C_j^\theta(\xi_i^\theta) \varpi_i^\theta \mathcal{R}(\xi_i^\theta, \tau), & \eta_j(\tau) &= \frac{1}{h_j^\theta} \sum_{i=0}^{\mathcal{K}} C_j^\theta(\xi_i^\theta) \varpi_i^\theta \mathcal{S}(\xi_i^\theta, \tau).
 \end{aligned}
 \tag{12.47}$$

In this case, the approximations in (12.46) take the form

$$\begin{aligned}
 \mathcal{P}(\xi, \tau) &= \sum_{i,j=0,\dots,\mathcal{K}} \frac{1}{h_j^\theta} C_j^\theta(\xi_i^\theta) C_j^\theta(\xi) \varpi_i^\theta \mathcal{P}(\xi_i^\theta, \tau), \\
 \mathcal{Q}(\xi, \tau) &= \sum_{i,j=0,\dots,\mathcal{K}} \frac{1}{h_j^\theta} C_j^\theta(\xi_i^\theta) C_j^\theta(\xi) \varpi_i^\theta \mathcal{Q}(\xi_i^\theta, \tau), \\
 \mathcal{R}(\xi, \tau) &= \sum_{i,j=0,\dots,\mathcal{K}} \frac{1}{h_j^\theta} C_j^\theta(\xi_i^\theta) C_j^\theta(\xi) \varpi_i^\theta \mathcal{R}(\xi_i^\theta, \tau), \\
 \mathcal{S}(\xi, \tau) &= \sum_{i,j=0,\dots,\mathcal{K}} \frac{1}{h_j^\theta} C_j^\theta(\xi_i^\theta) C_j^\theta(\xi) \varpi_i^\theta \mathcal{S}(\xi_i^\theta, \tau).
 \end{aligned}
 \tag{12.48}$$

Similarly to (12.31) and (12.33), we get

$$\begin{aligned}
 -{}_1\mathcal{D}_\xi^\beta \mathcal{P}(\xi_n^\theta, \tau) &= \sum_{i=0}^{\mathcal{K}} \wp_{n,i} \mathcal{P}(\xi_i^\theta, \tau), & -{}_1\mathcal{D}_\xi^\beta \mathcal{Q}(\xi_n^\theta, \tau) &= \sum_{i=0}^{\mathcal{K}} \wp_{n,i} \mathcal{Q}(\xi_i^\theta, \tau), \\
 -{}_1\mathcal{D}_\xi^\beta \mathcal{R}(\xi_n^\theta, \tau) &= \sum_{i=0}^{\mathcal{K}} \wp_{n,i} \mathcal{R}(\xi_i^\theta, \tau), & -{}_1\mathcal{D}_\xi^\beta \mathcal{S}(\xi_n^\theta, \tau) &= \sum_{i=0}^{\mathcal{K}} \wp_{n,i} \mathcal{S}(\xi_i^\theta, \tau), \\
 n &= 0, 1, \dots, \mathcal{K},
 \end{aligned}
 \tag{12.49}$$

$$\begin{aligned}
 {}_\xi \mathcal{D}_1^\beta \mathcal{P}(\xi_n^\theta, \tau) &= \sum_{i=0}^{\mathcal{K}} \ell_{n,i} \mathcal{P}(\xi_i^\theta, \tau), & {}_\xi \mathcal{D}_1^\beta \mathcal{Q}(\xi_n^\theta, \tau) &= \sum_{i=0}^{\mathcal{K}} \ell_{n,i} \mathcal{Q}(\xi_i^\theta, \tau), \\
 {}_\xi \mathcal{D}_1^\beta \mathcal{R}(\xi_n^\theta, \tau) &= \sum_{i=0}^{\mathcal{K}} \ell_{n,i} \mathcal{R}(\xi_i^\theta, \tau), & {}_\xi \mathcal{D}_1^\beta \mathcal{S}(\xi_n^\theta, \tau) &= \sum_{i=0}^{\mathcal{K}} \ell_{n,i} \mathcal{S}(\xi_i^\theta, \tau), \\
 n &= 0, 1, \dots, \mathcal{K},
 \end{aligned}
 \tag{12.50}$$

where $\wp_{n,i}$ and $\ell_{n,i}$ are given by (12.32) and (12.34), respectively.

Combining the boundary conditions with the abovementioned equations and equating the residual of (12.44) by zero at the Gegenbauer–Gauss–Lobatto nodes leads to

$$\begin{aligned}
 \dot{\mathcal{P}}_n(\tau) - \gamma \left(\frac{2}{\mathcal{B} - \mathcal{A}} \right)^\beta \frac{1}{2 \cos(\frac{\pi\beta}{2})} \sum_{i=1}^{\mathcal{K}-1} (\wp_{n,i} + \ell_{n,i}) \mathcal{Q}_i(\tau) \\
 + \rho (\mathcal{P}_n^2(\tau) + \mathcal{Q}_n^2(\tau) + \varrho \mathcal{R}_n^2(\tau) + \varrho \mathcal{S}_n^2(\tau)) \mathcal{Q}_n(\tau) &= 0, \\
 -\dot{\mathcal{Q}}_n(\tau) - \gamma \left(\frac{2}{\mathcal{B} - \mathcal{A}} \right)^\beta \frac{1}{2 \cos(\frac{\pi\beta}{2})} \sum_{i=1}^{\mathcal{K}-1} (\wp_{n,i} + \ell_{n,i}) \mathcal{P}_i(\tau) \\
 + \rho (\mathcal{P}_n^2(\tau) + \mathcal{Q}_n^2(\tau) + \varrho \mathcal{R}_n^2(\tau) + \varrho \mathcal{S}_n^2(\tau)) \mathcal{P}_n(\tau) &= 0, \\
 \dot{\mathcal{R}}_n(\tau) - \gamma \left(\frac{2}{\mathcal{B} - \mathcal{A}} \right)^\beta \frac{1}{2 \cos(\frac{\pi\beta}{2})} \sum_{i=1}^{\mathcal{K}-1} (\wp_{n,i} + \ell_{n,i}) \mathcal{S}_i(\tau) \\
 + \rho (\varrho \mathcal{P}_n^2(\tau) + \varrho \mathcal{Q}_n^2(\tau) + \mathcal{R}_n^2(\tau) + \mathcal{S}_n^2(\tau)) \mathcal{S}_n(\tau) &= 0, \\
 -\dot{\mathcal{S}}_n(\tau) - \gamma \left(\frac{2}{\mathcal{B} - \mathcal{A}} \right)^\beta \frac{1}{2 \cos(\frac{\pi\beta}{2})} \sum_{i=1}^{\mathcal{K}-1} (\wp_{n,i} + \ell_{n,i}) \mathcal{R}_i(\tau) \\
 + \rho (\varrho \mathcal{P}_n^2(\tau) + \varrho \mathcal{Q}_n^2(\tau) + \mathcal{R}_n^2(\tau) + \mathcal{S}_n^2(\tau)) \mathcal{R}_n(\tau) &= 0, \\
 n &= 1, 2, \dots, \mathcal{K} - 1,
 \end{aligned}
 \tag{12.51}$$

with the initial values

$$\begin{aligned} \mathcal{P}_n(0) &= \mathcal{P}(\xi_n^\theta, 0), & \mathcal{Q}_n(0) &= \mathcal{Q}(\xi_n^\theta, 0), & \mathcal{R}_n(0) &= \mathcal{R}(\xi_n^\theta, 0), \\ \mathcal{S}_n(0) &= \mathcal{S}(\xi_n^\theta, 0), & n &= 1, \dots, \mathcal{K} - 1. \end{aligned} \quad (12.52)$$

The numerical approach for solving the systems (12.35)–(12.36) and (12.51)–(12.52) will be listed in Section 12.4.2.

12.4.2 Temporal discretization

The IRK method has many applications for efficiently solving SODEs numerically (see [62,63]). Let

$$\dot{\mathbf{u}}(\tau) = \Omega(\tau, \mathbf{u}(\tau)), \quad \mathbf{u}(0) = \delta_0. \quad (12.53)$$

Then, the iterative solution is

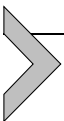
$$\begin{aligned} \mathbf{U}_{i,j} &= \mathbf{u}_i + \Delta\tau \sum_{l=1}^s a_{j,l} \Omega(\tau_i + c_l \Delta\tau, \mathbf{U}_{i,l}), \quad j = 1, \dots, s, \\ \mathbf{u}_{i+1} &= \mathbf{u}_i + \Delta\tau \sum_{j=1}^s b_j \Omega(\tau_i + c_j \Delta\tau, \mathbf{U}_{i,j}), \quad \forall i, \end{aligned} \quad (12.54)$$

where $\Delta\tau$ is the step size, $\tau_i = \tau_0 + i\Delta\tau$, and \mathbf{u}_i are approximations to $\mathbf{u}(\tau_i)$. Moreover, a_{ij} , b_j , and c_j are constants and $i, j = 1, 2, \dots, s$, which are given by

$$\begin{array}{c|ccc} c_1 & a_{11} & \cdots & a_{1s} \\ \vdots & \vdots & \ddots & \vdots \\ c_s & a_{s1} & \cdots & a_{ss} \\ \hline & b_1 & \cdots & b_s \end{array}.$$

For the two-stage IRK method, the Butcher array is given by

$$\begin{array}{c|cc} \frac{1}{2} - \frac{\sqrt{3}}{6} & \frac{1}{4} & \frac{1}{4} - \frac{\sqrt{3}}{6} \\ \frac{1}{2} + \frac{\sqrt{3}}{6} & \frac{1}{4} - \frac{\sqrt{3}}{6} & \frac{1}{4} \\ \hline & \frac{1}{2} & \frac{1}{2} \end{array}.$$



12.5. Numerical experiments

In this section, we clarify the robustness and accuracy of the Runge–Kutta/Gegenbauer spectral collocation scheme by implementing the algorithm to several test problems. In our simulations we chose $\mathcal{K} = 256$.

12.5.1 Convergence test

We start with the nonlinear Riesz space FSE [64]

$$i \frac{\partial \psi(\xi, \tau)}{\partial \tau} - \gamma (-\Delta)^{\beta/2} \psi(\xi, \tau) + |\psi|^2 \psi(\xi, \tau) = f(\xi, \tau), \quad (12.55)$$

$$(\xi, \tau) \in (0, 1) \times (0, 1],$$

given the conditions

$$\psi(\xi, 0) = \xi^2(1 - \xi)^2, \quad \xi \in [0, 1],$$

$$\psi(0, \tau) = \psi(1, \tau) = 0, \quad \tau \in (0, 1],$$

and $f(\xi, \tau)$ is given when $\psi(\xi, \tau) = e^{it} \xi^2(1 - \xi)^2$.

Space discretization has been introduced by Yang [64] based on the so-called fractional central difference scheme. A modified Crank–Nicolson leapfrog technique has been used for temporal discretization. Table 12.1 lists a comparison between our results and those in [64] for dissimilar values of parameters. Obviously, the proposed scheme shows better numerical results

Table 12.1 The maximum absolute errors for different choices of β for problem (12.55).

	\mathcal{K}	$\beta = 1.2$	$\beta = 1.5$	$\beta = 1.8$
Method I [64]	2^6	4.62×10^{-4}	3.66×10^{-3}	8.90×10^{-5}
	2^8	1.39×10^{-4}	1.08×10^{-3}	3.01×10^{-5}
	2^{10}	3.64×10^{-5}	2.71×10^{-4}	7.93×10^{-6}
Method II [64]	2^6	9.92×10^{-5}	6.70×10^{-5}	7.35×10^{-5}
	2^8	6.89×10^{-6}	4.57×10^{-6}	4.35×10^{-6}
	2^{10}	4.69×10^{-7}	3.25×10^{-7}	3.25×10^{-7}
Method III [64]	2^6	5.09×10^{-5}	3.83×10^{-5}	5.61×10^{-5}
	2^8	3.32×10^{-6}	2.62×10^{-6}	3.26×10^{-6}
	2^{10}	2.32×10^{-7}	1.89×10^{-7}	2.15×10^{-7}
Method IV [64]	2^6	1.55×10^{-5}	1.36×10^{-5}	4.11×10^{-5}
	2^8	9.85×10^{-7}	9.77×10^{-7}	2.34×10^{-6}
	2^{10}	8.45×10^{-8}	7.86×10^{-8}	1.61×10^{-7}
Present method	4	2.90×10^{-2}	2.36×10^{-2}	2.19×10^{-2}
	6	1.34×10^{-11}	3.54×10^{-11}	7.98×10^{-11}
	8	1.19×10^{-11}	4.08×10^{-11}	8.85×10^{-11}
	10	1.36×10^{-11}	3.69×10^{-11}	7.30×10^{-11}

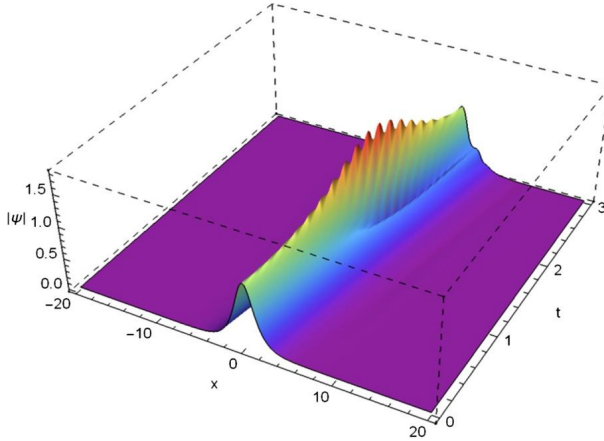


Figure 12.1 Evaluation of the approximate solution for different fractional orders, where $\beta = 1.4$.

than those reported in [64]. It is also observed that excellent approximations with a low number of collocation points are achieved.

12.5.2 A single equation

Firstly, we consider the nonlinear Riesz space FSE (12.19) in the following form:

$$i \frac{\partial \psi}{\partial \tau} - \gamma (-\Delta)^{\beta/2} \psi + \rho |\psi|^2 \psi = 0, \quad (12.56)$$

subject to the initial condition

$$\psi(\xi, 0) = e^{2i\xi} \operatorname{sech}(\xi). \quad (12.57)$$

For this problem, we take the parameters $\gamma = 1$, $\rho = 2$. When $\beta = 2$, the exact solution is given by

$$\psi(\xi, \tau) = e^{i(2\xi - 3\tau)} \operatorname{sech}(\xi - 4\tau).$$

In this example, we chose $a = -20$ and $b = 20$. In Figs. 12.1–12.4, we display the numerical approximations for different values of β . We note that the shape of the soliton is affected by the fractional order (see the details also in Fig. 12.5). The shape of the soliton will change quickly when β becomes smaller, and when β tends to 2, the approximate solutions converge to the solutions of the integer-order equation.

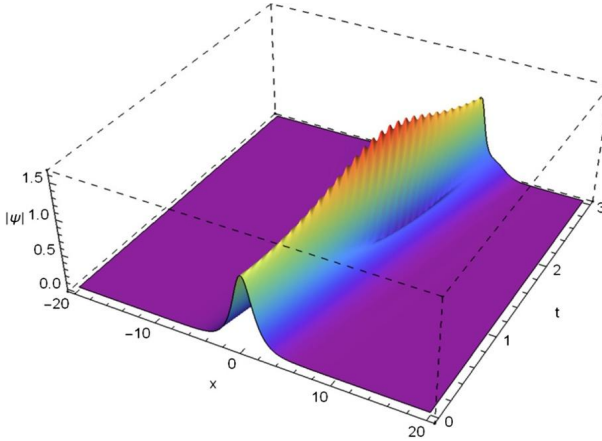


Figure 12.2 Evaluation of the approximate solution for different fractional orders, where $\beta = 1.6$.

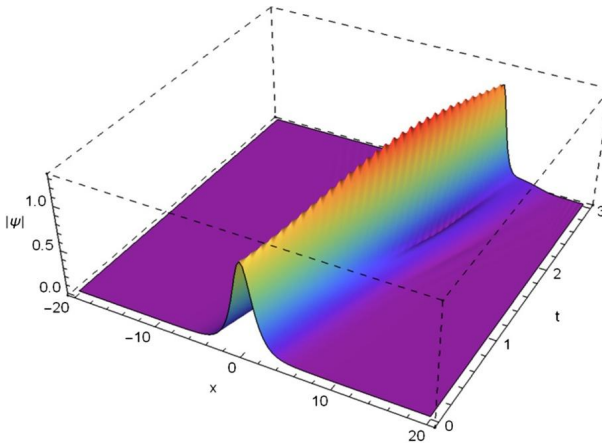


Figure 12.3 Evaluation of the approximate solution for different fractional orders, where $\beta = 1.8$.

12.5.3 Coupled equations

Example 12.1. Consider the coupled system

$$\begin{aligned}
 i \frac{\partial \psi}{\partial \tau} - \gamma (-\Delta)^{\beta/2} \psi + \rho (|\psi|^2 + \varrho |\varphi|^2) \psi &= 0, \\
 i \frac{\partial \varphi}{\partial \tau} - \gamma (-\Delta)^{\beta/2} \varphi + \rho (|\varphi|^2 + \varrho |\psi|^2) \varphi &= 0,
 \end{aligned}
 \tag{12.58}$$

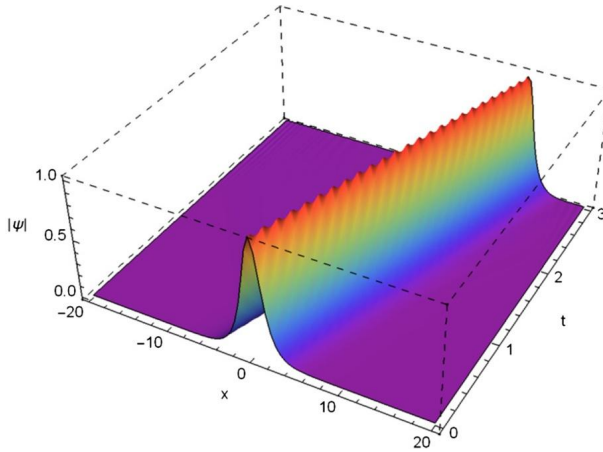


Figure 12.4 Evaluation of the approximate solution for different fractional orders, where $\beta = 1.99$.

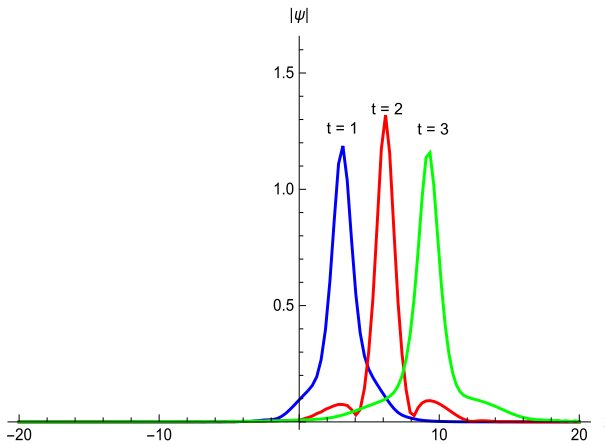


Figure 12.5 Numerical solution at $t = 1, 2, 3$ with $\beta = 1.8$.

where $\varrho \neq 0$, with the following initial conditions:

$$\begin{aligned} \psi(\xi, 0) &= e^{iQ_0\xi} \operatorname{sech}(\xi + R_0), \\ \phi(\xi, 0) &= e^{-iQ_0\xi} \operatorname{sech}(\xi - R_0). \end{aligned} \tag{12.59}$$

In this example, we choose the parameters $R_0 = 5$, $Q_0 = 3$, $\gamma = \varrho = 1$, and $\rho = 2$. The numerical results indicate that when β tends to 2, collision is elastic and the shapes of the two solitons are unchanged (Figs. 12.6–12.9).

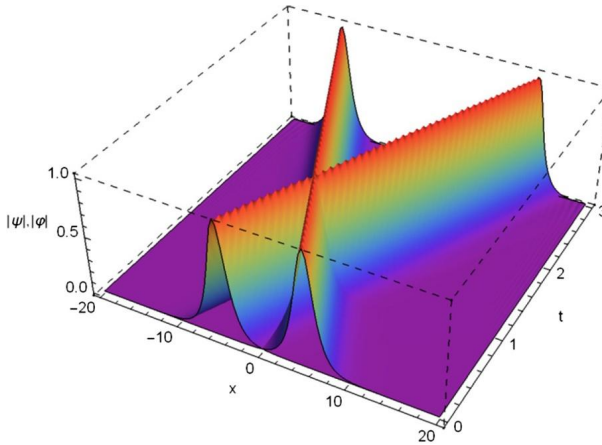


Figure 12.6 Evaluation of the approximate solution, where $\beta = 1.99$.

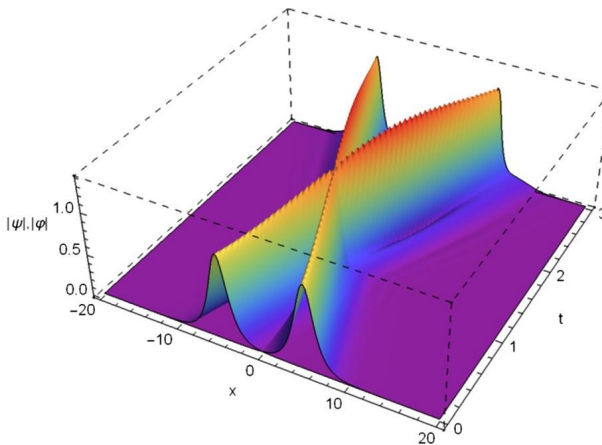


Figure 12.7 Evaluation of the approximate solution for different fractional orders, where $\beta = 1.8$.

We also find that when $\beta \neq 2$, the collisions are not elastic. These results show that the order β seriously affects the shape of the solitons.

Example 12.2. Finally, we introduce

$$\begin{aligned} i \frac{\partial \psi}{\partial \tau} - (-\Delta)^{\beta/2} \psi + (|\psi|^2 + |\varphi|^2) \psi &= f_1(\xi, \tau), \\ i \frac{\partial \varphi}{\partial \tau} - (-\Delta)^{\beta/2} \varphi + (|\varphi|^2 + |\psi|^2) \varphi &= f_2(\xi, \tau), \end{aligned} \quad (12.60)$$

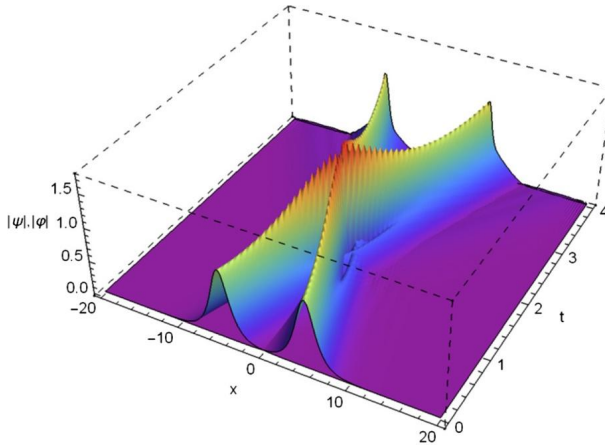


Figure 12.8 Evaluation of the approximate solution, where $\beta = 1.6$.

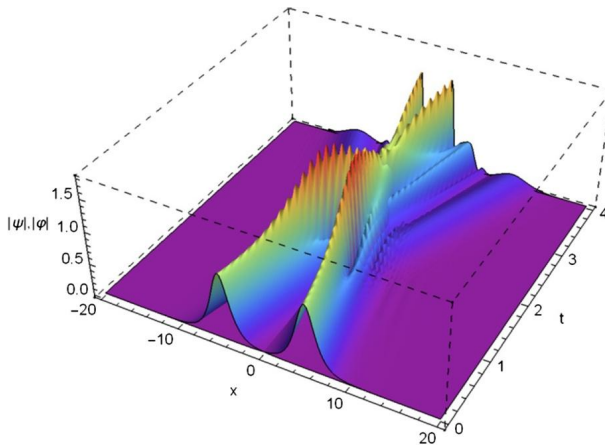


Figure 12.9 Evaluation of the approximate solution for different fractional orders, where $\beta = 1.4$.

given the conditions

$$\begin{aligned} \psi(\xi, 0) &= x^4(1-x)^4, & \psi(0, \tau) &= \psi(1, \tau) = 0, \\ \phi(\xi, 0) &= x^4(1-x)^4, & \phi(0, \tau) &= \phi(1, \tau) = 0, \end{aligned} \quad (12.61)$$

and $f_1(\xi, \tau)$ and $f_2(\xi, \tau)$ are given when $\psi(\xi, \tau) = e^{-it}\xi^4(1-\xi)^4$ and $\phi(\xi, \tau) = e^{it}\xi^4(1-\xi)^4$. Table 12.2 lists a comparison between our results and exact solutions for dissimilar values of parameters. Space-time graphs

Table 12.2 Maximum absolute errors of problem (12.60).

β	(N, M)	$M_{P_{N,M}}$	$M_{Q_{N,R}}$	$M_{R_{N,M}}$	$M_{M_{S,M}}$
1.1	(4,4)	2.86927×10^{-3}	1.88846×10^{-3}	2.50934×10^{-3}	3.0645×10^{-3}
	(6,6)	6.60009×10^{-4}	5.67821×10^{-4}	7.79847×10^{-4}	7.89858×10^{-4}
	(8,8)	8.74126×10^{-5}	7.00946×10^{-5}	8.98759×10^{-5}	9.40342×10^{-5}
	(10,10)	6.54949×10^{-13}	6.33758×10^{-13}	3.213436×10^{-8}	4.06006×10^{-8}
1.5	(4,4)	4.443×10^{-3}	4.63618×10^{-3}	4.8823×10^{-3}	4.85871×10^{-3}
	(6,6)	6.67378×10^{-4}	6.64512×10^{-4}	7.30094×10^{-4}	7.83298×10^{-4}
	(8,8)	8.74126×10^{-5}	8.16411×10^{-5}	1.02859×10^{-4}	1.07615×10^{-4}
	(10,10)	1.81612×10^{-12}	1.67684×10^{-13}	2.80548×10^{-8}	2.68269×10^{-8}
1.8	(4,4)	5.94956×10^{-3}	5.05091×10^{-3}	6.56518×10^{-3}	6.53194×10^{-3}
	(6,6)	7.62834×10^{-4}	6.82844×10^{-4}	9.31914×10^{-4}	9.74952×10^{-4}
	(8,8)	8.97187×10^{-5}	8.65576×10^{-5}	1.02615×10^{-4}	1.08416×10^{-4}
	(10,10)	3.52175×10^{-12}	2.90958×10^{-12}	1.93218×10^{-8}	1.86377×10^{-8}

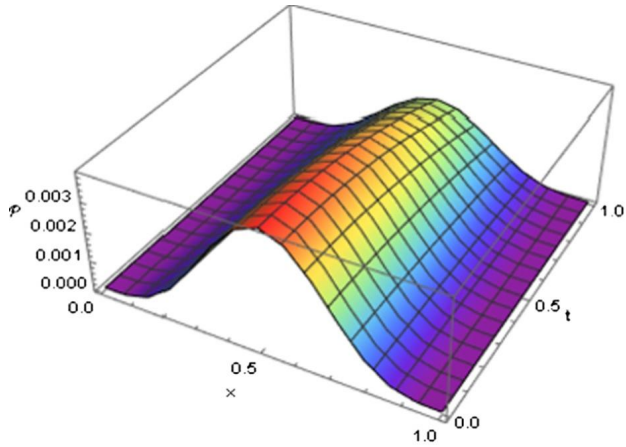


Figure 12.10 Evaluation of the real part of the approximate solution ψ , where $\beta = 1.8$.

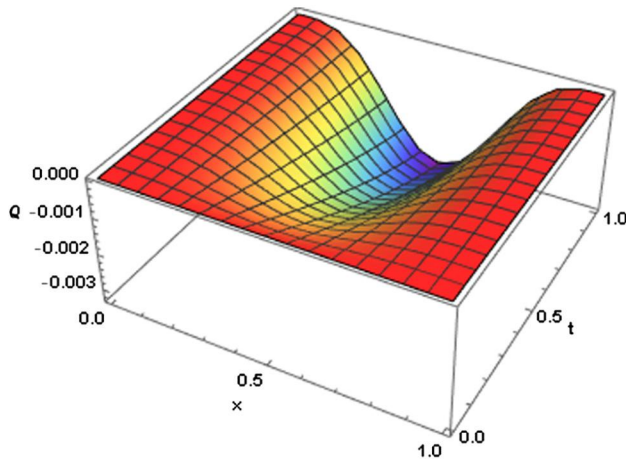


Figure 12.11 Evaluation of the imaginary part of the approximate solution ψ , where $\beta = 1.8$.

of real and imaginary parts of the numerical solution of problem (12.60) are shown in Figs. 12.10–12.13. While in Figs. 12.14–12.17, we recognize the outright matching of numerical and exact solutions in its real and imaginary parts. Also, space-time graphs of real and imaginary parts of the absolute errors of problem (12.60) are plotted in Figs. 12.18–12.21.

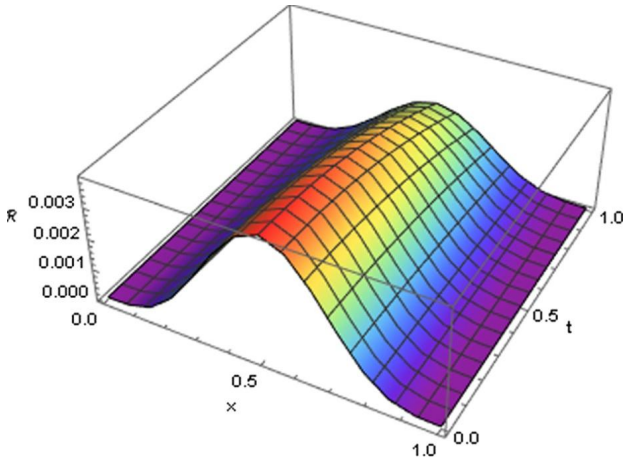


Figure 12.12 Evaluation of the real part of the approximate solution ϕ , where $\beta = 1.8$.

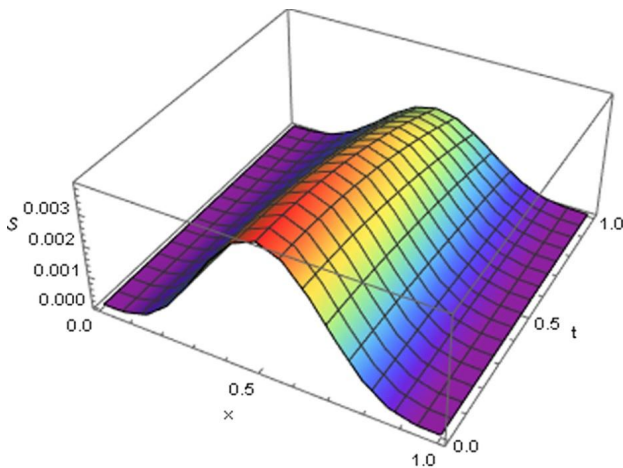


Figure 12.13 Evaluation of the imaginary part of the approximate solution ϕ , where $\beta = 1.8$.

12.6. Conclusion and discussion

In this chapter, we developed a Runge–Kutta/Gegenbauer-based spectral collocation scheme for the coupled nonlinear Riesz space FSEs. It is a continuation of the authors' previous works on Chebyshev and Legendre pseudospectral methods for the fractional Schrödinger equations.

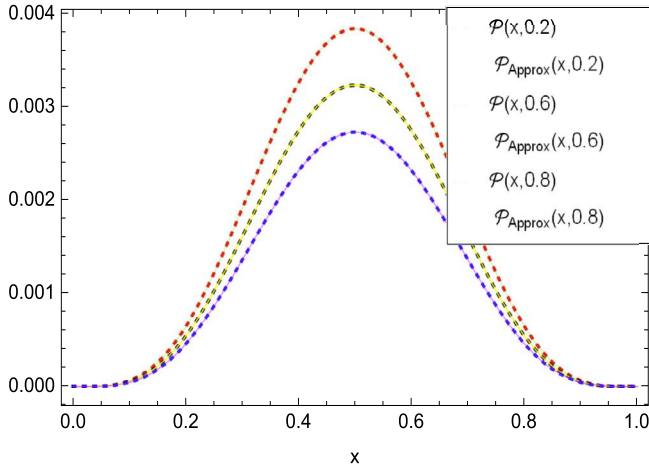


Figure 12.14 Space curves of the real part of the approximate solution ϕ , where $\beta = 1.8$.

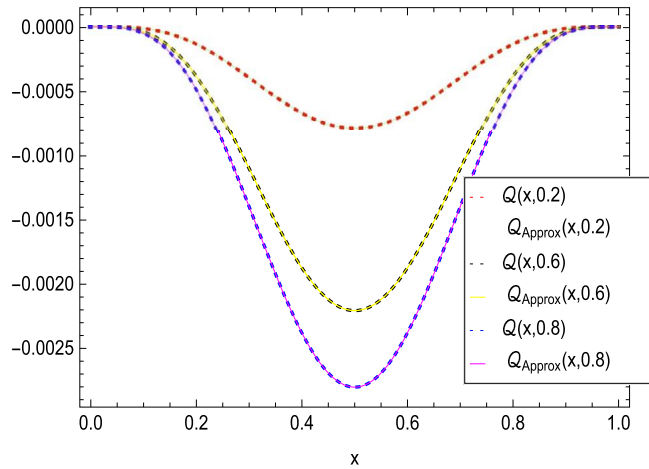


Figure 12.15 Space curves of the imaginary part of the approximate solution ϕ , where $\beta = 1.8$.

The governing equations exhibited both nonlinear and nonlocal behavior, making the numerical computations challenging. We derived a spatially Gegenbauer-based spectral collocation scheme to the Riesz fractional operator on a bounded domain and related differentiation matrices are derived. Then, a fully discrete scheme was obtained by applying the implicit Runge–

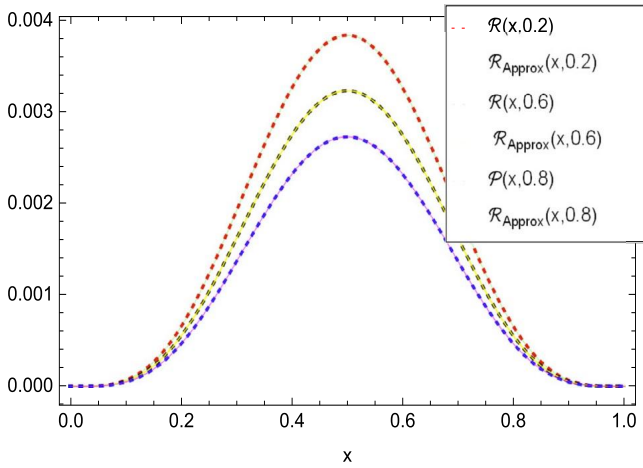


Figure 12.16 Space curves of the real part of the approximate solution ψ , where $\beta = 1.8$.

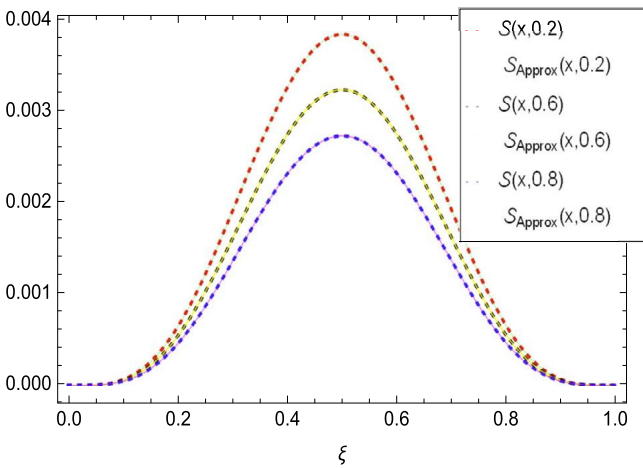


Figure 12.17 Space curves of the imaginary part of the approximate solution ψ , where $\beta = 1.8$.

Kutta scheme of fourth order in time. Finally, numerical simulations were provided to verify the effectiveness of the numerical schemes. The effects of fractional-order parameters on the pattern formations of the wave packets in the coupled Schrödinger equations were discussed.

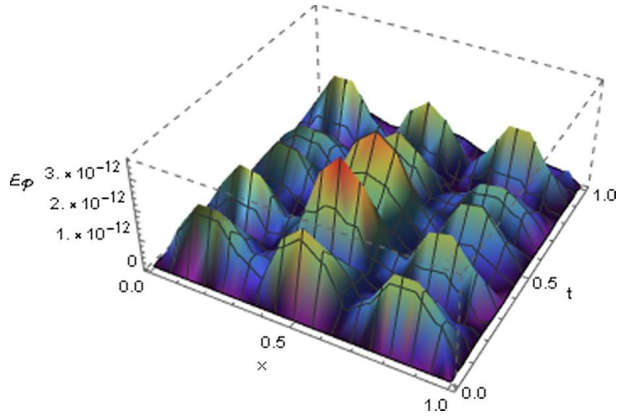


Figure 12.18 Evaluation of the absolute errors of the real part of the approximate solution ψ , where $\beta = 1.8$.

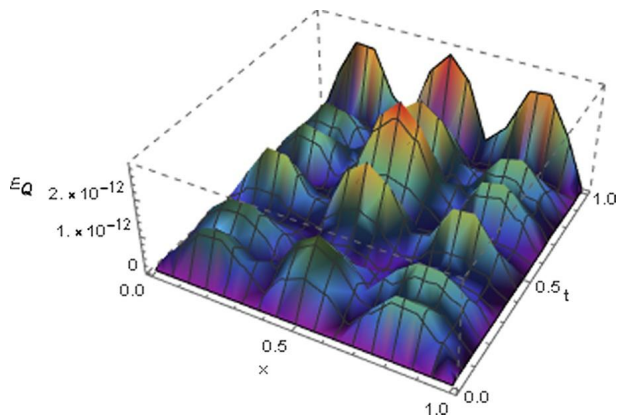


Figure 12.19 Evaluation of the absolute errors of the imaginary part of the approximate solution ψ , where $\beta = 1.8$.

References

- [1] E.F. Hefter, Application of the nonlinear Schrödinger equation with a logarithmic inhomogeneous term to nuclear physics, *Physical Review A* 32 (2) (1985) 1201.
- [2] E. Schrödinger, An undulatory theory of the mechanics of atoms and molecules, *Physical Review* 28 (6) (1926) 1049.
- [3] N. Zettili, *Quantum Mechanics: Concepts and Applications*, 2nd ed., John Wiley and Sons, New York, 2009.
- [4] W.J. Sonnier, Dynamics of repelling soliton collisions in coupled Schrödinger equations, *Wave Motion* 48 (8) (2011) 805–813.
- [5] N. Laskin, Fractional quantum mechanics and Lévy path integrals, *Physics Letters A* 268 (4–6) (2000) 298–305.

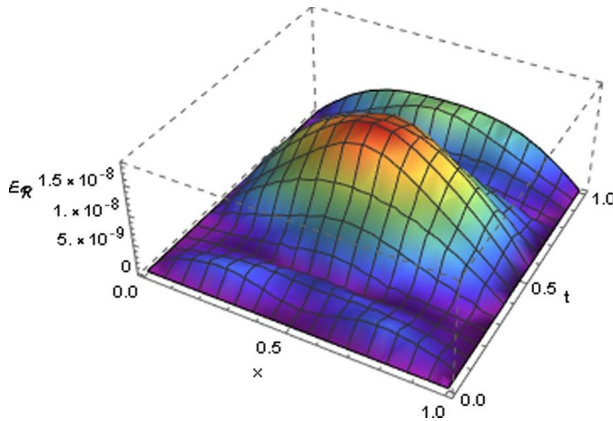


Figure 12.20 Evaluation of the absolute errors of the real part of the approximate solution ϕ , where $\beta = 1.8$.

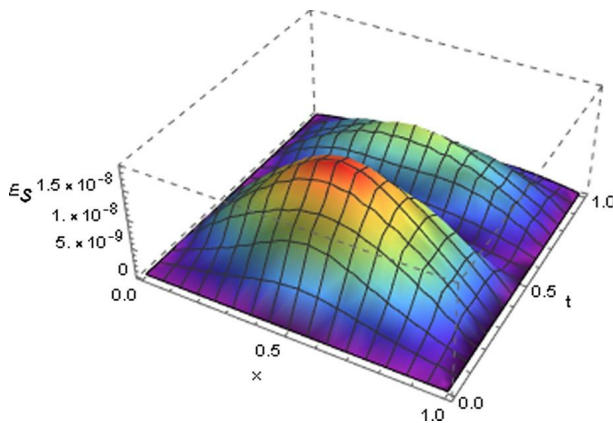


Figure 12.21 Evaluation of the absolute errors of the imaginary part of the approximate solution ϕ , where $\beta = 1.8$.

- [6] B.A. Stickler, Potential condensed-matter realization of space-fractional quantum mechanics: the one-dimensional Lévy crystal, *Physical Review E* 88 (1) (2013) 012120.
- [7] S. Longhi, Fractional Schrödinger equation in optics, *Optics Letters* 40 (6) (2015) 1117–1120.
- [8] X. Guo, M. Xu, Some physical applications of fractional Schrödinger equation, *Journal of Mathematical Physics* 47 (8) (2006) 082104.
- [9] B. Guo, Y. Han, J. Xin, Existence of the global smooth solution to the period boundary value problem of fractional nonlinear Schrödinger equation, *Applied Mathematics and Computation* 204 (1) (2008) 468–477.
- [10] J. Hu, J. Xin, H. Lu, The global solution for a class of systems of fractional nonlinear Schrödinger equations with periodic boundary condition, *Computers & Mathematics with Applications* 62 (3) (2011) 1510–1521.

- [11] Y. Cho, G. Hwang, S. Kwon, S. Lee, Well-posedness and ill-posedness for the cubic fractional Schrödinger equations, *Discrete and Continuous Dynamical Systems. Series A* 35 (7) (2015) 2863.
- [12] R. Metzler, J. Klafter, The random walk's guide to anomalous diffusion: a fractional dynamics approach, *Physics Reports* 339 (1) (2000) 1–77.
- [13] M. Naber, Time fractional Schrödinger equation, *Journal of Mathematical Physics* 45 (8) (2004) 3339–3352.
- [14] J.T. Machado, V. Kiryakova, F. Mainardi, Recent history of fractional calculus, *Communications in Nonlinear Science and Numerical Simulation* 16 (3) (2011) 1140–1153.
- [15] J. Dong, M. Xu, Space–time fractional Schrödinger equation with time-independent potentials, *Journal of Mathematical Analysis and Applications* 344 (2) (2008) 1005–1017.
- [16] S. Wang, M. Xu, Generalized fractional Schrödinger equation with space-time fractional derivatives, *Journal of Mathematical Physics* 48 (4) (2007) 043502.
- [17] M.A. Zaky, A.S. Hendy, J.E. Macías-Díaz, High-order finite difference/spectral-Galerkin approximations for the nonlinear time–space fractional Ginzburg–Landau equation, *Numerical Methods for Partial Differential Equations* (2020) 1–26, <https://doi.org/10.1002/num.22630>.
- [18] H. Abo-Gabal, M.A. Zaky, R.M. Hafez, E.H. Doha, On Romanovski–Jacobi polynomials and their related approximation results, *Numerical Methods for Partial Differential Equations* 36 (6) (2020) 1982–2017.
- [19] M.A. Zaky, An accurate spectral collocation method for nonlinear systems of fractional differential equations and related integral equations with nonsmooth solutions, *Applied Numerical Mathematics* 154 (2020) 205–222.
- [20] A.S. Hendy, M.A. Zaky, Graded mesh discretization for coupled system of nonlinear multi-term time-space fractional diffusion equations, *Engineering With Computers* (2020) 1–13.
- [21] M.A. Zaky, I.G. Ameen, A novel Jacob spectral method for multi-dimensional weakly singular nonlinear Volterra integral equations with nonsmooth solutions, *Engineering With Computers* (2020) 1–9.
- [22] M.A. Zaky, J.A. Tenreiro Machado, Multi-dimensional spectral tau methods for distributed-order fractional diffusion equations, *Computers & Mathematics with Applications* 79 (2) (2020) 476–488.
- [23] M.A. Zaky, Recovery of high order accuracy in Jacobi spectral collocation methods for fractional terminal value problems with non-smooth solutions, *Journal of Computational and Applied Mathematics* 357 (2019) 103–122.
- [24] M.A. Zaky, I.G. Ameen, N.A. Elkot, E.H. Doha, A unified spectral collocation method for nonlinear systems of multi-dimensional integral equations with convergence analysis, *Applied Numerical Mathematics* 161 (2021) 27–45.
- [25] R.M. Hafez, M.A. Zaky, M.A. Abdelkawy, Jacobi spectral Galerkin method for distributed-order fractional Rayleigh–Stokes problem for a generalized second grade fluid, *Frontiers in Physics* 7 (2019) 240.
- [26] A.H. Bhrawy, M.A. Zaky, An improved collocation method for multi-dimensional space–time variable-order fractional Schrödinger equations, *Applied Numerical Mathematics* 111 (2017) 197–218.
- [27] A.H. Bhrawy, M.A. Zaky, Highly accurate numerical schemes for multi-dimensional space variable-order fractional Schrödinger equations, *Computers & Mathematics with Applications* 73 (6) (2017) 1100–1117.
- [28] A.H. Bhrawy, M.A. Zaky, Numerical simulation of multi-dimensional distributed-order generalized Schrödinger equations, *Nonlinear Dynamics* 89 (2) (2017) 1415–1432.

- [29] A.H. Bhrawy, M.A. Abdelkawy, A fully spectral collocation approximation for multi-dimensional fractional Schrödinger equations, *Journal of Computational Physics* 294 (2015) 462–483.
- [30] A.H. Bhrawy, F. Mallawi, M.A. Abdelkawy, New spectral collocation algorithms for one- and two-dimensional Schrödinger equations with a Kerr law nonlinearity, *Advances in Difference Equations* 2016 (1) (2016) 18.
- [31] A.H. Bhrawy, J.F. Alzaidy, M.A. Abdelkawy, A. Biswas, Jacobi spectral collocation approximation for multi-dimensional time-fractional Schrödinger equations, *Nonlinear Dynamics* 84 (3) (2016) 1553–1567.
- [32] N.H. Sweilam, T.A. Assiri, M.M. Abou Hasan, Numerical solutions of nonlinear fractional Schrödinger equations using nonstandard discretizations, *Numerical Methods for Partial Differential Equations* 33 (5) (2017) 1399–1419.
- [33] N.H. Sweilam, M.M. Abou Hasan, Numerical solutions for 2-D fractional Schrödinger equation with the Riesz–Feller derivative, *Mathematics and Computers in Simulation* 140 (2017) 53–68.
- [34] N.H. Sweilam, M.M. Abou Hasan, Numerical studies for the fractional Schrödinger equation with the quantum Riesz–Feller derivative, *Progress in Fractional Differentiation and Applications* 2 (4) (2016) 231–245.
- [35] A.H. Bhrawy, E.H. Doha, S.S. Ezz-Eldien, R.A. Van Gorder, A new Jacobi spectral collocation method for solving $1 + 1$ fractional Schrödinger equations and fractional coupled Schrödinger systems, *The European Physical Journal Plus* 129 (12) (2014) 260.
- [36] A.S. Hendy, M.A. Zaky, Global consistency analysis of L1-Galerkin spectral schemes for coupled nonlinear space-time fractional Schrödinger equations, *Applied Numerical Mathematics* 156 (2020) 276–302.
- [37] M.A. Zaky, A.S. Hendy, Convergence analysis of an L1-continuous Galerkin method for nonlinear time-space fractional Schrödinger equations, *International Journal of Computer Mathematics* 89 (2020) 1420–1437.
- [38] A.S. Hendy, M.A. Zaky, R.M. Hafez, R.H. De Staelen, The impact of memory effect on space fractional strong quantum couplers with tunable decay behavior and its numerical simulation, *Scientific Reports* 11 (2021) 10275.
- [39] M. Li, C. Huang, P. Wang, Galerkin finite element method for nonlinear fractional Schrödinger equations, *Numerical Algorithms* 74 (2) (2017) 499–525.
- [40] D. Wang, A. Xiao, W. Yang, Crank–Nicolson difference scheme for the coupled nonlinear Schrödinger equations with the Riesz space fractional derivative, *Journal of Computational Physics* 242 (2013) 670–681.
- [41] H. Zhang, X. Jiang, Spectral method and Bayesian parameter estimation for the space fractional coupled nonlinear Schrödinger equations, *Nonlinear Dynamics* 95 (2) (2019) 1599–1614.
- [42] M. Ran, C. Zhang, A conservative difference scheme for solving the strongly coupled nonlinear fractional Schrödinger equations, *Communications in Nonlinear Science and Numerical Simulation* 41 (2016) 64–83.
- [43] M.A. Zaky, A.S. Hendy, J.E. Macías-Díaz, Semi-implicit Galerkin–Legendre spectral schemes for nonlinear time-space fractional diffusion–reaction equations with smooth and nonsmooth solutions, *Journal of Scientific Computing* 82 (1) (2020) 13.
- [44] M.A. Zaky, I.G. Ameen, A priori error estimates of a Jacobi spectral method for nonlinear systems of fractional boundary value problems and related Volterra–Fredholm integral equations with smooth solutions, *Numerical Algorithms* 84 (2020) 63–89.
- [45] R.M. Hafez, M.A. Zaky, High-order continuous Galerkin methods for multi-dimensional advection–reaction–diffusion problems, *Engineering With Computers* (2019) 1–17.

- [46] S.S. Ezz-Eldien, Y. Wang, M.A. Abdelkawy, M.A. Zaky, A.A. Aldraiweesh, J.T. Machado, Chebyshev spectral methods for multi-order fractional neutral pantograph equations, *Nonlinear Dynamics* 100 (2020) 3785–3797.
- [47] P. Barthélemy, J. Bertolotti, D.S. Wiersma, A Lévy flight for light, *Nature* 453 (7194) (2008) 495–498.
- [48] C. Conti, N. Ghofraniha, G. Ruocco, S. Trillo, Laser beam filamentation in fractal aggregates, *Physical Review Letters* 97 (12) (2006) 123903.
- [49] Yiqi Zhang, Hua Zhong, Milivoj R. Belić, Yi Zhu, Weiping Zhong, Yanpeng Zhang, Demetrios N. Christodoulides, Min Xiao, PT symmetry in a fractional Schrödinger equation, *Laser & Photonics Reviews* 10 (3) (2016) 526–531.
- [50] Y. Zhang, X. Liu, M.R. Belić, W. Zhong, Y. Zhang, M. Xiao, Propagation dynamics of a light beam in a fractional Schrödinger equation, *Physical Review Letters* 115 (18) (2015) 180403.
- [51] D. Zhang, Y. Zhang, Z. Zhang, N. Ahmed, Y. Zhang, F. Li, M.R. Belić, M. Xiao, Unveiling the link between fractional Schrödinger equation and light propagation in honeycomb lattice, *Annalen der Physik* 529 (9) (2017) 1700149.
- [52] A. Liemert, A. Kienle, Fractional Schrödinger equation in the presence of the linear potential, *Mathematics* 4 (2) (2016) 31.
- [53] M. Solaimani, S. Dong, Quantum information entropies of multiple quantum well systems in fractional Schrödinger equations, *International Journal of Quantum Chemistry* 120 (5) (2020) e26113.
- [54] P. Zhuang, F. Liu, V. Anh, I. Turner, Numerical methods for the variable-order fractional advection-diffusion equation with a nonlinear source term, *SIAM Journal on Numerical Analysis* 47 (3) (2009) 1760–1781.
- [55] Z. Xie, L.-L. Wang, X. Zhao, On exponential convergence of Gegenbauer interpolation and spectral differentiation, *Mathematics of Computation* 82 (282) (2013) 1017–1036.
- [56] C. Canuto, M.Y. Hussaini, A. Quarteroni, T.A. Zang, *Spectral Methods: Fundamentals in Single Domains*, Springer Science & Business Media, 2007.
- [57] E.H. Doha, A.H. Bhrawy, M.A. Abdelkawy, R.A. Van Gorder, Jacobi–Gauss–Lobatto collocation method for the numerical solution of 1 + 1 nonlinear Schrödinger equations, *Journal of Computational Physics* 261 (2014) 244–255.
- [58] M.A. Zaky, S.S. Ezz-Eldien, E.H. Doha, J.A. Tenreiro Machado, A.H. Bhrawy, An efficient operational matrix technique for multidimensional variable-order time fractional diffusion equations, *Journal of Computational and Nonlinear Dynamics* 11 (6) (2016) 1–8.
- [59] M.A. Zaky, E.H. Doha, J.A. Tenreiro Machado, A spectral numerical method for solving distributed-order fractional initial value problems, *Journal of Computational and Nonlinear Dynamics* 13 (10) (2018) 1–6.
- [60] S.S. Ezz-Eldien, E.H. Doha, Y. Wang, W. Cai, A numerical treatment of the two-dimensional multi-term time-fractional mixed sub-diffusion and diffusion-wave equation, *Communications in Nonlinear Science and Numerical Simulation* 91 (2020) 105445.
- [61] S.S. Ezz-Eldien, E.H. Doha, Fast and precise spectral method for solving pantograph type Volterra integro-differential equations, *Numerical Algorithms* 81 (1) (2019) 57–77.
- [62] J.C. Butcher, Implicit Runge-Kutta processes, *Mathematics of Computation* 18 (85) (1964) 50–64.
- [63] K. Atkinson, W. Han, D.E. Stewart, *Numerical Solution of Ordinary Differential Equations*, vol. 108, John Wiley & Sons, 2011.
- [64] Z. Yang, A class of linearized energy-conserved finite difference schemes for nonlinear space-fractional Schrödinger equations, *International Journal of Computer Mathematics* 93 (3) (2016) 609–626.

This page intentionally left blank

Transmission line modeling by fractional and topological generalization of the telegrapher's equation

Dušan Zorica^{a,b} and Stevan M. Cvetičanin^c

^aSerbian Academy of Arts and Sciences, Mathematical Institute, Beograd, Serbia

^bUniversity of Novi Sad, Faculty of Sciences, Department of Physics, Novi Sad, Serbia

^cUniversity of Novi Sad, Faculty of Technical Sciences, Department of Power, Electronic and Telecommunication Engineering, Novi Sad, Serbia

13.1. Classical and fractional telegrapher's equations

Using the traditional approach, a transmission line (TL) is modeled using Heaviside's elementary circuit shown in Fig. 13.1, which consists of the inductor of inductivity ΔL [H] and the resistor of resistivity ΔR [Ω] in its series branch, modeling magnetic field effects, a part of energy loss, and voltage drop along the line, as well as of the capacitor of capacitivity ΔC [F] and the resistor of conductivity ΔG [S] in its shunt branch, modeling electric field effects, a part of energy loss, and current leakage. Assuming instantaneous connection of the physical quantities describing accumulative electric elements for all time instants $t > 0$, the classical constitutive relations for inductor and capacitor

$$\phi(t) = \Delta L i_L(t) \quad \text{and} \quad q(t) = \Delta C u_C(t), \quad (13.1)$$

where ϕ and i_L are inductor magnetic flux and current, while q and u_C are capacitor charge and voltage, by the Faraday law of electromagnetic induction and the definition of electric current imply the inductor voltage and capacitor current as

$$u_L(t) = \frac{d}{dt}\phi(t) = \Delta L \frac{d}{dt}i_L(t) \quad \text{and} \quad i_C(t) = \frac{d}{dt}q(t) = \Delta C \frac{d}{dt}u_C(t),$$

so that by applying Kirchhoff's laws to the elementary circuit from Fig. 13.1, which is of length Δx and located at position x along the TL, and

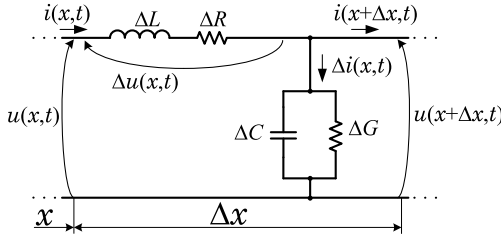


Figure 13.1 Elementary circuit of classical TL model.

after the passage to the continuum, i.e., in the limit $\Delta x \rightarrow 0$, the classical telegrapher's equation (TE)

$$\left(LC \frac{\partial^2}{\partial t^2} + (LG + RC) \frac{\partial}{\partial t} + RG \right) u(x, t) = \frac{\partial^2}{\partial x^2} u(x, t) \quad (13.2)$$

is derived, where the model parameters inductance, resistance, capacitance, and conductance by-length are respectively given by

$$L = \lim_{\Delta x \rightarrow 0} \frac{\Delta L}{\Delta x} \left[\frac{\text{H}}{\text{m}} \right], \quad R = \lim_{\Delta x \rightarrow 0} \frac{\Delta R}{\Delta x} \left[\frac{\Omega}{\text{m}} \right],$$

$$C = \lim_{\Delta x \rightarrow 0} \frac{\Delta C}{\Delta x} \left[\frac{\text{F}}{\text{m}} \right], \quad G = \lim_{\Delta x \rightarrow 0} \frac{\Delta G}{\Delta x} \left[\frac{\text{S}}{\text{m}} \right],$$

as Oliver Heaviside has done in [22]. Heaviside's contributions in the analysis of classical electric TLs and electromagnetic theory are accounted for in the survey paper [12]. The alternative form

$$K^2 \left(\tau_L \tau_C \frac{\partial^2}{\partial t^2} + (\tau_L + \tau_C) \frac{\partial}{\partial t} + 1 \right) u(x, t) = \frac{\partial^2}{\partial x^2} u(x, t)$$

of the classical TE (13.2) is obtained by introducing a static attenuation coefficient $K = \sqrt{RG}$ [m^{-1}] and time constants $\tau_L = \frac{L}{R}$ [s], $\tau_C = \frac{C}{G}$ [s], giving the characteristic time of the charge/discharge of energy accumulated in the inductor through the resistor in the series branch, as well of the energy accumulated in the capacitor through the resistor in the shunt branch. The classical TE (13.2) is the wave type equation in the sense that the signal propagation speed is finite and determined by

$$c = \frac{1}{\sqrt{LC}} = \frac{1}{K \sqrt{\tau_L \tau_C}} \left[\frac{\text{m}}{\text{s}} \right], \quad (13.3)$$

thanks to the term containing the second-order time partial derivative of voltage, however displaying the dissipation effects as well, which are due to the term containing the first-order time derivative of voltage and the term linear in voltage. Solitary waves, representing the solutions of the classical TE, are analyzed in [37,48,51], while the traveling waves solutions are reported in [44]. Signals in nonlinear TLs, assumed as solitons and in the elliptic forms, are studied in [27]. The classical TE (13.2) proved to be a good model for signal transmission in classical conductors and also through the large-scale systems. In particular, the use of the classical TE (13.2) is reasonable when modeling low-frequency power TLs. On the other hand, the classical TE proved inadequate (see [46]) in modeling transmission of high-frequency signals of terahertz order, i.e., in modeling THz lines and composite right/left-handed TLs (CRLHT lines), where the fractional TL models are proved to be more adequate.

If an electric signal is transmitted through some more exotic material, or through a small-scale system, the instantaneous constitutive relations for inductor and capacitor (13.1) might become inappropriate, since the hereditarity of magnetization and polarization processes in material might be prominent; hence the magnetic flux and current in the inductor, so as the charge and voltage in capacitor, are connected through the phenomenological constitutive relations

$$\phi(t) = \Delta L_{\xi} {}_0I_t^{1-\xi} i_L(t) \quad \text{and} \quad q(t) = \Delta C_{\xi} {}_0I_t^{1-\xi} u_C(t), \quad \xi \in (0, 1), \quad (13.4)$$

with ΔL_{ξ} and ΔC_{ξ} denoting the fractional inductance and capacitance measured in $\text{Hs}^{\xi-1}$ and $\text{Fs}^{\xi-1}$, which account for the long tail memory through the hereditarity kernel assumed as the power type function, due to the Riemann–Liouville fractional integral

$${}_0I_t^{\xi} f(t) = \frac{1}{\Gamma(\xi)} \int_0^t (t-\tau)^{\xi-1} f(\tau) d\tau = \frac{t^{\xi-1}}{\Gamma(\xi)} * f(t), \quad \xi > 0,$$

where Γ is the Euler Gamma function and $*$ denotes the convolution, defined by $f(t) * g(t) = \int_0^t f(t') g(t-t') dt'$ for the causal function. For more details regarding the field of fractional calculus and its various applications see for example [28,38]. Using the Faraday law of electromagnetic induction and the definition of the current, constitutive relations (13.4) for the fractional inductor and capacitor become

$$u_L(t) = \frac{d}{dt} \phi(t) = \Delta L_{\xi} \frac{d}{dt} {}_0I_t^{1-\xi} i_L(t) = \Delta L_{\xi} {}_0D_t^{\xi} i_L(t), \quad (13.5)$$

$$i_C(t) = \frac{d}{dt}q(t) = \Delta C_\xi \frac{d}{dt} {}_0I_t^{1-\xi} u_C(t) = \Delta C_\xi {}_0D_t^\xi u_C(t), \quad (13.6)$$

where ${}_0D_t^\xi$ stands for the Riemann–Liouville fractional derivative of order $\xi \in (0, 1)$, defined by

$${}_0D_t^\xi f(t) = \frac{d}{dt} {}_0I_t^{1-\xi} f(t) = \frac{d}{dt} \left(\frac{t^{-\xi}}{\Gamma(1-\xi)} * f(t) \right). \quad (13.7)$$

Constitutive equation (13.5) for the fractional inductor describes the element with performance between resistor and classical inductor, obtained in the limiting cases of the fractional differentiation orders $\xi = 0$ and $\xi = 1$, respectively, while the model of fractional capacitor (13.6) describes the element with performance between resistor and classical capacitor in the same limiting cases.

The phenomenological constitutive relations (13.4) take into account only the hereditary effects of the element, while in [20] the instantaneous contribution corresponding to the classical element is also included into the constitutive model, thus yielding

$$\begin{aligned} \phi(t) &= \Delta L i_L(t) + \Delta L_\xi {}_0I_t^{1-\xi} i_L(t) \quad \text{and} \\ q(t) &= \Delta C u_C(t) + \Delta C_\xi {}_0I_t^{1-\xi} u_C(t), \quad \xi \in (0, 1), \end{aligned} \quad (13.8)$$

which, by thermodynamic considerations, proved to model the dissipative electric elements, contrary to

$$\begin{aligned} i_L(t) &= \frac{1}{\Delta L} \phi(t) + \frac{1}{\Delta L_\xi} {}_0I_t^{1-\xi} \phi(t) \quad \text{and} \\ u_C(t) &= \frac{1}{\Delta C} q(t) + \frac{1}{\Delta C_\xi} {}_0I_t^{1-\xi} q(t), \quad \xi \in (0, 1), \end{aligned}$$

which model generative electric elements. Constitutive models (13.8) are further used in [21] to model electric elements in *RLC* circuits in transient and steady-state regimes. In [24,25], the constitutive equations (13.5) and (13.6) are generalized by including the instantaneous effects through the term corresponding to the resistor, rather than the classical inductor or capacitor, and further used in modeling the transient response of series and parallel connections of such generalized electric elements.

A constitutive equation similar to (13.5) is used in [45] in modeling magnetic core coils, while the electrochemical double layer capacitors (EDLCs), or supercapacitors or ultracapacitors, are often modeled using the fractional capacitor in an equivalent electrical scheme (see

[13,14,26,35,40]). The fractional electric elements are fabricated with pre-defined specifications (see [29,36]) and the analysis of electric circuits containing such elements is performed in [15,47], while the fractional *RLC* filters are studied in [41,42]. Coils and resistors, modeled using the fractional approach, are used to model the skin effect in [34].

The assumption that the accumulative electric elements, appearing in the elementary circuit from Fig. 13.1, are of the hereditary type and modeled by the constitutive relations (13.4) leads to the fractional generalization of the classical TE (13.2), obtained as

$$(L_\mu C_v {}_0D_t^{\mu+\nu} + L_\mu G {}_0D_t^\mu + RC_v {}_0D_t^\nu + RG) u(x, t) = \frac{\partial^2}{\partial x^2} u(x, t), \quad (13.9)$$

with the fractional inductance and capacitance by-length given by

$$L_\mu = \lim_{\Delta x \rightarrow 0} \frac{\Delta L_\mu}{\Delta x} \left[\frac{\text{H s}^{\mu-1}}{\text{m}} \right], \quad C_v = \lim_{\Delta x \rightarrow 0} \frac{\Delta C_v}{\Delta x} \left[\frac{\text{F s}^{\nu-1}}{\text{m}} \right],$$

which rewritten in terms of the attenuation coefficient K and fractional time constants $\tau_\mu = \frac{L_\mu}{R}$ [s $^\mu$] and $\tau_\nu = RC_\nu$ [s $^\nu$] takes the form

$$K^2 (\tau_\mu \tau_\nu {}_0D_t^{\mu+\nu} + \tau_\mu {}_0D_t^\mu + \tau_\nu {}_0D_t^\nu + 1) u(x, t) = \frac{\partial^2}{\partial x^2} u(x, t),$$

where the highest order of the fractional time derivative can be either $\mu + \nu \in (0, 1)$ or $\mu + \nu \in (1, 2)$, in which case the Riemann–Liouville derivative of order $\xi + n \in (n, n + 1)$, $n \in \mathbb{N}_0$, is defined by

$${}_0D_t^{\xi+n} f(t) = \frac{d^{n+1}}{dt^{n+1}} {}_0I_t^{1-\xi} f(t) = \frac{d^{n+1}}{dt^{n+1}} \left(\frac{t^{-\xi}}{\Gamma(1-\xi)} * f(t) \right).$$

Due to the fractional derivatives, being the consequences of the generalization of elements' constitutive equation, the fractional TE (13.9) is nonlocal in time, while nonlocality in space may be achieved by considering the classical elements' models and assuming the magnetic coupling between inductors in all elementary circuits through the superposition of local and nonlocal magnetic fluxes, yielding

$$\phi = \phi_L + \phi_{\text{NL}}, \quad \text{with}$$

$$\phi_L(x, t) = L i(x, t) \quad \text{and} \quad \phi_{\text{NL}}(x, t) = \int_a^b m(x, \xi) i(\xi, t) d\xi,$$

in the continuum limit, with the cross-inductivity kernel m constitutively given, leading to the nonlocal TE, derived and analyzed in [10].

Fractionalizing the inductor and capacitor appearing in the elementary circuit, the frequency characteristics of such obtained fractional TE are analyzed analytically, while the Laplace transform inversion is performed by numerical methods in [2,3]. The space and time fractionalization of TE in [17–19] is performed by replacing the integer-order derivatives with the fractional ones, with the solutions of TE assumed as plane waves. The diffusion of ions in nerve cells, i.e., electro-diffusion in spiny dendrites, can also be described by the fractional TE, like in [7,23,30–33,49,52].

Introducing simultaneous fractionalization of accumulative elements' constitutive models and topological modifications of the elementary circuit, as shown in Fig. 13.2, not only the hereditary effects in material polarization and magnetization, described by the fractional models (13.5) and (13.6) for inductor and capacitor, are taken into account instead of the instantaneous polarization and magnetization effects accounted for by the classical constitutive models (13.1), but also the charge accumulation effects along the TL are included by introducing the additional fractional capacitor in the series branch of the elementary circuit, which is either in parallel connection with the resistor, as in Fig. 13.2a, or in series connection with the resistor, as in Fig. 13.2b.

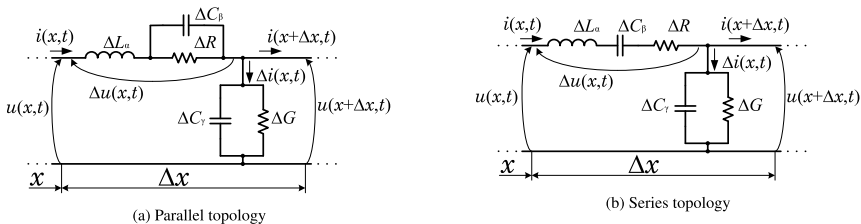


Figure 13.2 Topological modifications of the classical elementary circuit.

The differences in modeling charge accumulation effects using elementary circuits from Fig. 13.2 lie in the origin of energy losses and magnetic phenomena, since the energy losses are due to the motion of either free charges, in the case of parallel topology from Fig. 13.2a, or polarization charges, in the case of series topology from Fig. 13.2b, while magnetic phenomena are due to the total current, consisting of the motion of both free and polarization charges, in the case of parallel topology, and only of the motion of polarization charges in the case of series topology

(Figs. 13.2a and 13.2b, respectively). Further differences between topologies lie in characteristics of signal transmission, since for low signal frequencies transmission is either allowed, in the case of parallel topology, or blocked, in the case of series topology, due to the capacitor in the series branch, while in the case of both topologies the high-frequency signal transmission is blocked, due to the inductor in the series branch. Therefore, parallel topology corresponds to the band-pass filter, while the series topology corresponds to the low-pass filter. Moreover, the parallel topology behaves similarly to the classical one regarding the signal transmission at both high and low frequencies.

The fractional TE corresponding to the parallel topology from Fig. 13.2a takes two equivalent forms:

$$\begin{aligned} (L_\alpha C_\beta C_\gamma R_0 D_t^{\alpha+\beta+\gamma} + L_\alpha C_\beta R G_0 D_t^{\alpha+\beta} + L_\alpha C_\gamma {}_0D_t^{\alpha+\gamma} + L_\alpha G_0 D_t^\alpha \\ + R C_\gamma {}_0D_t^\gamma + R G) u(x, t) = \left(R C_\beta {}_0D_t^\beta + 1 \right) \frac{\partial^2}{\partial x^2} u(x, t) \end{aligned} \quad (13.10)$$

and

$$\begin{aligned} (L_\alpha C_\beta C_\gamma R_0 D_t^{\alpha+\gamma} + L_\alpha C_\beta R G_0 D_t^\alpha + L_\alpha C_\gamma {}_0D_t^{\alpha+\gamma} {}_0I_t^\beta + L_\alpha G_0 D_t^\alpha {}_0I_t^\beta \\ + R C_\gamma {}_0D_t^\gamma {}_0I_t^\beta + R G_0 I_t^\beta) u(x, t) = \left(R C_\beta + {}_0I_t^\beta \right) \frac{\partial^2}{\partial x^2} u(x, t), \end{aligned} \quad (13.11)$$

while the fractional TE corresponding to the series topology from Fig. 13.2b, is written either in the form

$$\begin{aligned} (L_\alpha C_\beta C_\gamma {}_0D_t^{\alpha+\beta+\gamma} + L_\alpha C_\beta G_0 D_t^{\alpha+\beta} + C_\beta C_\gamma R_0 D_t^{\beta+\gamma} + C_\beta R G_0 D_t^\beta \\ + C_\gamma {}_0D_t^\gamma + G) u(x, t) = C_\beta {}_0D_t^\beta \frac{\partial^2}{\partial x^2} u(x, t) \end{aligned} \quad (13.12)$$

or in the form

$$\begin{aligned} (L_\alpha C_\beta C_\gamma {}_0D_t^{\alpha+\gamma} + L_\alpha C_\beta G_0 D_t^\alpha + C_\beta C_\gamma R_0 D_t^\gamma + C_\beta R G \\ + C_\gamma {}_0D_t^\gamma {}_0I_t^\beta + G_0 I_t^\beta) u(x, t) = C_\beta \frac{\partial^2}{\partial x^2} u(x, t), \end{aligned} \quad (13.13)$$

where in addition to the previously defined resistance and conductance by-length, fractional inductance and capacitance by-length as well as the

fractional relaxation time are introduced by

$$L_\alpha = \lim_{\Delta x \rightarrow 0} \frac{\Delta L_\alpha}{\Delta x} \left[\frac{H s^{\alpha-1}}{m} \right], \quad C_\gamma = \lim_{\Delta x \rightarrow 0} \frac{\Delta C_\gamma}{\Delta x} \left[\frac{F s^{\gamma-1}}{m} \right],$$

$$RC_\beta = \lim_{\Delta x \rightarrow 0} (\Delta R \Delta C_\beta) [s^\beta].$$

It appears that the fractional TEs (13.10) and (13.12) are of the order belonging to the interval $(0, 3)$, since $\alpha, \beta, \gamma \in (0, 1)$, implying that the TEs (13.10) and (13.12), apart from the subdiffusion and diffusion-wave phenomena, having the equation orders belonging to $(0, 1)$ and $(1, 2)$, respectively, cover phenomena modeled by the equation of order higher than the order of the wave equation. However, it is obvious from the equivalent forms of the fractional TEs (13.11) and (13.13) that the highest order of fractional differentiation is $\alpha + \gamma \in (0, 2)$, since the differentiation operator of order β on the right-hand side of (13.10) and (13.12), unlike the integral operator on the right-hand side of (13.11) and (13.13), actually reduces the order of TEs. Thus, if $\alpha + \gamma \in (0, 1)$ in (13.11) and (13.13), then one expects the impulse response of the diffusive type, while if $\alpha + \gamma \in (1, 2)$ in (13.11) and (13.13), then the wave type response is expected. The diffusive or wave type response refers to the propagation of the impulse response's peak in space during time, while the wave propagation speed, given by (13.3) for the classical TE (13.2), defining the furthestmost position in space reached by the response during its propagation time, is not obtained to be finite. Fractional TE (13.10), corresponding to the parallel topology, is derived in the time domain in [8] and the transient impulse response is analytically obtained and numerically verified.

Similarly as the classical TE (13.2) and the fractional TE (13.9), TEs (13.10)–(13.13) are derived in the time domain by reducing the system of fractional TEs, obtained by applying Kirchhoff's laws to the elementary circuit with the accumulative elements modeled by the fractional constitutive relations (13.5) and (13.6), and subsequently by the continuum limit $\Delta x \rightarrow 0$. Derivation of TEs can also be performed in the complex domain by considering the impedance of the series and admittance of the shunt branch of the elementary circuit and subsequently using the continuum limit and the inverse Laplace transform. Both types of derivations are performed in Section 13.3.

The equivalent models (13.10) and (13.11) of the hereditary TL corresponding to the parallel topology take the form

$$K^2(\tau_\alpha \tau_\beta \tau_\gamma {}_0D_t^{\alpha+\beta+\gamma} + \tau_\alpha \tau_\beta {}_0D_t^{\alpha+\beta} + \tau_\alpha \tau_\gamma {}_0D_t^{\alpha+\gamma} + \tau_\alpha {}_0D_t^\alpha + \tau_\gamma {}_0D_t^\gamma + 1)u(x, t) = \left(\tau_\beta {}_0D_t^\beta + 1\right) \frac{\partial^2}{\partial x^2} u(x, t), \quad (13.14)$$

$$K^2(\tau_\alpha \tau_\beta \tau_\gamma {}_0D_t^{\alpha+\gamma} + \tau_\alpha \tau_\beta {}_0D_t^\alpha + \tau_\alpha \tau_\gamma {}_0D_t^{\alpha+\gamma} {}_0I_t^\beta + \tau_\alpha {}_0D_t^\alpha {}_0I_t^\beta + \tau_\gamma {}_0D_t^\gamma {}_0I_t^\beta + {}_0I_t^\beta)u(x, t) = \left(\tau_\beta + {}_0I_t^\beta\right) \frac{\partial^2}{\partial x^2} u(x, t), \quad (13.15)$$

while the models (13.12) and (13.13), corresponding to the series topology, are of the form

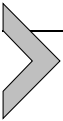
$$K^2(\tau_\alpha \tau_\beta \tau_\gamma {}_0D_t^{\alpha+\beta+\gamma} + \tau_\alpha \tau_\beta {}_0D_t^{\alpha+\beta} + \tau_\beta \tau_\gamma {}_0D_t^{\beta+\gamma} + \tau_\beta {}_0D_t^\beta + \tau_\gamma {}_0D_t^\gamma + 1)u(x, t) = \tau_\beta {}_0D_t^\beta \frac{\partial^2}{\partial x^2} u(x, t), \quad (13.16)$$

$$K^2(\tau_\alpha \tau_\beta \tau_\gamma {}_0D_t^{\alpha+\gamma} + \tau_\alpha \tau_\beta {}_0D_t^\alpha + \tau_\beta \tau_\gamma {}_0D_t^\gamma + \tau_\beta + \tau_\gamma {}_0D_t^\gamma {}_0I_t^\beta + {}_0I_t^\beta)u(x, t) = \tau_\beta \frac{\partial^2}{\partial x^2} u(x, t), \quad (13.17)$$

if rewritten in terms of the static attenuation coefficient K and fractional time constants $\tau_\alpha = \frac{L_\alpha}{R}$ [s^α], $\tau_\beta = RC_\beta$ [s^β], and $\tau_\gamma = \frac{C_\gamma}{G}$ [s^γ]. The time constant τ_α describes the dynamics of magnetic flux in the fractional inductor, facilitated by the series branch resistor, while the time constants τ_β and τ_γ describe the dynamics of charge accumulation on the fractional capacitor, facilitated by the series branch resistor and the shunt branch conductor, respectively.

Frequency characteristics of the fractional TEs (13.14) and (13.16), corresponding to the parallel and series topologies, are analyzed in [9] along with their asymptotics. The fractional inductor can also be included into the shunt branch of the elementary circuit, like in [50], and moreover, the classical elementary circuit is extended into two dimensions, as done in [16].

The aim is to review and extend the results on the derivation, transient regime response, frequency, and asymptotic analysis of the fractional TE as the hereditary TL model, published in [9].



13.2. Reduction of fractional telegrapher's equations to special cases

The elementary circuit from Fig. 13.2 represents the topological modification of Heaviside's elementary circuit from Fig. 13.1, which introduces the additional capacitor in the series branch, having also the constitutive models of all accumulative electric elements generalized using fractional constitutive relations (13.4). The aim is to investigate TL models originating from the elementary circuit from Fig. 13.2 for the limiting cases of the parameters appearing in the constitutive equation of the additional fractional capacitor

$$i_C(t) = \Delta C_\beta {}_0D_t^\beta u_C(t), \quad \beta \in (0, 1),$$

(see also (13.6)), which becomes an open circuit if $\Delta C_\beta = 0$, a short circuit if $\Delta C_\beta \rightarrow \infty$, a resistor of conductance ΔC_β if $\beta = 0$, and a classical capacitor if $\beta = 1$, as well as in the cases of an ideal conductive element ($\Delta R = 0$) and an ideal insulative element ($\Delta G = 0$).

Although an ideal insulative element ($\Delta G = 0$) is assumed in the elementary circuits from Fig. 13.2, the shunt branch remains conductive due to the fractional capacitor ΔC_γ , which is an element between classical resistor and capacitor, implying special models of the TL

$$K^2(\tau_\lambda \tau_\mu \tau_\nu {}_0D_t^{\lambda+\mu+\nu} + \tau_\lambda \tau_\mu {}_0D_t^{\lambda+\mu} + \tau_\lambda {}_0D_t^\lambda)u(x, t) = (\tau_\nu {}_0D_t^\nu + 1) \frac{\partial^2}{\partial x^2} u(x, t),$$

$$K^2(\tau_\lambda \tau_\mu \tau_\nu {}_0D_t^{\lambda+\mu+\nu} + \tau_\lambda \tau_\mu {}_0D_t^{\lambda+\mu} + \tau_\lambda {}_0D_t^\lambda)u(x, t) = \tau_\mu {}_0D_t^\mu \frac{\partial^2}{\partial x^2} u(x, t),$$

corresponding to the parallel and series topology, respectively, as a reduction of fractional TEs (13.10) and (13.12) when $G = 0$. If, in addition to $G = 0$, one assumes either $\beta = 0$ in the case of both topologies, implying that the fractional capacitor in the series branch is actually the resistor, or $\Delta C_\beta = 0$ in the parallel topology, implying that there is no additional element in the series branch, one obtains the reduced fractional TE

$$K^2(\tau_\mu \tau_\nu {}_0D_t^{\mu+\nu} + \tau_\mu {}_0D_t^\mu)u(x, t) = \frac{\partial^2}{\partial x^2} u(x, t), \quad (13.18)$$

while the same assumptions ($G = 0$ and $\Delta C_\beta = 0$) in series topology yield

$${}_0D_t^\lambda u(x, t) = 0,$$

since there is an open circuit in the series branch. The reduced fractional TE is often used in modeling diffusion-wave phenomena (see for example [4–6,43,53] and reference therein).

The series branch remains resistive as well if an ideal conductive element ($\Delta R = 0$) is assumed in the elementary circuits from Fig. 13.2, due to the fractional inductor ΔL_α , which is an element between classical resistor and inductor, implying the reduced fractional TE (13.18) as a reduction of the TL model (13.10) corresponding to the parallel topology, regardless of the fractional capacitor, since there is a short circuit instead of the resistor, as well as

$$K^2(\tau_\lambda \tau_\mu \tau_v {}_0D_t^{\lambda+\mu+\nu} + \tau_\lambda \tau_\mu {}_0D_t^{\lambda+\mu} + \tau_v {}_0D_t^\nu + 1)u(x, t) = \tau_\mu {}_0D_t^\mu \frac{\partial^2}{\partial x^2} u(x, t),$$

in the case of series topology, originating from (13.12). If, in addition to $\Delta R = 0$, for the series topology one assumes $\beta = 0$ as well, which implies that the fractional capacitor is actually a resistor, the fractional TE

$$K^2(\tau_\mu \tau_v {}_0D_t^{\mu+\nu} + \tau_\mu {}_0D_t^\mu + \tau_v {}_0D_t^\nu + 1)u(x, t) = \frac{\partial^2}{\partial x^2} u(x, t) \quad (13.19)$$

is obtained from (13.12), while if $\Delta C_\beta = 0$, i.e., the open circuit in the series branch of the series topology, is additionally assumed, one has the fractional relaxation equation

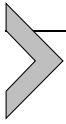
$$(\tau_\lambda {}_0D_t^\lambda + 1)u(x, t) = 0. \quad (13.20)$$

The assumption of the open circuit ($\Delta C_\beta = 0$) instead of the fractional capacitor in the series branch of the elementary circuits from Fig. 13.2 leads to the fractional TE (13.19) in the case of parallel topology and to the fractional relaxation equation (13.20) in the case of series topology, while the assumption of the short circuit ($\Delta C_\beta \rightarrow \infty$) instead of the fractional capacitor leads to the reduced fractional TE (13.18) in the case of parallel topology and to the fractional TE (13.19) in the case of series topology.

Assuming $\beta = 0$, the resistor is considered instead of the fractional capacitor in the series branch of the elementary circuits from Fig. 13.2, leading to the fractional TE (13.19) in the case of both topologies.

With respect to the model parameters, the attenuation coefficient K [m^{-1}] and fractional time constants τ_λ [s^λ], τ_μ [s^μ], and τ_ν [s^ν], appearing in all of the previously mentioned models, are obtained from the appropriate resistance, conductance, and fractional inductance and capacitance

by-length when the fractional TEs (13.10) and (13.12) are reduced to a special case.



13.3. Transmission line model

Fractional TEs (13.10) and (13.12), as models of the hereditary TL, are derived in time and complex domains by considering the parallel and series topologies from Figs. 13.2a and 13.2b, respectively. Derivation in the time domain of the TL model corresponding to the parallel topology is performed in [8], while in [9] the TL models for both topologies are presented in the complex domain and the part of these results is given in this section.

13.3.1 Model formulation in the time domain

Fractional TEs (13.10) and (13.12), corresponding to the parallel and series topologies of the elementary circuits from Fig. 13.2, are derived in the time domain. Application of the first and second Kirchhoff's laws to the elementary circuit gives

$$-i(x, t) + i(x + \Delta x, t) + \Delta i(x, t) = 0, \quad (13.21)$$

$$-u(x, t) + u(x + \Delta x, t) + \Delta u(x, t) = 0, \quad (13.22)$$

where the leakage current

$$\Delta i(x, t) = (\Delta C_{\gamma} {}_0D_t^{\gamma} + \Delta G) u(x + \Delta x, t) \quad (13.23)$$

is the same for both topologies and it is a consequence of the first Kirchhoff law for the shunt branch, with the fractional capacitor current constitutively given by (13.6), while the voltage drop in the series branch, according to the second Kirchhoff's law, is

$$\Delta u(x, t) = \Delta L_{\alpha} {}_0D_t^{\alpha} i(x, t) + u_{RC_{\beta}}(x, t), \quad (13.24)$$

with the fractional inductor voltage constitutively given by (13.5) and having the voltage $u_{RC_{\beta}}$ implicitly obtained either as

$$i(x, t) = \left(\frac{1}{\Delta R} + \Delta C_{\beta} {}_0D_t^{\beta} \right) u_{RC_{\beta}}(x, t), \quad (13.25)$$

in the case of parallel topology from Fig. 13.2a, or as

$$\Delta C_{\beta 0} D_t^\beta u_{RC_\beta}(x, t) = \left(\Delta R \Delta C_{\beta 0} D_t^\beta + 1 \right) i(x, t), \quad (13.26)$$

in the case of series topology from Fig. 13.2b, so that Kirchhoff's laws (13.21) and (13.22), leakage current (13.23), and voltage drop (13.24) divided by the elementary circuit's length Δx yield

$$\frac{i(x + \Delta x, t) - i(x, t)}{\Delta x} = - \left(\frac{\Delta C_\gamma}{\Delta x} {}_0 D_t^\gamma + \frac{\Delta G}{\Delta x} \right) u(x + \Delta x, t), \quad (13.27)$$

$$\frac{u(x + \Delta x, t) - u(x, t)}{\Delta x} = - \frac{\Delta L_\alpha}{\Delta x} {}_0 D_t^\alpha i(x, t) - \frac{u_{RC_\beta}(x, t)}{\Delta x}, \quad (13.28)$$

coupled either with

$$\frac{\Delta R}{\Delta x} i(x, t) = \left(1 + \Delta R \Delta C_{\beta 0} D_t^\beta \right) \frac{u_{RC_\beta}(x, t)}{\Delta x}, \quad (13.29)$$

obtained by (13.25) in the case of parallel topology, or with

$$\Delta R \Delta C_{\beta 0} D_t^\beta \frac{u_{RC_\beta}(x, t)}{\Delta x} = \frac{\Delta R}{\Delta x} \left(\Delta R \Delta C_{\beta 0} D_t^\beta + 1 \right) i(x, t), \quad (13.30)$$

obtained by (13.26) in the case of series topology.

The system of fractional TEs corresponding either to the parallel or to the series topology is obtained from Eqs. (13.27) and (13.28), coupled either with (13.29) or with (13.30), in the continuum limit when $\Delta x \rightarrow 0$ as

$$\frac{\partial}{\partial x} i(x, t) = - \left(C_\gamma {}_0 D_t^\gamma + G \right) u(x, t), \quad (13.31)$$

$$\frac{\partial}{\partial x} u(x, t) = - L_\alpha {}_0 D_t^\alpha i(x, t) - u'_{RC_\beta}(x, t), \quad (13.32)$$

in the case of parallel topology coupled with

$$R i(x, t) = \left(1 + R C_{\beta 0} D_t^\beta \right) u'_{RC_\beta}(x, t), \quad (13.33)$$

and in the case of series topology coupled with

$$C_{\beta 0} D_t^\beta u'_{RC_\beta}(x, t) = \left(R C_{\beta 0} D_t^\beta + 1 \right) i(x, t), \quad (13.34)$$

where

$$\begin{aligned} u'_{RC\beta}(x, t) &= \lim_{\Delta x \rightarrow 0} \frac{u_{RC\beta}(x, t)}{\Delta x}, \quad L_\alpha = \lim_{\Delta x \rightarrow 0} \frac{\Delta L_\alpha}{\Delta x}, \quad C_\gamma = \lim_{\Delta x \rightarrow 0} \frac{\Delta C_\gamma}{\Delta x}, \\ R &= \lim_{\Delta x \rightarrow 0} \frac{\Delta R}{\Delta x}, \quad G = \lim_{\Delta x \rightarrow 0} \frac{\Delta G}{\Delta x}, \\ RC_\beta &= \frac{R}{W_\beta} = \frac{\lim_{\Delta x \rightarrow 0} \frac{\Delta R}{\Delta x}}{\lim_{\Delta x \rightarrow 0} \frac{\Delta W_\beta}{\Delta x}} = \lim_{\Delta x \rightarrow 0} \frac{\frac{\Delta R}{\Delta x}}{\frac{\Delta W_\beta}{\Delta x}} = \lim_{\Delta x \rightarrow 0} \frac{\Delta R}{\Delta W_\beta} = \lim_{\Delta x \rightarrow 0} (\Delta R \Delta C_\beta), \\ &\quad \text{with } \Delta W_\beta = \frac{1}{\Delta C_\beta}. \end{aligned}$$

Assuming both current and voltage to be bounded at the initial time instant, the fractional TEs corresponding to the parallel topology (13.10) and (13.11) are derived from the system of fractional TEs (13.31), (13.32), and (13.33) either by eliminating voltage by-length $u'_{RC\beta}$ from (13.33) using Eq. (13.32) as well as its fractional derivative of order β , so that

$$\left(L_\alpha C_\beta R {}_0D_t^{\alpha+\beta} + L_\alpha {}_0D_t^\alpha + R \right) i(x, t) = - \left(RC_\beta {}_0D_t^\beta + 1 \right) \frac{\partial}{\partial x} u(x, t) \quad (13.35)$$

is obtained by the composition of fractional derivatives of orders $\xi, \zeta \in (0, 1)$

$${}_0D_t^\xi {}_0D_t^\zeta f(t) = {}_0D_t^{\xi+\zeta} f(t) - \frac{d^2}{dt^2} {}_0I_t^{1-\xi} \left[{}_0I_t^{1-\zeta} f(t) \right]_{t=0} = {}_0D_t^{\xi+\zeta} f(t), \quad (13.36)$$

which holds for f bounded at zero, or by eliminating voltage by-length $u'_{RC\beta}$ from Eq. (13.33) integrated by fractional integral of order β using Eq. (13.32) as well as its fractional integral of order β , so that

$$\left(L_\alpha C_\beta R {}_0D_t^\alpha + L_\alpha {}_0D_t^\alpha {}_0I_t^\beta + R {}_0I_t^\beta \right) i(x, t) = - \left(RC_\beta + {}_0I_t^\beta u(x, t) \right) \frac{\partial}{\partial x} u(x, t) \quad (13.37)$$

is obtained by the composition of the fractional integral of order $\xi \in (0, 1)$ and the derivative of order $\zeta \in (0, 1)$ applied to function f bounded at zero,

$${}_0I_t^\xi {}_0D_t^\zeta f(t) = {}_0D_t^\zeta {}_0I_t^\xi f(t) - \frac{d}{dt} {}_0I_t^\xi \left[{}_0I_t^{1-\zeta} f(t) \right]_{t=0} = {}_0D_t^\zeta {}_0I_t^\xi f(t), \quad (13.38)$$

reducing to

$${}_0I_t^\xi {}_0D_t^\xi f(t) = f(t) - \frac{d}{dt} {}_0I_t^\xi \left[{}_0I_t^{1-\xi} f(t) \right]_{t=0} = f(t), \quad (13.39)$$

and by subsequent differentiation of (13.35) and (13.37) with respect to x and eliminating current i from (13.31) using the composition of fractional derivatives (13.36) as well as the composition of derivatives of different orders $\xi \in (1, 2)$ and $\zeta \in (0, 1)$,

$${}_0D_t^\xi {}_0D_t^\zeta f(t) = {}_0D_t^{\xi+\zeta} f(t) - \frac{d^3}{dt^3} {}_0I_t^{2-\xi} \left[{}_0I_t^{1-\zeta} f(t) \right]_{t=0} = {}_0D_t^{\xi+\zeta} f(t), \quad (13.40)$$

holding for f bounded at zero.

Similarly, assuming both current and voltage to be bounded at initial time instant, the fractional TEs corresponding to the series topology (13.12) and (13.13) are derived from the system of fractional TEs (13.31), (13.32), and (13.34) either by eliminating voltage by-length $u'_{RC\beta}$ from (13.34) using the fractional derivative of order β applied to Eq. (13.32), so that

$$\left(L_\alpha C_\beta {}_0D_t^{\alpha+\beta} + RC_\beta {}_0D_t^\beta + 1 \right) i(x, t) = -C_\beta {}_0D_t^\beta \frac{\partial}{\partial x} u(x, t) \quad (13.41)$$

is obtained according to the composition of fractional derivatives (13.36), or by eliminating voltage by-length $u'_{RC\beta}$ from the fractional integral of order β of (13.34) using Eq. (13.32), so that

$$\left(L_\alpha C_\beta {}_0D_t^\alpha + RC_\beta + {}_0I_t^\beta \right) i(x, t) = -C_\beta \frac{\partial}{\partial x} u(x, t) \quad (13.42)$$

is obtained using (13.39) and by subsequent differentiation of (13.41) and (13.42) with respect to x and eliminating current i from (13.31) according to the composition of fractional derivatives (13.36) and (13.40) as well as the composition of the fractional integral and derivative (13.38).

Note that the fractional TEs (13.11) and (13.13) can also be obtained by applying the fractional integral of order β to Eqs. (13.10) and (13.12), respectively, using the composition of the fractional integral and derivative (13.38) and (13.39) under assumption of the boundedness of both current and voltage at the initial time instant.

13.3.2 Model formulation in the complex domain

Regardless of the topology of the series and shunt branches of the elementary circuit, as far as the constitutive equations of the elements constituting the branches are linear with constant coefficients, the TE can be derived using the Laplace transform of physical quantities, i.e., the TE can be derived in the complex domain (see also the classical literature [39]). The TE

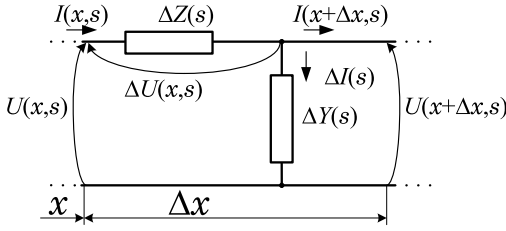


Figure 13.3 Elementary circuit in the complex domain.

in the complex domain

$$\frac{\partial^2}{\partial x^2} U(x, s) - k^2(s) U(x, s) = 0, \quad \text{with} \quad k(s) = \sqrt{\psi(s)} = \sqrt{Z(s)Y(s)} \quad (13.43)$$

being the (complex) propagation constant (PC) and

$$Z(s) = \lim_{\Delta x \rightarrow 0} \frac{\Delta Z(s)}{\Delta x} \left[\frac{\Omega}{\text{m}} \right], \quad Y(s) = \lim_{\Delta x \rightarrow 0} \frac{\Delta Y(s)}{\Delta x} \left[\frac{\text{S}}{\text{m}} \right]$$

being series impedance and shunt admittance by-length, is obtained by applying Kirchhoff's laws to the elementary circuit from Fig. 13.3, yielding

$$I(x + \Delta x, s) - I(x, s) = -\Delta I(x, s) = -\Delta Y(s)U(x + \Delta x, s), \quad (13.44)$$

$$U(x + \Delta x, s) - U(x, s) = -\Delta U(x, s) = -\Delta Z(s)I(x, s), \quad (13.45)$$

where ΔZ is the impedance of series and ΔY is the admittance of shunt branch of the elementary circuit, so that (13.44) and (13.45), divided by the elementary circuit's length Δx , give

$$\begin{aligned} \frac{I(x + \Delta x, s) - I(x, s)}{\Delta x} &= -\frac{\Delta Y(s)}{\Delta x} U(x + \Delta x, s) \quad \text{and} \\ \frac{U(x + \Delta x, s) - U(x, s)}{\Delta x} &= -\frac{\Delta Z(s)}{\Delta x} I(x, s), \end{aligned}$$

which after taking the continuum limit $\Delta x \rightarrow 0$ becomes the system of TEs in the complex domain

$$\frac{\partial}{\partial x} U(x, s) = -Z(s)I(x, s) \quad \text{and} \quad \frac{\partial}{\partial x} I(x, s) = -Y(s)U(x, s),$$

yielding (13.43) after being reduced to a single equation in voltage U .

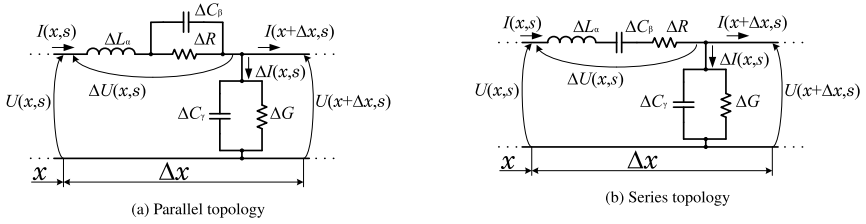


Figure 13.4 Topological modifications of the classical elementary circuit.

In order to derive the fractional TEs in the complex domain corresponding either to the parallel or to the series topology from the elementary circuit shown in Figs. 13.4a and 13.4b, which take the respective forms

$$K^2(\tau_\alpha \tau_\beta s^{\alpha+\beta} + \tau_\alpha s^\alpha + 1)(\tau_\gamma s^\gamma + 1)U(x, s) = (\tau_\beta s^\beta + 1) \frac{\partial^2}{\partial x^2} U(x, s), \quad (13.46)$$

$$K^2(\tau_\alpha \tau_\beta s^{\alpha+\beta} + \tau_\beta s^\beta + 1)(\tau_\gamma s^\gamma + 1)U(x, s) = \tau_\beta s^\beta \frac{\partial^2}{\partial x^2} U(x, s), \quad (13.47)$$

the series impedances by-length Z_p and Z_s for the parallel and series topology, as well as the shunt admittance by-length Y , which is the same for both topologies, appearing in PC (13.43)₂, are calculated as

$$Z_p(s) = \lim_{\Delta x \rightarrow 0} \frac{\Delta Z_{L_\alpha}(s) + \Delta R \parallel \Delta Z_{C_\beta}(s)}{\Delta x},$$

$$Z_s(s) = \lim_{\Delta x \rightarrow 0} \frac{\Delta R + \Delta Z_{L_\alpha}(s) + \Delta Z_{C_\beta}(s)}{\Delta x}, \quad (13.48)$$

$$Y(s) = \lim_{\Delta x \rightarrow 0} \frac{\Delta Y_{C_\gamma}(s) + \Delta G}{\Delta x}, \quad (13.49)$$

where the impedances ΔZ_{L_α} and ΔZ_{C_β} , as well as the admittance ΔY_{C_γ} , follow from the phenomenological constitutive relations (13.4) for fractional inductor and capacitor, obtained as

$$\Delta Z_{L_\alpha}(s) = \frac{U_L(s)}{I_L(s)} = s^\alpha \Delta L_\alpha, \quad \Delta Z_{C_\beta}(s) = \frac{U_C(s)}{I_C(s)} = \frac{1}{s^\beta \Delta C_\beta},$$

$$\Delta Y_{C_\gamma}(s) = \frac{I_C(s)}{U_C(s)} = s^\gamma \Delta C_\gamma,$$

by the Laplace transform

$$F(s) = \mathcal{L}[f(t)](s) = \int_0^{\infty} f(t) e^{-st} dt,$$

of the constitutive relation (13.5) for inductor and (13.6) for capacitor, due to the Laplace transform of the Riemann–Liouville fractional derivative (13.7)

$$\mathcal{L}\left[{}_0D_t^{\xi} f(t)\right](s) = s^{\xi} F(s) - \left[{}_0I_t^{1-\xi} f(t)\right]_{t=0} = s^{\xi} F(s), \quad (13.50)$$

holding for f bounded at zero, so that the impedances and the admittance by-length, by (13.48) and (13.49), are

$$\begin{aligned} Z_p(s) &= \frac{RL_{\alpha} C_{\beta} s^{\alpha+\beta} + L_{\alpha} s^{\alpha} + R}{RC_{\beta} s^{\beta} + 1} = R \frac{\tau_{\alpha} \tau_{\beta} s^{\alpha+\beta} + \tau_{\alpha} s^{\alpha} + 1}{\tau_{\beta} s^{\beta} + 1}, \\ Z_s(s) &= \frac{L_{\alpha} C_{\beta} s^{\alpha+\beta} + RC_{\beta} s^{\beta} + 1}{C_{\beta} s^{\beta}} = R \frac{\tau_{\alpha} \tau_{\beta} s^{\alpha+\beta} + \tau_{\beta} s^{\beta} + 1}{\tau_{\beta} s^{\beta}}, \\ Y(s) &= C_{\gamma} s^{\gamma} + G = G(\tau_{\gamma} s^{\gamma} + 1), \end{aligned}$$

yielding, by (13.43)₂, PCs corresponding to the parallel and series topology as

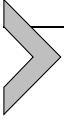
$$\begin{aligned} k_p(s) &= \sqrt{\frac{(RL_{\alpha} C_{\beta} s^{\alpha+\beta} + L_{\alpha} s^{\alpha} + R)(C_{\gamma} s^{\gamma} + G)}{RC_{\beta} s^{\beta} + 1}} \\ &= K \sqrt{\frac{(\tau_{\alpha} \tau_{\beta} s^{\alpha+\beta} + \tau_{\alpha} s^{\alpha} + 1)(\tau_{\gamma} s^{\gamma} + 1)}{\tau_{\beta} s^{\beta} + 1}}, \end{aligned} \quad (13.51)$$

$$\begin{aligned} k_s(s) &= \sqrt{\frac{(L_{\alpha} C_{\beta} s^{\alpha+\beta} + RC_{\beta} s^{\beta} + 1)(C_{\gamma} s^{\gamma} + G)}{C_{\beta} s^{\beta}}} \\ &= K \sqrt{\frac{(\tau_{\alpha} \tau_{\beta} s^{\alpha+\beta} + \tau_{\beta} s^{\beta} + 1)(\tau_{\gamma} s^{\gamma} + 1)}{\tau_{\beta} s^{\beta}}}. \end{aligned} \quad (13.52)$$

Fractional TEs (13.14) and (13.16), corresponding to the parallel and series topologies, are obtained by the Laplace transform inversion of fractional TEs in the complex domain (13.46) and (13.47), using the Laplace transform of fractional derivative (13.50), while the equivalent forms of the fractional TEs (13.15) and (13.17) are obtained by dividing Eqs. (13.46) and (13.47) by s^{β} and using the inverse Laplace transform of fractional

derivative and (13.50) integral

$$\mathcal{L} \left[{}_0 I_t^{\xi} f(t) \right] (s) = \frac{1}{s^{\xi}} F(s).$$



13.4. Transmission line in transient regime

A transient regime of the hereditary TL is considered for the semi-infinite line $x \in [0, \infty)$, which initially has neither voltage nor current, but is however forced by the external voltage applied at its boundary. The transient regime analysis of the TL corresponding to the parallel topology is performed in [8], where the numerical examples illustrating the impulse responses are also provided and the part of these results is presented in this section.

13.4.1 Response in transient regime

The transient regime of the TL corresponds to the initial boundary value problem on the half axis for the system of fractional TEs (13.31), (13.32), coupled either with (13.33), in the case of parallel topology, or with (13.34), in the case of series topology, rewritten in terms of the fractional time constants as

$$\frac{\partial}{\partial x} i(x, t) = -G (\tau_{\gamma} {}_0 D_t^{\gamma} + 1) u(x, t), \quad (13.53)$$

$$\frac{\partial}{\partial x} u(x, t) = -R \tau_{\alpha} {}_0 D_t^{\alpha} i(x, t) - u'_{RC\beta}(x, t), \quad (13.54)$$

coupled with

$$R i(x, t) = \left(1 + \tau_{\beta} {}_0 D_t^{\beta} \right) u'_{RC\beta}(x, t) \quad (13.55)$$

in the case of parallel topology and with

$$\tau_{\beta} {}_0 D_t^{\beta} u'_{RC\beta}(x, t) = R \left(\tau_{\beta} {}_0 D_t^{\beta} + 1 \right) i(x, t) \quad (13.56)$$

in the case of series topology, subject to zero initial

$$i(x, 0) = 0, \quad u(x, 0) = 0, \quad \text{and} \quad u'_{RC\beta}(x, 0) = 0, \quad x \in [0, \infty) \quad (13.57)$$

and boundary conditions

$$u(0, t) = u_0(t) \quad \text{and} \quad \lim_{x \rightarrow \infty} u(x, t) = 0, \quad t > 0. \quad (13.58)$$

Equivalently, one may consider either the fractional TE (13.11) corresponding to the parallel topology, or TE (13.13) corresponding to the series topology, subject to initial condition

$$u(x, 0) = 0, \quad x \in [0, \infty),$$

and boundary conditions given by (13.58).

Applying the Laplace transform to the system of fractional TEs (13.53), (13.54), with either (13.55), or (13.56), one has

$$\begin{aligned} \frac{\partial}{\partial x} I(x, s) &= -G(\tau_\gamma s^\gamma + 1) U(x, s), \\ \frac{\partial}{\partial x} U(x, s) &= -R \tau_\alpha s^\alpha i(x, s) - U'_{RC_\beta}(x, s), \end{aligned}$$

coupled either with

$$RI(x, s) = (1 + \tau_\beta s^\beta) I'_{RC_\beta}(x, s),$$

or with

$$\tau_\beta s^\beta U'_{RC_\beta}(x, s) = R(\tau_\beta s^\beta + 1) I(x, s),$$

yielding, when reduced to a single equation expressed in terms of voltage U , either

$$\frac{\partial^2}{\partial x^2} U(x, s) - K^2 \frac{(\tau_\alpha \tau_\beta s^{\alpha+\beta} + \tau_\alpha s^\alpha + 1)(\tau_\gamma s^\gamma + 1)}{\tau_\beta s^\beta + 1} U(x, s) = 0, \quad (13.59)$$

in the case of parallel topology, or

$$\frac{\partial^2}{\partial x^2} U(x, s) - K^2 \frac{(\tau_\alpha \tau_\beta s^{\alpha+\beta} + \tau_\beta s^\beta + 1)(\tau_\gamma s^\gamma + 1)}{\tau_\beta s^\beta} U(x, s) = 0, \quad (13.60)$$

in the case of series topology.

Since the system of fractional TEs (13.53), (13.54), coupled either with (13.55), in the case of parallel topology, or with (13.56), in the case of series topology, is equivalent to the fractional TE (13.14) or (13.16), by the application of the Laplace transform to (13.14) one reobtains the fractional TE in the complex domain (13.59), corresponding to the parallel topology, while the Laplace transform applied to Eq. (13.16) leads to Eq. (13.60), corresponding to the series topology, which is written in a unified way as (13.43), with PC given by (13.51) for the parallel topology or by (13.52) for the series topology.

Solution of the ordinary differential equations with the constant coefficients (13.59) and (13.60), complying with the boundary conditions (13.58), is

$$U(x, s) = U_0(s) e^{-k_{p/s}(s)x}, \quad (13.61)$$

with $k_{p/s}$ already given by (13.51) and (13.52), assuming that model parameters are chosen such that $\arg k_{p/s}^2(s) \in (-\pi, \pi)$ for all $\operatorname{Re} s > 0$ guaranteeing that $\operatorname{Re} k_{p/s}(s) > 0$ for $\operatorname{Re} s > 0$. The condition $\arg k_p^2(s) \in (-\pi, \pi)$ for $\operatorname{Re} s > 0$ is satisfied in the case of the parallel topology either if $\alpha + \gamma \in (0, 1]$ or if $\beta = \gamma$ and $\tau_\beta < \tau_\gamma$, since the real and imaginary parts of k_p^2 , obtained as

$$\begin{aligned} \operatorname{Re} k_p^2(\rho, \varphi) = & \frac{K^2}{|\tau_\beta \rho^\beta e^{i\beta\varphi} + 1|^2} \left(\tau_\alpha \tau_\beta^2 \tau_\gamma \rho^{\alpha+2\beta+\gamma} \cos((\alpha + \gamma)\varphi) \right. \\ & + \tau_\alpha \tau_\beta^2 \rho^{\alpha+2\beta} \cos(\alpha\varphi) \\ & + 2\tau_\alpha \tau_\beta \tau_\gamma \rho^{\alpha+\beta+\gamma} \cos(\beta\varphi) \cos((\alpha + \gamma)\varphi) \\ & + 2\tau_\alpha \tau_\beta \rho^{\alpha+\beta} \cos(\alpha\varphi) \cos(\beta\varphi) + \tau_\alpha \tau_\gamma \rho^{\alpha+\gamma} \cos((\alpha + \gamma)\varphi) \\ & + \tau_\beta \tau_\gamma \rho^{\beta+\gamma} \cos((\beta - \gamma)\varphi) + \tau_\alpha \rho^\alpha \cos(\alpha\varphi) \\ & \left. + \tau_\beta \rho^\beta \cos(\beta\varphi) + \tau_\gamma \rho^\gamma \cos(\gamma\varphi) + 1 \right), \end{aligned} \quad (13.62)$$

$$\begin{aligned} \operatorname{Im} k_p^2(\rho, \varphi) = & \frac{K^2}{|\tau_\beta \rho^\beta e^{i\beta\varphi} + 1|^2} \left(\tau_\alpha \tau_\beta^2 \tau_\gamma \rho^{\alpha+2\beta+\gamma} \sin((\alpha + \gamma)\varphi) \right. \\ & + \tau_\alpha \tau_\beta^2 \rho^{\alpha+2\beta} \sin(\alpha\varphi) + 2\tau_\alpha \tau_\beta \tau_\gamma \rho^{\alpha+\beta+\gamma} \cos(\beta\varphi) \sin((\alpha + \gamma)\varphi) \\ & + 2\tau_\alpha \tau_\beta \rho^{\alpha+\beta} \sin(\alpha\varphi) \cos(\beta\varphi) + \tau_\alpha \tau_\gamma \rho^{\alpha+\gamma} \sin((\alpha + \gamma)\varphi) \\ & - \tau_\beta \tau_\gamma \rho^{\beta+\gamma} \sin((\beta - \gamma)\varphi) + \tau_\alpha \rho^\alpha \sin(\alpha\varphi) \\ & \left. - \tau_\beta \rho^\beta \sin(\beta\varphi) + \tau_\gamma \rho^\gamma \sin(\gamma\varphi) \right), \end{aligned}$$

by substituting $s = \rho e^{i\varphi}$, $\rho \in (0, \infty)$, $\varphi \in (-\frac{\pi}{2}, \frac{\pi}{2})$ in (13.51), yield that all terms in (13.62) are positive for $\varphi \in (-\frac{\pi}{2}, \frac{\pi}{2})$ if $\alpha + \gamma \in (0, 1]$, since $\alpha, \beta, \gamma \in (0, 1)$ and also, if $\beta = \gamma$ and $\tau_\beta < \tau_\gamma$, then $\operatorname{Im} k_p^2 \geq 0$ for $\varphi \in [0, \frac{\pi}{2})$ (and also $\operatorname{Im} k_p^2 < 0$ for $\varphi \in (-\frac{\pi}{2}, 0)$). Note that the condition $\beta = \gamma$ implies that the capacitances in the series and shunt branch are of the same order, while $\tau_\beta < \tau_\gamma$ means that the fractional time relaxation in the series is smaller than in its shunt branch, supporting the fact that the series branch is conductive,

while the shunt branch is insulative. The condition $\arg k_s^2(s) \in (-\pi, \pi)$ for $\text{Re } s > 0$ is satisfied in the case of the series topology if $\alpha + \gamma \in (0, 1]$, since the substitution $s = \rho e^{i\varphi}$, $\rho \in (0, \infty)$, $\varphi \in (-\frac{\pi}{2}, \frac{\pi}{2})$ in (13.52) as a result gives

$$\begin{aligned} \text{Re } k_s^2(\rho, \varphi) = & K^2 \left(\tau_\alpha \tau_\gamma \rho^{\alpha+\gamma} \cos((\alpha + \gamma)\varphi) + \tau_\alpha \rho^\alpha \cos(\alpha\varphi) + \tau_\gamma \rho^\gamma \cos(\gamma\varphi) \right. \\ & \left. + 1 + \frac{\tau_\gamma}{\tau_\beta} \rho^{\gamma-\beta} \cos((\gamma - \beta)\varphi) + \frac{1}{\tau_\beta \rho^\beta} \cos(\beta\varphi) \right), \end{aligned} \tag{13.63}$$

$$\begin{aligned} \text{Im } k_s^2(\rho, \varphi) = & K^2 \left(\tau_\alpha \tau_\gamma \rho^{\alpha+\gamma} \sin((\alpha + \gamma)\varphi) + \tau_\alpha \rho^\alpha \sin(\alpha\varphi) + \tau_\gamma \rho^\gamma \sin(\gamma\varphi) \right. \\ & \left. + \frac{\tau_\gamma}{\tau_\beta} \rho^{\gamma-\beta} \sin((\gamma - \beta)\varphi) - \frac{1}{\tau_\beta \rho^\beta} \sin(\beta\varphi) \right), \end{aligned}$$

where all terms in (13.63) are positive for $\varphi \in (-\frac{\pi}{2}, \frac{\pi}{2})$ if $\alpha + \gamma \in (0, 1]$. Nevertheless, the geometrical considerations of k_p^2 and k_s^2 (see (13.51) and (13.52)) imply that the condition $\text{Re } k_{p/s}(s) > 0$ for $\text{Re } s > 0$ for the validity of the solution (13.61) is satisfied for the whole range of the model parameters: $\alpha, \beta, \gamma \in (0, 1)$ and $K, \tau_\alpha, \tau_\beta, \tau_\gamma > 0$.

Inverting the Laplace transform in (13.61), the voltage in the transient regime as a solution to the system of fractional TEs (13.53), (13.54), coupled either with (13.55), in the case of parallel topology, or with (13.56), in the case of series topology, subject to (13.57) and (13.58), takes the form

$$u(x, t) = u_0(t) * u_\delta(x, t), \tag{13.64}$$

where the impulse response (inversion of the transfer function [TF]), i.e., the voltage response to the boundary voltage assumed as a Dirac δ -distribution, is obtained in Appendix 13.A.1 by inverting the Laplace transform by the definition

$$u_\delta(x, t) = \mathcal{L}^{-1} \left[e^{-k_{p/s}(s)x} \right] (x, t) = \frac{1}{2\pi i} \int_{Br} e^{-k_{p/s}(s)x} e^{st} ds, \tag{13.65}$$

with Br being the Bromwich path, in the following forms:

$$u_\delta^{(I,II)}(x, t) = \frac{1}{\pi} \int_0^\infty \sin(\text{Im } k_{p/s}(\rho e^{i\pi}) x) e^{-(\rho t + \text{Re } k_{p/s}(\rho e^{i\pi}) x)} d\rho, \tag{13.66}$$

$$\begin{aligned} u_\delta^{(III)}(x, t) = & \frac{1}{\pi} \int_0^\infty \sin(\rho t \sin \varphi_0 - \text{Im } k_{p/s}(\rho e^{i\varphi_0}) x + \varphi_0) \\ & \times e^{-(\rho t |\cos \varphi_0| + \text{Re } k_{p/s}(\rho e^{i\varphi_0}) x)} d\rho, \end{aligned} \tag{13.67}$$

depending on the nature of branching points (BPs) of the TF $e^{-k_{p/s}(s)x}$, other than $s = 0$, i.e., on their number and position in the complex plane. The impulse responses have the same form, given by (13.66), if the TF has either no BPs or a negative real branch point, while the impulse response is of the form (13.67) if the TF has a pair of complex conjugated BPs $s_0 = \rho_0 e^{i\varphi_0}$ and \bar{s}_0 having a negative real part.

BPs of the TF $e^{-k_{p/s}(s)x}$, which are actually the BPs of k_p and k_s , given by (13.51) and (13.52), are obtained as the zeros of numerators of PCs squared, since terms $s^\beta + \frac{1}{\tau_\beta}$ and $s^\gamma + \frac{1}{\tau_\gamma}$, appearing in the denominator and numerator of PCs, respectively, do not have zeros in the first Riemann sheet, i.e., for $\arg s \in (-\pi, \pi)$, and $s = 0$ is a BP of function s^ξ , for ξ being noninteger, so the BPs of k_p and k_s are obtained as solutions of

$$s^{\alpha+\beta} + \frac{1}{\tau_\beta} s^\alpha + \frac{1}{\tau_\alpha \tau_\beta} = 0 \quad \text{and} \quad s^{\alpha+\beta} + \frac{1}{\tau_\alpha} s^\beta + \frac{1}{\tau_\alpha \tau_\beta} = 0. \quad (13.68)$$

Eq. (13.68)₁ does not have zeros if $\alpha + \beta \in (0, 1]$, while if $\alpha + \beta \in (1, 2)$, then the sign of

$$f_p(\alpha, \beta, \tau_\alpha, \tau_\beta) = \left(-\frac{\sin(\alpha\pi)}{\tau_\beta \sin((\alpha + \beta)\pi)} \right)^{\frac{\alpha}{\beta}} \frac{\sin(\beta\pi)}{\tau_\beta \sin((\alpha + \beta)\pi)} + \frac{1}{\tau_\alpha \tau_\beta}$$

determines the nature of its zeros: if $f_p < 0$, then (13.68)₁ has no zeros for $\arg s \in (-\pi, \pi)$; if $f_p = 0$, then (13.68)₁ has one negative real zero; if $f_p > 0$, then (13.68)₁ has a pair of complex conjugated zeros with negative real part. Since Eqs. (13.68)₁ and (13.68)₂ are of the same form, the function

$$f_s(\alpha, \beta, \tau_\alpha, \tau_\beta) = \left(-\frac{\sin(\beta\pi)}{\tau_\alpha \sin((\alpha + \beta)\pi)} \right)^{\frac{\beta}{\alpha}} \frac{\sin(\alpha\pi)}{\tau_\alpha \sin((\alpha + \beta)\pi)} + \frac{1}{\tau_\alpha \tau_\beta}$$

determines the nature of zeros of Eq. (13.68)₂ with the same conditions as in the previous case. The proof of this claim is provided in Section 4.2 of [8].

13.4.2 Numerical examples

Considering three different types of voltage forcing at the boundary (impulse, step, and harmonic), the voltage responses of the TL are qualitatively and quantitatively analyzed through the numerical examples in the case of parallel topology of the elementary circuit. The voltage responses are obtained as solutions to the time-fractional model of TL, represented by the

system of fractional TEs (13.53)–(13.55), subject to initial and boundary conditions (13.57) and (13.58), or equivalently represented by the fractional TE (13.14), subject to zero initial and boundary conditions (13.58), with the explicit form of voltage responses given by (13.64) as a convolution of the external voltage forcing and impulse response, either represented by (13.66) when k_p , given by (13.51), except for $s = 0$ has no other BPs, as well as when it has one negative real BP, or represented by (13.67) when PC has a pair of complex conjugated BPs with negative real part. The impulse responses are calculated in Appendix 13.A.1 by inverting the Laplace transform analytically using the contour integration in the complex plane.

13.4.2.1 Time evolution and space profiles of impulse response

Fig. 13.5 presents time evolution of the impulse response, depending on the nature of PC's BPs, which can be aperiodic if k_p has no other BPs than $s = 0$ (see Fig. 13.5a), critically aperiodic if k_p has a negative real BP in addition to $s = 0$, as depicted in Fig. 13.5b, and damped oscillatory if k_p , except for $s = 0$, has a pair of complex conjugated BPs, as illustrated in Fig. 13.5c. The responses obtained through the analytical expressions (13.66) and (13.67), depicted by solid lines, are in perfect agreement with the responses depicted by dots, which are calculated by de Hoog's method of numerical Laplace transform inversion (see [11]).

Fig. 13.6 illustrates two distinct types of disturbance propagation: diffusion- and wave-like behavior of the impulse response, which occur if the highest order of fractional differentiation in the fractional TE corresponding to the parallel topology (13.15) is $\alpha + \gamma \in (0, 1)$ and $\alpha + \gamma \in (1, 2)$, respectively. Diffusion- and wave-like impulse responses differ in their space profiles, so that for the former one, as time passes, disturbance does not propagate or propagates in the small spatial domain (see Figs. 13.6a, 13.6c, and 13.6e), while for the latter one there is disturbance propagation on the large spatial scale during time, as depicted in Figs. 13.6b, 13.6d, and 13.6f.

If the highest order of fractional differentiation in TE (13.15) is $\alpha + \gamma \in (0, 1)$, the critically aperiodic impulse response, as obvious from Fig. 13.6a, has a diffusive character, since its space profiles display a gradual decrease in peak height, while their position gradually shifts to the higher value of coordinate still being confined to a small spatial scale. One would expect that peaks of the aperiodic impulse response shift on an even smaller scale, while their height decreases. The damped oscillatory impulse response displays peculiar, yet diffusive type, behavior, since after some time, a negative

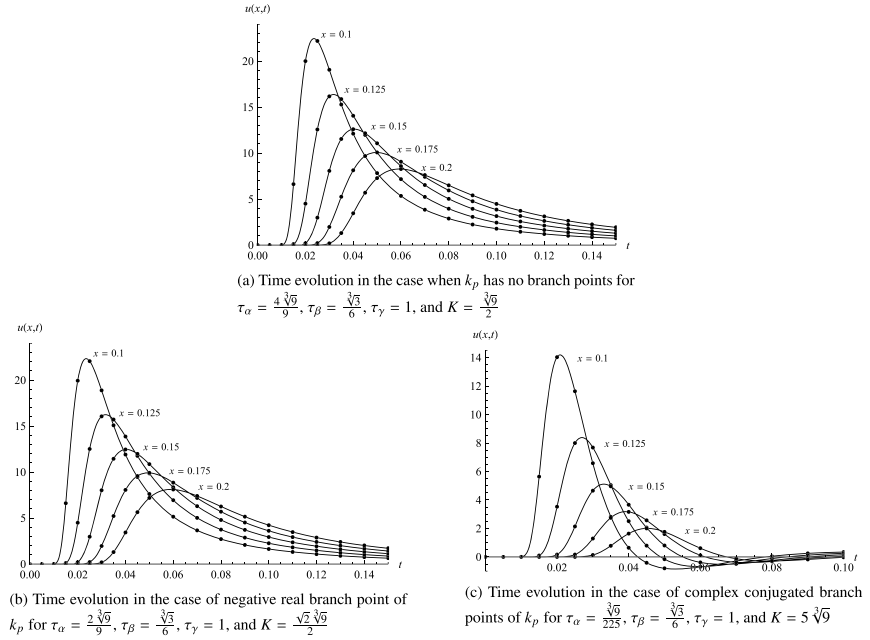


Figure 13.5 Time evolution of the impulse response at discrete positions for $\alpha = \frac{5}{6}$ and $\beta = \gamma = \frac{2}{3}$.

peak emerges alongside the positive one, as clear from Fig. 13.6c, and the negative peak progressively gains height while the positive peak loses height until it completely vanishes. Further time evolution of the negative peak is such that its height also decreases and it utterly vanishes as well, as illustrated in Fig. 13.6e. As time passes, both positive and negative peaks eventually disappear, while the whole process is spatially confined; hence the impulse response’s behavior is classified as diffusion-like.

On the other hand, if the highest order of fractional differentiation in TE (13.15) is $\alpha + \gamma \in (1, 2)$, the aperiodic impulse response from Fig. 13.6b is clearly wave-like, due to the peak’s large-scale shift during time, while the peak’s loss of height and gain in width is due to the dissipativity properties of the hereditary TL. Again, the critically aperiodic impulse response is expected to have the same character as the aperiodic one. The space profiles of the damped oscillatory impulse response, shown in Fig. 13.6d, have a negative peak emerging alongside the positive one, so that as time passes the negative peak gains height, while the positive one loses height, until the secondary positive peak appears, which gradually increases, while

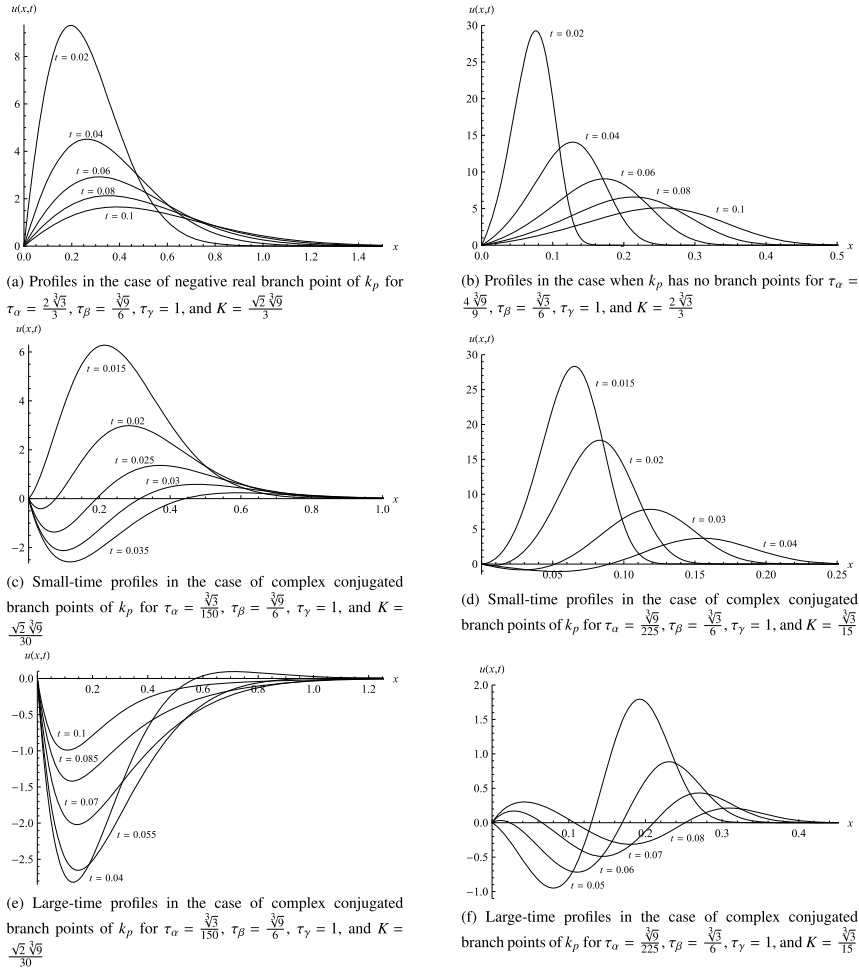


Figure 13.6 Diffusion-like space profiles of the impulse response at discrete time instants for $\alpha = \frac{2}{3}$, $\beta = \frac{5}{6}$, and $\gamma = \frac{1}{4}$.

the primary positive and negative peaks' heights decrease, as illustrated in Fig. 13.6f. It is also evident that all peaks propagate in space during time; hence the impulse response's behavior is classified as wave-like.

13.4.2.2 Time evolution of step response

Fig. 13.7 presents plots of the TL's voltage response to voltage forcing at its boundary, taken in the form of a Heaviside step function, implying that the

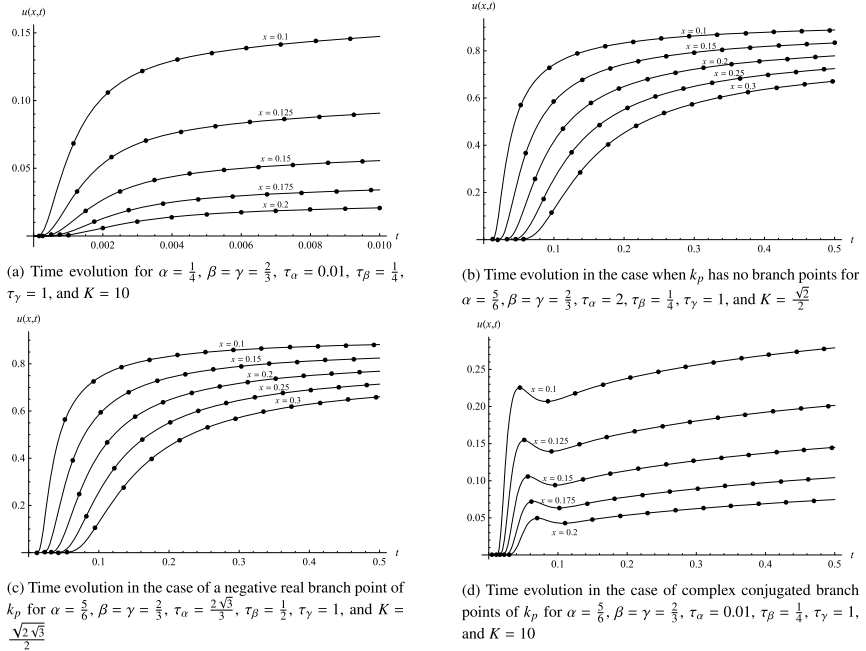


Figure 13.7 Time evolution of step response at discrete positions.

response is either a monotonic or a damped oscillatory function increasing from zero to a finite value of voltage depending on the spatial coordinate, as predicted by the Tauber initial and final value theorem

$$u(x, 0) = \lim_{s \rightarrow \infty} sU(x, s) = 0 \quad \text{and} \quad \lim_{t \rightarrow \infty} u(x, t) = \lim_{s \rightarrow 0} sU(x, s) = e^{-Kx},$$

since by (13.61) one has $sU(x, s) = e^{-k_p(s)x}$ as the Laplace transform of the step response, with k_p given by (13.51). The monotonic character of the step response is obtained in Figs. 13.7a–13.7c either if $\alpha + \beta \in (0, 1)$ or if $\alpha + \beta \in (1, 2)$ and PC in addition to $s = 0$ may only have a negative real BP, while the response displays a damped oscillatory character if $\alpha + \beta \in (1, 2)$ and PC has a pair of complex conjugated BPs in addition to $s = 0$, as illustrated in Fig. 13.7d. Interestingly, the height of the voltage maximum is lower than the asymptotic value of voltage for large time. The step responses, calculated according to the analytical expressions and depicted by solid lines, are in perfect agreement with the responses depicted by dots, obtained through the fixed Talbot algorithm for numerical inversion of the Laplace transform (see [1]).

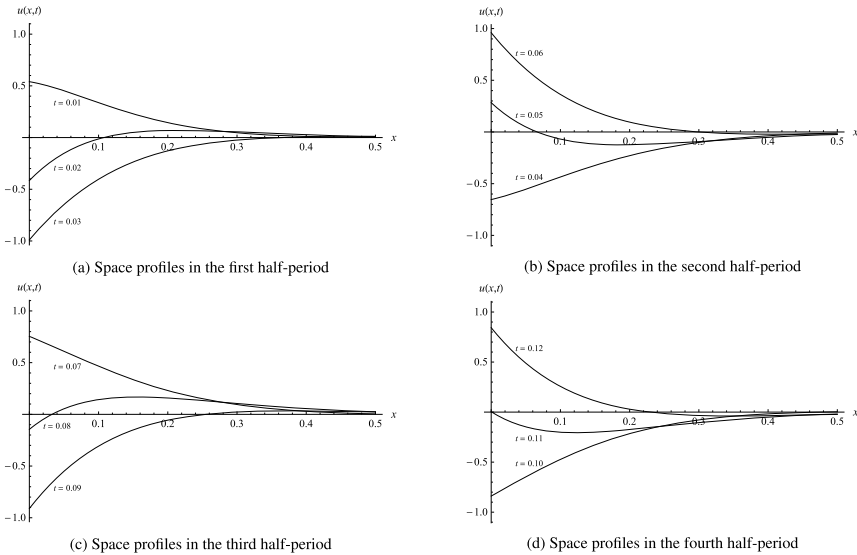


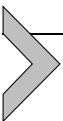
Figure 13.8 Space profiles of the response to harmonic function $u_0(t) = \mathcal{U}_0 \cos(\omega t)$ at discrete time instants in the case of complex conjugated branch points of k_p for $\mathcal{L}_0 = 1$, $\omega = 100$, $\alpha = \frac{2}{3}$, $\beta = \frac{5}{6}$, $\gamma = \frac{1}{4}$, $\tau_\alpha = 0.01$, $\tau_\beta = \frac{1}{3}$, $\tau_\gamma = 1$, and $K = 10$.

13.4.2.3 Space profiles of harmonic response

Assuming harmonic voltage forcing at the boundary of TL in the form

$$u_0(t) = \mathcal{U}_0 \cos(\omega t),$$

the space profiles of the voltage response are shown in Figs. 13.8 and 13.9 for time instants belonging to the first two periods of the forcing. It is evident that there are voltage oscillations in time having decreasing amplitudes as the spatial coordinate increases, as well as that there are nonpropagating space profiles, since the highest order of the fractional TE $\alpha + \gamma \in (0, 1)$ implies the diffusive character of the response (see Fig. 13.8) and that there are propagating space profiles, as depicted in Fig. 13.9, since the highest order of TE $\alpha + \gamma \in (1, 2)$ implies the wave type of the response.



13.5. Transmission line in steady-state regime and its frequency characteristics

In order to examine the hereditary TL in the steady-state regime, as well as to analyze its frequency characteristics, a transmission line is

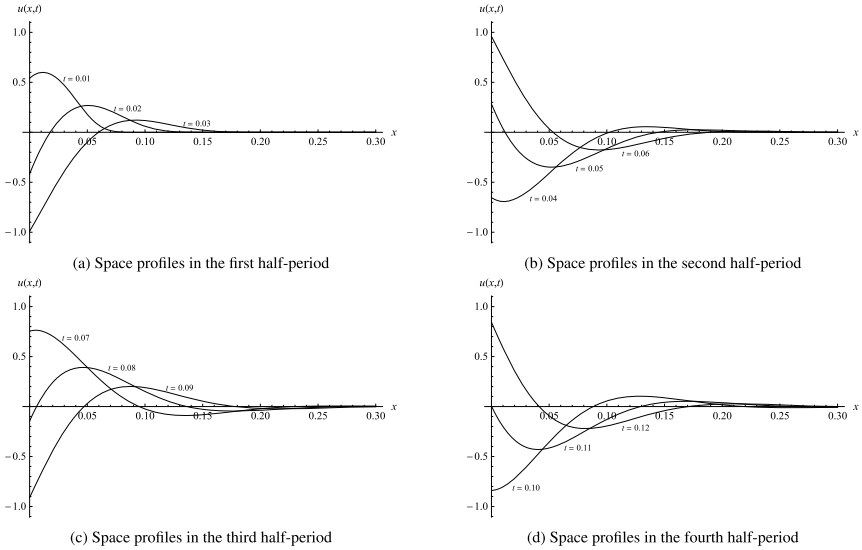


Figure 13.9 Space profiles of the response to harmonic function $u_0(t) = \mathcal{U}_0 \cos(\omega t)$ at discrete time instants in the case of complex conjugated branch points of k_p for $\mathcal{U}_0 = 1$, $\omega = 100$, $\alpha = \frac{5}{6}$, $\beta = \gamma = \frac{2}{3}$, $\tau_\alpha = 0.01$, $\tau_\beta = \frac{1}{4}$, $\tau_\gamma = 1$, and $K = 10$.

subjected to harmonic voltage forcing at its boundary, i.e., the fractional TEs (13.14) and (13.16), corresponding to the parallel and series topologies of the elementary circuit, are subject to the boundary condition (13.58)₁ assumed as

$$u_0(t) = \mathcal{U}_0 \cos(\omega t) = \text{Re}(\mathcal{U}_0 e^{i\omega t}), \tag{13.69}$$

where ω is the angular frequency, in addition to zero initial and boundary condition (13.58)₂.

13.5.1 Response in steady-state regime

Aiming to derive the steady-state response of the TL from the transient one, rather than using the solution (13.64) to TEs (13.14) and (13.16), expressed in terms of convolution of boundary condition and impulse response, the voltage response in the complex domain (13.61), yielding

$$U(x, s) = \mathcal{U}_0 \frac{s}{s^2 + \omega^2} e^{-k_p/s(s)x}, \tag{13.70}$$

by (13.69), is inverted in Appendix 13.A.2 by definition of the inverse Laplace transform using the Cauchy residues theorem and contour integra-

tion, so that the harmonic voltage response is obtained as

$$u(x, t) = \mathcal{L}^{-1} [U(x, s)](x, t) = \frac{\mathcal{U}_0}{2\pi i} \int_{Br} \frac{s}{s^2 + \omega^2} e^{-k_{p/s}(s)x} e^{st} ds, \quad (13.71)$$

$$u^{(I,II)}(x, t) = \frac{\mathcal{U}_0}{2\pi i} \int_0^\infty \left(e^{-k_{p/s}(\rho e^{i\pi})x} - e^{-k_{p/s}(\rho e^{-i\pi})x} \right) \frac{\rho e^{-\rho t}}{\rho^2 + \omega^2} d\rho + \mathcal{U}_0 e^{-\text{Re } k_{p/s}(i\omega)x} \cos(\omega t - \text{Im } k_{p/s}(i\omega)x), \quad (13.72)$$

$$u^{(III)}(x, t) = \frac{\mathcal{U}_0}{2\pi i} \int_0^\infty \left(\frac{e^{-k_{p/s}(\rho e^{i\varphi_0})x} e^{i(2\varphi_0 + \rho t \sin \varphi_0)}}{\rho^2 e^{2i\varphi_0} + \omega^2} - \frac{e^{-k_{p/s}(\rho e^{-i\varphi_0})x} e^{-i(2\varphi_0 + \rho t \sin \varphi_0)}}{\rho^2 e^{-2i\varphi_0} + \omega^2} \right) e^{-\rho t |\cos \varphi_0|} \rho d\rho + \mathcal{U}_0 e^{-\text{Re } k_{p/s}(i\omega)x} \cos(\omega t - \text{Im } k_{p/s}(i\omega)x), \quad (13.73)$$

with Br being the Bromwich path. Again, the BPs of TF $e^{-k_{p/s}(s)x}$ determine the form of the solution, so that (13.72) is obtained either if TF has no BPs or if it has a negative real BP in addition to $s = 0$, while the solution takes the form (13.73) if TF, except for $s = 0$, has a pair of complex conjugated BPs $s_0 = \rho_0 e^{i\varphi_0}$ and \bar{s}_0 having a negative real part. The steady-state voltage response of the TL becomes

$$u_{ss}(x, t) = \mathcal{U}_0 e^{-\text{Re } k_{p/s}(i\omega)x} \cos(\omega t - \text{Im } k_{p/s}(i\omega)x) \quad \text{as } t \rightarrow \infty, \quad (13.74)$$

assuming that the integrals in harmonic responses, given by (13.72) and (13.73), actually corresponding to the transient regime, can be approximated by zero for time large enough.

Traditionally, the steady-state response is obtained by considering the TF (impulse response in the complex domain), obtained by rewriting (13.61) as

$$W_{p/s}(x, s) = \frac{U(x, s)}{U_0(s)} = e^{-k_{p/s}(s)x}, \quad (13.75)$$

which, after substitution $s = i\omega$ and separation of real and imaginary parts in PC, yields the TF modulus and argument in the form

$$|W_{p/s}(x, \omega)| = e^{-\text{Re } k_{p/s}(\omega)x}, \quad \text{i.e.,} \quad (13.76)$$

$$\arg W_{p/s}(x, \omega) = -20 x \text{Re } k_{p/s}(\omega) \log e, \quad \text{and} \quad (13.77)$$

$$\arg W_{p/s}(x, \omega) = -x \text{Im } k_{p/s}(\omega),$$

with the notation $f(\omega) = f(s)|_{s=i\omega}$ used, so that the steady-state response to harmonic forcing

$$U_0^{(t)}(\omega) = \mathcal{U}_0 e^{i\omega t}$$

is

$$u_{ss}(x, t) = \operatorname{Re} U^{(t)}(x, \omega) = \mathcal{U}_0 e^{-\operatorname{Re} k_{p/s}(\omega)x} \cos(\omega t - \operatorname{Im} k_{p/s}(\omega)x),$$

since $U^{(t)}$ is obtained by (13.75), (13.76), and (13.77) as

$$\begin{aligned} U^{(t)}(x, \omega) &= U_0^{(t)}(\omega) W_{p/s}(x, \omega) = \mathcal{U}_0 |W_{p/s}(x, \omega)| e^{i(\omega t + \arg W_{p/s}(x, \omega))} \\ &= \mathcal{U}_0 e^{-\operatorname{Re} k_{p/s}(\omega)x} e^{i(\omega t - \operatorname{Im} k_{p/s}(\omega)x)}. \end{aligned}$$

Note that the TF $W_{p/s}$ in the form (13.75) can be directly obtained from the fractional TEs in the complex domain (13.46) and (13.47), corresponding to the parallel and series topologies of the elementary circuit, i.e., from (13.43)₁ with $k_{p/s}$ given by (13.51) and (13.52), as a solution complying with the boundary conditions (13.58).

Figs. 13.10 and 13.11 illustrate the time evolution of harmonic responses, or more precisely responses' transitions from transient to the steady-state regime, since the plots from figures are respectively obtained according to expressions (13.72) and (13.73), representing the solution to the fractional TE (13.14), corresponding to the parallel topology of the elementary circuit, in the case of harmonic boundary forcing taken in the form (13.69). It is clear that the harmonic responses quite quickly (presumably after only one period) enter the steady state, with the shape of the transient regime depending on the existence of TF's BPs other than $s = 0$, so that if there are no other BPs, the response resembles the steady-state response from the very beginning (see Fig. 13.10), while if there is a pair of complex conjugated BPs, the response has an additional maximum prior to maxima and minima originating from the harmonic forcing, as clear from Fig. 13.11. Moreover, the harmonic response resembles the step response for small time (compare Figs. 13.7b and 13.10), as well as Figs. 13.7d and 13.11, since initially both (causal) harmonic and step forcing jump to the same value. The decrease of amplitudes and the increase of the phase delay as the position increases is clearly noticeable from Figs. 13.10 and 13.11, since the steady-state response (13.74) predicts the exponential decrease of amplitude and the linear decrease of phase angle as the spatial coordinate increases.

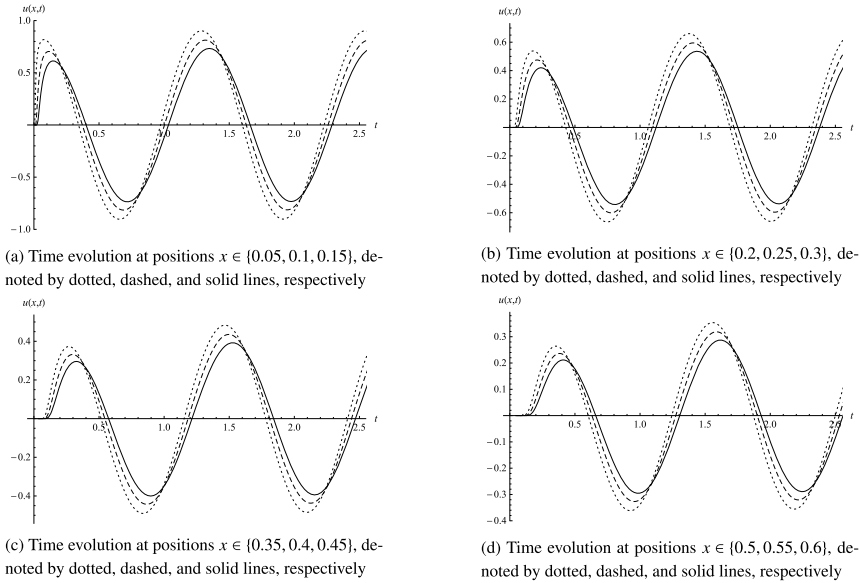


Figure 13.10 Time evolution of the response to harmonic function $u_0(t) = \mathcal{U}_0 \cos(\omega t)$ at discrete positions in the case when k_p has no branch points for $\mathcal{L}_0 = 1$, $\omega = 5$, $\alpha = \frac{5}{6}$, $\beta = \gamma = \frac{2}{3}$, $\tau_\alpha = 1$, $\tau_\beta = \frac{1}{4}$, $\tau_\gamma = 1$, and $K = 1$.

13.5.2 Frequency characteristics and their asymptotic

Considering the hereditary TL subject to the harmonic boundary voltage forcing (13.69), the dependence of TF (13.75) on frequency is analyzed, i.e., frequency characteristics of the TF modulus and argument (13.76)₂ and (13.77), which are linear functions of the spatial coordinate, while their frequency dependence is governed by the topology of the elementary circuit through k_p and k_s , defined by (13.51) and (13.52). The frequency analysis of the TL corresponding to parallel and series topologies is performed in [9], where the numerical examples illustrating the behavior of TF modulus and argument are also provided and the part of these results is presented in this section.

Modulus (13.76) and argument (13.77) of the TF require real and imaginary parts of PC expressed in terms of angular frequency, which are obtained by

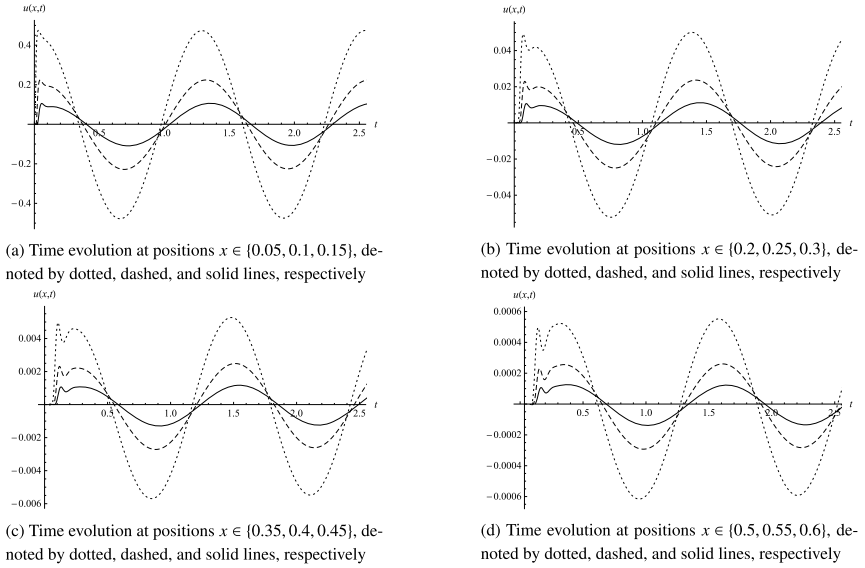


Figure 13.11 Time evolution of the response to harmonic function $u_0(t) = \mathcal{U}_0 \cos(\omega t)$ at discrete positions in the case of complex conjugated branch points of k_p for $\mathcal{U}_0 = 1$, $\omega = 5$, $\alpha = \frac{5}{6}$, $\beta = \gamma = \frac{2}{3}$, $\tau_\alpha = 0.01$, $\tau_\beta = \frac{1}{4}$, $\tau_\gamma = 1$, and $K = 10$.

$$\begin{aligned} \operatorname{Re} k_{p/s}(\omega) &= \sqrt{\frac{|k_{p/s}^2(\omega)| + \operatorname{Re} k_{p/s}^2(\omega)}{2}} \quad \text{and} \\ \operatorname{Im} k_{p/s}(\omega) &= \operatorname{sgn}(\operatorname{Im} k_{p/s}^2(\omega)) \sqrt{\frac{|k_{p/s}^2(\omega)| - \operatorname{Re} k_{p/s}^2(\omega)}{2}} \end{aligned} \quad (13.78)$$

from the square of PC, yielding in the case of parallel topology

$$\begin{aligned} \operatorname{Re} k_p^2(\omega) &= \frac{K^2}{|\tau_\beta(i\omega)^\beta + 1|^2} \left(\tau_\alpha \tau_\beta^2 \tau_\gamma \omega^{\alpha+2\beta+\gamma} \cos \frac{(\alpha+\gamma)\pi}{2} \right. \\ &\quad + \tau_\alpha \tau_\beta^2 \omega^{\alpha+2\beta} \cos \frac{\alpha\pi}{2} + 2\tau_\alpha \tau_\beta \tau_\gamma \omega^{\alpha+\beta+\gamma} \cos \frac{\beta\pi}{2} \cos \frac{(\alpha+\gamma)\pi}{2} \\ &\quad + 2\tau_\alpha \tau_\beta \omega^{\alpha+\beta} \cos \frac{\alpha\pi}{2} \cos \frac{\beta\pi}{2} + \tau_\alpha \tau_\gamma \omega^{\alpha+\gamma} \cos \frac{(\alpha+\gamma)\pi}{2} \\ &\quad + \tau_\beta \tau_\gamma \omega^{\beta+\gamma} \cos \frac{(\beta-\gamma)\pi}{2} + \tau_\alpha \omega^\alpha \cos \frac{\alpha\pi}{2} \\ &\quad \left. + \tau_\beta \omega^\beta \cos \frac{\beta\pi}{2} + \tau_\gamma \omega^\gamma \cos \frac{\gamma\pi}{2} + 1 \right), \end{aligned} \quad (13.79)$$

$$\begin{aligned}
\operatorname{Im} k_p^2(\omega) = & \frac{K^2}{|\tau_\beta(i\omega)^\beta + 1|^2} \left(\tau_\alpha \tau_\beta^2 \tau_\gamma \omega^{\alpha+2\beta+\gamma} \sin \frac{(\alpha+\gamma)\pi}{2} \right. \\
& + \tau_\alpha \tau_\beta^2 \omega^{\alpha+2\beta} \sin \frac{\alpha\pi}{2} + 2\tau_\alpha \tau_\beta \tau_\gamma \omega^{\alpha+\beta+\gamma} \cos \frac{\beta\pi}{2} \sin \frac{(\alpha+\gamma)\pi}{2} \\
& + 2\tau_\alpha \tau_\beta \omega^{\alpha+\beta} \sin \frac{\alpha\pi}{2} \cos \frac{\beta\pi}{2} + \tau_\alpha \tau_\gamma \omega^{\alpha+\gamma} \sin \frac{(\alpha+\gamma)\pi}{2} \\
& - \tau_\beta \tau_\gamma \omega^{\beta+\gamma} \sin \frac{(\beta-\gamma)\pi}{2} + \tau_\alpha \omega^\alpha \sin \frac{\alpha\pi}{2} - \tau_\beta \omega^\beta \sin \frac{\beta\pi}{2} \\
& \left. + \tau_\gamma \omega^\gamma \sin \frac{\gamma\pi}{2} \right), \tag{13.80}
\end{aligned}$$

and in the case of series topology

$$\begin{aligned}
\operatorname{Re} k_s^2(\omega) = & K^2 \left(\tau_\alpha \tau_\gamma \omega^{\alpha+\gamma} \cos \frac{(\alpha+\gamma)\pi}{2} + \tau_\alpha \omega^\alpha \cos \frac{\alpha\pi}{2} + \tau_\gamma \omega^\gamma \cos \frac{\gamma\pi}{2} \right. \\
& \left. + 1 + \frac{\tau_\gamma}{\tau_\beta} \omega^{\gamma-\beta} \cos \frac{(\gamma-\beta)\pi}{2} + \frac{1}{\tau_\beta \omega^\beta} \cos \frac{\beta\pi}{2} \right), \tag{13.81}
\end{aligned}$$

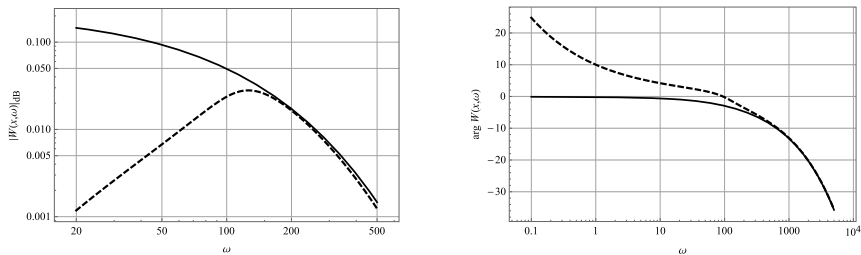
$$\begin{aligned}
\operatorname{Im} k_s^2(\omega) = & K^2 \left(\tau_\alpha \tau_\gamma \omega^{\alpha+\gamma} \sin \frac{(\alpha+\gamma)\pi}{2} + \tau_\alpha \omega^\alpha \sin \frac{\alpha\pi}{2} + \tau_\gamma \omega^\gamma \sin \frac{\gamma\pi}{2} \right. \\
& \left. + \frac{\tau_\gamma}{\tau_\beta} \omega^{\gamma-\beta} \sin \frac{(\gamma-\beta)\pi}{2} - \frac{1}{\tau_\beta \omega^\beta} \sin \frac{\beta\pi}{2} \right). \tag{13.82}
\end{aligned}$$

Writing explicitly PC's real and imaginary parts, determined by (13.78) using (13.79)–(13.82), makes sense only in the limiting cases of low and high frequencies, as done in the sequel.

Frequency characteristics of the TF modulus and argument, according to (13.76)₂ governed by the real part of k_p and k_s , given by (13.78)₁, and according to (13.77) governed by the imaginary part of k_p and k_s , given by (13.78)₂, respectively, are depicted in Fig. 13.12 for different cases of the number and nature of PCs' BPs.

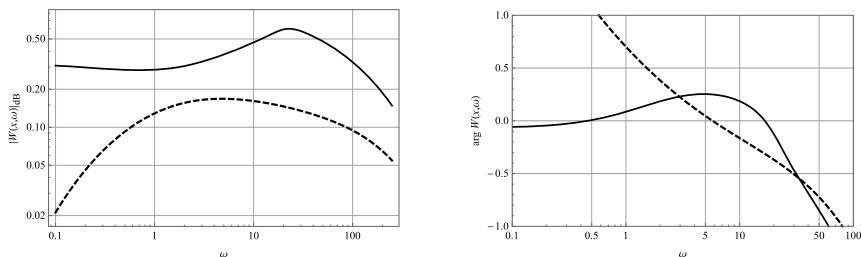
The monotonicity properties of the TF modulus' frequency characteristics for the parallel topology depend on the nature of PCs' BPs, so that if k_p has a pair of complex conjugated BPs, the frequency characteristics are a nonmonotonic function having both minimum and maximum, and otherwise it is a monotonically decreasing function (compare Figs. 13.12c and 13.12e with Fig. 13.12a). On the other hand, for the series topology, the TF modulus' frequency characteristics do not depend on the number and nature of PCs' BPs, since they have only one maximum in each case (see Figs. 13.12a, 13.12c, and 13.12e).

Contrary to the frequency characteristics of the TF modulus for the parallel topology, a pair of complex conjugated BPs of k_p does not guar-



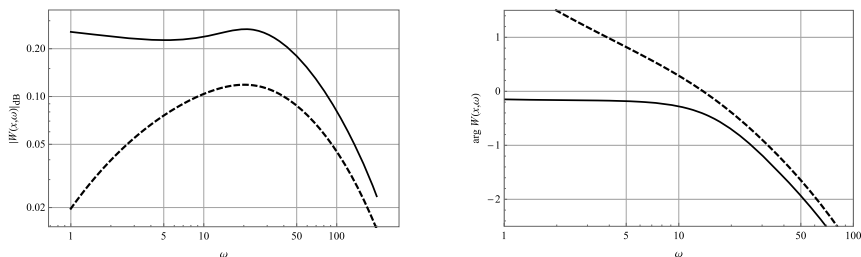
(a) TF modulus (b) TF argument

Case when k_p has no BPs and k_s has a pair of complex conjugated BPs, obtained for $\tau_\alpha = 0.05$, $\tau_\beta = 0.005$, and $\tau_\gamma = 1$.



(c) TF modulus (d) TF argument

Case when k_p has a pair of complex conjugated BPs and k_s has no BPs, obtained for $\tau_\alpha = 0.01$, $\tau_\beta = 0.5$, and $\tau_\gamma = 1$.



(e) TF modulus (f) TF argument

Case when both k_p and k_s have a pair of complex conjugated BPs, obtained for $\tau_\alpha = 0.05$, $\tau_\beta = 0.1$, and $\tau_\gamma = 1$.

Figure 13.12 Frequency characteristics corresponding to parallel and series topologies, depicted by solid and dashed lines, respectively, at $x = 1$, for $K = 1$, $\alpha = 0.9$, $\beta = 0.85$, $\gamma = \frac{1}{3}$.

ante the nonmonotonicity of the argument's characteristics (compare Figs. 13.12d and 13.12f). Similarly to the frequency characteristics of the TF argument for the series topology, the argument's characteristics do not depend on the existence of BPs of k_s , since the characteristics are

monotonically decreasing functions in each case (see Figs. 13.12b, 13.12d, and 13.12f).

In the low frequency limit, i.e., as $\omega \rightarrow 0$, the real and imaginary parts of the square of k_p , given by (13.79) and (13.80), become

$$\begin{aligned} \operatorname{Re} k_p^2(\omega) &\sim K^2 \left(1 + \tau_\alpha \omega^\alpha \cos \frac{\alpha\pi}{2} - \tau_\beta \omega^\beta \cos \frac{\beta\pi}{2} + \tau_\gamma \omega^\gamma \cos \frac{\gamma\pi}{2} \right. \\ &\quad \left. - \tau_\beta^2 \omega^{2\beta} \left(1 - 2 \cos^2 \frac{\beta\pi}{2} \right) + \tau_\alpha \tau_\gamma \omega^{\alpha+\gamma} \cos \frac{(\alpha+\gamma)\pi}{2} \right. \\ &\quad \left. - \tau_\beta \tau_\gamma \omega^{\beta+\gamma} \cos \frac{(\beta+\gamma)\pi}{2} \right) \end{aligned} \quad (13.83)$$

and

$$\operatorname{Im} k_p^2(\omega) \sim K^2 \left(\tau_\alpha \omega^\alpha \sin \frac{\alpha\pi}{2} - \tau_\beta \omega^\beta \sin \frac{\beta\pi}{2} + \tau_\gamma \omega^\gamma \sin \frac{\gamma\pi}{2} \right), \quad (13.84)$$

using approximation

$$\frac{1}{|\tau_\beta(i\omega)^\beta + 1|^2} \sim 1 - 2\tau_\beta \omega^\beta \cos \frac{\beta\pi}{2} - \tau_\beta^2 \omega^{2\beta} \left(1 - 4 \cos^2 \frac{\beta\pi}{2} \right),$$

calculated by

$$(1+x)^\xi \sim 1 + \xi x + \frac{\xi(\xi-1)}{2} x^2, \quad \text{for } |x| \ll 1. \quad (13.85)$$

Further, (13.83) and (13.84) are used to calculate

$$\begin{aligned} |k_p^2(\omega)| &= \sqrt{\operatorname{Re}^2 k_p^2(\omega) + \operatorname{Im}^2 k_p^2(\omega)} \\ &\sim K^2 \left(1 + \tau_\alpha \omega^\alpha \cos \frac{\alpha\pi}{2} - \tau_\beta \omega^\beta \cos \frac{\beta\pi}{2} + \tau_\gamma \omega^\gamma \cos \frac{\gamma\pi}{2} \right. \\ &\quad \left. + \frac{1}{2} \tau_\alpha^2 \omega^{2\alpha} \sin^2 \frac{\alpha\pi}{2} - \frac{1}{2} \tau_\beta^2 \omega^{2\beta} \left(1 - 3 \cos^2 \frac{\beta\pi}{2} \right) \right. \\ &\quad \left. + \frac{1}{2} \tau_\gamma^2 \omega^{2\gamma} \sin^2 \frac{\gamma\pi}{2} - \tau_\alpha \tau_\beta \omega^{\alpha+\beta} \sin \frac{\alpha\pi}{2} \sin \frac{\beta\pi}{2} \right. \\ &\quad \left. + \tau_\alpha \tau_\gamma \omega^{\alpha+\gamma} \left(\cos \frac{(\alpha-\gamma)\pi}{2} - \sin \frac{\alpha\pi}{2} \sin \frac{\gamma\pi}{2} \right) \right. \\ &\quad \left. - \tau_\beta \tau_\gamma \omega^{\beta+\gamma} \left(\cos \frac{(\beta-\gamma)\pi}{2} - \sin \frac{\beta\pi}{2} \sin \frac{\gamma\pi}{2} \right) \right), \end{aligned}$$

with approximation (13.85) used again, so that, by (13.78), the PC's real and imaginary parts in the low frequency limit are

$$\begin{aligned} \operatorname{Re} k_p(\omega) &\sim K \quad \text{and} \\ \operatorname{Im} k_p(\omega) &\sim K \operatorname{sgn}\left(\operatorname{Im} k_p^2(\omega)\right) \frac{\sqrt{2}}{2} \left(\frac{1}{2} \tau_\alpha^2 \omega^{2\alpha} \sin^2 \frac{\alpha\pi}{2} + \frac{1}{2} \tau_\beta^2 \omega^{2\beta} \sin^2 \frac{\beta\pi}{2} \right. \\ &\quad \left. + \frac{1}{2} \tau_\gamma^2 \omega^{2\gamma} \sin^2 \frac{\gamma\pi}{2} - \tau_\alpha \tau_\beta \omega^{\alpha+\beta} \sin \frac{\alpha\pi}{2} \sin \frac{\beta\pi}{2} \right. \\ &\quad \left. + \tau_\alpha \tau_\gamma \omega^{\alpha+\gamma} \sin \frac{\alpha\pi}{2} \sin \frac{\gamma\pi}{2} - \tau_\beta \tau_\gamma \omega^{\beta+\gamma} \right)^{\frac{1}{2}} \\ &\sim \frac{1}{2} K \operatorname{sgn}\left(\operatorname{Im} k_p^2(\omega)\right) \tau_\xi \omega^\xi \sin \frac{\xi\pi}{2}, \end{aligned}$$

with $\xi = \min\{\alpha, \beta, \gamma\}$ and $\operatorname{sgn}\left(\operatorname{Im} k_p^2(\omega)\right) = \begin{cases} 1, & \text{if } \xi \in \{\alpha, \gamma\}, \\ -1, & \text{if } \xi = \beta, \end{cases}$ due to (13.84).

Thus, in the case of the parallel topology the TF modulus and argument (13.76) and (13.77) in the low frequency limit are

$$W_p(x, \omega) \sim e^{-xK}, \quad \text{i.e.,} \quad |W_p(x, \omega)|_{\text{dB}} \sim -20 xK \log e, \quad \text{and} \quad (13.86)$$

$$\arg W_p(x, \omega) \sim -\frac{1}{2} \operatorname{sgn}\left(\operatorname{Im} k_p^2(\omega)\right) x \omega^\xi K \tau_\xi \sin \frac{\xi\pi}{2}. \quad (13.87)$$

Clearly, the real and imaginary parts of the square of k_s , given by (13.81) and (13.82), in the low frequency limit are

$$\operatorname{Re} k_s^2(\omega) \sim \frac{K^2}{\tau_\beta} \frac{1}{\omega^\beta} \cos \frac{\beta\pi}{2} \quad \text{and} \quad \operatorname{Im} k_s^2(\omega) = -\frac{K^2}{\tau_\beta} \frac{1}{\omega^\beta} \sin \frac{\beta\pi}{2},$$

implying $|k_s^2(\omega)| \sim \frac{K^2}{\tau_\beta} \frac{1}{\omega^\beta}$, yielding

$$\operatorname{Re} k_s(\omega) \sim \frac{K}{\sqrt{\tau_\beta} \omega^\beta} \cos \frac{\beta\pi}{4} \quad \text{and} \quad \operatorname{Im} k_s(\omega) \sim -\frac{K}{\sqrt{\tau_\beta} \omega^\beta} \sin \frac{\beta\pi}{4}$$

by (13.78); hence in the case of series topology the TF modulus and argument (13.76) and (13.77) in the low frequency limit are

$$\begin{aligned} W_s(x, \omega) &\sim e^{-\frac{x}{\omega^{\beta/2}} \frac{K}{\sqrt{\tau_\beta}} \cos \frac{\beta\pi}{4}}, \quad \text{i.e.,} \\ |W_s(x, \omega)|_{\text{dB}} &\sim -20 \frac{x}{\omega^{\beta/2}} \frac{K}{\sqrt{\tau_\beta}} \cos \frac{\beta\pi}{4} \log e, \quad \text{and} \quad (13.88) \end{aligned}$$

$$\arg W_s(x, \omega) \sim \frac{x}{\omega^{\frac{\beta}{2}}} \frac{K}{\sqrt{\tau_\beta}} \sin \frac{\beta\pi}{4}. \quad (13.89)$$

In the high frequency limit, i.e., as $\omega \rightarrow \infty$, for both parallel and series topologies, the real and imaginary parts of the square of k_p and k_s , given by (13.79)–(13.82), are

$$\begin{aligned} \operatorname{Re} k_{p/s}^2(\omega) &\sim K^2 \tau_\alpha \tau_\gamma \omega^{\alpha+\gamma} \cos \frac{(\alpha+\gamma)\pi}{2} \quad \text{and} \\ \operatorname{Im} k_{p/s}^2(\omega) &\sim K^2 \tau_\alpha \tau_\gamma \omega^{\alpha+\gamma} \sin \frac{(\alpha+\gamma)\pi}{2}, \end{aligned}$$

implying $|k_s^2(\omega)| \sim K^2 \tau_\alpha \tau_\gamma \omega^{\alpha+\gamma}$, yielding

$$\begin{aligned} \operatorname{Re} k_{p/s}(\omega) &\sim K \sqrt{\tau_\alpha \tau_\gamma} \omega^{\alpha+\gamma} \cos \frac{(\alpha+\gamma)\pi}{4} \quad \text{and} \\ \operatorname{Im} k_{p/s}(\omega) &\sim K \sqrt{\tau_\alpha \tau_\gamma} \omega^{\alpha+\gamma} \sin \frac{(\alpha+\gamma)\pi}{4} \end{aligned}$$

by (13.78); hence, in the case of both topologies the TF modulus and argument (13.76) and (13.77) in the high frequency limit are

$$W_{p/s}(x, \omega) \sim e^{-x\omega^{(\alpha+\gamma)/2} K \sqrt{\tau_\alpha \tau_\gamma} \cos \frac{(\alpha+\gamma)\pi}{4}}, \quad \text{i.e.,}$$

$$|W_{p/s}(x, \omega)|_{\text{dB}} \sim -20 x \omega^{\frac{\alpha+\gamma}{2}} K \sqrt{\tau_\alpha \tau_\gamma} \cos \frac{(\alpha+\gamma)\pi}{4} \log e, \quad \text{and} \quad (13.90)$$

$$\arg W_{p/s}(x, \omega) \sim -x \omega^{\frac{\alpha+\gamma}{2}} K \sqrt{\tau_\alpha \tau_\gamma} \sin \frac{(\alpha+\gamma)\pi}{4}. \quad (13.91)$$

In conclusion, for the parallel topology of the TL, the signal propagation is enabled in the low frequency limit, opposing the case of series topology in which signal propagation is disabled, as can be respectively seen from the TF modulus (13.86)₁, which is not frequency-dependent, and (13.88)₁, which tends to zero. In the high frequency limit, the signal propagation is disabled in the cases of both topologies because of the TF modulus (13.90)₁ tending to zero. Taking the logarithm of TF arguments in the low frequency limit (13.87) and (13.89), as well as of the TF argument in the high frequency limit (13.91), one obtains $\log |\arg W|$ as a linear function of $\log \omega$, given by

$$\begin{aligned} \log |\arg W_p(x, \omega)| &\sim \xi \log \omega + \log \left(\frac{1}{2} x K \tau_\xi \sin \frac{\xi\pi}{2} \right) \quad \text{and} \\ \log |\arg W_s(x, \omega)| &\sim -\frac{\beta}{2} \log \omega + \log \left(x \frac{K}{\sqrt{\tau_\beta}} \sin \frac{\beta\pi}{4} \right), \quad \text{as } \omega \rightarrow 0, \quad (13.92) \end{aligned}$$

$$\log \left| \arg W_{p/s}(x, \omega) \right| \sim \frac{\alpha + \gamma}{2} \log \omega + \log \left(x K \sqrt{\tau_\alpha \tau_\gamma} \sin \frac{(\alpha + \gamma)\pi}{4} \right), \quad \text{as } \omega \rightarrow \infty, \quad (13.93)$$

so that in the low frequency limit, according to (13.92), the slope of $\log |\arg W|$ determines the lowest order of fractional differentiation $\xi = \min \{\alpha, \beta, \gamma\}$ in the case of parallel topology and fractional differentiation order β , corresponding to the series branch capacitor, in the case of series topology, while in the high frequency limit, according to (13.93), the slope of $\log |\arg W|$ determines the highest fractional differentiation order of the fractional TEs (13.14) and (13.16).

Frequency characteristics of TF modulus and argument, combined with their low- and high-frequency asymptotes, are presented in Fig. 13.13. The fact that the TL corresponding to the parallel topology models the low-pass filter (voltage propagation is enabled for low frequencies and disabled for high frequencies), while the line corresponding to the series topology models the band-pass filter (voltage propagation is enabled for medium frequencies and disabled for both low and high frequencies), is obvious from the TF modulus' frequency characteristics, depicted in Fig. 13.13a. The low- and high-frequency asymptotes of both modulus and argument, calculated by (13.86)₂, (13.88)₂, and (13.92) as $\omega \rightarrow 0$, as well as by (13.90) and (13.93) as $\omega \rightarrow \infty$, agree very well with the frequency characteristics of modulus and argument calculated by (13.76)₂ and (13.77), with $\text{Re } k_{p/s}$ and $\text{Im } k_{p/s}$ given by (13.78). It is clear from Fig. 13.13b that the logarithm of the TF argument behaves as a linear function in the low and high frequency limit.

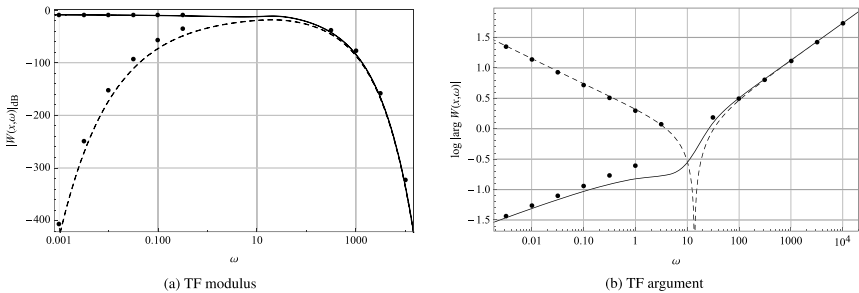
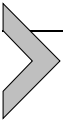


Figure 13.13 Frequency characteristics corresponding to parallel and series topologies, depicted by solid and dashed lines, respectively, along with their asymptotic behavior, depicted by dots, at $x = 1$, for $K = 1$, $\alpha = 0.9$, $\beta = 0.85$, $\gamma = \frac{1}{3}$, $\tau_\alpha = 0.05$, $\tau_\beta = 0.1$, and $\tau_\gamma = 1$.



Appendix 13.A.

13.A.1 Calculation of impulse response

In order to calculate the impulse response by definition of the inverse Laplace transform (13.65), the Cauchy integral theorem

$$\oint_{\Gamma^{(i)}} e^{-k_{p/s}(s)x} e^{st} ds = 0, \quad \text{with } i \in \{\text{I, II, III}\}, \quad (13.A.94)$$

is used, where the contour $\Gamma^{(i)}$, containing the Bromwich path Br , is chosen differently, as shown in Fig. 13.14, ensuring that the TF $e^{-k_{p/s}(s)x}$ is analytic within the domain encircled by the contour, so that the contour $\Gamma^{(\text{I})}$ corresponds to the case when $k_{p/s}$ has no BPs other than $s = 0$, contour $\Gamma^{(\text{II})}$ is chosen if $k_{p/s}$ has a negative real BP s_0 , and finally the contour $\Gamma^{(\text{III})}$ is used if $k_{p/s}$ has complex conjugated BPs $s_0 = \rho_0 e^{i\varphi_0}$ and \bar{s}_0 having a negative real part. Impulse responses of the TL corresponding to the parallel topology are calculated in [8] and here calculation of the impulse responses is extended to the case of series topology as well.

The impulse response calculation is performed only for the case of PC's complex conjugated BPs $s_0 = \rho_0 e^{i\varphi_0}$ and \bar{s}_0 , since the other two cases correspond to $\varphi_0 = \pi$ and therefore the contour in the Cauchy integral theorem (13.A.94) is chosen to be $\Gamma^{(\text{III})}$ from Fig. 13.14c.

The integrals along contours $\Gamma_{3a} \cup \Gamma_{3b}$ (parameterized by $s = \rho e^{i\varphi_0}$, $\rho \in (r, \rho_0 - r) \cup (\rho_0 + r, R)$) and $\Gamma_{5a} \cup \Gamma_{5b}$ (parameterized by $s = \rho e^{-i\varphi_0}$, $\rho \in (r, \rho_0 - r) \cup (\rho_0 + r, R)$) read

$$\begin{aligned} \lim_{\substack{R \rightarrow \infty, \\ r \rightarrow 0}} \int_{\Gamma_{3a} \cup \Gamma_{3b}} e^{-k_{p/s}(s)x} e^{st} ds &= \int_{-\infty}^0 e^{-k_{p/s}(\rho e^{i\varphi_0})x} e^{\rho t e^{i\varphi_0}} e^{i\varphi_0} d\rho \\ &= - \int_0^{\infty} e^{-k_{p/s}(\rho e^{i\varphi_0})x} e^{i(\varphi_0 + \rho t \sin \varphi_0)} e^{\rho t \cos \varphi_0} d\rho, \\ \lim_{\substack{R \rightarrow \infty, \\ r \rightarrow 0}} \int_{\Gamma_{5a} \cup \Gamma_{5b}} e^{-k_{p/s}(s)x} e^{st} ds &= \int_0^{\infty} e^{-k_{p/s}(\rho e^{-i\varphi_0})x} e^{\rho t e^{-i\varphi_0}} e^{-i\varphi_0} d\rho \\ &= \int_0^{\infty} e^{-k_{p/s}(\rho e^{-i\varphi_0})x} e^{-i(\varphi_0 + \rho t \sin \varphi_0)} e^{\rho t \cos \varphi_0} d\rho, \end{aligned}$$

and with the inverse Laplace transform (13.65), i.e.,

$$\lim_{\substack{R \rightarrow \infty, \\ r \rightarrow 0}} \int_{\Gamma_0} e^{-k_{p/s}(s)x} e^{st} ds = 2\pi i u_{\delta}^{(\text{III})}(x, t),$$

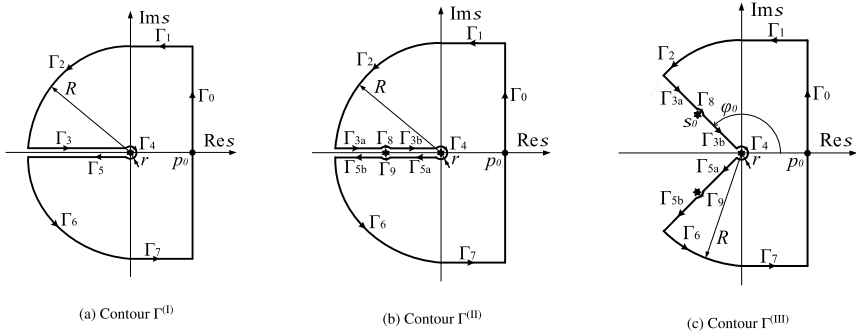


Figure 13.14 Integration contours depending on the nature and number of TF’s BPs.

by the Cauchy integral theorem (13.A.94), the impulse response is obtained as

$$u_{\delta}^{(III)}(x, t) = \frac{1}{2\pi i} \int_0^{\infty} \left(e^{-k_{p/s}(\rho e^{i\varphi_0})x} e^{i(\varphi_0 + \rho t \sin \varphi_0)} - e^{-k_{p/s}(\rho e^{-i\varphi_0})x} e^{-i(\varphi_0 + \rho t \sin \varphi_0)} \right) e^{-\rho t |\cos \varphi_0|} d\rho, \quad (13.A.95)$$

transforming to (13.67) by separating the real and imaginary parts in $k_{p/s}(\rho e^{\pm i\varphi_0})$ and by using $\bar{k}_{p/s}(s) = k_{p/s}(\bar{s})$, since the integrals along all other contours tend to zero as $R \rightarrow \infty$ and $r \rightarrow 0$, as proved below. By setting $\varphi_0 = \pi$ in (13.A.95), one obtains impulse responses

$$u_{\delta}^{(I,II)}(x, t) = \frac{1}{2\pi i} \int_0^{\infty} \left(e^{-k_{p/s}(\rho e^{-i\pi})x} - e^{-k_{p/s}(\rho e^{i\pi})x} \right) e^{-\rho t} d\rho,$$

which transform to (13.66) using the same arguments as in the previous case.

The parameterization of contour Γ_1 is $s = p + iR$, $p \in (0, p_0)$, implying the estimate of integral along Γ_1 as follows:

$$\begin{aligned} |I_{\Gamma_1}| &\leq \int_{\Gamma_1} \left| e^{-k_{p/s}(s)x} e^{st} \right| ds = \int_0^{p_0} \left| e^{-k_{p/s}(p+iR)x} e^{(p+iR)t} \right| dp \\ &\leq \int_0^{p_0} \left| e^{-k_{p/s}(p+iR)x} \right| e^{pt} dp = \int_0^{p_0} e^{-x|k_{p/s}(p+iR)| \cos(\arg(k_{p/s}(p+iR)))} e^{pt} dp. \end{aligned} \quad (13.A.96)$$

Assuming $s = \rho e^{i\varphi}$, with $\rho = \sqrt{p^2 + R^2} \sim R$ and $\varphi = \arctan \frac{R}{p} \sim \frac{\pi}{2}$, as $R \rightarrow \infty$, expressions (13.51) and (13.52) for k_p and k_s are estimated by

$$k_{p/s}(p + iR) \sim K \tau_\alpha \tau_\gamma R^{\frac{\alpha+\gamma}{2}} e^{i\frac{(\alpha+\gamma)\pi}{4}}, \quad \text{as } R \rightarrow \infty, \quad (13.A.97)$$

so that (13.A.96) in the limit as $R \rightarrow \infty$ becomes

$$\lim_{R \rightarrow \infty} |I_{\Gamma_1}| \leq \lim_{R \rightarrow \infty} \int_0^{p_0} e^{-xK \tau_\alpha \tau_\gamma R^{\frac{\alpha+\gamma}{2}} \cos \frac{(\alpha+\gamma)\pi}{4}} e^{pt} dp = 0,$$

for $\alpha + \gamma \in (0, 2)$. Analogously, it can be proved that $\lim_{R \rightarrow \infty} |I_{\Gamma_7}| = 0$.

The parameterization of contour Γ_2 is $s = Re^{i\varphi}$, with $\varphi \in (\frac{\pi}{2}, \varphi_0)$, so that the estimate of the integral along Γ_2 is

$$\begin{aligned} |I_{\Gamma_2}| &\leq \int_{\Gamma_2} \left| e^{-k_{p/s}(s)x} e^{st} \right| ds = \int_{\frac{\pi}{2}}^{\varphi_0} R \left| e^{-k_{p/s}(Re^{i\varphi})x} e^{Rte^{i\varphi}} \right| d\varphi \\ &\leq \int_{\frac{\pi}{2}}^{\varphi_0} R e^{-x|k_{p/s}(Re^{i\varphi})| \cos(\arg(k_{p/s}(Re^{i\varphi})))} e^{Rt \cos \varphi} d\varphi. \end{aligned} \quad (13.A.98)$$

Again, by (13.51) and (13.52), as in (13.A.97), one has

$$k_{p/s}(Re^{i\varphi}) \sim K \tau_\alpha \tau_\gamma R^{\frac{\alpha+\gamma}{2}} e^{i\frac{(\alpha+\gamma)\varphi}{2}}, \quad \text{as } R \rightarrow \infty,$$

which along with $\alpha + \gamma \in (0, 2)$ and $\cos \varphi < 0$ for $\varphi \in (\frac{\pi}{2}, \pi)$ implies that (13.A.98) becomes

$$\begin{aligned} \lim_{R \rightarrow \infty} |I_{\Gamma_2}| &\leq \lim_{R \rightarrow \infty} \int_{\frac{\pi}{2}}^{\varphi_0} R e^{-xK \tau_\alpha \tau_\gamma R^{\frac{\alpha+\gamma}{2}} \cos \frac{(\alpha+\gamma)\varphi}{2}} e^{Rt \cos \varphi} d\varphi \\ &\leq \lim_{R \rightarrow \infty} \int_{\frac{\pi}{2}}^{\varphi_0} R e^{Rt \cos \varphi} d\varphi = 0. \end{aligned}$$

By the similar arguments, $\lim_{R \rightarrow \infty} |I_{\Gamma_6}| = 0$.

The parameterization of contour Γ_4 is $s = re^{i\varphi}$, with $\varphi \in (-\varphi_0, \varphi_0)$, so that the estimate of the integral along Γ_4 is

$$\begin{aligned} |I_{\Gamma_4}| &\leq \int_{\Gamma_4} \left| e^{-k(s)x} e^{st} \right| ds = \int_{-\varphi_0}^{\varphi_0} r \left| e^{-k_{p/s}(re^{i\varphi})x} e^{rte^{i\varphi}} \right| d\varphi \\ &\leq \int_{-\varphi_0}^{\varphi_0} r e^{-x|k_{p/s}(re^{i\varphi})| \cos(\arg(k_{p/s}(re^{i\varphi})))} e^{rt \cos \varphi} d\varphi. \end{aligned} \quad (13.A.99)$$

The asymptotics of PCs, given by (13.51) and (13.52), are

$$k_p^2(s) \sim K^2 \quad \text{and} \quad k_s^2(s) \sim \frac{K^2}{\tau_\beta} \frac{1}{s^\beta} \quad \text{as } r \rightarrow 0,$$

so that, using the fact that $\frac{\beta\varphi}{2} \in (-\frac{\varphi_0}{2}, \frac{\varphi_0}{2})$, implying $\cos \frac{\beta\varphi}{2} > 0$, estimate (13.A.99) becomes

$$\lim_{r \rightarrow 0} |I_{\Gamma_4}| \leq \begin{cases} \lim_{r \rightarrow 0} \int_{-\varphi_0}^{\varphi_0} r e^{-xK} e^{rt \cos \varphi} d\varphi = 0, & \text{for } k_p, \\ \lim_{r \rightarrow 0} \int_{-\varphi_0}^{\varphi_0} r e^{-x \frac{K}{\sqrt{\tau\beta}} \frac{1}{r\beta/2} \cos \frac{\beta\varphi}{2}} e^{rt \cos \varphi} d\varphi = 0, & \text{for } k_s. \end{cases}$$

The parameterization of contour Γ_8 is $s - s_0 = r e^{i\varphi}$, with $\varphi \in (\varphi_0 - \pi, \varphi_0)$, implying the estimate of integral along Γ_8 as

$$\begin{aligned} |I_{\Gamma_8}| &\leq \int_{\Gamma_8} \left| e^{-k_{p/s}(s)x} e^{st} \right| ds = \int_{-\pi+\varphi_0}^{\varphi_0} r \left| e^{-k_{p/s}(s_0+re^{i\varphi})x} e^{(s_0+re^{i\varphi})t} \right| d\varphi \\ &\leq e^{s_0 t} \int_{-\pi+\varphi_0}^{\varphi_0} r \left| e^{-k_{p/s}(s_0+re^{i\varphi})x} \right| e^{rt \cos \varphi} d\varphi, \end{aligned} \quad (13.A.100)$$

so that, by (13.A.100),

$$\lim_{r \rightarrow 0} |I_{\Gamma_8}| \leq e^{s_0 t} \lim_{r \rightarrow 0} \int_{-\pi+\varphi_0}^{\varphi_0} r e^{rt \cos \varphi} d\varphi = 0,$$

since PCs, by (13.51) and (13.52), yield

$$k_{p/s}^2(s_0 + r e^{i\varphi}) \sim k_{p/s}^2(s_0) = 0 \quad \text{as } r \rightarrow 0.$$

By similar arguments, one also has $\lim_{r \rightarrow 0} |I_{\Gamma_9}| = 0$.

13.A.2 Calculation of harmonic response

The harmonic response is calculated by inverting the Laplace transform of U in (13.70) by the definition, i.e., by (13.71), using the Cauchy residues theorem

$$\begin{aligned} \oint_{\Gamma^{(i)}} U(x, s) e^{st} ds &= 2\pi i \left(\text{Res} \left(U(x, s) e^{st}, i\omega \right) + \text{Res} \left(U(x, s) e^{st}, -i\omega \right) \right), \\ \text{with } i &\in \{\text{I, II, III}\}, \end{aligned} \quad (13.A.101)$$

where the contour $\Gamma^{(i)}$, containing the Bromwich path Br , is chosen differently, as already discussed in Appendix 13.A.1 and shown in Fig. 13.14, since in addition to BPs that the TF $e^{-k_{p/s}(s)x}$ may have, function U has a pair of complex conjugated poles $\pm i\omega$, each of the first order, due to the term $\frac{s}{s^2 + \omega^2}$. The harmonic response, as in Appendix 13.A.1, is calculated only using the contour $\Gamma^{(\text{III})}$ from Fig. 13.14c, i.e., if PC has complex conjugated BPs $s_0 = \rho_0 e^{i\varphi_0}$ and \bar{s}_0 apart from $s = 0$, since the other two cases correspond to $\varphi_0 = \pi$.

The integrals along contours $\Gamma_{3a} \cup \Gamma_{3b}$ (parameterized by $s = \rho e^{i\varphi_0}$, $\rho \in (r, \rho_0 - r) \cup (\rho_0 + r, R)$) and $\Gamma_{5a} \cup \Gamma_{5b}$ (parameterized by $s = \rho e^{-i\varphi_0}$, $\rho \in (r, \rho_0 - r) \cup (\rho_0 + r, R)$) read

$$\begin{aligned} \lim_{\substack{R \rightarrow \infty \\ r \rightarrow 0}} \int_{\Gamma_{3a} \cup \Gamma_{3b}} U(x, s) e^{st} ds &= \mathcal{U}_0 \int_0^{\infty} \frac{\rho e^{i\varphi_0}}{\rho^2 e^{2i\varphi_0} + \omega^2} e^{-k_{p/s}(\rho e^{i\varphi_0})x} e^{\rho t e^{i\varphi_0}} e^{i\varphi_0} d\rho \\ &= -\mathcal{U}_0 \int_0^{\infty} \frac{e^{-k_{p/s}(\rho e^{i\varphi_0})x} e^{i(2\varphi_0 + \rho t \sin \varphi_0)}}{\rho^2 e^{2i\varphi_0} + \omega^2} e^{\rho t \cos \varphi_0} \rho d\rho, \\ \lim_{\substack{R \rightarrow \infty \\ r \rightarrow 0}} \int_{\Gamma_{5a} \cup \Gamma_{5b}} U(x, s) e^{st} ds &= \mathcal{U}_0 \int_0^{\infty} \frac{\rho e^{-i\varphi_0}}{\rho^2 e^{-2i\varphi_0} + \omega^2} e^{-k_{p/s}(\rho e^{-i\varphi_0})x} e^{\rho t e^{-i\varphi_0}} e^{-i\varphi_0} d\rho \\ &= \mathcal{U}_0 \int_0^{\infty} \frac{e^{-k_{p/s}(\rho e^{-i\varphi_0})x} e^{-i(2\varphi_0 + \rho t \sin \varphi_0)}}{\rho^2 e^{-2i\varphi_0} + \omega^2} e^{\rho t \cos \varphi_0} \rho d\rho, \end{aligned}$$

and with the inverse Laplace transform (13.71), i.e.,

$$\lim_{\substack{R \rightarrow \infty \\ r \rightarrow 0}} \int_{\Gamma_0} U(x, s) e^{st} ds = 2\pi i u^{(\text{III})}(x, t),$$

by the Cauchy residues theorem (13.A.101), the harmonic response is obtained as

$$\begin{aligned} u^{(\text{III})}(x, t) &= \frac{\mathcal{U}_0}{2\pi i} \int_0^{\infty} \left(\frac{e^{-k_{p/s}(\rho e^{i\varphi_0})x} e^{i(2\varphi_0 + \rho t \sin \varphi_0)}}{\rho^2 e^{2i\varphi_0} + \omega^2} \right. \\ &\quad \left. - \frac{e^{-k_{p/s}(\rho e^{-i\varphi_0})x} e^{-i(2\varphi_0 + \rho t \sin \varphi_0)}}{\rho^2 e^{-2i\varphi_0} + \omega^2} \right) e^{-\rho t |\cos \varphi_0|} \rho d\rho \\ &\quad + \mathcal{U}_0 e^{-\operatorname{Re} k_{p/s}(i\omega)x} \cos(\omega t - \operatorname{Im} k_{p/s}(i\omega)x), \end{aligned} \quad (13.A.102)$$

with the residues in (13.A.101) calculated as

$$\begin{aligned} \operatorname{Res}(U(x, s) e^{st}, i\omega) + \operatorname{Res}(U(x, s) e^{st}, -i\omega) \\ &= \frac{\mathcal{U}_0}{2} \left(e^{-k_{p/s}(i\omega)x} e^{i\omega t} + e^{-k_{p/s}(-i\omega)x} e^{-i\omega t} \right) \\ &= \mathcal{U}_0 e^{-\operatorname{Re} k_{p/s}(i\omega)x} \cos(\omega t - \operatorname{Im} k_{p/s}(i\omega)x), \end{aligned}$$

due to the separation of real and imaginary parts in $k_{p/s}(\pm i\omega)$ and the use of $\bar{k}_{p/s}(s) = k_{p/s}(\bar{s})$, since the integrals along all other contours tend to zero as $R \rightarrow \infty$ and $r \rightarrow 0$. The proof is omitted, since it uses a similar argumentation as in Appendix 13.A.1. By setting $\varphi_0 = \pi$ in (13.A.102), one obtains

the harmonic responses

$$u^{(I,II)}(x, t) = \frac{\mathcal{U}_0}{2\pi i} \int_0^\infty \left(e^{-k_{p/s}(\rho e^{i\pi})x} - e^{-k_{p/s}(\rho e^{-i\pi})x} \right) \frac{\rho e^{-\rho t}}{\rho^2 + \omega^2} d\rho \\ + \mathcal{U}_0 e^{-\operatorname{Re} k_{p/s}(i\omega)x} \cos(\omega t - \operatorname{Im} k_{p/s}(i\omega)x).$$

References

- [1] J. Abate, P.P. Valkó, Multi-precision Laplace transform inversion, *International Journal for Numerical Methods in Engineering* 60 (2004) 979–993.
- [2] N. Al-Zubaidi R-Smith, A. Kartci, L. Brančík, Fractional-order lossy transmission line with skin effect using NILT method, in: 40th International Conference on Telecommunications and Signal Processing (TSP), Barcelona, Spain, 2017.
- [3] N. Al-Zubaidi R-Smith, A. Kartci, L. Brančík, Application of numerical inverse Laplace transform methods for simulation of distributed systems with fractional-order elements, *Journal of Circuits, Systems, and Computers* 27 (2018) 1850172.
- [4] T.M. Atanackovic, S. Pilipovic, D. Zorica, Diffusion wave equation with two fractional derivatives of different order, *Journal of Physics A: Mathematical and Theoretical* 40 (2007) 5319–5333.
- [5] T.M. Atanackovic, S. Pilipovic, D. Zorica, Time distributed-order diffusion-wave equation. I. Volterra type equation, *Proceedings of the Royal Society A. Mathematical, Physical and Engineering Sciences* 465 (2009) 1869–1891.
- [6] T.M. Atanackovic, S. Pilipovic, D. Zorica, Time distributed-order diffusion-wave equation. II. Applications of the Laplace and Fourier transformations, *Proceedings of the Royal Society A. Mathematical, Physical and Engineering Sciences* 465 (2009) 1893–1917.
- [7] E. Bazhlekova, I. Dimovski, Exact solution for the fractional cable equation with non-local boundary conditions, *Central European Journal of Physics* 11 (2013) 1304–1313.
- [8] S.M. Cvetičanin, D. Zorica, M.R. Rapaić, Generalized time-fractional telegrapher's equation in transmission line modeling, *Nonlinear Dynamics* 88 (2017) 1453–1472.
- [9] S.M. Cvetičanin, D. Zorica, M.R. Rapaić, Frequency characteristics of two topologies representing fractional order transmission line model, *Circuits, Systems, and Signal Processing* 39 (2020) 456–473.
- [10] S.M. Cvetičanin, D. Zorica, M.R. Rapaić, Non-local telegrapher's equation as a transmission line model, *Applied Mathematics and Computation* 390 (2021) 125602.
- [11] E.R. de Hoog, J.H. Knight, A.N. Stokes, An improved method for numerical inversion of Laplace transforms, *SIAM Journal on Scientific and Statistical Computing* 3 (1982) 357–366.
- [12] C. Donaghy-Spargo, On Heaviside's contributions to transmission line theory: waves, diffusion and energy flux, *Philosophical Transactions - Royal Society. Mathematical, Physical and Engineering Sciences* 376 (2018) 20170457.
- [13] A. Dzieliński, G. Sarwas, D. Sierociuk, Comparison and validation of integer and fractional order ultracapacitor models, *Advances in Difference Equations* 2011 (2011) 11.
- [14] A. Dzieliński, D. Sierociuk, G. Sarwas, Some applications of fractional order calculus, *Bulletin of the Polish Academy of Sciences. Technical Sciences* 58 (2010) 583–592.
- [15] R. Süße, A. Domhardt, M. Reinhard, Calculation of electrical circuits with fractional characteristics of construction elements, *Forschung im Ingenieurwesen* 69 (2005) 230–235.
- [16] E. Fendzi-Donfack, J.P. Nguenang, L. Nana, Fractional analysis for nonlinear electrical transmission line and nonlinear Schroedinger equations with incomplete sub-equation,

- The European Physical Journal Plus 133 (2018) 32, <https://doi.org/10.1140/epjp/i2018-11851-1>.
- [17] J.F. Gómez-Aguilar, D. Baleanu, Fractional transmission line with losses, *Zeitschrift für Naturforschung A* 69 (2014) 539–546.
 - [18] J.F. Gómez-Aguilar, D. Baleanu, Solutions of the telegraph equations using a fractional calculus approach, *Proceedings of the Romanian Academy Series A* 15 (2014) 27–34.
 - [19] J.F. Gómez-Aguilar, M. Miranda-Hernández, M.G. López-López, V.M. Alvarado-Martínez, D. Baleanu, Modeling and simulation of the fractional space-time diffusion equation, *Communications in Nonlinear Science and Numerical Simulation* 30 (2016) 115–127.
 - [20] K. Haška, S.M. Cvetičanin, D. Zorica, Dissipative and generative fractional electric elements in modeling RC and RL circuits, *Nonlinear Dynamics* 105 (2021) 3451–3474.
 - [21] K. Haška, D. Zorica, S.M. Cvetičanin, Fractional RLC circuit in transient and steady state regimes, *Communications in Nonlinear Science and Numerical Simulation* 96 (2021) 105670, pp. 1–17.
 - [22] O. Heaviside, *Electromagnetic Theory*, vol. II, Chelsea Publishing Company, New York, 1899.
 - [23] B.I. Henry, T.A.M. Langlands, S.L. Wearne, Fractional cable models for spiny neuronal dendrites, *Physical Review Letters* 100 (2008) 128103.
 - [24] A. Jakubowska, J. Włczak, Analysis of the transient state in a series circuit of the class $RL_{\beta}C_{\alpha}$, *Circuits, Systems, and Signal Processing* 35 (2016) 1831–1853.
 - [25] A. Jakubowska-Ciszek, J. Włczak, Analysis of the transient state in a parallel circuit of the class $RL_{\beta}C_{\alpha}$, *Applied Mathematics and Computation* 319 (2018) 287–300.
 - [26] I.S. Jesus, J.A.T. Machado, Development of fractional order capacitors based on electrolyte processes, *Nonlinear Dynamics* 56 (2009) 45–55.
 - [27] E. Kengne, W.M. Liu, Exact solutions of the derivative nonlinear Schrödinger equation for a nonlinear transmission line, *Physical Review E* 73 (2006) 026603.
 - [28] A.A. Kilbas, H.M. Srivastava, J.J. Trujillo, *Theory and Applications of Fractional Differential Equations*, Elsevier B.V., Amsterdam, 2006.
 - [29] M.S. Krishna, S. Das, K. Biswas, B. Goswami, Fabrication of a fractional order capacitor with desired specifications: a study on process identification and characterization, *IEEE Transactions on Electron Devices* 58 (2011) 4067–4073.
 - [30] T.A.M. Langlands, B.I. Henry, S.L. Wearne, Fractional cable equation models for anomalous electrodiffusion in nerve cells: infinite domain solutions, *Journal of Mathematical Biology* 59 (2009) 761–808.
 - [31] T.A.M. Langlands, B.I. Henry, S.L. Wearne, Fractional cable equation models for anomalous electrodiffusion in nerve cells: finite domain solutions, *SIAM Journal on Applied Mathematics* 71 (2011) 1168–1203.
 - [32] Y. Lin, X. Li, C. Xu, Finite difference/spectral approximations for the fractional cable equation, *Mathematics of Computation* 80 (2011) 1369–1396.
 - [33] F. Liu, Q. Yang, I. Turner, Two new implicit numerical methods for the fractional cable equation, *Journal of Computational and Nonlinear Dynamics* 6 (2011) 011009.
 - [34] J.A.T. Machado, A.M.S.F. Galhano, Fractional order inductive phenomena based on the skin effect, *Nonlinear Dynamics* 68 (2012) 107–115.
 - [35] R. Martín, J.J. Quintana, A. Ramos, I. Nuez, Modeling electrochemical double layer capacitor, from classical to fractional impedance, in: *Electrotechnical Conference, MELECON 2008, The 14th IEEE Mediterranean*, Ajaccio, Corsica, France, 2008, pp. 61–66.
 - [36] D. Mondal, K. Biswas, Packaging of single-component fractional order element, *IEEE Transactions on Device and Materials Reliability* 13 (2013) 73–80.
 - [37] F.B. Pelap, M.M. Faye, Solitonlike excitations in a one-dimensional electrical transmission line, *Journal of Mathematical Physics* 46 (2005) 033502.

- [38] I. Podlubny, *Fractional Differential Equations*, Academic Press, San Diego, 1999.
- [39] Z.B. Popović, B.D. Popović, *Introductory Electromagnetics*, Prentice Hall, New Jersey, 1999.
- [40] J.J. Quintana, A. Ramos, I. Nuez, Modeling of an EDLC with fractional transfer functions using Mittag-Leffler equations, *Mathematical Problems in Engineering* 2013 (2013) 807034.
- [41] A.G. Radwan, M.E. Fouda, Optimization of fractional-order *RLC* filters, *Circuits, Systems, and Signal Processing* 32 (2013) 2097–2118.
- [42] A.G. Radwan, K.N. Salama, Fractional-order *RC* and *RL* circuits, *Circuits, Systems, and Signal Processing* 31 (2012) 1901–1915.
- [43] M.R. Rapačić, Z.D. Jeličić, Optimal control of a class of fractional heat diffusion systems, *Nonlinear Dynamics* 62 (2010) 39–51.
- [44] A. Sardar, S.M. Husnine, S.T.R. Rizvi, M. Younis, K. Ali, Multiple travelling wave solutions for electrical transmission line model, *Nonlinear Dynamics* 82 (2015) 1317–1324.
- [45] I. Schäfer, K. Krüger, Modelling of coils using fractional derivatives, *Journal of Magnetism and Magnetic Materials* 307 (2006) 91–98.
- [46] Y. Shang, W. Fei, H. Yu, A fractional-order RLGC model for terahertz transmission line, in: *IEEE MTT-S International Microwave Symposium Digest (IMS)*, Seattle, WA, 2013, pp. 1–3.
- [47] A.L. Soubhia, R.F. Camargo, E. Capelas de Oliveira, J. Vaz Jr., Theorem for series in three-parameter Mittag-Leffler function, *Fractional Calculus and Applied Analysis* 13 (2010) 9–20.
- [48] F. Tchier, A. Yusuf, A.I. Aliyu, M. Inc, Soliton solutions and conservation laws for lossy nonlinear transmission line equation, *Superlattices and Microstructures* 107 (2017) 320–336.
- [49] S. Vitali, G. Castellani, F. Mainardi, Time fractional cable equation and applications in neurophysiology, *Chaos, Solitons and Fractals* 102 (2017) 467–472.
- [50] C. Yang, H. Yu, Y. Shang, W. Fei, Characterization of CMOS metamaterial transmission line by compact fractional-order equivalent circuit model, *IEEE Transactions on Electron Devices* 62 (2015) 3012–3018.
- [51] M. Younis, S. Ali, Solitary wave and shock wave solitons to the transmission line model for nano-ionic currents along microtubules, *Applied Mathematics and Computation* 246 (2014) 460–463.
- [52] P. Zhuang, F. Liu, I. Turner, V. Anh, Galerkin finite element method and error analysis for the fractional cable equation, *Numerical Algorithms* 72 (2016) 447–466.
- [53] D. Zorica, S.M. Cvetičanin, Fractional telegrapher's equation as a consequence of Cattaneo's heat conduction law generalization, *Theoretical and Applied Mechanics* 45 (2018) 35–51.

This page intentionally left blank

System approach for the frequency analysis of a fractional-order acoustic tube: application for the resonator of the flute instrument

Xavier Moreau^a, Gaby Abou Haidar^{a,b}, and Roy Abi Zeid Daou^{c,d}

^aBordeaux University, CNRS, IMS Lab., Bordeaux, France

^bAmerican University of Science and Technology, Faculty of Engineering, Zahle, Lebanon

^cLebanese German University, Biomedical Technologies Department, Jounieh, Lebanon

^dMART, Learning, Education and Training Center, Chananiir, Lebanon

14.1. Introduction

Fractional calculus is a relatively old mathematical tool that was introduced during letter exchanges between l'Hopital and Leibniz in 1695 [1,2]. Until the middle of the 20th century, no effort was made to implement this mathematical tool in industrial applications.

From the 1960s onwards, the number of research groups, journals, books, special issues, and conferences dedicated to fractional calculus increased dramatically due mainly to the advantages that the fractional order presents to engineering systems [3,4]. In fact, the fractional behavior may appear due to natural phenomena, as in the case of diffusive interfaces [5,6], magnetic fields [7], and seismic waves [8], or it can be introduced manually integrated as in the case of controllers (CRONE, fractional PID, fractional sliding mode [9–11]) and other applications, such as the control of car suspensions [12], image processing [13,14], electrical components [15], audio filters [16], economical modeling [17], and others [18].

In 1964, in order to develop a real system exhibiting fractional-order behavior, Carlson proposed the fractional inductive effect [19]. In 1975, Oustaloup introduced arrangements of resistive and capacitive (RC) cells to synthesize fractional behavior [20]. Other representations based also on RC cells were proposed by Podlubny [19], whereas Abi Zeid Daou et al. introduced for the first time the inductive effects and showed how to implement fractional-order systems using RLC components [20].

To facilitate the simulation and the implementation of such systems, numerical simulators have been developed, such as the CRONE controller, which ensures the conversion from the fractional to the rational form of the transfer function [21]. These numerical simulators have been developed first for simple models (conservative plane waves) and they were based on signal processing tools. These were known as digital waveguide forms [22–25] and they were presented in a factorized system as developed by Kelly–Lochbaum [26]. Added to that, the plane wave equations were divided into two operators, each one decoupled into progressive waves, from which one could derive a delay system for the simulation.

Furthermore, 3D and 2D models with realistic boundary conditions are too complex to be considered, as the case of real-time sound synthesis. They can be effectively simplified to a 1D wave equation including a variable that models the medium dimensions. It is known as the *equation of the pavilions* and it is also called model of Webster [27–29]. A more elaborate version of this conservative model includes the effect of viscous–thermal losses due to the boundary layers in the vicinity of the walls. This dissipative model, known as *Webster–Lokshin 1D*, includes a term which involves a fractional derivation in time of order $3/2$ [30–33]. This operator plays a crucial role from a perceptual point of view on sound realism [34].

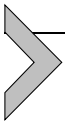
Concerning the flute musical instrument, the fractional order is a natural phenomenon that resides in the resonator. In fact, the thermal losses on the boundaries of the tube create a viscous–thermal effect as was already identified by Matignon [25,26,28–33].

In previous works, the musician–flute system was implemented and modeled [35,36]; in fact, an air compressor, a servo-valve, and an artificial mouth have been mounted to replace the musician lungs and mouth. A control system was also developed to regulate the pressure and the flow delivered to the artificial mouth. Added to that, the flute exciter is directly coupled with the artificial mouth and some pressure and temperature sensors are placed within the resonator.

The objective of this chapter is, first, to establish a *knowledge model* from partial differential equations which define the Webster–Lokshin model of an acoustic tube of constant radius r . Thus, a conventional resolution in the operational domain leads to the analytical expression of the acoustic impedance and admittance of the tube as a function of the position x , its length L , and its radius r . This working methodology will be similar to the one used for the modeling of the diffusive phenomenon in a semiinfinite homogeneous bar already proposed in previous works [37]. Then, a system

vision is proposed aiming to causally decompose the whole model into submodels in order to facilitate the analysis in the frequency domain.

This chapter is organized as follows. In Section 14.2, the modeling of the acoustic resonator will be presented. Section 14.3 will show the system approach and the block configuration. In Section 14.4, the simulations and the frequency domain analysis of this system will be proposed. Finally, Section 14.5 will conclude the work and propose some ideas to be implemented in future works.



14.2. Modeling

14.2.1 Schematization, configuration, and setting in equation

Let us consider an acoustic tube of length L and constant radius r subjected to an acoustic flow (also called volume flow) $Q_v(t)$ at $x = 0$ where $x \in [0, L]$, as shown in Fig. 14.1.

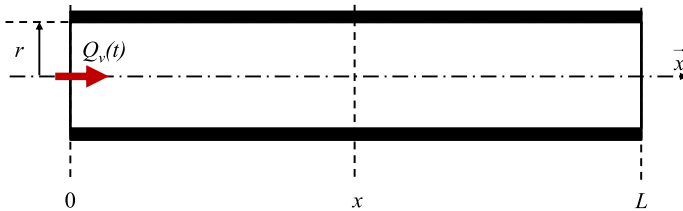


Figure 14.1 1D schematic of an acoustic tube of radius r and of finite length L subjected to an acoustic flow $Q_v(t)$ with $x = 0$.

When an acoustic wave propagates in air, this sets the particles of the fluid in motion which vibrate at a speed $v(t)$ around their equilibrium position. The acoustic flow $Q_v(t)$ then measures the flow [in m^3/s] of this speed through the surface. The acoustic flow is therefore a scalar quantity [38–42].

The acoustic impedance Z_{ac} (also called *specific* acoustic impedance, because it is an intensive quantity) of a medium is defined in steady state by the ratio between the acoustic pressure (in Pa) and the speed (in m/s) of the associated particle. When the medium is air, Z_{ac} is equal to the product between the density of air, ρ_a , and the speed of sound in air, c_a ; thus, $Z_{ac} = \rho_a * c_a$. These two parameters depend also on the air temperature T_a . As an illustration, Table 14.1 presents the values of the sound speed c_a , the

Table 14.1 Values of the speed of sound c_a , the density ρ_a , and the characteristic acoustic impedance Z_{ac} as a function of the air temperature T_a .

T_a (°C)	-10	-5	0	5	10	15	20	25	30
c_a (m/s)	325.4	328.5	331.5	334.5	337.5	340.5	343.4	346.3	349.2
ρ_a (kg/m ³)	1.341	1.316	1.293	1.269	1.247	1.225	1.204	1.184	1.164
Z_{ac} (Pa·s/m)	436.5	432.4	428.3	424.5	420.7	417	413.5	410	406.6

sound density ρ_a , and the acoustic impedance Z_{ac} as a function of the air temperature T_a .

The model used in this work is based on Webster–Lokshin [28]. It is a model with a monospatial dependence which characterizes the linear propagation of acoustic waves in tubes with axial symmetry. This model takes also into account viscous–thermal losses at the wall boundaries with the assumption of wide tubes [43]. Thus, in an axisymmetric tube of constant section $S = \pi r^2$, the acoustic pressure $P(x, t, L)$ and the acoustic flow $Q_v(x, t, L)$ are governed by the *equation of the pavilions*, also called Webster–Lokshin, and the Euler equation, leading to the following system:

$$\left\{ \begin{array}{l} \frac{r}{c_a} \frac{\partial^2}{\partial t^2} P(x, t, L) + 2\varepsilon \frac{r}{c_a} \frac{\partial^{3/2}}{\partial t^{3/2}} P(x, t, L) - r \frac{\partial^2}{\partial x^2} P(x, t, L) = 0, \\ x \in [0; L], \quad t > 0, \\ \frac{\rho_a}{S} \frac{\partial}{\partial t} Q_v(x, t, L) + \frac{\partial}{\partial x} P(x, t, L) = 0, \end{array} \right. \quad (14.1)$$

where ε is a parameter associated with the viscous–thermal losses.

More precisely, ε is given by the relation

$$\varepsilon = \frac{K_0}{r}, \quad \text{with} \quad K_0 = \sqrt{l_v} + (\gamma - 1) \sqrt{l_h}, \quad (14.2)$$

where l_v and l_h represent the characteristic lengths of viscous ($l_v = 4 \times 10^{-8}$ m) and thermal ($l_h = 6 \times 10^{-8}$ m) effects, γ being the ratio of specific heats.

The phenomenon of viscous–thermal losses is a dissipative effect at the wall boundary of the tube, which is due to the viscosity of the air and to the thermal conduction [43,44]. For the case of wind musical instrument resonators, the assumption of wide tubes is used. This hypothesis is expressed by the following relation:

$$r \gg \max[r_v = (l_v \lambda)^{0.5}; r_h = (l_h \lambda)^{0.5}], \quad (14.3)$$

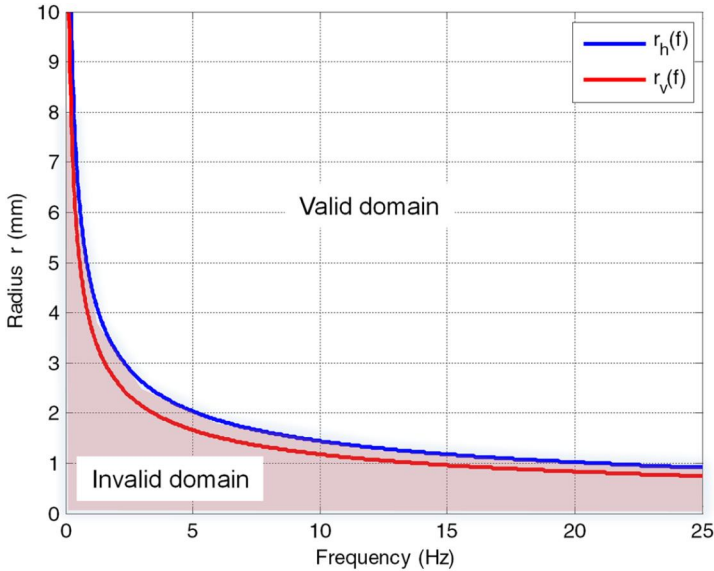


Figure 14.2 Curves $r_v(f) = (l_v c_a / f)^{0.5}$ (in red; light gray in print version) and $r_h(f) = (l_h c_a / f)^{0.5}$ (in blue; dark gray in print version) with respect to the frequency f .

where $\lambda = c_a / f$ represents the wavelength (in m) and f the frequency (in Hz).

Thus, for the sound speed c_a and a frequency f_{min} corresponding to the lower frequency limit of the model studied, it is possible to determine the minimum value of the radius r_{min} of the acoustic tube below which the model is not valid.

As an illustration where $l_v = 4 \times 10^{-8}$ m, $l_h = 6 \times 10^{-8}$ m, and $c_a = 346.3$ m/s (at a constant temperature $T_a = 25^\circ\text{C}$), Fig. 14.2 presents the curves of $r_v(f) = (l_v c_a / f)^{0.5}$ (in red; light gray in print version) and $r_h(f) = (l_h c_a / f)^{0.5}$ (in blue; dark gray in print version) with respect to the frequency f .

If we consider that the operational frequency domain of the Webster–Lokshin model is relative to the audible frequencies, i.e., frequencies ranging between 20 Hz (most serious frequency) and 20,000 Hz (most acute frequency), then $f_{min} = 20$ Hz. For this value of f_{min} , the model is valid for acoustic tube radius greater than 1 mm (in Section 14.3, $r = 5$ mm).

14.2.2 Resolution in the symbolic domain

Under the assumption of zero initial conditions (I.C. = 0), the Laplace transformation applied to system (14.1) leads to

$$\begin{cases} \left[\left[\left(\frac{s}{c_a} \right)^2 + 2\varepsilon \left(\frac{s}{c_a} \right)^{3/2} \right] - \frac{\partial^2}{\partial x^2} \right] r\bar{P}(x, s, L) = 0, \\ \frac{\rho_a}{S} s \bar{Q}_v(x, s, L) + \frac{\partial}{\partial x} \bar{P}(x, s, L) = 0, \end{cases} \quad (14.4)$$

with $\bar{P}(x, s, L) = \text{TL}\{P(x, t, L)\}$ and $\bar{Q}_v(x, s, L) = \text{TL}\{Q_v(x, t, L)\}$, s being the Laplace variable and TL its transformation. Solving the Webster-Lokshin equation [28] gives the solution $\bar{P}(x, s, L)$ in its general form:

$$\bar{P}(x, s, L) = \frac{A(s)}{r} e^{x\Gamma(s)} + \frac{B(s)}{r} e^{-x\Gamma(s)}, \quad (14.5)$$

where $A(s)$ and $B(s)$ are rational functions of s which depend on the boundary conditions and $\Gamma(j\omega) = jk(\omega)$, $k(\omega)$ being a standard complex wave number; $\Gamma(s)$ is given in the Laplace domain by the following relation [45]:

$$\Gamma(s) = \sqrt{\left(\frac{s}{c_a} \right)^2 + 2\varepsilon \left(\frac{s}{c_a} \right)^{3/2}}, \quad \text{with } R_e(\Gamma(s)) \geq 0 \text{ if } \varepsilon \geq 0. \quad (14.6)$$

The expression of the $\bar{Q}_v(x, s, L)$ solution is deduced in two ways:

1. using the Euler equation in the Laplace domain (the second equation of system (14.4)), that is,

$$\bar{Q}_v(x, s, L) = -\frac{S}{\rho_a} \frac{1}{s} \frac{\partial}{\partial x} \bar{P}(x, s, L), \quad (14.7)$$

2. introducing the general solution of $\bar{P}(x, s, L)$ in relation (14.7), that is,

$$\bar{Q}_v(x, s, L) = -\frac{S}{\rho_a} \frac{1}{s} \frac{\partial}{\partial x} \left(\frac{A(s)}{r} e^{x\Gamma(s)} + \frac{B(s)}{r} e^{-x\Gamma(s)} \right). \quad (14.8)$$

Finally, the solution of $\bar{Q}_v(x, s, L)$ is expressed as

$$\bar{Q}_v(x, s, L) = -\left(\frac{S}{\rho_a r} \right) \frac{1}{s} \Gamma(s) A(s) e^{x\Gamma(s)} + \left(\frac{S}{\rho_a r} \right) \frac{1}{s} \Gamma(s) B(s) e^{-x\Gamma(s)}. \quad (14.9)$$

Then, taking into account the boundary conditions makes it possible to determine the two unknowns $A(s)$ and $B(s)$, in addition to the impedance $Z(x, s, L) = \bar{P}(x, s, L) / \bar{Q}_v(x, s, L)$ of the finite medium of length L .

As an example, consider a zero impedance at $x = L$, that is, $Z(L, s, L) = 0$, which leads to $\bar{P}(L, s, L) = 0$. According to relation (14.5), we obtain

$$\frac{A(s)}{r} e^{L\Gamma(s)} + \frac{B(s)}{r} e^{-L\Gamma(s)} = 0, \quad (14.10)$$

from which one deduces that

$$B(s) = -A(s)e^{2L\Gamma(s)}. \quad (14.11)$$

Then, replacing $B(s)$ by its expression (14.11) in the relation (14.5) of $\bar{P}(x, s, L)$, we obtain

$$\bar{P}(x, s, L) = \frac{A(s)}{r} e^{x\Gamma(s)} (1 - e^{2(L-x)\Gamma(s)}). \quad (14.12)$$

In the same way, by replacing $B(s)$ by its expression (14.11) in the relation (14.9) of $\bar{Q}_v(x, s, L)$, we obtain

$$\bar{Q}_v(x, s, L) = -\left(\frac{S}{\rho_a r}\right) \frac{1}{s} \Gamma(s) A(s) e^{x\Gamma(s)} (1 + e^{2(L-x)\Gamma(s)}). \quad (14.13)$$

Finally, the impedance $Z(x, s, L)$ is given by the ratio of relations (14.12) and (14.13), that is,

$$Z(x, s, L) = -\frac{\frac{A(s)}{r} e^{x\Gamma(s)} (1 - e^{2(L-x)\Gamma(s)})}{\left(\frac{S}{\rho_a r}\right) \frac{1}{s} \Gamma(s) A(s) e^{x\Gamma(s)} (1 + e^{2(L-x)\Gamma(s)})}, \quad (14.14)$$

which gives, after simplification,

$$Z(x, s, L) = -\frac{\rho_a}{S} \frac{s}{\Gamma(s)} \left(\frac{1 - e^{2(L-x)\Gamma(s)}}{1 + e^{2(L-x)\Gamma(s)}} \right), \quad (14.15)$$

and knowing that $\tanh(y) = -(1 - e^{2y})/(1 + e^{2y})$, \tanh being the tangent hyperbolic function, $Z(x, s, L)$ can finally be written as follows:

$$Z(x, s, L) = \frac{\rho_a}{S} \frac{s}{\Gamma(s)} \tanh((L-x)\Gamma(s)). \quad (14.16)$$

From the perspective of a system approach representation, the function $\Gamma(s)$ defined in relation (14.6) is rewritten as

$$\Gamma(s) = \left(\frac{s}{c_a}\right) \sqrt{1 + 2\varepsilon \left(\frac{c_a}{s}\right)^{1/2}}, \quad (14.17)$$

or again, in canonical form,

$$\Gamma(s) = \left(\frac{s}{c_a}\right) \sqrt{\frac{1 + \left(\frac{s}{\omega_{r,m}}\right)^m}{\left(\frac{s}{\omega_{r,m}}\right)^m}}, \quad \text{where} \quad \begin{cases} m = 0.5, \\ \varepsilon = 2m \frac{K_0}{r}, \\ \omega_{r,m} = (2\varepsilon)^{1/m} c_a, \end{cases} \quad (14.18)$$

where $\omega_{r,m}$ is a transitional frequency (in rad/s). Note that in the theoretical case where the system is conservative, that is, $\varepsilon = 0$, the function $\Gamma(s)$ (relation (14.17)) is reduced to $\Gamma(s) = s/c_a$. By replacing $\Gamma(s)$ of relation (14.18) in relation (14.14), $Z(x, s, L)$ can be expressed as follows:

$$Z(x, s, L) = \frac{\rho_a c_a}{S} \sqrt{\frac{\left(\frac{s}{\omega_{r,m}}\right)^m}{1 + \left(\frac{s}{\omega_{r,m}}\right)^m}} \tanh \left((L-x) \left(\frac{s}{c_a}\right) \sqrt{\frac{1 + \left(\frac{s}{\omega_{r,m}}\right)^m}{\left(\frac{s}{\omega_{r,m}}\right)^m}} \right), \quad (14.19)$$

or again, by introducing the acoustic impedance $Z_{ac} = \rho_a c_a$ and the transitional frequency $\omega_{Lx} = c_a/(L-x)$ (in rad/s), $Z(x, s, L)$ becomes

$$Z(x, s, L) = \frac{Z_{ac}}{S} \sqrt{\frac{\left(\frac{s}{\omega_{r,m}}\right)^m}{1 + \left(\frac{s}{\omega_{r,m}}\right)^m}} \tanh \left(\left(\frac{s}{\omega_{L,x}}\right) \sqrt{\frac{1 + \left(\frac{s}{\omega_{r,m}}\right)^m}{\left(\frac{s}{\omega_{r,m}}\right)^m}} \right). \quad (14.20)$$

Thus, from the analytical expression of the impedance $Z(x, s, L)$ (14.20), knowing the flow $\bar{Q}_v(x, s, L)$ at any point x of the acoustic tube of length L makes it possible to deduce the pressure $\bar{P}(x, s, L)$ [46].

Remarks.

At $\mathbf{x} = \mathbf{L}$, $1/\omega_{Lx} = 0$; hence, knowing that $\tanh(0) = 0$, we verify that $Z(L, s, L) = 0$.

At $\mathbf{x} = \mathbf{0}$, the input impedance $Z_{in}(s, L) = Z(0, s, L)$ of the finite medium of length L is given by

$$Z_{in}(s, L) = \frac{\rho_a}{S} \frac{s}{\Gamma(s)} \tanh(L\Gamma(s)). \quad (14.21)$$

Always at $\mathbf{x} = \mathbf{0}$, but for a semiinfinite medium **semiinfini** ($L \rightarrow \infty$), knowing that $\lim_{y \rightarrow \infty} \tanh(y) = 1$, the input impedance $Z_{in}(s, \infty) = Z(0, s, \infty)$ becomes

$$Z_{in}(s, \infty) = \lim_{L \rightarrow \infty} Z(x=0, s, L) = \frac{\rho_a}{S} \frac{s}{\Gamma(s)}. \quad (14.22)$$

Finally, in the theoretical case of a purely conservative system ($\varepsilon = 0$), the acoustic impedance $Z(x, s, L)$, noted in this case $Z_0(x, s, L)$, of a finite medium is expressed as

$$Z_0(x, s, L) = \frac{Z_{ac}}{S} \tanh\left(\frac{s}{\omega_{L,x}}\right), \quad (14.23)$$

and that of a semiinfinite medium, denoted $Z_0(x, s, \infty)$, is equal to

$$Z_0(x, s, \infty) = \lim_{L \rightarrow \infty} Z(x, s, L) = \frac{Z_{ac}}{S} = cste. \quad (14.24)$$

Note that the conservative case, although purely theoretical, allows by comparison to better observe the effect of viscous-thermal losses. \square

To conclude this paragraph concerning the resolution in the symbolic domain, the study of asymptotic behaviors of $Z(x, s, L)$, that is,

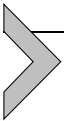
$$\lim_{s \rightarrow 0} Z(x, s, L) = \frac{Z_{ac}}{S} \frac{1}{\omega_{r,m}^m} \frac{1}{\omega_{L,x}} \lim_{s \rightarrow 0} s^{m+1} \quad (14.25)$$

and

$$\lim_{s \rightarrow \infty} Z(x, s, L) \rightarrow \frac{Z_{ac}}{S} = cste, \quad (14.26)$$

highlights that $Z(x, s, L)$ tends towards a behavior of the type:

- *fractional derivative* of order $m + 1$, i.e., 1.5 with $m = 0.5$, when s tends to zero;
- *proportional* whose gain value is fixed by Z_{ac}/S , when s tends to infinity.



14.3. Frequency response analysis

In the stationary harmonic regime, the frequency response $Z(x, j\omega, L)$ is given by

$$Z(x, j\omega, L) = \frac{Z_{ac}}{S} \sqrt{\frac{\left(\frac{j\omega}{\omega_{r,m}}\right)^m}{1 + \left(\frac{j\omega}{\omega_{r,m}}\right)^m}} \tanh\left(\left(\frac{j\omega}{\omega_{L,x}}\right) \sqrt{\frac{1 + \left(\frac{j\omega}{\omega_{r,m}}\right)^m}{\left(\frac{j\omega}{\omega_{r,m}}\right)^m}}\right), \quad (14.27)$$

where the transitional frequencies $\omega_{r,m}$ and $\omega_{L,x}$ have the following expressions:

$$\omega_{r,m} = \frac{c_a}{(r/4mK_0)^{1/m}} \quad \text{and} \quad \omega_{L,x} = \frac{c_a}{L-x}. \quad (14.28)$$

Thus, $\omega_{r,m}$ decreases when the radius r increases and, on the contrary, $\omega_{L,x}$ increases when the position x moves away from the origin and approaches the endpoint L of the acoustic tube.

For illustration, and in order to plot the frequency response $Z(x, j\omega, L)$ in the stationary harmonic regime, let us consider an acoustic tube whose dimensions are as follows:

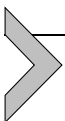
- radius $r = 5 \times 10^{-3}$ m (value perfectly in accordance with the domain of validity of the Webster–Lokshin model);
- length $L = 0.3$ m;
- a temperature of 25°C ;
- density $\rho_a = 1.184$ kg/m³;
- a speed of sound in the air of $c_a = 346.3$ m/s (refer to Table 14.1).

Note that these values of r and L are representative of the resonator of a recorder and lead to the values of the transitional frequencies $\omega_{r,m} = 4.92$ rad/s (0.78 Hz) and $\omega_{L,x} = 1154$ rad/s (184 Hz) when $x = 0$, thus showing for such an instrument that $\omega_{r,m} \ll \omega_{L,x}$.

Fig. 14.3 presents at $x = 0$ the Bode diagrams of $Z(0, j\omega, L)$ on the frequency range [20; 20,000] Hz (frequencies audible by the human ear (Fig. 14.3(a))), and on the frequency range [20; 4000] Hz (frequencies attainable with a recorder (Fig. 14.3(b))).

Although an in-depth analysis of the frequency response of the model is developed in the following paragraph, the observation of these diagrams over the range of audible frequencies leads to the identification of two very distinct behaviors:

- the first on the frequency range [20; $\omega_{L,x}/2\pi = 184$] Hz with a derivative behavior of order 1, highlighting the absence of the fractional behavior in this frequency range which exists for frequencies lower than $\omega_{r,m}/2\pi = 0.78$ Hz;
- the second on the frequency range [$\omega_{L,x}/2\pi = 184$; 20,000] Hz with an alternation of resonances and antiresonances.



14.4. System approach

From a causal point of view, the input of the resonator at $x = 0$ is defined by the pressure at the output of the nonlinear exciter. This is the reason why the system approach developed in this paragraph considers the admittance $Y(x, s, L) = Z^{-1}(x, s, L)$ and not the impedance $Z(x, s, L)$. More specifically, it is the input admittance at $x = 0$, denoted $Y_{in}(s, L) = Y(0, s, L)$. Note that this consideration of the admittance $Y_{in}(j\omega, L)$ leads

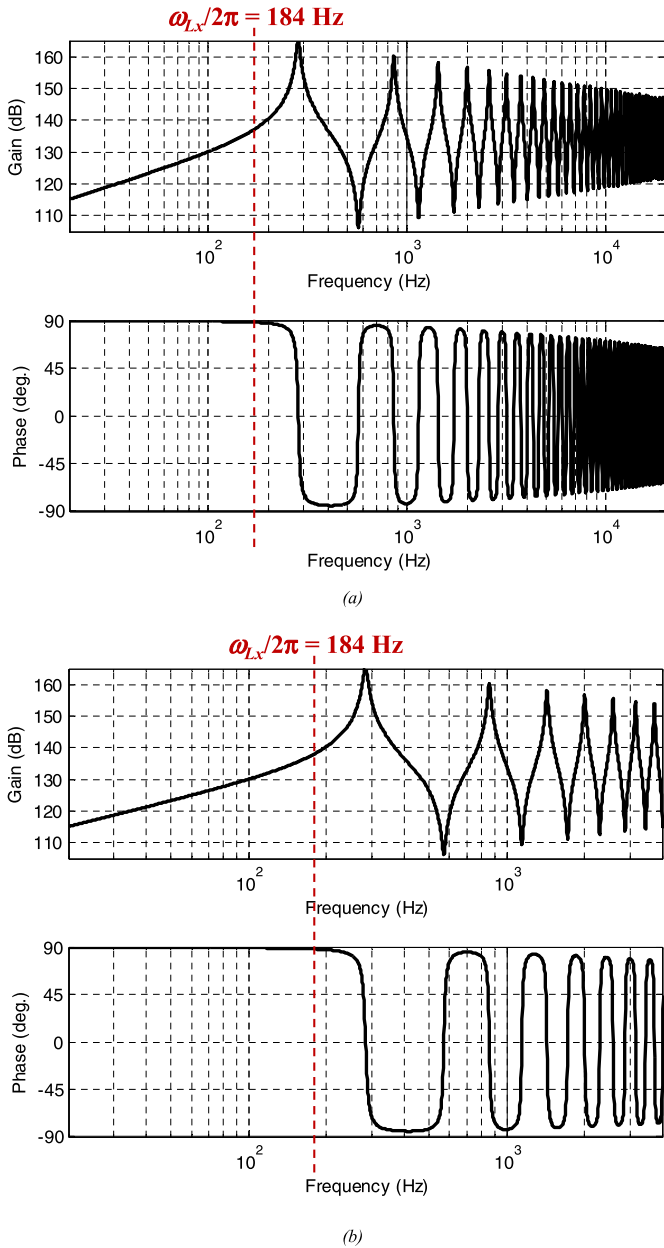


Figure 14.3 Bode diagrams of $Z(0, j\omega, L)$ (a) in the range [20; 20,000] Hz of the frequencies audible by the human ear and (b) in the range [20; 4000] Hz of frequencies attainable with a recorder.

to an integrator behavior for frequencies lower than $\omega_{L,x}$ (derivation for $Z(x, s, L)$), thus respecting integral causality, a fundamental notion in a system approach.

In addition, the admittance $Y(x, s, L)$ is broken down into a cascade of local transfer functions where the parameters, as well as all the input and output variables, have a physical meaning. This decomposition facilitates the frequency analysis of the Webster–Lokshin model, thus reaching a reduced model to be implemented in the simulator.

14.4.1 Decomposition of admittance $Y(x, s, L)$ into subsystems

The admittance $Y(x, s, L) = Z^{-1}(x, s, L)$ of an acoustic tube of length L at a point x between 0 and L is therefore defined by

$$Y(x, s, L) = \frac{\bar{Q}_v(x, s, L)}{\bar{P}(x, s, L)} = \frac{S}{Z_{ac}} \sqrt{\frac{1 + \left(\frac{s}{\omega_{r,m}}\right)^m}{\left(\frac{s}{\omega_{r,m}}\right)^m}} \frac{1}{\tanh\left(\left(\frac{s}{\omega_{L,x}}\right) \sqrt{\frac{1 + \left(\frac{s}{\omega_{r,m}}\right)^m}{\left(\frac{s}{\omega_{r,m}}\right)^m}}\right)}, \quad (14.29)$$

a relation that can be expressed as

$$Y(x, s, L) = H_0 I_m(s) T(x, s, L), \quad (14.30)$$

knowing that

$$H_0 = \frac{S}{Z_{ac}} = \frac{S}{\rho_a c_a}, \quad (14.31)$$

$$I_m(s) = \sqrt{\frac{1 + \left(\frac{s}{\omega_{r,m}}\right)^m}{\left(\frac{s}{\omega_{r,m}}\right)^m}}, \quad (14.32)$$

and

$$T(x, s, L) = \frac{1}{\tanh(F(x, s, L))}, \quad (14.33)$$

where

$$F(x, s, L) = \left(\frac{s}{\omega_{L,x}}\right) I_m(s). \quad (14.34)$$

For the remaining part, the concept of *acoustic admittance* $Y(x, s, L)$ is replaced by the concept of *transfer function* $H(x, s, L)$ defined between the

pressure source $\bar{P}_{in}(s) = \bar{P}(x=0, s)$ at the input of the tube at $x=0$ and the flow $\bar{Q}_v(x, s, L)$ at any point x of the tube of length L and of constant radius r . The transfer function can be expressed as follows:

$$H(x, s, L) = \frac{\bar{Q}_v(x, s, L)}{\bar{P}_{in}(s)} = H_0 I_m(s) T(x, s, L). \quad (14.35)$$

At $x=0$, for this finite medium, the input admittance $Y_{in}(s, L)$ has therefore the following expression:

$$Y_{in}(s, L) = H(0, s, L) = \frac{\bar{Q}_v(0, s, L)}{\bar{P}_{in}(s)} = H_0 I_m(s) T(0, s, L). \quad (14.36)$$

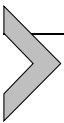
Always for $x=0$, but for a semiinfinite medium ($L \rightarrow \infty$), the input admittance $Y_{in}(s, \infty)$ is reduced to

$$Y_{in}(s, \infty) = H(0, s, \infty) = \frac{\bar{Q}_v(0, s, \infty)}{\bar{P}_{in}(s)} = H_0 I_m(s). \quad (14.37)$$

Fig. 14.4 presents the block diagrams associated with this system approach where the different transfer functions are defined by

$$\left\{ \begin{array}{l} H_0 = \frac{\bar{Q}_{in}(s)}{\bar{P}_{in}(s)} = \frac{S}{Z_{ac}} = cste, \\ I_m(s) = \frac{\bar{Q}_v(0, s, \infty)}{\bar{Q}_{in}(s)} = \sqrt{\frac{1 + \left(\frac{s}{\omega_{r,m}}\right)^m}{\left(\frac{s}{\omega_{r,m}}\right)^m}}, \\ T(x, s, L) = \frac{\bar{Q}_v(x, s, L)}{\bar{Q}_v(0, s, \infty)} = \frac{1}{\tanh\left(\left(\frac{s}{\omega_{L,x}}\right) I_m(s)\right)}. \end{array} \right. \quad (14.38)$$

Note that the quantity $H_0 \bar{P}_{in}(s)$ is homogeneous with respect to the flow, denoted $\bar{Q}_{in}(s)$, and corresponds to the conversion of the pressure source applied at $x=0$ (Dirichlet condition) into an equivalent source of flow always applied at $x=0$ (Neumann condition) [37].



14.5. Frequency analysis of the system approach

In stationary harmonic mode, relation (14.35) becomes

$$H(x, j\omega, L) = \frac{\bar{Q}_v(x, j\omega, L)}{\bar{P}_{in}(j\omega)} = H_0 I_m(j\omega) T(x, j\omega, L), \quad (14.39)$$

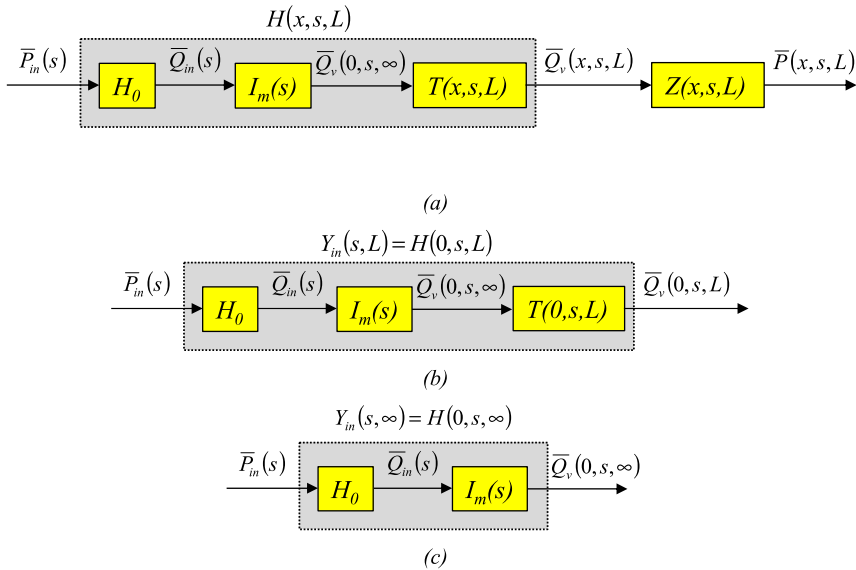


Figure 14.4 Block diagrams associated with the system approach: Whatever x is between 0 and L (a), at $x = 0$ for the finite system L (b), at $x = 0$ for a semifinite system (c).

with

$$I_m(j\omega) = \frac{\bar{Q}_v(0, j\omega, \infty)}{\bar{Q}_{in}(j\omega)} = \sqrt{\frac{1 + \left(j\frac{\omega}{\omega_{r,m}}\right)^m}{\left(j\frac{\omega}{\omega_{r,m}}\right)^m}} \tag{14.40}$$

and

$$T(x, j\omega, L) = \frac{\bar{Q}_v(x, j\omega, L)}{\bar{Q}_v(0, j\omega, \infty)} = \frac{1}{\tanh(F(x, j\omega, L))}, \tag{14.41}$$

where

$$F(x, j\omega, L) = \left(\frac{j\omega}{\omega_{L,x}}\right) I_m(j\omega). \tag{14.42}$$

The remaining part of this paragraph is devoted to a detailed analysis of the frequency responses $I_m(j\omega)$, $F(x, j\omega, L)$, and $T(x, j\omega, L)$ of each subsystem and of the frequency response $H(x, j\omega, L)$ of the whole system.

14.5.1 Analysis of $I_m(j\omega)$

The analysis of $I_m(j\omega)$ highlights two behaviors whose transition zone is fixed by the transitional frequency $\omega_{r,m}$. These behaviors are:

- For $\omega \ll \omega_{r,m}$, we observe a fractional integration behavior of order $m/2 = 0.25$. Indeed,

$$\begin{aligned} \forall \omega \ll \omega_{r,m}, \quad I_m(j\omega) &= \sqrt{\frac{1 + \left(j\frac{\omega}{\omega_{r,m}}\right)^m}{\left(j\frac{\omega}{\omega_{r,m}}\right)^m}} \underset{\omega \ll \omega_{r,m}}{\approx} \left(\frac{\omega_{r,m}}{j\omega}\right)^{m/2} \\ \Rightarrow \quad \begin{cases} |I_m(j\omega)| = \left(\frac{\omega_{r,m}}{\omega}\right)^{m/2}, \\ \arg I_m(j\omega) = -m\frac{\pi}{4}. \end{cases} & \quad (14.43) \end{aligned}$$

- For $\omega \gg \omega_{r,m}$, we observe a proportional behavior. Indeed,

$$\begin{aligned} \forall \omega \gg \omega_{r,m}, \quad I_m(j\omega) &= \sqrt{\frac{1 + \left(j\frac{\omega}{\omega_{r,m}}\right)^m}{\left(j\frac{\omega}{\omega_{r,m}}\right)^m}} \underset{\omega \gg \omega_{r,m}}{\approx} 1 \\ \Rightarrow \quad \begin{cases} |I_m(j\omega)| = 1, \\ \arg I_m(j\omega) = 0. \end{cases} & \quad (14.44) \end{aligned}$$

As an illustration, let us take the acoustic tube whose nominal dimensions are fixed by a radius $r = 5 \times 10^{-3}$ m and a length $L = 0.3$ m at a temperature of 25°C, with $\rho_a = 1.184$ kg/m³ and $c_a = 346.3$ m/s. In this case, and as a reminder, the numerical value of the transitional frequency $\omega_{r,m}$ (relation (14.28)) is equal to 4.92 rad/s (0.784 Hz).

Fig. 14.5 presents the Bode diagrams of the frequency response $I_m(j\omega)$ over the range $[10^{-4}; 10^4]$ Hz. Two behaviors appear clearly:

- For $\omega \ll \omega_{r,m}$, a gain diagram appears with a straight line with slope $p = -m/2 \times 20$ dB/dec = -5 dB/dec and a phase diagram appears with a horizontal line at $-m/2 \times 90^\circ = -22.5^\circ$.
- For $\omega \gg \omega_{r,m}$, a gain diagram appears with a horizontal line at 0 dB and a phase diagram with a horizontal line appears at 0° .

Fig. 14.6 presents the same frequency response of $I_m(j\omega)$ but only over the frequency audible range $[20; 20,000]$ Hz. A gain diagram in linear-

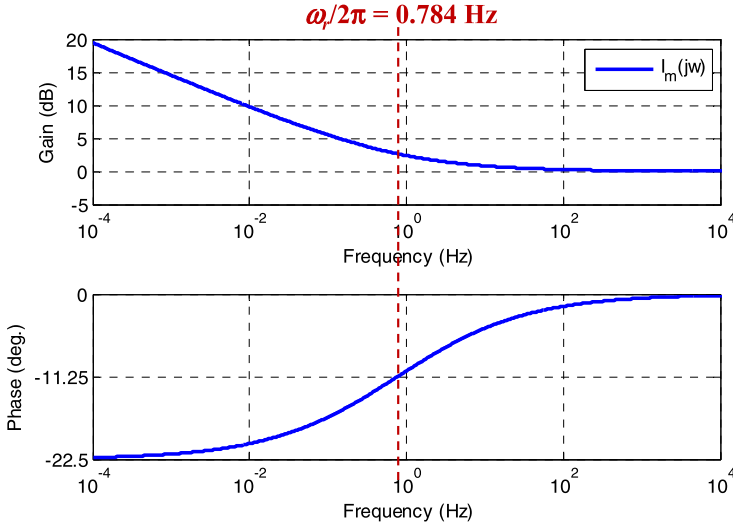


Figure 14.5 Bode diagrams of $I_m(j\omega)$ in the range $[10^{-4}; 10^4]$ Hz.

linear scale and a phase diagram with the frequency axis also in linear scale are observed. This result makes it possible to confirm, for this recorder example, that the unit proportional behavior is dominant, that is,

$$\forall \omega \geq 2\pi 20 \text{ rad/s}, \quad I_m(j\omega) = \frac{\bar{Q}_v(0, j\omega, \infty)}{\bar{Q}_{in}(j\omega)} \approx 1. \quad (14.45)$$

Thus, for the domain of study considered in this work, where the audible frequency ranges over $[20; 20,000]$ Hz, the transfer $I_m(s)$ can be reduced to the unit which leads to $\bar{Q}_v(0, s, \infty) = \bar{Q}_{in}(s)$, allowing a reduction in the block diagrams of Fig. 14.4. The direct consequence is that in the case of a semiinfinite medium at $x = 0$ (Fig. 14.4(c)), the fractional integration behavior has no influence in the range of audible frequencies.

14.5.2 Analysis of $F(0, j\omega, L)$

Knowing that in the case of a recorder $\omega_{r,m} \ll \omega_{L,x}$, the analysis of $F(0, j\omega, L)$ highlights again two behaviors whose transition zone is fixed

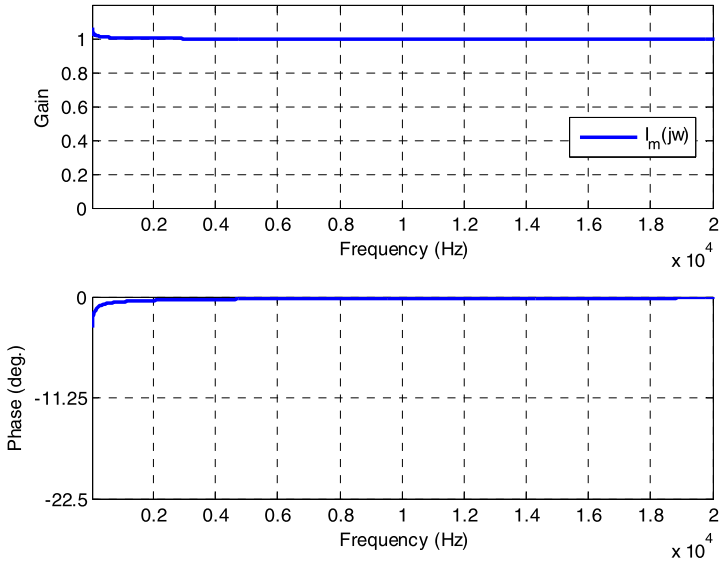


Figure 14.6 Frequency response of $I_m(j\omega)$ in the range [20; 20,000] Hz of the audible frequencies in linear scale.

by the transitional frequency $\omega_{r,m}$. These behaviors are:

- For $\omega \ll \omega_{r,m}$, a *fractional derivative* behavior of order $(1 - m/2) = 0.75$ is observed. Indeed,

$$\forall \omega \ll \omega_{r,m},$$

$$F(x, j\omega, L) = \left(\frac{j\omega}{\omega_{L,x}} \right) \sqrt{\frac{1 + \left(j \frac{\omega}{\omega_{r,m}} \right)^m}{\left(j \frac{\omega}{\omega_{r,m}} \right)^m}} \underset{\omega \ll \omega_{r,m}}{\approx} \left(\frac{\omega_{r,m}^{m/2}}{\omega_{L,x}} \right) (j\omega)^{(1-m/2)}, \quad (14.46)$$

and hence the module and the argument of $F(x, j\omega, L)$ can be expressed as

$$\begin{cases} |F(x, j\omega, L)| = \left(\frac{\omega_{r,m}^{m/2}}{\omega_{L,x}} \right) \omega^{(1-m/2)}, \\ \arg F(x, j\omega, L) = \left(1 - \frac{m}{2} \right) \frac{\pi}{2}. \end{cases} \quad (14.47)$$

- For $\omega_r \ll \omega$, a *derivative* behavior of order 1 is observed. Indeed,

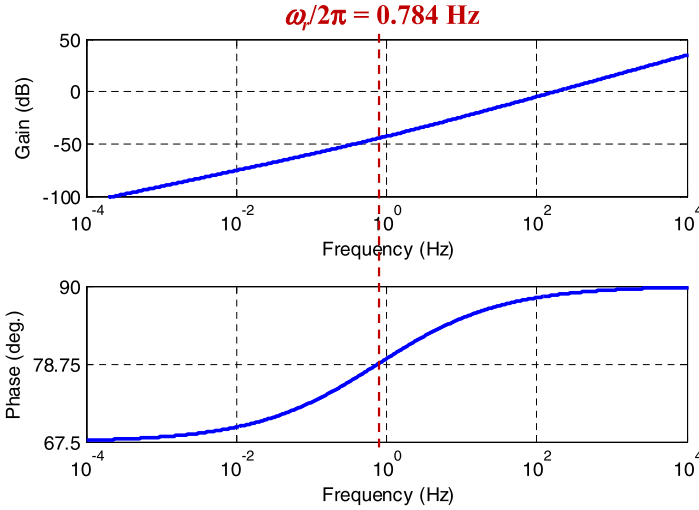


Figure 14.7 Bode diagrams of $F(0, j\omega, L)$ in the range $[10^{-4}; 10^4]$ Hz.

$$\forall \omega_{r,m} \ll \omega, \quad F(x, j\omega, L) = \left(\frac{j\omega}{\omega_{L,x}} \right) \sqrt{\frac{1 + \left(j\frac{\omega}{\omega_{r,m}} \right)^m}{\left(j\frac{\omega}{\omega_{r,m}} \right)^m}} \underset{\omega_{r,m} \ll \omega}{\approx} \left(\frac{j\omega}{\omega_{L,x}} \right)$$

$$\Rightarrow \begin{cases} |F(x, j\omega, L)| = \frac{\omega}{\omega_{L,x}}, \\ \arg F(x, j\omega, L) = \frac{\pi}{2}. \end{cases} \quad (14.48)$$

Fig. 14.7 presents, at $x = 0$, the Bode diagrams of the frequency response $F(0, j\omega, L)$ in the range $[10^{-4}; 10^4]$ Hz. The two behaviors appear clearly:

- For $\omega \ll \omega_{r,m}$, a gain diagram with a straight line is observed with $p_1 = (1 - m/2) \times 20$ dB/dec = 15 dB/dec and a phase diagram with a horizontal line is observed at $(1 - m/2) \times 90^\circ = 67.5^\circ$.
- For $\omega \gg \omega_{r,m}$, a gain diagram with a straight line is observed with slope $p_2 = 20$ dB/dec and a phase diagram is observed with a horizontal straight line at 90° .

14.5.3 Analysis of $T(0, j\omega, L)$

The analysis of $T(x, j\omega, L)$ highlights three behaviors whose transition zones are fixed by the transitional frequencies $\omega_{r,m}$ and $\omega_{L,x}$:

- For $\omega \ll \omega_{L,x}$, an *integration behavior with two different orders* according to the frequency range is observed. Indeed,

$$\forall \omega \ll \omega_{L,x}, \quad T(x, j\omega, L) = \frac{1}{\tanh(F(x, j\omega, L))} \underset{\omega \ll \omega_{L,x}}{\approx} \frac{1}{F(x, j\omega, L)}, \quad (14.49)$$

with, for $\omega \ll \omega_{r,m}$, an orderly *fractional integrative* behavior equal to $-(1 - m/2) = -0.75$, that is,

$$\begin{aligned} \forall \omega \ll \omega_{r,m}, \quad \frac{1}{F(x, j\omega, L)} \underset{\omega \ll \omega_{r,m}}{\approx} \left(\frac{\omega_{L,x}}{\omega_r^{m/2}} \right) \frac{1}{(j\omega)^{(1-m/2)}} \\ \Rightarrow \begin{cases} |T(x, j\omega, L)| = \left(\frac{\omega_{L,x}}{\omega_r^{m/2}} \right) \frac{1}{\omega^{(1-m/2)}}, \\ \arg T(x, j\omega, L) = \left(1 - \frac{m}{2}\right) \frac{\pi}{2}, \end{cases} \end{aligned} \quad (14.50)$$

and, for $\omega_{r,m} \ll \omega$, a *derivative* behavior of order 1, that is,

$$\begin{aligned} \forall \omega_{r,m} \ll \omega, \quad \frac{1}{F(x, j\omega, L)} \underset{\omega_{r,m} \ll \omega}{\approx} \left(\frac{\omega_{L,x}}{j\omega} \right) \\ \Rightarrow \begin{cases} |T(x, j\omega, L)| = \frac{\omega_{L,x}}{\omega}, \\ \arg T(x, j\omega, L) = -\frac{\pi}{2}. \end{cases} \end{aligned} \quad (14.51)$$

- For $\omega_{L,x} \ll \omega$, a behavior composed of an alternation of *antiresonances* and *resonances* is observed; thus, $T(x, j\omega, L)$ can be expressed as

$$\forall \omega_{L,x} \ll \omega, \quad T(x, j\omega, L) = \frac{1}{\tanh\left(\left(\frac{j\omega}{\omega_{L,x}}\right) \sqrt{\frac{1 + \left(\frac{j\omega}{\omega_{r,m}}\right)^m}{\left(\frac{j\omega}{\omega_{r,m}}\right)^m}}\right)}. \quad (14.52)$$

Fig. 14.8 shows the Bode diagrams of $1/F(0, j\omega, L)$ (in red; light gray in print version) and of $T(0, j\omega, L)$ (in blue; dark gray in print version) over the range $[10^{-4}; 10^4]$ Hz (Fig. 14.8(a)) and in the range $[20; 4000]$ Hz of the audible and achievable frequencies with a recorder (Fig. 14.8(b)).

Below the first cut-off frequency $[10^{-4}; \omega_{L,x}/2\pi = 184]$ Hz, the responses of $1/F(0, j\omega, L)$ (in red; light gray in print version) and $T(0, j\omega, L)$ (in blue; dark gray in print version) overlap where:

- a *fractional integration behavior* of order -0.75 over the range $[10^{-4}; \omega_r/2\pi = 0.784]$ Hz is observed;

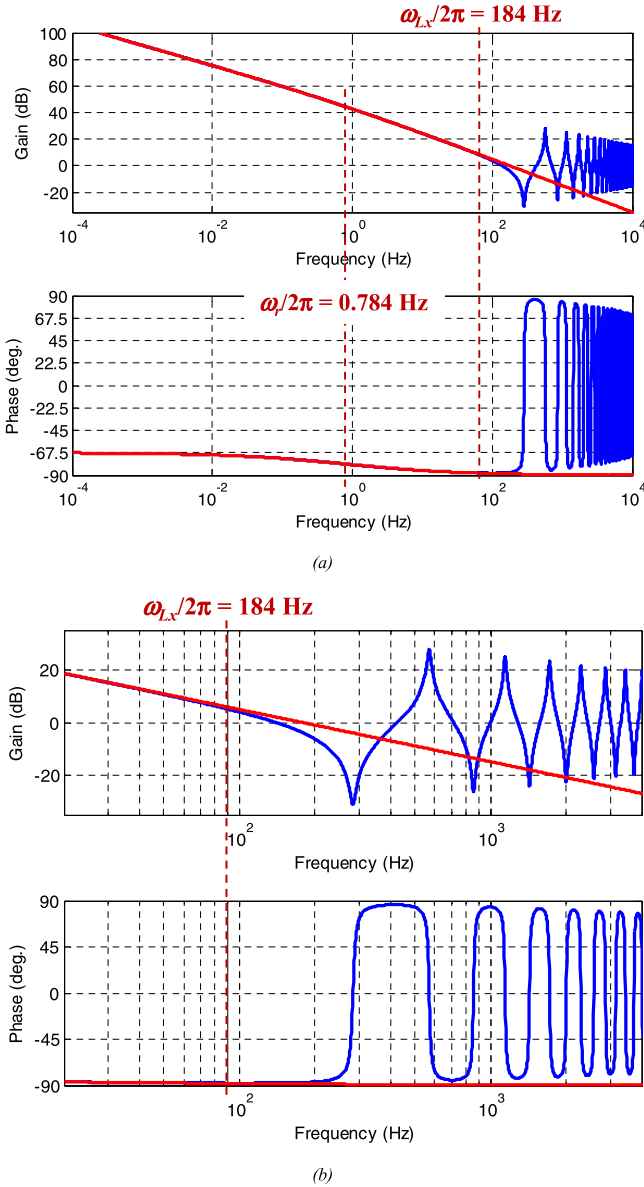


Figure 14.8 Bode diagrams of $1/F(0, j\omega, L)$ (in red; light gray in print version) and of $T(0, j\omega, L)$ (in blue; dark gray in print version) (a) in the range $[10^{-4}; 10^4]$ Hz and (b) in the range $[20; 4000]$ Hz.

- an *integrative behavior* of order 1 over the range $[\omega_{r,m}/2\pi = 0.784; \omega_{L,x}/2\pi = 184]$ Hz is observed.

Beyond 184 Hz, the frequency response $T(0, j\omega, L)$ (in blue; dark gray in print version) clearly presents an alternation of antiresonances and resonances introduced by the hyperbolic tangent function.

14.5.4 Analysis of $H(x, j\omega, L)$

Finally, the analysis of $H(x, j\omega, L)$ highlights three behaviors whose transition zones are fixed by the transitional frequencies ω_r and $\omega_{L,x}$:

- For $\omega \ll \omega_r \ll \omega_{L,x}$, an orderly *fractional integrative behavior* $-(1 - m/2) = -0.75$ is observed. Indeed,

$$\begin{aligned} \forall \omega \ll \omega_{r,m}, \quad H(x, j\omega, L) &\underset{\omega \ll \omega_{r,m}}{\approx} \left(\frac{\omega_{L,x}}{\omega_{r,m}^{m/2}} \right) \frac{H_0}{(j\omega)^{(1-m/2)}} \\ \Rightarrow \quad \left\{ \begin{array}{l} |H(x, j\omega, L)| = \left(\frac{\omega_{L,x}}{\omega_{r,m}^{m/2}} \right) \frac{H_0}{\omega^{(1-m/2)}}, \\ \arg H(x, j\omega, L) = \left(1 - \frac{m}{2} \right) \frac{\pi}{2}. \end{array} \right. & \quad (14.53) \end{aligned}$$

- For $\omega_{r,m} \ll \omega \ll \omega_{L,x}$, a *derivative behavior* of order 1 is observed. Indeed,

$$\begin{aligned} \forall \omega_{r,m} \ll \omega \ll \omega_{L,x}, \quad H(x, j\omega, L) &\underset{\omega_{r,m} \ll \omega \ll \omega_{L,x}}{\approx} H_0 \left(\frac{\omega_{L,x}}{j\omega} \right) \\ \Rightarrow \quad \left\{ \begin{array}{l} |H(x, j\omega, L)| = H_0 \frac{\omega_{L,x}}{\omega}, \\ \arg H(x, j\omega, L) = -\frac{\pi}{2}. \end{array} \right. & \quad (14.54) \end{aligned}$$

- For $\omega_{L,x} \ll \omega$, a behavior composed of an alternation of *antiresonances* and *resonances* is observed. Indeed,

$$\forall \omega_{L,x} \ll \omega, \quad H(x, j\omega, L) \underset{\omega_{L,x} \ll \omega}{\approx} \frac{H_0}{\tanh \left(\left(\frac{j\omega}{\omega_{L,x}} \right) \sqrt{1 + \left(\frac{\omega}{\omega_{r,m}} \right)^m} \right)}. \quad (14.55)$$

Fig. 14.9 presents, at $x = 0$ ($\omega_{L,x}/2\pi = 184$ Hz), at $x = L/2$ ($\omega_{L,x}/2\pi = 368$ Hz), and at $x = 3L/4$ ($\omega_{L,x}/2\pi = 735$ Hz), the Bode diagrams of $H(0, j\omega, L)$ (in black), of $H(L/2, j\omega, L)$ (in blue; dark gray in print version), and of $H(3L/4, j\omega, L)$ (in red; light gray in print version) over the audible frequency range [20; 4000] Hz.

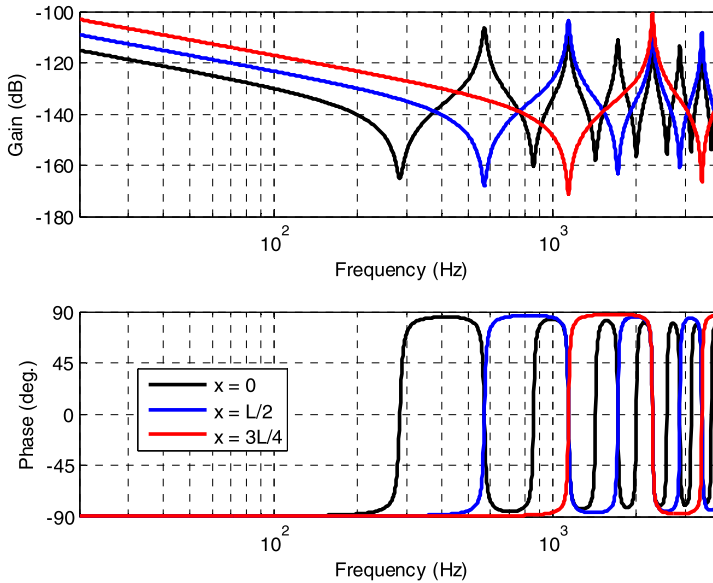


Figure 14.9 Bode diagrams in $x = 0$ ($\omega_{Lx}/2\pi = 184$ Hz), in $x = L/2$ ($\omega_{Lx}/2\pi = 368$ Hz), and in $x = 3L/4$ ($\omega_{Lx}/2\pi = 735$ Hz) of $x = 3L/4$ ($\omega_{Lx}/2\pi = 735$ Hz) (in black), of $H(L/2, j\omega, L)$ (in blue; dark gray in print version), and of $H(3L/4, j\omega, L)$ (in red; light gray in print version) in the range [20; 4000] Hz of audible and achievable frequencies.

Over the range $[20; \omega_{Lx}/2\pi]$ Hz, the three responses of $H(x, j\omega, L)$ present an integration behavior of order 1. The fractional integration behavior of order -0.75 does not appear over this range as it is present within a much lower frequency (0.784 Hz). Beyond ω_{Lx} , the three responses present a succession of alternation of antiresonances and resonances introduced by the hyperbolic tangent (\tanh) function. In [47], the authors show that the influence of the order m is essentially located:

- for *gain diagrams*, at the peaks of resonances and antiresonances, quantifiable effects using quality factors for antiresonances and for resonances illustrating well the phenomenon of dissipation associated with visco-thermal losses;
- for *phase diagrams*, at the crossing points at 0 degrees with a local slope which is all the more important as the order is small, a slope which becomes infinite for $m = 0$ (purely conservative case).

Moreover, note that the farther the position x moves away from the origin, the higher the transitional frequency ω_{Lx} pushes the antiresonance and resonance frequencies towards the high frequencies.

In addition, the position x having no influence on the transitional frequency $\omega_{r,m}$, the fractional integrative behavior of order -0.75 still does not appear in this frequency range.



14.6. Conclusions and future work

To sum up this work, we have presented the dynamic behavior of an acoustic tube of constant radius and showed the effects of viscous thermal losses as well as the frequency range where fractional-order behavior is observed.

First, from the two partial differential equations which define the Webster–Lokshin model, a classical resolution in the operational domain leads to the analytical expression of the acoustic impedance and admittance of the function tube of position x , its length L , and its radius r .

Second, a system approach is proposed aiming to causally decompose the overall model into submodels, thus facilitating analysis in the frequency domain. One of the conclusions of this frequency analysis is that the fractional model can be simplified over the range [20; 20,000] Hz of the audible frequencies. Although the fractional-order behavior (fractional integrator) is only present for very low nonaudible frequencies (less than 1 Hz), the influence of the fractional order m does appear at resonances and antiresonances (in the audible frequencies), illustrating well the phenomenon of dissipation associated with visco-thermal losses.

As for the future work, more precise measurements of the pressure and the flow on the real test bench will be conducted and the resulting impedance will be compared to the simulated one. Added to that, the influence of the fractional-order derivative will be analyzed. Thus, the hardware-in-the-loop method will be implemented where the physical resonator will be replaced by a numerical simulator in order to study the effects of the fractional order and the other resonator parameter on the delivered sound.

References

- [1] K. Oldham, J. Spanier, *The Fractional Calculus*, Academic Press, New York, 1974.
- [2] S. Samko, A. Kilbas, O. Marichev, *Fractional Integrals and Derivatives: Theory and Applications*, Gordon and Breach, Amsterdam, 1993.
- [3] A. Oustaloup, *Etude et Réalisation d'un système d'asservissement d'ordre 3/2 de la fréquence d'un laser à colorant continu*, Universitu of Bordeaux, Bordeaux, 1975.
- [4] R. Abi Zeid Daou, X. Moreau, *Fractional Calculus: Theory*, Nova Science Publishers Inc., New York, 2014.

- [5] R. Abi Zeid Daou, X. Moreau, F. Christophy, Temperature control of a finite diffusive interface medium applying CRONE second generation, in: 3rd International Conference on Advances in Computational Tools for Engineering Applications, Lebanon, 2016.
- [6] J.-C. Trigeassou, N. Maamri, State space modelling of fractional differential equations and the initial condition problem, in: IEEE Systems, Signals and Devices SSD'09, Djerba, 2009.
- [7] N. Engheta, Fractional kernels and intermediate zones in electromagnetism: planar geometries, in: IEEE Antennas and Propagation Society International Symposium, Atlanta, 1998.
- [8] A. Lopes, J. Tenreiro Machado, C. Pinto, A. Galhanob, Fractional dynamics and MDS visualization of earthquake phenomena, *Computers & Mathematics with Applications* 66 (5) (2013) 647–658.
- [9] A. Oustaloup, La commande CRONE, Hermes, Paris, 1991.
- [10] A. Charef, N. Fergani, PID μ controller tuning for desired closed-loop response using impulse response, in: Workshop on Fractional Derivation and Applications, Spain, 2010, pp. 350–371.
- [11] B. Zhang, Y. Pi, Y. Luo, Fractional order sliding-mode control based on parameters auto-tuning for velocity control of permanent magnet synchronous motor, *ISA Transactions* 51 (5) (2012) 649–656.
- [12] R. Abi Zeid Daou, X. Moreau, C. Francis, Effect of hydropneumatic components nonlinearities on the CRONE suspension, *IEEE Transactions on Vehicular Technology* 61 (2) (2011) 466–474.
- [13] R. Abi Zeid Daou, F. Samarani, C. Yaacoub, X. Moreau, Fractional derivatives for edge detection: application to road obstacles, in: Smart City Performability, Cognition, & Security, EAI/Springer Innovations in Communication and Computing, Switzerland, Springer, Cham, 2020, https://doi.org/10.1007/978-3-030-14718-1_6.
- [14] B. Hennelly, J. Sheridan, Image encryption and the fractional Fourier transform, *Optik* 114 (6) (2003) 251–265.
- [15] S. Coman, V. Comnac, C. Boldisor, D. Dumitrache, Fractional order control for DC electrical drives in networked control systems, in: 12th International Conference on Optimization of Electrical and Electronic Equipment (OPTIM), Brasov, Romania, 2010, <https://doi.org/10.1109/OPTIM.2010.5510503>.
- [16] G. Apaydin, Realization of reduced-delay finite impulse response filters for audio applications, *Digital Signal Processing* 20 (2010) 620–629.
- [17] J. Blackledge, Application of the fractal market hypothesis for modelling macroeconomic time series, *ISAST Transactions on Electronics and Signal Processing* 1 (2) (2008) 1–22.
- [18] R. Abi Zeid Daou, X. Moreau, *Fractional Calculus: Applications*, Nova, New York, 2015.
- [19] I. Podlubny, Geometric and physical interpretation of fractional integration and fractional differentiation, in: *Fractional Differentiation and Its Applications*, U-books, Ed., 2005, pp. 3–18.
- [20] R. Abi Zeid Daou, C. Francis, M. Moreau, Synthesis and implementation of non-integer integrators using RLC devices, *International Journal of Electronics* 96 (12) (2009) 1207–1223.
- [21] P. Lanusse, R. Malti, P. Melchior, CRONE control system design toolbox for the control engineering community: tutorial and a case study, *Philosophical Transactions of the Royal Society A: Mathematical, Physical and Engineering Sciences* 371 (1990) (2013) 20120149, <https://doi.org/10.1098/rsta.2012.0149>.
- [22] S. Tassart, Modélisation, simulation et analyse des instruments à vent avec retards fractionnaires, Université Paris VI, Paris, 1999.

- [23] T. Hélie, Modélisation physique d'instruments de musique en systèmes dynamiques et inversion, *Journal Européen des Systèmes Automatisés (JESA)* 37 (10) (2003) 1305–1310.
- [24] T. Hélie, Unidimensional models of acoustic propagation in axisymmetric wave guides, *The Journal of the Acoustical Society of America* 114 (5) (2003) 2633, <https://doi.org/10.1121/1.1608962>.
- [25] R. Mignot, T. Hélie, D. Matignon, Simulation en guides d'ondes numériques stables pour des tubes acoustiques à profil convexe, *Journal Européen des Systèmes Automatisés (JESA)* 45 (2011) 547–574.
- [26] T. Hélie, R. Mignot, D. Matignon, Waveguide modeling of lossy flared acoustic pipes: derivation of Kelly-Lochbaum structure for real-time simulations, in: *IEEE Workshop on Applications of Signal Processing to Audio and Acoustics*, New Paltz, NY, 2007.
- [27] A. Lokshin, V. Rok, Fundamental solutions of the wave equation with retarded time, *Doklady Akademii Nauk SSSR* 239 (1978) 1305–1308.
- [28] H. Haddar, T. Hélie, D. Matignon, A Webster-Lokshin model for waves with viscothermal losses and impedance boundary conditions: strong solutions, in: *International Congress in Mathematical and Numerical Aspects of Wave Propagation*, Jyväskylä, Finland, 2003, https://doi.org/10.1007/978-3-642-55856-6_10.
- [29] H. Haddar, D. Matignon, Analyse théorique et numérique du modèle de Webster Lokshin, in: RR-6558, INRIA. 2008. ffinria-00288254v2f, France Toulouse, 2008.
- [30] H. Haddar, J. Li, D. Matignon, Efficient solution of a wave equation with fractional-order dissipative terms, *Journal of Computational and Applied Mathematics* 234 (2010) 2003–2010.
- [31] D. Matignon, B. d'Andréa-Novel, P. Depalle, A. Oustaloup, Viscothermal losses in wind instruments: a non-integer model, in: *Systems and Networks: Mathematical Theory and Applications*, Akademie Verlag, 1994, pp. 789–790.
- [32] D. Matignon, Représentation en variables d'état de modèles de guides d'ondes avec dérivation fractionnaire, Paris XI University, Paris, 1994.
- [33] B. Lombard, D. Matignon, Y. Le Gorrec, A fractional Burgers equation arising in nonlinear acoustics: theory and numerics, *IFAC Proceeding Volumes* 46 (23) (2013) 406–411.
- [34] P. Vigué, C. Vergez, B. Lombard, B. Cochelin, Continuation of periodic solutions for systems with fractional derivatives, *Nonlinear Dynamics* 95 (1) (2019) 479–493.
- [35] G. Abou Haidar, R. Abi Zeid Daou, X. Moreau, Modelling and identification of the musicians blowing part and the flute musical instrument, in: *Fourth International Conference on Advances in Computational Tools for Engineering Applications*, Zouk, Lebanon, 2019, <https://doi.org/10.1109/ACTEA.2019.8851093>.
- [36] G. Abou Haidar, X. Moreau, R. Abi Zeid Daou, Modelling, implementation and control of a wind musical instrument, in: *21st IFAC World Congress*, Berlin, 2020.
- [37] R. Assaf, Modélisation des phénomènes de diffusion thermique dans un milieu fini homogène en vue de l'analyse, de la synthèse et de la validation de commandes robustes, Université de Bordeaux, Bordeaux, 2015.
- [38] F. Blanc, Production de son par couplage écoulement/résonateur: étude des paramètres de facture des flûtes par expérimentations et simulations numériques d'écoulements, in: *OAI*, Paris, 2009.
- [39] E. Ducasse, Modélisation d'instruments de musique pour la synthèse sonore: application aux instruments à vent, *Journal de Physique Colloques* 51 (1990) C2-837–C2-840, <https://doi.org/10.1051/jphyscol:19902194>.
- [40] C. Ségoufin, Production du son par interaction écoulement/résonateur acoustique, Université Paris VI, Paris, 2000.
- [41] E. Ducasse, Modélisation et simulation dans le domaine temporel d'instruments à vent à anche simple en situation de jeu: méthodes et modèles, Université du Maine, Maine, 2001.

- [42] S. Terrien, Instrument de la famille des flûtes: analyse des transitions entre régimes, Université Aix-Marseille, HAL Id: tel-01142359, version 1, Marseille, 2014.
- [43] R. Mignot, Réalisation en guides d'ondes numériques stables d'un modèle acoustique réaliste pour la simulation en temps réel d'instruments à vent, Télécom ParisTech, HAL Id: tel-00456997, version 2, Paris, 2009.
- [44] H. Boutin, S. Le Conte, J.L. Le Carrou, B. Fabre, Modèle de propagation acoustique dans un tuyau cylindrique à paroi poreuse, in: Conference: CFA'18, 14ème Congrès Français d'AcoustiqueAt: Le Havre, France, Le Havre, 2018.
- [45] R. Mignot, T. Hélie, D. Matignon, From a model of lossy flared pipes to a general framework for simulation of waveguides, *Acta Acustica united with Acustica* 97 (3) (2011) 477–491.
- [46] T. Hélie, G. Gandolfi, T. Hezard, Estimation paramétrique de la perce d'un instrument à vent à partir de la mesure de son impédance d'entrée, in: Congrès Français d'Acoustique, Poitiers, 2014.
- [47] G. Abou Haidar, X. Moreau, R. Abi Zeid Daou, Identification and analysis of the effects of the viscous thermal losses in the flute musical instruments, *Fractal and Fractional* 5 (1) (2021) 11, <https://doi.org/10.3390/fractalfract5010011>.

Fractional-order dynamics to study neuronal function

Antonio Coronel-Escamilla^a, Rohisha Tuladhar^a, Ivanka Stamova^b,
and Fidel Santamaria^a

^aDepartment of Biology, University of Texas at San Antonio, San Antonio, TX, United States

^bDepartment of Mathematics, University of Texas at San Antonio, San Antonio, TX, United States

15.1. Introduction

The nervous system is composed of networks of neurons that, in the majority of cases, communicate via electrical pulses known as action potentials [85]. Each action potential, also referred to as a spike, is the result of the flow of ions across the cell membrane through membrane conductances. In response to constant or varying stimulation, neurons generate trains of action potentials [29]. The response of a given neuron is usually characterized by the firing rate of these action potentials (Fig. 15.1). There is increasing evidence that the response of neurons is history-dependent [6,25]. This means that the reaction rates, or time constants of adaptation, of a neuron change to identical stimuli based on its previous activity [95,96]. Actually, this phenomenon can be observed across all scales of neuronal organization, sensory modalities, and species [7,23,49]. History dependence seems to underlie important computational functions such as efficient adaptive coding of natural stimuli and contrast adaptation over multiple scales of input strength [8,96]. A search of only experimental publications in recent years shows an increasing number of neuroscience laboratories that have concluded that their phenomena require a history-dependent approach [2,6,15–17,20,24,31–34,38,41,49,53,56,58,66–68,74,75,77,80,87,94,100,104,105]. Thus, it is important to generate mathematical frameworks that can model history-dependent responses in neurons independently of their particular biophysical properties.

Fractional-order differential equations are a natural mathematical tool to model history-dependent phenomena [36,86]. As can be seen in this chapter and elsewhere in this volume, a fractional-order derivative implies an intrinsic memory trace [88,97]. The memory trace integrates all the previous activity of the system in order to calculate its next value [14]. This is

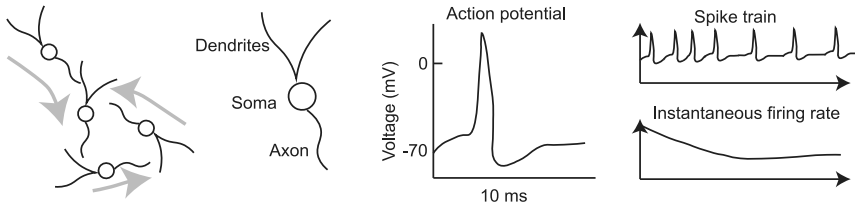
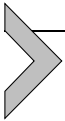


Figure 15.1 *Neurons form networks that communicate via action potentials.* Neurons make synaptic connections to form networks. Usually, synapses form at dendrites, and the activity of all synapses is integrated at the soma. If enough synaptic input is integrated, then the neuron generates an action potential that travels along the axon. In response to a stimulus, neurons generate trains of action potentials. From the interspike interval, it is possible to calculate the instantaneous firing rate.

important for membrane conductances since they are characterized by their time constant of reaction [89,91]. In a neuron without history dependence the time constant of all the membrane conductances remains identical, independently of previous activity [98]. Thus, the activity of the neuron could be characterized by averaging its behavior over multiple repetitions of an identical input [44]. However, if the dynamics of the neuronal activity are history-dependent, then the reaction rates of the conductances change as a function of time [25]. Thus, history dependence could provide a temporal dimension that increases the repertoire of responses of neurons, allowing them to change their responses to an ever-adapting input.

In this chapter, we will summarize our work on fractional-order models to study history dependence in the generation of action potentials. In the first example, we demonstrate that many properties of action potential firing rate adaptation can be reproduced with a simplified model that considers the membrane voltage being dominated by fractional-order dynamics. In the second example, we study the case in which single membrane conductances show history dependence. In this part of the chapter, we will show that such assumption is enough to replicate a myriad of spiking patterns across neuronal types. Finally, we will also present a different angle, in which we investigate the advantages of using fractional-order proportional integral derivative (FO-PID) controllers to control pathological neuronal oscillations. Overall, our work shows that we can use fractional-order integro-differential equations to build models of neuronal function and to design controllers for potential brain-machine applications.



15.2. Fractional calculus definitions

There are several definitions of fractional-order derivatives and integrals [71]. In this chapter we use Riemann–Liouville (RL), Grunwald–Letnikov (GL), and Caputo definitions.

Let $f : (0, \infty) \rightarrow \mathbb{R}$ be a continuous function. Then the fractional RL integral definition is formulated as

$${}^{\text{RL}}I_t^\alpha f(t) = \frac{1}{\Gamma(\alpha)} \frac{d^m}{dt^m} \int_0^t f(\eta)(t - \eta)^{\alpha-1} d\eta, \quad t > 0, \tag{15.1}$$

where $\alpha > 0$ is the fractional order in the integral and $\alpha \in \mathbb{R}$, $\Gamma(\cdot)$ is the Gamma function defined as

$$\Gamma(z) = \int_0^\infty t^{z-1} \exp(-t) dt. \tag{15.2}$$

If $\alpha = 1$, then the RL integral is equal to the classical integral definition [39].

The fractional RL derivative of order β , with $\beta > 0$ and $m = [\beta] + 1$, is formulated as

$${}^{\text{RL}}D_t^\beta f(t) = \frac{1}{\Gamma(m - \beta)} \frac{d^m}{dt^m} \int_0^t f(\eta)(t - \eta)^{m-\beta-1} d\eta, \quad t > 0. \tag{15.3}$$

Note that when $\beta = 1$, the RL derivative is equal to the classical derivative definition.

Finally, the Caputo derivative of order β is defined as

$${}^{\text{C}}D_t^\beta f(t) = \frac{1}{\Gamma(m - \beta)} \int_0^t f^{(m)}(\eta)(t - \eta)^{m-\beta-1} d\eta, \quad t > 0. \tag{15.4}$$

If $\beta = 1$, then the Caputo derivative is the same as the classical derivative definition.

15.2.1 Numerical algorithms to solve fractional-order differential equations

We present two algorithms that allow us to compute a numerical solution of fractional-order differential equations. The first method is based on the GL derivative and is used to find a numerical approximation of the solution when the RL derivative is considered [65]. The second approach is the L1 scheme, which allows us to compute a numerical solution of a fractional-order differential equation when the Caputo derivative is considered [37].

The use and performance of these two approaches have been widely studied and their effectiveness and robustness have also been demonstrated [12,54,79].

15.2.1.1 The Grunwald–Letnikov derivative and its numerical integration

The GL definition allows to solve numerically fractional-order differential equations [65,71] and is formulated as

$${}_0^{GL}D_t^\theta f(t) = \lim_{h \rightarrow 0} \frac{1}{h^\theta} \sum_{j=0}^{\lceil t/h \rceil} (-1)^j \binom{\theta}{j} f(t - jh), \quad (15.5)$$

where θ is the fractional order in the derivative, $\theta \in \mathbb{R}$, and j is the time increment. Note that when $\theta < 0$, this is the fractional integral ($\theta = \alpha$), and when $\theta > 0$, it is the fractional derivative ($\theta = \beta$). The binomial coefficients are computed by using the relation between Euler's Gamma function and factorial as

$$\binom{\theta}{j} = \frac{\Gamma(\theta + 1)}{\Gamma(j + 1) \Gamma(\theta - j + 1)}. \quad (15.6)$$

Using the fractional-order GL definition, we can calculate the numerical solution of a fractional-order differential equation expressed as

$${}_0^{GL}D_t^\theta f(t) = g(f(t)) \quad (15.7)$$

as follows [12,98]:

$$f(t_k) = g(f(t_{k-1})) h^\theta - \sum_{j=1}^k c_j^\theta f(t_{k-j}), \quad (15.8)$$

$$c_j^\theta = \left(1 - \frac{1 + \theta}{j}\right) c_{j-1}^\theta, \quad (15.9)$$

where h is the time step and the initial coefficient value is set to $c_0^\theta = \theta$. Note that the summation part of Eq. (15.8) is the *intrinsic memory trace*.

15.2.1.2 The L1 scheme applied to integrate the Caputo derivative

The L1 scheme is an algorithm based on the finite difference method that allows us to find a numerical solution of a fractional-order differential equation considering the Caputo derivative. The L1 scheme in the classical case

for a differential equation given as

$$\frac{d}{dt}f(t) = g(f(t), t) \tag{15.10}$$

is defined as the following approximation of the derivative [46]:

$$\frac{d}{dt}f(t) \approx \frac{1}{dt} \left[\sum_{k=0}^{N-1} [f(t_{k+1}) - f(t_k)] \right]. \tag{15.11}$$

We take the right-hand side of Eqs. (15.10) and (15.11), and solving for f at time $t_N(f(t_N))$, from $f(t_0)$ to $f(t_{N-1})$, we get

$$g(f(t), t) \approx \frac{1}{dt} \left[f(t_N) - f(t_{N-1}) + \sum_{k=0}^{N-2} [f(t_{k+1}) - f(t_k)] \right], \tag{15.12}$$

where $f(t_0)$ represents the initial condition, k is the time increment for past events, t_k is the k -th value of time such that $t_k = kdt$, and N represents the value of time at which the function f is integrated. Then, applying some algebraic rules to Eq. (15.12), we obtain the numerical solution of Eq. (15.10) as

$$f(t_N) \approx dtg(f(t_{N-1})) + f(t_{N-1}) - \sum_{k=0}^{N-2} [f(t_{k+1}) - f(t_k)]. \tag{15.13}$$

Now, we present the generalized scheme for solving a fractional-order differential equation. First, let us define a system with fractional dynamics represented with the following equation:

$${}_0^C D_t^\beta f(t) = g(f(t), t). \tag{15.14}$$

Then, with the L1 scheme a fractional derivative in the sense of Caputo can be approximated as

$$\begin{aligned} {}_0^C D_t^\beta f(t) \approx & \frac{dt^{-\beta}}{\Gamma(2-\beta)} \\ & \times \left[\sum_{k=0}^{N-1} [f(t_{k+1}) - f(t_k)] \left[(N-k)^{(1-\beta)} - (N-1-k)^{(1-\beta)} \right] \right]. \end{aligned} \tag{15.15}$$

Now, if we take the right-hand side of Eqs. (15.14) and (15.15), solving for f at time $t_N(f(t_N))$ that depends on all past values of f , that is, from $f(t_0)$ to $f(t_{N-1})$, we get

$$g(f(t), t) \approx \frac{dt^{-\beta}}{\Gamma(2-\beta)} \left[f(t_N) - f(t_{N-1}) + \sum_{k=0}^{N-2} [f(t_{k+1}) - f(t_k)] \left[(N-k)^{(1-\beta)} - (N-1-k)^{(1-\beta)} \right] \right]. \quad (15.16)$$

With some algebraic manipulations of Eq. (15.16) we obtain the numerical solution of Eq. (15.14) as

$$f(t_N) \approx dt^\beta \Gamma(2-\beta) g(f(t_{N-1})) + f(t_{N-1}) - \sum_{k=0}^{N-2} [f(t_{k+1}) - f(t_k)] \left[(N-k)^{(1-\beta)} - (N-1-k)^{(1-\beta)} \right], \quad (15.17)$$

where the Markov term weighted by the Gamma function is defined as

$$dt^\beta \Gamma(2-\beta) g(f(t_{N-1})) + f(t_{N-1}), \quad (15.18)$$

the kernel is $dt^\alpha \Gamma(2-\beta)$, and the *memory trace* is defined as

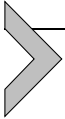
$$\sum_{k=0}^{N-2} [f(t_{k+1}) - f(t_k)] \left[(N-k)^{(1-\beta)} - (N-1-k)^{(1-\beta)} \right]. \quad (15.19)$$

Eq. (15.19) can be divided into differentiation of the past values of $(\Delta f(t_k))$, weighted by a function $W_N(\beta, k)$ as

$$(\Delta f(t_k)) = f(t_{k+1}) - f(t_k), \quad \text{for } k = 0, 1, 2, \dots, N-1, \quad (15.20)$$

$$W_N(\beta, k) = (N-k)^{(1-\beta)} - (N-1-k)^{(1-\beta)}. \quad (15.21)$$

It is important to recall that the *memory trace* contains information of all previous activity of f . As we can see, in this numerical method there is a computational problem due to the matrix expansion over the time. We also want to recall that this solution requires at least two points at the begging. Then $f(t_1)$ is computed using some classical integration method, such as Euler or Runge–Kutta.



15.3. Fractional-order dynamics in neuroscience

In this part of the chapter, we focus our attention on the study of the effects to use fractional-order dynamics in three different neuronal systems. The first example is the fractional leaky integrate-and-fire (LIF) model and the second is the Hodgkin–Huxley model. In these two examples, we study the generation of action potentials while the order range is $(0, 1)$ and the adaptation when we use fractional-order dynamics. In the last example, we study the effects of using fractional-order controllers applied to treat pathological conditions which are modeled with oscillatory behavior in a neural network. We use a PID controller that considers the fractional integral and the fractional derivative terms and is known as $PI^\alpha D^\beta$ controller.

15.3.1 History dependence in abstract models of action potential generation

The classical version of the LIF model (Eq. (15.22)) is widely used to describe the spiking activity of neurons [9]. The system consists of a leaky integrator and a voltage threshold. After the voltage crosses the threshold, an action potential is generated and the voltage is reset to a resting value for a fixed period (refractory period):

$$C_m \frac{d}{dt} V(t) = -g_L (V(t) - V_L) + I(t), \tag{15.22}$$

where $g_L = 1/R_m$ is the conductance, $V(t)$ is the membrane voltage, V_L is the resting potential, C_m is the membrane capacitance, and $I(t)$ is the input current. From Eq. (15.22) we can define the passive membrane time constant as $\tau_m = \frac{C_m}{g_L}$. The reset condition is as follows: if $V(t) = V_{th}$, then there is a spike at time t and $V(t) = V_{reset}$, where V_{th} is the voltage threshold and V_{reset} is the reset membrane voltage.

In order to provide long-term adaptation to the LIF model we made use of fractional-order derivatives (Eq. (15.23)). We have

$$C_{m0} {}^C D_t^\beta V(t) = -g_L (V(t) - V_L) + I(t), \tag{15.23}$$

where ${}^C D_t^\beta$ represents the Caputo fractional derivative and $0 < \beta \leq 1$ is the order of the derivative. The motivation to do such implementation stems from increasing experimental evidence that shows that the firing rate of real neurons follows multiple time scale dynamics [44,93] that arise from the interaction of multiple active membrane conductances [48,92,101].

To calculate an analytical solution Eq. (15.23) can be rewritten after applying ${}_0^C D_t^{1-\beta}$ to both sides:

$${}_0^C D_t^1 V(t) = -\frac{1}{\tau_m} {}_0^C D_t^{\beta-1} \left[(V(t) - V_L) + \frac{I(t)}{g_L} \right]. \quad (15.24)$$

Using the Fourier–Laplace transform, we find the solution of Eq. (15.24) as

$$V(t) = \left(V_L + \frac{I(t)}{g_L} \right) + \left(V(t_0) - V_L - \frac{I(t)}{g_L} \right) E_\beta \left(-\frac{(t-t_0)^\beta}{\tau_m} \right), \quad (15.25)$$

where $E_\beta(x)$ is the Mittag-Leffler function defined as

$$E_\beta(x) = \sum_{k=0}^{\infty} \frac{x^k}{\Gamma(\beta k + 1)}. \quad (15.26)$$

Note that the solution of Eq. (15.24) is guaranteed if and only if $g_L, C_m > 0$ for all $t > t_0$. A comparison of the analytical and numerical solution of this model can be found in [89]. For all the simulations presented here, we used the parameters in Table 15.1.

Table 15.1 Leaky integrate-and-fire model parameters values.

Parameter	Value
C_m	0.5 nF
V_L	-70 mV
V_{reset}	-70 mV
V_{th}	-50 mV
g_L	25 nS

The subthreshold response of the fractional LIF model reflects the effects of the fractional-order derivative. We injected a step current in a model with $\beta = 1$, corresponding to the classical case (Fig. 15.2(A)), and $\beta = 0.2$, corresponding to a model with strong history dependence. As expected, the membrane voltage follows a power-law behavior for the case of $\beta = 0.2$ (Fig. 15.2(B)).

The complete model, with the spiking mechanism, shows adaptation to constant input (Fig. 15.3). When $\beta = 1$, the model shows no adaptation in the firing rate (Fig. 15.3(A)). As the value of β decreases, the response of the neuron to the same constant input results in an adapting train of action potentials (Fig. 15.3(B) and (C)).

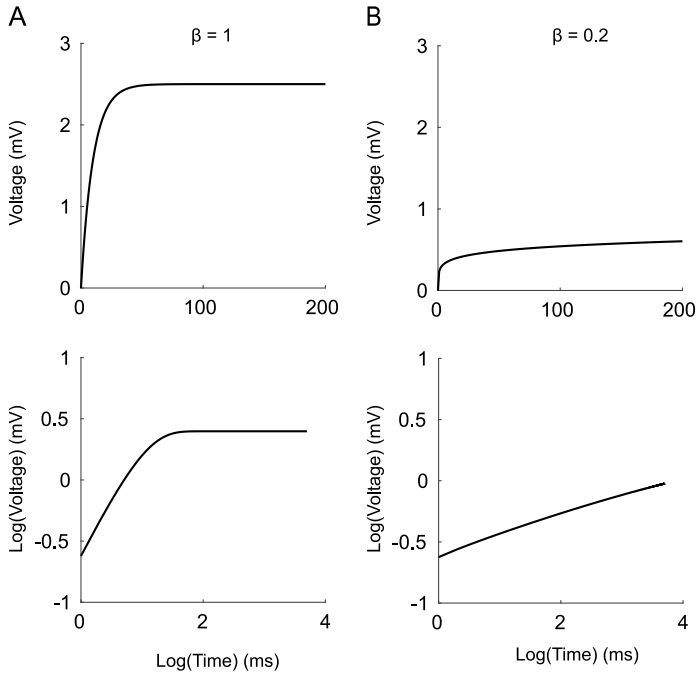


Figure 15.2 *The membrane voltage response of the fractional leaky integrate-and-fire model.* (A) Top: Membrane voltage in the LIF with $\beta = 1.0$ in response to a 2.5-nA step input current. The stimulus does not make the neuron reach the membrane threshold. Bottom: The same data as in the top panel but in log-log scale. (B) The same as in (A) but with the value of the fractional-order integral $\beta = 0.2$.

As mentioned in the introduction, history dependence results in neurons changing their reaction rates, even when stimulated with identical stimuli. In order to show this, we injected a sinusoidal current with constant frequency and amplitude (Fig. 15.4(A)) into the fractional-order model. We set the parameters in order to generate suprathreshold spiking at the peak of the curve when $\beta = 1$ (not shown). Our results show that when the value of β decreases (to 0.7 and 0.4), the spiking response of the neuron decreases (Fig. 15.4(B)–(D)). For a value of $\beta = 0.3$ the neuron does not generate action potentials during the first cycle of the sinusoidal input (Fig. 15.4(D)). After the first cycle, the cell increasingly generates more action potentials per cycle. A detailed description of these results can be found in [89].

We have extended our studies to investigate the behavior of networks composed of fractional FIL neurons. As a first step, we built a two-neuron

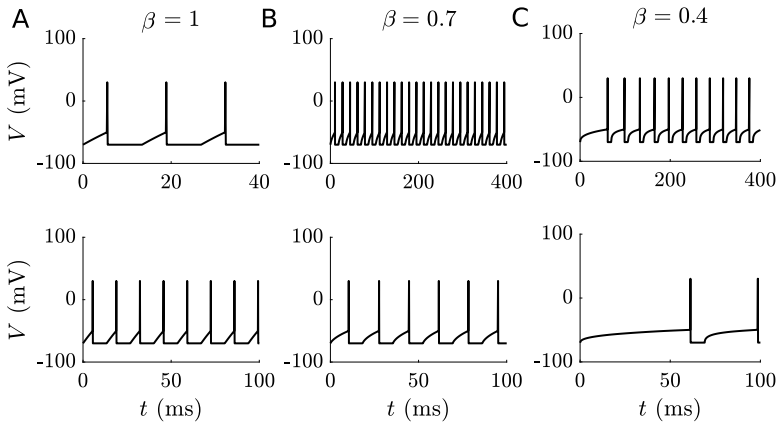


Figure 15.3 Spike adaptation in the classical and fractional leaky integrate-and-fire model. (A) The classical model generates regular spiking when we inject a constant input. (B and C) The fractional model shows the first spike latency and spike adaptation. We applied the same input current to both models (3 nA).

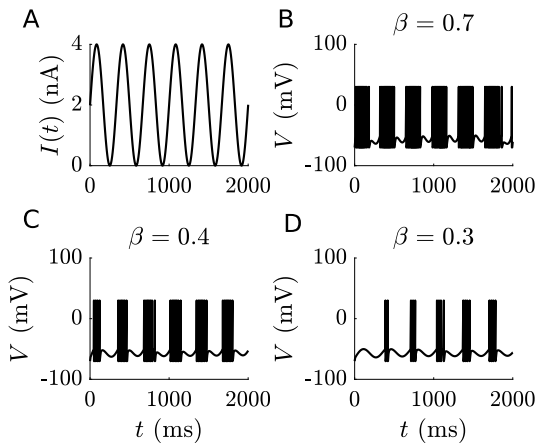


Figure 15.4 Suprathreshold and spiking fractional dynamics to oscillatory inputs. (A) Injected input current to the fractional model. (B–D) Spiking response in the fractional model to the sinusoidal input (A).

network to study the effects of synaptic coupling and input noise:

$$\begin{aligned}
 C_{m_0}^C D_t^\beta V_1(t) &= -g_L (V_1(t) - V_L) + I_1(t), \\
 C_{m_0}^C D_t^\beta V_2(t) &= -g_L (V_2(t) - V_L) + I_2(t).
 \end{aligned}
 \tag{15.27}$$

Both neurons had identical parameters. The neurons were connected through synaptic weights ω_{ij} . The weights were positive and chosen randomly. In this case, the input current is defined as

$$I_i(t) = \sum_{j=1}^i \omega_{ij} \delta_j(t) + I_{ext}(t) + I_{noise}, \quad (15.28)$$

where δ_j is the postsynaptic current generated by neuron j after it reaches the threshold, $I_{ext}(t)$ is the injected input current, I_{noise} is a noisy input current, and i is the neuron number. We did not consider connections between each neuron and itself, with the weights being $\omega_{12} = 0.17$ and $\omega_{21} = 0.19$. Both neurons received identical $I_{ext} = 3.5$ nA. On top of that input, we added white noise with an amplitude of 10 nA. When both neurons were in classical mode ($\beta = 1$) the instantaneous firing rate of both neurons was $18.23 \text{ Hz} \pm 8.10 \text{ Hz STD}$ (see Fig. 15.5(A)). In contrast, the network consisting of two fractional LIFs ($\beta = 0.6$) had a lower and more stable firing rate ($6.8 \text{ Hz} \pm 3.55 \text{ Hz STD}$) (see Fig. 15.5(B)). This analysis suggests that fractional-order neural networks could be more robust to the effects of noise.

15.3.2 History dependence in biophysical models of action potentials

Individual conductances are modeled using the Hodgkin–Huxley equations. In the basic form of this model, the passive properties of the membrane are complemented by adding voltage-dependent conductances for the sodium and potassium currents [40]:

$$C_m \frac{dV(t)}{dt} = -[g_m(V(t) - V_l) + g_k n^4(t)(V(t) - E_k) + g_{Na} m^3(t)h(t)(V(t) - E_{Na})] + I(t), \quad (15.29)$$

where g_k is the maximum potassium conductance, g_{Na} is the maximum sodium conductance, and E_k and E_{Na} are the reversal potential for the potassium and sodium currents, respectively. The variables $m(t)$, $n(t)$, and $h(t)$ are called the gating variables and are defined by the general equation

$$\frac{d}{dt}x(t) = \alpha_x(V(t))(1 - x(t)) - \beta_x(V(t))x(t), \quad (15.30)$$

where $x(t) = [n(t), m(t), h(t)]$. The gating variables $n(t)$ and $m(t)$ are activation variables and the gating variable $h(t)$ is an inactivation variable. The

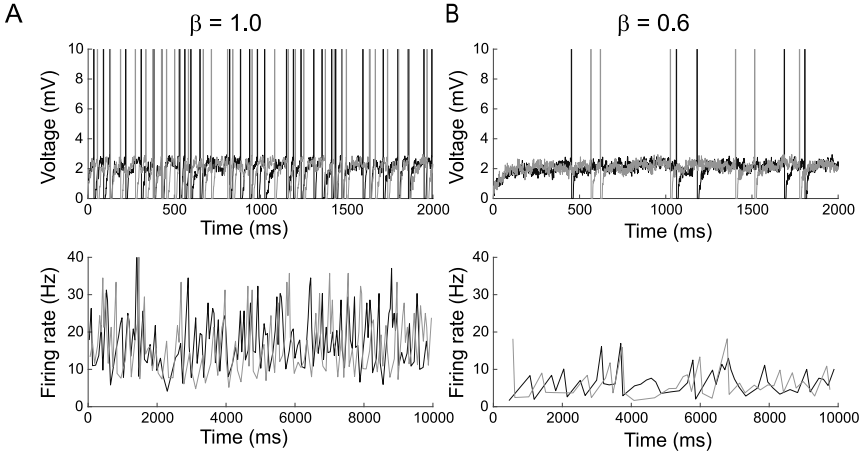


Figure 15.5 *The effects of noise on a network of fractional-order integrate-and-fire neurons.* (A) Top: The spiking response of a network composed of two neurons (black and gray). Both neurons are identical with $\beta = 1.0$, which corresponds to the classical LIF model. The neurons receive strong noisy input and are synaptically coupled (see text for details). Bottom: The instantaneous firing rate of each neuron. (B) Identical synaptic and input current parameters as in (A) but with both neurons having a fractional order of $\beta = 0.6$.

functions $\alpha_x(V(t))$ and $\beta_x(V(t))$ are the forward rate and the backward rate, respectively; these functions are defined as

$$\alpha_n(V(t)) = \frac{0.1 - 0.01(V(t) - V_0)}{e^{(1-0.1(V(t)+V_0))} - 1}, \quad (15.31)$$

$$\beta_n(V(t)) = 0.125e^{-\frac{(V(t)+V_0)}{80}}, \quad (15.32)$$

$$\alpha_m(V(t)) = \frac{2.5 - 0.1(V(t) - V_0)}{e^{(2.5-0.1(V(t)+V_0))} - 1}, \quad (15.33)$$

$$\beta_m(V(t)) = 4e^{-\frac{(V(t)+V_0)}{18}}, \quad (15.34)$$

$$\alpha_h(V(t)) = 0.07e^{-\frac{(V(t)+V_0)}{20}}, \quad (15.35)$$

$$\beta_h(V(t)) = \frac{1}{1 + e^{(3-0.1(V(t)+V_0))}}. \quad (15.36)$$

There is evidence that individual conductances can have history dependence [23]. In order to investigate the effect of history dependence on the voltage-gated conductances, we introduce the fractional operator ${}_0^C D_t^\beta$.

Now Eq. (15.30) results in

$${}^C_0D_t^\beta x(t) = \alpha_x (V(t)) (1 - x(t)) - \beta_x (V(t)) x(t), \tag{15.37}$$

where ${}^C_0D_t^\beta$ represents the fractional derivative in the sense of Caputo and $0 < \beta \leq 1$ is the order of the derivative. For the simulations presented here we used the parameters in Table 15.2.

Table 15.2 Hodgkin–Huxley model parameters values.

Parameter	Value
C_m	1.5 μ F
g_{Na}	120 ms
g_k	36 ms
g_m	0.3 ms
E_{Na}	50 mV
E_k	-77 mV
E_l	-54 mV

In the past, we have studied the spike generation of the fractional-order Hodgkin–Huxley model in response to a constant input current [90]. In that study, we conducted a systematic analysis of the types of action potentials generated by the model as a function of the value of the fractional order for the three different gates (n, m, and h). We found that we could reproduce the shapes of action potentials generated by different neuronal types. Furthermore, application of a constant input for long periods resulted in the generation of complex spiking patterns. For example, when using the classical version of the models ($\beta = 1.0$) the neuron generates a constant firing rate (Fig. 15.6(A)). For the same parameters but with $\beta = 0.6$ in the n-gate, the neuron generates a spike train that has an adaptation in the interspike interval with subthreshold oscillations (Fig. 15.6(B), top). Now, following our work on the fractional LIF we applied a sinusoidal current (5 Hz) to this same simulation. The results show that the model generates action potentials on the rising phase of the oscillation, but the action potentials are not phase-locked. This variability is in the absence of noise and is due to the combination of the spike time adaptation and subthreshold oscillations with the slow oscillatory input current.

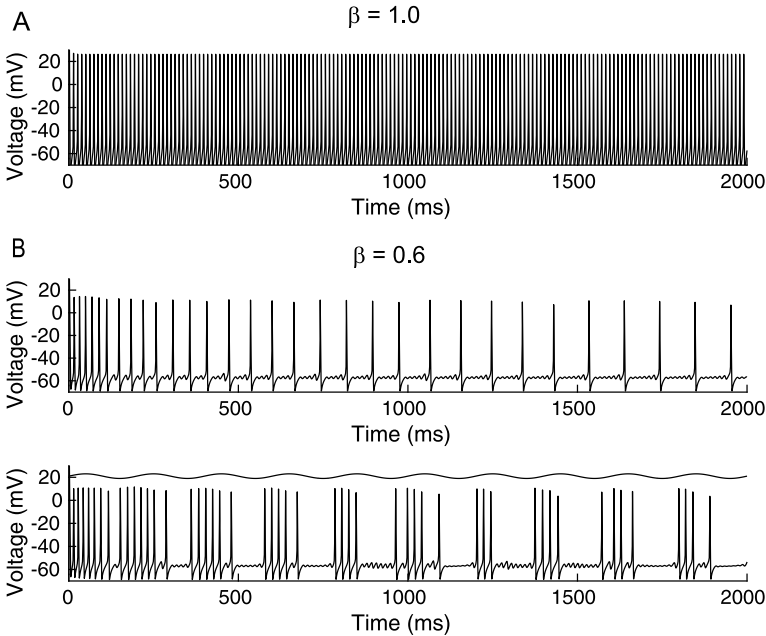


Figure 15.6 *Complex spiking patterns in the fractional-order Hodgkin–Huxley model.* (A) In response to constant (21 nA) input the classical ($\beta = 1.0$) Hodgkin–Huxley model generates a spike train with constant firing rate. (B) Top: The same model as in (A) but with a fractional order of $\beta = 0.6$ for the n-gate. Bottom: The same as top but with an added oscillatory input current (5 Hz, 2 nA amplitude).

15.3.3 Fractional controllers applied to neuronal networks

So far, we have shown how to use fractional-order dynamics to model the generation of action potentials. In this section, we will turn the problem around. Instead of using fractional differential equations to model neuronal function, we will use them to design controllers that could modulate the activity of the brain. In particular, we are interested in an application known as deep brain stimulation (DBS), which is used to control pathological oscillatory neuronal activity [4,26,30,45,55]. For example, in Parkinson’s disease (PD) there are abnormal firing rate oscillations in the activity of the neurons within the basal ganglia. These oscillations are usually in what is called the beta range: ~ 12.5 Hz to 30 Hz [5,28,61,64,76]. Fractional-order controllers are of great interest for DBS applications because they are robust to time changes in model parameters [57], they provide a fast response to external perturbations [102], and, since they have intrinsic memory, they can

be used to predict sudden changes in the model and controller parameters [50].

We designed a fractional-order PID (FO-PID) controller applied to a mathematical model of the basal ganglia in order to treat oscillatory behavior related to PD. For PD, DBS consists of applying short-period stimuli to the internal segment of the globus pallidus (GP) or to the subthalamic nucleus (STN) at a constant high frequency. The stimuli are performed by implanting a multicontact lead to one of these parts [22,59]. The stimulation is usually performed with fixed parameters and sporadic manual adjustments are made when necessary [1,3,42,43,69,76]. Our model implements a circuit of the basal ganglia with connections between the GP, STN, striatum, and cortex (Fig. 15.7) [28,63,64]:

$$\tau_s \frac{d}{dt} STN(t) = -STN(t) + F_s (-\omega_{gs} GP(t - \delta_{gs}) + \omega_{cs} v_s + u(t)), \quad (15.38)$$

$$\tau_g \frac{d}{dt} GP(t) = -GP(t) + F_g (-\omega_{sg} STN(t - \delta_{sg}) - \omega_{gg} GP(t - \delta_{gg}) + \omega_{gg} v_g), \quad (15.39)$$

where the firing rates of the STN and GP are represented by $STN(t)$ and $GP(t)$, respectively. The activation functions F_s and F_g can be defined as

$$F_s = \frac{M_s}{1 + \left(\frac{M_s - B_s}{B_s}\right) e^{\left(\frac{-4x}{M_s}\right)}}, \quad (15.40)$$

$$F_g = \frac{M_g}{1 + \left(\frac{M_g - B_g}{B_g}\right) e^{\left(\frac{-4x}{M_g}\right)}}, \quad (15.41)$$

where x is the input as shown in Eqs. (15.40) and (15.41). All parameters are described in Table 15.3.

The function $u(t)$ represents the input of the controller. In our work, we use the fractional-order derivative with order in a range of $0 < \alpha \leq 1$ and the fractional-order integral with order in a range of $1 \leq \beta < 2$ to get a general representation of the PID controller. Then $u(t)$ takes the form

$$u(t) = K_P e(t) + K_I {}^{RL}I_t^\alpha e(t) + K_D {}^{RL}D_t^\beta e(t), \quad (15.42)$$

where K_P , K_I , and K_D are the action gains of the proportional, integral, and differential components, respectively. The operators ${}^R L I_t^\alpha$ and ${}^R L D_t^\beta$ represent the fractional integral and the fractional derivative, respectively

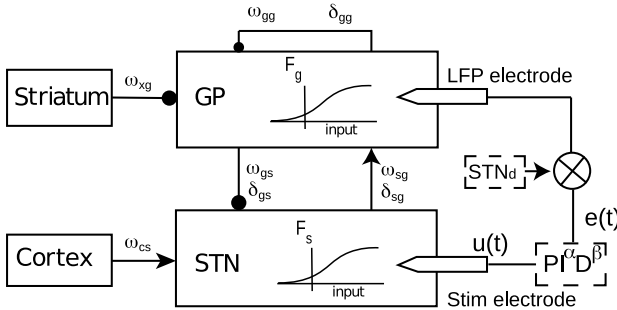


Figure 15.7 *Diagram of the basal ganglia model with the FO-PID controller.* The network model is composed of the globus pallidus (GP), the subthalamic nucleus (STN), striatum and the cortex. The FO-PID controller measures the local field potential (LFP) signal with an electrode in the GP, it calculates the error signal $e(t)$, which is the difference between the STN and the STN_d (setpoint), and injects the signal $u(t)$ in the STN. The synaptic weights (ω_{gs} , ω_{sg} , ω_{gg} , ω_{xg} , ω_{cs}) and propagation delays (δ_{gg} , δ_{gs} , δ_{sg}) affect the dynamics of the system. Synapses marked with \rightarrow are excitatory and those marked with \bullet are inhibitory.

[70,71]. Note that when $\alpha = \beta = 1$, the controller takes the form of a classical PID controller.

We define the error function as

$$e(t) = STN_d - LFP(t), \tag{15.43}$$

where STN_d is the target firing rate for the STN, $LFP(t)$ represents the local field potential in the GP, which receives inputs from the STN and striatum. The $LFP(t)$ is defined as

$$LFP(t) = \omega_{sg} STN(t - \delta_{sg}), \tag{15.44}$$

which is the weighted delayed activity of the STN (see Eqs. (15.40) and (15.41)). According to Fig. 15.7 the controller measures the error and its output is applied to the STN. A change in the synaptic weights between the STN and the GP, the striatum and the GP, and the cortex and the STN [28] results in the PD condition (see Table 15.4). All simulations were performed using the GL numerical algorithm.

15.3.4 Lyapunov analysis

We performed a Lyapunov-based stability analysis to the model (Eqs. (15.38) and (15.39)) with the FO-PID controller given in Eq. (15.42). First, we

Table 15.3 Network parameters.

Parameter	Value	Description
δ_{sg}	6 ms	Delay STN→GP
δ_{gs}	6 ms	Delay GP→STN
δ_{gg}	4 ms	Delay GP→GP
τ_s	6 ms	Reaction time STN
τ_g	14 ms	Reaction time GP
M_s	300 spk/s	STN maximum firing rate
B_s	17 spk/s	STN resting firing rate
M_g	400 spk/s	GP maximum firing rate
B_g	75 spk/s	GP resting firing rate
ν_s	27 spk/s	Cortical input to STN
ν_g	2 spk/s	Striatal input to GP

Table 15.4 Synaptic weights values.

Parameter	Healthy	Disease	Connections
ω_{gs}	1.12	10.7	GP→STN
ω_{sg}	19.0	20.0	STN→GP
ω_{gg}	6.60	12.3	GP→GP
ω_{cs}	2.42	9.2	Cortex→STN
ω_{xg}	15.1	139.4	Striatum→GP

denote $\delta = \max \{ \delta_{gs}, \delta_{sg}, \delta_{gg} \}$, and we define $x_t(\gamma) = x(t + \gamma)$, for $t \geq 0$ and $x_t \in C[[-\delta, 0], \mathbb{R}]$ with $-\delta \leq \gamma \leq 0$. Let

$$f(t, \varphi_t, \phi_t) = -\varphi(t) + F_s \left(-\omega_{gs}\phi_t + \omega_{cs}\nu_s + K_P e(t) + K_{I_0}^{RL} I_t^\alpha e(t) + K_{D_0}^{RL} D_t^\beta e(t) \right), \tag{15.45}$$

$$g(t, \varphi_t, \phi_t) = -\phi(t) + F_g (\omega_{sg}\varphi_t - \omega_{gg}\phi_s - \omega_{xg}\nu_g),$$

and let $(STN(t), GP(t))$ be a solution of Eq. (15.43) with initial conditions

$$\begin{cases} STN(t; 0, \varphi_0, \phi_0) = \varphi_0(t), & -\delta \leq t \leq 0, \\ GP(t; 0, \varphi_0, \phi_0) = \phi_0(t), & -\delta \leq t \leq 0, \end{cases} \tag{15.46}$$

where φ_0, ϕ_0 are continuous functions on $[-\delta, 0]$.

Now, we denote by GP_d the state corresponding to STN_d . Consider the Lyapunov-like functions

$$V(t, STN, GP) = |STN - STN_d| + |GP - GP_d|. \tag{15.47}$$

We evaluate the derivative of the continuous function $V(t, STN, GP)$ with respect to the system given in Eqs. (15.38) and (15.39) as follows:

$$\begin{aligned}
 &D_4^+ V(t, \varphi(t), \phi(t)) \\
 &= \limsup_{h \rightarrow 0^+} \frac{1}{\delta} \left[V(t+h, \varphi(t) + hf(t, \varphi_t, \phi_t), \phi(t) + hg(t, \varphi_t, \phi_t)) \right. \\
 &\quad \left. - V(t, \varphi(t), \phi(t)) \right]. \tag{15.48}
 \end{aligned}$$

There are positive constants L_s and L_g for the sigmoid activation functions F_s and F_g such that

$$\begin{aligned}
 |F_s(x) - F_s(y)| &\leq L_s |x - y|, \\
 |F_g(x) - F_g(y)| &\leq L_g |x - y|,
 \end{aligned} \tag{15.49}$$

for all $x, y \in \mathbb{R}$, $x \neq y$, and we also have $F_g(0) = B_g \geq 0$, $F_s(0) = B_s \geq 0$.

Then for $t \geq 0$ and for any $\varphi \in C[[t - \delta, t], \mathbb{R}]$, $\phi \in C[[t - \delta, t], \mathbb{R}]$ such that $V(t + \gamma, \varphi(t + \gamma), \phi(t + \gamma)) < V(t, \varphi(t), \phi(t))$, $\gamma \in [-\delta, 0)$, we have

$$D_7^+ V(t, \varphi(t), \phi(t)) \leq \left(-\frac{1}{\tau} + A \right) V(t, \varphi(t), \phi(t)), \tag{15.50}$$

where $-\frac{1}{\tau} = \min \left\{ \frac{1}{\tau_s}, \frac{1}{\tau_g} \right\}$ and

$$\begin{aligned}
 A = \max \left\{ \frac{\omega_{gs} L_s}{\tau_s} + \frac{\omega_{gg} L_g}{\tau_g}, \right. \\
 \left. \omega_{sg} \left(\frac{1}{\tau_s} L_s \left(K_P + K_I \frac{I_c}{\Gamma(\alpha)} + K_D \frac{D_c}{\Gamma(m - \beta)} \right) + \frac{1}{\tau_g} L_g \right) \right\}, \tag{15.51}
 \end{aligned}$$

where I_c and D_c are constants that allow to compute the reference gain from the fractional integral action and fractional derivative action.

If $\frac{1}{\tau} \geq A$, then $D_4^+ V(t, \varphi(t), \phi(t)) \leq 0$, and based on the theory of delayed systems (see [27]), the state (STN_d, GP_d) is stable. Note that if there is a constant $c > 0$ such that $\frac{1}{\tau} - A \geq c > 0$, then $D_4^+ V(t, \varphi(t), \phi(t)) \leq -cV(t, \varphi(t), \phi(t))$; this assumption guarantees exponential stability. Some results using this approach can be found in [82–84]. In these systems the Mittag-Leffler stability generalizes the exponential stability concept. Our Lyapunov-based stability analysis indicates that the state variables $STN(t)$ and $GP(t)$ could be controlled and synchronized. However, the condition $\frac{1}{\tau} - A \geq c > 0$ is very restrictive.

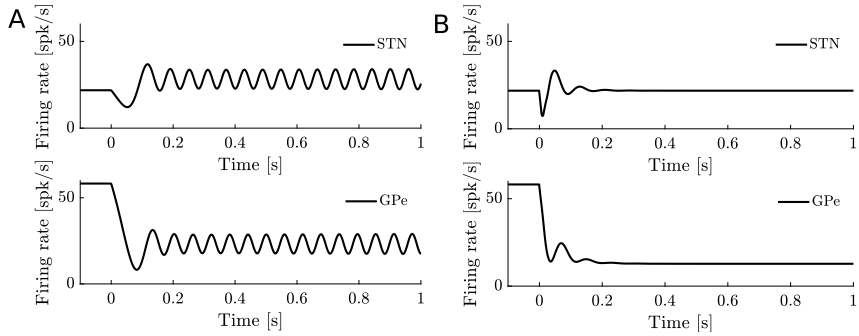


Figure 15.8 System response in Parkinson's disease condition and with the PID controller. (A) The firing rate of the subthalamic nucleus (STN) and the globus pallidus (GP) is constant when $t < 0$; when $t > 0$ the synaptic parameters change and the system presents pathological oscillatory behavior (see Table 15.2). (B) The same simulation as in (A) but now the system is in a closed-loop with the PID controller with $K_p = 15$, $K_i = 115$, and $K_d = 0.15$. The firing rate of the STN now is regulated to the set point (22 Hz).

15.3.5 Reducing pathological neuronal oscillations with a FO-PID controller

A nonpathological condition is when the firing rate in the neural network has a stable firing rate in the STN and GP (Fig. 15.8(A), $t < 0$). If the synaptic parameters change (Table 15.4), then the firing rates in both areas present oscillation in the beta range (12 Hz, Fig. 15.8(A), $t > 0$). We considered the system under control when the STN activity has a value within 10% of the desired firing rate (22 Hz) in the last 0.2 seconds of the simulation. In order to regulate this oscillatory activity, we first tuned the PID controller. We fixed the proportional gain to $K_p = 15$, performed a parameter sweep of each gain separately, and determined the range of values in which the system was under control. In the case when $K_D = 0$ and $K_p = 15$, the gain sweep of K_I resulted in a range of $K_I = (0, 856)$, and when $K_I = 0$ and $K_p = 15$, the gain sweep of K_D resulted in a range of $K_D = (0, 0.19)$. We chose the set of gains ($K_I = 115$, $K_D = 0.15$, $K_p = 15$) to show how the controller damped the oscillatory behavior to the target firing rate in the STN and GP (Fig. 15.8(B)).

Using the same approach, we calculated the gain range of the FO-PID controller. In this case we also changed the fractional orders of the differential and integral components. We fixed $K_D = 0.15$ and performed a sweep of the K_I gain while increasing the order in the integral term. This analysis showed an increase in the range of $K_I = (0, 1967)$. Then, we

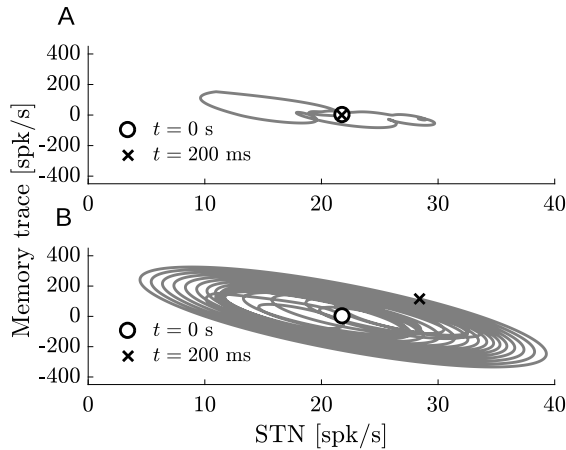


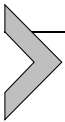
Figure 15.9 Phase plane of the memory trace of a FO-PID controller against the spiking activity in a computer model of Parkinson's disease. (A) Phase portrait between the memory trace and the subthalamic nucleus (STN) when the system is under control ($K_I = 115$, $K_D = 0.15$, $K_P = 15$). The memory trace and the STN generate an attractor which takes the system into a stable state. (B) The same as in (A) but now without the control; the system never gets into the attractor and hence it is unstable.

performed a similar analysis but now fixing $K_I = 115$ to determinate the range of the K_D gain while we decreased the order in the derivative term. This result shows that the range of K_D expands to $K_D = 22$. These analyses show that the ranges of K_I and K_D are expanded in the fractional case which indicates a multifold increase in the range of operational gains compared to the classical PID controller.

We analyzed the system phase portrait between the memory trace and the STN in the stable and unstable cases. When the system is stable the memory trace generates an attractor, which takes the system into a stable state (Fig. 15.9(A)). In contrast, when the system is not under control, the system never falls into the attractor; in fact, the system behavior grows unbounded, which proves that the system is not stable (Fig. 15.9(B)). We show that the memory trace provides a negative feedback which generates an attractor and takes the system into a stable state. When no control is applied, the system never gets into an attractor and hence the system is unstable.

We also studied the robustness of the neural network to changes in synaptic parameters. In the system, the oscillatory conditions occur when there is an increase in synaptic weights between GP→STN (ω_{gs}),

STN→GP (ω_{sg}), and GP→GP (ω_{gg}); other synaptic changes did not generate oscillations. In order to determinate the synaptic parameter space, we randomly ran 760 simulations with the combination of the three parameters distributed from 0% to 200% of the values given in Table 15.4. At each simulation we used the fractional order of the integral $\alpha = (1, 1.3, 1.5, 1.7)$ and derivative $\beta = (0.3, 0.5, 0.7, 1)$. Each time simulation lasted 5 seconds, with the first 2.5 seconds with the normal synaptic parameters and the last 2.5 seconds with the increased values of these parameters. Our results show that only the values of ω_{gs} and ω_{sg} affect the system when it is under control. The value of ω_{gg} did not contribute to the control of the simulation, except for the cases in which there was a strong self-inhibition that shuts down the activity in the GP. Our analysis shows that when we used a classical PID controller, only 57% of the simulations converge; in contrast, when we used the FO-PID controller this percentage increased to 82%. Our complete analysis of the data proves that maximum robustness of the FO-PID controller is obtained when $\alpha = 1.3$ and $\beta = [0.5, 1]$. Thus, a FO-PID controller can expand the robustness in controlling the onset of oscillations due to changes in synaptic weight parameters that affect the network dynamics. A detailed description of this work can be found in [13].



15.4. Discussions and conclusions

In this chapter, we presented an overview of how to use fractional-order differential equation models in neuroscience. We concentrated on two different aspects. In one, we showed that fractional-order dynamics in the membrane voltage or the activation of membrane conductances replicate complex spiking activity. From a different perspective, we showed that fractional-order PID controllers could be a robust solution for DBS systems. Altogether, our work shows that fractional-order systems can be widely applied in neuroscience, from modeling to neuro-engineering.

Fractional-order dynamics is not only applied to modeling membrane voltage and spiking activity. In fact, our original experimental and modeling work concentrated on the diffusion rates of intracellular signals. Here we found that diffusion in complex dendritic trees follows subanomalous diffusion, a well-known process described with fractional-order equations [77,78]. In these studies, we linked the shape and density of dendritic spines, the site of most excitatory synapses, to the anomalous exponent (the fractional order of the diffusion equation in time). The models not only replicated experimental results, but also provided a new perspective in

understanding the function of dendritic spines as “traps” for diffusing signals along dendrites. Multiple theoretical works have been inspired by our results [35,62,81,100].

If, indeed, neurons follow fractional-order dynamics, it is necessary to understand how those properties are reflected in neural network dynamics. It is well known that the fractional differentiation of order β of a signal with a power spectrum that follows a power law of the same order results in an output signal with a flat power spectrum [51,99]. This is known as whitening the noise and is a hallmark of optimal coding [60]. This could indicate that neurons that perform a fractional-order derivative of their input could be optimally coding their inputs, thus facilitating efficient computation in the brain [36]. There are multiple challenges to investigate the effects of fractional-order neuro-dynamics on networks; some of the ones that we think are more pressing are in the areas of coding and of learning and memory [18,52,72].

We also presented a very different application of fractional dynamics in which we used it to design a FO-PID controller to reduce modeled pathological oscillations. Here we combined mathematical analysis with simulations. Lyapunov stability analysis is a powerful and universal method for investigating dynamical systems [11,47]. The well-constructed Lyapunov function that we presented allows the area of stability to be evaluated in the phase space as well as in the space of the parameters. Our analysis indicates that the state variables $STN(t)$ and $GP(t)$ could be controlled and synchronized. The simulations showed that the robustness of the FO-PID controller was multiple times that of the classical controller. This study allows us to understand how fractional dynamics improve the robustness in the controller and, while the neuronal model was highly simplified, our objective was to provide a proof-of-principle about the increase in robustness of history-dependent controllers for DBS applications. Future work should include realistic neural networks and an expanded stability analysis in order to guarantee convergence over a wide range of changes in neuronal activity [10,19,73]. The neuronal phenomena we are trying to control consist of the sudden emergence of pathological oscillations; therefore, Lyapunov stability extended to non-smooth systems should be considered in future extensions of this research [103]. Although closed-loop controllers have been studied to suppress the pathological beta oscillations associated with PD, there are still some challenges on how to properly tune the controllers considering the DBS signal constraints, and since this is an invasive technique there is a need to be careful with its proper application [21]. Thus, our study

provides a proper background on the implementation, tuning, and future applications of closed-loop controllers.

As a final comment, we want to point out that fractional-order dynamical systems are a promising tool to study neuronal function and behavior. However, there are multiple challenges to tackle. For example, what is the biophysical origin of the scale-free behavior? In some cases, we have experimentally shown that the complex dendritic structure of neurons is directly related to anomalous diffusion phenomena in different types of neurons [78]. However, while fractional-order behavior is observed at all neurobiological scales, the biophysical substrates of such activity remain unknown. Another question is whether the emergence of fractional-order dynamics is related to systems with a large number of time constants or whether it is because there are strong interactions across scales that result in systems outside equilibrium. This could be happening in the open-closed states of voltage-gated channels; however, this requires further study. Ultimately, it is important to determine if fractional-order dynamics provides an advantageous computational strategy to the organism. We have suggested that history dependence is a mechanism to increase the computational capacity of neurons, and as such, we propose that scale-free history-dependent processes produced by evolutionary pressures allow organisms to continuously adapt to an ever-changing environment.

References

- [1] R. Agarwal, S.V. Sarma, Restoring the basal ganglia in Parkinson's disease to normal via multi-input phase-shifted deep brain stimulation, in: *Engineering in Medicine and Biology Society (EMBC), 2010 Annual International Conference of the IEEE*, 2010, pp. 1539–1542.
- [2] E. Álvarez-Salvado, A. Licata, E.G. Connor, M.K. McHugh, B.M. King, N. Stavropoulos, J.P. Crimaldi, K.I. Nagel, Elementary sensory-motor transformations underlying olfactory navigation in walking fruit-flies, *Elife* (2018) e37815.
- [3] B.-P. Bejjani, P. Damier, I. Arnulf, L. Thivard, A.-M. Bonnet, D. Dormont, P. Cornu, B. Pidoux, Y. Samson, Y. Agid, Transient acute depression induced by high-frequency deep-brain stimulation, *The New England Journal of Medicine* 1999 (340) (1999) 1476–1480.
- [4] A.L. Benabid, Deep brain stimulation for Parkinson's disease, *Current Opinion in Neurobiology* 13 (6) (2003) 696–706.
- [5] A. Beuter, J. Bélair, C. Labrie, Feedback and delays in neurological diseases: a modeling study using dynamical systems, *Bulletin of Mathematical Biology* 55 (3) (1993) 525–541.
- [6] V. Botella-Soler, S. Deny, G. Martius, O. Marre, G. Tkačik, Nonlinear decoding of a complex movie from the mammalian retina, *PLoS Computational Biology* 14 (5) (2018) e1006057.
- [7] J.W. Brascamp, T.H.J. Knapen, R. Kanai, A.J. Noest, R. van Ee, A.V. van den Berg, Multi-timescale perceptual history resolves visual ambiguity, *PLoS ONE* 3 (1) (2008) e1497.

- [8] C.D. Brody, R. Romo, A. Kepecs, Basic mechanisms for graded persistent activity: discrete attractors, continuous attractors, and dynamic representations, *Current Opinion in Neurobiology* 13 (2) (2003) 204–211.
- [9] A.N. Burkitt, A review of the integrate-and-fire neuron model: I. Homogeneous synaptic input, *Biological Cybernetics* 95 (1) (2006) 1–19.
- [10] J. Cao, S. Zhong, Y. Hu, Global stability analysis for a class of neural networks with varying delays and control input, *Applied Mathematics and Computation* 189 (2) (2007) 1480–1490.
- [11] W. Chen, H. Dai, Y. Song, Z. Zhang, Convex Lyapunov functions for stability analysis of fractional order systems, *IET Control Theory & Applications* 11 (7) (2017) 1070–1074.
- [12] A. Coronel-Escamilla, J. Gómez-Aguilar, E. Alvarado-Méndez, G. Guerrero-Ramírez, R. Escobar-Jiménez, Fractional dynamics of charged particles in magnetic fields, *International Journal of Modern Physics C* 27 (08) (2016) 1650084.
- [13] A. Coronel-Escamilla, J.F. Gomez-Aguilar, I. Stamova, F. Santamaria, Fractional order controllers increase the robustness of closed-loop deep brain stimulation systems, *Chaos, Solitons and Fractals* 140 (2020) 110149.
- [14] M. Du, Z. Wang, H. Hu, Measuring memory with the order of fractional derivative, *Scientific Reports* 3 (1) (2013) 1–3.
- [15] A. Dutta, H. Wagner, Y. Gutfreund, Responses to pop-out stimuli in the barn owl's optic tectum can emerge through stimulus-specific adaptation, *The Journal of Neuroscience* 36 (17) (2016) 4876–4887.
- [16] R. Dvorkin, N.E. Ziv, Relative contributions of specific activity histories and spontaneous processes to size remodeling of glutamatergic synapses, *PLoS Biology* 14 (10) (2016) e1002572.
- [17] E.D. Fagerholm, G. Scott, W.L. Shew, C. Song, R. Leech, T. Knopfel, D.J. Sharp, Cortical entropy, mutual information and scale-free dynamics in waking mice, *Cerebral Cortex* 26 (10) (2016) 3945–3952.
- [18] M. Famulare, A. Fairhall, Feature selection in simple neurons: how coding depends on spiking dynamics, *Neural Computation* 22 (3) (2010) 581–598.
- [19] C. Feng, R. Plamondon, On the stability analysis of delayed neural networks systems, *Neural Networks* 14 (9) (2001) 1181–1188.
- [20] I.R. Fiete, W. Senn, C.Z. Wang, R.H. Hahnloser, Spike-time-dependent plasticity and heterosynaptic competition organize networks to produce long scale-free sequences of neural activity, *Neuron* 65 (4) (2010) 563–576.
- [21] J.E. Fleming, E. Dunn, M.M. Lowery, Simulation of closed-loop deep brain stimulation control schemes for suppression of pathological beta oscillations in Parkinson's disease, *Frontiers in Neuroscience* 14 (2020) 166.
- [22] K.A. Follett, F.M. Weaver, M. Stern, K. Hur, C.L. Harris, P. Luo, W.J. Marks Jr., J. Rothlind, O. Sagher, C. Moy, et al., Pallidal versus subthalamic deep-brain stimulation for Parkinson's disease, *The New England Journal of Medicine* 362 (22) (2010) 2077–2091.
- [23] A. Gal, D. Eytan, A. Wallach, M. Sandler, J. Schiller, S. Marom, Dynamics of excitability over extended timescales in cultured cortical neurons, *The Journal of Neuroscience* 30 (48) (2010) 16332–16342.
- [24] A. Gal, S. Marom, Entrainment of the intrinsic dynamics of single isolated neurons by natural-like input, *The Journal of Neuroscience* 33 (18) (2013) 7912–7918.
- [25] G. Gilboa, R. Chen, N. Brenner, History-dependent multiple-time-scale dynamics in a single-neuron model, *The Journal of Neuroscience* 25 (28) (2005) 6479–6489.
- [26] B.D. Greenberg, D.A. Malone, G.M. Friehs, A.R. Rezai, C.S. Kubu, P.F. Malloy, S.P. Salloway, M.S. Okun, W.K. Goodman, S.A. Rasmussen, Three-year outcomes in deep brain stimulation for highly resistant obsessive-compulsive disorder, *Neuropsychopharmacology* 31 (11) (2006) 2384–2393.

- [27] J.K. Hale, S.M.V. Lunel, L.S. Verduyn, S.M.V. Lunel, *Introduction to Functional Differential Equations*, vol. 99, Springer Science & Business Media, 1993.
- [28] A.J.N. Holgado, J.R. Terry, R. Bogacz, Conditions for the generation of beta oscillations in the subthalamic nucleus-globus pallidus network, *The Journal of Neuroscience* 30 (37) (2010) 12340–12352.
- [29] A.R. Houweling, M. Brecht, Behavioural report of single neuron stimulation in somatosensory cortex, *Nature* 451 (7174) (2008) 65–68.
- [30] B. Hu, Q. Wang, Controlling absence seizures by deep brain stimulus applied on substantia nigra pars reticulata and cortex, *Chaos, Solitons and Fractals* 80 (2015) 13–23.
- [31] C.G. Huang, M.J. Chacron, Optimized parallel coding of second-order stimulus features by heterogeneous neural populations, *The Journal of Neuroscience* 36 (38) (2016) 9859.
- [32] R. Huda, M.J. Goard, G.N. Pho, M. Sur, Neural mechanisms of sensorimotor transformation and action selection, *European Journal of Neuroscience* 49 (8) (2019) 1055–1060.
- [33] E.J. Hwang, J.E. Dahlen, M. Mukundan, T. Komiyama, History-based action selection bias in posterior parietal cortex, *Nature Communications* 8 (1) (2017) 1242.
- [34] J.M. Hyman, C.B. Holroyd, J.K. Seamans, A novel neural prediction error found in anterior cingulate cortex ensembles, *Neuron* 95 (2) (2017) 447–456, e3.
- [35] A. Iomin, V. Méndez, Reaction-subdiffusion front propagation in a comblike model of spiny dendrites, *Physical Review E* 88 (1) (2013) 012706.
- [36] C. Ionescu, A. Lopes, D. Copot, J.T. Machado, J. Bates, The role of fractional calculus in modeling biological phenomena: a review, *Communications in Nonlinear Science and Numerical Simulation* 51 (2017) 141–159.
- [37] B. Jin, R. Lazarov, Z. Zhou, An analysis of the L1 scheme for the subdiffusion equation with nonsmooth data, *IMA Journal of Numerical Analysis* 36 (1) (2016) 197–221.
- [38] Y. Karimipناه, Z. Ma, J.K. Miller, R. Yuste, R. Wessel, Neocortical activity is stimulus- and scale-invariant, *PLoS ONE* 12 (5) (2017) e0177396.
- [39] A.A. Kilbas, H.M. Srivastava, J.J. Trujillo, *Theory and Applications of Fractional Differential Equations*, vol. 204, Elsevier Science Limited, 2006.
- [40] C. Koch, *Biophysics of Computation: Information Processing in Single Neurons*, Oxford University Press, 2004.
- [41] N. Kolling, M.K. Wittmann, T.E. Behrens, E.D. Boorman, R.B. Mars, M.F. Rushworth, Value, search, persistence and model updating in anterior cingulate cortex, *Nature Neuroscience* 19 (10) (2016) 1280.
- [42] R. Kumar, A. Lozano, Y. Kim, W. Hutchison, E. Sime, E. Halket, A. Lang, Double-blind evaluation of subthalamic nucleus deep brain stimulation in advanced Parkinson's disease, *Neurology* 51 (3) (1998) 850–855.
- [43] R. Kumar, A.M. Lozano, E. Sime, A.E. Lang, Long-term follow-up of thalamic deep brain stimulation for essential and parkinsonian tremor, *Neurology* 61 (11) (2003) 1601–1604.
- [44] G. La Camera, A. Rauch, D. Thurbon, H.-R. Luscher, W. Senn, S. Fusi, Multiple time scales of temporal response in pyramidal and fast spiking cortical neurons, *Journal of Neurophysiology* 96 (6) (2006) 3448–3464.
- [45] A.W. Laxton, D.F. Tang-Wai, M.P. McAndrews, D. Zumsteg, R. Wennberg, R. Keren, J. Wherrett, G. Naglie, C. Hamani, G.S. Smith, A phase I trial of deep brain stimulation of memory circuits in Alzheimer's disease, *Annals of Neurology* 68 (4) (2010) 521–534.
- [46] Z. Li, Z. Liang, Y. Yan, High-order numerical methods for solving time fractional partial differential equations, *Journal of Scientific Computing* 71 (2) (2017) 785–803.

- [47] S. Liu, W. Jiang, X. Li, X.-F. Zhou, Lyapunov stability analysis of fractional nonlinear systems, *Applied Mathematics Letters* 51 (2016) 13–19.
- [48] R.R. Llinás, The intrinsic electrophysiological properties of mammalian neurons: insights into central nervous system function, *Science* 242 (4886) (1988) 1654–1664.
- [49] B.N. Lundstrom, M.H. Higgs, W.J. Spain, A.L. Fairhall, Fractional differentiation by neocortical pyramidal neurons, *Nature Neuroscience* 11 (11) (2008) 1335.
- [50] J. Machado, Discrete-time fractional-order controllers, *Fractional Calculus and Applied Analysis* 4 (2001) 47–66.
- [51] R. Magin, M.D. Ortigueira, I. Podlubny, J. Trujillo, On the fractional signals and systems, *Signal Processing* 91 (3) (2011) 350–371.
- [52] R.L. Magin, Fractional calculus models of complex dynamics in biological tissues, *Computers & Mathematics with Applications* 59 (5) (2010) 1586–1593.
- [53] B. Maniscalco, J.L. Lee, P. Abry, A. Lin, T. Holroyd, B.J. He, Neural integration of stimulus history underlies prediction for naturalistically evolving sequences, *The Journal of Neuroscience* 38 (2018) 1541–1557.
- [54] T. Marinov, N. Ramirez, F. Santamaria, Fractional integration toolbox, *Fractional Calculus and Applied Analysis* 16 (3) (2013) 670–681.
- [55] H.S. Mayberg, A.M. Lozano, V. Voon, H.E. McNeely, D. Seminowicz, C. Hamani, J.M. Schwab, S.H. Kennedy, Deep brain stimulation for treatment-resistant depression, *Neuron* 45 (5) (2005) 651–660.
- [56] S. Mensi, O. Hagens, W. Gerstner, C. Pozzorini, Enhanced sensitivity to rapid input fluctuations by nonlinear threshold dynamics in neocortical pyramidal neurons, *PLoS Computational Biology* 12 (2) (2016) e1004761.
- [57] C.A. Monje, A.J. Calderon, B.M. Vinagre, Y. Chen, V. Feliu, On fractional PI λ controllers: some tuning rules for robustness to plant uncertainties, *Nonlinear Dynamics* 38 (1–4) (2004) 369–381.
- [58] A.S. Morcos, C.D. Harvey, History-dependent variability in population dynamics during evidence accumulation in cortex, *Nature Neuroscience* 19 (12) (2016) 1672–1681.
- [59] E. Moro, A.M. Lozano, P. Pollak, Y. Agid, S. Rehncrona, J. Volkmann, J. Kulisevsky, J.A. Obeso, A. Albanese, M.I. Hariz, et al., Long-term results of a multicenter study on subthalamic and pallidal stimulation in Parkinson's disease, *Movement Disorders* 25 (5) (2010) 578–586.
- [60] B. Ninness, Estimation of $1/f$ noise, *IEEE Transactions on Information Theory* 44 (1) (1998) 32–46.
- [61] J.A. Obeso, M.C. Rodriguez-Oroz, M. Rodriguez, J.L. Lanciego, J. Artieda, N. Gonzalo, C.W. Olanow, Pathophysiology of the basal ganglia in Parkinson's disease, *Trends in Neurosciences* 23 (2000) S8–S19.
- [62] A. Ochab-Marcinek, S.A. Wieczorek, N. Ziębacz, R. Hołyst, The effect of depletion layer on diffusion of nanoparticles in solutions of flexible and polydisperse polymers, *Soft Matter* 8 (43) (2012) 11173–11179.
- [63] W. Pasillas-Lépine, Delay-induced oscillations in Wilson and Cowan's model: an analysis of the subthalamo-pallidal feedback loop in healthy and parkinsonian subjects, *Biological Cybernetics* 107 (3) (2013) 289–308.
- [64] A. Pavlides, S. John Hogan, R. Bogacz, Improved conditions for the generation of beta oscillations in the subthalamic nucleus-globus pallidus network, *European Journal of Neuroscience* 36 (2) (2012) 2229–2239.
- [65] I. Petras, *Fractional-Order Nonlinear Systems: Modeling, Analysis and Simulation*, Springer Science & Business Media, 2011.
- [66] E.A. Phillips, C.E. Schreiner, A.R. Hasenstaub, Cortical interneurons differentially regulate the effects of acoustic context, *Cell Reports* 20 (4) (2017) 771–778.

- [67] E.A. Phillips, C.E. Schreiner, A.R. Hasenstaub, Distinct regulation of history-dependent responses by two cortical interneuron populations, *bioRxiv* (2017) 129593.
- [68] E.A. Phillips, C.E. Schreiner, A.R. Hasenstaub, Diverse effects of stimulus history in waking mouse auditory cortex, *Journal of Neurophysiology* 118 (2) (2017) 1376–1393.
- [69] P. Plaha, S.S. Gill, Bilateral deep brain stimulation of the pedunculopontine nucleus for Parkinson's disease, *NeuroReport* 16 (17) (2005) 1883–1887.
- [70] I. Podlubny, Fractional-order systems and $PI^{\lambda}D^{\mu}$ -controllers, *IEEE Transactions on Automatic Control* 44 (1) (1999) 208–214.
- [71] I. Podlubny, *Fractional Differential Equations: An Introduction to Fractional Derivatives, Fractional Differential Equations, to Methods of Their Solution and Some of Their Applications*, vol. 198, Academic Press, 1998.
- [72] S.A. Prescott, T. Sejnowski, Spike-rate coding and spike-time coding are affected oppositely by different adaptation mechanisms, *The Journal of Neuroscience* 28 (50) (2008) 13649–13661.
- [73] H. Qiao, J. Peng, Z.-B. Xu, B. Zhang, A reference model approach to stability analysis of neural networks, *IEEE Transactions on Systems, Man, and Cybernetics, Part B* 33 (6) (2003) 925–936.
- [74] A. Rastogi, Surbhi, S. Malik, S. Rani, V. Kumar, Annual life-history dependent seasonal differences in neural activity of the olfactory system between non-migratory and migratory songbirds, *Behavioural Brain Research* 296 (2016) 233–239.
- [75] T. Ros, P. Frewen, J. Theberge, A. Michela, R. Kluetsch, A. Mueller, G. Candrian, R. Jetly, P. Vuilleumier, R.A. Lanius, Neurofeedback tunes scale-free dynamics in spontaneous brain activity, *Cerebral Cortex* 27 (10) (2017) 4911–4922.
- [76] J.E. Rubin, D. Terman, High frequency stimulation of the subthalamic nucleus eliminates pathological thalamic rhythmicity in a computational model, *Journal of Computational Neuroscience* 16 (3) (2004) 211–235.
- [77] F. Santamaria, S. Wils, E. De Schutter, G.J. Augustine, Anomalous diffusion in Purkinje cell dendrites caused by spines, *Neuron* 52 (4) (2006) 635–648.
- [78] F. Santamaria, S. Wils, E. De Schutter, G.J. Augustine, The diffusional properties of dendrites depend on the density of dendritic spines, *European Journal of Neuroscience* 34 (4) (2011) 561–568.
- [79] R. Scherer, S.L. Kalla, Y. Tang, J. Huang, The Grünwald–Letnikov method for fractional differential equations, *Computers & Mathematics with Applications* 62 (3) (2011) 902–917.
- [80] D.J. Smit, E.J. de Geus, M.E. van de Nieuwenhuijzen, C.E. van Beijsterveldt, G.C. van Baal, H.D. Mansvelder, D.I. Boomsma, K. Linkenkaer–Hansen, Scale-free modulation of resting-state neuronal oscillations reflects prolonged brain maturation in humans, *The Journal of Neuroscience* 31 (37) (2011) 13128–13136.
- [81] I.M. Sokolov, Models of anomalous diffusion in crowded environments, *Soft Matter* 8 (35) (2012) 9043–9052.
- [82] I. Stamova, Mittag-Leffler stability of impulsive differential equations of fractional order, *Quarterly of Applied Mathematics* 73 (3) (2015) 525–535.
- [83] I. Stamova, On the Lyapunov theory for functional differential equations of fractional order, *Proceedings of the American Mathematical Society* 144 (4) (2016) 1581–1593.
- [84] I. Stamova, G. Stamov, *Functional and Impulsive Differential Equations of Fractional Order: Qualitative Analysis and Applications*, CRC Press, 2017.
- [85] G. Stuart, N. Spruston, B. Sakmann, M. Häusser, Action potential initiation and backpropagation in neurons of the mammalian CNS, *Trends in Neurosciences* 20 (3) (1997) 125–131.

- [86] H. Sun, Y. Zhang, D. Baleanu, W. Chen, Y. Chen, A new collection of real world applications of fractional calculus in science and engineering, *Communications in Nonlinear Science and Numerical Simulation* 64 (2018) 213–231.
- [87] Y. Sun, A. Nern, R. Franconville, H. Dana, E.R. Schreiter, L.L. Looger, K. Svoboda, D.S. Kim, A.M. Hermundstad, V. Jayaraman, Neural signatures of dynamic stimulus selection in *Drosophila*, *Nature Neuroscience* 20 (8) (2017) 1104–1113.
- [88] V.E. Tarasov, Generalized memory: fractional calculus approach, *Fractal and Fractional* 2 (4) (2018) 23.
- [89] W. Tekka, T.M. Marinov, F. Santamaria, Neuronal spike timing adaptation described with a fractional leaky integrate-and-fire model, *PLoS Computational Biology* 10 (3) (2014) e1003526.
- [90] W. Tekka, D. Stockton, F. Santamaria, Power-law dynamics of membrane conductances increase spiking diversity in a Hodgkin–Huxley model, *PLoS Computational Biology* 12 (3) (2016) e1004776.
- [91] W. Tekka, R.K. Upadhyay, A. Mondal, Spiking and bursting patterns of fractional-order Izhikevich model, *Communications in Nonlinear Science and Numerical Simulation* 56 (2018) 161–176.
- [92] S. Temporal, M. Desai, O. Khorkova, G. Varghese, A. Dai, D.J. Schulz, J. Golowasch, Neuromodulation independently determines correlated channel expression and conductance levels in motor neurons of the stomatogastric ganglion, *Journal of Neurophysiology* 107 (2) (2012) 718–727.
- [93] N. Ulanovsky, L. Las, D. Farkas, I. Nelken, Multiple time scales of adaptation in auditory cortex neurons, *The Journal of Neuroscience* 24 (46) (2004) 10440–10453.
- [94] A. Vinograd, Y. Livneh, A. Mizrahi, History-dependent odor processing in the mouse olfactory bulb, *The Journal of Neuroscience* 37 (2017) 12018–12030.
- [95] B. Wark, A. Fairhall, F. Rieke, Timescales of inference in visual adaptation, *Neuron* 61 (5) (2009) 750–761.
- [96] B. Wark, B.N. Lundstrom, A. Fairhall, Sensory adaptation, *Current Opinion in Neurobiology* 17 (4) (2007) 423–429.
- [97] Y. Wei, Y. Chen, S. Cheng, Y. Wang, A note on short memory principle of fractional calculus, *Fractional Calculus and Applied Analysis* 20 (6) (2017) 1382.
- [98] S.H. Weinberg, F. Santamaria, History dependent neuronal activity modeled with fractional order dynamics, *Computational Models of Brain and Behavior* (2017) 531–548.
- [99] B.J. West, Fractal physiology and the fractional calculus: a perspective, *Frontiers in Physiology* 1 (2010) 12.
- [100] F. Xiao, J. Hrabec, S. Hrabetova, Anomalous extracellular diffusion in rat cerebellum, *Biophysical Journal* 108 (9) (2015) 2384–2395.
- [101] W. Yamada, Multiple channels and calcium dynamics, in: C. Koch, I. Segev (Eds.), *Methods in Neuronal Modeling*, MIT Press, New York, 1989.
- [102] B. Yang, T. Yu, H. Shu, D. Zhu, N. An, Y. Sang, L. Jiang, Perturbation observer based fractional-order sliding-mode controller for MPPT of grid-connected PV inverters: design and real-time implementation, *Control Engineering Practice* 79 (2018) 105–125.
- [103] K. Zarei-nia, N. Sepehri, Lyapunov stable displacement-mode haptic manipulation of hydraulic actuators: theory and experiment, *International Journal of Control* 85 (9) (2012) 1313–1326.
- [104] Y. Zhang, D. Bucher, F. Nadim, Ionic mechanisms underlying history-dependence of conduction delay in an unmyelinated axon, *eLife* 6 (2017) e25382.
- [105] A. Zhigalov, G. Arnulfo, L. Nobili, S. Palva, J.M. Palva, Relationship of fast- and slow-timescale neuronal dynamics in human MEG and SEEG, *The Journal of Neuroscience* 35 (13) (2015) 5385–5396.

Modeling woody plant tissue using different fractional-order circuits

Menna Mohsen^a, Mohamed S. Ghoneim^a, Lobna A. Said^a,
Ahmed S. Elwakil^{a,b,c}, Ahmed H. Madian^{a,d}, and Ahmed G. Radwan^{e,f}

^aNanoelectronics Integrated Systems Center (NISC), Nile University, Giza, Egypt

^bDepartment of Electrical and Computer Engineering, University of Sharjah, Sharjah, United Arab Emirates

^cDepartment of Electrical and Computer Engineering, University of Calgary, Calgary, AB, Canada

^dRadiation Engineering Dept., NCRRT, Egyptian Atomic Energy, Cairo, Egypt

^eEngineering Mathematics and Physics Department, Cairo University, Giza, Egypt

^fSchool of Engineering and Applied Sciences, Nile University, Giza, Egypt

ChapterPoints

- This chapter discusses the concept of bio-impedance measurements and the woody plant stem structure.
- A comparison between the traditional bio-impedance models used for woody plants and a modified model is provided.
- The employed bio-impedance models parameters are extracted to find the best characterizing model.

16.1. Introduction

Bio-electrics is the study of the electrical properties and behaviors of biological tissues [1]. Our focus here is on plant tissues with different functions depending on their location in the leaf, stem, or root [2,3], and particularly on woody tissue, which is composed of two main cell types: the xylem and the phloem. Xylem cells are responsible for one-directional transportation, forming long chains of small interconnected tubes to transport water and nutrients to the leaves. Phloem cells are responsible for two-directional transportation, transporting sugar and food [4].

Bio-impedance is the produced electrical impedance spectra (magnitude and phase) of biological cells under sufficiently small AC signal (voltage or current) stimulus, as shown in Fig. 16.1(a). Two-electrode, three-electrode, or four-electrode configurations can be used to measure bio-impedance, which changes significantly based on the tissue morphology, extra- and

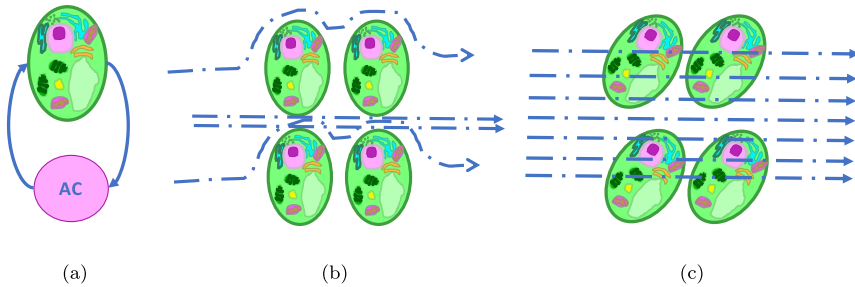


Figure 16.1 Current path inside a tissue due to (a) an AC signal applied over tissue (b) at low frequencies and (c) at high frequencies.

intracellular resistance, shape, type, structure, location, health status, and chemical composition [1]. When excited by a voltage signal, the current paths through the tissue differ depending on the applied frequency [5–7]. At low frequencies, current passes mainly through the extracellular space around the cells, as shown in Fig. 16.1(b), while at higher frequencies, the impedance of the cell becomes lower due to its capacitive nature, and hence the current flows everywhere according to local ionic conductivity, as depicted in Fig. 16.1(c). Thus, it is important to cover a wide range of frequencies when measuring bio-impedance with a sufficient number of points in this range. This task is usually conducted using an electro-chemical station, as shown in Fig. 16.2. Bio-impedance measurements contribute greatly to the study of plant responses to certain conditions such as fruit ripening [8], the analysis of fruits under heating conditions [9], and maturity assessment of fruit [10]. It is also used in many medical applications such as blood storage [11], noninvasive health monitoring [12], and disease determination [13]. Also, bio-impedance measurements are conducted to estimate the quality of wood, such as its chemical structure, which has a significant effect on the development of mold on the wood [14]. The interaction between mold development and wood characteristics is used as the main factor in evaluating the effect of wood quality on its robustness against mold and decay. Wood characteristics under mold growth were investigated using bio-impedance measurements in [15].

Fractional calculus is the study of integrals and derivatives of noninteger order, where the ordinary integer calculus is a limited set of fractional calculus. Fractional-order modeling has many benefits, including the added degree of freedom and the memory dependency in the fractional derivative definition, which increase the flexibility and controllability of any de-



Figure 16.2 Impedance measurement of *Schefflera Arboricola* using a Biologic SP150 station.

sign [16,17]. Fractional-order derivatives are nonlocal operators containing memory traces. This means that the present response of a system modeled with such derivatives is a result of all past excitations up mostly until the characteristic time constant of the system which is important to the understanding of many applications. Recently, fractional calculus has become the pioneer in many fields such as bio-engineering [18,19], chemistry [20], chaotic systems [21–23], filters [24,25], physics [26], mechanics [27,28], robotics [29], encryption [30,31], control systems [32], finance [33], wireless power transmission [34], viscoelasticity [35], oscillators [16,36], and supercapacitor modeling [37].

Several definitions were introduced in the literature for fractional-order differentiation; the most famous definition, preferably employed in analog designs, is the Caputo derivative [38] defined as follows:

$${}^C_a D_t^\alpha f(t) = \frac{1}{\Gamma(m-\alpha)} \int_a^t (t-\tau)^{(m-\alpha-1)} f^{(m)}(\tau) d\tau, \quad (16.1)$$

where $m-1 < \alpha \leq m$, $m \in \mathbb{N}$. By setting $a=0$, the Laplacian transform of Eq. (16.1) is given by [38]

$$\mathcal{L}[{}_0^C D_t^\alpha f(t)] = s^\alpha F(s) - \sum_{K=0}^{m-1} s^{\alpha-K-1} D^K f(0). \quad (16.2)$$

At zero initial condition the definition reduces to [39]

$$\mathcal{L}[{}_0^C D_t^\alpha f(t)] = s^\alpha F(s). \quad (16.3)$$

Using these extra degrees of freedom from the fractional order, it is possible to define a general fractance device [39]. A special case of fractance devices is the constant phase element (CPE), whose impedance is represented by

$$Z_{CPE} = 1/(s^\alpha C), \quad (16.4)$$

where C is a pseudocapacitance value and α is the fractional order, typically in the range of $(0 < \alpha < 1)$. This continuous range of the fractional order enables capturing the self-similar fractal-like structure of biological tissues, which translates into an equivalent infinite self-similar resistor-capacitor impedance network.

Various bio-impedance circuits were introduced in the literature to model the electrical properties of plant tissues [18]. The single dispersion Cole-impedance model is the first representation for the bio-impedance introduced by the Cole brothers in 1940 [40]. It became a popular model to represent biological tissues because of its simplicity in fitting with actual data. The double dispersion Cole-impedance model is a second generation of the single dispersion Cole-impedance model, which was used for a wide range of frequencies [2]. In 1969, the Hayden model was introduced in [41], which consists of a resistance representation of the extracellular resistance, the intercellular resistance, the plasma membrane resistance, and a capacitance representation of the plasma membrane capacitance. However, the model showed some defects between the theoretical impedance and the measured one, as it is more generic to mimic the plant tissues precisely because of the negligence of the vacuole representation in the tissue [1]. The double-shell model was introduced in 1990 to overcome the Hayden model's defects, as it took into consideration the vacuole representation in the tissue [5–7]. However, the model showed many defects in fitting data at low frequencies [2]. A more detailed model was also introduced in [42] where two resistances were added, representing the plasma membrane and tonoplast resistances. It was more complicated than the original double-shell model, and it did not improve the accuracy of curve fitting, so it was not used practically. In [1], the Hayden and double-shell models were

generalized into the fractional-order forms to get a better fitting for the measured data.

In [43–45], bio-impedance models were used for human skin measurements, while in [46] and [47] they were used for diagnosis of aging and to measure the pressure on the human skin, receptively. Also, bio-impedance was used on mouse muscles [48,49], on rat brains [50], and for testing the effect of the chilling process on pork loins [51]. In agriculture, it was used for monitoring fruits during pre- and postharvest [52–54] and for quantifying the physical changes in fruits during freezing and heating processes [9,55,56]. Bio-impedance was also used for environmental purposes [57–60].

There are two types of measuring bio-impedance: direct and indirect methods. Direct methods use portable/bench devices such as Livium, PalmSense3, SP150, and PSM3750 Newton4th. The indirect methods depend on embedding the tested tissue inside an analog circuit and then post-processing through an optimization technique to extract the bio-impedance model parameters. From the perspective of the indirect method, step response measurements were used to extract the Cole-impedance model parameters for fruit samples in [61]. In [19], a new technique is used by embedding the sample in an oscillator circuit to estimate its parameters using two measurements. A Kramers–Kronig transform was used in [62] to estimate the phase while measuring only the magnitude response. Then the measured magnitude and the estimated phase are used to extract the model parameters [62]. In [63–65], magnitude-only response measurements were used to identify the model parameters.

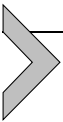
A common woody house plant, *Schefflera Arboricola*, is used in this work (See Fig. 16.2) [66]. It is a member of the flowering woody plants in the Araliaceae family, which can grow very tall and is widely used in medicinal herbal products [67] since it contains fumaric gamma-hydroxybutyric acids [68,69]. It has also been used in liver meridian disease medicine [70] since it enhances blood circulation, relieves pain, and stops bleeding [71]. It has also been used recently to treat rheumatoid arthritis, numbness in the limbs, abdominal pain, headaches, arthralgia, and swollen throat [72]. Also, *S. Arboricola* can be grounded into a paste to treat injuries and stop bleeding [71].

Plant wood is a complex tissue where several studies proposed suitable circuit models to properly fit its measured impedance values, such as in [73], where the fractional-order double-shell model was used. The Cole-impedance model was used in modeling the wood tissue in [74] as well as

a modified version in [75]. Other studies modeled wood by using different approximations for the CPE [76].

This chapter proposes a modified model for wood tissue and compares it with the fractional-order double-shell model, triple dispersion Cole-impedance model, and the model introduced in [75]. In particular, we employ a triple Cole impedance model, chosen to increase the degrees of freedom to improve the fitting accuracy. The modified model was inspired by double-shell model, which offers the best fitting of the measured data using the optimizer Z_{fit} of the impedance analyzer SP150. The models are tested experimentally on *S. Arboricola* plant sample using SP150.

This chapter is organized as follows. Section 16.2 describes the wood cell structure's characteristics. Section 16.3 shows an overview of the employed bio-impedance circuit models. Section 16.4 discusses the experimental setup, presents the results, and provides a discussion. Section 16.5 concludes the chapter.



16.2. Woody cell structure

Woody plants are the source of essential products such as food, medicines, oils, lumber, and fuel. Trees modify their growth according to their environment, such as light intensity, wind, temperature, and soil fertility [77].

Woody plants have two different types of transportation cells, as shown in Fig. 16.3. Xylem (Fig. 16.3(a)) moves water and solutes from the roots to the leaves. Phloem (Fig. 16.3(b)) moves glucose made in the leaves by the photosynthesis process and amino acids to the rest of the plant [78].

The arrangement of the xylem and the phloem is different in the stem and the roots. The xylem and the phloem are found in groups called vascular bundles. The position of these bundles changes from one part of the plant to another. Both xylem and phloem are made of rows of cells that form a continuous tube running the whole length of the plant [79].

Xylem vessels, which act as hydraulic systems, are made of dead cells impermeable to water. The walls contain woody materials, so xylem vessels are rigid, and the vascular bundles of the roots are in the center. The presence of the vascular bundles of the roots in the center helps the plant protect itself and adds more stability to it, as it is hard to pull out. In the stem, the vascular bundles are near the edge to give the stem strength and prevent it from bending [78,79].

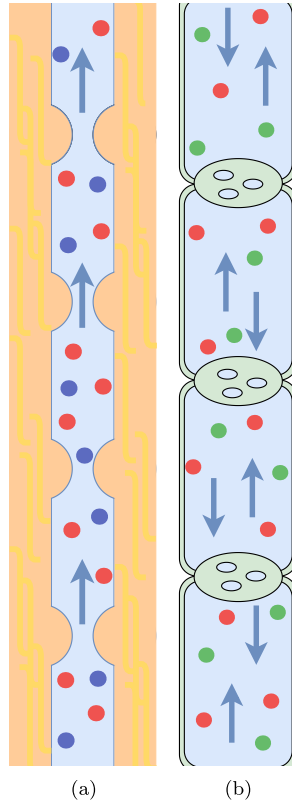
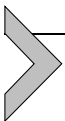


Figure 16.3 Woody transportation in (a) xylem and (b) phloem cells.

Phloem vessels are made of living cells. These cells are called sieve cells, forming sieve elements connected by sieve plates (small pores). They are responsible for transporting sucrose and amino acids up and down the plant, depending on where they are needed [77,79].



16.3. Bio-impedance models overview

Four different circuit models for wood tissue are shown in Fig. 16.4. The fractional wood model (FWM) is depicted in Fig. 16.4(a), the double-shell model is shown in Fig. 16.4(b), and Fig. 16.4(c) shows the triple dispersion Cole-impedance model. Finally, a modified wood model is proposed in Fig. 16.4(d).

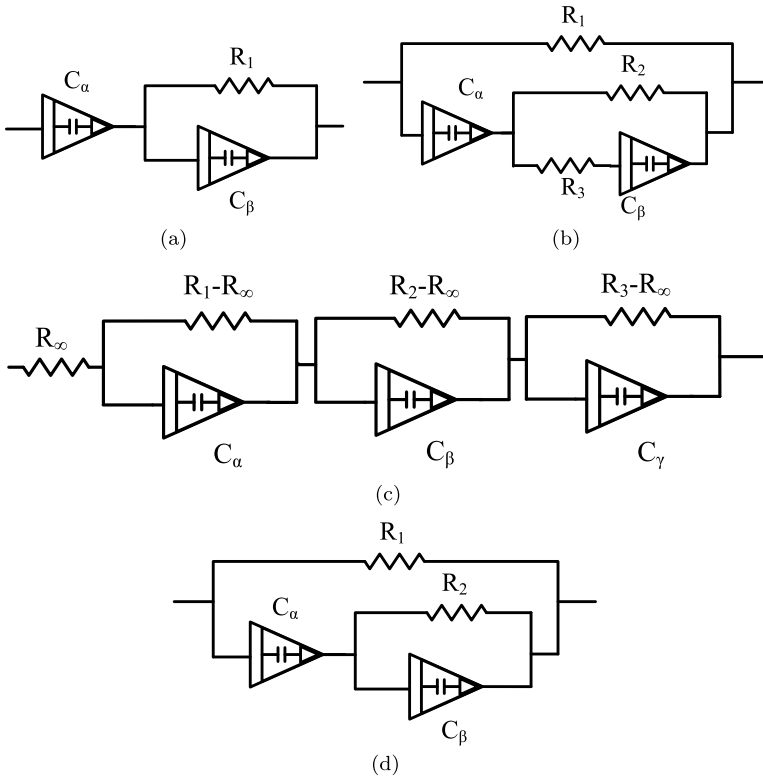


Figure 16.4 Most common bio-impedance models used for plant tissue modeling. (a) Fractional wood impedance circuit [75]. (b) Double-shell model [7]. (c) Triple dispersion Cole-impedance circuit. (d) Modified wood model impedance circuit.

An integer-order circuit model for wood tissue was introduced in [75], which consists of an RC ladder. However, It was large and did not provide the best fitting results. A fractional-order model (FWM) was introduced in [75], to reduce the number of elements in the RC ladder-equivalent network. The components of the circuit shown in Fig. 16.4(a) have an equivalent impedance given by

$$Z_{FWM} = \frac{1}{s^\alpha C_\alpha} + \frac{R_1}{1 + s^\beta R_1 C_\beta}. \tag{16.5}$$

The fractional-order double-shell model presented in Fig. 16.4(b) was used to characterize the plant tissues and was also used to characterize the

wood tissue in [5–7]. The impedance can be written as follows:

$$Z_{FDS} = \frac{R_1(R_2 + \frac{R_3}{1+s^\alpha C_\alpha R_3})}{R_1 + (R_2 + \frac{R_3}{1+s^\alpha C_\alpha R_3})}. \quad (16.6)$$

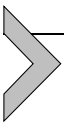
The double dispersion Cole-impedance model is the extended version of the single dispersion Cole-impedance model to describe the impedance for more complex material over a wide range of frequencies. The triple Cole-impedance model (TCM) shown in Fig. 16.4(c) is the third extension, and the equivalent impedance is written as follows:

$$Z_{TCM} = R_\infty + \frac{(R_1 - R_\infty)}{1 + s^\alpha R_1 C_\alpha} + \frac{(R_2 - R_\infty)}{1 + s^\beta R_2 C_\beta} + \frac{(R_3 - R_\infty)}{1 + s^\gamma R_3 C_\gamma}. \quad (16.7)$$

Finally, a modified wood model (NM) is proposed in Fig. 16.4(d). The modification is the addition of the parallel resistor R_1 to the wood model shown in Fig. 16.4(a). The equivalent impedance of this model is

$$Z_{NW} = \frac{R_1 Z_1}{R_1 + Z_1}, \quad (16.8a)$$

$$Z_1 = \frac{1}{s^\alpha C_\alpha} + \frac{R_2}{1 + s^\beta R_2 C_\beta}. \quad (16.8b)$$



16.4. Experimental setup

The woody plant *S. Arboricola*, from the Araliaceae family, which is widely used in medicinal herbal products, was selected. The woody stem of *S. Arboricola* was first measured using the SP150 impedance analyzer module, as shown in Fig. 16.2, where the plant is 1 m above the floor. Two crocodile electrodes were used for measuring the woody stem of the plant, where the length of the stem is about 10 cm and the diameter is about 11 mm. The interelectrode distance was first set to 8 cm and subsequently changed to 3 cm, 5 cm, and 8 cm, as shown in Fig. 16.5.

The measured impedance data were fitted to the four mentioned circuit models using the optimizer Z_{fit} of the impedance analyzer SP150. The results were then recorded to be compared, as shown in Table 16.1.



Figure 16.5 Experimental setup for three different interelectrode positions. (a) Position 1. (b) Position 2. (c) Position 3.

16.4.1 Results and discussion

The results for each interelectrode position using each of the models are given in Table 16.1, where the first position is 3 cm, the second is 5 cm, and the third is 8 cm. The impedance Nyquist plots for all used models at each position are shown in Fig. 16.6. As shown in Fig. 16.7, the fractional-order double-shell model has the highest percentage of error in all positions as it moves between 31% and 49%. The highest percentage of error is the result of the nonreasonable parameter values reported in Table 16.1. For example, in position 1, the value of R_2 is equal to 0.537 n Ω (which is nearly zero), while for position 2, C_β is 0.25e-21 F, which means that it is an open circuit. R_2 is very high as it also mimics an open circuit, and R_3 is zero, which means a short circuit. This means that the double-shell model failed to fit.

The FWM has reasonable parameters for all three positions, but the percentage error is still high: they are 15%, 35%, and 11% for positions 1, 2, and 3, respectively. The percentage error for the most significant position (position 3) is the least. Meanwhile, this model could fit well for high impedances only. However, the percentage error for position 3 is still high.

The triple Cole-impedance model has a smaller percentage error compared with the previous two models, as shown in Fig. 16.7, where the highest error values are 4.55%, 11%, and 5.4% for positions 1, 2, and 3, respectively. However, the parameter values are unreasonable, and the model has the highest number of elements. This means that this model's higher

Table 16.1 Fractional wood model parameters.

Model	Parameter	Position		
		Position 1	Position 2	Position 3
FDS	α	0.5172	0.4840	0.4823
	C_α	1.272 μF	0.128 μF	1.42 nF
	β	0.5584	0.6812	0.5788
	C_β	93.61 nF	0.206e-21 F	33.15 μF
	R_1	273.016 k Ω	247.958 k Ω	1444 k Ω
	R_2	0.557 n Ω	0.17e309 Ω	1.529 k Ω
	R_3	52.108 k Ω	0 Ω	183.396 k Ω
FWM	α	0.3802	0.3021	0.6206
	C_α	3.827 μF	4.45 μF	15.5 nF
	β	0.5796	0.6213	0.2743
	C_β	84.5 nF	26.7 nF	2.27 μF
	R_1	40.178 k Ω	108.7 k Ω	101.58 k Ω
TCM	R_∞	9.827 f Ω	27.16 f Ω	4.2e-114 Ω
	α	0.5074	0.4722	0.4186
	C_α	1.878 μF	1.988 μF	1.839 μF
	$(R_1 - R_\infty)$	235.871 k Ω	490 k Ω	1.6 M Ω
	β	3.491 μ	0.53884 μ	0
	C_β	18300 GF	30 nF	7.68e-192 F
	$(R_2 - R_\infty)$	12.093 k Ω	112.5 k Ω	124 m Ω
	γ	0.5596	0.9252	0.5934
	C_γ	18.5 nF	0.121 pF	27 nF
	$(R_3 - R_\infty)$	44.134 k Ω	5.39e-12 Ω	141.67 k Ω
NM	α	0.5172	0.4784	0.4228
	C_α	1.27 μF	1.293 μF	1.55 μF
	β	0.5584	0.5819	0.5940
	C_β	93.61 nF	31.91 nF	27.59 nF
	R_1	273.016 k Ω	597.275 k Ω	177 k Ω
	R_2	52.108 k Ω	137.826 k Ω	154.446 k Ω

number of degrees of freedom is not enough to give reasonable parameters. For example, the value of R_1 in all positions is very low, which means it is a short circuit all the time. Also, the dispersion coefficient β is nearly zero, which acts as an open circuit. That means the triple dispersion Cole-impedance model is not the optimum circuit model to represent the wood structure.

Finally, the modified wood model results shown in Table 16.1 have reasonable values, whereby increasing the interelectrode distance increases R_2 ,

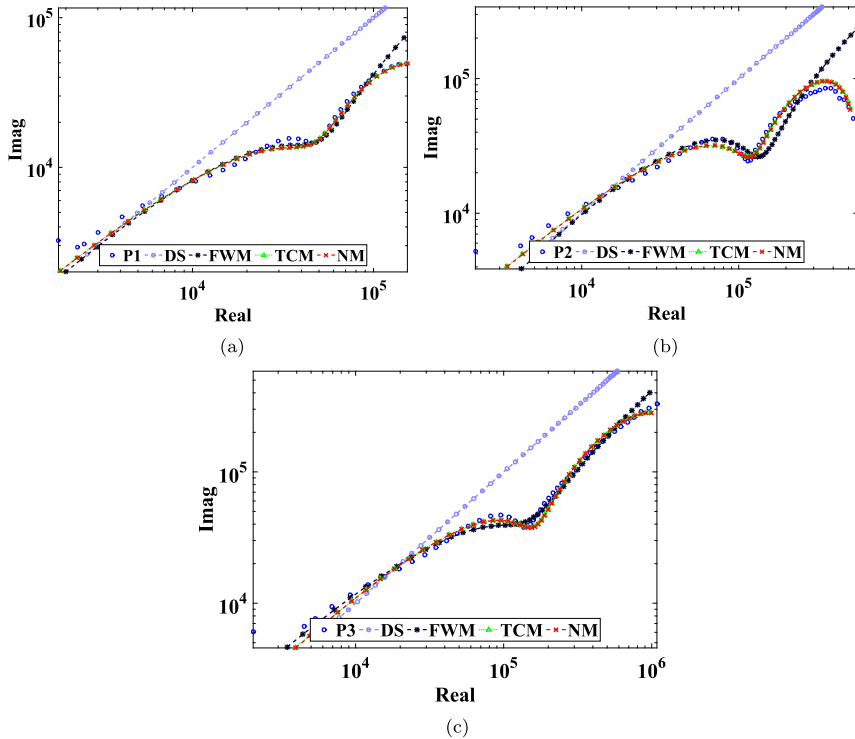
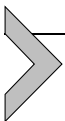


Figure 16.6 Experimental Nyquist plots and fittings for the three interelectrode positions using all models. (a) Position 1. (b) Position 2. (c) Position 3.

decreases C_β , and increases C_α . This model has the smallest percentage errors, as shown in Fig. 16.7, which are 4.55%, 11%, and 5.4% for positions 1, 2, and 3, respectively. That proves the modified wood model is the best circuit model to represent the wood structure.



16.5. Conclusion

This chapter surveyed the most suitable bio-impedance models for wood tissue. A modified model was introduced and compared to three different models (double-shell, modified triple dispersion Cole model, and traditional wood model). The modified circuit model showed the smallest percentage of fitting error when compared to the measured data. Three different electrode positions were tested, where the modified wood model

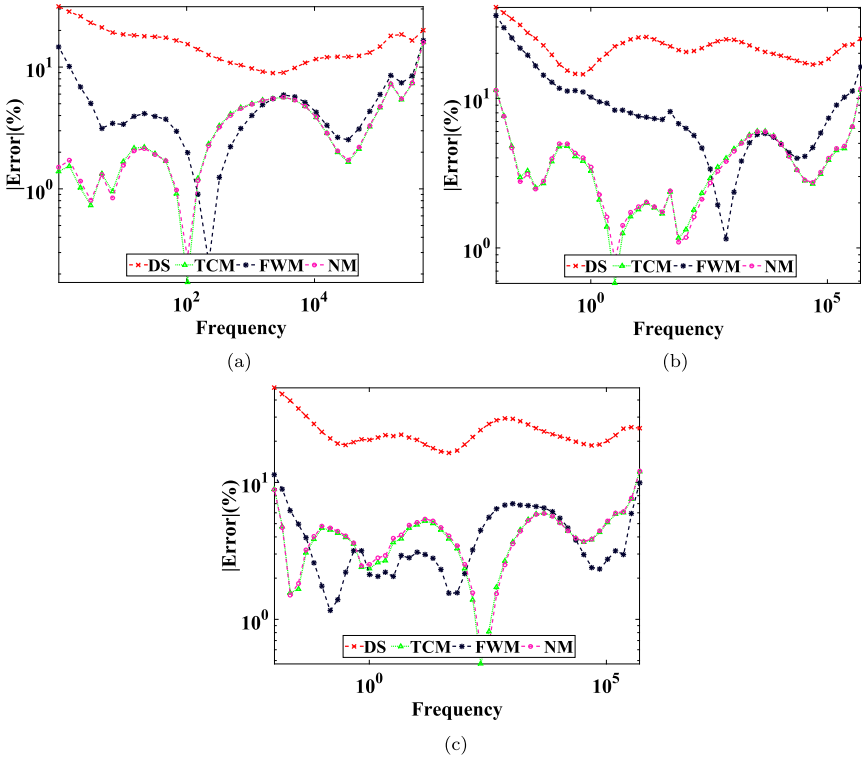


Figure 16.7 Percentage error for the three positions in all models. (a) Position 1. (b) Position 2. (c) Position 3.

managed to fit well over the different positions with the smallest percentage error. Other optimizations could be used in future studies such as metaheuristic optimizations and different woody plant types, giving better accuracy and a lower fitting error, overcoming some models' limitations. (See Table 16.2.)

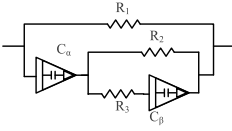
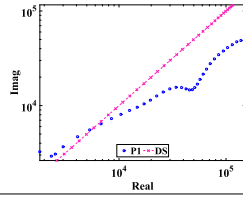
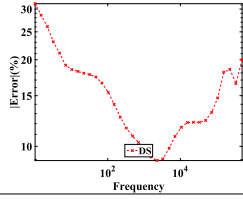
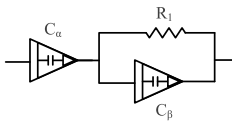
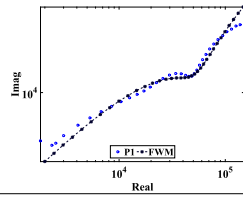
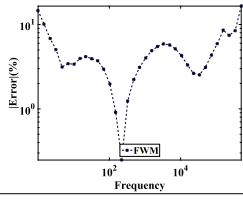
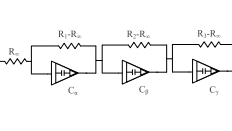
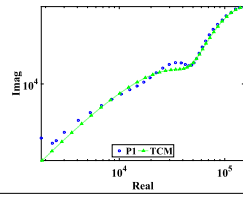
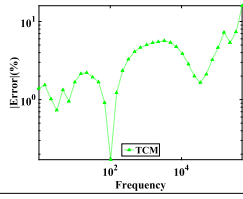
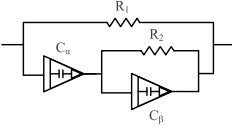
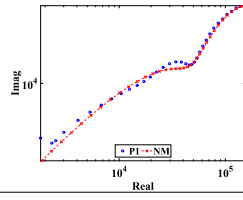
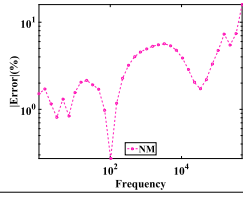
Acknowledgment

This chapter is based upon work supported by the Egyptian Academy of Science, Research, and Technology (ASRT) under a grant of JESOR project #5280.

References

- [1] A. AboBakr, L.A. Said, A.H. Madian, A.S. Elwakil, A.G. Radwan, Experimental comparison of integer/fractional-order electrical models of plant, *AEÜ. International Journal of Electronics and Communications* 80 (2017) 1–9.

Table 16.2 Wood models and their accuracy.

	Wood model	Nyquist plot	Error plot (%)
FDS			
FWM			
TCM			
NM			

- [2] D. Yousri, A.M. AbdelAty, L.A. Said, A. AboBakr, A.G. Radwan, Biological inspired optimization algorithms for Cole-impedance parameters identification, *AEÜ. International Journal of Electronics and Communications* 78 (2017) 79–89.
- [3] T.K. Bera, S. Bera, K. Kar, S. Mondal, Studying the variations of complex electrical bio-impedance of plant tissues during boiling, *Procedia Technology* 23 (2016) 248–255.
- [4] J.A. Romberger, Z. Hejnowicz, J.F. Hill, et al., *Plant Structure: Function and Development. A Treatise on Anatomy and Vegetative Development With Special Reference to Woody Plants*, Springer-Verlag GmbH & Co. KG, 1993.
- [5] M. Zhang, D. Stout, J. Willison, Electrical impedance analysis in plant tissues3, *Journal of Experimental Botany* 41 (3) (1990) 371–380.
- [6] M. Zhang, J. Willison, Electrical impedance analysis in plant tissues11, *Journal of Experimental Botany* 42 (11) (1991) 1465–1475.
- [7] M. Zhang, J. Willison, Electrical impedance analysis in plant tissues: the effect of freeze-thaw injury on the electrical properties of potato tuber and carrot root tissues, *Canadian Journal of Plant Science* 72 (2) (1992) 545–553.

- [8] F.R. Harker, S.K. Forbes, Ripening and development of chilling injury in persimmon fruit: an electrical impedance study, *New Zealand Journal of Crop and Horticultural Science* 25 (2) (1997) 149–157.
- [9] B.M. Aboalnaga, L.A. Said, A.H. Madian, A.S. Elwakil, A.G. Radwan, Cole bio-impedance model variations in *Daucus Carota Sativus* under heating and freezing conditions, *IEEE Access* 7 (2019) 113254–113263.
- [10] J. Li, Y. Xu, W. Zhu, X. Wei, H. Sun, Maturity assessment of tomato fruit based on electrical impedance spectroscopy, *International Journal of Agricultural and Biological Engineering* 12 (4) (2019) 154–161.
- [11] Y. Ülgen, S. Mana, Storage effects on whole blood: physiological and electrical measurements, in: *13th International Conference on Electrical Bioimpedance and the 8th Conference on Electrical Impedance Tomography*, Springer, 2007, pp. 66–69.
- [12] T.K. Bera, Bioelectrical impedance methods for noninvasive health monitoring: a review, *Journal of Biomedical Engineering* 2014 (2014) 381251.
- [13] F. Lopot, B. Nejedlý, H. Novotna, M. Mackova, S. Sulkova, Age-related extracellular to total body water volume ratio (ECV/TBW) – can it be used for “dry weight” determination in dialysis patients? Application of multifrequency bioimpedance measurement, *The International Journal of Artificial Organs* 25 (8) (2002) 762–769.
- [14] O. Theander, J. Bjurman, J. Boutelje, Increase in the content of low-molecular carbohydrates at lumber surfaces during drying and correlations with nitrogen content, yellowing and mould growth, *Wood Science and Technology* 27 (5) (1993) 381–389.
- [15] M. Tiitta, L. Tomppo, H. Järnström, M. Löjja, T. Laakso, A. Harju, M. Venäläinen, H. Iitti, L. Paajanen, P. Saranpää, et al., Spectral and chemical analyses of mould development on Scots pine heartwood, *European Journal of Wood and Wood Products* 67 (2) (2009) 151–158.
- [16] O. Elwy, L.A. Said, A.H. Madian, A.G. Radwan, All possible topologies of the fractional-order Wien oscillator family using different approximation techniques, *Circuits, Systems, and Signal Processing* 38 (9) (2019) 3931–3951.
- [17] A.M. AbdelAty, D. Yousri, L.A. Said, A.G. Radwan, Identifying the parameters of Cole impedance model using magnitude only and complex impedance measurements: a metaheuristic optimization approach, *Arabian Journal for Science and Engineering* 45 (8) (2020) 6541–6558.
- [18] T.J. Freeborn, A survey of fractional-order circuit models for biology and biomedicine, *IEEE Journal on Emerging and Selected Topics in Circuits and Systems* 3 (3) (2013) 416–424.
- [19] M. Mohsen, L.A. Said, A.S. Elwakil, A.H. Madian, A.G. Radwan, Extracting optimized bio-impedance model parameters using different topologies of oscillators, *IEEE Sensors Journal* 20 (2020) 9947–9954.
- [20] A.B. Malinowska, T. Odziejewicz, D.F. Torres, *Advanced Methods in the Fractional Calculus of Variations*, Springer, 2015.
- [21] M.F. Tolba, A.H. Elsafty, M. Armanyos, L.A. Said, A.H. Madian, A.G. Radwan, Synchronization and FPGA realization of fractional-order Izhikevich neuron model, *Microelectronics Journal* 89 (2019) 56–69.
- [22] N.S. Soliman, M.F. Tolba, L.A. Said, A.H. Madian, A.G. Radwan, Fractional x-shape controllable multi-scroll attractor with parameter effect and FPGA automatic design tool software, *Chaos, Solitons and Fractals* 126 (2019) 292–307.
- [23] A.H. ElSafty, M.F. Tolba, L.A. Said, A.H. Madian, A.G. Radwan, A study of the non-linear dynamics of human behavior and its digital hardware implementation, *Journal of Advanced Research* 25 (2020) 111–123.
- [24] E.M. Hamed, L.A. Said, A.H. Madian, A.G. Radwan, On the approximations of CFOA-based fractional-order inverse filters, *Circuits, Systems, and Signal Processing* 39 (1) (2020) 2–29.

- [25] M. Ghoneim, R. Hesham, H. Yassin, A. Madian, α -order universal filter realization based on single input multi-output differential voltage current conveyor, *Analog Integrated Circuits and Signal Processing* 107 (2021) 411–422.
- [26] H. Rudolf, *Applications of Fractional Calculus in Physics*, World Scientific, 2000.
- [27] C.M. Pinto, A.R. Carvalho, New findings on the dynamics of HIV and TB coinfection models, *Applied Mathematics and Computation* 242 (2014) 36–46.
- [28] F. Jarad, S. Hari Krishnan, K. Shah, K. Kanagarajan, Existence and stability results to a class of fractional random implicit differential equations involving a generalized Hilfer fractional derivative, *Discrete and Continuous Dynamical Systems. Series S* (2019) 209–219.
- [29] A. Dumlu, K. Erenturk, Trajectory tracking control for a 3-DOF parallel manipulator using fractional-order control, *IEEE Transactions on Industrial Electronics* 61 (7) (2013) 3417–3426.
- [30] S.M. Ismail, L.A. Said, A.A. Rezk, A.G. Radwan, A.H. Madian, M.F. Abu-Elyazeed, A.M. Soliman, Generalized fractional logistic map encryption system based on FPGA, *AEÜ. International Journal of Electronics and Communications* 80 (2017) 114–126.
- [31] A.H. Elsafty, M.F. Tolba, L.A. Said, A.H. Madian, A.G. Radwan, Enhanced hardware implementation of a mixed-order nonlinear chaotic system and speech encryption application, *AEÜ. International Journal of Electronics and Communications* 125 (2020) 153347.
- [32] Z. Li, L. Liu, S. Dehghan, Y. Chen, D. Xue, A review and evaluation of numerical tools for fractional calculus and fractional order controls, *International Journal of Control* 90 (6) (2017) 1165–1181.
- [33] F. Mainardi, *Fractional Calculus and Waves in Linear Viscoelasticity: An Introduction to Mathematical Models*, World Scientific, 2010.
- [34] X. Shu, B. Zhang, The effect of fractional orders on the transmission power and efficiency of fractional-order wireless power transmission system, *Energies* 11 (7) (2018) 1774.
- [35] S. Majumdar, S. Hazra, M.D. Choudhury, S.D. Sinha, S. Das, T.R. Middy, S. Tarafdar, T. Dutta, A study of the rheological properties of visco-elastic materials using fractional calculus, *Colloids and Surfaces. A, Physicochemical and Engineering Aspects* 516 (2017) 181–189.
- [36] O. Elwy, A.M. AbdelAty, L.A. Said, A.H. Madian, A.G. Radwan, Two implementations of fractional-order relaxation oscillators, *Analog Integrated Circuits and Signal Processing* (2020) 1–12.
- [37] A.S. Elwakil, A. Allagui, T. Freeborn, B. Maundy, Further experimental evidence of the fractional-order energy equation in supercapacitors, *AEÜ. International Journal of Electronics and Communications* 78 (2017) 209–212.
- [38] A.A. Kilbas, H.M. Srivastava, J.J. Trujillo, *Theory and Applications of Fractional Differential Equations*, vol. 204, Elsevier, 2006.
- [39] M. Nakagawa, K. Sorimachi, Basic characteristics of a fractance device, *IEICE Transactions on Fundamentals of Electronics, Communications and Computer Sciences* 75 (12) (1992) 1814–1819.
- [40] K.S. Cole, Permeability and impermeability of cell membranes for ions, in: *Cold Spring Harbor Symposia on Quantitative Biology*, vol. 8, Cold Spring Harbor Laboratory Press, 1940, pp. 110–122.
- [41] R. Hayden, C. Moyses, F. Calder, D. Crawford, D. Fensom, Electrical impedance studies on potato and alfalfa tissue, *Journal of Experimental Botany* 20 (2) (1969) 177–200.
- [42] M. Chang, D. Stout, J. Willison, Electrical impedance analysis in plant tissues: symplasmic resistance and membrane capacitance in the Hayden model, *Journal of Experimental Botany* 41 (1990) 371–380.
- [43] D.J. Bora, R. Dasgupta, Various skin impedance models based on physiological stratification, *IET Systems Biology* 14 (3) (2020) 147–159.

- [44] Z.B. Vosika, G.M. Lazovic, G.N. Misevic, J.B. Simic-Krstic, Fractional calculus model of electrical impedance applied to human skin, *PLoS ONE* 8 (4) (2013) e59483.
- [45] B. Fu, T. Freeborn, Electrical equivalent network modeling of forearm tissue bioimpedance, in: 2019 SoutheastCon, IEEE, 2019, pp. 1–7.
- [46] J.B. Simić-Krstić, A.J. Kalauzi, S.N. Ribar, L.R. Matija, G.N. Misevic, Electrical properties of human skin as aging biomarkers, *Experimental Gerontology* 57 (2014) 163–167.
- [47] B. Taji, A.D. Chan, S. Shirmohammadi, Effect of pressure on skin-electrode impedance in wearable biomedical measurement devices, *IEEE Transactions on Instrumentation and Measurement* 67 (8) (2018) 1900–1912.
- [48] B. Sanchez, J. Li, T. Geisbush, R.B. Bardia, S.B. Rutkove, Impedance alterations in healthy and diseased mice during electrically induced muscle contraction, *IEEE Transactions on Biomedical Engineering* 63 (8) (2014) 1602–1612.
- [49] B. Sanchez, J. Li, S. Yim, A. Pacheck, J.J. Widrick, S.B. Rutkove, Evaluation of electrical impedance as a biomarker of myostatin inhibition in wild type and muscular dystrophy mice, *PLoS ONE* 10 (10) (2015) e0140521.
- [50] G. Kumar, U. Kasiviswanathan, S. Mukherjee, S.K. Mahto, N. Sharma, R. Patnaik, Changes in electrolyte concentrations alter the impedance during ischemia-reperfusion injury in rat brain, *Physiological Measurement* 40 (10) (2019) 105004.
- [51] Y. Leng, Y. Sun, X. Wang, J. Hou, X. Zhao, Y. Zhang, Electrical impedance estimation for pork tissues during chilled storage, *Meat Science* 161 (2020) 108014.
- [52] M.T. Mbezi, H.P.E. Fouda, C.B. Tabi, T.C. Kofané, et al., Estimated photosynthetic activity from its electrical impedance spectroscopy, *American Scientific Research Journal for Engineering, Technology, and Sciences (ASRJETS)* 13 (1) (2015) 178–193.
- [53] A. AboBakr, M. Mohsen, L.A. Said, A.H. Madian, A.S. Elwakil, A.G. Radwan, Banana ripening and corresponding variations in bio-impedance and glucose levels, in: 2019 Novel Intelligent and Leading Emerging Sciences Conference (NILES), vol. 1, IEEE, 2019, pp. 130–133.
- [54] P. Ibba, A. Falco, B.D. Abera, G. Cantarella, L. Petti, P. Lugli, Bio-impedance and circuit parameters: an analysis for tracking fruit ripening, *Postharvest Biology and Technology* 159 (2020) 110978.
- [55] T. Watanabe, Y. Ando, T. Orikasa, T. Shiina, K. Kohyama, Effect of short time heating on the mechanical fracture and electrical impedance properties of spinach (*Spinacia oleracea* L.), *Journal of Food Engineering* 194 (2017) 9–14.
- [56] T. Watanabe, Y. Ando, N. Nakamura, T. Orikasa, T. Shiina, M. Nagata, Electric and mechanical detection of changes in heated apple flesh, *Journal of Food Engineering* 261 (2019) 26–31.
- [57] D. Lei, C. Zhao, Y. Zhang, S. Liu, Experimental study on characteristics of water containing coal complex resistivity dispersion, *Journal of Loss Prevention in the Process Industries* 56 (2018) 328–333.
- [58] J. Li, D. Lei, C. Zhao, H. Meng, Complex resistivity dispersion characteristics of water-bearing coal based on Double Cole–Cole model, *Advances in Civil Engineering* 2019 (2019) 4913767.
- [59] H. de Souza, E.E. Sampaio, Apparent resistivity and spectral induced polarization in the submarine environment, *Anais Da Academia Brasileira de Ciências* 73 (3) (2001) 429–444.
- [60] M.H. Najar, K. Majid, Investigation of the transport properties of PPy/[Co(EDTA)NH₃Cl]·H₂O nanocomposite prepared by chemical oxidation method, *RSC Advances* 6 (30) (2016) 25449–25459.
- [61] T.J. Freeborn, B. Maundy, A.S. Elwakil, Cole impedance extractions from the step-response of a current excited fruit sample, *Computers and Electronics in Agriculture* 98 (2013) 100–108, <https://doi.org/10.1016/j.compag.2013.07.017>.

- [62] A. Al-Ali, A.S. Elwakil, B. Maundy, T.J. Freeborn, Extraction of phase information from magnitude-only bio-impedance measurements using a modified Kramers–Kronig transform, *Circuits, Systems, and Signal Processing* 37 (8) (2018) 3635–3650.
- [63] T.J. Freeborn, B. Maundy, A.S. Elwakil, Extracting the parameters of the double-dispersion Cole bioimpedance model from magnitude response measurements, *Medical & Biological Engineering & Computing* 52 (9) (2014) 749–758.
- [64] T.J. Freeborn, A.S. Elwakil, B. Maundy, Variability of Cole-model bioimpedance parameters using magnitude-only measurements of apples from a two-electrode configuration, *International Journal of Food Properties* 20 (sup1) (2017) S507–S519.
- [65] B.J. Maundy, A.S. Elwakil, A. Allagui, Extracting the parameters of the single-dispersion Cole bioimpedance model using a magnitude-only method, *Computers and Electronics in Agriculture* 119 (2015) 153–157.
- [66] E.F. Gilman, D.G. Watson, *Schefflera arboricola: Dwarf Schefflera*, EDIS Publication, 1993.
- [67] C. Ng, Z.J. Wang, J.J. Ni, Effects of plant morphology on root–soil hydraulic interactions of *Schefflera heptaphylla*, *Canadian Geotechnical Journal* 58 (5) (2021) 666–681.
- [68] Y. Wang, D. Liang, F.A. Khan, C.L. Zhang, Y.F. Liu, R.Y. Chen, M.I. Choudhary, D.Q. Yu, Chemical constituents from *Schefflera leucantha* R. Vig. (Araliaceae), *Biochemical Systematics and Ecology* 91 (2020) 104076.
- [69] M. Fathi, S. Sedaghatpour, S.K. Abbasnia, The variations of physiological and antioxidant properties in *Schefflera arboricola* cuttings over the rooting period, *Agriculturae Conspectus Scientificus* 85 (1) (2020) 79–85.
- [70] J. Zhou, G. Xie, X. Yan, *Encyclopedia of Traditional Chinese Medicines, Isolated Compounds AB*, vol. 1, Springer, 2011.
- [71] G. Xie, J. Zhou, X. Yan, *Encyclopedia of Traditional Chinese Medicines: Molecular Structures, Pharmacological Activities, Natural Sources and Applications*, vol. 2 DG, Springer-Verlag Berlin Heidelberg, 2011.
- [72] F. Li, Z. Cao, H. Wang, C. Li, J. Fu, J. Xie, B. Li, R. Chen, J. Kang, Inhibition of IL-6 expression by lignans and other constituents isolated from *Schefflera rubriflora* C.J. Tseng & G. Hoo, *Fitoterapia* 140 (2020) 104417.
- [73] T. Repo, M. Zhang, Modelling woody plant tissues using a distributed electrical circuit, *Journal of Experimental Botany* 44 (5) (1993) 977–982.
- [74] M. Zhang, T. Repo, J. Willison, S. Sutinen, Electrical impedance analysis in plant tissues: on the biological meaning of Cole–Cole α in Scots pine needles, *European Biophysics Journal* 24 (2) (1995) 99–106.
- [75] M. Tiitta, H. Olkkonen, Electrical impedance spectroscopy device for measurement of moisture gradients in wood, *Review of Scientific Instruments* 73 (8) (2002) 3093–3100.
- [76] S. Mahata, A. Ghosh, R. Kar, D. Mandal, S. Saha, Approximation of fractional order wood tissue impedance model using flower pollination algorithm, in: 2018 15th International Conference on Electrical Engineering/Electronics, Computer, Telecommunications and Information Technology (ECTI-CON), IEEE, 2018, pp. 664–667.
- [77] P. Kramer, *Physiology of Woody Plants*, Elsevier, 2012.
- [78] T. Hölttä, T. Vesala, S. Sevanto, M. Perämäki, E. Nikinmaa, Modeling xylem and phloem water flows in trees according to cohesion theory and Münch hypothesis, *Trees* 20 (1) (2006) 67–78.
- [79] T. Hölttä, M. Mencuccini, E. Nikinmaa, Linking phloem function to structure: analysis with a coupled xylem–phloem transport model, *Journal of Theoretical Biology* 259 (2) (2009) 325–337.

Analog and digital implementation of fractional-order FitzHugh–Nagumo (FO-FHN) neuron model

Mohammad Rafiq Dar^a, Nasir Ali Kant^a, Farooq Ahmad Khanday^a, Shakeel Ahmad Malik^b, and Mubashir Ahmad Kharadi^a

^aDepartment of Electronics and Instrumentation Technology, University of Kashmir, Srinagar, India

^bDepartment of Electronics and Communication Engineering, Islamic University of Science and Technology, Awantipora, India

17.1. Introduction

The momentous responsiveness of academic and industrial research and development (R&D) towards the investigation, enhancement, and implementation of neuron models is outstanding. A number of applications of artificial neural networks (ANNs) have been explored and spiking neural networks [2] like artificial intelligence (AI), deep learning (DL), and machine learning (ML) are results of such research. Consequently, numerous models and designs have been offered and realized for procurement of ANNs and/or SNNs to efficaciously impersonate the characteristics of the brain, like image and voice recognition, pattern classification, chat bots, attribute identification, memory, etc. However, in [44,45], it has been confirmed that electrical properties of some membranes are exactly governed by fractional-order differential equations (FODEs). It is worth to note that the fractional-order calculus (FOC) was an unexplored branch of mathematics and engineering because of its intrinsic complexity. The unexploredness of FOC [22] was due to the fact that it does not have completely satisfactory geometrical or physical interpretation [43,69]. The fractional-order derivative can be defined as “the derivative that has arbitrary order and order can be complex or real.” However, it characterizes more precisely some natural behavior associated with different areas of engineering, and now it is used as a promissory tool in bioengineering [46,60], viscoelas-

ticity [15,25], electronics [38,56], robotics [39,58], control theory [7,16], signal processing [53,66], etc. The fractional-order neural networks (FONNs) are also well suited for the development and investigation of other allied areas, as depicted in [14,57], and provide the added feature for governing dynamical system performance. In addition, the FO derivative is governed by preceding responses, i.e., FO systems have memory and as the fractional order approaches a minimum value, the dependency of the output on earlier states rises. In the recent past, a lot of effort has been made towards the development and investigation of FO complex dynamical behavior of the ANNs [4,8,19,21,31,34–36,42,64,65,72].

Due to the rapid advent of modern computer technology, the computing power has increased tremendously. However, despite the obvious advantages of the ANNs, like the ones discussed above, hardware design approached of ANNs have not advanced so much. The hardware design of ANNs is efficient due to intrinsic speed and an extremely parallel nature. During the recent past, there has been a tremendous growth in the hardware implementation of the neuron models and networks based on them [6,12,20,23,47,48,52,55,61,68,70].

The rudimentary component of ANNs is a “neuron.” Therefore, numerous mathematical models have been proposed [1,5,18,23,26–28,30,37,50,59,62,64]. One of the most important characteristic models that portrays a huge diversity of dynamics is the FitzHugh–Nagumo (FHN) model [29,30]. For conventional-order, i.e., integer-order, FHN neuron models, quite a few digital as well as analog (field programmable analog array [FPAA])-based realizations exist in the literature [9–11,24,32,40,52,70]. However, a more important version of the FHN model, i.e., the FO-FHN neuron model, is investigated and implemented in [3,4,41,49,67,71]. For analog realization of the neuron models, discrete or off-the-shelf components like resistors, capacitors, inductors, etc., are employed, which consume much power and are very bulky, which makes them unsuitable to fabricate large ANNs and unfit for the realization of complex ANNs. However, VLSI realization of complete FHN models employs transistors (bipolar junction transistors [BJTs], complementary metal oxide semiconductors [CMOS]), operational amplifiers (Op-Amps), and operational transconductor amplifiers (OTAs), consume low power, and are suitable to fabricate large ANNs. Another analog realization uses FPAA boards which consist of switched capacitor circuits for realizing the various models. For digital realization, i.e., field-programmable gate array (FPGA)-based design, there are

various FPGA boards available commercially that are used to realize various models.

In this chapter we demonstrate the realization of FO-FHN models in three ways: (i) using low-voltage low-power CMOS circuits in companding mode, i.e., using sinh-domain implementation, (ii) using FPAA boards, and (iii) using FPGA boards.



17.2. Fractional-order FitzHugh–Nagumo (FO-FHN) neuron model

In 1961 Richard FitzHugh developed a mathematical neuron model [68]. The FHN model is alternatively called the Bonhoeffer–van der Pol model. In the following year, J. Nagumo created the equivalent circuit of this model [51] and described a prototype of an excitable system. The FHN model is a superior version of the relaxation oscillator as it displays a specific excursion in phase space. The main characteristics of the FHN model are electrical impulses along nerve and cardiac fibers [23].

Having said that, fractional-order modeling will add to the dynamical characteristics of the neuron model in terms of the controllability and generation of frequency [4], memory, etc. It is due to the fact that the FO derivative accommodates and considers the historical responses in estimating the system response at any instant of time. Hence it adds to the advantages of memory. Further, the reliance on memory of the system can be meticulously handled through the FO derivative and the system will become highly dependent on the history as the order of the FO derivative approaches zero, and vice versa. The detailed account of the FO-FHN model is discussed in [36]. The FO-FHN model can be given as

$$\begin{aligned} \frac{d^{\alpha_1} x_1(t)}{dt^{\alpha_1}} &= x_1(t) - \frac{1}{c} x_1(t)^3 - x_2(t) + I(t), \\ a \frac{d^{\alpha_2} x_2(t)}{dt^{\alpha_2}} &= x_1(t) - b x_2(t) + d, \end{aligned} \quad (17.1)$$

where x_1 and x_2 are the membrane current and recovery variable current, respectively.

The state space representation of (17.1) can be written as

$$\begin{bmatrix} \frac{d^{\alpha_1} x_1(t)}{dt^{\alpha_1}} \\ \frac{d^{\alpha_2} x_2(t)}{dt^{\alpha_2}} \end{bmatrix} = \begin{bmatrix} g(x_1) & -1 \\ \frac{1}{a} & -\frac{b}{a} \end{bmatrix} \begin{bmatrix} x_1(t) \\ x_2(t) \end{bmatrix} + \begin{bmatrix} I(t) \\ \frac{d}{a} \end{bmatrix},$$

where $g(x_1) = \left(1 - \frac{x_1^2}{c}\right)$, $x_1(t)$ represents the sheath potential and recovery variable, $x_2(t)$ represents the activation of an outward current, $I(t)$ is the external current, and α_1 and α_2 are fractional orders. When $\alpha_1 = \alpha_2 = \alpha = 1$, the FO-FHN neuron model becomes the conventional integer-order model.

17.2.1 Dynamical analysis of FO-FHN neuron model

Let (x^*, γ^*) be the equipoise of the FO-FHN neuronal model given in (17.1). Dynamical characteristics of the FO-FHN neuronal model can be found using

$$\begin{aligned} \frac{d^{\alpha_1} x_1(t)}{dt^{\alpha_1}} &= x_1(t) \left(1 - \frac{1}{c} x_1(t)^2\right) - x_2(t), \\ \frac{d^{\alpha_2} x_2(t)}{dt^{\alpha_2}} &= \frac{x_1(t)}{a} - \frac{b x_2(t)}{a}. \end{aligned} \tag{17.2}$$

The eigenvalues of the Jacobian matrix are

$$\lambda_{1,2} = \frac{1 - x_1^{*2} \pm \sqrt{\left(x_1^{*2} + \frac{b}{a} - 1\right)^2 - \frac{4b}{a} \left(1 - b(1 - x_1^{*2})\right)}}{2}. \tag{17.3}$$

The stability of the equipoise is governed by:

Case 1: If $|\arg(\lambda_i)| > \frac{\alpha\pi}{2}$, then equipoise (x^*, γ^*) is stable.

Case 2: If $|\arg(\lambda_i)| < \frac{\alpha\pi}{2}$, then equipoise (x^*, γ^*) is unstable ($i = 1, 2$).

Using the parameters $a = 13$, $b = 0.8$, and $I = 0.37$, the equilibrium points of (17.1) will be $(-0.9339, -0.2924)$. Hence the corresponding eigenvalues of the linearized system given in (17.3) are $\lambda_{1,2} = 0.0331 \pm 0.2607i$ with $|\arg(\lambda_{1,2})| = 1.4445$ in radians. Letting $|\arg(\lambda_{1,2})| = \frac{\pi\alpha_{critical}}{2}$, we will get the critical value of the fractional order as 0.9196. Hence, we can have the following cases:

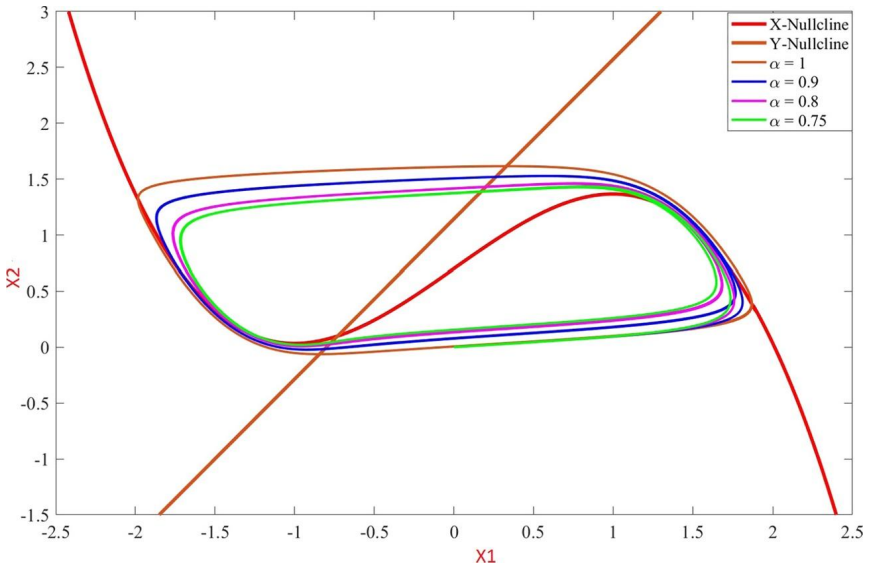


Figure 17.1 Nullcline diagram of the FO-FHN neuron model.

Case 1: If $\alpha > \alpha_{critical}$, the equilibrium point $(-0.9339, -0.2924)$ is unstable and hence the neuron is under periodic spiking.

Case 2: If $\alpha < \alpha_{critical}$, the equilibrium point $(-0.9339, -0.2924)$ is stable and hence the neuron is at quiescence.

The nullcline diagram of the FO-FHN neuron model is shown in Fig. 17.1, and the transient behavior of the FO-FHN neuron model is shown in Fig. 17.2.

17.2.2 Coupling of FO-FHN neuron model

The FO-FHN neuron model is coupled with other FO-FHN neuron models/units [29] by a coupling factor or coupling function. It is imperative to note here that the neural network produces different dynamics/behaviors depending on the coupling function used and coupling parameters varied. Depending on coupling, FO-FHN models will have applications like image synthesis, learning, etc. The kind of the coupling used here is called unidirectional coupling. It guarantees exponentially fast synchronization of neurons [13]. The coupling of neurons is given as

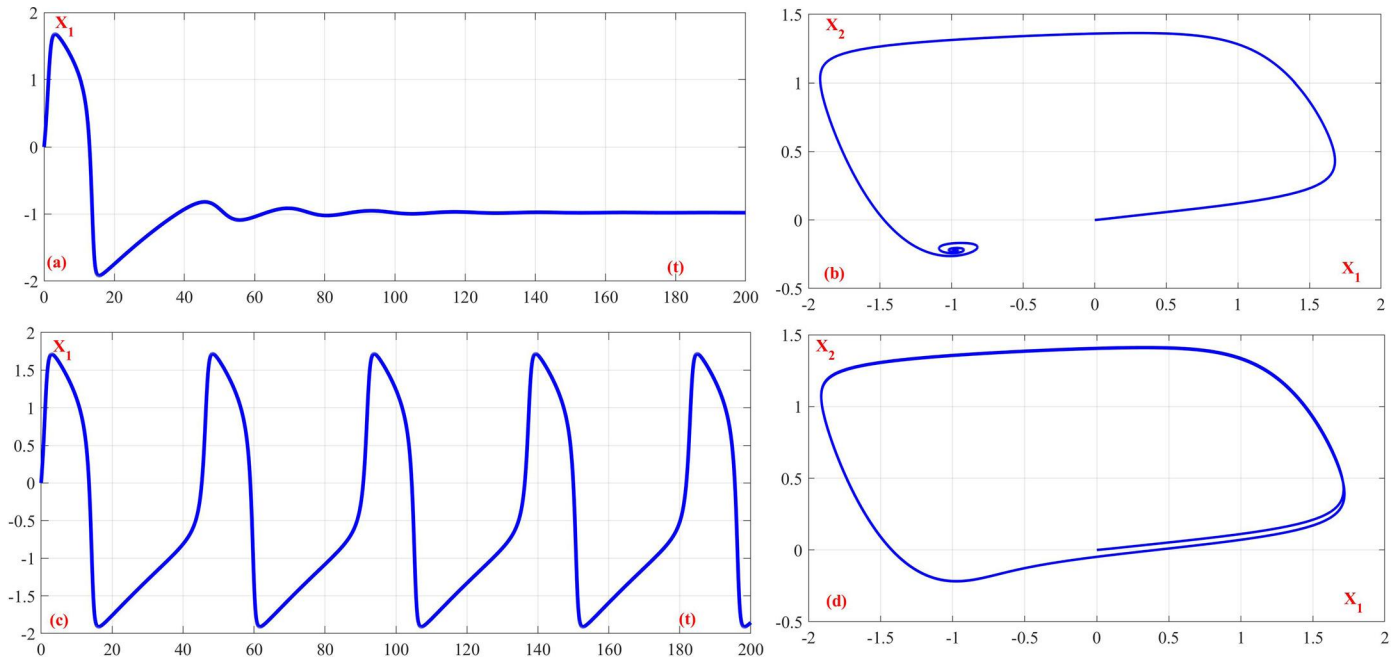
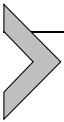


Figure 17.2 Transient response and phase portrait of the FO-FHN neuron model.

$$\begin{aligned}
\frac{d^\alpha x_{11}(t)}{dt^\alpha} &= x_{11}(t) - \frac{x_{11}^3}{c} - x_{21}(t) + I(t) + k(x_{12} - x_{11}), \\
a \frac{d^\alpha x_{21}(t)}{dt^\alpha} &= x_{11}(t) - bx_{21}(t) + d, \\
\frac{d^\alpha x_{12}(t)}{dt^\alpha} &= x_{12}(t) - \frac{x_{12}^3}{c} - x_{22}(t) + I(t) + k(x_{13} - x_{12}), \\
a \frac{d^\alpha x_{22}(t)}{dt^\alpha} &= x_{12}(t) - bx_{22}(t) + d, \\
\frac{d^\alpha x_{13}(t)}{dt^\alpha} &= x_{13}(t) - \frac{x_{13}^3}{c} - x_{23}(t) + I(t) + k(x_{14} - x_{13}), \\
a \frac{d^\alpha x_{23}(t)}{dt^\alpha} &= x_{13}(t) - bx_{23}(t) + d, \\
\frac{d^\alpha x_{14}(t)}{dt^\alpha} &= x_{14}(t) - \frac{x_{14}^3}{c} - x_{24}(t) + I(t) + k(x_{13} - x_{14}), \\
a \frac{d^\alpha x_{24}(t)}{dt^\alpha} &= x_{14}(t) - bx_{24}(t) + d.
\end{aligned} \tag{17.4}$$

Here k is the coupling coefficient and is changed to highlight the numerous dynamical behaviors of the ANNs. Having thus stated the FO-FHN neuron model, in the upcoming sections various types of implementations of the FO-FHN neuron model will be discussed.



17.3. Analog implementations of the FO-FHN neuron model

In the analog domain, the FO-FHN model, like any other circuit, can be realized by employing the conventional discrete off-the-shelf components (i.e., resistors, capacitors, inductors) alongside with off-the-shelf semiconductor components (BJTs, MOSFETS, etc.), which employ high voltages and low integration density while the contemporary VLSI technology employs low voltages and has high integration density. In this chapter we will implement the FO-FHN model by employing the companding design technique.

The companding technique is popularly known as externally linear and internally nonlinear (ELIN) circuit design. Using the sinh-domain companding technique, we can reduce power consumption because of the intrinsic class AB nature of this technique [33,63]. The main features of companding methods are: (i) low power consumption, (ii) resistor-free design, (iii) usage of only grounded capacitors, and (iv) electronic reconfigurability (tunability).

17.3.1 Sinh-domain building blocks for FO-FHN neuron model

From (17.1) and (17.2), one can assess that the FO-FHN neuron model can be realized in sinh-domain companding mode by employing sinh-domain-FO integrators, sinh-domain gain blocks, and sinh-domain multipliers.

17.3.1.1 Sinh-domain nonlinear transconductor

Sinh-domain realization of any differential equation can be fundamentally done by a nonlinear transconductor, as shown in Fig. 17.3, and its input-output relation is given as

$$i_{out} = 2I_0 \mathbf{Sinh}\left(\frac{\hat{v}_{IN+} - \hat{v}_{IN-}}{nV_T}\right). \tag{17.5}$$

Using a typical current mirror in the circuit given in Fig. 17.3, we can have Cosh and $-\mathbf{Sinh}$ as

$$i_{out} = 2I_0 \mathbf{Cosh}\left(\frac{\hat{v}_{IN+} - \hat{v}_{IN-}}{nV_T}\right), \tag{17.6}$$

$$i_{out} = -2I_0 \mathbf{Sinh}\left(\frac{\hat{v}_{IN+} - \hat{v}_{IN-}}{nV_T}\right), \tag{17.7}$$

where V_T is the thermal voltage (26 mV @ 27°C), n is the subthreshold slope factor ($1 < n < 2$), and, \hat{v}_{IN+} , \hat{v}_{IN-} are the noninverting and inverting input voltages, respectively.

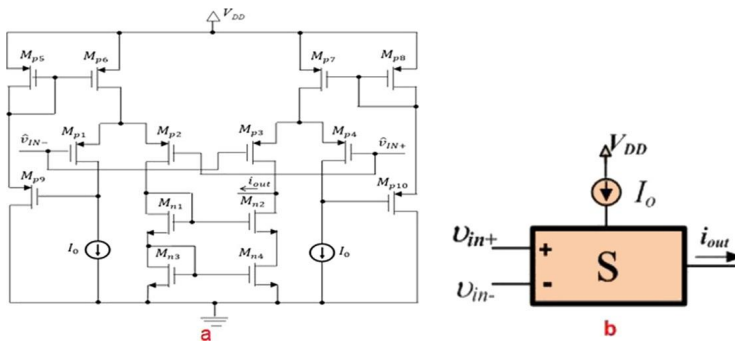


Figure 17.3 Nonlinear transconductor. (a) MOS realization. (b) Employed symbol.

17.3.1.2 Sinh-domain two-quadrant multiplier/divider

A sinh-domain two-quadrant (2Q) multiplier/divider circuit is given in Fig. 17.4, and its relationship is given as

$$i_{out} = I_0 \frac{i_1}{i_2} \tag{17.8}$$

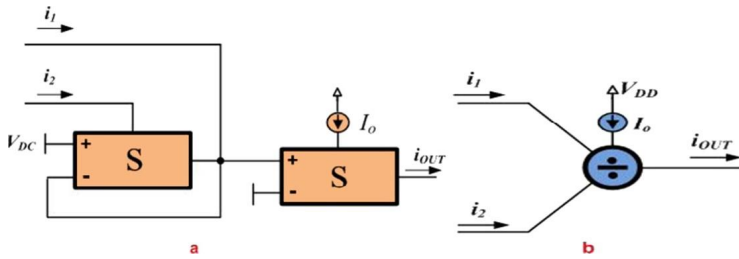


Figure 17.4 (a) 2Q multiplier/divider. (b) Employed symbol.

17.3.1.3 Sinh-domain lossless integrator

The integrator in sinh-domain mode is depicted in Fig. 17.5(a) and the symbol used is depicted in Fig. 17.5(b). The mathematical relationship of the lossless integrator is

$$\tau \frac{d}{dt} [\mathbf{Sinh}(\hat{v}_{OUT})] = \mathbf{Sinh}(\hat{v}_{IN}) \tag{17.9}$$

Here $\tau = \frac{\hat{C}_{int} n V_T}{2 I_{int}}$ is the time constant of the integrator.

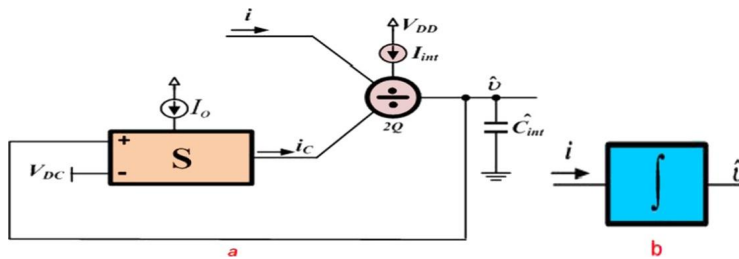


Figure 17.5 (a) Sinh-domain integrator. (b) Employed symbol.

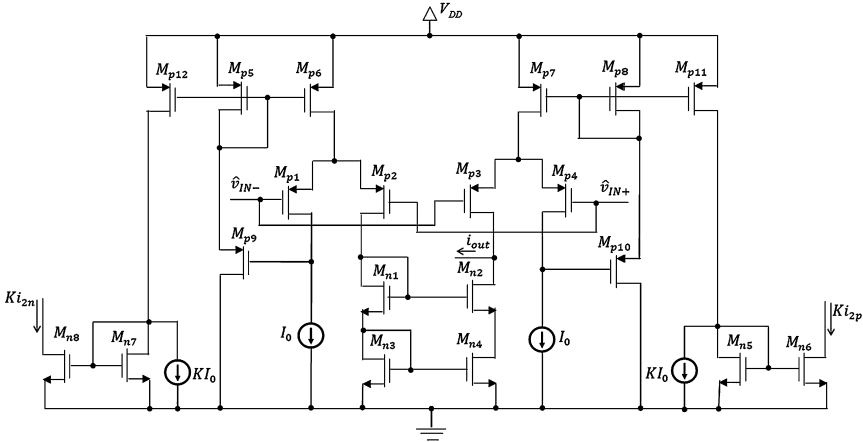


Figure 17.6 MOS realization of splitter.

17.3.1.4 Sinh-domain four-quadrant multiplier

In order to implement a sinh-domain four-quadrant (4Q) multiplier, a current splitter [63] block is required. Its sinh-domain implementation is shown in Fig. 17.6. Using the current splitter, the 4Q multiplier has been realized as shown in Fig. 17.7. The governing equations for the current splitter and 4Q multiplier are

$$i_{2p} = \frac{i_2 + \sqrt{i_2^2 + 4I_o^2}}{2}, \tag{17.10}$$

$$i_{2n} = \frac{-i_2 + \sqrt{i_2^2 + 4I_o^2}}{2}, \tag{17.11}$$

$$i_{out} = \mathbf{K} \frac{i_1 i_2}{I_0}. \tag{17.12}$$

17.3.1.5 Sinh-domain fractional-order lossless integrator

The fractional-order lossless integrator (FOLLI) [17] is given as

$$H(s) = \frac{1}{(\tau.s)^\alpha}. \tag{17.13}$$

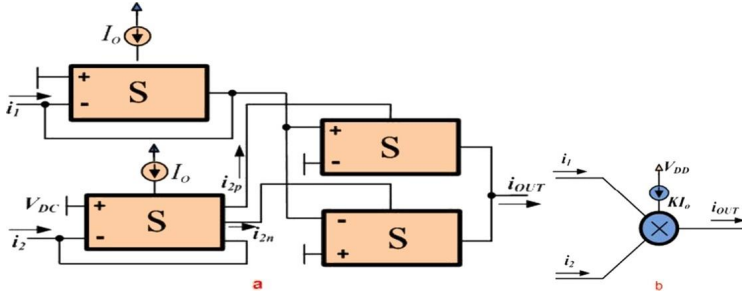


Figure 17.7 4Q multiplier. (a) Sinh-domain implementation. (b) Employed symbol.

The magnitude of FOLLI is represented by $|H(\omega)| = (\omega_u/\omega)^\alpha$ and the phase response of FOLLI is denoted by $\phi = -\alpha\pi/2$. Here, $\omega_u \equiv 1/\tau$ is the unity gain frequency.

The second-order continued fraction expansion approximation of $1/s^\alpha$ is given by

$$\frac{1}{s^\alpha} = \frac{(\alpha^2 - 3\alpha + 2)s^2 + (\alpha^2 + 3\alpha + 2)}{(\alpha^2 + 3\alpha + 2)s^2 + (8 - 2\alpha^2)s + (\alpha^2 - 3\alpha + 2)} \quad (17.14)$$

or

$$\frac{1}{(\tau s)^\alpha} = \frac{\left(\frac{\alpha^2 - 3\alpha + 2}{\alpha^2 + 3\alpha + 2}\right)s^2 + \frac{1}{\tau} \left(\frac{8 - 2\alpha^2}{\alpha^2 + 3\alpha + 2}\right)s + \frac{1}{\tau^2}}{s^2 + \frac{1}{\tau} \left(\frac{8 - 2\alpha^2}{\alpha^2 + 3\alpha + 2}\right)s + \frac{1}{\tau^2} \left(\frac{\alpha^2 - 3\alpha + 2}{\alpha^2 + 3\alpha + 2}\right)}. \quad (17.15)$$

The FOLLI described above can be comprehended by follow-the-leader feedback (FLF) topology shown in Fig. 17.8, which is characterized as

$$H(s) = \frac{1}{(s\tau)^\alpha} = \frac{G_2 s^2 + \frac{G_1}{\tau_1} s + \frac{G_0}{\tau_1 \tau_2}}{s^2 + \frac{1}{\tau_1} s + \frac{1}{\tau_1 \tau_2}}. \quad (17.16)$$

Using FLF of Fig. 17.8, sinh-domain implementation of FOLLI is presented in Fig. 17.9(a) and its symbol is presented in Fig. 17.9(b). Comparing (17.16) and (17.17), the time constant values and coefficients were computed and are given in Table 17.1. Using FOLLI, the sinh-domain FO-FHN neuron circuit is shown in Fig. 17.10.

17.3.2 Simulation results of FO-FHN neuron model

The circuit simulator used for performing the simulation is HSPICE. It is pertinent to mention that the Synopsys HSPICE circuit simulator is the

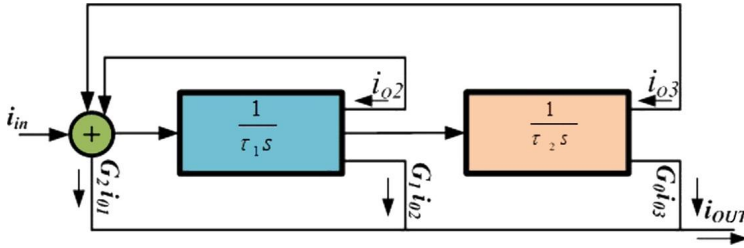


Figure 17.8 FLF structure of FOLLI.

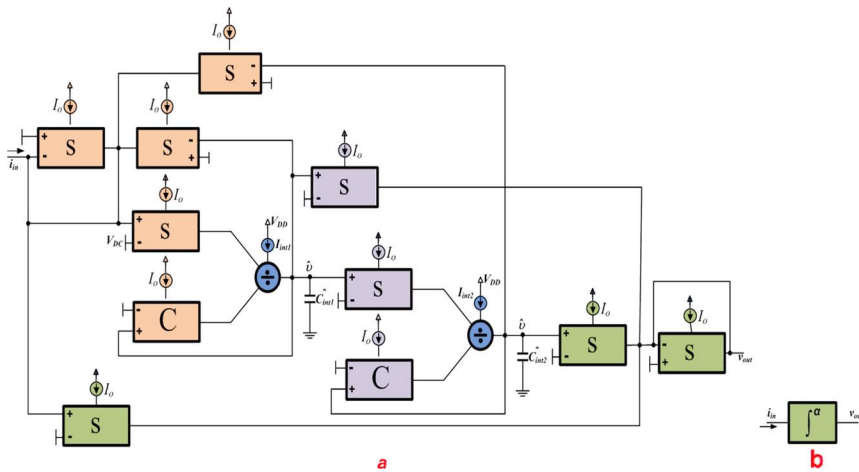


Figure 17.9 FOLLI. (a) Sinh-domain implementation. (b) Employed symbol.

Table 17.1 Time constants and gain coefficients of the FOI.

G_2	G_1	G_0	τ_1	τ_2
$\frac{\alpha^2 - 3\alpha + 2}{\alpha^2 + 3\alpha + 2}$	1	$\frac{\alpha^2 + 3\alpha + 2}{\alpha^2 - 3\alpha + 2}$	$\tau \left(\frac{\alpha^2 + 3\alpha + 2}{8 - 2\alpha^2} \right)$	$\tau \left(\frac{8 - 2\alpha^2}{\alpha^2 - 3\alpha + 2} \right)$

industry’s golden standard for accurate circuit simulation. HSPICE is a key part of the Synopsys Analog and Mixed Signal (AMS) verification suite. HSPICE is capable of performing steady-state, transient, and frequency-domain analysis along with the statistical analysis. HSPICE also allows hierarchical node naming, circuit optimization, input, output, and behavioral algebraics for parameterized cells, and interactive waveform viewing. The performance of the sinh-domain realization of the FO-FHN model is performed via the HSPICE simulator using the TSMC 130 nm CMOS process. The values for voltage source ($V_{DD} = 650$ mV, $V_{DC} = 350$ mV)

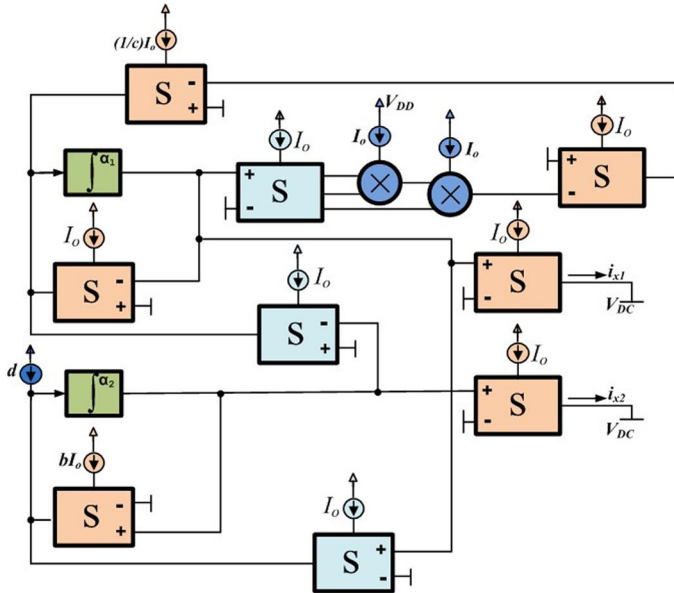


Figure 17.10 Sinh-domain implementation of the FO-FHN neuron model.

and current source ($I_0 = 200$ pA) were used in simulation. PMOS transistors having a W/L ratio of $55 \mu\text{m}/1.5 \mu\text{m}$ were used to obtain the DC current sources. Aspect ratios of MOS transistors of transconductor and current splitter are given in Table 17.2. By adjusting the aspect ratios of M_{p11} and M_{p12} , the gain factor “K” can be set to any value. The DC transfer characteristics of the 4Q multiplier are depicted in Fig. 17.11(a). The current i_1 is changed from -200 pA to 200 pA and i_2 is changed from -200 pA to 200 pA. The transient response of a multiplier with sinusoidal input having a frequency of 10 Hz and an amplitude of 100 pA is depicted in Fig. 17.11(b).

For achieving sinh-domain implementation of the FO-FHN neuron model as shown in Fig. 17.10, the parameters for FOLLI of Fig. 17.9 are given in Table 17.3. For FOLLI, the values used for \hat{C}_{int1} and \hat{C}_{int2} were 200 pF and 2 nF, respectively. The obtained results for FOLLI are shown in Fig. 17.12, and the phase responses of FOLLI with orders 0.5, 0.6, and 0.7 are plotted for $\tau = 16.2$ ms in Fig. 17.12(b) and the simulation results of phase responses with orders 0.5, 0.6, and 0.7 in the case $\tau = 211$ ms are given in Fig. 17.12(b). The results associated with FOLLI and the results

Table 17.2 Aspect ratio of nonlinear transconductor and current splitter MOS transistors.

Nonlinear transducer		Current splitter	
MOS transistor	Aspect ratio	MOS transistor	Aspect ratio
$M_{p1} - M_{p4}$	4 $\mu\text{m}/4 \mu\text{m}$	$M_{p1} - M_{p4}$	4 $\mu\text{m}/4 \mu\text{m}$
$M_{p5} - M_{p8}$	1 $\mu\text{m}/1 \mu\text{m}$	$M_{p5} - M_{p8}$	4 $\mu\text{m}/4 \mu\text{m}$
$M_{p9} - M_{p10}$	1 $\mu\text{m}/10 \mu\text{m}$	$M_{p9} - M_{p10}$	1 $\mu\text{m}/10 \mu\text{m}$
$M_{n1} - M_{n4}$	2 $\mu\text{m}/2 \mu\text{m}$	$M_{p11} - M_{p12}$	1 $\mu\text{m}/1 \mu\text{m}$
		$M_{n1} - M_{n8}$	2 $\mu\text{m}/2 \mu\text{m}$

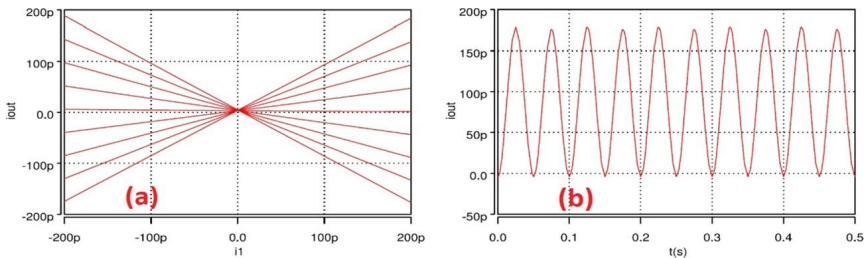


Figure 17.11 (a) Characteristics of the 4Q multiplier. (b) Output transient behavior of the 4Q multiplier.

Table 17.3 Bias currents and coefficients of sinh-domain FOI with various orders and time constants.

τ (ms)	α	I_{int1} (pA)	I_{int2} (pA)	G_2	G_1	G_0
16.2		831	416			
211	0.5	63.9	32	0.2	1	5
16.2		728	320			
211	0.6	56	24	0.134	1	7.43
16.2		636	231			
211	0.7	48.9	17.8	0.085	1	11.77

conforming to a multiplier with $I_0 = 150 \text{ pA}$, 200 pA , and 250 pA are given in Fig. 17.13.

Using the FO-FHN model of Fig. 17.10 and the FOLLI block of Fig. 17.9, the acquired results of the FO-FHN model were obtained by changing the input impetus I . The FO-FHN neuron model of commensurate order (i.e., $\alpha_1 = \alpha_2 = \alpha$) is designed. With $\alpha = 0.5$, the results hence obtained are given in Fig. 17.14. Fig. 17.14(a)–(f) gives the x_2 vs. x_1 phase portrait for the FO-FHN model having different excitation current values,

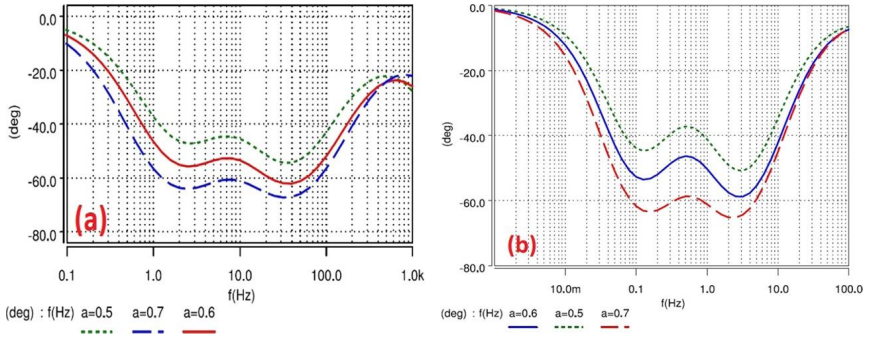


Figure 17.12 Phase response of FOI with $\alpha = 0.5, 0.6,$ and $0.7.$ (a) $\tau = 16.2$ ms. (b) $\tau = 211$ ms.

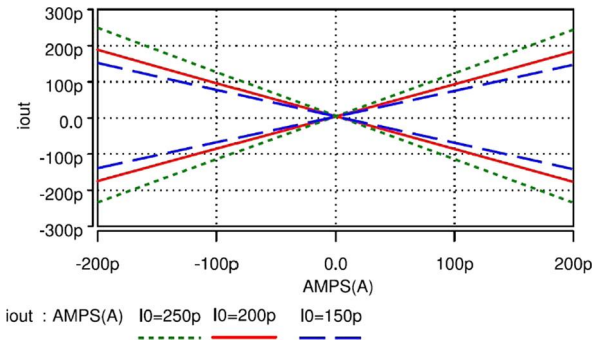


Figure 17.13 Demonstration of the electronic tunability of the 4Q multiplier.

as depicted in the caption of the figure. The corresponding obtained results for $\alpha = 0.6$ and $\alpha = 0.7$ are given in Fig. 17.15 and Fig. 17.16, respectively.

Further, the simulation of incommensurate order i.e., for different values of α of integrators is obtained. The x_2 vs. x_1 results of the FO-FHN neuron model using $\alpha_1 = 0.5$ and $\alpha_2 = 0.6$ are displayed in Fig. 17.17. The conforming results for $\alpha_1 = 0.6$ and $\alpha_2 = 0.7$ are given in Fig. 17.18. Obtained results suggest that the firing rate of the fractional-order model increases as the integrator order increases, as shown in Fig. 17.19(a). Also, the firing rate of the neuron model increases as the impetus of neurons increases, as shown in Fig. 17.19(b). The estimated silicon area for the FO-FHN neuron model was 2.2 mm^2 and the maximum working frequency of fractional-order neuron circuits is 856 Hz.

The corner analysis was performed to assess the integrated circuit (IC) realization with variants such as speed of the PMOS and NMOS. Corners

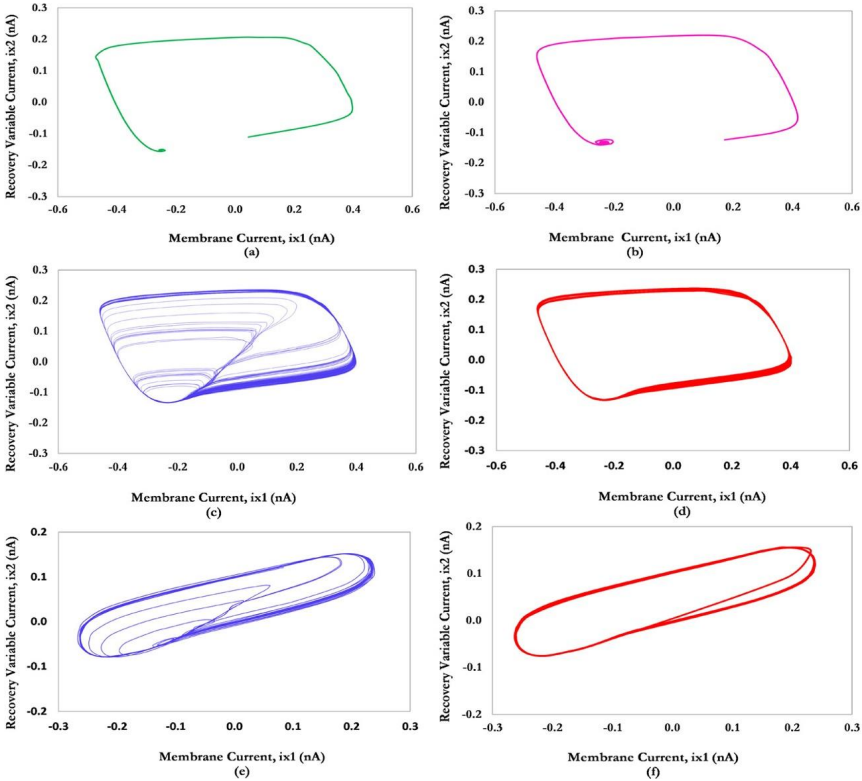


Figure 17.14 x_2 vs. x_1 portrait for the FO-FHN neuron model with $\alpha_1 = \alpha_2 = \alpha = 0.5$ for (a) $I = 15$ pA, (b) $I = 34$ pA, (c) $I = 43.4$ pA, (d) $I = 45$ pA, (e) $I = 61.5$ pA, and (f) $I = 62.5$ pA.

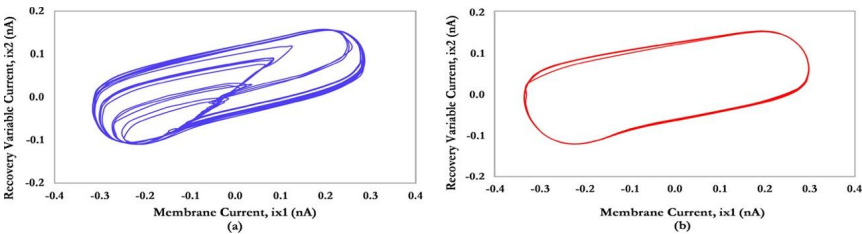


Figure 17.15 x_2 vs. x_1 portrait for the FO-FHN neuron model with $\alpha_1 = \alpha_2 = \alpha = 0.6$ for (a) $I = 48.7$ pA and (b) $I = 50$ pA.

such as “typical NMOS” and “typical PMOS (TT),” “fast NMOS and fast PMOS (FF),” “slow NMOS and slow PMOS (SS),” “fast NMOS and slow PMOS (FS),” and “slow NMOS and fast PMOS (SF)” are deliberated to

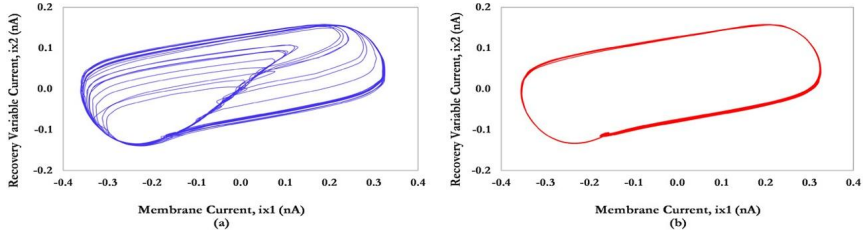


Figure 17.16 x_2 vs. x_1 portrait for the FO-FHN neuron model with $\alpha_1 = \alpha_2 = \alpha = 0.7$ for (a) $I = 33.2$ pA and (b) $I = 35$ pA.

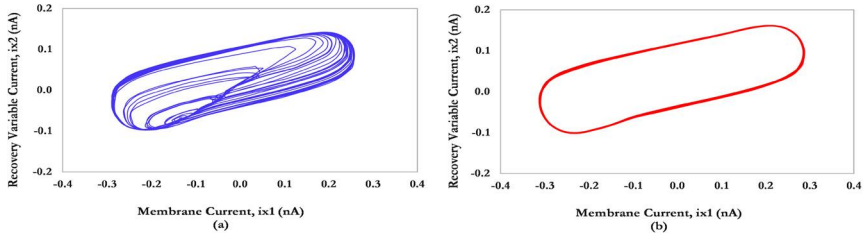


Figure 17.17 x_2 vs. x_1 portrait for the FO-FHN neuron model with $\alpha_1 = 0.5, \alpha_2 = 0.6$ for (a) $I = 46.2$ pA and (b) $I = 50$ pA.

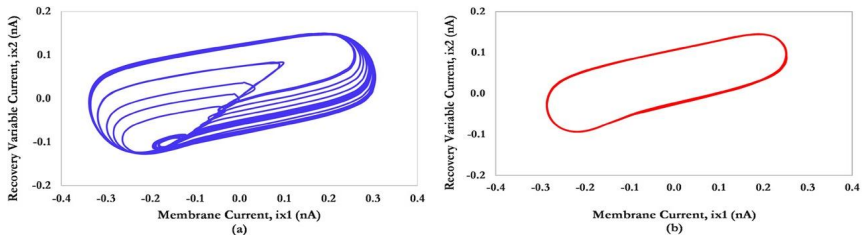


Figure 17.18 x_2 vs. x_1 portrait for the FO-FHN neuron model with $\alpha_1 = 0.6, \alpha_2 = 0.7$ for (a) $I = 34$ pA and (b) $I = 37.5$ μ A.

estimate the performance of IC realization with process variations. The attained outcomes for the FO-FHN neuron model with $\alpha_1 = \alpha_2 = 0.5$ and a stimulus of $I = 65$ pA in the process corners TT, FE, SS, FS, and SF are shown in Fig. 17.20. It is observed that there is a change in the shape and frequency of the signal. The R^2 fitting test was performed to check the matching of attained corner results; corner outcomes provide a respectable fit to typical results for the designs.

The Monte Carlo analysis was performed for the FO-FHN neuron model with $\alpha_1 = \alpha_2 = 0.5$ for calculating the threshold voltage variations on

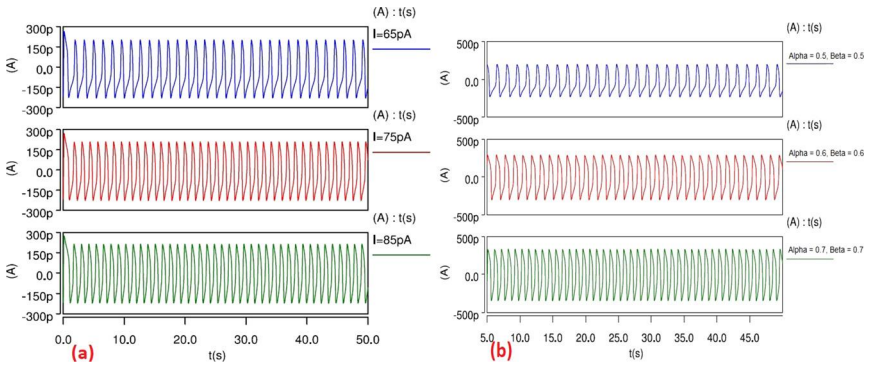


Figure 17.19 Illustration of (a) the increase in firing rate with input impetus and (b) the increase in firing rate with the order of the neuron.

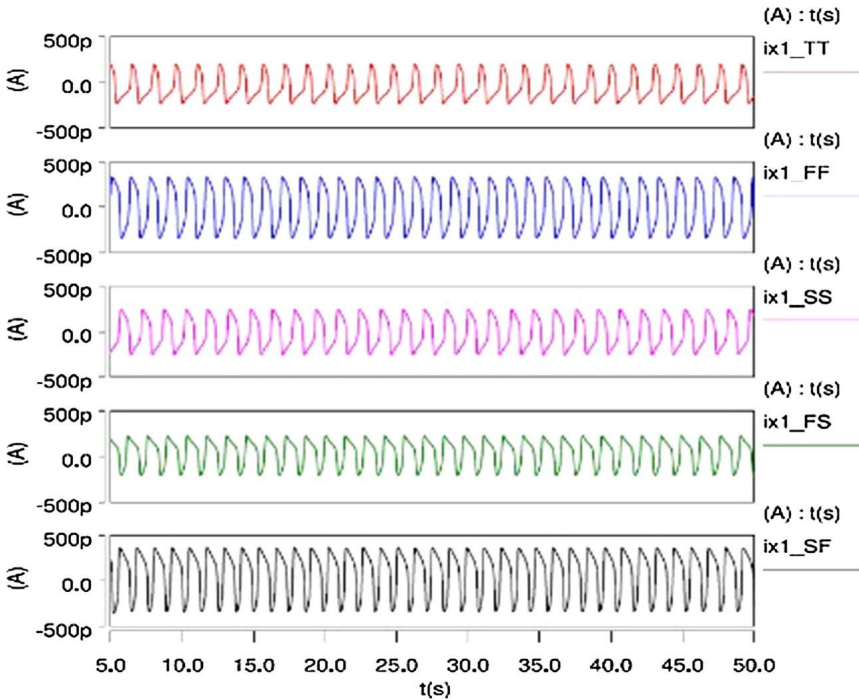


Figure 17.20 Corner analysis for the FO-FHN neuron model.

the performance of the circuit. The attained results are shown in Fig. 17.21. The standard deviation of the amplitude (peak to peak) was 89 pA and the standard deviation for frequency of the output waveform is 45 mHz. In

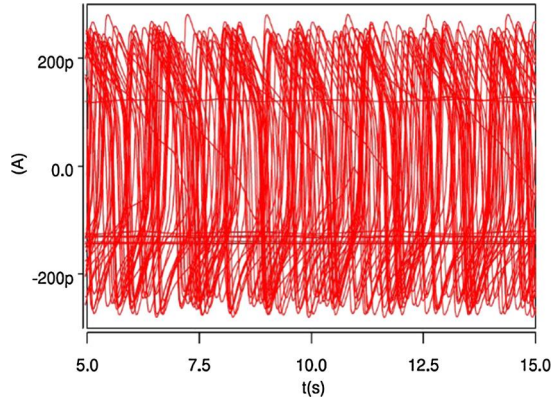
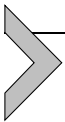


Figure 17.21 The response of the FO-FHN neuron model with threshold variation.

addition, the linearly coupled four-neuron FO-FHN neuron model given in (17.4) was designed with $\alpha_1 = \alpha_2 = 0.5$ to assess the application performance. As the dynamics of the coupled neurons depend on coupling function and coupling strength (k), for different coupling strength values, the attained results are shown in Fig. 17.22. It is verified that as k increases, the dynamics change.



17.4. FPAА implementation of FO-FHN neuron network

For FPAА implementation of the FO-FHN, the Anadigm FPAА AN231E04 kit was employed. The kit is comprised of configurable analog modules (CAMs). The CAM blocks are basically switched capacitor circuits and hence the clock frequency is used to set frequencies. The various CAM blocks of the Anadigm kit are bilinear filters, sumintegrator, biquad filters, analog-to-digital converters (ADCs), sumfilter, sumdiff, multipliers, Hold circuits, etc. Since FPAА does not contain FOLLI, we need to implement it using filterbiquad CAM as used by [17]. The transfer function for the filterbiquad CAM is given as

$$T(s) = -\frac{G_H \left(s^2 + \left(\frac{2\pi f_z}{Q_z} \right) s + 4\pi^2 f_z^2 \right)}{s^2 + \left(\frac{2\pi f_p}{Q_p} \right) s + 4\pi^2 f_p^2}. \quad (17.17)$$

Here, G_H , f_z , Q_z , f_p , and Q_p are various factors of the filterbiquad CAM.

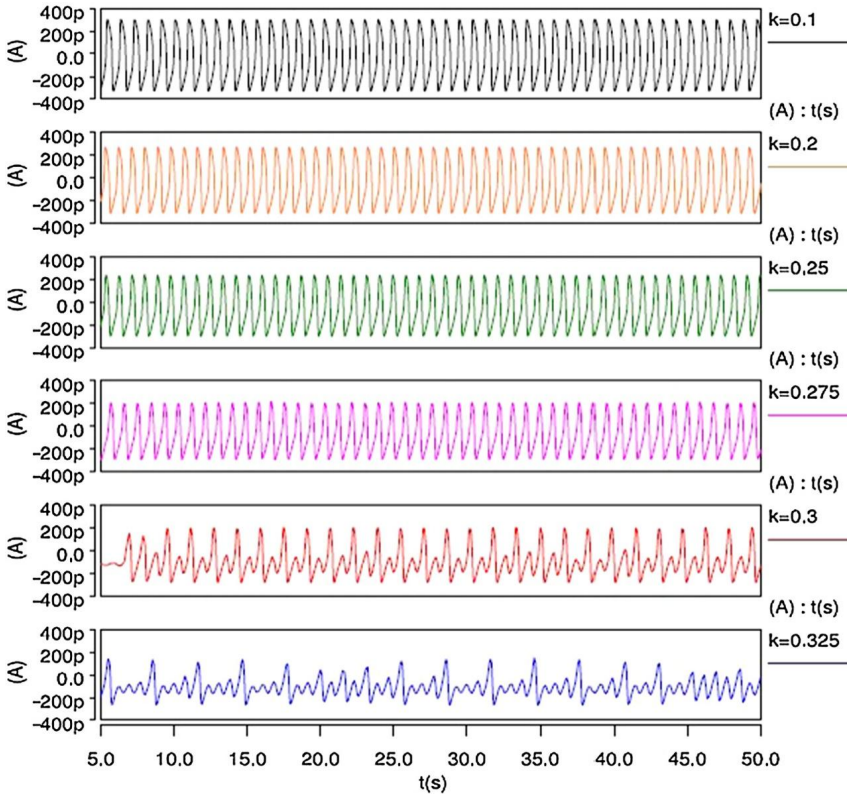


Figure 17.22 Variation of k in a linearly coupled four-neuron FO-FHN neural network.

Eq. (17.15) can be rewritten as

$$\frac{1}{(\tau s)^\alpha} = \frac{\left(\frac{\alpha^2 - 3\alpha + 2}{\alpha^2 + 3\alpha + 2}\right) \left(s^2 + \frac{1}{\tau} \left(\frac{8 - 2\alpha^2}{\alpha^2 - 3\alpha + 2}\right) s + \frac{1}{\tau^2} \left(\frac{\alpha^2 + 3\alpha + 2}{\alpha^2 - 3\alpha + 2}\right)\right)}{s^2 + \frac{1}{\tau} \left(\frac{8 - 2\alpha^2}{\alpha^2 + 3\alpha + 2}\right) s + \frac{1}{\tau^2} \left(\frac{\alpha^2 - 3\alpha + 2}{\alpha^2 + 3\alpha + 2}\right)}. \tag{17.18}$$

On comparing (17.17) and (17.18),

$$G_H = \frac{\alpha^2 - 3\alpha + 2}{\alpha^2 + 3\alpha + 2}, \quad f_z = \frac{1}{2\pi\tau} \left(\frac{\alpha^2 + 3\alpha + 2}{\alpha^2 - 3\alpha + 2}\right)^{\frac{1}{2}},$$

$$Q_z = \frac{\left((\alpha^2 + 3\alpha + 2)(\alpha^2 - 3\alpha + 2)\right)^{\frac{1}{2}}}{8 - 2\alpha^2}, \quad f_p = \frac{1}{2\pi\tau} \left(\frac{\alpha^2 - 3\alpha + 2}{\alpha^2 + 3\alpha + 2}\right)^{\frac{1}{2}},$$

Table 17.4 Values of G_H , f_z , Q_z , f_p , and Q_p for various FOs with $\tau = 16.2 \mu\text{s}$.

Order	G_H	G_L	f_z (kHz)	Q_z	f_p (kHz)	Q_p
0.5	0.2	5	22	0.223	4.39	0.223
0.6	0.134	7.42	26.8	0.209	3.61	0.209
0.7	0.085	11.76	33.7	0.190	2.86	0.190

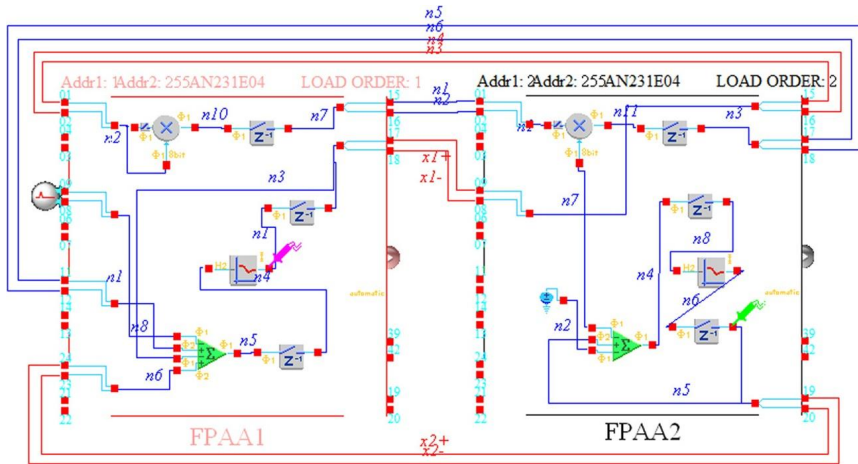


Figure 17.23 FPAA realization of the FO-FHN neuron model.

$$Q_p = \frac{\left((\alpha^2 + 3\alpha + 2)(\alpha^2 - 3\alpha + 2) \right)^{\frac{1}{2}}}{8 - 2\alpha^2}$$

Besides, the low-frequency gain G_L can be given by

$$G_L = \frac{\alpha^2 + 3\alpha + 2}{\alpha^2 - 3\alpha + 2}$$

Values of G_H , f_z , Q_z , f_p , and Q_p with different FOs are tabulated in Table 17.4.

The filter biquad CAMs with other CAMs were used to implement the required circuit as given in Fig. 17.23. The FPAA results are shown in Fig. 17.24.

17.5. FPGA implementation of FO-FHN neuron model

The first step in hardware realization of any system is to recognize the hardware to be used. FPGA is chosen here because of its rapid proto-

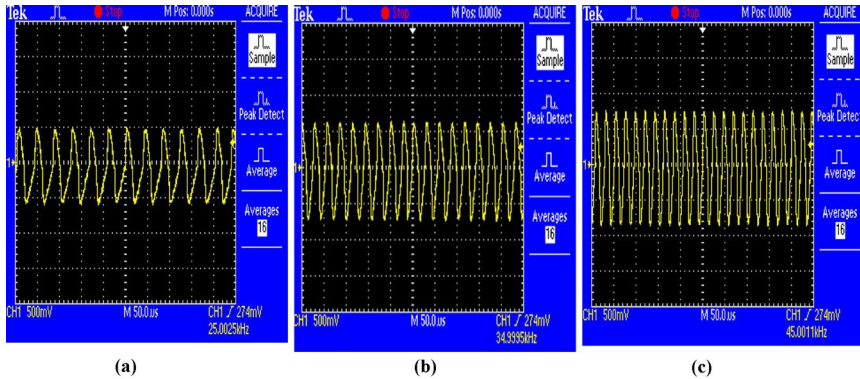


Figure 17.24 Experimental FPAA results for the FO-FHN neuron model (x_1) with an input impetus of 0.95 V. (a) $\alpha_1 = \alpha_2 = 0.5$. (b) $\alpha_1 = \alpha_2 = 0.6$. (c) $\alpha_1 = \alpha_2 = 0.7$.

typing and its inherent properties of reconfigurability and parallelism. The discretization or numerical simulations of fractional differential equations $D_v^\alpha y(t) = f(y(t), t)$ can be obtained by using the Grünwald–Letnikov (GL) definition of fractional derivatives [17,54], which is given as

$$y(t_{n+1}) = (f(y(t_n), t_n))h^\alpha - \sum_{j=\nu}^n C_j^\alpha y(t_{n-j}), \tag{17.19}$$

where

$$C_j^\alpha = \left(1 - \frac{1+\alpha}{j}\right) C_{j-1}^\alpha, \quad C_0^\alpha = 1. \tag{17.20}$$

Therefore, using (17.19), the numerical solution of FHN neuron can be written as

$$\begin{aligned} x_1(t_{n+1}) &= \left(x_1(t_n) - \frac{x_1^3(t_n)}{3} - x_2(t_n) + I(t_n)\right)h^{\alpha_1} - \sum_{j=\nu}^n C_j^{\alpha_1} x_1(t_{n-j}), \\ x_2(t_{n+1}) &= \frac{1}{a} \left(x_1(t_n) - bx_2(t_n) + d\right)h^{\alpha_2} - \sum_{j=\nu}^n C_j^{\alpha_2} x_2(t_{n-j}). \end{aligned} \tag{17.21}$$

The coefficient C_j is referred to as the memory part. Simulation for different values of α_1 , α_2 , and $I(t)$ are shown in Figs. 17.25–17.28. Fig. 17.29 shows the nullcline diagram of the membrane potential variable and recovery variable and phase space diagrams for different values of α_1 and α_2 when $I(t) = 0.7$.

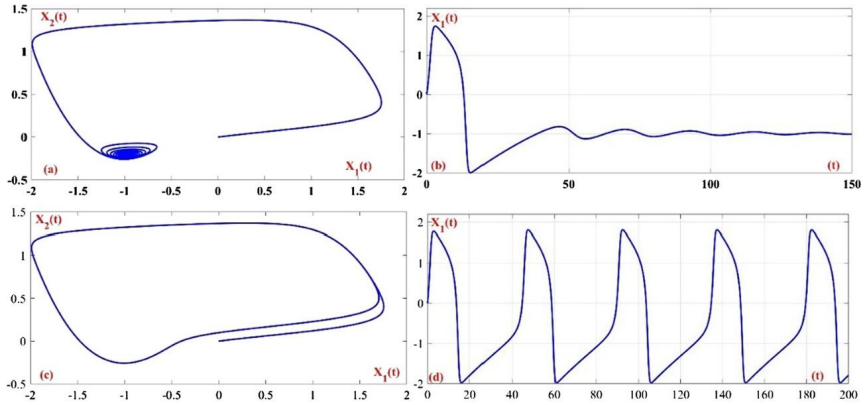


Figure 17.25 FO-FHN neuron model with variable input stimulus and $a = 13, b = 0.8, d = 0.8,$ and $c = 1/3$. (a) Phase space bet. $x_1(t)$ and $x_2(t)$ when $\alpha_1 = 1, \alpha_2 = 1,$ and $l(t) = 0.4$. (b) Membrane pot. $x_1(t)$ when $\alpha_1 = 1, \alpha_2 = 1,$ and $l(t) = 0.4$. (c) Phase space bet. $x_1(t)$ and $x_2(t)$ when $\alpha_1 = 1, \alpha_2 = 1,$ and $l(t) = 0.45$. (d) Membrane pot. $x_1(t)$ when $\alpha_1 = 1, \alpha_2 = 1,$ and $l(t) = 0.45$.

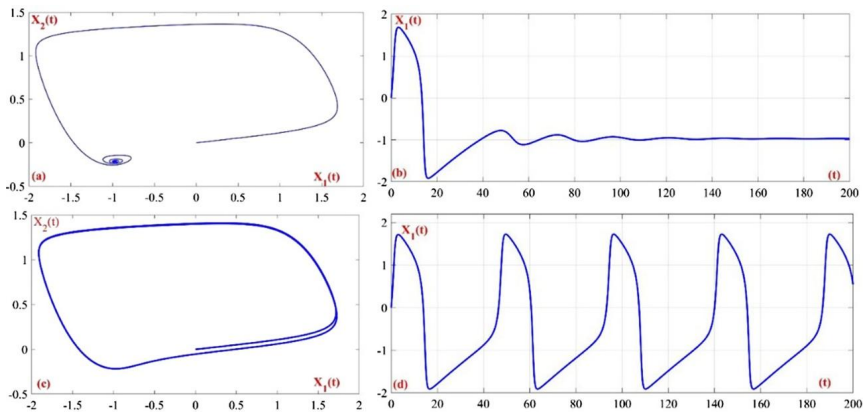


Figure 17.26 FO-FHN neuron model with variable input stimulus and $a = 13, b = 0.8, d = 0.8,$ and $c = 1/3$. (a) Phase space bet. $x_1(t)$ and $x_2(t)$ when $\alpha_1 = 0.9, \alpha_2 = 1,$ and $l(t) = 0.448$. (b) Membrane pot. $x_1(t)$ when $\alpha_1 = 0.9, \alpha_2 = 1,$ and $l(t) = 0.448$. (c) Phase space bet. $x_1(t)$ and $x_2(t)$ when $\alpha_1 = 0.9, \alpha_2 = 1,$ and $l(t) = 0.5$. (d) Membrane pot. $x_1(t)$ when $\alpha_1 = 0.9, \alpha_2 = 1,$ and $l(t) = 0.5$.

The first step in FPGA implementation of any variable or function is attaining bit length of the variables in the model. From above, we see that the membrane potential values vary from -2 to 2.5 ; therefore, a bit width has to be 3. Nevertheless, to elude overflow and accurately represent the

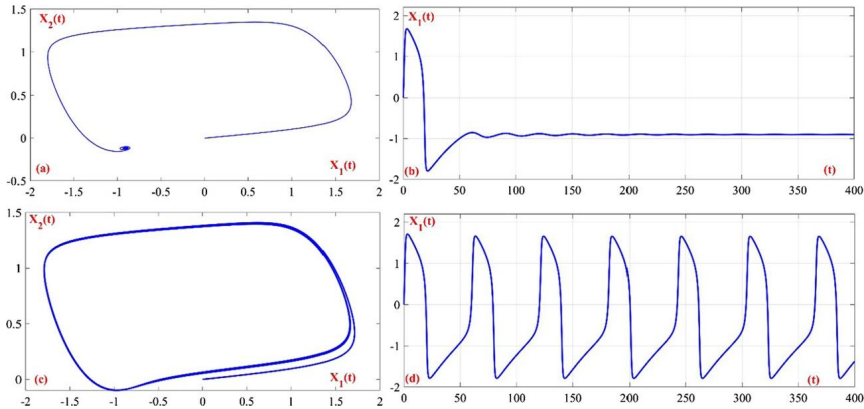


Figure 17.27 FO-FHN neuron model with variable input impetus and $a = 13$, $b = 0.8$, $d = 0.8$, and $c = 1/3$. (a) Phase space bet. $x_1(t)$ and $x_2(t)$ when $\alpha_1 = 0.8$, $\alpha_2 = 0.9$, and $I(t) = 0.53$. (b) Membrane pot. $x_1(t)$ when $\alpha_1 = 0.8$, $\alpha_2 = 0.9$, and $I(t) = 0.53$. (c) Phase space bet. $x_1(t)$ and $x_2(t)$ when $\alpha_1 = 0.8$, $\alpha_2 = 0.9$, and $I(t) = 0.60$. (d) Membrane pot. $x_1(t)$ when $\alpha_1 = 0.8$, $\alpha_2 = 0.9$, and $I(t) = 0.60$.

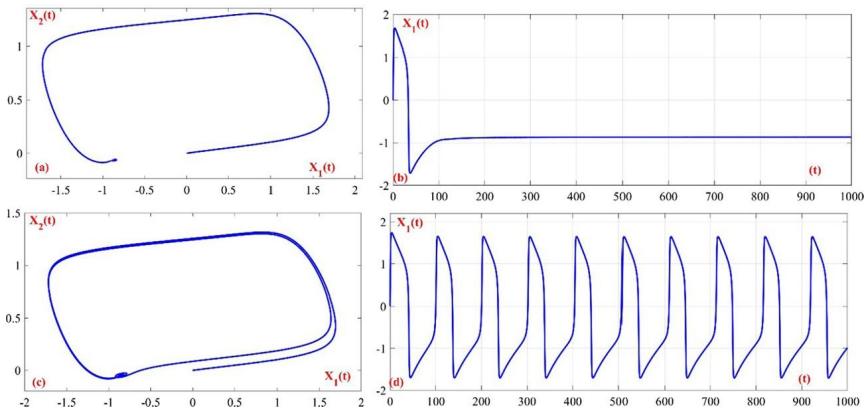


Figure 17.28 FO-FHN neuron model with variable input impetus and $a = 13$, $b = 0.8$, $d = 0.8$, and $c = 1/3$. (a) Phase space bet. $x_1(t)$ and $x_2(t)$ when $\alpha_1 = 0.75$, $\alpha_2 = 0.75$, and $I(t) = 0.55$. (b) Membrane pot. $x_1(t)$ when $\alpha_1 = 0.75$, $\alpha_2 = 0.75$, and $I(t) = 0.55$. (c) Phase space bet. $x_1(t)$ and $x_2(t)$ when $\alpha_1 = 0.75$, $\alpha_2 = 0.75$, and $I(t) = 0.70$. (d) Membrane pot. $x_1(t)$ when $\alpha_1 = 0.75$, $\alpha_2 = 0.75$, and $I(t) = 0.70$.

decimal part, especially the constants C_j of each variable, we are using a bit width of 24 bits, where 4 bits are reserved for the integer part and 20 bits are used for the decimal part. Further, the hardware flow diagram is shown in Fig. 17.30. It is pertinent to mention that the main challenge in

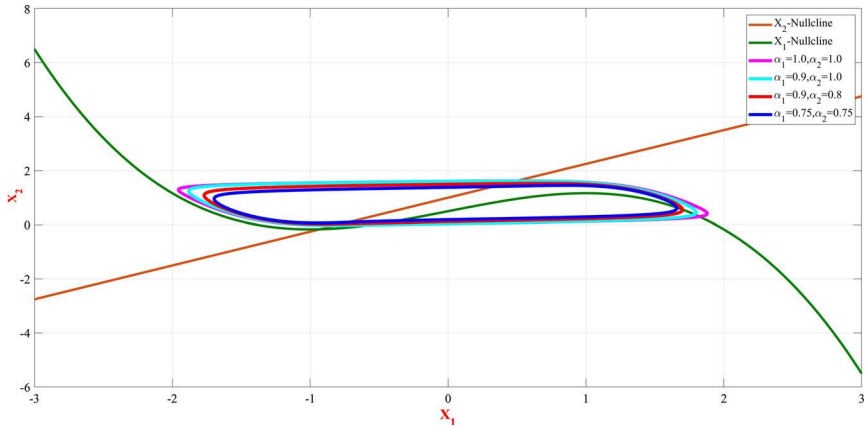


Figure 17.29 Nullcline diagrams of membrane pot. $x_1(t)$ and recovery variable $x_2(t)$. Phase space diagrams for different values of fractional operators α_1 and α_2 when $a = 13$, $b = 0.8$, $d = 0.8$, $c = 1/3$, and $I(t) = 0.7$.

Table 17.5 Resource exhausted of the board DE2-115. Available Resources (AVI).

Neuron model	Resource type							
	Logic		Registers		Memory bits		DSP blocks	
	Used	AVI	Used	AVI	Used	AVI	Used	AVI
FHZ	2440		2208		1960		2	
Neuron	<3%	114,480	<2%	114,480	<1%	3,981,312	<1%	266

implementing the FODE on a practical FPGA board is that in the second part of the numerical GL equation, which is also referred to as memory, the values of the coefficients in the designed equation are mostly very small and consume a lot of hardware resource.

The FPGA board employed is DE2-115 for the circuit implementation of the FO-FHN neuron. Table 17.5 depicts the hardware resource exhausted by the FO-FHN.

17.6. Conclusion

In this chapter a detailed account of the analog and digital realization of the FO-FHN neuron model has been investigated and various aspects of implementations of FO modeling have been discussed. In analog implementation, two techniques have been employed. One is the VLSI implementable low-voltage low-power companding technique, which offers the advantages of low voltage and reconfigurability. The other analog

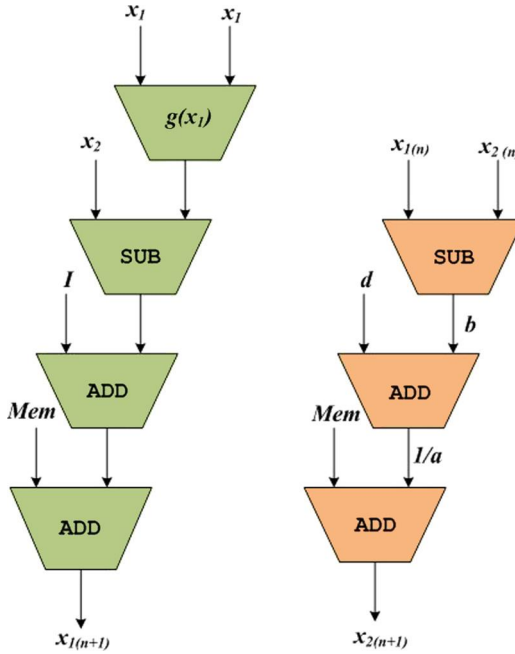


Figure 17.30 Hardware flow diagram of FO-FHN.

implementation technique used is FPAA, which offers the advantage of experimental verification of FO design with on-board switched capacitor design. Besides, FPGA implementation of the FO-FHN neuron model has been achieved, which offers advantages of flexible design. In along implementation, the detailed dynamical aspects of the FO-FHN model are discussed in this chapter. In addition, the coupling scheme of the neuron models is also given for application purposes.

Being very advantageous, FO circuit design of analog and/or digital nature is still difficult because of unavailability of off-the-shelf FO elements. The difficulty level of FO circuit design increases to a great extent due to the approximated design employed for the FO element. The approximated design not only increases the circuit complexity but also consumes more memory in the case of FPGA implementation and more power in the case of analog design. This is further aggravated in the case of FO-NNs, where a large part of the neurons are required to perform a specific task such as data classification. Therefore, future research of the FO-NN design must focus on the optimization of the designs for achieving low power and high speed features. This may raise the need to use different design techniques

or algorithms. Furthermore, some practical applications of FO-NNs can be designed to verify the performance of FO-NNs for real-world applications.

References

- [1] Larry F. Abbott, Lopicque's introduction of the integrate-and-fire model neuron (1907), *Brain Research Bulletin* 50 (5–6) (1999) 303–304.
- [2] Alma Y. Alanis, Nancy Arana-Daniel, Carlos Lopez-Franco, *Artificial Neural Networks for Engineering Applications*, Academic Press, 2019.
- [3] Javad Alidousti, R. Khoshsiar Ghaziani, Spiking and bursting of a fractional order of the modified FitzHugh–Nagumo neuron model, *Mathematical Models and Computer Simulations* 9 (3) (2017) 390–403.
- [4] Mina Armanios, Ahmed G. Radwan, Fractional-order FitzHugh–Nagumo and Izhikevich neuron models, in: 2016 13th International Conference on Electrical Engineering/Electronics, Computer, Telecommunications and Information Technology (ECTI-CON), IEEE, 2016, pp. 1–5.
- [5] Laurent Badel, Sandrine Lefort, Romain Brette, Carl C.H. Petersen, Wulfram Gerstner, Magnus J.E. Richardson, Dynamic IV curves are reliable predictors of naturalistic pyramidal-neuron voltage traces, *Journal of Neurophysiology* 99 (2) (2008) 656–666.
- [6] Stéphane Binczak, Sabir Jacquir, Jean-Marie Bilbault, Viktor B. Kazantsev, Vladimir I. Nekorkin, Experimental study of electrical FitzHugh–Nagumo neurons with modified excitability, *Neural Networks* 19 (5) (2006) 684–693.
- [7] Gary W. Bohannon, Analog fractional order controller in temperature and motor control applications, *Journal of Vibration and Control* 14 (9–10) (2008) 1487–1498.
- [8] Arefeh Boroomand, Mohammad B. Menhaj, Fractional-order Hopfield neural networks, in: *International Conference on Neural Information Processing*, Springer, 2008, pp. 883–890.
- [9] Nikola Burić, Kristina Todorović, Nebojša Vasović, Dynamics of noisy FitzHugh–Nagumo neurons with delayed coupling, *Chaos, Solitons and Fractals* 40 (5) (2009) 2405–2413.
- [10] Mo Chen, Jianwei Qi, Quan Xu, Bocheng Bao, Quasi-period, periodic bursting and bifurcations in memristor-based FitzHugh–Nagumo circuit, *AEÜ. International Journal of Electronics and Communications* 110 (2019) 152840.
- [11] Mo Chen, JianWei Qi, HuaGan Wu, Quan Xu, BoCheng Bao, Bifurcation analyses and hardware experiments for bursting dynamics in non-autonomous memristive FitzHugh–Nagumo circuit, *Science China. Technological Sciences* (2020) 1–10.
- [12] Jordi Cosp, Stéphane Binczak, Jordi Madrenas, Daniel Fernández, Realistic model of compact VLSI FitzHugh–Nagumo oscillators, *International Journal of Electronics* 101 (2) (2014) 220–230.
- [13] Dalibor Hrg, Synchronization of two Hindmarsh–Rose neurons with unidirectional coupling, *Neural Networks* 40 (73) (2017) 73–79.
- [14] Mohammad Rafiq Dar, Nasir Ali Kant, Farooq Ahmad Khanday, Realization of fractional-order double-scroll chaotic system using operational transconductance amplifier (OTA), *Journal of Circuits, Systems, and Computers* 27 (01) (2018) 1850006.
- [15] José João De Espíndola, Carlos Alberto Bavastri, Eduardo Márcio de Oliveira Lopes, Design of optimum systems of viscoelastic vibration absorbers for a given material based on the fractional calculus model, *Journal of Vibration and Control* 14 (9–10) (2008) 1607–1630.
- [16] Lokenath Debnath, Recent applications of fractional calculus to science and engineering, *International Journal of Mathematics and Mathematical Sciences* 2003 (2003).
- [17] Todd J. Freeborn, Brent Maundy, Ahmed S. Elwakil, Field programmable analogue array implementation of fractional step filters, *IET Circuits, Devices & Systems* 4 (6) (2010) 514–524.

- [18] Antonio Galves, Eva Löcherbach, Infinite systems of interacting chains with memory of variable length—a stochastic model for biological neural nets, *Journal of Statistical Physics* 151 (5) (2013) 896–921.
- [19] Tene Alain Giresse, Kofane Timoleon Crepin, Tchhoffo Martin, Generalized synchronization of the extended Hindmarsh–Rose neuronal model with fractional order derivative, *Chaos, Solitons and Fractals* 118 (2019) 311–319.
- [20] Shaghayegh Gomar, Arash Ahmadi, Digital multiplierless implementation of biological adaptive-exponential neuron model, *IEEE Transactions on Circuits and Systems I: Regular Papers* 61 (4) (2013) 1206–1219.
- [21] Emile Franc Doungmo Goufo, Melusi Khumalo, Patrick M. Tchepmo Djomegni, Perturbations of Hindmarsh–Rose neuron dynamics by fractional operators: bifurcation, firing and chaotic bursts, *Discrete and Continuous Dynamical Systems. Series S* 13 (3) (2020) 663.
- [22] Ricardo Enrique Gutierrez, Joao Mauricio Rosario, J.A. Machado, Fractional order calculus: basic concepts and engineering applications, *Mathematical Problems in Engineering* 2010 (2010) 1–19.
- [23] Saeed Haghiri, Ali Naderi, Behzad Ghanbari, Arash Ahmadi, High speed and low digital resources implementation of Hodgkin–Huxley neuronal model using base-2 functions, *IEEE Transactions on Circuits and Systems I: Regular Papers* (2020).
- [24] Mohsen Hayati, Moslem Nouri, Saeed Haghiri, Derek Abbott, A digital realization of astrocyte and neural glial interactions, *IEEE Transactions on Biomedical Circuits and Systems* 10 (2) (2015) 518–529.
- [25] Nicole Heymans, Dynamic measurements in long-memory materials: fractional calculus evaluation of approach to steady state, *Journal of Vibration and Control* 14 (9–10) (2008) 1587–1596.
- [26] Alan L. Hodgkin, Andrew F. Huxley, Bernard Katz, Measurement of current-voltage relations in the membrane of the giant axon of *Loligo*, *The Journal of Physiology* 116 (4) (1952) 424.
- [27] Allan L. Hodgkin, Andrew F. Huxley, Currents carried by sodium and potassium ions through the membrane of the giant axon of *Loligo*, *The Journal of Physiology* 116 (4) (1952) 449.
- [28] Allan L. Hodgkin, Andrew F. Huxley, The components of membrane conductance in the giant axon of *Loligo*, *The Journal of Physiology* 116 (4) (1952) 473.
- [29] Anderson Hoff, Juliana V. dos Santos, Cesar Manchein, Holokx A. Albuquerque, Numerical bifurcation analysis of two coupled FitzHugh–Nagumo oscillators, *The European Physical Journal B* 87 (7) (2014) 151.
- [30] Eugene M. Izhikevich, Richard FitzHugh, FitzHugh–Nagumo model, *Scholarpedia* 1 (9) (2006) 1349.
- [31] Dong Jun, Zhang Guang-jun, Xie Yong, Yao Hong, Wang Jue, Dynamic behavior analysis of fractional-order Hindmarsh–Rose neuronal model, *Cognitive Neurodynamics* 8 (2) (2014) 167–175.
- [32] Nasir Ali Kant, Mohammad Rafiq Dar, Farooq Ahmad Khanday, Costas Psychalinos, Ultra-low-voltage integrable electronic realization of integer- and fractional-order Liao’s chaotic delayed neuron model, *Circuits, Systems, and Signal Processing* 36 (12) (2017) 4844–4868.
- [33] C. Kasimis, C. Psychalinos, 0.65 V class-AB current-mode four-quadrant multiplier with reduced power dissipation, *AEÜ. International Journal of Electronics and Communications* 65 (7) (2011) 673–677.
- [34] Eva Kaslik, Analysis of two- and three-dimensional fractional-order Hindmarsh–Rose type neuronal models, *Fractional Calculus and Applied Analysis* 20 (3) (2017) 623–645.
- [35] Eva Kaslik, Seenith Sivasundaram, Nonlinear dynamics and chaos in fractional-order neural networks, *Neural Networks* 32 (2012) 245–256.

- [36] Farooq Ahmad Khanday, Nasir Ali Kant, Mohammad Rafiq Dar, Tun Zainal Azni Zulkifli, Costas Psychalinos, Low-voltage low-power integrable CMOS circuit implementation of integer- and fractional-order FitzHugh–Nagumo neuron model, *IEEE Transactions on Neural Networks and Learning Systems* 30 (7) (2018) 2108–2122.
- [37] Christof Koch, Idan Segev, et al., *Methods in Neuronal Modeling: From Ions to Networks*, MIT Press, 1998.
- [38] B.T. Krishna, K.V.V.S. Reddy, Active and passive realization of fractance device of order $1/2$, *Active and Passive Electronic Components* 2008 (2008) 369421.
- [39] Miguel F.M. Fima, J.A. Tenreiro Machado, Manuel Crisóstomo, Experimental signal analysis of robot impacts in a fractional calculus perspective, *Journal of Advanced Computational Intelligence and Intelligent Informatics* 11 (2007) 1079–1085.
- [40] Bernabe Linares-Barranco, Edgar Sánchez-Sinencio, Angel Rodríguez-Vázquez, José L. Huertas, A CMOS implementation of FitzHugh–Nagumo neuron model, *IEEE Journal of Solid-State Circuits* 26 (7) (1991) 956–965.
- [41] Yong Liu, Yong Xie, Yanmei Kang, Ning Tan, Jun Jiang, Jian-Xue Xu, Dynamical characteristics of the fractional-order FitzHugh–Nagumo model neuron, in: *Advances in Cognitive Neurodynamics (II)*, Springer, 2011, pp. 253–258.
- [42] Brian N. Lundstrom, Matthew H. Higgs, William J. Spain, Adrienne L. Fairhall, Fractional differentiation by neocortical pyramidal neurons, *Nature Neuroscience* 11 (11) (2008) 1335.
- [43] J.A.T. Machado, A probabilistic interpretation of the fractional-order differentiation, *Fractional Calculus and Applied Analysis* 1 (6) (2003) 73–80.
- [44] Richard L. Magin, Fractional calculus in bioengineering, part 3, *Critical Reviews in Biomedical Engineering* 32 (3&4) (2004).
- [45] Richard L. Magin, Fractional calculus models of complex dynamics in biological tissues, *Computers & Mathematics with Applications* 59 (5) (2010) 1586–1593.
- [46] R.L. Magin, M. Ovardia, Modeling the cardiac tissue electrode interface using fractional calculus, *Journal of Vibration and Control* 14 (9–10) (2008) 1431–1442.
- [47] S.A. Malik, A.H. Mir, Synchronization of Hindmarsh Rose neurons, *Neural Networks* 123 (2020) 372–380.
- [48] S.A. Malik, A.H. Mir, FPGA realization of fractional order neuron, *Applied Mathematical Modelling* 81 (2020) 372–385.
- [49] Argha Mondal, Sanjeev Kumar Sharma, Ranjit Kumar Upadhyay, Arnab Mondal, Firing activities of a fractional-order FitzHugh–Rinzel bursting neuron model and its coupled dynamics, *Scientific Reports* 9 (1) (2019) 1–11.
- [50] Catherine Morris, Harold Lecar, Voltage oscillations in the barnacle giant muscle fiber, *Biophysical Journal* 35 (1) (1981) 193–213.
- [51] J. Nagumo, A. Uchiyama, S. Kimoto, T. Watanuki, M. Hori, K. Suma, A. Ouchi, M. Kumano, H. Watanabe, Echo capsule for medical use (a batteryless endoradiosonde), *IRE Transactions on Bio-Medical Electronics* 9 (3) (1962) 195–199.
- [52] Moslem Nouri, Gh.R. Karimi, Arash Ahmadi, Derek Abbott, Digital multiplierless implementation of the biological FitzHugh–Nagumo model, *Neurocomputing* 165 (2015) 468–476.
- [53] Rutuparna Panda, Madhumita Dash, Fractional generalized splines and signal processing, *Signal Processing* 86 (9) (2006) 2340–2350.
- [54] Ivo Petráš, *Fractional-Order Nonlinear Systems: Modeling, Analysis and Simulation*, Springer Science & Business Media, 2011.
- [55] A. Petrovas, S. Lissauskas, A. Slepikas, Electronic model of FitzHugh–Nagumo neuron, *Elektronika Ir Elektrotechnika* 122 (6) (2012) 117–120.
- [56] Yifei Pu, Xiao Yuan, Ke Liao, Jiliu Zhou, Ni Zhang, Xiaoxian Pu, Yi Zeng, A recursive two-circuits series analog fractance circuit for any order fractional calculus, in: *ICO20: Optical Information Processing*, vol. 6027, International Society for Optics and Photonics, 2006, p. 60271Y.

- [57] Mohammad Rafiq Dar, Nasir Ali Kant, Farooq Ahmad Khanday, Electronic implementation of fractional-order Newton–Leipnik chaotic system with application to communication, *Journal of Computational and Nonlinear Dynamics* 12 (5) (2017).
- [58] J.M. Rosario, Didier Dumur, J.A. Tenreiro Machado, Analysis of fractional-order robot axis dynamics, *IFAC Proceedings Volumes* 39 (11) (2006) 367–372.
- [59] William M. Siebert, Some implications of the stochastic behavior of primary auditory neurons, *Kybernetik* 2 (5) (1965) 206–215.
- [60] Laurent Sommacal, Pierre Melchior, Alain Oustaloup, J.-M. Cabelguen, Auke Jan Ijspeert, Fractional multi-models of the frog gastrocnemius muscle, *Journal of Vibration and Control* 14 (9–10) (2008) 1415–1430.
- [61] Elena Tamaševičiūtė, Gytis Mykolaitis, Analogue modelling an array of the FitzHugh–Nagumo oscillators, *Nonlinear Analysis: Modelling and Control* 17 (1) (2012) 118–125.
- [62] Wondimu Teka, Toma M. Marinov, Fidel Santamaria, Neuronal spike timing adaptation described with a fractional leaky integrate-and-fire model, *PLoS Computational Biology* 10 (3) (2014) e1003526.
- [63] Georgia Tsirimokou, Costas Psychalinos, Ultra-low voltage fractional-order differentiator and integrator topologies: an application for handling noisy ECGs, *Analog Integrated Circuits and Signal Processing* 81 (2) (2014) 393–405.
- [64] Yong Xie, YanMei Kang, Yong Liu, Ying Wu, Firing properties and synchronization rate in fractional-order Hindmarsh–Rose model neurons, *Science China. Technological Sciences* 57 (5) (2014) 914–922.
- [65] Xujun Yang, Qiankun Song, Yurong Liu, Zhenjiang Zhao, Uniform stability analysis of fractional-order BAM neural networks with delays in the leakage terms, *Abstract and Applied Analysis* 2014 (2014), Hindawi.
- [66] Zhu-Zhong Yang, Ji-Liu Zhou, An improved design for the IIR-type digital fractional-order differential filter, in: 2008 International Seminar on Future BioMedical Information Engineering, IEEE, 2008, pp. 473–476.
- [67] Mehmet Yavuz, Asif Yokus, Analytical and numerical approaches to nerve impulse model of fractional-order, *Numerical Methods for Partial Differential Equations* 36 (6) (2020) 1348–1368.
- [68] Abdulhamid Zahedi, Saeed Haghiri, Mohsen Hayati, Multiplierless digital implementation of time-varying FitzHugh–Nagumo model, *IEEE Transactions on Circuits and Systems I: Regular Papers* 66 (7) (2019) 2662–2670.
- [69] Qing-Shan Zeng, Guang-Yi Cao, Xin-Jian Zhu, The effect of the fractional-order controller's orders variation on the fractional-order control systems, in: *Proceedings. International Conference on Machine Learning and Cybernetics*, vol. 1, IEEE, 2002, pp. 367–372.
- [70] Jun Zhao, Yong-Bin Kim, Circuit implementation of FitzHugh–Nagumo neuron model using field programmable analog arrays, in: 2007 50th Midwest Symposium on Circuits and Systems, IEEE, 2007, pp. 772–775.
- [71] Qianqian Zheng, Jianwei Shen, Turing instability induced by random network in FitzHugh–Nagumo model, *Applied Mathematics and Computation* 381 (2020) 125304.
- [72] Shangbo Zhou, Hua Li, Zhengzhou Zhu, Chaos control and synchronization in a fractional neuron network system, *Chaos, Solitons and Fractals* 36 (4) (2008) 973–984.

Index

A

- Abnormal firing rate, 442
- Accumulative electric elements, 355, 359, 364
- Acoustic
 - admittance concept, 414
 - impedance, 404–406, 410, 411, 425
 - tube, 404, 405, 407, 410, 412, 414, 417, 425
 - tube radius, 407
- Action potentials, 429, 430, 435–437, 439, 441, 442
- Adaptive
 - control, 216
 - controller, 153, 154
 - controller structure, 153
 - feedback control, 216
 - sliding mode controller design, 244
- ADRC framework control, 155
- Analog-to-digital converter (ADC), 493
- Antiresonances, 412, 421, 423–425
- Aperiodic impulse response, 378, 379
- Artificial intelligence (AI), 475
- Artificial neural network (ANN), 475, 476, 481
- Associative memory, 214, 215
- Atangana derivative, 217
- Attitude
 - controllers, 155
 - subsystem, 153–155, 164
- Audible
 - frequency, 407, 412, 418, 425
 - frequency range, 423

B

- Behavior
 - derivative, 412, 419, 421, 423
 - fractional, 403, 412
 - fractional derivative, 419
 - solution, 112, 280
- Behavioral algebraics, 486

- Bipolar junction transistor (BJT), 476, 481
- Black–Scholes
 - equation, 11
 - model, 11
- Bode diagram, 412, 413, 417, 418, 420–424
- Branching point (BP), 377, 378, 381, 384, 385

C

- Capacitor
 - charge, 355
 - current, 355
 - fractional, 215, 312, 313, 358, 360, 363–366
 - voltage, 355
- Caputo (C)
 - approach, 2, 14
 - definition, 98, 156, 431
 - derivative, 15, 23, 25, 52, 64, 97, 98, 125, 127, 133, 135–137, 139–141, 144, 218, 431, 432, 459
 - discrete form, 107
 - fractional, 121, 125, 218
 - fractional derivative, 15, 20, 33, 43, 71, 73, 80, 83, 97, 106, 121–124, 126, 129, 216–218, 221, 435
 - operator, 111, 156
 - operator derivative, 98
 - type, 120, 124, 127
 - type derivatives, 127
 - type fractional derivatives, 123
- Chaotic
 - behavior, 97
 - models, 110
 - models hybrid fractional, 99
- Chebyshev type
 - methods, 133, 135–137, 139, 141, 144
 - methods fractional, 144
 - point-to-point schemes, 120
- Circuit
 - models, 465
 - models for wood tissue, 463

- simulation, 486
 - topology relative, 312
 - Classical vector control (CVC), 180, 182, 201, 203–207
 - scheme, 180, 204, 205, 207
 - structure, 203, 207
 - Cohen–Grossberg neural network (CGNN), 214, 215, 239
 - Cohen–Grossberg neural network (CGNN) discontinuous, 215
 - Colliding bodies optimization (CBO), 295, 298
 - Complementary metal oxide semiconductor (CMOS), 476, 477, 486
 - Concept
 - fractional calculus, 41, 42
 - fuzzy, 40–42, 63, 65
 - Configurable analog module (CAM), 493
 - blocks, 493
 - filter biquad, 493, 495
 - Conformal
 - fractional energy, 284
 - mapping, 273, 281, 284, 289
 - Conformal antenna (CA), 271–273, 283
 - Conformal map (CM), 271
 - Conformal mapping, 277
 - Conformal thermal antenna (CTA), 272, 273, 289
 - cylindrical, 282
 - optimization, 273, 281
 - quasicylindrical, 284
 - system, 272
 - Constant phase element (CPE), 294, 296, 460, 462
 - Constant proportional Caputo (CPC) operator, 98, 99, 106
 - Constitutive models, 358, 360, 364
 - Continued fraction expansion (CFE), 298, 313
 - Continued fraction expansion (CFE) approximant biquadratic, 298
 - Continuous symmetry, 11, 13, 21, 22, 25, 28, 30
 - analysis applications, 7
 - for fractional differential equation, 14
 - for fractional ODE, 16
 - for fractional PDE, 22
 - groups, 7, 9, 11
 - method, 3
 - Control
 - action, 153
 - adaptive, 216
 - approach, 180
 - architectures, 152
 - DFIG, 188–190
 - FOPI, 181, 190
 - gains, 234, 237, 240
 - IFOSMC, 165
 - input, 168, 223, 240
 - input command, 153
 - laws, 161, 163, 165–168, 174
 - loops, 190
 - method, 189
 - objectives, 249, 264
 - optimal, 215
 - pathological neuronal oscillations, 430
 - performance, 203, 205
 - problems, 155
 - scheme, 153, 154, 180–182, 187, 189, 201, 208
 - signals, 190, 192
 - strategy, 152, 209, 234–236, 238
 - structures, 187, 202, 203, 205, 208
 - system, 40, 174, 180, 196, 249, 253, 254, 264, 265, 404
 - technique sliding, 234
 - techniques, 181, 216
 - theory, 215
 - Controller
 - adaptive, 153, 154
 - parameters, 155, 169, 265, 443
 - rotor current, 194
 - structure, 152
 - Critically aperiodic impulse response, 378, 379
 - Cuckoo search algorithm (CSA), 295, 297
- D**
- Deep brain stimulation (DBS), 442, 443, 449, 450
 - Deep learning (DL), 475

Derivative

- behavior, 412, 419, 421, 423
- Caputo, 15, 23, 25, 52, 64, 97, 98, 125, 127, 133, 135–137, 139–141, 144, 218, 431, 432, 459
- term, 448

Differential equation (DE), 40

Differential evolution (DE) algorithm, 298

Discontinuous

- CGNNs, 215
- FCGNNs, 216

Discrete symmetry method, 7

Disease control strategies, 39

Disturbance

- rejection, 152, 154, 181
- rejection control scheme, 155
- voltage, 206, 210

Doubly fed induction generator (DFIG),

- 179, 180, 182, 184, 185, 190, 205, 206, 208

control, 188–190

control scheme, 187

control strategy, 201

generator, 209

parameter variations, 187, 206

power control system, 197

power regulation loops, 197, 200

rotor shaft, 203

wind turbine, 180, 182, 202, 203

WPS, 180, 203, 206

Dynamic surface control (DSC), 154, 155

Dynamics

- change, 493
- fractional, 433, 450
- nonlinear, 210

E

Electrochemical double layer capacitor (EDLC), 358

Electromagnetic frequency array, 271

Equivalent impedance, 464, 465

Existence solution, 217, 226

Exponential stability, 446

Exponential stability concept, 446

Extended state observer (ESO), 153–155

F

FCGNN, 215, 216

FCGNN discontinuous, 216

Field programmable analog array (FPAA), 476, 493, 495, 500

boards, 476, 477

implementation, 493

Field-programmable gate array (FPGA), 476, 495

boards, 477, 499

implementation, 495, 497, 500

Filippov solution, 222

existence, 226, 244

fractional differential system, 222

Finite time

settling time, 240

sliding mode control law, 217

sliding model control, 226, 240

sliding model control strategy, 236, 240

stability criteria, 230

stability theory, 217

synchronization criteria, 216, 238, 239

Firing rate, 429, 435, 436, 443, 447, 489

abnormal, 442

action potential, 430

constant, 441

instantaneous, 439

stable, 439, 447

target, 444, 447

FitzHugh–Nagumo (FHN)

model, 476

neuron, 496

neuron model, 476

Flower pollination algorithm (FPA), 295, 296, 299, 301

Fractional

approach, 359

behavior, 403, 412

calculus, 2, 14, 33, 41, 65, 69, 70, 75, 97, 98, 119, 127, 181, 188, 210, 214,

249, 293, 357, 403, 431, 458, 459

concept, 41, 42

in control system design, 181

capacitor, 215, 312, 313, 358, 360, 363–366

Caputo, 121, 125, 218

- Chebyshev type methods, 144
- controllers, 174, 181, 442
- CPC derivatives, 99
- derivation, 404
- derivative, 2, 14, 18, 24, 41, 63, 69–74,
 - 76, 82, 83, 92, 93, 97, 116, 119,
 - 120, 122–125, 127, 129, 217, 324,
 - 326, 359, 368, 369, 411, 432, 433,
 - 435, 441, 443, 446, 458, 496
- behavior, 419
- inverse Laplace transform, 372
- Laplace transform, 372
- mass conservation equation, 87
- models, 69
- differential
 - Filippov solution, 222
 - operator applications, 326
- differentiation, 65, 358, 362, 378, 379,
 - 393, 450
- differentiation matrices, 325
- dimensionless transformations, 79
- dynamics, 433, 450
- electric elements, 359
- FIL neurons, 437
- form fuzzy, 61
- generalization, 359
- Harry Dym equation, 2, 30, 32, 33
- inductor, 357, 358, 363, 365, 371
- integral, 2, 42, 70, 122, 233, 252, 286,
 - 368, 369, 432, 435, 443, 446
- integral sliding mode, 217, 226
- integration behavior, 417, 418, 421, 424
- integrative behavior, 421, 423, 425
- integrator, 425
- Kolmogorov equation, 2
- Laplacian operator, 326
- LIFs, 439, 441
- Lyapunov stability, 217
- mass conservation equation, 70, 75, 91
- mass equation, 85, 90
- methods, 124, 127
- modeling, 69, 75
- models, 70, 81, 91, 93, 97, 360, 425
- momentum, 89
- Navier–Stokes equation, 75
- Newton type methods, 144
- operator, 78, 106, 326, 440
- operator calculus, 98
- PID, 403
- power series, 70, 79, 84
- relaxation, 365
- Riccati equation, 21
- Riesz space, 333
- RL derivative, 431
- RL integral definition, 431
- Schrödinger equations, 346
- sliding mode, 403
- Taylor development, 120
- Taylor series, 70, 73, 85
- TEs, 359–369, 371–374, 376, 378, 382,
 - 383, 385, 393
- time, 75, 359, 363, 365, 373
- time derivative, 359
- TL models, 357
- transformation, 69
- Traub type methods, 129
- Traub type schemes, 144
- Fractional differential equation (FDE), 2,
 - 14, 33, 75, 79, 97, 106, 213, 214,
 - 442
- Fractional ODE (FODE), 16, 20, 22, 33
- Fractional order (FO), 41, 53, 55, 57, 120,
 - 161, 181, 188, 214, 219, 222, 238,
 - 339, 404, 425, 431, 432, 441, 447,
 - 449, 460, 476, 478
- chaotic system, 103
- derivative, 476, 477
- derivatives, 39, 56, 97, 119
- differential, 55, 57, 74
- Fractional PDE (FPDE), 22, 33
- Fractional Schrödinger equation (FSE),
 - 324, 325
- Fractional variable-order fractional
 - proportional integral derivative
 - (FVOPID), 249, 264
- Fractional vector control (FVC), 182, 201,
 - 203–205
- schemes, 204
- structures, 207
- Fractional wood model (FWM), 463, 464,
 - 466
- Fractional-chaotic FPA (FC-FPA), 301

Fractional-order Butterworth filter
 (FOBF), 296–299, 301
 approximants, 308
 model, 301
 modeling, 299

Fractional-order calculus (FOC), 475

Fractional-order CGMNN (FCGMNN),
 215

Fractional-order differential equation
 (FODE), 40, 475

Fractional-order differentiator (FOD), 295

Fractional-order discontinuous
 Cohen–Grossberg type memristive
 neural network (FDCGMNN),
 217, 221, 226, 236, 239
 dynamics, 244
 solution, 227

Fractional-order fast terminal SMC
 (FOFTSMC), 152, 169

Fractional-order FitzHugh–Nagumo
 (FO-FHN)
 model, 477
 neuron model, 476–479

Fractional-order FPA (FO-FPA), 301

Fractional-order integrator (FOI), 295

Fractional-order lossless integrator
 (FOLLI), 484, 485, 487
 block, 488
 responses, 485, 487

Fractional-order memristor-based neural
 network (FOMBNN), 215

Fractional-order neural network (FO-NN),
 476, 500, 501

Fractional-order PI (FOPI), 181
 control, 181, 190
 controller, 181, 182, 187, 190–192, 194,
 196, 197, 200, 209
 controller design, 181

Fractional-order sliding mode controller
 (FOSMC), 152, 160

Fractional-order sliding mode controller
 (FOSMC) time derivative, 163

Fractional-order transfer function (FOTF)
 approximants, 297
 approximation, 298
 model, 297, 298, 300, 308, 311, 312

Frequency
 analysis, 415, 425
 audible range, 417
 axis, 418
 characteristics, 360, 363, 382, 386, 388,
 389, 393
 dependence, 386
 domain, 294, 405, 407, 425
 range, 189, 299, 412, 421
 response, 196, 201, 265, 411, 412, 416,
 417, 420, 423

Function evaluation (FE), 302

Function neuronal, 430, 451

Fuzzy

concept, 40–42, 63, 65
 form, 40, 42
 fractional differential equations, 40
 fractional form, 61
 integral equations, 41
 Laplace transform, 42
 solutions, 63

G

Gain margin (GM), 196

Gamma function, 70, 73, 121, 132, 133,
 156, 188, 218, 302, 431, 432, 434

Gegenbauer polynomials, 327–329

Genetic algorithm (GA), 295–298

Global Wind Energy Council (GWEC),
 179

Globus pallidus (GP), 443, 444, 447

Gravitational search algorithm (GSA), 295,
 298

Grunwald–Letnikov (GL)

definition, 431, 432
 derivative, 431
 numerical algorithm, 444

H

Hadamard derivative, 217

Harmonic

response, 382, 384, 385, 397–399
 voltage forcing, 382, 383
 voltage response, 384

Harry Dym equation, 13, 14

Harry Dym equation fractional, 2, 30, 32,
 33

Healthy population, 53, 55, 56, 61, 65
 Healthy population density, 57
 Hierarchical control technique, 155
 History dependence, 429, 430, 435, 437, 439, 440
 Hybrid controller, 154
 Hybrid fractional, 103
 Bloch model, 103
 chaotic models, 99
 hyperchaotic finance, 100
 models, 106
 order, 110

I

IFOSMC, 169, 172, 174
 control, 165
 design structure for UAV systems, 165
 methods, 169
 outperforms, 174
 structure for attitude subsystem, 167
 Imaginary parts, 345, 375, 384, 386, 388, 390–392, 395, 398
 Impedance
 acoustic, 404–406, 410, 411, 425
 analyzer, 462, 465
 appearances, 272
 characteristics, 294, 313
 converter, 296
 Nyquist plots, 466
 series, 370
 Impulse response, 362, 373, 376–379, 383, 384, 394, 395
 aperiodic, 378, 379
 infinite, 295
 Impulsive control, 216
 Inductor
 fractional, 357, 358, 363, 365, 371
 voltage, 355
 Infinite impulse response (IIR), 295
 Instability characteristics, 214
 Integer-order transfer function (IOTF), 295, 298
 Integral
 equations, 2, 46
 fractional, 2, 42, 70, 122, 233, 252, 286, 368, 369, 432, 435, 443, 446
 gains, 181, 191, 200

Laplace transform, 250
 MPC, 153
 operator, 2, 362
 predictive controller, 154
 Integral backstepping (IB), 154
 Integrated circuit (IC), 489, 491
 Interior search algorithm (ISA), 296, 297
 Intrinsic memory trace, 429, 432
 Invariant solutions, 7, 25
 Inverse Laplace transform, 53, 60, 231, 362, 383, 394, 398
 Inverse Laplace transform fractional derivative, 372

L

Laplace domain, 192, 220, 250, 408
 Laplace transform, 43, 44, 52, 58, 65, 220, 231, 253–256, 259, 372, 374, 376, 378, 381, 397
 fractional derivative, 372
 fuzzy, 42
 integral, 250
 inverse, 53, 60, 231, 362, 383, 394, 398
 inversion, 360, 372
 physical quantities, 369
 system error, 258
 Leaky integrate-and-fire (LIF) model, 435, 436, 440
 Local field potential (LFP) signal, 444
 Lyapunov stability
 analysis, 450
 fractional, 217
 theory, 216

M

Machine learning (ML), 475
 Mass conservation equation, 72, 74, 88
 fractional, 70, 75, 91
 fractional derivative, 87
 Mathematical
 model, 38, 39, 326, 476
 neuron model, 477
 Maximum
 power, 182, 184, 190, 202, 204
 robustness, 449

- Maximum power point tracking (MPPT),
 - 180, 190, 203, 207, 301
 - control law, 186, 204
 - control scheme, 186, 187
 - law, 185, 202
 - scheme, 182, 186
 - Membrane
 - conductances, 429, 430, 449
 - voltage, 430, 435, 436, 449
 - Memory
 - part, 496
 - space, 70, 82, 91
 - trace, 429, 434, 448, 459
 - Memristive connection weights, 221, 223, 238
 - Model predictive control (MPC), 154
 - integral, 153
 - regular, 153
 - theory, 153
 - Models
 - circuit, 465
 - fractional, 70, 81, 91, 93, 97, 360, 425
 - fractional derivative, 69
 - hybrid fractional, 106
 - neuron, 475–477, 489, 500
 - neuronal, 442
 - nonlinear, 85
 - Modified Rodrigues parameter (MRP), 155
 - Moth flame optimization (MFO), 296, 298
 - Multipoint Traub type procedures, 120
- N**
- Network
 - dynamics, 449
 - voltage faults, 202
 - Neuronal
 - activity, 430, 442, 450
 - function, 430, 451
 - models, 442, 450
 - networks, 442
 - organization, 429
 - phenomena, 450
 - systems, 435
 - Neurons
 - models, 475–477, 489, 500
 - responses, 429, 430
 - Newton type methods, 125, 133, 135–137, 139, 141
 - Newton type methods fractional, 144
 - Nominal backstepping controller (NBC), 152
 - Nonlinear
 - controller, 154
 - dynamics, 210
 - fractional Riesz space, 330
 - models, 85
 - resilient control scheme, 153
 - space FSEs, 326
 - Nonstandard finite difference method (NSFDM), 98, 106, 111, 114
 - Numerical
 - simulations, 109, 156, 169, 172, 201, 259–261, 265
 - solution, 325, 345, 431–434, 436
- O**
- Operational amplifier (Op-Amp), 476
 - Operational transconductor amplifier (OTA), 476
 - Optimal
 - control, 215
 - solution, 279
 - TSR, 184, 186, 187
 - OrCAD PSpice, 300, 312, 315
 - Ordinary differential equation (ODE), 1, 33
 - Oscillatory behavior, 435, 443, 447
- P**
- Parallel topology, 361, 367, 368, 374, 375, 378, 387, 388, 394
 - Parallel topology models, 393
 - Parametric disturbances, 205
 - Parkinson's disease (PD), 442–444, 447, 448, 450
 - Partial differential equation (PDE), 1, 2, 33, 41
 - Particle swarm optimization (PSO), 295–297
 - Particle swarm optimization (PSO) algorithms, 298
 - Pathological neuronal oscillations, 447
 - Pathological neuronal oscillations control, 430

- Phase
 - response, 294
 - response simulation results, 487
 - Phase margin (PM), 192, 194, 196, 198, 201, 263
 - Phloem, 457, 462
 - cells, 457, 463
 - vessels, 463
 - Pinning
 - control, 216
 - feedback control, 216
 - Population dynamics model, 39
 - Power
 - control loops, 204
 - flow control, 180
 - Propagation constant (PC), 370, 371
 - Proportional integral derivative (PID)
 - controller, 154, 181, 430, 435, 443, 444, 447–450
 - Proportional integral (PI), 180
 - Proportional integral (PI) controllers, 180, 182, 187, 192
- Q**
- Quadcopter system, 152, 154, 157
- R**
- Reactive power, 185, 190, 201, 204, 206, 207
 - Reactive power control, 179
 - Regulation loops, 181, 187, 188, 190, 205
 - Reset membrane voltage, 435
 - Resistive and capacitive (RC) cells, 403
 - Response
 - frequency, 196, 201, 265, 411, 412, 416, 417, 420, 423
 - phase, 294
 - voltage, 376–378, 380, 382, 383
 - Riemann–Liouville (RL)
 - approach, 14
 - definition, 156, 431
 - derivative, 15, 431
 - fractional derivative, 15, 121, 431
 - fractional integral, 14
 - fractional time derivative, 97
 - integral, 15, 431
 - type, 124
 - Riesz
 - fractional derivative, 325–327
 - fractional operator, 347
 - space FSE, 324, 325, 327, 330, 333, 338, 339, 346
 - Robustness
 - condition, 199
 - evaluation, 205, 206
 - performance, 205
 - Rotational subsystem controller, 163
 - Rotor
 - circuit voltages, 185
 - current, 196, 204
 - control loop, 194
 - controller, 194
 - regulation loop, 182, 192, 194, 209
 - regulator, 192, 197
 - system, 196
 - voltages, 189
 - Runge–Kutta/Gegenbauer spectral collocation scheme, 325, 337
- S**
- Semianalytical solution, 52, 58
 - Series
 - branch, 355, 356, 361, 365, 366
 - branch capacitor, 393
 - branch resistor, 363
 - coefficients, 80
 - impedance, 370
 - solution, 52, 53, 58, 61, 65, 328
 - topology, 360, 361, 363–367, 369, 371–374, 376, 383, 385, 386, 388, 389, 391, 392
 - topology models, 393
 - Severe acute respiratory syndrome
 - coronavirus 2 (SARS-CoV-2), 38
 - Shunt branch, 355, 356, 362–364, 366, 369, 375, 376
 - Shunt branch admittance, 370
 - Sigmoid tracking differentiator (STD), 155
 - Simulated annealing (SA), 296, 297
 - Simulation
 - circuit, 486
 - purposes, 202
 - results, 169, 182, 265, 485
 - studies, 188

- Sliding
 - control technique, 234
 - mode, 155, 163, 180, 216, 230, 233, 234, 240, 244
 - mode control, 216, 217, 238
 - problem, 216
 - scheme, 216
 - strategies control, 216
 - technique, 238
 - theory, 238, 244
 - surface, 161, 167, 176, 216, 230, 234–236, 238
 - surface derivatives, 167
 - Solution
 - behavior, 112
 - existence, 217, 226
 - existence theory, 40
 - optimal, 279
 - series, 52, 53, 58, 61, 65, 328
 - Space
 - FSEs, 324, 325
 - generalized fractional, 92
 - memory, 70, 82, 91
 - Spatial-fractional mass conservation equation, 72
 - Stability
 - analysis, 98, 115, 155, 163, 308, 450
 - condition, 103
 - margin, 299, 308, 317
 - Stable
 - firing rate, 439, 447
 - method, 109
 - state, 448
 - State feedback control, 216
 - Stator
 - circuit voltages, 185
 - real, 204, 206
 - voltages, 189
 - Step response, 264, 380, 381, 385, 461
 - Subthalamic nucleus (STN), 443, 444, 447
 - Supercapacitors, 358
 - Swarm intelligence (SI)
 - algorithms, 296
 - techniques, 295
 - Symbiotic organisms search (SOS), 295, 297, 298
 - Synapse resistors, 215
 - Synchronization criteria, 216, 238
 - finite time, 216, 238, 239
 - for memristive FCGNNs, 217
 - sliding mode control problem, 216
 - Synchronization error
 - dynamic, 225, 230, 237
 - norms, 240
 - system, 235, 236, 238
 - trajectories, 240
- ## T
- Taylor series, 73
 - Taylor series fractional, 70, 73, 85
 - Telegrapher's equation (TE), 356, 357, 359
 - Thermal
 - optimization approach, 276
 - simulation, 272
 - Topology series, 360, 361, 363–367, 369, 371–374, 376, 383, 385, 386, 388, 389, 391, 392
 - Total error (TE), 304
 - index, 308
 - metric, 308–310
 - plots, 308
 - responses, 304
 - values, 304
 - Trajectory tracking, 152, 153, 155, 169, 171, 172
 - controller, 154
 - performance, 152, 165
 - Transfer function (TF), 376, 377, 384, 385
 - modulus, 384, 386, 388, 391, 392
 - modulus behavior, 386
 - modulus frequency characteristics, 393
 - Transitional frequencies, 410–412, 417, 419, 420, 423–425
 - Translational
 - subsystem control signals, 161
 - subsystem controller, 160
 - Transmission line (TL), 355–357, 360
 - hereditary, 363, 366, 373, 379, 382, 386
 - model, 356
 - models, 364, 366
 - models fractional, 357

Traub type methods, 133, 135, 136, 139,
141, 143, 144
Traub type methods fractional, 129
Triple Cole impedance model, 462
Truncated series, 330
Truncated series representation, 328

U

Ultracapacitors, 358
Unmanned aerial vehicle (UAV), 151, 153,
155
Unmanned aerial vehicle (UAV) system,
155, 159, 165

V

Variable-order
circuit, 263
derivative, 251
derivative operators, 250
function, 250
integrator, 250, 254
operators, 250, 251
system, 251, 256, 257, 259, 260, 266
Vector control, 180, 189
fractional, 182
technology, 189
Viscoelastic behavior, 2

Voltage

change, 207
disturbances, 206, 210
drop, 206–208, 355, 366, 367
drop disturbance rejection, 207
faults, 180, 210
forcing, 377, 380, 386
oscillations, 382
partial derivative, 357
response, 376–378, 380, 382, 383
signal, 458
threshold, 435

W

Whale optimization (WO), 295, 296
Wind power system (WPS), 179, 181, 182,
184–186, 206, 210
Wood tissue, 461–465, 468
Woody
cell structure, 462
materials, 462
plants, 461, 462, 465, 469
stem, 465
transportation, 463

X

Xylem, 457, 462
cells, 457, 463
vessels, 462

Series Editor: Quan Min Zhu

Fractional-Order Modeling of Dynamic Systems with Applications in Optimization, Signal Processing, and Control

Edited by

Ahmed G. Radwan, Farooq Ahmad Khanday, and Lobna A. Said

Fractional-Order Modeling of Dynamic Systems with Applications in Optimization, Signal Processing, and Control aims to provide an overview of recent advances in the fractional-order modeling of different physical, biological, and chemical systems.

Fractional-order systems play an essential role in our day-to-day activities. Therefore, several researchers around the globe endeavor to work in the different domains of fractional-order systems. The efforts include developing the mathematics to solve fractional-order calculus/systems and to achieve feasible designs for various applications of fractional-order systems. These applications vary from biomedical engineering to control systems, robotics, bio-impedance modeling, chaotic systems, signal processing, and more.

Fractional-order models of a system give better predictions compared with their integer-order counterparts. This book discusses the fractional-order modeling of systems ranging from the COVID-19 pandemic to fluid flow, chaotic systems, controllers, neural networks, antennas, acoustic tubes, plant tissues, and more. Thus, the book gives details of fractional-order modeling to readers in a comprehensive manner, which they can then use to design efficient fractional-order systems.

Ahmed G. Radwan (SM-IEEE, Fellow AAS) is the Vice President for Research at Nile University and Professor at the Faculty of Engineering, Cairo University, Egypt. He is a former director of the Technical Center for Career Development (TCCD), Cairo University and the former director of the Nanoelectronics Integrated Systems Center (NISC), Nile University. He is among the top authors worldwide for two research tracks (T.21555 & T.8806) based on the SciVal database. His research interests include interdisciplinary concepts between mathematics and engineering applications such as fractional-order systems, bifurcation, chaos, memristors, and encryption.

Farooq A. Khanday is a full-time Senior Assistant Professor at the Department of Electronics and Instrumentation Technology, University of Kashmir, J&K, India. He has more than 100 publications in peer-reviewed indexed international and national journals/conference proceedings. His research interests include fractional-order circuits, nano-electronics, hardware neural network design, and stochastic computing

Lobna A. Said is a full-time Associate Professor at the Faculty of Engineering and Applied Science and the NISC, Nile University. She has over 115 publications distributed between high-impact journals, conference proceedings, and book chapters. In 2019, she was selected as a member of the Egyptian Young Academy of Sciences (EYAS), and in 2020 she was elected as EYAS Co-Chair, as an affiliate member of the African Academy of Science (AAS), and as a Member of the Arab-German Young Academy of Sciences and Humanities (AGYA).



ACADEMIC PRESS

An imprint of Elsevier

elsevier.com/books-and-journals

ISBN 978-0-323-90089-8



9 780323 900898